

Introduction to the Numerical Modeling of Groundwater and Geothermal Systems

Fundamentals of Mass, Energy and Solute Transport in Poroelastic Rocks

J. Bundschuh and M.C. Suárez Arriaga

INTRODUCTION TO THE NUMERICAL MODELING
OF GROUNDWATER AND GEOTHERMAL SYSTEMS

THE COVER

The main figure represents a conductive-convective geothermal system with fluid, heat and solute transport through pores and fractures. The simplified geological model corresponds to the Los Azufres, Mexico geothermal field.

The equations (from top to bottom) are mathematical models of:

- 1) The groundwater flow equation in terms of pressure, density and permeability (eq. 4.16).
- 2) The Terzaghi effective stresses and the pore-fluid pressure (eq. 2.69b).
- 3) The poroelastic strains, the stresses and the inverse matrix of poroelastic coefficients (eq. 2.77b).
- 4) The pore-fluid pressure in terms of mechanical and thermal stresses (eq. 2.120).
- 5) The general solute transport equation with dispersion and advection (eq. 4.111).
- 6) The Fourier's law of heat conduction (eq. 4.79).
- 7) The general heat flow equation with conduction and convection (eq. 4.104a).

Multiphysics Modeling

Series Editors

Jochen Bundschuh

*University of Applied Sciences, Institute of Applied Research,
Karlsruhe, Germany*

Royal Institute of Technology (KTH), Stockholm, Sweden

Mario César Suárez Arriaga

*Department of Applied Mathematics and Earth Sciences,
Faculty of Physics and Mathematical Sciences, Michoacán University UMSNH,
Morelia, Michoacán, Mexico*

ISSN: 1877-0274

Volume 2

Introduction to the Numerical Modeling of Groundwater and Geothermal Systems

Fundamentals of Mass, Energy and Solute Transport in Poroelastic Rocks

Jochen Bundschuh

*University of Applied Sciences, Institute of Applied Research,
Karlsruhe, Germany
Royal Institute of Technology (KTH), Stockholm, Sweden*

Mario César Suárez Arriaga

*Department of Applied Mathematics and Earth Sciences,
Faculty of Physics and Mathematical Sciences,
Michoacán University UMSNH, Morelia, Michoacán, Mexico*



CRC Press

Taylor & Francis Group

Boca Raton London New York Leiden

CRC Press is an imprint of the
Taylor & Francis Group, an **informa** business

A BALKEMA BOOK

CRC Press
Taylor & Francis Group
6000 Broken Sound Parkway NW, Suite 300
Boca Raton, FL 33487-2742

© 2010 by Taylor & Francis Group, LLC
CRC Press is an imprint of Taylor & Francis Group, an Informa business

No claim to original U.S. Government works
Version Date: 20140602

International Standard Book Number-13: 978-0-203-84810-4 (eBook - PDF)

This book contains information obtained from authentic and highly regarded sources. Reasonable efforts have been made to publish reliable data and information, but the author and publisher cannot assume responsibility for the validity of all materials or the consequences of their use. The authors and publishers have attempted to trace the copyright holders of all material reproduced in this publication and apologize to copyright holders if permission to publish in this form has not been obtained. If any copyright material has not been acknowledged please write and let us know so we may rectify in any future reprint.

Except as permitted under U.S. Copyright Law, no part of this book may be reprinted, reproduced, transmitted, or utilized in any form by any electronic, mechanical, or other means, now known or hereafter invented, including photocopying, microfilming, and recording, or in any information storage or retrieval system, without written permission from the publishers.

For permission to photocopy or use material electronically from this work, please access www.copyright.com (<http://www.copyright.com/>) or contact the Copyright Clearance Center, Inc. (CCC), 222 Rosewood Drive, Danvers, MA 01923, 978-750-8400. CCC is a not-for-profit organization that provides licenses and registration for a variety of users. For organizations that have been granted a photocopy license by the CCC, a separate system of payment has been arranged.

Trademark Notice: Product or corporate names may be trademarks or registered trademarks, and are used only for identification and explanation without intent to infringe.

Visit the Taylor & Francis Web site at
<http://www.taylorandfrancis.com>

and the CRC Press Web site at
<http://www.crcpress.com>

About the book series

Numerical modeling is the process of obtaining approximate solutions to problems of scientific and/or engineering interest. The book series addresses novel mathematical and numerical techniques with an interdisciplinary emphasis that cuts across all fields of science, engineering and technology. It focuses on breakthrough research in a richly varied range of applications in physical, chemical, biological, geoscientific, medical and other fields in response to the explosively growing interest in numerical modeling in general and its expansion to ever more sophisticated physics. The goal of this series is to bridge the knowledge gap among engineers, scientists, and software developers trained in a variety of disciplines and to improve knowledge transfer among these groups involved in research, development and/or education.

This book series offers a unique collection of worked problems in different fields of engineering and applied mathematics and science, with a welcome emphasis on coupling techniques. The book series satisfies the need for up-to-date information on numerical modeling. Faster computers and newly developed or improved numerical methods such as boundary element and meshless methods or genetic codes have made numerical modeling the most efficient state-of-the-art tool for integrating scientific and technological knowledge in the description of phenomena and processes in engineered and natural systems. In general, these challenging problems are fundamentally coupled processes that involve dynamically evolving fluid flow, mass transport, heat transfer, deformation of solids, and chemical and biological reactions.

This series provides an understanding of complicated coupled phenomena and processes, its forecasting, and approaches in problem solving for a diverse group of applications, including natural resources exploration and exploitation (e.g. water resources and geothermal and petroleum reservoirs), natural disaster risk reduction (earthquakes, volcanic eruptions, tsunamis), evaluation and mitigation of human induced phenomena (climate change), and optimization of engineering systems (e.g. construction design, manufacturing processes).

Jochen Bundschuh
Mario César Suárez Arriaga
(*Series Editors*)

Editorial board of the book series

- Iouri Balachov *Advanced Power Generation, Physical Sciences Division,
SRI International, Menlo Park, CA 94025, USA
E-mail: iouri.balachov@sri.com*
- Jacob Bear *Dept. of Civil and Environmental Eng., Technion,
Israel Inst. of Technology, Haifa 32000, Israel
E-mail: cvrbear@techunix.technion.ac.il*
- Angelika Bunse-Gerstner *Center of Industrial Mathematics, Faculty of Mathematics
and Computer Science, University of Bremen,
Bremen, Germany
Email: Bunse-Gerstner@math.uni-bremen.de*
- Chun-Jung Chen *Chen Life Science Group, Research Division,
National Synchrotron Radiation Research Center,
and Department of Physics, National Tsing
Hua University, Hsinchu 30076, Taiwan
Email: cjchen@nsrrc.org.tw*
- Alexander H.D. Cheng *Department of Civil Engineering, University of Mississippi,
MS 38677-1848
E-mail: acheng@olemiss.edu*
- Martín A. Díaz Viera *Instituto Mexicano del Petróleo (IMP), Mexico City, Mexico
E-mail: mdiazv@imp.mx*
- Hans J. Diersch *Groundwater Modelling Centre, DHI-WASY GmbH,
12526 Berlin, Germany
E-mail: H.Diersch@dhi-wasy.de*
- Jesus A. Dominguez *ASRC Aerospace Corporation, Kennedy Space Center,
FL, USA
E-mail: jesus.a.dominguez@nasa.gov*
- Donald Estep *Department of Mathematics, Department of Statistics,
Program for Interdisciplinary Mathematics,
Ecology, & Statistics; Director, Center for
Interdisciplinary Mathematics and Statistics,
Colorado State University, Fort Collins, CO 80523, USA
E-mail: don.estep@gmail.com*
- Ed Fontes *COMSOL, SE-111 40, Stockholm, Sweden
E-mail: ed@comsol.com*
- Edward Furlani *Device Physics and Simulation, OCTO,
Device Science & Technology Research,
Fluidics Dept., Eastman Kodak Company,
NY 14650-2216, USA
E-mail: edward.furlani@kodak.com*

- Ismael Herrera *Institute of Geophysics, National University of Mexico (UNAM), 14000, Mexico D.F., Mexico*
E-mail: iherrera@unam.mx
- Jim Knox *Life Support Systems Development Team, NASA Marshall Space Flight Center, Huntsville, AL 35812, USA*
E-mail: Jim.Knox@nasa.gov
- William Layton *Department of Mathematics, University of Pittsburgh, Pittsburgh, PA 15260, USA*
E-mail: wjl@math.pitt.edu
- Kewen Li *Stanford University, Department of Energy Resources Engineering, Stanford, CA 94305-2220, USA*
E-mail: kewenli@stanford.edu
- Jen-Fin Lin *Center for Micro/Nano Science and Technology, National Cheng Kung University, Tainan, Taiwan*
E-mail: jflin@mail.ncku.edu.tw
- Rainald Löhner *School of Computational Sciences, George Mason University, MS 6A2, USA*
E-mail: rlohner@gmu.edu
- Emily Nelson *Bio Science and Technology Branch, NASA Glenn Research Center, Cleveland, OH 44135, USA*
E-mail: emily.s.nelson@nasa.gov
- Enrico Nobile *Department of Naval Architecture, Ocean and Environmental Engineering (DINMA), University of Trieste, Trieste, Italy*
E-mail: nobile@units.it
- Jennifer Ryan *Delft Institute of Applied Mathematics, Delft University of Technology, 2628 CD Delft, The Netherlands*
E-mail: j.k.ryan@tudelft.nl
- Rosalind Sadleir *Department of Biomedical Engineering, University of Florida, Gainesville, FL 32611-6131, USA*
E-mail: rsadleir@bme.ufl.edu
- Fernando Samaniego V. *Faculty of Engineering, National University of Mexico (UNAM), 14000, Mexico City, Mexico*
E-mail: fsamaniegov@pep.pemex.com
- Peter Schätzl *Groundwater Modelling Centre, DHI-WASY GmbH, 12526 Berlin, Germany*
E-mail: p.schaetzl@dhi-wasy.de
- Xinpu Shen *Landmark Graphics Corporation, Houston, TX 77042-3021, USA*
E-mail: xinpshen@yahoo.com
- Roger Thunvik *Dept. Land & Water Resources Engineering, Royal Institute of Technology (KTH), SE-100 44 Stockholm, Sweden*
E-mail: roger@kth.se
- Clifford I. Voss *U.S. Geological Survey, Reston, VA 20192, USA*
E-mail: cvoss@usgs.gov
- Thomas Westermann *Karlsruhe University of Applied Sciences, 76133 Karlsruhe, Germany*
E-mail: thomas.westermann@hs-karlsruhe.de
- Michael Zilberbrand *Hydrological Service of Israel, Jerusalem 91360, Israel*
E-mail: michaelz20@water.gov.il

This book is dedicated to my wife Teresa
—Jochen Bundschuh

This book is dedicated to my wife Elke who has enriched my life
—Mario César Suárez Arriaga

The Pioneers of fluid flow and thermoporoelasticity



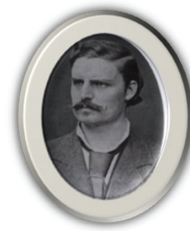
Sir Isaac Newton
(1643–1727)

$$\vec{F} = \frac{d}{dt}(m\vec{v})$$



Henry Darcy
(1803–1858)

$$\vec{\nabla} \cdot (\mathbf{K}_H \cdot \vec{\nabla} h) = S_{sp} \frac{\partial h}{\partial t}$$



Adolf E. Fick
(1829–1901)

$$\vec{\nabla} \cdot (\varphi \mathbf{D} \cdot \vec{\nabla} C) = \varphi \frac{\partial C}{\partial t}$$



Joseph Fourier
(1768–1830)

$$c_p \rho \frac{\partial T}{\partial t} - \vec{\nabla} \cdot (\mathbf{k}_T \cdot \vec{\nabla} T) = Q_H$$



Hermann Ludwig
von Helmholtz
(1821–1894)

$$\Delta F_s = \Delta U_s - T \Delta S_s$$



Josiah W. Gibbs
(1839–1903)

$$\Delta G_s = \Delta H_s - T \Delta S$$



Karl Terzaghi
(1883–1963)

$$\sigma_T = \tau - \mathbf{b} p_f$$



Maurice A. Biot
(1905–1985)

$$p_f = M \zeta - C \varepsilon_B$$

Source: Wikimedia Commons; the photo of M.A. Biot is from Poronet (2009).

Table of contents

About the book series	VII
Editorial board of the book series	IX
Dedications	XI
The Pioneers of fluid flow and thermoporoelasticity	XIII
Preface	XXXIII
Foreword	XXXV
Authors' prologue	XXXVII
About the authors	XXXIX
Acknowledgements	XLI
1 Introduction	1
1.1 The water problem—The UN vision	1
1.2 The energy problem—Vision of the Intergovernmental Panel of Climate Change	3
1.3 Multiphysics modeling of isothermal groundwater and geothermal systems	5
1.4 Modeling needs in the context of social and economic development	6
1.4.1 The role of groundwater for drinking, irrigation, and other purposes	7
1.4.2 Geothermal resources	9
1.5 The need to accelerate the use of numerical modeling of isothermal aquifers and geothermal systems	10
2 Rock and fluid properties	13
2.1 Mechanical and thermal properties of porous rocks	13
2.1.1 Absolute permeability	13
2.1.2 The skeleton: Bulk, pore and solid volumes; porosity	15
2.1.2.1 The variation of the fluid mass content	17
2.1.2.2 The advective derivative of the density	17

2.1.3	The principle of conservation of mass in porous rocks	17
2.1.4	Thermal conductivity of porous rocks	19
2.1.5	Heat conduction, Fourier's law and thermal gradient	21
2.1.6	Heat capacity and enthalpy of rocks	21
2.1.7	Rock heat capacity and geothermal electric power	26
2.1.8	Thermal diffusivity and expansivity of rocks	27
2.1.8.1	Thermal diffusivity	27
2.1.8.2	Volumetric thermal expansivity	28
2.1.9	Mechanical parameters of rocks	29
2.1.9.1	Stress and strain	29
2.1.9.2	Young's modulus	29
2.1.9.3	Poisson's modulus	30
2.1.9.4	Bulk modulus	30
2.1.9.5	Rock compressibility	30
2.1.9.6	Rigidity and Lamé moduli	30
2.1.9.7	Volumetric strain	30
2.1.10	Elasticity equations for Hookean rocks	31
2.2	Linear thermoporoelastic rock deformation	32
2.2.1	Effects of the fluid on porous rock properties	32
2.2.2	A simple model for the collapse of fractures in poroelastic rocks	33
2.2.3	Linear deformation of rocks containing isothermal fluid	35
2.2.3.1	Differential relationships between porosity and volumes	36
2.2.4	Poroelastic rock parameters: Drained and undrained conditions	36
2.2.4.1	Drained bulk compressibility	37
2.2.4.2	Undrained bulk compressibility	37
2.2.4.3	Compressibility of the solid phase	38
2.2.4.4	Compressibility of the pore volume	38
2.2.5	The Biot-Willis coefficient	39
2.2.6	Biot's classical poroelasticity theory	40

2.2.6.1	Fundamental concepts and coefficients in Biot's poroelastic theory	40
2.2.6.2	The fundamental parameters of poroelasticity	41
2.2.6.3	Relationships among the bulk moduli and other poroelastic coefficients	43
2.2.7	Porosity and the low-frequency Gassmann-Biot equation	44
2.2.8	Numerical values of the poroelastic coefficients	47
2.2.9	Tensorial form of Biot's poroelastic theory in 4D	48
2.2.9.1	Terzaghi effective stresses in poroelastic rocks	49
2.2.9.2	Vectorial formulation of the poroelastic equations	50
2.2.10	Mathematical model of the fluid flow in poroelastic rocks	52
2.2.10.1	Dynamic and static poroelastic equations for Hookean rocks	53
2.2.11	Diffusion equations for consolidation	56
2.2.12	Basic thermodynamics of porous rocks	57
2.2.12.1	The first and second laws of thermodynamics for porous rocks	57
2.2.12.2	Differential and integral forms of the first and second law	59
2.2.12.3	The Helmholtz free energy: A thermoelastic potential for the matrix	60
2.2.12.4	The Gibbs free enthalpy: Skeleton thermodynamics with null dissipation	63
2.2.12.5	Thermodynamics of the fluid mass content	66
2.2.12.6	Numerical values of the thermal expansivity coefficients	69
2.2.12.7	Tensorial form of the thermoporoelastic equations	69
2.3	Mechanical and thermodynamical water properties	70
2.3.1	Practical correlations for aquifers and low-enthalpy geothermal systems	71
2.3.2	A brief history of the equation of state for water	74
2.3.3	The IAPWS-95 formulation for the equation of state of water	75
2.3.4	Exact properties of low-enthalpy water (0 to 150°C)	77
2.3.4.1	Density and enthalpy of the liquid	77
2.3.4.2	Isobaric heat capacity and thermal conductivity	77

2.3.4.3	Compressibility and expansivity	78
2.3.4.4	Dynamic viscosity and speed of sound	78
2.3.5	Exact properties of high-enthalpy water (150 to 350°C)	79
2.3.6	Properties of two-phase geothermal water (100 to 370°C)	81
2.3.6.1	Thermodynamic range of validity of the code AquaG370.For	82
2.3.6.2	Temperature of saturation (subroutine T_{sat})	82
2.3.6.3	Saturation pressure (subroutine P_{sat})	82
2.3.6.4	Density and enthalpy of liquid and steam (subroutines Likid and Vapor)	82
2.3.6.5	Dynamic viscosity of two-phase water (subroutine Visf)	83
2.3.6.6	Thermal conductivity of two-phase water (subroutine Terk)	83
2.3.6.7	Specific heat of two-phase water (subroutines CPliq and CPvap)	84
2.3.6.8	Surface tension of two-phase water (subroutine Tensa)	84
2.3.6.9	Practical correlations for two-phase flow	84
2.3.7	Capillary pressure	85
2.3.8	Practical correlations for capillary pressures	88
2.3.8.1	Correlation of Van Genuchten	88
2.3.8.2	Correlation of Schulz and Kehrwald	89
2.3.8.3	Correlation of Li and Horne	89
2.3.8.4	Correlation of Brooks-Corey	90
2.3.8.5	Correlation of Li and Horne for geothermal reservoirs	90
2.3.8.6	The Li-Horne general fractal capillary pressure model	92
2.3.9	Relative permeabilities	92
2.3.10	Practical correlations for relative permeabilities	94
2.3.10.1	Constant functions for perfectly mobile phases	94
2.3.10.2	Linear functions	94
2.3.10.3	Functions of Purcel	95
2.3.10.4	Functions of Corey	95
2.3.10.5	Functions of Brooks-Corey	95

2.3.10.6	Functions of Schulz-Kehrwald	96
2.3.10.7	Functions for three-phase relative permeabilities	96
2.3.10.8	Li-Horne universal relative permeability functions based on fractal modeling of porous rocks	96
2.3.10.9	Linear X-functions for relative permeability in fractures	97
2.3.10.10	Relative permeabilities in fractures: The Honarpour-Diomampo model	97
2.3.11	Observed effects of dissolved salts (NaCl) and non-condensable gases (CO ₂)	98
3	Special properties of heterogeneous aquifers	101
3.1	The problem of heterogeneity in aquifers	101
3.2	The concept of multiple porosity in heterogeneous aquifers	102
3.3	The triple porosity-permeability concept in geothermics	103
3.4	Averages of parameters at different interfaces	103
3.4.1	Permeability and thermal conductivity	103
3.4.2	Special average for thermal conductivity in dry rock	104
3.4.3	Heat capacity of the rock-fluid system	104
3.4.4	Linear Lagrange interpolation for densities	105
3.5	Averages for systems with two and three components: General models of mixtures	105
3.5.1	Parallel and serial models	105
3.5.2	Geometrical model	106
3.5.3	Model of Griethe	106
3.5.4	Model of Budiansky	106
3.5.5	Model of Hashin-Shtrikman	106
3.5.6	Model of Brailsford-Major	107
3.5.7	Model of Waff	107
3.5.8	Model of Walsh-Decker	107
3.5.9	Model of Maxwell	107
3.5.10	Maxwell's dispersive model	107
3.5.11	Model of Russel	108

3.6	Some applications to field data	108
3.6.1	Application to data from rocks of the Los Azufres and Los Humeros geothermal fields (Mexico)	108
3.7	Discontinuities of parameters when crossing heterogeneous interfaces	110
3.8	Examples of heterogeneous non-isothermal aquifers—Petrophysical properties in Mexican geothermal fields	112
3.8.1	Cerritos Colorados (La Primavera), Jalisco	112
3.8.2	Los Humeros, Puebla	113
3.8.3	Los Azufres, Michoacán	114
4	Fluid flow, heat and solute transport	115
4.1	The conservation of mass for fluids	115
4.2	General model of fluid flow: The Navier-Stokes equations	117
4.2.1	Flow of fluids at the scale of the pores	119
4.3	Darcy's law: pressure and head	119
4.3.1	Pressure formulation of the general groundwater flow equation	122
4.3.2	Darcy's law in terms of hydraulic head and conductivity	122
4.3.3	The hydraulic head governing equation of groundwater flow	124
4.3.3.1	Storativity and transmissivity	125
4.3.3.2	Two-dimensional groundwater flow—The Boussinesq approximation	126
4.3.4	Reservoir anisotropy in two dimensions	128
4.4	Flow to wells in homogeneous isotropic aquifers	129
4.4.1	Simple geometries for isothermal stationary groundwater flow	129
4.4.1.1	Radial flow	129
4.4.1.2	Linear flow	130
4.4.1.3	Spherical flow	130
4.4.2	Darcy's law and the equation of state of slightly compressible water	131
4.4.3	Transient flow of slight compressible fluids, Theis solution	132
4.4.4	Flow to a well of finite radius, wellbore storage	135
4.4.5	The Brinkman equation and the coupled flow to wells	136

4.4.5.1	Coupling the Darcy-Brinkman-Navier-Stokes equations in the flow to wells	138
4.5	Pumping test fundamentals	139
4.5.1	Stationary flow towards a well—Dupuit and Thiem well equations	140
4.5.1.1	Confined aquifer	140
4.5.1.2	Unconfined aquifer	141
4.5.2	Transient flow—explicit Theis equation for confined aquifers	142
4.5.3	Transient flow—Hantush equation (semiconfined aquifer)	145
4.5.4	Turbulence and the Forchheimer’s law	146
4.6	Heat transport equations	147
4.6.1	Heat conduction	148
4.6.2	Heat convection	149
4.7	Flow of mass and energy in two-phase reservoirs	150
4.7.1	Darcy’s law for two-phase systems	150
4.7.2	Flow of energy in reservoirs with single-phase fluid	151
4.7.3	Flow of energy in reservoirs with two-phase fluid	152
4.7.3.1	The Garg’s model for two-phase fluid	153
4.7.4	Heat pipe transfer in two-phase reservoirs	153
4.7.5	The general heat flow equation	154
4.8	Solute transport equations	154
4.8.1	Fick’s law of diffusion	155
4.8.2	Fick’s law with advection and dispersion	157
4.8.3	General solute transport equations	159
5	Principal numerical methods	165
5.1	The finite difference method	166
5.1.1	Fundamentals	166
5.1.2	Stationary two-dimensional groundwater flow	168
5.1.2.1	Difference method for model nodes and centers	168
5.1.2.1.1	Forward difference method	169

5.1.2.1.2	Centered difference method	170
5.1.2.1.3	Backward difference method	170
5.1.2.2	Difference method for boundary nodes	171
5.1.3	Transient groundwater flow	172
5.1.3.1	Time discretization	172
5.1.3.2	Explicit difference method ($\varepsilon = 1$)	173
5.1.3.3	Implicit difference method ($\varepsilon = 0$)	174
5.1.3.4	Crank-Nicholson difference method ($\varepsilon = 0.5$)	175
5.1.3.5	Difference method for an inhomogeneous, anisotropic, confined aquifer	175
5.1.4	Calculating the groundwater flow velocity (average pore velocity)	178
5.1.5	Solute and heat transport	179
5.1.6	Stability and accuracy criteria	180
5.1.6.1	Courant criterion	181
5.1.6.2	Neumann criterion	181
5.2	Introduction to the finite element method (FEM)	182
5.2.1	Brief description of the method fundamentals	183
5.2.2	Finite elements using linear Lagrange interpolation polynomials	183
5.2.3	Numerical solution of the Poisson's equation with the FEM—Galerkin method	186
5.2.3.1	Numerical method 1: General test functions	188
5.2.3.2	Numerical method 2: Linear polynomials	190
5.2.3.3	Variable permeability in the weak form of the Galerkin method	194
5.2.3.4	The general diffusion equation in the weak form of the Galerkin method	194
5.2.4	Galerkin weighted residuals method; weak formulation of the heat equation for a stationary temperature in two dimensions	196
5.2.5	Finite elements using bilinear Lagrange interpolation polynomials over triangles	197
5.2.6	Finite elements using bilinear Lagrange interpolation polynomials over rectangles	199
5.2.7	Solution of the transient heat equation using finite elements in 1D	201

5.3	The finite volume method (FVM)	202
5.3.1	The FVM in the solution of single-phase mass flow	202
5.3.2	The FVM in the numerical solution of single-phase energy flow	205
5.3.3	The FVM in the numerical solution of two-phase mass flow	206
5.3.4	The FVM in the numerical solution of two-phase energy flow	207
5.3.5	Numerical approximations of the time-level	209
5.3.5.1	Explicit numerical approximation of the time-level	209
5.3.5.2	Implicit numerical approximation of the time-level	210
5.3.5.3	Three time-level numerical approximations	210
5.4	The boundary element method for elliptic problems	211
5.4.1	The Dirac distribution (a generalized function)	213
5.4.2	The fundamental solution in free space	213
5.4.3	BEM solution of the Poisson's equation	214
5.4.4	The BEM numerical implementation: An example	215
6	Procedure of a numerical model elaboration	217
6.1	Introduction	217
6.2	Defining the objectives of the numerical model	219
6.3	Conceptual model	221
6.4	Types of conceptual models	223
6.4.1	The porous medium continuum model (granular medium)	224
6.4.2	Conceptual models of fracture flow	226
6.4.2.1	Equivalent porous medium (EPM) approach	227
6.4.2.2	Dual and multiple continuum approach	227
6.4.2.3	Explicit discrete fracture approach	228
6.4.2.4	Discrete-fracture network (DFN) approach	229
6.4.3	Simplification by using 2-dimensional horizontal models	229
6.5	Field data required for constructing the conceptual model	230
6.5.1	General evaluation of sufficiency of available field data	230
6.5.2	Types of model boundaries and boundary values	232

6.5.3	Aquifer geometry, type, solid and fluid properties	233
6.5.4	Sources and sinks within the model area	235
6.6	Numerical formulation of the conceptual model	237
6.6.1	From the conceptual to the mathematical and numerical model	237
6.6.2	Discretizing the model domain of an aquifer	237
6.6.3	Initial values	239
6.6.4	Ready for numerical simulations	239
6.7	Parameter estimation	239
6.7.1	Remote sensing	239
6.7.2	Field surveys of cold (non-geothermal) aquifer systems	241
6.7.2.1	Geological and hydrogeological studies	241
6.7.2.2	Hydro(geo)chemical surveys	241
6.7.2.3	Geophysical survey	243
6.7.2.4	Aquifer tests	244
6.7.2.5	Tracer tests	246
6.7.2.5.1	Overview on principal artificial tracers and their applications	246
6.7.2.5.2	Field-scale tracer tests performed in boreholes (wells)	246
6.7.3	Field survey of geothermal systems	247
6.7.3.1	Geological and hydrogeological surface studies	248
6.7.3.2	Hydro(geo)chemical surveys	248
6.7.3.3	Geophysical surveys	248
6.7.3.4	Tests performed in drillings	249
6.7.4	Laboratory tests and experiments	250
6.8	Selection of model type and code	250
6.8.1	Model types	251
6.8.2	Public domain and commercial software for numerical modeling	254
6.8.3	ASM (Aquifer Simulation Model)	254
6.8.4	SUTRA	255

6.8.5	Visual MODFLOW	256
6.8.6	Processing MODFLOW for Windows (PMWIN)	257
6.8.7	FEFLOW (Finite Element Subsurface Flow and Transport Simulation System)	258
6.8.8	TOUGH, TOUGHREACT and related codes and modules	260
6.8.9	STAR—General Purpose Reservoir Simulation System	261
6.8.9.1	RIGHTS: Single-phase geothermal reservoir simulator	262
6.8.9.2	DIAGNS: Well test data diagnostics and interpretation	262
6.8.9.3	GEOSYS: Data management and visualization system	262
6.8.10	COMSOL Multiphysics	263
6.9	Calibration, validation and sensitivity analysis	263
6.9.1	Model calibration	264
6.9.2	Model validation (history matching)	265
6.9.3	Sensitivity analysis	268
6.10	Performing numerical simulations	269
6.11	How good is the model? Assessing uncertainties	271
6.12	Model misuse and mistakes	272
6.13	Example of model construction—Assessment of the contamination of an aquifer	273
6.13.1	Situation and tasks	273
6.13.1.1	Existing field data and information	275
6.13.2	Design of the investigation program	275
6.13.3	Preliminary investigations—Contamination assessment	275
6.13.4	Acquisition of groundwater level and contaminant concentration	275
6.13.5	Groundwater flow and advective transport as a first approach	276
6.13.5.1	Delimitation of the area to model and aquifer geometry	276
6.13.5.2	Hydrogeological parameters	276
6.13.5.3	Simulation of groundwater flow lines and flow times	278
6.13.5.4	Results	278
6.13.6	Transport model with dispersion, sorption, and resulting solutions	279

6.13.6.1	Introduction	279
6.13.6.2	Simulation of solute propagation with a permanent inflow of contaminants	280
6.13.6.3	Simulation of solute propagation with an immediate suspension of inflow of contaminants	282
6.13.6.4	Water works: Diagnosis and recommended solutions	282
6.13.6.5	Farm wells: Diagnosis and recommended solutions	283
7	Parameter identification and inverse problems (by Longina Castellanos and Angel Pérez)	285
7.1	Introduction	285
7.2	Ill-posedness of the inverse problem	288
7.2.1	Existence of a solution	289
7.2.2	Uniqueness of the solution (identifiability)	289
7.2.3	Continuous dependency on the data	290
7.3	Linear least-squares (LLS)	291
7.3.1	Condition number of an invertible square matrix	292
7.3.2	Linear least-squares solution: Direct method	292
7.3.3	Tikhonov's regularization method	293
7.3.4	An iterative method for solving LLS: Linear conjugate gradients	294
7.3.4.1	L-curve regularization algorithm	295
7.3.4.2	Linear preconditioned conjugate gradient method	296
7.4	Nonlinear least-squares (NLS)	297
7.4.1	The Levenberg-Marquardt method	298
7.4.2	Using an optimization routine (TRON) to solve NLS problems	300
7.4.3	Regularization techniques in NLS	301
7.5	Application examples	302
7.5.1	Groundwater modeling	302
7.5.1.1	Multiscale optimization	303
7.5.1.2	An elementary example	305
7.5.1.2.1	Experimental results	305

7.5.2	Inverse problems in geophysics	306
7.5.2.1	An elementary geophysical inverse problem	307
7.5.2.2	Formulation of the inverse problem	308
8	Groundwater modeling application examples	311
8.1	Periodical extraction of groundwater	311
8.1.1	Situation and tasks	311
8.1.2	Aquifer specifications	311
8.1.3	Tasks	312
8.1.4	Elaboration of a numerical model and problem solution	312
8.1.4.1	Elaboration of the numerical flow model	312
8.1.4.2	Evaluation of the piezometric pattern	314
8.1.4.3	Evaluation of the water balance of the model area	314
8.2	Water exchange between an aquifer and a surface water body by leakage	315
8.2.1	Problem and tasks	315
8.2.2	Hydrogeological setting, available data and measurements	315
8.2.3	Formulating surface water-groundwater interactions by leakage	315
8.2.4	Execution of infiltration tests along the river	316
8.2.5	Elaboration of a numerical model and problem solution	319
8.3	Scenario modeling of multi-layer aquifers and distribution of groundwater ages caused by exploitation	320
8.3.1	Problem	320
8.3.2	Aquifer specifications	321
8.3.3	Objectives of the modeling	322
8.3.4	Elaboration of a numerical model	323
8.3.4.1	Aquifer properties	324
8.3.4.2	Boundary conditions	325
8.3.4.3	Groundwater extraction	325
8.3.5	Results	325
8.3.5.1	Groundwater balance in models with two or three geological layers	325

8.3.5.2	Influence of groundwater exploitation	325
8.3.5.3	Influence of clay layers	338
8.3.5.4	Contamination threat for deeper aquifers	339
8.4	Point source contamination and aquifer remediation	340
8.4.1	Situation	340
8.4.2	Aquifer specifications	340
8.4.3	Objectives	340
8.4.4	Elaboration of a numerical model and problem solution	342
8.4.4.1	Groundwater flow pattern	342
8.4.4.2	Isochrones	343
8.4.4.3	Designing the remediation well	343
8.5	Boron contamination propagation	344
8.5.1	Situation and objectives	344
8.5.2	Existing data	345
8.5.3	Elaboration of a numerical model	346
8.5.4	Results of the simulations	346
8.6	Annual temperature oscillations in a shallow stratified aquifer	347
8.6.1	Introduction and objectives	347
8.6.2	Elaboration of a numerical model	349
8.6.2.1	Geometry	349
8.6.2.2	Aquifer properties	349
8.6.2.3	Boundary conditions	350
8.6.2.4	Initial conditions	351
8.6.3	Simulations of spring water temperatures and their results (scenarios 1–8)	351
8.6.3.1	Groundwater flow field	351
8.6.3.2	Annual periodic oscillations of spring water temperature	351
8.6.3.3	Results summary	351
8.6.4	Scenario 1 and 3: Simulations and results	352
8.6.4.1	Scenario 1	355

8.6.4.1.1	Aquifer configuration, flow field and water balance	355
8.6.4.1.2	Temperature field	355
8.6.4.1.3	Spring water temperature	355
8.6.4.2	Scenario 3	355
8.6.4.2.1	Aquifer configuration, flow pattern and water balance	355
8.6.4.2.2	Temperature field	355
8.6.4.2.3	Spring water temperature	356
9	Geothermal systems modeling examples	357
9.1	What is geothermal energy?	357
9.1.1	Characteristics of geothermal reservoirs in Mexico as examples of heterogeneous non-isothermal aquifers	360
9.1.1.1	Cerro Prieto, Baja California	361
9.1.1.2	Los Azufres, Michoacán	362
9.1.1.3	Los Humeros, Puebla	364
9.1.1.4	Las Tres Virgenes, Baja California	366
9.1.1.5	Cerritos Colorados (La Primavera), Jalisco	366
9.2	Transient radial-vertical heat conduction in wells	367
9.2.1	Transient radial-vertical flow of heat	367
9.2.1.1	Radial portion of the model	369
9.2.1.2	Radial temperature distribution inside the cement	371
9.2.1.3	Vertical portion of the model	372
9.2.1.4	The well-rock radial flow of heat	373
9.3	The Model of Avdonin	374
9.3.1	Transient radial flow of hot water in 1D	374
9.4	The invasion of geothermal brine in oil reservoirs	376
9.4.1	Geothermal aquifers and oil reservoirs: Available data	376
9.4.2	A general 3D mathematical model	378
9.4.2.1	The one-dimensional Buckley-Leverett model	380

9.4.3	Formulation and numerical solution using the finite element method	381
9.4.4	Numerical simulation of brine invasion	383
9.5	Modeling submarine geothermal systems	384
9.5.1	Brief description of submarine geothermal systems	385
9.5.1.1	Geothermal discharge chimneys and plumes	386
9.5.1.2	Models to compute the heat flux related to the plumes	387
9.5.1.3	Modeling the radial heat conduction in chimneys	388
9.5.2	Submarine geothermal potential	388
9.5.2.1	Submarine potential of the Gulf of California	388
9.5.2.2	Using the boundary element method to estimate the initial conditions of submarine geothermal systems	390
9.6	Modeling processes in fractured geothermal systems	392
9.6.1	Single porosity and fractured volcanic systems	393
9.6.2	The double porosity model	393
9.6.3	The triple porosity model	393
9.6.4	Fluid transport through faults	395
9.6.5	General equations for single, double and triple porosity models	396
9.6.6	Numerical comparison between single porosity and fractured media	396
9.6.6.1	Graphical results of the simulations	398
9.6.7	Effective thermal conductivity and reservoir natural state; Flow problem with CO ₂	401
9.6.8	Simultaneous heat and mass flow in fractured reservoirs: Conclusions	405

APPENDIXES

A:	Mathematical appendix	407
A.1	Introduction to interpolation techniques	407
A.1.1	Approximation and basis of interpolation in one dimension	408
A.1.2	Basis of a linear functional space	409
A.1.2.1	Karl Weierstrass approximation theorem (1885)	409
A.1.3	Support and matrix of the interpolation	409

A.1.4	Numerical examples of interpolation	410
A.1.4.1	Example 1	410
A.1.4.2	Example 2	411
A.1.5	The Lagrange interpolation polynomials	412
A.1.5.1	Example 1	414
A.1.5.2	Example 2	415
A.2	Interpolation in two and three dimensions	415
A.3	Elements of tensor analysis	416
A.3.1	Index notation for vectors and tensors	416
A.3.2	Differential operators in curvilinear coordinates	417
A.3.3	Tensorial notation for differential operators in cartesian coordinates	418
A.4	The integral theorem of Stokes	418
A.4.1	Riemann's theorem	419
A.4.2	Green's first identity	419
A.4.3	Green's second identity	420
A.4.4	The divergence theorem	420
A.4.5	The Dirac distribution	420
B:	Tabulated thermal conductivities	422
	Nomenclature	429
	References	439
	Book series page	479

Preface

No comprehensive textbook on the groundwater related issues of geothermal energy use is available yet. This book addresses this gap and appears at a crucial point in time where we all need to explore non-fossil alternative energy sources. Despite some recent irritations related to earthquakes induced by geothermal projects there is no way to ignore this vast energy resource and I am sure it will prevail in the long run. In all design and scoping tasks involved in its development the tool of numerical modelling will be essential. It is this tool which is described in depth and detail in this book.

The treatment of heat related groundwater flows requires the coupling of the ordinary isothermal Darcy flow with heat transport, density changes, deformation of the matrix, two-phase flow under steam conditions and eventually the geochemistry and thermodynamics of dissolved minerals. This leads to a highly complex, highly non-linear problem, the mere numerical solution of which even today still presents a major scientific challenge, not to speak of the problems associated with the natural heterogeneity of the subsurface properties.

The book limits itself to the physical aspects, leaving out the geochemical coupling. It describes in great detail the thermal and mechanical properties of the rock and the transported fluids. The aspect of heterogeneity is taken into account by its treatment through the conceptualisation of the medium as multi-porous. This is a pragmatic way of parameterizing unresolved and unknown heterogeneity of the medium. However it has to be remembered that it is not predictive but rather requires substantial observation data in order to be identifiable.

After discussion all partial aspects of the modelling procedure, in the final chapter, the coupled approach is applied in a more integral fashion to a geothermal field in Mexico, giving the student a practical example of how to approach the geothermal modelling task.

The text is very comprehensive and can therefore be used not only as a textbook but also as a reference source especially on all temperature related properties of rocks and fluids.

I wish this book a friendly reception in the scientific and engineering communities involved with geothermal energy and its groundwater and hydrogeology aspects.

Zürich, February, 2010
Wolfgang Kinzelbach

Foreword

Modern theory of flow through deformable porous media is based on Darcy's law, which owes its origin to a simple one-dimensional filtration experiment first performed by Henry Darcy in 1856. By varying the experimental parameters, Darcy showed that the volumetric flow rate is directly proportional to the area of the filtration bed, and the liquid head gradient across the bed. The constant of proportionality K , introduced by Darcy, is now known as hydraulic conductivity and depends on the properties of both the fluid and the porous media. Since the publication of Darcy's monograph in 1856, Darcy's law has been generalized to describe multi-phase multi-component compressible fluid flow through anisotropic and heterogeneous porous and fractured media. An understanding of the theoretical framework for flow through porous media and material properties is essential for modeling groundwater and geothermal systems. The current volume contains a thorough exposition of poroelasticity and thermomechanical properties of porous rocks and water in addition to mass and energy transport in geologic media.

Until the availability of computing machines in the second half of the 20th century, only a few groundwater problems could be solved analytically. The advent of computers has radically altered the situation. These days large-scale multidimensional computer codes are in routine use for complex groundwater, geothermal, oil and gas, and environmental applications. The authors provide a discussion of all the principal numerical methods used to solve the system of partial differential equations that govern mass and energy transport in porous media. Application of computer codes to solve practical groundwater and geothermal problems requires an estimation of certain model parameters (e.g. formation porosity and permeability). It is only fitting that the authors have devoted considerable space to model parameter estimation, construction of the conceptual model, and procedures for developing numerical models.

Readers new to numerical modeling will find the groundwater and geothermal examples contained in the last part of the book to be very helpful in learning the "art" and "science" of the numerical modeling of groundwater and geothermal systems. Experienced modelers and researchers will find this volume to be a valuable addition to their reference shelf. The authors and the publisher are to be congratulated for producing an interesting and comprehensive work.

Sabodh K. Garg
Science Applications International Corporation
San Diego, California

Authors' prologue

I don't know where I'm going But I know I'm on the way...

American Folk Song

The main purpose of writing this book was to make basic knowledge on mathematical modeling and fundamental concepts of the flow of mass and energy in deformable porous rocks available to a broad readership. It is impossible to cover this subject within the space limitations of any normal book. Therefore, a selection of topics has been made among those essential for a full understanding of the area. However, almost all the developments described herein are discussed in detail. The fundamental concepts, the physical laws, and the majority of equations modeling different phenomena are described and presented in a simple and logical manner. Some mathematical knowledge is required by the reader, including an understanding of differential and integral calculus in two or three variables, basic matrix algebra, and some interpolation techniques for the numerical approximation of functions and the solution of differential equations. The laws of conservation of mass, momentum and energy, including the two laws of thermodynamics, are gradually introduced in the context of natural reservoirs formed by poroelastic rocks subjected to pressure and temperature changes. The experimental coefficients supporting the theory are presented from a practical point of view, with a short description of how they are measured in the laboratory.

This book is oriented to the presentation of the scientific fundamentals of groundwater and geothermal systems. It explains in a simple and didactic manner the different water and energy problems and the existing mathematical and numerical tools that lead to modeling and solving them. We believe that this approach provides the reader with a thorough understanding of several subjects including the basic physical laws of poroelastic rocks, the partial differential equations representing these laws and the principal numerical methods, which allow finding approximate solutions of the corresponding mathematical models. The book also presents the form in which specific useful models can be generated and solved.

The text is introductory in the sense that it discusses elementary topics in three areas: mathematics, physics and engineering of the mentioned systems. All the laws and equations introduced in this book are formulated carefully from physical principles. In this way, the reader will understand the key importance of mathematics applied to all the subjects. Simple models are emphasized and solved with numerous examples. The numerical techniques are described and developed carefully for the more sophisticated and advanced models. In all cases we emphasize the physical interpretation of equations and mathematical results. The various parameters and coefficients appearing in both isothermal and geothermal aquifers are introduced after explanations based on well documented experimental outcomes. We introduced several new ideas, including, for example, a four-dimensional formulation of linear poroelastic theory and the use of the Gibbs and Helmholtz potentials to deduce the thermoporoelastic matrix equations also in four dimensions. An exact model to estimate the collapse of fractures and faults, direct examples of porous rock thermodynamics, relationships and numerical values of the poroelastic coefficients, practical correlations for aquifers, low-enthalpy and two-phase hydrothermal reservoirs, the graphical properties of water and various modeling examples of groundwater and geothermal systems are also novel in this introductory context.

Water and energy related sciences play a major, but often overlooked role in regard to economic and social development. During recent decades, the world has witnessed an unrelenting succession

of problems related to shortage of water resources and energy supply. Risks have increased sharply during the last few decades and will continue to grow in the near future. Reasons for this dangerous increase include population growth and human activities such as industry in continually expanding economies.

Geologic resources need to be better assessed, via improved exploration and exploitation. Geothermal resources can be exploited as an environmentally sound domestic energy source to cover large parts of the world's projected electricity demand. Freshwater resources are becoming increasingly limited and thus are assuming the status of the world's "gold" of the 3rd millennium. Energy and water, their purification, and equitable distribution pose great social and political challenges for humanity. A better understanding of these natural resources can contribute to reduce such menaces on our planet. Numerical modeling is an indispensable tool for any wise decision-making.

Particularly within the last 20 years, numerous important investigations have been performed in different fields of numerical modeling in different systems, and new methods and concepts were introduced by various groups of researchers. The most important results of these investigations are presented in numerous publications which are covering either highly specific topics or which are restricted to very special types of systems. This indicates the need of a synoptic compendium of the fundamentals of fluid, solute and heat transport, which is applicable for all types of sub-surface systems, ranging from shallow aquifers down to deep geothermal reservoirs. We wanted to showcase these new studies, as well as the trends of ongoing research in a broad spectrum of topics in numerical modeling applied to groundwater resources and geothermal reservoirs. Additionally, the book clearly reveals that a lot of further investigations need to be performed, and it hopefully will give the reader appropriate stimulus. We show that numerical models are tools and that their results must be considered critically. The quality of the results depends on the preparation of the model, the knowledge of the hydrogeological situation, and data as well as on the knowledge of the initial and boundary values of the reservoir.

The book aims to address professionals and academics equally. It shall further assist key institutions that deal with water and energy resources planning as an introduction for what and how numerical modeling can be applied in these fields. This also includes international and bilateral bodies concerned with technical and economic cooperation in developing countries—like those of the United Nations family and the international and regional development banks, financial institutions, donors, etc. Referring to this group it addresses in particular the newly founded International Renewable Energy Agency IRENA. We hope this book will become a standard, used by educational institutions, and Research and Development establishments involved in the respective issues. The book should prove to be a useful textbook to senior undergraduate and graduate students, postgraduates, professional geologists and geophysicists, engineers, mathematicians and others working in the areas concerned to groundwater and geothermal resources.

Not least, this book fills a gap in the literature, not only in the combination of deep insights into numerical modeling, but it also joins diverse specialist into a framework of a closer cooperation related to better using the world's freshwater and geothermal resources contributing to global climate change mitigation. We hope that the book will not only benefit its readers, but that it also will contribute to bring scientists of geosciences, engineering and applied mathematics closer together, through cooperative work in problem solving, and that this effort will prove to be a catalyst and starting point for many new collaborations and scientific research projects. We hope that this book will help us all to rededicate ourselves to wise and responsible use of the world's geological resources. Our goal must be to use water and energy resources in an optimal and sustainable way, to fulfill the water and energy needs of our present generation and to maintain and to protect them for the sake of the subsequent generations, and to avoid jeopardizing their future through inept use of natural resources.

Jochen Bundschuh
Mario-César Suárez Arriaga
June 2010

About the authors



Jochen Bundschuh (1960, Germany), finished his PhD in numerical modeling of heat transport in aquifers in Tübingen in 1990. He is working in geothermics, subsurface and surface hydrology and integrated water resources management, and connected disciplines. From 1993 to 1999 he served as an expert for the German Agency of Technical Cooperation (GTZ) and as a long-term professor for the DAAD (German Academic Exchange Service) in Argentina. From 2001 to 2008 he worked within the framework of the German governmental cooperation (Integrated Expert Program of CIM; GTZ/BA) as an adviser in mission to Costa Rica at the Instituto Costarricense de Electricidad (ICE). Here, he assisted the country in evaluation and development of its huge low-enthalpy geothermal resources for power generation. In 2005, he was appointed as an affiliate professor of the Royal Institute of Technology, Stockholm, Sweden. In 2006, he was elected Vice-President of the International Society of Groundwater for Sustainable Development ISGSD.

Dr. Bundschuh is editor of the books “Geothermal Energy Resources for Developing Countries” (2002), “Natural Arsenic in Groundwater” (2005), and the two-volume monograph “Central America: Geology, Resources and Hazards” (2007), “Groundwater for Sustainable Development” (2008), “Natural Arsenic in Groundwater of Latin America” (2008). He is co-author of the book “Low-Enthalpy Geothermal Resources for Power Generation” (2008) (CRC Press/Balkema—Taylor & Francis Group). Dr. Bundschuh is editor of the book series “Multiphysics Modeling” and of the book series “Arsenic in the Environment” (both CRC Press/Balkema—Taylor & Francis Group).

Since June 2009 he is teaching as professor in the area of renewable energies, in particular geothermics, at the University of Applied Sciences in Karlsruhe (Germany) and is researcher at the Institute of Applied Research of the same university, where he works in geothermics and the groundwater arsenic issue. Research is performed in close cooperation with the Department of Earth Sciences at the National Cheng Kung University, Tainan, Taiwan, where he is visiting professor.



Mario-César Suárez Arriaga (1950, Mexico City), studied Physics and Mathematics at the National Autonomous University of Mexico (UNAM) and Applied Mathematics and Mechanics in the Universities of Toulouse III and Paris VI, France (1980). He obtained his PhD in Petroleum & Geothermal Engineering at the Faculty of Engineering of the UNAM (2000). His areas of scientific research include the mathematical modeling of Complex Natural Systems, Continuum Mechanics and Geothermal Reservoir Engineering. At present he is working as a Research-Professor at the Faculty of Physics and Mathematics of the Universidad Michoacana de San Nicolas de Hidalgo (FCFM-UMSNH) in central Mexico. He worked several years (1982–2000) in the Comisión Federal de Electricidad (CFE), the Mexican federal utility which produces electricity from several sources, including geothermal. He was in charge of the evaluation and numerical simulation of geothermal reservoirs, covering several volcanic systems in Mexico. He developed and completed more than 30 different technical projects for CFE since 1982. He has a wide experience in the elaboration of conceptual models, in the analysis and synthesis of geological, geophysical, geochemical and production data and in the numerical modeling of two-phase flow geothermal systems. He has developed several modeling techniques for CFE from simple analytical models to complex numerical simulators. He started the first practical evaluations of deep Submarine Geothermal Reservoirs in Mexico, with the objective of producing electricity in the proximal future. He has published approximately eighty technical and scientific papers and reports on geothermal reservoir engineering and applied mathematics. He was co-founder and editor (1987–1994) of GEOTERMIA, a journal devoted to geothermal energy and published by the CFE since 1985. He is one of the founders of the Mexican Geothermal Association (1992). He is member of the following organizations: International Geothermal Association (IGA), International Society of Groundwater for Sustainable Development, Society of Industrial and Applied Mathematics, American Mathematical Society, American Association for the Advancement of Science, Asociación Geotérmica Mexicana, Sociedad Matemática Mexicana, Unión Geofísica Mexicana and Asociación Mexicana de Métodos Numéricos en Ingeniería y Ciencias Aplicadas. He is a member of the National System of Scientific Researchers (SNI) since 1991. He has been Professor of Mathematics, Mechanics, Transport Phenomena, Differential Equations and History of Science at the FCFM-UMSNH. He is co-author of the book “Stories from a Heated Earth: Our Geothermal Heritage”, published by the Geothermal Resources Council and the IGA (1999). He is the editor of the book series “Multiphysics Modeling” and of the book “Numerical Modeling of Coupled Phenomena in Science and Engineering: Practical Use and Examples”—Volume 1 (2009), both published by CRC Press/Balkema—Taylor & Francis Group.

Acknowledgements

This book would be incomplete without an expression of our sincere and deep gratitude to Michael Zilberbrand at Hydrological Service of Israel (Jerusalem) and Dina L. López at Ohio University (Athens, OH) for their careful reading and suggestions that greatly improved chapter 6 and to Emily Nelson from the NASA Glenn Research Center (Cleveland, OH) and Cliff Voss (USGS, VA) whose valuable reviews and comments significantly contributed to improve the chapters 6 and 8. We express our gratitude to Jennifer Ryan at Delft University of Technology, (The Netherlands) who contributed significantly to improve chapter 5. Many thanks also to Sarah Pasela (Canada), for devoting valuable time in providing grammatical corrections. We wish to express our sincere thanks to all of the above, whose efforts contributed to the high quality of the book.

Many thanks to Wolfgang Kinzelbach at ETH Zürich at Institute of Environmental Engineering (ETH Zürich, Switzerland) for his valuable comments on chapter 2. Additionally, we thank the following scientists who read parts of the examples of chapters 5, 8 and 9 and made a number of very useful suggestions for its improvement: Peter Birkle (IIE, Mexico), Ondra Sracek (Masaryk University, Czech Republic), Roger Thunvik and Vladimir Cvetkovic (Royal Institute of Technology, Sweden), Hans J. Diersch and Peter Schätzl (Groundwater Modelling Centre, DHI-WASY GmbH, Germany), Clifford I. Voss (U.S. Geological Survey, VA), Saugata Datta (Georgia College & State University, GA) and Francisco Domínguez, Gerardo Tinoco and Salvador Jara (Faculty of Sciences, Michoacan University UMSNH).

We particularly thank the editorial board members of the book series Multiphysics Modeling for their editorial help. Our special acknowledgement to John Gittins, Nadia Suarez, Thomas Mortlock and Pete Martin from the National Oceanography Centre (NOCS), University of Southampton, England; to John Garner from Shalimar, Florida; Susan F. Hodgson, from Sacramento, CA.; Corrie Clark, from Argonne National Laboratory, Washington, DC; Joshua Mendez Harper, from Boston University; Meredith Robin Mendez, Boston University Alumnus; Nita D. Schubert, Institute of Physics & Mathematics, UMSNH, and to William Layton, Department of Mathematics, University of Pittsburgh, Pittsburgh, PA for their invaluable help, comments and suggestions in the English language revision of this volume. The authors also thank the technical people of Taylor & Francis Group, for the excellent typesetting of the manuscript.

JB is especially grateful for the support provided by the Integrated Expert Program of CIM (GTZ/BA)*, Frankfurt, Germany, which delegated me [JB] as long-term integrated expert to the Instituto Costarricense de Electricidad (ICE) in San José, to assist Costa Rica in the better exploration and exploitation of its huge yet unused low-enthalpy geothermal resources. This mission allowed, within the framework of the German governmental cooperation, the compilation of this book, which will remain as one of the solid outcomes of this cooperative effort between the governments of Germany and Costa Rica. Many thanks to the Instituto Costarricense de Electricidad (ICE), which supported the compilation of this book in this framework and allowed the use of its facilities. JB would further like to thank the National Cheng Kung University and the National Science Council, Taiwan for the visiting professorship and the time for the final editorial work for the volume.

* Auftraggeber: Bundesministerium für Wirtschaftliche Zusammenarbeit und Entwicklung—(BMZ), Centrum für Internationale Migration und Entwicklung (CIM). [Federal Ministry for Economic Cooperation and Development (BMZ), Center for International Migration and Development (CIM)].

Mario-Cesar is especially grateful to the assistance provided by Dr. Rigoberto Vera, director of the Faculty of Sciences of the Michoacán University (UMSNH), by the authorities of the UMSNH itself and by the CONACYT (National Council of Science and Technology) of Mexico. Both institutions allowed the accomplishment of this book, providing the means and financial support for my sabbatical year in 2008. The help and hospitality provided by Professor Y. Tsompanakis of the Technical University of Crete, Greece, who invited me to spend a large part of my Sabbatical year in Xania at the Department of Applied Sciences is gratefully acknowledged. Special thanks goes also to my students, V. Chavez and F. Sanchez of the UMSNH for the elaboration and corrections of some graphics and figures. Additionally I express my sincere gratitude to the Coordinación de la Investigación Científica (UMSNH) and to the Consejo Estatal de Ciencia y Tecnología (COECyT) for their support of my research projects. I would like to thank the managers of the Comisión Federal de Electricidad—Geotermia in Morelia, Mexico, for their permission to reproduce some of the geothermal data herein presented.

Jochen Bundschuh
Mario-César Suárez Arriaga
March 2010

CHAPTER 1

Introduction

Accessibility to water and energy in sufficient quantity and quality are essential for human development. Hence provision of both these commodities accounting for their sustainable use and the need to mitigate global climate change by reducing greenhouse gas emissions are primary tasks of the 21st century. Increasing stress on water resources, and the need to better assess 'clean' energy resources such as geothermal energy, require the development and application of sophisticated, state-of-the-art tools such as numerical modeling. To illustrate this present-day world concern, we will start this introductory chapter with some information, mostly from the *UN organizations* on the global water problem and from the *Intergovernmental Panel on Climate Change* about the process of global warming related to the energy issue and cite their most important findings (sections 1.1 and 1.2). These reports highlight the importance of better addressing these issues guaranteeing the development and survival of humanity.

1.1 THE WATER PROBLEM—THE UN VISION

“Global freshwater consumption rose sixfold between 1900 and 1995—more than twice the rate of population growth. About one third of the world’s population already lives in countries considered to be ‘water stressed’—that is, where consumption exceeds 10% of total supply. If present trends continue, two out of every three people on Earth will live in that condition by 2025.”

Kofi Annan (2000)*

No one can live without water. Water and air are the essential elements for life in this planet and for the development and survival of humanity. Neither nature nor human technology can generate or create more water. The water existing on Earth transits through the continuous hydrological cycle of evaporation, condensation, infiltration, and flow. This water is the same fluid that existed for millions of years. The great difference nowadays is its quality and distribution.

It has recently entered public awareness that drinking water is a fragile and rare commodity. The immensity of the oceans and the constant renewal of the water cycle create the illusion that water is a simple and eternal fluid. However, recent figures from the UN (UNEP 2009) show that some 1200 million human beings lack access to drinking water and another 2000 million receive contaminated water. In other words, serious deficiencies in the supply and quality of this vital liquid currently affect almost half of humanity (February 2010: 6,912,334,200; source: <http://www.breathingearth.net/>). The ecological, social, technical, and political problems related to the supply of water are not caused by its amount, but by the irregular distribution of water on the planet, as well as the polluting influence of human activity.

The Earth contains approximately $1400 \times 10^6 \text{ km}^3$ of water and the oceans contain 97.5% of this total ($1365 \times 10^6 \text{ km}^3$, UNEP 2009). Freshwater resources represent about 2.5% of the total volume (35 million km^3). Of the total water, 1.7% (24 million km^3) is in the form of ice and perennial snow cover in the mountains, the Antarctic and Arctic regions. Therefore, only 0.8%

* Source: Kofi Annan in: *We the Peoples*, 2000.

(11 million km³) of the Earth's vital fluid is available to humanity and even this small portion is subject to constant pollution. (UNEP 2009).

Each year the oceans lose some 5×10^5 km³ of water into the atmosphere by evaporation. Only 9% of this amount falls as rain on land. Some 8 million km³ is stored in the form of groundwater basins, soil moisture and permafrost. This constitutes about 73% of all the freshwater that is potentially available for human use. Lakes and rivers contain approximately 105,000 km³ (0.3%) of the world's freshwater (UNEP 2009). Many ecologists, scientists and international experts believe that water availability will become a critical factor for the survival of mankind in the very near future. Water issues will determine the very future of life on Earth.

Today, water is considered as a finite, valuable resource of inequitable and unbalanced worldwide distribution in both social and geographical spaces. Industrial wastes, pesticides, natural arsenic, and diverse chemicals cause contamination of drinkable water. The demand increment produced by the demographic augmentation and water wastage creates a dangerous situation. Population pressures, increasing demands for space and resources, and poor economic performances can all undermine the sustainable use of water. Since 1900, water demand has been multiplied six times (UNEP 2009). Since 1940 the world population has an annual growth of about 2% while water extraction increases about 3% per year (León Diez 2005). At the present time people need an average of between 27 and 200 liters per day to satisfy their needs (León Diez 2005). Africa and the Middle East are the two regions of the world where there is less water. The American continent is the richest in hydraulic resources (León Diez 2005). The inequity in the consumption of water is evident when comparing figures of the UN (2003): Brazil, Canada, China, United States, India and Russia have the 40% of rivers and lakes of the planet. In Canada each inhabitant disposes of 91,640 m³ of water per year; in Australia, 26,032 m³; in Mexico, 4547 m³; in South Africa, 1109 m³ and in Egypt, 29 m³. According to the UN, (León Diez 2005) the quantity of water that a person needs is about 5000 m³/year. Having less than 1700 m³/year is called water stress; having less than 1000 m³/year is considered scarcity.

The United Nations Environment Programme (UNEP) compiled an updated a very useful report (*Vital Water Graphics*) on the state of the world's waters. This report focuses on the critical issues of water quantity, quality and availability—issues that are vital to the quality of life on Earth. Highlights from assessment activities over the past two decades, reveal the following conclusions (cited from UNEP 2009):

- Freshwater resources are unevenly distributed, with much of the water located far from human populations. Many of the world's largest river basins run through thinly populated regions.
- Groundwater represents about 90% of the world's readily available freshwater resources, and some 1.5 billion people depend upon groundwater for their drinking water supply. Groundwater is by far the most abundant and readily available source of freshwater, followed by lakes, reservoirs, rivers and wetlands.
- The amount of groundwater withdrawn annually is roughly estimated between 600 and 700 km³, representing about 20% of global water withdrawals. A comprehensive picture of the quantity of groundwater withdrawn and consumed annually around the world does not exist.
- Agricultural water use accounts for about 75% of total global consumption, mainly through crop irrigation, while industrial use accounts for about 20%, and the remaining 5% is used for domestic purposes.
- It is estimated that two out of every three people will live in water-stressed areas by the year 2025. In Africa alone, it is estimated that 25 countries will be experiencing water stress (below 1700 m³ per capita per year) by 2025. Today, 450 million people in 29 countries suffer from water shortages.
- Clean water supplies and sanitation remain major problems in many parts of the world, with 20% of the global population lacking access to safe drinking water. Water-borne diseases from faecal pollution of surface waters continue to be a major cause of illness in developing countries.

Polluted water is estimated to affect the health of 1.2 billion people, and contributes to the death of 15 million children annually.

1.2 THE ENERGY PROBLEM—VISION OF THE INTERGOVERNMENTAL PANEL OF CLIMATE CHANGE

“Modern society continues to rely largely on fossil fuels to preserve economic growth and today’s standard of living. However, for the first time, physical limits of the Earth are met in our encounter with finite resources of oil and natural gas and its impact of greenhouse gas emissions onto the global climate. Never before has accurate accounting of our energy dependency been more pertinent to developing public policies for a sustainable development of our society, both in the industrial world and the emerging economies.”

Minutes, Debate of Senate (Eerste Kamer), 2009 (in Dutch)*

Today (2010) the world is consuming about 85 millions barrels of oil/day (Mbod). In 2008, this consumption was 86 Mbod and was growing in that period by more than one Mbod per year. This increment is equivalent to discover a new oil province like Azerbaijan each year. Oil prices in July 2008 reached 145.29 USD per barrel (WTI). Because of the economical crisis, oil consumption reduced 0.5 Mbod in 2008 and 1.75 Mbod in 2009, and the oil prices decreased as well. However, the price in February 2010 was around 80 USD per barrel and the trend is to grow again (Oil-Price.Net 2010). Between 40 and 50% of worldwide oil demand is for transportation. In addition to the huge amount of gasoline required by the industrialized territories, there is an uncontrollable increase in the appetite for automotive fuel in several countries of Asia, Latin America, and Africa. On the other hand, the production costs of oil in reservoirs located in different regions are increasingly high (Chevron Corporation 2009). The total OPEC’s oil spare capacity was 10 Mbod in 1995; this capacity decreased to 2 Mbod in 2008. With or without crisis, there is no longer a safety margin to ensure price stability in the face of demand spikes and supply interruptions. Therefore, in the very near future we will have limited oil supply, increasing demand, higher oil prices, increasing pollution, and environmental impact from global emissions of greenhouse gases.

The Working Group I of the Intergovernmental Panel on Climate Change (IPCC), (Solomon *et al.* 2007, and IPCC homepage <http://ipcc-wg1.ucar.edu/wg1/>) provided an authoritative international assessment of how the activities of the human industry are affecting the radiative energy balance in the atmosphere. Their objective is to provide a scientific understanding of climate change. Concerning the key question: how are temperatures on Earth changing? the Working Group I furnished the following conclusive information:

“Instrumental observations over the past 157 years show that temperatures at the surface have risen globally, with important regional variations. . . . An increasing rate of warming has taken place over the last 25 years, . . . Confirmation of global warming comes from warming of the oceans, rising sea levels, glaciers melting, sea ice retreating in the Arctic and diminished snow cover in the Northern Hemisphere, . . . (and) decreases in the length of river and lake ice seasons. . . . the oceans are warming; and sea level is rising due to thermal expansion of the oceans and melting of land ice . . . Expressed as a global average, surface temperatures have increased by about 0.74°C over the past hundred years (between 1906 and 2005; Figs. 1.1 and 1.2).”

The human impact on climate during this era greatly exceeds that due to known changes in natural processes, such as solar changes and volcanic eruptions (Solomon *et al.* 2007) (Fig. 1.2). In the light of the available information, there is an urgent need to replace hydrocarbons by other, diversified, and clean primary sources of energy. Solar, wind, and geothermal energy

* Source: Minutes of the debat of the Senate (Eerste Kamer) of the Dutch Parliament, March 31st, 2009 http://www.eerstekamer.nl/stenogram/stenogram_254/f=x.pdf.

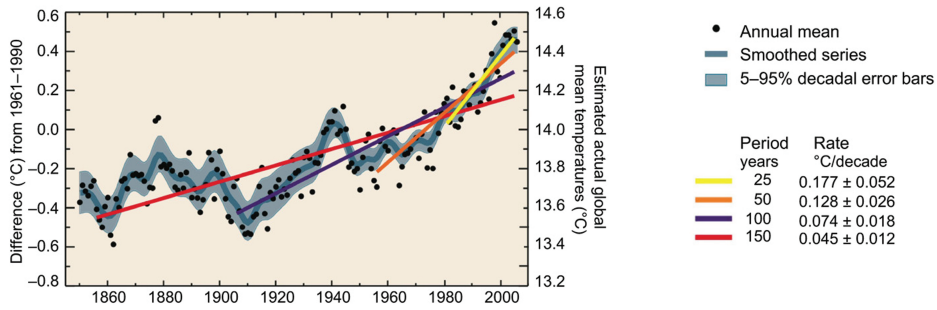


Figure 1.1. Annual global mean observed temperatures (black dots, from the HadCRUT3 data set) along with simple fits to the data. The left hand axis shows anomalies relative to the 1961 to 1990 average and the right hand axis shows the estimated actual temperature. Linear trend fits to the last 25 (yellow), 50 (orange), 100 (purple) and 150 years (red) are shown, and correspond to 1981 to 2005, 1956 to 2005, 1906 to 2005, and 1856 to 2005, respectively. From about 1940 to 1970 the increasing industrialisation following World War II increased pollution in the northern hemisphere, contributing to cooling, and increases in carbon dioxide and other greenhouse gases dominate the observed warming after the mid-1970s. (Solomon *et al.* 2007).

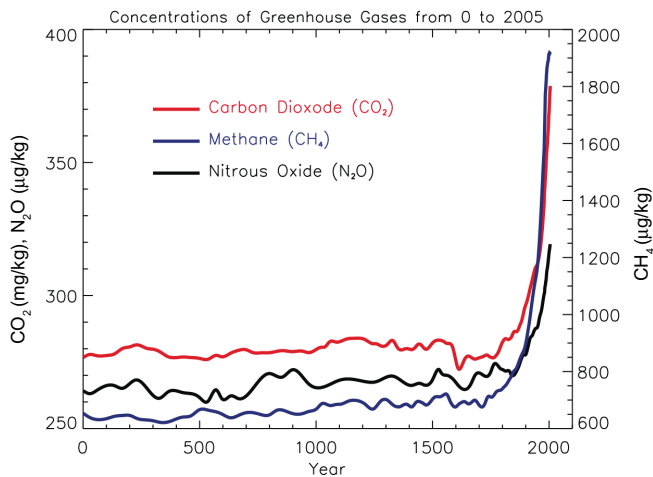


Figure 1.2. Summary of the principal components of the radiative forcing of climate change (Solomon *et al.* 2007).

are some of these sources able to replace advantageously coal, oil, gas and nuclear. Particularly, submarine offshore hydrothermal energy is one of the most important and enormous geothermal source that has never been used on Earth (Suárez-Bosche *et al.* 2005). Supercritical geothermal resources will enable the generation of electricity on an efficient, economical basis through turbine-generators on the ocean floor that will supply the grid's demand for electricity. This approach generates electricity from geothermal energy from a vast, high-temperature resource never before accessed. Technological improvements will increase efficiency enough to enable geothermal energy to compete with traditional power plants on cost. This approach will also access much more extensive geothermal resources than the land conventional resources currently used.

1.3 MULTIPHYSICS MODELING OF ISOTHERMAL GROUNDWATER AND GEOTHERMAL SYSTEMS

“Scientific computing has often been called the third approach to scientific discovery, emerging as a peer to experimentation and theory. Historically, the synergy between theory and experimentation has been well understood. Experiments give insight into possible theories, theories inspire experiments, experiments reinforce or invalidate theories, and so on. As scientific computing has evolved to increasingly produce computational results that meet or exceed the quality of theoretical and experimental results, it has become an indispensable third approach. . . The synergy of theory, experimentation, and computation is very rich.”

Michael A. Heroux, Padma Raghavan and Horst D. Simon, 2006*

The scientific study of transport processes in natural porous fractured systems, such as aquifers, petroleum, gas and geothermal reservoirs, is relatively recent. Over the last 40 years, several research methods have been developed based on experimental data and mathematical approaches. To understand the complicated mechanisms of flow occurring in these scenarios, various mathematical methods have been employed: analytical methods were initially used, followed by analog models and most recently, numerical models. One of the main problems is the difficulty in accurately representing the dimensions and spatial distribution of fractures and faults created by geologic and tectonic processes of a random nature. In hydrothermal systems (convection-dominated geothermal reservoirs), the transport of mass, momentum and energy is a non-isothermal process with phase changes, where dissolved salts, non-condensable gases and the distribution of petrophysical parameters are of great importance.

In the scientific study of nature it is necessary to make numerical operations of diverse degrees of complexity, from elementary to high mathematical sophistication. The development of mathematical models is justified by the help they bring in the understanding and verification of specific mechanisms and behaviors of natural systems. In addition, their cost is considerably lower compared to any other technique. Furthermore, numerical models can be subjected, without any risk, to the most critical operation conditions. The utility of modeling is specific to the natural systems because physical scale models of them cannot be made in the laboratory. The “prediction” and “retro-diction” capacities of mathematical models allow the quantitative estimation of future behaviors that are yet to be observed, as well as the estimation of processes that are no longer observed, but that were the antecedent of the current phenomenon. Numerical simulation is irreplaceable as a tool for analysis and synthesis, to achieve an ongoing coherent integration of information on the reservoir, as its lifespan advances. Other research techniques offer only a partial perspective on the global system. The mathematical model and its associated numerical code can be used to combine and to verify several complex hypotheses and to test them against the observed facts and data. Petroleum, gas, water and heat reservoirs are examples of complex natural systems. To understand the mass and energy flows in these systems, the development of integrated models is required.

In this book we define aquifers in the classical sense: groundwater systems of low temperature ($<37^{\circ}\text{C}$), which correspond generally to freshwater resources, providing water for drinking, irrigation and industrial purposes. With very few exceptions, these aquifers can generally be treated as isothermal systems, where temperature variations in time and space are not of interest. In addition, we will focus on geothermal systems of variable temperature ($>37^{\circ}\text{C}$), which are used as energy resources either for direct use or for electric power generation. These systems—with the exception of very simple cases—should be treated as non-isothermal reservoirs and in some instances, the occurrence of both the liquid and the vapor phase of water has to be considered. The presence of other phases such as non-condensable gases and dissolved species such as ions,

* Source: Parallel Processing for Scientific Computing, SIAM, 2006.

further increase the complexity of the system. To simplify the nomenclature, we will distinguish these two groups with regard to their use, by referring to the first group as “*cold aquifers*” (isothermal groundwater, freshwater aquifers, etc.) and the second group as “*geothermal systems*” (geothermal reservoirs, geothermal resources, geothermal fluid, etc.). It is worth remembering that the physical laws and mathematical descriptions which apply to geothermal systems are also valid for isothermal aquifer systems.

Numerous interacting parameters, variables and functions drive the movement of groundwater and steam, and the transport of heat, solutes and gases. With the exception of some very special cases, these transport processes are coupled through (1) the interstitial pore velocity, (2) the dependence of fluid density on pressure, temperature and solute-mass fraction, (3) the dependence of the fluid viscosity on temperature and solute-mass fraction, and (4) the rock poroelasticity. As a consequence these processes can only be described using numerical methods. The influences of the numerous variables, which may be functions of space and time and may also be dependent on temperature, pressure, etc., govern mass and heat transport and their interactions. All of these functions should be considered at the same time. Hence, mathematical, computational and numerical modeling become vital tools for the analysis of isothermal aquifers and geothermal systems.

The most important problem for the general scientific development of reservoir engineering is the dearth of data in some areas and its abundance in others. The nature of this discipline means that it is always necessary to formulate ideas based on incomplete information. It is also not possible to construct physical scale models which fully represent the reservoir. Computer numerical simulation can then achieve an integral detailed description of the reservoir by reproducing the available robust data. Once some approximate reproduction is achieved, extrapolation may be applied to predict the future behavior of the system as it is subjected to different exploitation scenarios with different levels of uncertainty.

As mentioned above, the principal difficulty in establishing an accurate numerical model is due to the very limited availability of spatial and chronological field data. This can be readily appreciated if we consider, for example, the parameter dispersivity. It is now well recognized that this parameter, which is important in modeling solute transport in aquifers, is not measurable in field situations unless we have a very well-defined simple aquifer fabric, such as that found at some experimental test sites. For real problems, dispersivity is merely a fitting parameter that covers our lack of knowledge of the true flow patterns. It cannot be inexpensively measured except in the immediate vicinity of a well. Furthermore, it is often spatial-scale-dependent and time-dependent; thus, a single constant value does not often adequately describe what we measure or wish to predict in the field. Such a lack of input data must be overcome by indirect estimation of data ranges, and the model has to be applied carefully to obtain useful results from the modeling analysis. Therefore, a good understanding of the limitations of the data and modeling tools is vital for the intelligent application of modeling.

1.4 MODELING NEEDS IN THE CONTEXT OF SOCIAL AND ECONOMIC DEVELOPMENT

The availability of freshwater and energy are intrinsically linked to human social and economic development. Water and energy resources are increasingly limited. At the same time, the demand for these resources is increasing sharply due to population and economic growth. This effect is greatest in the developing world with their higher population growth rates, their fast-expanding emerging economies and related increase in living standards. This can be clearly demonstrated using the parameter “electricity demand”, the world-average of which is predicted to increase by a factor of two from 2004 to 2030 (EIA 2007), with an annual average grow rate of 3.5% in developing countries (non-affiliated with OECD: Organization for Economic Cooperation and Development), compared with a growth rate of 1.3% in industrialized countries (OECD) (EIA 2007).

Several regions of the planet are experiencing a worsening water shortage. The supply of freshwater is a crucial issue in the many countries that have very limited resources. For example,

the Mediterranean region is considered to be “poor” in water because 180 million people living there have less than 1000 m³ per capita per year (LeMonde, 23 December, 2008). Of these, sixty million are surviving with less than 500 m³/year. This situation is worsening because of increasing population growth, the consequences of climate change and pollution, which renders the water unsuitable for consumption. In many regions, rivers and aquifers are shared between different countries, which increases the risk of conflict. Some examples are the Guaraní aquifer in South America, the Nubian sandstone aquifers in northern Africa, the Karoo aquifers in southern Africa, the Vechte aquifer in western Europe and the Slovak Karst-Aggtelek aquifer and the Praded aquifer in Central Europe. Nations facing a lack of water look first to secure new sources of supply by the expansion of drilling, the creation of dams, and the construction of pipelines. These policies have their limits due to problems associated with overexploitation of aquifers, jeopardizing the natural groundwater recharge, or drawing on fossil reserves.

In consequence, the security of long-term freshwater and energy supplies is a global cause of concern. In order to meet future freshwater and energy demands, it will be necessary to develop “improved tools” for better exploration and exploitation of groundwater resources, which constitute over 99% of the world’s freshwater and energy sources including the geothermal resources, which have a potential for power generation that is much greater than that of all fossil fuel resources combined. Geothermal resources can be tapped to meet the increasing demand for electric power by applying modern heat-exchanger technologies, binary-fluids, drilling-technologies, and submergible-pumps. These technologies allow the exploitation of previously technically and economically inaccessible low-enthalpy (<150°C) convection-dominated geothermal resources and conduction-dominated enhanced geothermal systems (EGS) (both, high- and low-enthalpy systems) that are found in practically every country on the Earth (Chandrasekharam and Bundschuh 2008).

Although numerical modeling has been used in past decades as a standard application in different fields of mechanical, civil engineering and design its application to isothermal groundwater systems and geothermal systems has developed slowly during the last four decades and still today is not implemented to its optimal capacity. The improvement of computer technologies during the last two decades allows actual modeling of complex coupled subsurface processes, which was not possible a few years ago. This development in hardware today makes the limitation of field-data the principal limitation of the application of numerical modeling in hydrogeology and geothermics.

Before we describe a natural real-world problem, such as an isothermal aquifer system (freshwater resources), or a geothermal system (non-isothermal fluids) by applying numerical modeling, it should be appreciated that these systems are much more complex than most other mechanical engineering problems, where numerical modeling has been used as a standard tool for several decades. An isothermal aquifer system is a complex natural underground system involving coupled mechanisms which control mass, solute, and energy transfer in poroelastic rocks, with the Earth’s surface acting as a boundary. In the case of geothermal systems, the circulation of hydrothermal fluids, comprising liquid, steam, and gases, is a fundamental complex coupled process controlling mass, solute and energy transfer from the Earth’s mantle and crust through the subsurface up to the surface, where geothermal fluids may emerge as hot springs, fumaroles or steam vents.

In the following part of this chapter we will discuss recent developments in the area of freshwater and energy resources and give some examples of the worldwide importance of increasing the implementation of numerical modeling for improved assessment and sustainable exploitation of these resources, and for problem solving.

1.4.1 *The role of groundwater for drinking, irrigation, and other purposes*

Increasing limitations on the availability of surface water caused by its seasonal fluctuations and its continuously quality degradation due to anthropogenic contamination, make groundwater the principal water source in many areas. The importance of groundwater will undoubtedly increase

in the future as it is required as drinking water and for crop irrigation to sustain food supplies to an increasing world population (Bhattacharya *et al.* 2008). However, groundwater resources are under increasing stress, both in terms of quantity and quality. This, together with the growing importance of groundwater, demands a better understanding of the critical processes related to aquifer systems, which necessitates the development and application of improved tools, such as numerical modeling, to permit the identification and quantification of processes occurring in the aquifer and allow the prediction of these processes and their effects. This action should mitigate the negative impacts of these processes and help to identify optimal approaches for the assessment, management, and protection of groundwater resources, in order to achieve long-term sustainability.

Groundwater flow simulation can be applied to investigate groundwater recharge and recovery, where the consequence of the groundwater withdrawal through wells, horizontal wells or filter galleries on the natural groundwater flow field (e.g. decrease of the groundwater table or pressure), can be simulated and used to determine the optimal type and location of a withdrawal installation (a group of wells and the location of single wells in it, horizontal well, filter gallery), and respective withdrawal rate(s). Beyond its use for groundwater management tasks, groundwater flow simulation can also be used for other applications, including the simulation of well hydraulics and the evaluation of pumping and infiltration tests to determine aquifer parameters, and for numerous tasks in civil engineering, such as designing proper drainage in excavation pits or determine water influx in tunnel constructions. In hydroelectric projects, the accurate simulation of water percolation through, below, and around storage dams, is important for the design of proper measures to reduce the respective flow rates, for example, by the use of liners or injections. In addition, the filling of storage lakes and the impact on the natural groundwater flow field can also be simulated. In areas with limited natural aquifers, numerical modeling is an important tool to optimize the augmentation of water supplies, e.g. by artificial recharge.

Groundwater flow simulation can be coupled with solute transport simulation and may be applied to model natural or anthropogenic-induced chemical species transport, including processes of solute sorption, production and decay. This procedure may be applied to analyze groundwater contaminant transport problems, and aquifer vulnerability (contamination hazard and risk), to define aquifer remediation measures in cases of contamination, and to delimit protection zones around groundwater capture areas. Numerical transport modeling can be further applied to the analysis of problems such as those related to subsurface-waste injection, landfill leaching, and the evaluation of tracer tests. It is suitable to simulate complex redox- and pH-dependent chemical and biochemical reactions which occur in the groundwater during its movement in an aquifer. One example is the occurrence of geogenic contaminants in groundwater such as arsenic, which is found at toxic levels in many regions of the world, making it a major environmental health risk for the 21st century (see e.g., Bundschuh *et al.* 2005, 2009, Bhattacharya *et al.* 2007a, b and 2008). In order to supply safe drinking water to the tens of millions of people affected, an improved understanding of the hydrogeochemical processes responsible for high levels of arsenic in groundwater is required. Hence, numerical modeling is a reliable tool with which to examine natural and anthropogenic contamination processes of aquifers, by forecasting contamination propagation, and defining optimal remediation measures.

Another important application is the modeling of salt water intrusions into freshwater aquifers. Worldwide, coastal aquifers are increasingly affected by salinization due to sea water intrusions caused by excessive groundwater exploitation in coastal areas. Here, numerical modeling combined with extensive groundwater monitoring, can optimize freshwater exploitation and avoid or reduce salinization of aquifers.

In special cases, heat transport has to be considered, e.g. in relation to applications such as seasonal heat storage underground, the storage of radioactive waste and other situations where temperature changes in aquifers are of importance. Heat transport may also be of interest if we wish to describe the mixing of waters of different temperatures, as occurs during groundwater-surface water interactions. In this case, heat may be used as a tracer to identify and quantify mixing processes, such as infiltration of river water into an aquifer, or groundwater recharge processes due

to precipitation, which can further be used for assessing the groundwater contamination potential from contaminated surfaces or rivers. In addition, heat transport is of interest, e.g. if we want to model processes resulting in temperature variations in spring water or shallow groundwater, which are related to temperature changes at the Earth's surface (Bundschuh 1992, 1993a, b, 1995).

1.4.2 Geothermal resources

The geothermal option for electricity generation has recently been recognized as the optimal—economically and environmentally sound—choice to meet much of the future electricity demand and guarantee energy security and energy independence of both developing and developed countries (Chandrasekharam and Bundschuh 2002, 2008, Aaheim and Bundschuh 2002, Bundschuh *et al.* 2002, 2007, Bundschuh and Coviello 2002; further information can be found on the homepages of the International Geothermal Association (IGA2009a, b) the Geothermal Resources Council (GRC 2009) and the Geothermal Education Office (GEO 2009)).

Recent innovations in the form of binary fluids, heat exchangers, and drilling technologies have made the commercial exploitation of low-enthalpy convective geothermal resources ($< 150^{\circ}\text{C}$) and conductive enhanced geothermal systems (low- and high-enthalpy) possible (Chandrasekharam and Bundschuh 2008).

Convection-dominated high-enthalpy geothermal systems (vapor- or liquid-dominated; $> 150^{\circ}\text{C}$) are related to volcanic and/or tectonic active areas, and therefore are only found along active plate boundaries in both the continents and the oceans. At these locations, uprising magma or deep-seated intrusives are the main source of heat for low- and high-enthalpy convective geothermal systems, whose main source of thermal fluid is meteoric water. Convective low-enthalpy resources have considerably greater geothermal potential than high-enthalpy systems, and much larger regional distribution since they are not limited to active tectonic plate boundaries. Despite these benefits, low-enthalpy systems are practically unutilized for electricity generation in both developed and developing countries (Chandrasekharam and Bundschuh 2002, 2008, Bundschuh and Chandrasekharam 2002, Bundschuh *et al.* 2002, 2007), even though geothermal water with temperatures as low as 80°C can be used for economical commercial electricity generation with currently available technologies.

Enhanced geothermal systems (EGS), which are not limited to volcanic and/or tectonic active areas such as convective high-enthalpy geothermal systems, have even greater potential. In these systems, heat is provided by the natural radioactivity of elements like U, Th, and K, and the conduction of heat from the mantle to shallower levels along deep continental crust (Chandrasekharam and Bundschuh 2008). EGS, which are available in practically every country, have received greater attention in recent years. According to the MIT report (MIT 2006), the USA alone has an EGS potential of about 13,000,000 Exa Joules ($\text{EJ} = 10^{18}$ Joules) (depth 3–10 km), of which 200,000 EJ can be extracted for utilization, which corresponds to about 2000 times the annual primary energy consumption of the country in 2005. By 2050 the USA could economically generate about 100,000 MW_e with modest R&D investment (MIT 2006). Recent increases in the cost and uncertainty surrounding conventional energy supplies make these EGS resources increasingly attractive. These developments in the USA are following the international progress in the development of EGS and related technologies, which has obtained considerable interest in Europe and Australia over the last few years. It is especially important that developing countries, which can all access low-enthalpy convective and conductive EGS sources for electricity generation, are aware of these resources. For many of these countries, the exploitation of low-enthalpy resources is not new since they have been used over the past centuries for bathing, and for direct applications the last few decades (Chandrasekharam and Bundschuh 2008). Lund *et al.* (2010) reported direct use production data from these systems in 78 countries in the year 2010 (72 in the year 2005).

The accelerated growth of interest in geothermal systems requires further development of sophisticated software and the creation of numerical models to facilitate geothermal exploration and exploitation, and to sustain long-term productivity. To understand both convective and conductive geothermal systems, the geological and tectonic features that control them needs to be

thoroughly understood. Simple numerical models of geothermal reservoirs (including scenario modeling) can assist in understanding these systems during pre-drilling stages, and as more data become available, more sophisticated models, e.g. those that include thermoporoelastic processes, can be developed. The development of these tools can be ongoing during drilling and exploitation, to help ensure that convection-dominated geothermal reservoirs are utilized optimally in a sustainable way. In the case of EGS, the heat exchange between rock and the artificially circulated fluids along the reservoir fractures can be modeled to assist managers during the exploration phase (e.g. in decisions about artificial fracturing used to increase the volume of the fluid space), and to ensure optimal exploitation of the system. This involves modeling hydraulic fracturing using high fluid pressure on a reservoir to enhance the existing permeability and establish connectivity between adjacent fractures by opening sealed joints or by creating new fractures to allow geofluids to move more freely through the rock formation. This is an interesting application that is used to assist in the design and to optimize the outcome of the fracturing process.

1.5 THE NEED TO ACCELERATE THE USE OF NUMERICAL MODELING OF ISOTHERMAL AQUIFERS AND GEOTHERMAL SYSTEMS

Compared to the aforementioned advances in computer technologies, numerical methods, and the identification of application possibilities, the use of numerical modeling in hydrogeology, particularly its application to geothermal systems, is still rare. The main reason for this is the gap between the people involved in this issue and their respective knowledge. The principal groups on one side include software developers, engineers, and applied mathematicians, who may have insufficient knowledge about the geological, hydrogeological or geothermal background and hence of the application possibilities of numerical models and the respective software needs, so that the design of the software is not optimal. An insufficient understanding of subsurface processes occurring in groundwater and geothermal systems makes the developers unaware of the numerical needs to optimize model calibration subprograms and tools that handle the problem of irregularly available data in time and space. On the other side, there are the hydrogeologists and other groundwater professionals or geothermists, who may have little knowledge of numerical methods, application possibilities, or the correct application of models. In particular these groups lack expertise in (1) the elaboration of an accurate conceptual model, (2) the selection of the appropriate model code suitable for the elaborated conceptual model (or in a few cases the proper elaboration of a numerical program code), (3) the discretization of the model area in space and time to establish the numerical model, (4) the correct calibration and validation of the model by selecting the appropriate calibration and validation parameters, and (5) the correct evaluation of the simulation results and reliability considering the model uncertainties, that are related to the uncertainty of the data used to test the selected conceptual model.

This book aims to bridge these knowledge gaps and to provide integrated information on numerical modeling in hydrogeology and geothermics for all those involved. We hope to show that numerical modeling is a reliable tool, which should be implemented for the improved integral management of groundwater and geothermal resources. However, users must always approach numerical models and their simulation results with a critical eye. It should be remembered that numerical models are tools and that the quality of the simulation results depends on the preparation of the conceptual model, knowledge of the geological situation, the hydrogeological and hydrogeochemical parameters and the data, particularly the initial and boundary values.

The basis of this book is the idea that specific mathematical models can be generated and solved: models that are useful in underground hydrology and in geothermal systems with transport of mass, heat and solutes. The fundamental laws and concepts of fluid, energy and solute transport in poroelastic rocks, as well as their mathematical representation, are introduced and discussed in detail. Thereby the mass and heat transport processes and models have been expressed in general form, valid for all types of aquifers: isothermal aquifers, where heat transport is normally not of interest, and convective geothermal systems, where heat transport and the presence of liquid

and steam are of particular interest. In addition, the models and methodologies that have been developed are valid for conductive enhanced geothermal systems, where the fluid is artificially circulated through natural or artificially produced fractures within the geothermal reservoir.

The major themes of the book are divided into chapters arranged according to their fundamental and practical importance. After a detailed overview of rock and fluid properties (chapter 2), special properties of heterogeneous aquifers are discussed (chapter 3) followed by a description of the hydraulic properties, the processes and respective governing equations of fluid flow, solute and heat transport (chapter 4). In chapter 5, the principal numerical methods, comprising the finite difference method (FDM), finite element method (FEM), surface-integrated finite difference method (SIFDM) or finite volume method (FVM), and the boundary element method (BEM) are addressed. Chapter 6 gives a step by step overview of how to construct a numerical model: (1) defining the specific objectives, (2) development of an accurate conceptual model suitable for the specific case and modeling objectives, (3) construction of the mathematical model, (4) elaboration of the numerical model and its calibration and validation, and finally sensitivity analysis. This process is illustrated by a simple practical example. In chapter 7, inverse methods for parameter estimation that are useful, e.g. for numerical model calibration, are introduced and applied to simple examples. Chapter 8 contains a number of simple illustrative examples of modeling applications used for different hydrogeological tasks, and shows how they were constructed based on limited data, while chapter 9 presents selected examples of modeling geothermal systems. Chapters 6, 8, and 9 describe the standard procedure for constructing models using simplified examples from practical applications. The correct formulation of the initial values and boundary values are treated in detail. Special emphasis is given to the incorporation of the field investigations and field data into the model, with consideration of the necessary and permitted simplifications and the resulting consequences to the quality of the simulation results. There is free software for the book available at the site: <http://www.fismat.umich.mx/~mario/c/> in FORTRAN, Mathematica and Matlab programming languages. This site will be interactive, containing software in continuous growth, and focusing on the numerical aspects of different topics treated in the book.

Each of the natural phenomena and processes discussed here are the product of several interacting components that form a “complex system”, or a so-called “multiphysics system”. The properties and behavior of complex systems cannot be thoroughly explained by understanding each of the separate parts in isolation. These systems act as a whole and the interactions of all components must be considered to understand their operation. Sophisticated numerical modeling is the only tool able to accomplish these integrated studies. For example, crustal rocks are poroelastic and the presence of fluid inside the pores affects their geomechanical properties; therefore, a realistic model of groundwater flow must take into account the rock deformation.

The most important step in engineering practice and in applied science is the idealization of reality, which is the process of creating a mathematical model from a physical system. The word “model” has the traditional meaning of a small-scale representation of a real object. Here, we use this term to mean a symbolic device built to compute, simulate, and predict aspects of reservoir processes. Mathematical modeling is an abstraction tool by which complexity can be controlled by “filtering out” physical details that are not relevant to the analysis process. A continuum material model of porous rocks, for example, filters out the crystal, molecular and atomic levels of matter. Creating a mathematical model is equivalent to choosing an information filter. In this book, different models and numerical techniques useful in reservoir engineering are explained in detail. To read the book it is not necessary to be an expert in mathematical modeling, or to have an extensive knowledge of computational mathematics. Each chapter is self contained, starting with an explanation of the problem, and then describing the form of the model and the numerical techniques available to solve it. It is hoped that the reader will acquire a thorough understanding of each topic covered. In the future other volumes will be dedicated to specific problem solving techniques and to real-world case studies, where numerical modeling has been applied to simulate non-isothermal processes in groundwater and geothermal systems.

CHAPTER 2

Rock and fluid properties

“Soil [and rock] mechanics arrived at the borderline between science and art. I use the term “art” to indicate mental processes leading to satisfactory results without the assistance of step-for-step logical reasoning. . . . To acquire competence in the field of earthwork engineering one must live with the soil [rock]. One must love it and observe its performance not only in the laboratory but also in the field, to become familiar with those of its manifold properties that are not disclosed by boring records. . . .”

Karl Terzaghi (1883–1963)*

2.1 MECHANICAL AND THERMAL PROPERTIES OF POROUS ROCKS

Porosity and conductivity (or permeability) are the two main hydraulic properties of rocks in subsurface reservoirs (freshwater aquifers, geothermal systems, hydrocarbon reservoirs). Porosity measures the ability of the rock to store fluids in pore spaces and in fractures. The hydraulic conductivity K_H describes the ease with which a fluid can move through open rock conduits. The main geomechanical parameters of rocks are: absolute permeability k , Young’s modulus of elasticity E , rock bulk compressibility C_B , Poisson’s ratio ν , Lamé coefficient λ , shear or rigidity modulus G , bulk modulus K_B and thermal expansivity γ_B . All the petrophysical properties are measured in the laboratory specifically for each system.

Apart from convection and radiation, there are three main modes of storage and heat exchange between rocks and fluids in aquifers and in geothermal reservoirs. These modes are thermal conductivity k_T , isobaric heat capacity c_p and thermal diffusivity δ_T . The conduction of heat occurs by contact, at the molecular level, between two media with different temperatures. Heat capacity measures the quantity of thermal energy required by a rock mass to change its temperature. This property quantifies the capacity of the reservoir to store heat. The thermal diffusivity is the reservoir’s property of driving heat with respect to its capacity to store it. We will introduce the rock parameters in this chapter from a practical and experimental point of view.

2.1.1 Absolute permeability

The permeability k of a porous rock is its natural capability to transmit fluids through interconnected pores. The permeability of a fractured rock is its intrinsic ability to transmit fluids through interconnected fissures. Fluids prefer the path of least resistance flowing always into trajectories with the highest permeability. Rocks that transmit fluids easily are described as permeable, having many large, well-connected pores and fractures. Absolute permeability is the measurement of this capacity when a single fluid is present in the rock. Global permeability depends on the quantity, size and form of the pores, on the topology of fissures and on their mutual interconnections (Fig. 2.1). These concepts can also be applied to the permeability of faults and fractures. The units of permeability are the m^2 , the Darcy [D] ($1 \text{ D} = 9.86923 \times 10^{-13} \text{ m}^2$), and the millidarcy [mD] ($1 \text{ mD} = 10^{-3} \text{ D} \approx 10^{-15} \text{ m}^2$). The permeability can be a simple number or a matrix

* Source: D. Goodman: *Karl Terzaghi, the Engineer as an Artist*. ASCE Press, 1999.

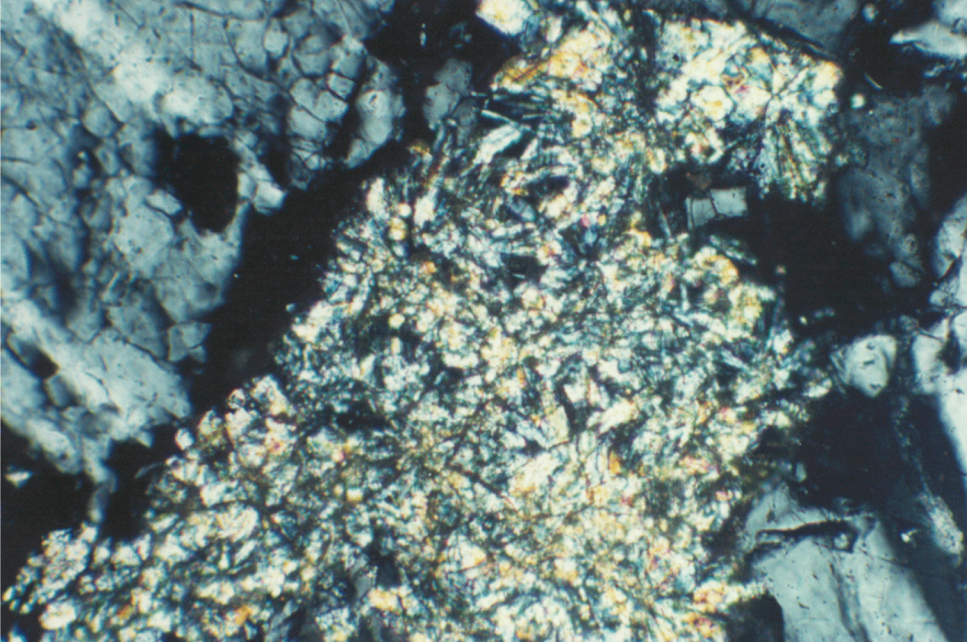


Figure 2.1. A microphotograph of a volcanic porous rock with a sealed fissure (~ 1 mm width) and microfractures ($\sim 10^{-3}$ mm), Los Azufres geothermal field (Mexico).

(tensor), depending on the availability of measured data. Cores from geothermal rocks show four types of coexistent permeabilities (Suárez 1995):

- permeability related to the intergranular spaces of the porous rock,
- micropermeability associated to interconnected microfractures,
- permeability related to nets of fractures,
- macropermeability of open faults.

The first two permeabilities obey Darcy's law of laminar flow. The last two permeabilities are especially sensitive to high fluid extraction rates that can generate turbulence. In this case non-linear or non-Darcian laws are applied (see section 4.5.4).

A purely quantitative definition of permeability is obtained directly from Darcy's law (see equation 4.12) in horizontal direction (x) of one dimensional flow:

$$v_x = -\frac{k_x}{\mu_f} \frac{\Delta p}{\Delta x} \Rightarrow k_x = \mu_f v_x \left(-\frac{\Delta x}{\Delta p} \right) > 0 \quad (2.0)$$

where v_x is specific flow rate [m/s], μ_f is fluid dynamic viscosity [Pa · s] and $\Delta p/\Delta x$ [Pa/m] is the pressure gradient. It follows that k_x has natural units of [m²]. A value of $k_x = 1$ D, for a $\Delta p/\Delta x = 10^5$ Pa/cm and $\mu_f = 10^{-3}$ Pa · s, gives $v_x = 1$ cm/s. Measurements of k_x in rock cores and pressure tests carried out in fractured reservoirs (Suárez 2000a, Suárez *et al.* 1989), show a very wide range of permeability values, from microdarcys up to hundreds of darcys (10^{-18} , 10^{-10} m²). The lower values correspond to porous rock without fractures; the higher values are typical of intensely fractured rocks (nets of fractures) or of open faults. Thermal and mechanical stresses affect the rock's absolute permeability. Experimental data show that, independently of the nature of the fluid, the compressions created by high confining pressures always reduce permeability. This poroelastic effect can cause the partial or total collapse of pores and fractures reducing the effective fluid flow area.

On the other hand, the temperature effect on the permeability depends on the type of fluid present. In oil saturated cores, a slight permeability increment has been observed when the temperature increases, possibly because of both the increment of pore pressure and the reduction of oil viscosity. In the case of gas-saturated rock cores, the permeability is independent of the temperature. However, in liquid water saturated cores, permeability reductions up to 65% have been observed inside an experimental range between 21°C and 163°C (Suárez 2000a). Ramey *et al.* (1974) reported similar results for cores of sandstone, where a permeability value of 1350 mD at 24°C, falls down to 500 mD at 163°C. This effect can be created by the extra thermo-mechanical stress in the rock, caused by dilatation of the solid due to increased temperature. The fluid-rock geochemical interaction also affects the absolute permeability by the accumulation of minerals in pores and fractures.

2.1.2 *The skeleton: Bulk, pore and solid volumes; porosity*

There exist two overlapping continua, the skeleton and the fluid, which form the reservoir porous rock. The volume of interconnected pores and fractures that contribute to fluid flow in the porous system is the effective pore volume V_{Φ} [m³]. The solid volume V_s is the volume of the rock solid grains, omitting the volume of the holes (Fig. 2.2). The volume of the simple pores V_P and the volume of the fractures V_F compose the total pore volume V_{Φ} . The bulk volume V_B is the skeleton formed by the union of V_{Φ} and V_s :

$$V_B = V_{\Phi} + V_s \tag{2.1a}$$

$$V_{\Phi} = V_P + V_F \tag{2.1b}$$

The natural porosity is the fraction of void space in the rock where the void may contain water, brine, oil, air or other fluids. In a fully saturated rock, the effective pore volume V_{Φ} defines the dimensionless effective porosity φ [ad] and V_s establishes the fraction of the solid phase in V_B :

$$\varphi_f = \varphi = \frac{V_{\Phi}}{V_B}, \quad \varphi_s = \frac{V_s}{V_B} = 1 - \varphi \tag{2.1c}$$

$$\varphi + \varphi_s = 1, \quad \frac{1}{V_B} = \frac{\varphi}{V_{\Phi}} = \frac{\varphi_s}{V_s} \tag{2.1d}$$

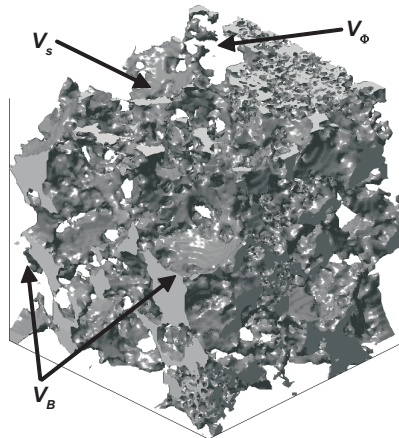


Figure 2.2. Skeleton of a sandstone with pore spaces in 3D. Dimensions: $\sim 3^3$ mm³ (adapted from Piri 2003).

The skeleton is the bulk or global volume V_B occupied by the solid rock with its pores and fractures. Note that φ and φ_s are the fractions of porous and solid volumes with respect to the bulk volume V_B . In this book we identify ΔV_B as the representative elementary volume (REV) of the porous rock, as it was accurately defined by Bear (1972). Total porosity also takes into account the rock isolated pores, but they do not contribute to the fluid flow. The sealed pores are considered as part of the solid. For this reason, we consider only the effective porosity. In a fractured porous rock, we can define two partial porosities, the porosity of the fractures, and the porosity of the simple pores. Their mathematical definitions are:

$$\varphi_P = \frac{V_P}{V_B}; \quad \varphi_F = \frac{V_F}{V_B}; \quad \varphi_P + \varphi_F + \varphi_s = 1 \quad (2.1e)$$

Effective rock porosity is an important parameter when evaluating the volume of water or hydrocarbons the system may contain. Effective porosity depends on many factors, but it is always reduced by the lithostatic load and decreases with depth. Permeability shows the same trend, it increases when porosity augments. Four common approximate relationships between porosity and depth and between porosity and permeability for homogeneous rocks are given by the following formulae:

a) Athy's equation (1930): $\varphi(z) = \varphi_1 e^{-c_k z}$ (2.2a)

b) Kozeny's equation (1927): $S_p = \frac{\text{surface area}}{\text{pore volume}} \Rightarrow \varphi(k) = k_z S_p^2$ (2.2b)

c) Pearson's equation (1976): $k(\varphi) = 10^{(13.614 \varphi - 1.8126)} \times 0.987 \times 10^{-15} \text{ [m}^2\text{]}$ (2.2c)

d) Rutqvist's equation (2002): $\varphi(k) = \varphi_0 \left(1 + C_0 \text{Ln} \frac{k}{k_0} \right)$ (2.2d)

where φ_1 is surface reference porosity, $c_k \text{ [m}^{-1}\text{]}$ is the compaction coefficient and $z \text{ [m]}$ is depth in equation (2.2a). For the second and third equations (eq. 2.2b,c), φ is porosity and k is the permeability. In equation (2.2b) $k_z (\approx 0.5 \text{ m}^2)$ is the Kozeny constant. In equation (2.2d), φ_0 and k_0 are porosity and permeability at zero stress and C_0 is an experimental parameter to be measured for different rocks. Using data from Table 2.1, we obtain $10^{-3} \leq c_k \leq 3.2 \times 10^{-4} \text{ m}^{-1}$

Table 2.1. Petrophysical properties of andesite cores from the Los Humeros, Mexico geothermal reservoir (adapted from Contreras *et al.* 1990).

Well	Depth (m)	ρ_r (kg/m ³)	φ (%)	k (mD)	E (10 ⁴ MPa)	ν	C_B (10 ⁻¹¹ Pa ⁻¹)	k_T (W/m ^o C)	c_p (J/kg ^o C)
H02	616	2160	19.7	0.019	2.09*	0.27	—	1.54	1046.7
H22	663	2250	18.1	0.096	2.08*	0.28	8.6	1.96	1088.6
H04	907	2240	19.4	0.086	1.60*	0.39	9.2	1.96	1046.7
H29	1200	2250	18.4	0.334 ^f	2.53	0.30	12.5	1.86	1046.7
H10	1469	2620	6.1	0.026	1.99*	0.18	7.3	1.61	1088.6
H27	1500	2400	10.1	0.145 ^f	3.32*	0.23	—	1.89	1130.4
H18	1750	2340	14.7	0.005	2.69	0.20	8.5	2.42	921.1
H19	1769	2460	11.5	0.147 ^f	2.05*	0.31	7.7	1.91	1172.3
H26	1810	2670	4.5	1.873 ^f	2.77*	0.42	7.7	1.95	1004.8
H23	1924	2370	13.9	1.252 ^f	3.19*	0.37	6.5	1.82	1088.6
H24	2297	2370	11.6	0.070	4.11*	0.42	4.8	2.14	1130.4

Superscript *f* means absolute permeability k in microfractures, φ is porosity, ρ_r is rock density, k_T is rock thermal conductivity, c_p is isobaric rock specific heat capacity, E is the Young's modulus, ν is Poisson's ratio and C_B is rock bulk compressibility measured at a confining pressure of 35 MPa. Measurements are reported in saturated rock. The symbol (*) means uniaxial tests.

and $C_0 \approx 1.9532$ for andesites (data from wells H-04 and H-24 of Los Humeros, Mexico), respectively.

2.1.2.1 The variation of the fluid mass content

Let M_f [kg] be the mass of the fluid in the pores and ρ_f [kg/m³] its density, the fluid mass content m_f per unit reference volume V_B of the porous rock is:

$$m_f = \frac{M_f}{V_B} = \frac{M_f V_f}{V_B V_f} = \frac{M_f \varphi}{V_f} = \rho_f \varphi \quad \left[\frac{\text{kg}}{\text{m}^3} \right] \quad (2.3a)$$

Biot introduced in 1941 a poroelastic dimensionless variable ζ , which he defined as “the volume of fluid which enters the pores of a unit volume of bulk material” (Biot 1941), or “the variation in water content”, or for a generic fluid, “the variation of fluid content” (eq. 2.3a). If m_0 and ρ_0 are the mass content and the fluid density in a reference state, respectively, then the variation of fluid content ζ in the pores is defined as:

$$\zeta = \frac{m_f - m_0}{\rho_0} = \frac{\Delta m_f}{\rho_0} = \frac{\rho_f \Delta \varphi + \varphi \Delta \rho_f}{\rho_0} \quad [\text{ad}] \quad (2.3b)$$

In other words, “ ζ is the volume of fluid transported into or out of storage” (Wang 2000). The variation of m_f occurs by changes in the fluid density and in the porosity.

2.1.2.2 The advective derivative of the density

The fluid and the rock in a reservoir are assumed to be continuum media. Both are changing in space and time. The changes in the rock are in general, very slow and small compared with the changes in the fluid, but we need to take the changes into account to study poroelastic strains. To understand the rock deformations we introduce here a very important mathematical concept which is useful to represent those variations. The advective or convective derivative of the density of each phase, fluid or solid, is the global rate of change or total time derivative of the phase density considered as a function of space and time $\rho(x, y, z, t)$. We can compute this total derivative $D\rho/Dt$ using the differential concept and the chain rule for functions of several variables:

$$\begin{aligned} \rho(\vec{r}(t), t) &\Rightarrow d\rho(x, y, z, t) = \frac{\partial \rho}{\partial x} dx + \frac{\partial \rho}{\partial y} dy + \frac{\partial \rho}{\partial z} dz + \frac{\partial \rho}{\partial t} dt \\ \Rightarrow \frac{D\rho}{Dt}(x, y, z, t) &= \frac{\partial \rho}{\partial x} \frac{dx}{dt} + \frac{\partial \rho}{\partial y} \frac{dy}{dt} + \frac{\partial \rho}{\partial z} \frac{dz}{dt} + \frac{\partial \rho}{\partial t} \frac{dt}{dt} = \frac{\partial \rho}{\partial t} + \vec{\nabla} \rho \cdot \vec{v} \end{aligned} \quad (2.4)$$

$$\text{where } \vec{v} = \left(\frac{dx}{dt}, \frac{dy}{dt}, \frac{dz}{dt} \right) \quad \text{and} \quad \vec{r}(t) = (x(t), y(t), z(t))$$

Vector \vec{v} is the phase velocity field and $\vec{r}(t)$ is the changing vector position of any particle of the porous rock. From this formula we deduce that the advective derivative originates from the fact that the phase density changes with time experiencing a spatial variation because of the phase motion. If $v = 0$ or the density gradient is null, then the advective derivative becomes equal to the traditional time derivative.

2.1.3 The principle of conservation of mass in porous rocks

The density of an object is equal to its mass divided by its volume. The total density of a porous rock should be defined taking into account the presence of the fluid (ρ_f) in the pores together with the solid phase (ρ_s). The global density is an average of both densities $\rho = \varphi \rho_f + \varphi_s \rho_s$. The total mass $M = M_f + M_s$ is the sum of the masses of both phases; at time $t \geq 0$. Their mathematical

definitions are:

$$\text{solid mass: } M_s = \int_{V_s} \varphi_s \rho_s(\vec{r}, t) dV, \quad \text{fluid mass: } M_f = \int_{V_f} \varphi \rho_f(\vec{r}, t) dV \quad (2.5)$$

Let $\vec{v}_i = \partial \vec{r} / \partial t$ be the vectorial velocity of a particle in the phase volume V_i ($i = f, s$). If the mass of each phase is conserved, then it remains constant under motion. Thus, the advective derivative D/Dt of each one of the integrals in equation (2.5) is zero. This derivative is computed for each phase velocity v_i ($i = f, s$) using equation (2.4):

$$\frac{DM_i}{Dt} = \frac{D}{Dt} \int_{V_i} \varphi_i \rho_i(\vec{r}, t) dV = \int_{V_0} \frac{D}{Dt} (\varphi_i \rho_i J) dV_0 = \int_{V_0} \left(\frac{D}{Dt} (\varphi_i \rho_i) J + \varphi_i \rho_i \frac{DJ}{Dt} \right) dV$$

$$\text{where: } dV = J(t) dV_0, \quad \frac{DJ}{Dt} = J \vec{\nabla} \cdot \vec{v}_i, \quad \text{and} \quad \frac{D}{Dt} (\varphi_i \rho_i) = \frac{\partial}{\partial t} (\varphi_i \rho_i) + \vec{\nabla} (\varphi_i \rho_i) \cdot \vec{v}_i$$

The term $J(t)$ is the determinant of the Jacobian matrix that transforms the initial volume V_0 into the deformed volume $V(t)$. The interested reader may consult any book on advanced calculus for more details on these concepts (e.g., Dill 2007). Therefore:

$$\frac{DM_i}{Dt} = \int_{V_i} \left(\frac{\partial (\varphi_i \rho_i)}{\partial t} + \vec{\nabla} \cdot (\varphi_i \rho_i \vec{v}_i) \right) dV = 0 \quad (2.6a)$$

This equation is the integral form of the principle of conservation of mass for a porous rock, valid in any part of the fluid-rock continuum. Assuming that V_i is any arbitrary part of phase i in the porous rock, the integrand of equation (2.6a) must be identical to zero, therefore:

$$\frac{\partial (\varphi_i \rho_i)}{\partial t} + \vec{\nabla} \cdot (\varphi_i \rho_i \vec{v}_i) = \frac{D(\varphi_i \rho_i)}{Dt} + (\varphi_i \rho_i) \vec{\nabla} \cdot \vec{v}_i = 0 \quad (2.6b)$$

where the advective derivative is:

$$\frac{D(\varphi_i \rho_i)}{Dt} = \frac{\partial (\varphi_i \rho_i)}{\partial t} + \vec{\nabla} (\varphi_i \rho_i) \cdot \vec{v}_i \quad \text{and} \quad \vec{\nabla} \cdot (\varphi_i \rho_i \vec{v}_i) = \vec{\nabla} (\varphi_i \rho_i) \cdot \vec{v}_i + \varphi_i \rho_i \vec{\nabla} \cdot \vec{v}_i$$

Formula (2.6b) is also known as the continuity equation which expresses the same principle of conservation of mass of equation (2.6a) in the form of a partial differential equation. This law can be related directly to the deformations of the fluid volume and of the solid phase in the porous rock. Applying equation (2.6b) to the fluid phase ($i = f$):

$$\frac{D(\varphi \rho_f)}{Dt} = -(\varphi \rho_f) \vec{\nabla} \cdot \vec{v}_f \quad \Rightarrow \quad \vec{\nabla} \cdot \vec{v}_f = \frac{-1}{\varphi \rho_f} \frac{D(\varphi \rho_f)}{Dt} = -\frac{1}{m_f} \frac{Dm_f}{Dt} \quad (2.7a)$$

Therefore, the divergence of the fluid phase velocity is equal to the advective derivative of the fluid mass content per unit mass. If we assume that the porosity is constant:

$$\vec{\nabla} \cdot \vec{v}_f = \frac{-v_f}{\varphi} \frac{D}{Dt} (\varphi v_f^{-1}) = \frac{-v_f}{-v_f^2} \frac{D}{Dt} (v_f) = \frac{1}{v_f} \frac{Dv_f}{Dt} \quad (2.7b)$$

In this case the divergence of the fluid phase velocity is equal to the advective derivative of the fluid specific volume $v_f = 1/\rho_f$. If we assume that the fluid mass is constant:

$$\vec{\nabla} \cdot \vec{v}_f = \frac{-1}{\varphi \rho_f} \frac{D(\varphi \rho_f)}{Dt} = -\frac{V_B \cancel{V_f}}{\cancel{V_f} \cancel{M_f}} \frac{D}{Dt} \left(\frac{\cancel{M_f}}{V_B} \right) = \frac{1}{V_B} \frac{D V_B}{Dt} = \frac{D \varepsilon_B}{Dt} \quad (2.7c)$$

The divergence of the fluid phase velocity is equal to the advective derivative of the bulk volumetric strain when the fluid mass M_f is constant. This is because:

$$\vec{\nabla} \cdot \vec{u}_B = \varepsilon_B = \frac{\Delta V_B}{V_B^0} \Rightarrow \frac{D \varepsilon_B}{Dt} = \frac{1}{V_B^0} \frac{D V_B}{Dt}$$

If we assume that both the fluid mass and the porosity are constants:

$$\vec{\nabla} \cdot \vec{v}_f = \frac{-V_f}{\cancel{\varphi} \cancel{M_f}} \frac{D}{Dt} \left(\frac{\cancel{M_f}}{V_f} \right) = \frac{1}{V_f} \frac{D V_f}{Dt} = \frac{D \varepsilon_f}{Dt} \quad (2.7d)$$

In this case the divergence of the fluid phase velocity is equal to the advective derivative of the fluid volumetric strain.

Applying equation (2.6b) to the solid phase ($i = s$) when the solid mass and the porosity are constants:

$$\begin{aligned} \frac{D}{Dt}(\varphi_s \rho_s) &= -(\varphi_s \rho_s) \vec{\nabla} \cdot \vec{v}_s \Rightarrow \vec{\nabla} \cdot \vec{v}_s = \frac{-1}{\varphi_s \rho_s} \frac{D(\varphi_s \rho_s)}{Dt} \\ &= \frac{-V_s}{\cancel{\varphi_s} \cancel{M_s}} \frac{D}{Dt} \left(\frac{\cancel{M_s}}{V_s} \right) = -V_s \frac{D}{Dt} (V_s)^{-1} = V_s \left(V_s^{-2} \frac{D V_s}{Dt} \right) = \frac{1}{V_s} \frac{D V_s}{Dt} \end{aligned}$$

Hence, the divergence of the solid phase velocity is equal to the advective derivative of the solid volumetric strain:

$$\vec{\nabla} \cdot \vec{v}_s = \frac{1}{V_s} \left(\frac{D V_s}{Dt} \right) = \frac{D \varepsilon_s}{Dt} \quad (2.7e)$$

The variable ε_s is defined as the volumetric deformation (dilatation or compaction) of the solid phase (see section 2.2.4). If the rock is assumed to be non-deformable or incompressible then $DV_s/Dt = 0$ and the divergence of the solid velocity is null. This is the most common approximation in reservoir engineering. If in equation (2.6b) we assume that the porosity is constant and that the density does not change with time:

$$\vec{\nabla} \cdot (\rho_i \vec{v}_i) = 0 \quad (2.7f)$$

Equations (2.7a–f) are other forms of the continuity equation; they give a clear physical interpretation of the divergence of the deformation velocity of both phases.

2.1.4 Thermal conductivity of porous rocks

Heat transfer in porous rocks saturated with fluids occurs by convection and by thermal conduction in the fluid, among the solid grains and between the grains and the fluid. The effective thermal conductivity in a porous system with fractures and microfractures depends on the thermal conductivity of the solid matrix, the fracturing intensity, the saturating phase, if the fluid is single phase, and on the saturation of both phases in two-phase fluids.

The thermal conductivity k_T [W/m²C] of rocks increases with lithostatic pressure at the low rate; e.g. those of granites at $\approx 2.6 \times 10^{-3}$ W/m/K per kilometer (Beardsmore and Cull, 2001).

Thus, the influence of pressure on rock thermal conductivity is negligible in the crust. In most reservoir rocks k_T decreases when the temperature increases up to 650°C. Starting at this temperature the rock thermal conductivity remains almost constant, until nearing the Earth's mantle, where it starts to grow linearly (Passmore and Archer 1985). Table B1 in the Appendix B indicates values of some rock forming minerals found in the upper part of the Earth's crust as function of temperature in the range generally found in aquifers and geothermal systems and in dependence of the direction in the crystal lattice.

Using data for granite (Beardmore and Cull 2001) and for andesite (Contreras *et al.* 1988), we deduced quadratic relations between thermal conductivity and temperature. The following formula for granite is valid in the range [0, 300]°C; the corresponding formula for andesite is valid in the range [20, 250]°C, at the confining pressure of 8 MPa (Fig. 2.3a):

$$\begin{aligned}
 k_{T\text{granite}}(T) &= 3.50 - 5.83333 \times 10^{-3}T + 8.33333 \times 10^{-6}T^2 \\
 k_{T\text{andesite}}(T) &= 2.02333 - 2.24889 \times 10^{-3}T + 4.62222 \times 10^{-6}T^2
 \end{aligned}
 \tag{2.8}$$

Data from the Los Humeros geothermal field, Mexico (Table 2.1) show that k_T has an irregular distribution in the vertical direction (Fig. 2.3b). This is because of the several factors influencing this parameter.

Laboratory experiments show that the thermal conductivity of the rock/fluid system is increased when the effective rock tensions increase (Contreras *et al.* 1988). The increment of confining pressure tends to improve the thermal contact among grains, resulting in a net increment of k_T .

Several experiments show that k_T increases with increasing hydraulic permeability (e.g., Passmore and Archer 1985). This effect can be due to convective heat transfer in pores and inside of interconnected micro-fractures. On the other hand, the porosity increment reduces the effective thermal conductivity. The fluid-rock geochemical interaction also affects the thermal conductivity, because the minerals are hydrothermally altered and some of the pores or fractures are filled modifying the nature of the intergranular contact. Experiments reported by Ramey *et al.* (1974) found that if the saturating fluid is water with its liquid and vapor phases in equilibrium, the effective thermal conductivity has much larger values than those predicted by empirical correlations. The increment depends on the permeability, on the latent heat of vaporization and on vapor saturation. Formulae to calculate effective averages of k_T in heterogeneous rocks are described in chapter 3.

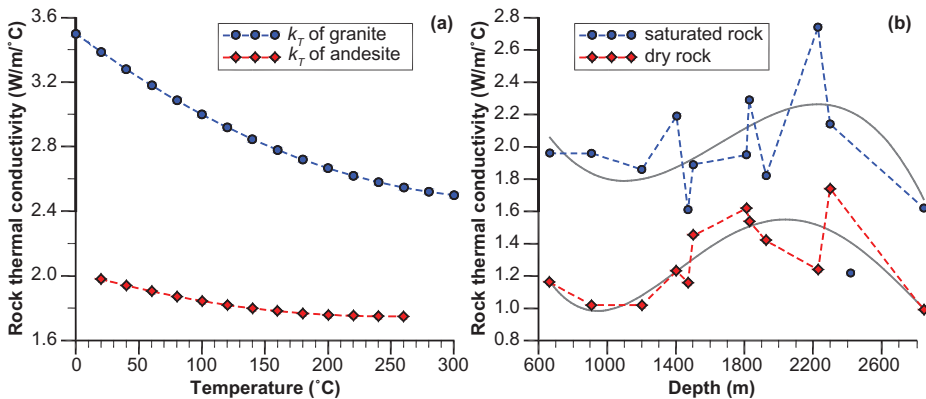


Figure 2.3. Thermal conductivity of volcanic rocks: (a) k_T of granite and of andesites as function of T ; (b) Distribution of k_T as function of depth (cores of andesites, data from Contreras *et al.* 1990).

2.1.5 Heat conduction, Fourier's law and thermal gradient

The conduction of heat is a macroscopic process, and is also a microscopic process originated from molecular agitation producing thermal energy, which is transported from one place to another in the porous rock. The conduction is reflected by changes in the temperature of the medium; this energy transit always takes place in the direction of decreasing temperature. If the temperature varies at two distinct points within the porous rock, this difference will produce heat conduction from the hotter point to the colder point. The physical process of heat conduction is different in solid rocks, liquids, and gases. This is because the molecular activity is different in each one of the three states (Alonso and Finn 1967). The fundamental equation describing this process is the experimental Fourier's law of heat conduction in one (1D), two (2D), or three dimensions (3D):

$$\begin{aligned}
 \text{in 1D:} \quad q_{Tz} &= -k_T \frac{dT}{dz} \\
 \text{in 2D or 3D:} \quad \vec{q}_T &= -\mathbf{k}_T \cdot \vec{\nabla} T \\
 \text{in 3D:} \quad \mathbf{k}_T &= \begin{pmatrix} k_{Tx} & 0 & 0 \\ 0 & k_{Ty} & 0 \\ 0 & 0 & k_{Tz} \end{pmatrix}, \quad \vec{\nabla} T = \begin{pmatrix} \partial_x T \\ \partial_y T \\ \partial_z T \end{pmatrix}, \quad \partial_x T = \frac{\partial T}{\partial x}
 \end{aligned} \tag{2.9}$$

The matrix \mathbf{k}_T is the thermal conductivity tensor for anisotropic media and is specific to each rock. The thermal conductivity has units of [J/m/s/K] or of [W/m/°C], because both temperature scales are parallel ($K = °C + 273.15$) and the temperature change is one to one ratio. The increment of one degree Celsius is exactly equal to the increment of one Kelvin. The vector thermal gradient $\vec{\nabla} T$ quantifies the variation of temperature in three directions of space (x, y, z), it has units of [°C/m = K/m]. The vector \vec{q}_T is the flow of heat and has units of power per unit area [W/m²]. The negative sign appears because heat always flows in the direction in which the temperature decreases. With respect to Earth surface temperatures, the normal average geothermal gradient is about 25°C/km in depth. In abnormal geothermal zones, this gradient is higher. For example at the Los Azufres hydrothermal field (Mexico), its values are between 87 and 138°C/km. The average heat flow at the Transmexican Volcanic Belt is 0.10 W/m² at the surface, while the estimated submarine heat flow in the Gulf of California is about 0.34 W/m² (Suárez 2000a, 2004). Concerning the whole Earth, the average heat flow for the continents is about 0.06 W/m² and about 0.10 W/m² for the oceans. The approximate total thermal power out of the Earth is 45×10^{12} W (Lautrup 2005).

2.1.6 Heat capacity and enthalpy of rocks

The heat capacity C_p [J/K] at constant pressure is defined as the amount of energy required to raise the temperature of a rock volume V_B by 1°C; C_V is the volumetric heat capacity under constant deformation per unit volume. Both parameters quantify the ability of rocks to store thermal energy. The specific heat capacity (or simply specific heat) is defined as the quantity of heat required to raise the temperature of one kilogram of rock mass by 1 K or 1°C. It is important to mention here that there are two types of specific heat: c_p at constant pressure p in terms of the enthalpy h , and c_V at constant volume V (or constant strain) in terms of the internal energy e . They are defined as follows:

$$\begin{aligned}
 c_p &= \left(\frac{\partial h}{\partial T} \right)_p, \quad c_V = \left(\frac{\partial e}{\partial T} \right)_V \rightarrow \left[\frac{\text{J}}{\text{kg K}} \right] \text{ both} \\
 C_p &= c_p \rho V_B \rightarrow \left[\frac{\text{J}}{\text{K}} \right], \quad C_V = \frac{C_p}{V_B} \rightarrow \left[\frac{\text{J}}{\text{m}^3 \text{K}} \right]
 \end{aligned} \tag{2.10}$$

The rock thermodynamic functions, specific internal energy e and specific enthalpy h are discussed in section 2.2.11. Their mutual relationships are:

$$\text{at constant pressure: } h = e + \nu p \quad \left[\frac{\text{J}}{\text{kg}} \right] \Rightarrow \frac{\partial h}{\partial T} = \frac{\partial e}{\partial T} + \frac{\partial \nu}{\partial T} p \quad (2.11a)$$

$$\text{at constant volume: } e = h - \nu p \quad \left[\frac{\text{J}}{\text{kg}} \right] \Rightarrow \frac{\partial e}{\partial T} = \frac{\partial h}{\partial T} - \frac{\partial p}{\partial T} \nu \quad (2.11b)$$

The function ν is the specific volume, p is pressure and T [K] is the rock temperature. Let q_H [W] be the power of a heat source producing a temperature growth of ΔT in the porous rock during a period Δt , in one-dimensional spatial interval $\Delta z = z_2 - z_1$. The amount of heat H_G [J] or geothermal energy transferred between both points of this interval is:

$$H_G = C_p \Delta T = q_H \Delta t \quad [\text{J}] \quad (2.12)$$

Using Fourier's law in one dimension, the volumetric heat generation $Q_H(z) = q_H/V_B$ produced by the source can be approximated by the following equation (Carslaw and Jaeger 1959):

$$q_z = k_T \frac{\Delta T}{\Delta z} \quad \text{and} \quad \frac{q_H}{V_B} = \frac{\Delta q_z}{\Delta z} \Rightarrow Q_H = k_T \frac{\Delta}{\Delta z} \left(\frac{\Delta T}{\Delta z} \right) \approx k_T \frac{\partial^2 T}{\partial z^2} \quad (2.13)$$

$$\left(Q_H = \frac{q_H}{V_B} = \text{volumetric heat generation in } \left[\frac{\text{W}}{\text{m}^3} \right] \right)$$

Then, we obtain from equation (2.12):

$$H_G = C_p \Delta T = q_H \Delta t \Rightarrow \frac{q_H}{V_B} = \frac{C_p}{V_B} \frac{\Delta T}{\Delta t} \approx k_T \frac{\partial^2 T}{\partial z^2} \quad (2.14)$$

Taking the limit when both $\Delta z \rightarrow 0$ and $\Delta t \rightarrow 0$ we obtain the exact equality:

$$C_V \frac{\partial T}{\partial t} = k_T \frac{\partial^2 T}{\partial z^2} \quad (2.15)$$

This equation relates the evolution of the temperature with its spatial changes, through the physical rock parameters, heat capacity, thermal conductivity, and volume. The more general heat equation in three dimensions is discussed in section 4.6. It is common to use the specific heat capacity at constant pressure c_p instead of C_p or C_V . Dividing by the rock mass M_r , we obtain the classical heat equation in one dimension for homogeneous and isotropic rocks:

$$C_V \frac{\partial T}{\partial t} = \frac{C_p}{M_r} \frac{M_r}{V_B} \frac{\partial T}{\partial t} \Rightarrow \boxed{c_p \rho \frac{\partial T}{\partial t} = k_T \frac{\partial^2 T}{\partial z^2}} \quad (2.16)$$

Several thermal characteristics of rocks can be estimated with these formulae. We use data from Table 2.1 to compute some useful parameters. Given a volume $V_B = 10 \text{ km}^3$, and the data for well H-29 $\rho_r = 2250 \text{ kg/m}^3$, and $c_p = 1046.7 \text{ J/kg}^\circ\text{C}$, the heat capacity can be determined $C_p = 2.36 \times 10^{16} \text{ J}^\circ\text{C}$. With additional data from the same well H-29, $k_T = 1.86 \text{ W/m}^\circ\text{C}$, $\Delta T = 100^\circ\text{C}$ and $\Delta z = 1000 \text{ m}$, we obtain the heat $H_G = 2.36 \times 10^{18} \text{ J}$, and the temperature gradient $dT/dz = 0.1^\circ\text{C/m}$. The heat flow is 0.183 W/m^2 at one point and 0.186 W/m^2 at another point located 1000 m deeper. The heat generation is estimated from the quotient $\Delta q_z/\Delta z = (0.186 - 0.183)/10^3 = 3 \times 10^{-6} \text{ W/m}^3$. Published data of radiogenic heat generation for rhyolites point out a value

of $q_H/V_B = 2.8 \times 10^{-6} \text{ W/m}^3$; as a general trend, acidic rocks present larger radiogenic heat production ($\sim 2 \times 10^{-6} \text{ W/m}^3$) than basic rocks ($[10^{-8}, 10^{-7}] \text{ W/m}^3$, Beardsmore and Cull 2001). These values are only for solid rocks; to take into account the fluid presence, the use of averages of ρ_s , c_p and k_T are necessary. The formulae to calculate effective averages are treated in chapter 3.

The heat capacities of complex heterogeneous, multiporosity reservoirs, are calculated using Kopp's law, which states that the heat capacity of a compound is equal to the sum of the heat capacities of its constituent elements. This law was experimentally verified for complex mixtures of sandstone and shales, with a maximum deviation smaller than 2% (Passmore and Archer 1985). This result supports the hypothesis that the heat capacity of saturated rocks can be estimated in a similar way.

Diverse experimental laboratory measurements demonstrate that the heat capacity of a fluid saturated rock depends on both pressure and temperature. Table 2.2 shows the specific heat capacity for principal rock forming minerals and some selected elements at temperatures in the

Table 2.2. Experimental measurements of specific heat capacity c_p (kJ/kg/K) for different temperatures in the range of (0–800°C) for rock forming minerals and some selected elements. (Ab: albite; An: anorthite). (After [Goranson 1942], modified from Clauser 2006).

Mineral/element	Formula	0°C	200°C	400°C	800°C
acanthite	Ag ₂ S	0.32	–	–	–
adularia	KAlSi ₂ O ₈	0.732	0.84	1	–
alabandite	MnS	0.569	–	–	–
albite	NaAlSi ₃ O ₈	0.709	0.99	1.09	1.2
amphibole	MgSiO ₃	0.74	1.03	1.13	1.24
andalusite	Al ₂ SiO ₅	0.77	1.03	1.11	1.17
andesine	3Ab · 2An	0.7	0.97	1.07	1.18
anglesite	PbSO ₄	0.364 at 60°C	–	–	–
anhydrite	CaSO ₄	0.52	0.58	0.6	0.64
anorthite	CaAl ₂ Si ₂ O ₈	0.7	0.95	1.05	1.17
aragonite	CaCO ₃	0.78	1	1.13	–
argentite	Ag ₂ S	–	0.37	–	–
arsenopyrite	FeAsS	0.43 at 55°C	–	–	–
barite	BaSO ₄	0.45	0.5	0.55	0.65
berzelianite (α)	Cu ₂ Se	0.42	–	–	–
berzelianite (β)	Cu ₂ Se	–	0.41	–	–
boracite (α)	Mg ₇ B ₁₆ Cl ₂ O ₂₅	0.796	1.18	–	–
boracite (β)	Mg ₇ B ₁₆ Cl ₂ O ₂₅	–	–	1.41	–
borax	Na ₂ B ₄ O ₇ · 10H ₂ O	0.161 at 35°C	–	–	–
bournonite	CuPbSbS ₃	0.31 at 50°C	–	–	–
brucite	Mg(OH) ₂	1.30 at 35°C	–	–	–
calcite	CaCO ₃	0.79	1	1.13	–
cassiterite	SnO ₃	0.34	0.43	0.48	0.55
cerussite	PbCO ₄	0.318	–	–	–
chalcocite (α)	Cu ₂ S	0.47	–	–	–
chalcocite (β)	Cu ₂ S	–	0.55	0.55	0.55
chalcopyrite	CuFeS ₂	0.54 at 50°C	–	–	–
chloromagnesite	MgCl ₂	0.805	0.84	0.87	–
chrysoberyl	BeAl ₂ O ₄	0.84 at 50°C	–	–	–
cinnabar (α)	HgS	0.214	0.23	0.24	–
copper (native)	Cu	0.384	0.4	0.42	0.46
corundum	Al ₂ O ₃	0.72	1	1.1	1.19
covellite	CuS	0.49	0.52	0.54	0.59
cryolite	Na ₃ AlF ₆	0.909	1.18	1.39	1.78
cuprite	Cu ₂ O	0.47	0.51	0.54	0.61
cyanite	Al ₂ SiO ₅	0.7	1	1.1	1.2

(Continued)

Table 2.2. (Continued)

Mineral/element	Formula	0°C	200°C	400°C	800°C
diamond	C	0.435	1.06	1.37	1.86
diopside	CaMgSi ₂ O ₆	0.69	0.98	1.06	1.15
diopside	CuSiO ₃ · H ₂ O	0.77 at 34°C			
dolomite	CaMg(CO) ₃	0.93 at 60°C			
epsomite	MgSO ₄ · 7H ₂ O	1.51 at 32°C			
fayalite	Fe ₂ SiO ₄	0.551	0.79	0.91	1.1
fluorite	CaF ₂	0.85	0.89	0.93	1.01
galena	PbS	0.207	0.22	0.24	–
garnet	Mg ₃ Al ₂ Si ₃ O ₁₂	0.74 at 58°C			
gehlenite	Ca ₂ Al ₂ SiO ₇	0.75	0.97	1.03	1.09
graphite (β)	C	0.635	1.18	1.45	1.88
greenockite	CdS	0.445	0.5	0.55	0.65
gypsum	CaSO ₄ · 2H ₂ O	1.03	–	–	–
halite	NaCl	0.855	0.92	0.98	1.1
hematite	Fe ₂ O ₃	0.61	0.79	0.9	1.08
hypersthene	Fe ₂ Si ₂ O ₆	0.80 at 60°C			
iron (α)	Fe	0.44	0.52	0.6	–
iron (β)	Fe	–	–	–	0.73
kaolin	Al ₂ Si ₂ O ₇ · 2H ₂ O	0.99	1.17	1.35	–
kaolinite	Al ₈ Si ₃ O ₁₈	0.93	1.02	–	–
kieserite	MgSO ₄ · H ₂ O	1.00 at 9°C			
labradorite	2Ab · 3An	0.82 at 60°C			
leucite	KAlSi ₂ O ₆	0.74 at 80°C			
limonite	2Fe ₂ O ₃ · 3H ₂ O	0.94 at 60°C			
magnesite	MgCO ₃	0.864	–	–	–
magnetite (α)	Fe ₃ O ₄	0.6	0.8	0.93	–
magnetite (β)	Fe ₃ O ₄	–	–	–	1.03
malachite	2CuO · CO ₂ · H ₂ O	0.74 at 57°C			
manganite	Mn ₂ O ₃ · H ₂ O	0.74 at 36°C			
metakaolin	Al ₂ Si ₂ O ₇	0.71	1	1.1	1.2
microcline	KAlSi ₂ O ₈	0.68	0.95	1.04	1.14
millerite	NiS	0.506	0.57	–	–
molybdenite	MoS ₂	0.537	0.55	0.57	–
mullite	Al ₆ Si ₂ O ₁₃	0.77	0.97	1.03	1.09
oligoclase	4Ab · 1An	0.85 at 60°C			
olivine	Mg ₂ Fe ₂ SiO ₄	0.79 at 36°C			
orthoclase	KAlSi ₂ O ₈	0.61	0.94	1.05	1.15
periclase	MgO	0.87	1.09	1.16	1.24
petalite	LiAlSi ₂ O ₅	0.85 at 58°C			
prehnite	Ca ₂ Al ₂ H ₂ (SiO ₄) ₃	0.84 at 50°C			
proustite	Ag ₃ AsS ₃	0.34 at 50°C			
pyrrargyrite	Ag ₃ SbS ₃	0.32 at 50°C			
pyrite	FeS ₂	0.5	0.59	0.69	–
pyrolusite	MnO ₂	0.975	1	1.01	–
pyroxene	MgSiO ₃	0.752	1.03	1.15	–
pyrrhotite	Fe ₇ S ₈	0.594	0.77	–	–
quartz (α)	SiO ₂	0.698	0.97	1.13	–
quartz (β)	SiO ₂	–	–	–	1.17
rhodochrosite	MnCO ₃	0.7	1.08	1.46	–
rutile	TiO ₂	0.7	0.8	0.88	–
scheelite	CaWO ₄	0.40 at 50°C			
sellaite	MgF ₂	0.906	1.08	1.21	1.43
siderite	FeCO ₃	0.68	–	–	–
sillimanite	Al ₂ SiO ₅	0.743	1	1.08	1.16

(Continued)

Table 2.2. (Continued)

Mineral/element	Formula	0°C	200°C	400°C	800°C
smithsonite	ZnCO ₃	0.632	–	–	–
sphalerite (β)	ZnS	0.45	0.53	0.56	0.59
spodumene	LiAlSi ₂ O ₆	0.90 at 60°C	–	–	–
stibnite	Sb ₂ S ₃	0.342	0.38	0.41	–
strontianite	SrCO ₃	0.536	–	–	–
sylvite	KCl	0.682	0.72	0.75	–
talc	Mg ₃ H ₂ Si ₄ O ₁₂	0.87 at 59°C	–	–	–
tenorite	CuO	0.52	0.63	0.68	–
topaz	2(AlF)O · SiO ₂	0.83 at 50°C	–	–	–
troilite (α)	FeS	0.606	–	–	–
troilite (β)	FeS	–	0.64	0.66	0.71
tungstite	WO ₃	0.33	0.36	0.38	0.44
villiaumite	NaF	1.034	1.1	1.29	–
witherite (α)	BaCO ₃	0.44	0.5	0.55	0.66
wurtzite (α)	ZnS	0.45	0.53	0.56	0.59
zincite	ZnO	0.48	0.58	0.62	0.66
zircon	ZrSiO ₄	0.61 at 60°C	–	–	–

range of 0–800°C. The presence of gas has a negligible effect in the corresponding coefficient. Nevertheless, the presence of liquid water can increase, by more than 35% the specific heat c_p of the sample (Passmore and Archer 1985). If the pores are saturated with oil, the saturated rock heat capacity is increased by less than 20%. The mathematical expression of the rock specific heat at constant pressure is given by the same rock enthalpy partial differential equation (2.11a). Faust and Mercer (1975) outlined an experimental formula for the calculation of c_p and rock enthalpy h_s in sandstones (Fig. 2.4):

$$\begin{aligned}
 c_p(T) &= 849.88860 + 0.752854 T \left[\frac{\text{J}}{\text{kg}^\circ\text{C}} \right] \\
 h_s(T) &= 204,061.52 + 849.8886 T + 0.376427 T^2 \left[\frac{\text{J}}{\text{kg}} \right]
 \end{aligned}
 \tag{2.17}$$

With these formulae, we can estimate the heat capacity and the specific enthalpy of sandstones as a function of temperature (T in °C). However, many high-enthalpy geothermal reservoirs are located in volcanic rocks. We extend the previous formulae to andesites in the following way (the same method can be applied to other rock types). In one core of well Az-19 of Los Azufres, a single value of specific heat capacity, equal to $c_{p19} = 1164.82 \text{ J/kg}^\circ\text{C}$, was measured at 8.0 MPa and 250°C (Contreras *et al.* 1988). In andesites, the relationship between specific heat and temperature continues to be linear and the slopes are assumed similar. Applying formula (2.17) to the previous temperature: $c_p(250) = 1038.1021 \text{ J/kg}^\circ\text{C}$. The difference between both coefficients is: $c_{p19} - c_p(250) = 126.7179 \text{ J/kg}^\circ\text{C}$; therefore:

$$\begin{aligned}
 c_p(T) &= 976.6065 + 0.752854 T, \quad dh_s \approx c_p dT \Rightarrow \int_0^{h_r} dh_s = \int_{-273.15}^T c_p dT \\
 \Rightarrow h_s(T) &= 238,674.50 + 976.6065 T + 0.376427 T^2 \left[\frac{\text{J}}{\text{kg}} \right]
 \end{aligned}
 \tag{2.18}$$

With both formulae the specific heat and enthalpy of andesites can be calculated, under the typical thermodynamic conditions of geothermal reservoirs ($\sim[150, 350]^\circ\text{C}$; Fig. 2.4).

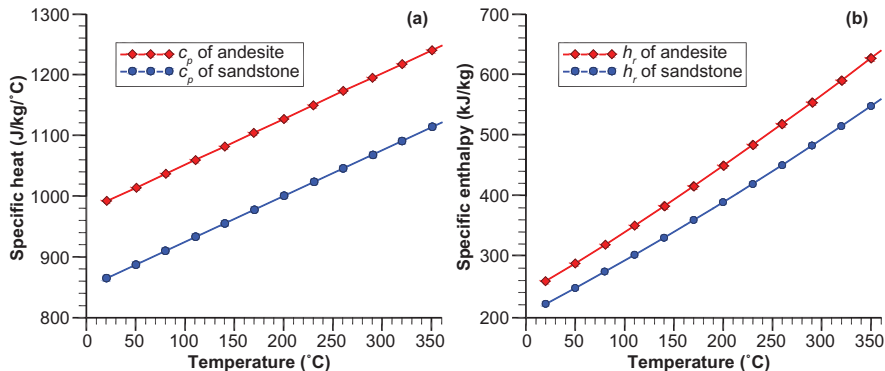


Figure 2.4. Specific heat (a) and enthalpy (b) of sandstones and andesites as functions of $T(^{\circ}\text{C})$.

2.1.7 Rock heat capacity and geothermal electric power

A practical important application of the heat capacity is the estimation of the electric power generation potential from a geothermal reservoir. This potential depends on the stored geothermal energy in the system and on the global efficiency factor with which the geothermal energy can be converted to electricity. The reservoir thermal energy is:

$$H_G = \rho_s c_p V_B (T_A - T_0) \quad (2.19)$$

where $\rho_s c_p$ is the isobaric volumetric specific heat of the reservoir rock, V_B is the volume of the reservoir, T_A is the characteristic average reservoir temperature, and T_0 is a reference value close to the average ground surface temperature. It is reasonable to compute first the energy contained in every cubic meter of rock, especially if the total volume of the reservoir is unknown. For example, using the following data from the Los Azufres reservoir (Table 3.7 in chapter 3): $p = 8$ MPa, $\Delta T = 250^{\circ}\text{C}$, $\rho_s = 2290$ kg/m³, $c_p = 1165$ J/kg/°C, the available volumetric geothermal energy is:

$$\frac{H_G}{V_B} = \rho_s c_p (T_A - T_0) = 2290 \times 1165 \times 250 \cong 667 \quad \left[\frac{\text{MJ}}{\text{m}^3} \right]$$

If the fluid is considered, ρ_s and c_p must be averaged (see chapter 3). This thermal energy can be related to electric power production through the application of appropriate recovery and conversion factors. The electric geothermal power [MW_e] is defined as:

$$G_P = \eta_G \frac{H_G}{t_E} = \eta_G \frac{\rho_s c_p V_B (T_A - T_0)}{t_E} \quad [\text{MW}_e] \quad (2.20)$$

where t_E represents a period of commercial exploitation of the reservoir, usually taken as 30 years (transformed to seconds) and η_G is the geothermal energy-electricity conversion factor. The global estimated η_G for the Los Azufres geothermal field is $\eta_G \approx 2.5\%$ (Suárez and Viggiano 1992). In this reservoir the volume of hot rock subjected to heat extraction is approximately 50 km³, thus its electric geothermal potential is:

$$G_P = 0.025 \times \frac{\rho_s c_p V_B (T - T_0)}{30 \times 365.25 \times 86400} \cong 880.6 \text{ MW}_e$$

This figure is close to five times the present installed capacity in this field (188 MW_e , Maya-González, R. and Gutiérrez-Negrín 2007) thus its real geothermal potential is larger. To make the conversion years to seconds we used the real duration of the year in days (1 year $\cong 365.25$ days).

2.1.8 Thermal diffusivity and expansivity of rocks

As a consequence of Fourier's law, of the isobaric specific heat c_p of the medium and of thermodynamic considerations (see chapter 4), the partial differential equation modeling the transitory heat conduction in the rock in three dimensions is:

$$\frac{k_T}{\rho_s c_p} \vec{\nabla} \cdot \vec{\nabla} T = \frac{k_T}{\rho_s c_p} \left(\frac{\partial^2 T}{\partial x^2} + \frac{\partial^2 T}{\partial y^2} + \frac{\partial^2 T}{\partial z^2} \right) = \frac{\partial T}{\partial t} \quad (2.21a)$$

2.1.8.1 Thermal diffusivity

The composed parameter δ_T affecting the Laplacian in equation (2.21a) is the rock thermal diffusion coefficient:

$$\delta_T = \frac{k_T}{\rho_s c_p} \Rightarrow \delta_T \nabla^2 T = \frac{\partial T}{\partial t} \quad (2.21b)$$

The differential equation (2.21b) is applicable only to homogeneous, isotropic rocks. δ_T represents the capacity of the porous rock to transfer heat with respect to its capacity of thermal storage per unit volume of rock. Any temperature increment results in an increase of heat capacity and in a decrement of thermal conductivity (Figs. 2.3 and 2.4). Using the data of Table 2.1 for well H-19, with the highest $\rho_s c_p$ value, we obtain $\delta_T = 6.62 \times 10^{-7} \text{ m}^2/\text{s}$, while for well H-18, with lower $\rho_s c_p$, we have $\delta_T = 11.2 \times 10^{-7} \text{ m}^2/\text{s}$. This is a typical range of diffusivity values for volcanic rocks (Fig. 2.5). For sandstones, $\delta_T = 9 \times 10^{-7} \text{ m}^2/\text{s}$ is an average value at 200°C (Contreras *et al.* 1990).

Therefore the effect of temperature on rock diffusivity can be significantly large. As a general trend, diffusivity is reduced when temperature increases. Experimental data show that many porous rocks have similar trends in this dependence of diffusivity on temperature, although one exception is the tufaceous sandstone (Passmore and Archer 1985), whose diffusivity decreases from 90°C up to 540°C and then it grows up to 980°C. To calculate accurately the rock diffusivity in every particular case, it is necessary to build semi-empiric correlations as those illustrated in equations (2.9) and (2.18).

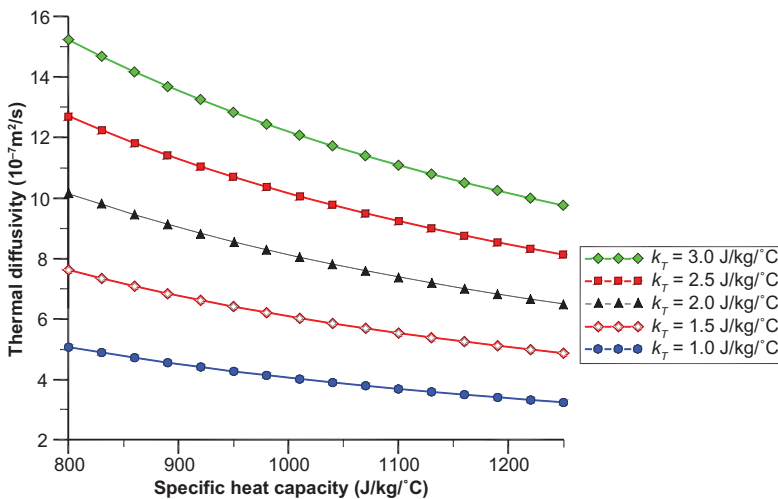


Figure 2.5. Thermal diffusivity of andesites as a function of c_p for different values of thermal conductivity: $k_T = 1.0, 1.5, 2.0, 2.5, 3.0$ [W/m°C]; rock density is $\rho_s = 2460 \text{ kg/m}^3$.

2.1.8.2 Volumetric thermal expansivity

The heat absorption is manifested as a dilatation of rock volume size. However, if the rock is cooling its volume decreases. This thermal rock expansion/contraction can be linear, areal or volumetric and it causes internal stresses. The volumetric expansivity concept is applicable to solids, liquids and gases. The bulk expansivity is measured by the volumetric thermal expansion coefficient at constant confining pressure p_k (see section 2.2.4):

$$\gamma_B = \frac{1}{V_B} \left(\frac{\partial V_B}{\partial T} \right)_{p_k} = - \frac{1}{\rho_s} \left(\frac{\partial \rho_s}{\partial T} \right)_{p_k} \quad \left[\frac{1}{\text{K}} \right] \text{ or } \left[\frac{1}{^\circ\text{C}} \right] \quad (2.22a)$$

The general trend is that thermal expansion increases when temperature rises. γ_B is about 10^{-5} K^{-1} for solids, 10^{-4} K^{-1} for liquids and 10^{-3} K^{-1} for gases. The thermal expansion coefficient of the pores at constant p_k and constant pore pressure p is:

$$\gamma_\varphi = \frac{1}{V_\varphi} \left(\frac{\partial V_\varphi}{\partial T} \right)_p = \frac{1}{\varphi V_B} \left(\frac{\partial (\varphi V_B)}{\partial T} \right)_p = \frac{1}{\varphi} \left(\frac{\partial \varphi}{\partial T} \right)_p \quad (2.22b)$$

The last term of equation (2.22b) defines the expansivity of the pores in the rock, coupling the fluid and heat flow to the rock deformation. The linear thermal expansion is commonly used in geomechanics and in mechanical and civil engineering:

$$\alpha_x = \frac{1}{x_0} \left(\frac{\partial x}{\partial T} \right)_{p_k} \quad (2.22c)$$

If the temperature difference $\Delta T = T - T_0$ is relatively small, a very practical formula can be deduced from equation (2.22c):

$$x \approx (1 + \alpha_x \Delta T) x_0 \quad (2.22d)$$

This equation allows to approximate the linear dilatation of cylindrical cores when temperature increases. For example, a core of granite of initial length $x_0 = 20 \text{ cm}$, with $\alpha_x = 20 \times 10^{-6} \text{ 1/}^\circ\text{C}$ will expand to $x \approx 20.02 \text{ cm}$, for a $\Delta T = 50^\circ\text{C}$.

The areal thermal expansion coefficient at constant pressure is defined as:

$$\alpha_A = \frac{1}{A_0} \left(\frac{\partial A}{\partial T} \right)_{p_k} \quad (2.22e)$$

For isotropic, homogeneous rocks, the bulk, areal and linear expansivities are related by approximate formulae that are constructed for a volume $V_B = x^3$ of area $A_B = x^2$. The approximation is based on the small deformation hypothesis; if $x \approx x_0$, we obtain:

$$\begin{aligned} \alpha_A &= \frac{1}{A_0} \left(\frac{\partial A}{\partial T} \right)_{p_k} = \frac{1}{x_0^2} \left(\frac{\partial x^2}{\partial T} \right)_{p_k} \approx \frac{2x_0}{x_0^2} \left(\frac{\partial x}{\partial T} \right)_{p_k} \\ \gamma_B &= \frac{1}{V_B} \left(\frac{\partial V_B}{\partial T} \right)_{p_k} = \frac{1}{x_0^3} \left(\frac{\partial x^3}{\partial T} \right)_{p_k} \approx \frac{3x_0^2}{x_0^3} \left(\frac{\partial x}{\partial T} \right)_{p_k} \\ \Rightarrow \quad \alpha_A &\approx 2\alpha_x, \quad \text{and} \quad \gamma_B \approx 3\alpha_x \end{aligned} \quad (2.22f)$$

Both approximations are valid only for small deformations. The thermal expansion of fluids is calculated using equation (2.22a), replacing V_B by the fluid volume V_f and ρ_s by the fluid density ρ_f . Other thermal expansion coefficients, for the rock and for the fluid, are defined in

section 2.2.1.1. The expansivity of geothermal rocks is relatively small, but its effects can produce severe structural damages in rocks subjected to strong temperature gradients, as happens during the injection of cold fluids. This is of great importance for enhanced geothermal systems, when the injected fluid circulates in the underground. This action can change both, the permeability and the rock thermal conductivity.

2.1.9 Mechanical parameters of rocks

Petrophysical properties are influenced by geomechanical stresses acting in the reservoir (Farmer 1968, Dandekar 2006). In this subsection, we introduce the fundamental parameters describing the solid rock elastic properties. In section 2.2.5 we define the corresponding poroelastic rock coefficients.

2.1.9.1 Stress and strain

Any applied force tends to modify the rock dimensions by tension or dilatation ($\sigma_x > 0$), compression ($\sigma_x < 0$), or shear ($\sigma_{xy} \neq 0$). The stress acting in the OX direction is defined as the applied force F_x per unit area A (Fig. 2.6):

$$\sigma_x = \frac{F_x}{A} \quad \left[\frac{\text{N}}{\text{m}^2} = \text{Pa} \right] \quad (2.23a)$$

The strain is a measure of the relative deformation of a rock when a stress is acting. If a cylindrical core of diameter d_0 and initial length x_0 is subjected to an axial stress σ_x (Fig. 2.6) in such a way that its original length changes to a value x , then the axial strain in the OX direction is:

$$\varepsilon_x = \frac{x - x_0}{x_0} = \frac{\Delta x}{x_0} = \frac{\partial u_x}{\partial x} \quad \left[\frac{\text{m}}{\text{m}} = \text{ad} \right] \quad (2.23b)$$

where u_x represents the displacement of the solid particles, defined in section 2.1.2. This experiment is extended to the other axis OY and OZ to define $\sigma_y, \sigma_z, \varepsilon_y$ and ε_z , respectively. An elastic deformation occurs if the strain becomes null when the stress is removed and the rock returns to its original shape. If the strain is not zero the deformation is called plastic or permanent.

2.1.9.2 Young's modulus

The Young's modulus is an elastic parameter, which is defined as the ratio of longitudinal stress to longitudinal strain; it describes the response to linear stress. In the same OX axis (uniaxial stress state):

$$E = \frac{F_x/A}{\Delta x/x_0} = \frac{\sigma_x}{\varepsilon_x} \quad \left[\frac{\text{N}}{\text{m}^2} = \text{Pa} \right] \quad (2.24a)$$

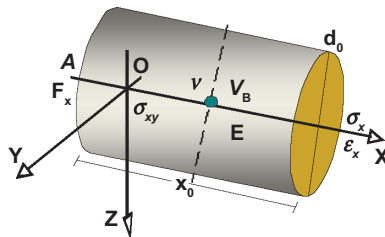


Figure 2.6. A cylindrical rock sample.

2.1.9.3 Poisson's modulus

The Poisson's modulus is an important elastic parameter that measures the rock compressibility perpendicular to applied stress. It is experimentally defined as the ratio of transversal (diameter in the OY or OZ axis) to longitudinal strain (OX axis). For the same cylinder in Figure 2.6 (uniaxial stress state):

$$\nu = \frac{\Delta d/d_0}{\Delta x/x_0} = -\frac{\varepsilon_y}{\varepsilon_x} = -\frac{\varepsilon_z}{\varepsilon_x} \quad [\text{ad}] \quad (2.24b)$$

The minus sign appears because when the cylinder is dilated in the OX direction, its diameter is reduced and *vice versa*, if the cylinder is compressed, ε_x decreases and both perpendicular strains ε_y and ε_z augment because the cylinder's diameter is dilated.

2.1.9.4 Bulk modulus

The bulk modulus is a coefficient, which measures the change in hydrostatic pressure when the rock volume changes with respect to an initial volume $V_0 = V_B$:

$$K_B = -\frac{\Delta p}{\Delta V_B/V_B} \quad [\text{Pa}] \quad (2.24c)$$

2.1.9.5 Rock compressibility

The rock compressibility is a coefficient, which measures the change in volume when the hydrostatic pressure changes with respect to an initial volume V_B . It is the reciprocal of the bulk modulus; when the test is done at constant temperature, C_B is the rock isothermal compressibility:

$$C_B = -\frac{1}{V_B} \frac{\Delta V_B}{\Delta p} = \frac{1}{K_B} \quad [\text{Pa}^{-1}] \quad (2.24d)$$

2.1.9.6 Rigidity and Lamé moduli

Rigidity and Lamé moduli are important elastic parameters, which measure the resistance of the rock to change in shape. The rigidity modulus describes the response to shear; that is why it is also known as the shear coefficient:

$$G = \frac{\text{shear stress}}{\text{shear strain}} = \frac{1}{2} \frac{\sigma_{xy}}{\varepsilon_{xy}} \quad [\text{Pa}] \quad (2.24e)$$

The Lamé module λ , expresses the rock response to tension or compression:

$$\lambda = K_B - \frac{2}{3}G \quad [\text{Pa}] \quad (2.24f)$$

Elastic energy conditions require that $K_B = \lambda + 2G/3 \geq 0$ and $-1 < \nu \leq 0.5$ always hold in isothermal, isotropic rocks (Mavko *et al.* 2003). Measured values of some of these coefficients in different rocks are shown in Tables 2.1, 2.3 and 2.4. For a complete description of laboratory measurements of all these basic rock elastic constants, the interested reader should consult the excellent book of Dandekar (2006).

2.1.9.7 Volumetric strain

Adding the three longitudinal strains in the OX, OY and OZ axis, respectively, we obtain the volumetric strain, a fundamental variable of porous mechanics (note that in classic elasticity $\varepsilon_B = \varepsilon_{kk} = \varepsilon_{xx} + \varepsilon_{yy} + \varepsilon_{zz}$):

$$\varepsilon_B = \varepsilon_x + \varepsilon_y + \varepsilon_z = \frac{\Delta x}{x_0} + \frac{\Delta y}{y_0} + \frac{\Delta z}{z_0} = \frac{y_0 z_0 \Delta x + x_0 z_0 \Delta y + x_0 y_0 \Delta z}{x_0 y_0 z_0} = \frac{\Delta V_B}{V_B^0} \quad (2.24g)$$

The ratio of volume change to the original rock volume is equal to the sum of the principal strains and is called the volumetric strain. In section 2.1.3 we showed that the divergence of the velocity of the rock deformation is equal to the rate of change of the rock volume (eq. 2.7). This was a consequence of the rock mass conservation. The same result can be obtained if we take the time derivatives of both sides of ε_B in the previous equation. As a numerical example we take the dimensions $x_0 = y_0 = z_0 = 2$ cm and $\Delta x_0 = \Delta y_0 = \Delta z_0 = 0.1$ cm. Then the volume $V_B = 8$ cm³, $\Delta V_B = 1.2$ cm³ and $\varepsilon_B = 0.15$.

Among the six elastic coefficients, only two are independent; the other four are deduced from them. The mutual relationships among the elastic parameters in isotropic rocks are (Mavko *et al.* 2003, Dill 2007):

$$\begin{aligned} \lambda &= \frac{E\nu}{(1+\nu)(1-2\nu)}, \quad G = \frac{E}{2(1+\nu)}, \quad K_B = \lambda + \frac{2}{3}G, \quad \lambda = \frac{2G\nu}{1-2\nu} \\ E &= \frac{3\lambda + 2G}{\lambda + G}G, \quad \nu = \frac{\lambda}{2(\lambda + G)}, \quad K_B = \frac{E}{3(1-2\nu)}, \quad \nu = \frac{E}{2G} - 1 \end{aligned} \quad (2.25)$$

2.1.10 Elasticity equations for Hookean rocks

We introduce the equations of simple elastic solids relating stresses and deformations (Mase and Mase 1999, Dill 2007). In this case, the bulk volume is the solid volume $V_B = V_s$ and $\varepsilon_B = \varepsilon_s$ because there are no pores. If the tensorial relations between stresses and strains are linear, the solid rock is called Hookean. In an inertial frame of reference OXYZ (Fig. 2.6), these classic relationships are (subscript s means solid phase):

$$\begin{aligned} \text{stress: } \boldsymbol{\sigma}_s &= \lambda \varepsilon_B \mathbf{I} + 2G\boldsymbol{\varepsilon}_s \quad \Leftrightarrow \quad \text{strain: } \boldsymbol{\varepsilon}_s = -\frac{\nu \sigma_{kk}}{E} \mathbf{I} + \frac{1+\nu}{E} \boldsymbol{\sigma}_s \\ \boldsymbol{\sigma}_s &= \begin{pmatrix} \sigma_x & \sigma_{xy} & \sigma_{xz} \\ \sigma_{xy} & \sigma_y & \sigma_{yz} \\ \sigma_{xz} & \sigma_{yz} & \sigma_z \end{pmatrix}_s = \begin{pmatrix} \lambda\varepsilon_B & 0 & 0 \\ 0 & \lambda\varepsilon_B & 0 \\ 0 & 0 & \lambda\varepsilon_B \end{pmatrix}_s + 2G \begin{pmatrix} \varepsilon_x & \varepsilon_{xy} & \varepsilon_{xz} \\ \varepsilon_{xy} & \varepsilon_y & \varepsilon_{yz} \\ \varepsilon_{xz} & \varepsilon_{yz} & \varepsilon_z \end{pmatrix}_s \\ \Leftrightarrow \quad \boldsymbol{\varepsilon}_s &= \begin{pmatrix} \varepsilon_x & \varepsilon_{xy} & \varepsilon_{xz} \\ \varepsilon_{xy} & \varepsilon_y & \varepsilon_{yz} \\ \varepsilon_{xz} & \varepsilon_{yz} & \varepsilon_z \end{pmatrix}_s = -\frac{\nu \sigma_{kk}}{E} \begin{pmatrix} 1 & 0 & 0 \\ 0 & 1 & 0 \\ 0 & 0 & 1 \end{pmatrix} + \frac{1+\nu}{E} \begin{pmatrix} \sigma_x & \sigma_{xy} & \sigma_{xz} \\ \sigma_{xy} & \sigma_y & \sigma_{yz} \\ \sigma_{xz} & \sigma_{yz} & \sigma_z \end{pmatrix}_s \end{aligned} \quad (2.26a)$$

$$\text{where: } \varepsilon_B = \varepsilon_x + \varepsilon_y + \varepsilon_z; \quad \sigma_{kk} = \sigma_x + \sigma_y + \sigma_z = 3\sigma_M = \frac{E}{1-2\nu} \varepsilon_B = 3K_B \varepsilon_B \quad (2.26b)$$

Let $u_s = (u_x, u_y, u_z)$ be the vector displacement of the solid particles. Using the compact tensorial notation described in books on continuum mechanics (e.g., Dill 2007), the components of the symmetric matrix equations (2.26a) for isotropic rocks have the equivalent form:

$$\begin{aligned} \sigma_{ij} &= \lambda \varepsilon_B \delta_{ij} + 2G \varepsilon_{ij} \Leftrightarrow \varepsilon_{ij} = \frac{1+\nu}{E} \sigma_{ij} - \frac{\nu}{E} \sigma_{kk} \delta_{ij}; \quad i, j = x, y, z \\ \text{where: } \varepsilon_{ij} &= \frac{1}{2} \left(\frac{\partial u_i}{\partial x_j} + \frac{\partial u_j}{\partial x_i} \right), \quad \varepsilon_i = \varepsilon_{ii} = \frac{\partial u_i}{\partial x_i}; \quad i, j = 1, 2, 3; \quad \left\{ \begin{array}{l} x_1 = x \\ x_2 = y \\ x_3 = z \end{array} \right\} \end{aligned} \quad (2.27)$$

Note that this is a three-dimensional generalization of previous relations between stress and strains introduced in section 2.1.9 (Fig. 2.6). The symbols in the preceding equation are of common and ordinary use: σ_{ij} holds for the six applied stresses in [Pa]; ε_{ij} are the six strains [ad], describing

the global elastic response of the solid. Coefficients λ , G , E and ν were already defined; δ_{ij} is the unit tensor ($\delta_{ii} = 1$, $\delta_{ij} = 0$ if $i \neq j$) and σ_M is the average stress. The term $\varepsilon_B = \varepsilon_{kk}$ represents the volumetric deformation of the solid rock and σ_{kk} is the trace of the stress tensor σ_s .

Tensors σ_s and ε_s are symmetric, this is a consequence of Newton's second law applied to solid dynamics (Duc and Bellet 1976). Both tensors are equivalent to a couple of six dimensional vectors and the matrix system can be transformed into a more convenient expression for the elastic deformation and poroelastic coupling. Adding a null column and a null row (to include later, in section 2.2.8 the fluid stress), and arranging the linear equations defined by the system (2.26a) in the order $(\sigma_x, \sigma_y, \sigma_z, \sigma_{xy}, \sigma_{xz}, \sigma_{yz})$, we obtain:

$$\vec{\sigma}_s = \begin{pmatrix} \sigma_x \\ \sigma_y \\ \sigma_z \\ \sigma_{xy} \\ \sigma_{xz} \\ \sigma_{yz} \\ 0 \end{pmatrix}_s = \begin{pmatrix} \lambda + 2G & \lambda & \lambda & 0 & 0 & 0 & 0 \\ \lambda & \lambda + 2G & \lambda & 0 & 0 & 0 & 0 \\ \lambda & \lambda & \lambda + 2G & 0 & 0 & 0 & 0 \\ 0 & 0 & 0 & 2G & 0 & 0 & 0 \\ 0 & 0 & 0 & 0 & 2G & 0 & 0 \\ 0 & 0 & 0 & 0 & 0 & 2G & 0 \\ 0 & 0 & 0 & 0 & 0 & 0 & 0 \end{pmatrix}_s \cdot \begin{pmatrix} \varepsilon_x \\ \varepsilon_y \\ \varepsilon_z \\ \varepsilon_{xy} \\ \varepsilon_{xz} \\ \varepsilon_{yz} \\ 0 \end{pmatrix}_s \quad (2.28)$$

This is the vectorial form of Hooke's law for an isotropic solid rock with zero porosity. It establishes a linear vector-tensor relationship between stresses and strains acting in a homogeneous rock. The elastic coefficients λ and G are assumed constant and the same at every point of the rock volume.

2.2 LINEAR THERMOPOROELASTIC ROCK DEFORMATION

The world literature on rock mechanics describes the existence of land subsidence in aquifers, in petroleum and gas fields, and in geothermal reservoirs caused by their exploitation (Biot 1962, Colback and Wiid 1965, Lippmann *et al.* 1977, Blés and Feuga 1986, Wang 2000). This phenomenon is a direct consequence of the rock deformation. In enhanced geothermal systems (EGS), artificial stimulation is applied to deform the rock and to increase porosity and permeability. Poroelasticity is the branch of geomechanics that studies the behavior of porous elastic rocks containing viscous fluids such as water, brine, gas and oil. A poroelastic rock is characterized by its porosity, its elastic moduli and by the physical properties of the fluids that it contains. The poroelastic rock deformation can be linear or non-linear, isothermal or non-isothermal. In this section, we describe the basic poroelasticity concepts.

2.2.1 Effects of the fluid on porous rock properties

Water contained in a rock, reduces its strength compared to dense rocks ($\varphi \approx 0$). The cohesive structure of rocks is weakened by the presence of liquid. All the geomechanical parameters are influenced by this cohesion and are directly affected by the pressure and amount of liquid present in both pores and fractures. This is generally called the *pore-water effect* (Terzaghi 1943). Rock compaction, fracturing, time dependent deformations, as well as creep and subsidence are essentially produced by volcanic and tectonic activities, by lithostatic pressure and by fluid extraction/injection.

In water-saturated rocks, density and wave propagation speed are increased compared with dry gas-saturated rocks, while strength is reduced. In aquifers and in geothermal reservoirs, the different values in parameters of dry rock and wet rock are determined by the amount of liquid water saturation, porosity, permeability, pressure and temperature. Compared with steam or with air, liquid water is almost incompressible, and this property tends to reduce both rock deformation and stiffness. The main hypothesis in linear poroelasticity is that the fluids flow through a deformable porous rock whose solid skeleton can be deformed elastically. Assuming

that rocks are only subjected to small deformations, Hooke's law (2.28) can be applied to relate strains and stresses.

Fluid extraction in natural reservoirs causes the reduction of the internal pore-fracture pressure and of the effective aperture of pores and fissures. Many naturally fractured systems experienced intense tectonic activity in their remote past and their original fracturing was equally intense. However, some of the systems contain fissured zones where most of the fractures appear closed (S. Arriaga and Verduzco 1998). This phenomenon is partially explained by the fact that dry rock deformation and saturated rock deformation are different. In the next subsection, we develop a simple model to calculate elastic fissure deformations.

2.2.2 A simple model for the collapse of fractures in poroelastic rocks

The reduction of the internal pore pressure in reservoir rocks produces subsidence. A similar event occurs in fissures of naturally fractured reservoirs. Fractures in these systems can also be closed because of fluid lost by natural means or through human activity. Some hydrothermal reservoirs contain portions of fractured rock where many fractures appear closed. Studies carried out in the Los Humeros, Mexico geothermal field, a prototype of this type of systems, strongly suggest that at the moment of its formation, for unknown reasons, the reservoir was unable to store enough water in its pores and fissures (Suárez and Samaniego 1995, Suárez 1998). This lack of fluid could produce the collapse of fractures and faults, which could result in a global drop in permeability. At the same time, the collapse of fissures permits the coexistence of very strong pressure gradients between the matrix blocks and the residual open fractures. Autosealing processes, during water-rock interactions at high temperature, can accentuate this last effect. The tectonic movements in this field did not have enough intensity to produce faults of great penetrability beneath the surface. At the same time, the shortage of water prevented the fracturing from being more intense. The created fractures collapsed because of the lack of hydraulic support. Based on the classical elastic continuum theory of rock mechanics (Farmer 1968, Asszonyi and Richter 1979, Blès and Feuga 1986), and using the following data and assumptions, we can calculate approximately how the fluid in a fractured rock matrix affects the internal stresses.

Let Ω be a rock portion of a reservoir saturated with water in liquid phase. The rock is confined and crossed by a single fracture f , which is perpendicular to the plane YZ (Fig. 2.7). The fracture is inclined at an angle θ with respect to the Z -axis. The water in Ω has very low compressibility and the pore-water pressure is almost equal to the hydraulic pressure p_w in Ω , which can be represented by a spherical tensor $p_w \delta_{ij}$. We assume that X, Y, Z are the principal axes and Ω is subjected to the stresses $(\sigma_X, \sigma_Y, \sigma_Z)$ as shown in Figure 2.7. To simplify, we also assume that the main pressure effects are contained in the plane YZ and that σ_Y (lateral confining stress)

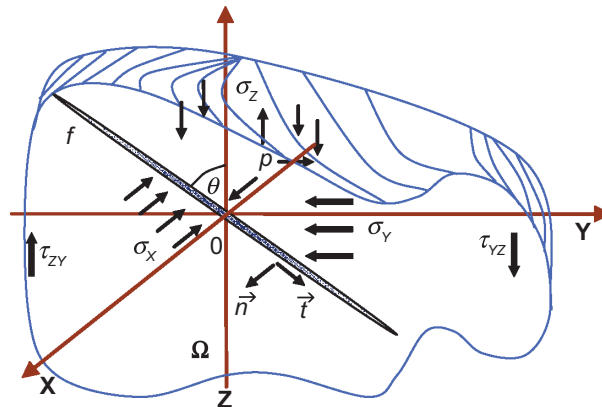


Figure 2.7. Principal stresses acting in a single fracture f of a porous rock.

and σ_Z (vertical stress) are the principal stresses, minimum and maximum, respectively, having a zero shear stress on this plane $\tau_{YZ} = \tau_{ZY} = 0$, after the fracture was created.

A compressive stress σ_Z is applied to Ω , as shown in Figure 2.7. The plane YZ is orthogonal to the plane of failure. The stress tensor inside the fracture can be simplified if it is represented by an orthonormal coordinate system (\vec{i}, \vec{n}) , where \vec{i} and \vec{n} are unit vectors, tangential and orthogonal to f , respectively. In this frame of reference, if the rock is dry, the normal stress σ and the tangential shear stress τ acting in the direction θ of the fracture are given by the following equations:

$$\tau = \frac{\sigma_Z - \sigma_Y}{2} \sin 2\theta \quad \text{and:} \quad \sigma = \frac{\sigma_Z + \sigma_Y}{2} + \frac{\sigma_Z - \sigma_Y}{2} \cos 2\theta \quad (2.29)$$

On the other hand, in saturated rock the effective stresses acting in the fracture will be decreased by p_w . Terzaghi (1943; section 2.2.6) discovered this effect when he showed experimentally that the effective stress tensor acting in saturated rocks is reduced by p_w in the form: $\sigma_I - p_w$ ($I = X, Y, Z$) in every principal stress component. Replacing these effective stresses in equation (2.29), we obtain the shear or tangential stress τ_w and the normal stress σ_w acting in the fracture saturated with liquid water. The following formulae show that the shear stresses in dry rock or in wet rock are the same, while the effective normal stress is reduced by an amount equal to p_w :

$$\begin{aligned} \sigma_w &= \frac{\sigma_Z + \sigma_Y}{2} + \frac{\sigma_Z - \sigma_Y}{2} \cos 2\theta - p_w \\ \tau_w &= \frac{(\sigma_Z - p_w) - (\sigma_Y - p_w)}{2} \sin 2\theta = \tau \end{aligned} \quad (2.30)$$

If the fracture is vertical, $\theta = 0^\circ$ and $\sigma_w = \sigma_Y - p_w$. If the fracture is horizontal $\theta = 90^\circ$ and $\sigma_w = \sigma_Z - p_w$. If the fracture is inclined at an angle $\theta = 45^\circ$, $\sigma_w = (\sigma_Z + \sigma_Y)/2 - p_w$. To illustrate an application of this model to the Los Humeros geothermal reservoir, we take the parameters of well H-27 in Table 2.1. The rock density is $\rho_s = 2400 \text{ kg/m}^3$ at a depth $z = 1500 \text{ m}$; the pore-water pressure p_w is 12.5 MPa. The corresponding temperature is 310°C and the liquid density is 700 kg/m^3 . The confining lateral pressure and the lithostatic load, respectively, are the numerical values of the principal stresses σ_Y and σ_Z : $\sigma_Z = \rho_s g z + p_0 = 35.38 \text{ MPa}$, $\sigma_Y = \alpha \rho_r g z = 31.75 \text{ MPa}$. Here $g = 9.8 \text{ m/s}^2$ is the acceleration of gravity, $p_0 = 0.1 \text{ MPa}$ is the atmospheric pressure, and α is an experimental correction coefficient, which ranges between 0.5 and 0.9 (Farmer 1968). The first value (0.5) corresponds to saturated rock with high porosity while the second one (0.9) is for almost dry rock with low porosity. Assuming $\alpha = 0.9$ and an angle $\theta = 60^\circ$ for the inclination of the fracture we obtain from equation (2.29) in dry rock: $\sigma_{\text{dry}} = 32.66 \text{ MPa}$, $\tau_{\text{dry}} = \tau_w = 1.57 \text{ MPa}$. The same data applied to equation (2.30) for saturated rock give: $\sigma_w = 20.16 \text{ MPa}$. In the same reference frame, (\vec{i}, \vec{n}) , the strain tensor is:

$$\varepsilon_t = -\frac{\nu\tau}{E}, \quad \varepsilon_n = \frac{\sigma}{E} \quad (2.31)$$

The average modulus of elasticity and Poisson's ratio are listed in Table 2.1. They are equal to $E = 3.32 \times 10^4 \text{ MPa}$ and $\nu = 0.23$. Elastic strain is also different in each case. For the practical purpose of estimating fracture deformation in the orthogonal direction, we define $\delta z_n = z \varepsilon_n$ as the small normal compression experienced by the fracture relative to dimension z in the orthogonal direction. We also assume that fractures are separated by a distance $z = 1 \text{ m}$. Introducing these data into equations (2.31) for dry rock we obtain:

$$\varepsilon_t = -\frac{0.23 \times 15.7}{3.32 \times 10^5} = -1.09 \times 10^{-5}, \quad \varepsilon_n = \frac{326.59}{3.32 \times 10^5} = 9.84 \times 10^{-4} \quad \Rightarrow \quad \delta z_n \cong 1 \text{ mm} \quad (2.32a)$$

Substituting the available data in equation (2.31) we obtain for saturated rocks:

$$\varepsilon_w = \frac{201.6}{3.32 \times 10^5} = 6.07 \times 10^{-4} \Rightarrow \delta z_n \cong 0.6 \text{ mm} \quad (2.32b)$$

In the previous example, we assumed that the modulus of elasticity E is not affected by the presence of water. Nevertheless, practical experiences show that liquid saturation affects the value of E in porous rocks. The behavior of this coefficient in rock with water is supported by experimental results obtained by Colback and Wiid (1965), when they measured a strength reduction of 50% in saturated sandstone. The effect of the pore-water pressure p_w on the elasticity of the rock leads to an equivalent decrease in strain that can be approximated by the next formula (Farmer 1968), which suggests a decreased modulus of elasticity:

$$\varepsilon_w = \left(\frac{0.5}{E} \right) \sigma_w = \frac{0.5 \times 201.6}{3.32 \times 10^5} = 3.04 \times 10^{-4} \Rightarrow \delta z_n \cong 0.3 \text{ mm} \quad (2.32c)$$

From this simple model, we can deduce that in dry, low porosity rocks, natural fractures present a clear tendency to be closed by normal lithostatic stresses. Under the same loading conditions, fractures filled with water will not collapse because of the presence of a fissure-pore-water pressure opposing the normal stress. High porosity saturated rocks will be considerably weakened by the presence of water even at low pressure, facilitating the formation of fractures. That is why artificial fracturing of the underground can be done with water injection. The Reh binder effect (Farmer 1968) postulates that p_w causes a reduction of the cohesive structure of the rock, which is weakened by the presence of liquid in the pores. Since all deformation and failure characteristics are influenced by this cohesion, they will be affected in direct proportion to the pressure and to the liquid saturation. Strength and elastic modulus will be decreased. The following practical conclusions are extracted from these results:

- Some reservoirs contain small amounts of liquid, but their original porosity and permeability were probably high. The lack of fluid can result in the collapse of pores and fissures because their internal hydraulic stresses could not balance the lithostatic load. Water-rock interaction facilitated the selfsealing of fractures. Under these natural conditions, fractures can be closed by the vertical compression, unless there is an opposite local force equilibrating the lithostatic load.

2.2.3 Linear deformation of rocks containing isothermal fluid

Several factors affect the geomechanical behavior of crustal rocks: porosity, pressure, temperature, and the presence of fluids, fissures and faults. Diverse phenomena produce rock deformations, compaction, fracturing, creep and subsidence in reservoirs. Stress variations lead to changes in seismic velocities affecting the time-lapse seismic response. These processes are thermodynamically irreversible, yielding permanent plastic deformations that could reduce the reservoirs' storage capacity. There are other important thermo-mechanical effects in aquifers, in geothermal reservoirs and in hydrocarbon fields. High pressure and temperature increase ductility and lower the yield point of the rock. The high confining pressure effects induce plastic flows.

Faults and fractures within geothermal systems are produced by stresses from tectonic events in brittle rocks producing deformations beyond the limit of elastic strain. We have observed that fissures and microfractures are more numerous near large, regional faults (S. Arriaga and Verdusco 1998). Other authors (e.g., Blès and Feuga 1986) reported similar experiences. This phenomenon occurs because at the time a fault is generated within massive rocks, the original stress distribution is modified in a neighborhood around the fault, producing the development of different tension fractures especially near the end of the fault. In volcanic geothermal reservoirs, highly heterogeneous structural systems are developed, whereas in large sedimentary basins and in old basement rock areas, both useful for EGS, heterogeneity is lower.

2.2.3.1 Differential relationships between porosity and volumes

The structural volume V_B or bulk volume is the global volume occupied by the solid rock V_s with its pores and fractures V_Φ . The differential relationships between these three volumes and the porosity (eq. 2.2), are:

$$\text{volumes: } V_B = V_\Phi + V_s \quad \Rightarrow \quad 1 = \frac{V_B}{V_B} = \frac{V_\Phi + V_s}{V_B} \quad \text{and} \quad dV_B = dV_\Phi + dV_s \quad (2.33a)$$

$$\text{differentials: } \frac{dV_B}{V_B} = \frac{dV_\Phi + dV_s}{V_B} = \frac{dV_\Phi}{V_B} + \frac{dV_s}{V_B} = \varphi \frac{dV_\Phi}{V_\Phi} + \varphi_s \frac{dV_s}{V_s} \quad (2.33b)$$

$$\frac{dV_\Phi}{\varphi V_B} = \frac{V_B d\varphi + \varphi dV_B}{\varphi V_B} \quad \Rightarrow \quad \frac{d\varphi}{\varphi} = \frac{dV_\Phi}{V_\Phi} - \frac{dV_B}{V_B} \quad (2.33c)$$

We can include explicitly the matrix and fractures volumes and porosities φ_M and φ_F introduced in section 2.1.2:

$$\begin{aligned} 1 &= \frac{V_M}{V_B} + \frac{V_F}{V_B} + \frac{V_s}{V_B} = \varphi_M + \varphi_F + \varphi_s \quad \Rightarrow \quad \frac{dV_B}{V_B} = \varphi_M \frac{dV_M}{V_M} + \varphi_F \frac{dV_F}{V_F} + \varphi_s \frac{dV_s}{V_s} \\ &\Rightarrow \frac{d(\varphi_M + \varphi_F)}{\varphi_s} = \frac{V_B d\varphi_M}{V_B \varphi_s} + \frac{V_B d\varphi_F}{V_B \varphi_s} = \frac{dV_M + dV_F}{V_B \varphi_s} - \frac{(\varphi_M + \varphi_F) dV_B}{V_B \varphi_s} = \frac{dV_B}{V_B} - \frac{dV_s}{V_s} \\ &\Rightarrow \frac{d\varphi}{\varphi_s} = \frac{dV_B}{V_B} - \frac{dV_s}{V_s} \end{aligned} \quad (2.34)$$

A detailed description of geomechanics coupled to a matrix-fractures dual porosity model was published by Chen *et al.* (1997). Let V_f be the volume of the fluid in the pores. Then the volumetric strains for the fluid ε_f , the bulk rock ε_B and the solid rock ε_s are:

$$\varepsilon_f = \frac{dV_f}{V_f}, \quad \varepsilon_B = \frac{dV_B}{V_B}, \quad \varepsilon_s = \frac{dV_s}{V_s} \quad \left[\frac{\text{m}^3}{\text{m}^3} = \text{ad} \right] \quad (2.35)$$

The physical meaning of a differential volume dV_B , when it is experimentally measured in the laboratory, is simply: $dV_B \approx \Delta V_B = V_B - V_0$ (see eq. 2.24g). These equations constitute an important part of the experimental bases of porous fractured rock mechanics.

2.2.4 Poroelastic rock parameters: Drained and undrained conditions

Different types of compressibility can be defined that are crucial to coupling the mass and energy flows to the rock deformation. The experimental relations between stress and volumetric deformations are based on the definition of the following pressures:

- confining lithostatic pressure: p_k
- fluid or pore pressure: $p_f = p = -\sigma_H$
- differential pressure: $p_d = p_k - p_f$
- effective pressure: $p_e = p_k - bp_f$

where b is the Biot-Willis coefficient defined in section 2.2.5; p_f is the pressure of the fluid filling up the pore space and considered positive. Note that the hydrostatic pressure is always compressive and opposed to the fluid pressure, thus $\sigma_H = -p_f < 0$. When the differential pressure is constant, the corresponding experiment is performed under unjacketed conditions. If the pressure p_f inside the pores increases, the absolute permeability is increased. This is the main benefit obtained with fluid reinjection.

Ramey *et al.* (1974) reported an empiric correlation to compute this effect in saturated sandstones, (the pressure is in atmospheres; k_0 is the initial permeability):

$$p_e = p_k - 0.85 p_f \Rightarrow k = k_0 \left(1 + \frac{127 \times 10^{-5}}{p_e} \right)^{-1} \quad (2.36)$$

In experimental poroelasticity, there are four different kinds of bulk moduli and two types of deformations, drained and undrained. Both modes represent limiting responses of the rock (Biot 1941, Fjaer *et al.* 1992, Wang 2000, Guéguen and Bouteca 2004):

- *Drained conditions*: During the test, the rock is confined and subjected to support an external hydrostatic pressure σ_H equal to σ_M (eq. 2.25b). In this test, the fluid in the pores is allowed to escape and the total stress is entirely supported by the rock skeleton. The deformations are achieved at constant pore-fluid pressure p_f . Biot (1962) called these conditions, an “open system”.
- *Undrained conditions*: During this test, the deformations are measured at constant fluid mass content m_f ($\Delta\zeta = 0$). The rock is entirely submerged in a fluid in such a way that the external hydrostatic pressure is balanced by the pore pressure $\sigma_H = -p_f$. In this test, the fluid in the pores remains constant; no fluid is allowed to move into or out of the control volume. The fluid remains trapped in the skeleton. For Biot (1962) this was characteristic of a “closed system”.

One of the central concepts in poroelasticity is the bulk elastic modulus (eq. 2.24c). For the bulk rock with pores and grains and for the solid without pores, the bulk elastic moduli are experimentally defined as the ratio of the hydrostatic stress σ_H relative to the volumetric strains under isothermal conditions:

$$\sigma_H = \sigma_M \Rightarrow K_B = \frac{\sigma_H}{\varepsilon_B}, \quad K_S = \frac{\sigma_H}{\varepsilon_S} \quad (2.37a)$$

2.2.4.1 Drained bulk compressibility

In a porous rock, the solid and the fluid phases are compressible; the skeleton has its own structural compressibility. The elastic modulus K_B measures the resistance of the bulk rock against deformations produced by the confining lithostatic pressure when the fluid pressure remains constant:

$$p_f \text{ constant} \Rightarrow \sigma_H = -p_d = -p_k, \quad \text{and} \quad K_B = - \left(\frac{\Delta p_k}{\Delta \varepsilon_B} \right)_{p_f} \quad (2.37b)$$

The jacketed volumetric or bulk compressibility, C_B , is defined as the drained deformation obtained when the rock is subjected to compressive stresses in all directions and the pressure of the fluid contained in the pores remains constant. Then $\Delta p_f = 0$ and $\Delta p_d = \Delta p_k$. The confining pressure is hydrostatic during the test. The rock compressibility C_B is the inverse of K_B . The measurements of C_B evaluate the changes of the bulk volume V_B , which includes pores, fractures and solid grains. Therefore, C_B is the compressibility of the rock’s skeleton, also known as the drained jacketed bulk compressibility (Chen *et al.* 1995). Its mathematical expression is:

$$C_B = - \frac{1}{V_B} \left(\frac{\partial V_B}{\partial p_k} \right)_{p_f} = - \frac{1}{V_B} \left(\frac{\partial V_B}{\partial p_d} \right)_{p_f} = \frac{1}{K_B} \quad (2.37c)$$

2.2.4.2 Undrained bulk compressibility

The elastic undrained bulk modulus K_U measures the resistance of the bulk rock against deformations produced by the confining lithostatic pressure when the fluid content ζ remains

constant (eq. 2.35a):

$$\sigma_H = -p_k, \quad \text{and} \quad \zeta \text{ constant} \quad \Rightarrow \quad K_U = -\left(\frac{\Delta p_k}{\Delta \varepsilon_B}\right)_\zeta \quad (2.38a)$$

The undrained bulk compressibility C_U is defined as the undrained deformation obtained when the rock is subjected to compressive stresses in all directions and the fluid contained in the pores remains constant:

$$C_U = -\frac{1}{V_B} \left(\frac{\partial V_B}{\partial p_k}\right)_\zeta = \frac{1}{K_U} \quad (2.38b)$$

2.2.4.3 *Compressibility of the solid phase*

The elastic modulus K_s measures the resistance of the solid rock against deformations produced by the hydrostatic compression:

$$\sigma_H = -p_f, \quad \text{and} \quad p_d \text{ constant} \quad \Rightarrow \quad K_s = -\left(\frac{\Delta p_f}{\Delta \varepsilon_s}\right)_{p_d} \quad (2.39a)$$

The non-jacketed volumetric compressibility C_s is defined as the undrained deformation obtained experimentally under constant differential pressure conditions, that means: $\Delta p_d = 0 \Rightarrow \Delta p_k = \Delta p_f$. In this case any change of the confining pressure is similar to the change of p_f ; the measurements evaluate the changes of the structural volume only when the fluid pressure changes. Therefore, C_s measures the grain compressibility of the solid matrix. The solid bulk modulus K_s is the inverse of C_s :

$$C_s = -\frac{1}{V_B} \left(\frac{\partial V_B}{\partial p_f}\right)_{p_d} = \frac{1}{K_s} \quad (2.39b)$$

If the porosity and the solid mass remain constant during the non-jacketed test:

$$C_s = -\frac{\varphi_s}{V_s} \left(\frac{1}{\varphi_s} \frac{\partial V_s}{\partial p_f}\right)_{p_d} = -\frac{1}{V_s} \left(\frac{\partial V_s}{\partial p_f}\right)_{p_d} = \frac{1}{\rho_s} \left(\frac{\partial \rho_s}{\partial p_f}\right)_{p_d} \quad (2.39c)$$

During this unjacketed, undrained test, the stress-strain response of the rock is completely given by the intrinsic elastic properties of the solid skeleton.

2.2.4.4 *Compressibility of the pore volume*

The unjacketed compressibility of the pore volume C_Φ , is defined as the change of pore volume with respect to the pore pressure change per unit volume when p_d remains constant:

$$C_\Phi = -\frac{1}{V_\Phi} \left(\frac{\partial V_\Phi}{\partial p_f}\right)_{p_d} = -\frac{1}{\varphi} \left(\frac{\partial \varphi}{\partial p_k}\right)_{p_d} \quad (2.40a)$$

The isothermal compressibility of the fluid C_f , when temperature T and fluid mass M_f are constants, is defined as the change of fluid volume with respect to the effective pressure change per unit volume:

$$C_f = -\frac{1}{V_f} \left(\frac{\partial V_f}{\partial p_f}\right)_T = -\frac{\rho_f}{M_f} \left(-\frac{M_f}{\rho_f^2} \frac{\partial \rho_f}{\partial p_f}\right)_T = \frac{1}{\rho_f} \left(\frac{\partial \rho_f}{\partial p_f}\right)_T \quad (2.40b)$$

Equations (2.39a) to (2.40b) define two different forms of unjacketed compressibilities C_s and C_Φ . The compressibility of the pore volume varies with the effective compression, the temperature and the porosity. If the pressure in the pores decreases during the reservoir's fall off, then important

reductions in the pore volume can occur, even with partial or total collapse of pores and fractures (S. Arriaga and Verduzco 1998). The bulk isothermal compressibility is:

$$C_T = -\frac{1}{V_B} \left(\frac{\partial V_B}{\partial p_k} \right)_T \quad (2.40c)$$

Reported effects of pressure in the pore volume (Ramey *et al.* 1974) show that its compressibility decreases when pressure increases within a range of 0.1 to 55 MPa, for temperatures between 24 and 205°C. For higher pressure values the variation is lower. The effect of temperature on the compressibility of the pore volume is appreciated in experiments with different rocks. Several results show that at 205°C the compressibility can be between 12 and 55% higher than at 24°C. The average of all the samples analyzed by Passmore and Archer (1985) shows a compressibility increment of 21% when the temperature increases inside this range. Other experimental results from the same authors, using sandstone cores, show that compressibility increases with porosity in the range between 19 to 28%. Below 19% porosity there was no trend.

2.2.5 The Biot-Willis coefficient

A very important parameter in poroelasticity, which will be used in the next sections, is the Biot-Willis coefficient b (Biot and Willis 1957, Wang 2000, Guéguen and Bouteca 2004). We deduce this coefficient adding both strains of equation (2.37a):

$$\varepsilon_B + \varepsilon_s = -\frac{p_k - p_f}{K_B} - \frac{p_f}{K_s} = -\frac{1}{K_B} \left(p_k - \left(1 - \frac{K_B}{K_s} \right) p_f \right) = \varepsilon \quad (2.41)$$

where ε is the overall volumetric strain. The coefficient b is defined as:

$$b = 1 - \frac{K_B}{K_s} = 1 - \frac{C_s}{C_B} \quad (2.42a)$$

Consequently, from equation (2.41) we can write:

$$-K_B \varepsilon = p_k - b p_f \quad \Rightarrow \quad b = \left(\frac{\partial p_k}{\partial p_f} \right)_\varepsilon \quad (2.42b)$$

Equation (2.42b) is another deduction of the Biot-Willis parameter, expressing that b is equal to the change of pressure p_k with respect to the fluid pressure change when the total volumetric strain remains constant. From experiments it is found that $C_s \leq C_B$ then $K_B \leq K_s$, thus: $0 \leq b \leq 1$; the Biot-Willis coefficient $b = 0$ if and only if there are no pores and $C_s = C_B$. Experimental relationships for porous rocks (Biot and Willis 1957, Fjaer *et al.* 1992, Wang 2000) showed that $\varphi \leq b \leq 1$. In the case of poroelastic soft media like soils and in unconsolidated rocks, it is obvious that $C_B \gg C_s$, therefore $K_B \ll K_s$ and thus $b \approx 1$, which results in the classical Terzaghi equation (2.30). Using the compressibility of the pore volume (eq. 2.40a), the total compressibility of the porous rock, for a drained experiment, is equal to the compressibility of the solid grains plus the compressibility of the pore space:

$$\frac{1}{K_B} = \frac{1}{K_s} + \frac{\varphi}{K_\Phi} \quad \Rightarrow \quad 1 = \frac{K_B}{K_s} + \varphi \frac{K_B}{K_\Phi} \quad (2.43a)$$

$$\Rightarrow \quad b = \varphi \frac{K_B}{K_\Phi} = \frac{-\frac{\varphi}{V_\Phi} \frac{\Delta V_\Phi}{\Delta p_k}}{-\frac{1}{V_B} \frac{\Delta V_B}{\Delta p_k}} = \left(\frac{\Delta V_\Phi}{\Delta V_B} \right)_{p_f} \quad (2.43b)$$



Figure 2.8. Karl Terzaghi (1883–1963). Photo taken in 1926.

This expression gives another definition of b as the ratio of pore volume change to total bulk volume change under drained conditions. Equations (2.43a,b) also provide two ways of computing the drained bulk modulus of the pore space K_{ϕ} . These formulae were obtained from an experiment in which pore fluids can flow in or out of the pores to maintain the pore pressure constant.

2.2.6 *Biot's classical poroelasticity theory*

Aquifers, hydrocarbon reservoirs and geothermal systems are compressible and elastic. Their elasticity is evidenced by the compression that results from the decline of the fluid pressure, which can shorten the pore volume. This reduction of the pore volume can be the principal source of fluid released from storage (Wang 2000). Karl von Terzaghi, an Austrian civil engineer considered the father of soil mechanics (Fig. 2.8), developed the first experimental studies to determine the concept of effective stress in a poroelastic rock containing water. This effect states that in saturated rock the pore-water pressure will decrease the effective stresses acting in the pores. In a porous fractured medium, this law is a *pore-fissure-water effect*. Fluid extraction, for example, causes the reduction of the internal pore-fracture pressure. Terzaghi (1943) explained that the effective total axial load in the porous medium is determined by the sum of the solid stress and the pore pressure $\sigma_z = \sigma_z^s - p_f$.

2.2.6.1 *Fundamental concepts and coefficients in Biot's poroelastic theory*

Maurice A. Biot (Fig. 2.9), an American, engineer, physicist and applied mathematician, born in Antwerp, Belgium in May 25, 1905, formulated the first consistent theory of coupled fluid-solid interaction in soil mechanics and consolidation in 1940. In the 1950s, Biot extended his theory to a general context of rock mechanics connected to problems in the oil industry (Poronet 2009). Biot published his work in a well-known series of classical papers (Biot 1941, 1955, 1962, and 1972; Biot and Willis 1957). Other people made improvements or added some new ideas to Biot's original work (Verruijt 1969, Rice and Cleary 1976, Brownell *et al.* 1977, Garg and Pritchett 1977, Lippmann *et al.* 1977, Garg, 1984 and 1985, Coussy 1991, 1995, Chen *et al.* 1995, Cheng *et al.* 1998, Wang 2000, Morland *et al.* 2004).

Poroelasticity is a continuum theory for the analysis of a porous medium consisting of an elastic matrix containing interconnected pores and fluids. Terzaghi's effective stress concept is the beginning of the first theory on the mechanics of deformation of porous rocks saturated with fluids. In physical terms, the theory postulates that when a porous material is subjected to stress, the resulting matrix deformation leads to volumetric changes in the pores saturated with a fluid. The presence of the moving fluid in the porous rock modifies its mechanical response. In this



Figure 2.9. M. Biot, (1905–1985). Photo supplied by Mme. Biot (Poronet 2009).

theory, the rock skeleton is treated as an elastic solid with a laminar flow of pore fluid coupled to the framework by equilibrium and continuity conditions. The main hypothesis in the classical theory of poroelasticity is that the fluid flows through a deformable porous rock whose framework can be elastically deformed. The pore fluid transport obeys Darcy's law integrating the mechanics of deformable solids. A central hypothesis in this theory is that the rock is Hookean and exposed only to small, reversible strains. Poroelasticity explains how the water inside the pores bears a portion of the total load supported by the porous rock. The solid matrix supports the remaining part of the load. Terzaghi's law is a special case of Biot's poroelastic theory, which is a macroscopic approach.

A geomechanical model is a group of differential equations capable of predicting the porous rock deformation under different internal and external forces. There are different objectives in this matter followed in different areas such as soil mechanics, hydrogeology, seismology, geomechanics, petroleum and geothermal reservoir engineering. That is why there are different coefficients and formulations to represent the porous rock deformation coupled to fluid flow. According to the several authors previously cited, there are two fundamental poroelastic phenomena and two mechanisms playing a key role in the interaction between the pore fluid and the rock:

- Solid-fluid coupling occurs when a change in applied stress produces a change in the fluid pressure or in the fluid mass.
- Fluid-solid coupling occurs when a change in the fluid pressure or in the fluid mass produces a change in the volume of the porous rock.
- An increase of pore pressure induces a dilation of the rock.
- Compression of the rock causes a rise of pore pressure, if the fluid is prevented from escaping the pores.

2.2.6.2 *The fundamental parameters of poroelasticity*

This subsection follows the basic developments of Wang (2000), “*who made a significant contribution to the poroelasticity field*” (Shemin Ge, *ibid.*). We use the concepts and some of the original notation of Biot and Willis (1957) and Biot (1962). In non-porous solids only two moduli, (λ , G) or (E , ν), are necessary to describe the relationship between strains and stresses (eq. 2.28). In isothermal poroelasticity, we need four poroelastic moduli for the same relationships, but only

three of them are independent. The Biot's field variables for an isotropic porous rock are the stress σ acting in the rock, the bulk volumetric strain ε_B , the pore pressure p_f and the variation of fluid content ζ . The linear relations among these variables are the foundations of Biot's poroelastic theory:

$$\varepsilon_B = \frac{\sigma}{K_B} + \frac{p_f}{H}, \quad \zeta = \frac{\sigma}{H} + \frac{p_f}{R} \quad (2.44a)$$

The matrix form of these relationships is:

$$\begin{pmatrix} \varepsilon_B \\ \zeta \end{pmatrix} = \begin{pmatrix} C_B & H^{-1} \\ H^{-1} & R^{-1} \end{pmatrix} \cdot \begin{pmatrix} \sigma \\ p_f \end{pmatrix} \Leftrightarrow \begin{pmatrix} \sigma \\ p_f \end{pmatrix} = \frac{1}{D_1} \begin{pmatrix} R^{-1} & -H^{-1} \\ -H^{-1} & C_B \end{pmatrix} \cdot \begin{pmatrix} \varepsilon_B \\ \zeta \end{pmatrix} \quad (2.44b)$$

$$\text{where the matrix determinant is: } \frac{1}{D_1} = \frac{K_B R H^2}{H^2 - K_B R} \neq 0 \quad \text{and} \quad \sigma = -p_k \quad (2.44c)$$

The sign conventions are: the stress $\sigma > 0$ in tension and $\sigma < 0$ in compression; the volumetric strain $\varepsilon_B > 0$ in expansion and $\varepsilon_B < 0$ in contraction; $\zeta > 0$ if fluid is added to ΔV_B and $\zeta < 0$ if fluid is extracted from ΔV_B ; the pore pressure $p_f > 0$ if it is larger than the atmospheric pressure. Here ΔV_B is the bulk control volume. The coefficients of both matrices (2.44b) are experimentally defined as follows (Wang 2000):

$$C_B = \frac{1}{K_B} = \left(\frac{\Delta \varepsilon_B}{\Delta \sigma} \right)_{p_f}, \quad \frac{1}{H} = \left(\frac{\Delta \varepsilon_B}{\Delta p_f} \right)_{\sigma} = \left(\frac{\Delta \zeta}{\Delta \sigma} \right)_{p_f}, \quad \frac{1}{R} = \left(\frac{\Delta \zeta}{\Delta p_f} \right)_{\sigma} \quad (2.45)$$

The drained coefficients K_B and C_B were introduced in equations (2.37a–c); $1/H$ is a special poroelastic expansion coefficient, which describes how much ΔV_B changes when p_f changes while keeping the applied stress σ constant; $1/H$ also measures the changes of ζ when σ changes and p_f remains constant. Finally $1/R$ is the unconstrained specific storage coefficient, which represents the changes of ζ when p_f changes. This parameter is measured when the applied stress σ remains constant, “the value of $1/R$ is determined by the compressibilities of the frame, the pores, the fluid and the solid grains” (Wang 2000). The three poroelastic coefficients given by equation (2.45) entirely describe the poroelastic response of the rock for isothermal, isotropic stresses. Writing explicitly the relationships for σ in equation (2.44a) and replacing the value of σ in ζ , we obtain:

$$\sigma = K_B \varepsilon_B - \frac{K_B}{H} p_f \Rightarrow \zeta = \frac{K_B}{H} \varepsilon_B + \left(\frac{1}{R} - \frac{K_B}{H^2} \right) p_f \quad (2.46)$$

Biot (1941) introduced a fourth poroelastic coefficient $1/M$, called the constrained specific storage, which is equal to the change of ζ when p_f changes and measured at constant strain. This parameter is expressed in terms of the three fundamental coefficients defined in equation (2.45). Using equation (2.46):

$$\frac{1}{M} = \left(\frac{\Delta \zeta}{\Delta p_f} \right)_{\varepsilon_B} = \frac{1}{R} - \frac{K_B}{H^2} \Rightarrow M = \frac{R H^2}{H^2 - K_B R} \quad (2.47)$$

There is an additional important parameter B , called the Skempton coefficient (Wang 2000, Guéguen and Boutéca 2004), which represents the change in pore pressure when the applied stress changes for undrained conditions (see section 2.2.9). This parameter is calculated directly,

using equation (2.44a):

$$\zeta = \frac{\sigma}{H} + \frac{p_f}{R} \Rightarrow B = \left(\frac{\Delta p_f}{\Delta p_k} \right)_{m_f} = - \left(\frac{\Delta p_f}{\Delta \sigma} \right)_{\zeta} = \frac{R}{H} \quad (2.48)$$

Biot (1962) introduced another important poroelastic coefficient C :

$$C = \frac{1}{D_1 H} = \frac{K_B R H}{H^2 - K_B R} = \frac{K_B}{H} M \quad (2.49a)$$

In this equation, if we take the limit when $\Delta p_f \rightarrow 0$ and $\sigma = -p_k$, in the definitions of K_b and H (eq. 2.45), we find three extra fundamental relationships for the Biot's coefficient:

$$\frac{C}{M} = \frac{K_B}{H} = \lim_{\Delta p_f \rightarrow 0} \left(\frac{\Delta p_k \Delta \varepsilon_B}{\Delta \varepsilon_B \Delta p_f} \right) = \left(\frac{\partial p_k}{\partial \varepsilon_B} \frac{\partial \varepsilon_B}{\partial p_f} \right) = \left(\frac{\partial p_k}{\partial p_f} \right)_{\varepsilon} = b \quad (2.49b)$$

The coefficient C represents the coupling of deformations between the solid grains and the fluid. The coefficient M is the inverse of the constrained specific storage, measured at constant strain (Wang 2000); this parameter characterizes the elastic properties of the fluid (Fjaer *et al.* 1992) because it measures how the fluid pressure changes when ζ changes. These three parameters b , M and C are the core of the poroelastic equations.

2.2.6.3 Relationships among the bulk moduli and other poroelastic coefficients

Writing explicitly the inverted relations for σ and p_f in the matrix equation (2.44b) and using equation (2.49a):

$$\sigma = \frac{K_B H^2}{H^2 - K_B R} \varepsilon_B - \frac{K_B R H}{H^2 - K_B R} \zeta = \frac{K_B}{R} M \varepsilon_B - C \zeta \quad (2.50a)$$

$$p_f = \frac{R H^2}{H^2 - K_B R} \zeta - \frac{K_B R H}{H^2 - K_B R} \varepsilon_B = M \zeta - C \varepsilon_B \quad (2.50b)$$

$$\zeta = \frac{p_f}{M} + b \varepsilon_B \quad (2.50c)$$

Using the definition of the undrained bulk modulus (eq. 2.38a) in equation (2.50a), we deduce that:

$$K_U = - \left(\frac{\Delta p_k}{\Delta \varepsilon_B} \right)_{\zeta} = \left(\frac{\Delta \sigma}{\Delta \varepsilon_B} \right)_{\zeta} = \frac{K_B}{R} M = \frac{K_B H^2}{H^2 - K_B R} = K_B \left(1 - \frac{K_B R}{H} \right)^{-1}$$

$$\Rightarrow \boxed{K_U = \frac{K_B}{1 - b B}} \quad (2.51a)$$

$$\boxed{B = \frac{K_U - K_B}{b K_U} = \frac{b M}{K_U}} \quad (2.51b)$$

From these relationships, we can define the fluid pressure in the undrained regime, when ζ remains constant. From equation (2.42b) and the definition of K_U :

$$\varepsilon_B = - \frac{p_k - b p_U}{K_B} = - \frac{p_k}{K_U} \Rightarrow p_U = - \frac{K_U - K_B}{b} \varepsilon_B = B p_k \quad (2.51c)$$

thus, the fluid pressure variation for undrained conditions is $\left(\frac{\partial p_U}{\partial p_k} \right)_{\zeta} = B$ (eq. 2.48).

Using expression (2.50c) we obtain the variation of the fluid content in the drained regime (eq. 2.49b):

$$\zeta = b \varepsilon_B + \frac{p_f}{M} = -b \frac{p_k}{K_U} + \frac{b p_f}{B K_U} = \frac{b}{B K_U} (p_f - B p_k) \quad (2.51d)$$

We have defined the bulk moduli K_B and K_s of the porous rock in equations (2.37b) and (2.39a). From equation (2.51a), we can construct several relationships between these three different bulk moduli and the other poroelastic parameters. Using equations (2.51a) and (2.49b):

$$K_B = K_U (1 - b B) = K_U - \frac{K_B}{R} M b B = K_U - \frac{K_B}{R} C B \quad (2.52a)$$

Using equations (2.48) and (2.49b):

$$K_B = K_U - \frac{K_B}{H} C = K_U - b C = K_U - b^2 M = K_U - \frac{C^2}{M} \quad (2.52b)$$

We can include K_s from equation (2.41):

$$1 = b + \frac{K_B}{K_s} \Rightarrow K_s = \frac{K_B}{1 - b} = \frac{K_U - b C}{1 - b} = \frac{K_U - b^2 M}{1 - b} = \frac{M K_U - C^2}{M - C} \quad (2.52c)$$

The symbol K_U is the rock undrained bulk modulus. The relationship given by equation (2.24f) is also valid for this undrained modulus, but the other elastic parameters, λ and G should be measured under the same conditions. Since there are no shear stresses in the fluid, the shear coefficient must be the same in both situations and $G = G_U = G_B$. For the undrained Lamé modulus, we have (Biot 1962, Wang 2000):

$$\lambda_U = K_U - \frac{2}{3} G \quad [\text{Pa}] \quad (2.53a)$$

From equation (2.53a) and with λ as the drained Lamé modulus, we deduce that:

$$\frac{2}{3} G = K_U - \lambda_U = K_B - \lambda \Rightarrow \boxed{\lambda_U = K_U - K_B + \lambda} \quad (2.53b)$$

From equation (2.52b) we obtain another useful expression for both coefficients:

$$K_U - K_B = b C = b^2 M \Rightarrow \boxed{\lambda_U = \lambda + b C} \quad (2.53c)$$

In a similar form, we deduce the undrained Poisson's coefficient:

$$\nu_U = \frac{3 \nu + b B (1 - 2 \nu)}{3 - b B (1 - 2 \nu)} \quad (2.53d)$$

2.2.7 Porosity and the low-frequency Gassmann-Biot equation

“One of the most important problems in the rock physics analysis of logs, cores and seismic data is the prediction of seismic velocities in rocks saturated with one fluid from rocks saturated with a second fluid or, equivalently, saturated rock velocities from dry rock velocities, and vice versa. This is the fluid substitution problem.” (Mavko et al. 2003). There are many examples of natural and artificially induced seismicity corresponding to this description. In The Geysers, California,

small earthquakes were reported when starting the fluid reinjection into the geothermal reservoir in 1999. In December 2006, several earthquakes were felt in the region of Alsace, France. A company of geothermal perforation near Bale recognized its responsibility (*Le Monde*, “*Le jour où la France tremblera*”, 10/04/2009).

Biot extended his theory to poroelastodynamic phenomena in two parts: low and high frequency ranges, respectively (Biot 1956a,b). The low frequency theory developed by Gassmann (1951) and Biot (1956a) allows to predict the resulting increase in the undrained bulk modulus K_U of a saturated rock when an increment of pore pressure is induced from a passing seismic wave (Mavko *et al.* 2003). This theory is condensed in the so called Gassmann-Biot equation, which combines porosity and all the poroelastic bulk moduli, in a single formula. Assuming a hydrostatic pressure σ_H acting in the rock solid grains, using the second part of equation (2.50b) and the relation (2.37a) for the solid phase and introducing the bulk modulus of water, we have from the analytic definition of the strain ζ (see eq. 2.65b):

$$K_f = \frac{\sigma_H}{\varepsilon_f}, K_s = \frac{\sigma_H}{\varepsilon_s}, \quad \text{and:} \quad \zeta = \varphi (\varepsilon_s - \varepsilon_f) \quad \Rightarrow \quad \frac{\zeta}{\sigma_H} = \varphi \left(\frac{1}{K_s} - \frac{1}{K_f} \right) \quad (2.54a)$$

On the other hand, the hydrostatic stress acting in the solid phase in equation (2.50b) is:

$$p_f = -\sigma_H = M\zeta - C\varepsilon_s \quad \Rightarrow \quad \frac{\zeta}{\sigma_H} = \frac{C}{M} \frac{\varepsilon_s}{\sigma_H} - \frac{1}{M} = \frac{b}{K_s} - \frac{1}{M} \quad (2.54b)$$

Equating both formulae (2.54a) and (2.54b):

$$\frac{\zeta}{\sigma_H} = \varphi \left(\frac{1}{K_s} - \frac{1}{K_f} \right) = \frac{b}{K_s} - \frac{1}{M} \quad \Rightarrow \quad M = \frac{K_f K_s}{\varphi K_s + (b - \varphi) K_f} \quad (2.54c)$$

This last expression leads to write the Biot coefficients C and M in terms of the bulk moduli. Directly from equations (2.49b) and (2.42a):

$$b = \frac{C}{M} \quad \Rightarrow \quad C = M \left(1 - \frac{K_B}{K_s} \right) = \frac{K_f K_s}{\varphi K_s + (b - \varphi) K_f} \left(1 - \frac{K_B}{K_s} \right)$$

$$\Rightarrow \quad \boxed{C = \frac{\frac{K_f}{\varphi} \left(1 - \frac{K_B}{K_s} \right)}{1 - \frac{K_f}{K_s} + \frac{K_f}{\varphi K_s} \left(1 - \frac{K_B}{K_s} \right)}} \quad \Rightarrow \quad \boxed{M = \frac{C}{1 - \frac{K_B}{K_s}}} \quad (2.55a)$$

From these coefficients, Biot (1962) derived another parameter N called the tangent modulus, defined as the pressure variation with respect to the porosity variation when both strain and temperature are held constant (Coussy 2004):

$$\frac{1}{N} = \frac{1}{M} - \frac{\varphi}{K_f} = \frac{b}{C} - \frac{\varphi}{K_f} = \frac{b - \varphi}{K_s} \quad (2.55b)$$

From equations (2.52b) and (2.55a) we finally obtain the Gassmann-Biot equation:

$$K_U - K_B = b^2 M \quad \Rightarrow \quad \boxed{K_U = K_B + \frac{b^2}{\frac{\varphi}{K_f} + \frac{b - \varphi}{K_s}}} \quad (2.56)$$

The Biot-Willis coefficient b is given by equation (2.55a). Another formulation of equation (2.56) is:

$$K_U = K_B + \frac{K_f}{\varphi} \left(1 - \frac{K_B}{K_s}\right)^2 \frac{1}{1 + \frac{K_f}{K_s} \left(\frac{1}{\varphi} \left(1 - \frac{K_B}{K_s}\right) - 1\right)} \quad (2.57)$$

The reciprocal form of equation (2.57) is obtained by computing $(K_U - K_B)/(K_U K_B)$:

$$\frac{1}{K_U} = \frac{1}{K_B} - \frac{\left(\frac{1}{K_B} - \frac{1}{K_s}\right)^2}{\frac{1}{K_B} - \frac{1}{K_s} + \varphi \left(\frac{1}{K_f} - \frac{1}{K_s}\right)} \quad (2.58)$$

Other equivalent formulations of equation (2.56) are obtained after doing some algebra:

$$\frac{K_U}{K_s - K_U} = \frac{K_B}{K_s - K_B} + \frac{K_f}{\varphi (K_s - K_f)} \quad (2.59)$$

From this equation, we obtain a formula for the porosity in terms of the bulk moduli:

$$\frac{1}{\varphi} = \frac{K_s - K_f}{K_f} \left(\frac{K_U}{K_s - K_U} - \frac{K_B}{K_s - K_B} \right) \quad (2.60)$$

From equation (2.56), we obtain another useful formula for the porosity, which includes the Biot coefficients and the Skempton parameter:

$$\varphi = \frac{K_f}{K_s - K_f} \left(\frac{K_s}{M(1-bB)} - \frac{b^2}{(1-b)} - b \right) \quad (2.61)$$

We can deduce the limit cases of poroelastic behavior from the Gassmann-Biot equation (2.56) that simplify equations (2.55a). For the case of a hard volcanic rock with very low porosity (Table 2.3):

$$b \approx 0 \Rightarrow K_U \approx K_B \approx K_s \gg K_f \Rightarrow C \approx \frac{K_f}{\varphi} \left(1 - \frac{K_B}{K_s}\right) \quad \text{and} \quad M \approx \frac{K_f}{\varphi} \quad (2.62)$$

The parameter C depends on both, the fluid properties and the bulk rock properties, whereas coefficient M depends only on the porosity and on the fluid bulk modulus. This last approximation corresponds to the case of a rigid frame.

The other limit case is for sedimentary rocks with high porosity, for example unconsolidated rocks or sandstones (Table 2.3). In this case equations (2.52c) and (2.56) become:

$$b \approx 1 \Rightarrow K_U \approx K_B + \frac{K_f}{\varphi}, \quad K_B \ll K_s \Rightarrow \frac{1}{K_U} \approx \frac{\varphi}{K_f} + \frac{\varphi_S}{K_s}, \quad C \approx M \approx \frac{K_f}{\varphi} \quad (2.63)$$

The non-negative character of the poroelastic energy (Biot 1962, Wang 2000; see also section 2.2.11.2) directly implies the same characteristic for the poroelastic constants: $E \geq 0$, $G \geq 0$, $K_B \geq 0$, $K_U \geq 0$, $M \geq 0$, $C \geq 0$, $\lambda \geq 0$, $\lambda_U \geq 0$, etc.

Tables 2.3 and 2.4 present both experimental and computed numerical values of the poroelastic parameters herein defined. Note that C , H and some other coefficients are not included in these tables, but they can be easily calculated using the formulae introduced in this section.

2.2.8 Numerical values of the poroelastic coefficients

Many coefficients are introduced to support poroelastic theory, but only three of these parameters are actually independent. Three basic parameters selected to constitute an experimental reference set were the drained bulk compressibility $C_B = 1/K_B$, the expansion coefficient $1/H$ and the unconstrained specific storage $1/R$ (Wang 2000). Other three possible basic coefficients are the drained bulk modulus K_B , the undrained bulk modulus K_U , and the Biot-Willis coefficient b (Detournay and Cheng 1993). However, it is impossible to compute all the coefficients of the theory using only the classical elastic constants (eq. 2.27), because at least five mixed coefficients are necessary for the whole poroelastic coupling. A sufficient set of measured parameters is for example $\{E, G, \varphi, K_s, K_f\}$. With these moduli, we can compute the full set of 16 poroelastic constants.

From an experimental point of view, it appears that some coefficients are more difficult to measure than others are. This is the case of the variation of the fluid mass content. To describe the saturating fluid, we need its pressure and its temperature. It is possible to make other choices of the basic experimental parameters using the relationships developed in this section.

Table 2.3. Poroelastic parameters measured and calculated for different types of rocks.

Rock type	φ (%)	E (GPa)	ν (ad)	ν_U (ad)	G (GPa)	λ (GPa)	λ_U (GPa)	K_B (GPa)	K_U (GPa)	K_s (GPa)	B (ad)	b (ad)	M (GPa)	R (GPa)
[0]	65.0	0.18	0.01	0.49	0.09	0.001	6.1	0.062	6.2	10 ⁵	0.99	1.00	6.1	0.06
[1]	26.0	9.7	0.15	0.31	4.2	1.8	7.3	4.6	10.1	42.0	0.61	0.89	6.9	3.2
[2]	19.0	13.1	0.17	0.30	5.6	2.9	10.9	6.6	14.6	28.9	0.71	0.77	13.4	6.1
[3]	13.0	30.5	0.26	0.32	12.1	13.1	23.2	21.2	31.2	72.6	0.46	0.71	20.0	13.6
[4]	2.0	60.0	0.25	0.27	24.0	24.2	28.3	40.0	44.3	50.0	0.49	0.19	107.3	97.0
[5]	0.5	42.2	0.42	0.42	14.9	73.9	74.0	83.8	83.9	85.0	0.06	0.01	384.3	384.0

The rock types are: [0] Clay ($K_f = 3.9$ GPa), [1] Boise sandstone ($K_f = 2.0$ GPa), [2] Berea sandstone ($K_f = 3.5$ GPa), [3] Indiana limestone ($K_f = 3.1$ GPa), (Wang 2000); [4] Tennessee marble ($K_f = 3.5$ GPa), (Detournay and Cheng 1993); [5] Rock with celestite ($K_f = 2.0$ GPa), (Mavko *et al.* 2003). Rocks of Type [0] and [5], are the two limit cases of linear poroelastic theory, for $b \approx 1$ and $b \approx 0$, respectively. The figures in italics were estimated using the poroelastic formulae.

Table 2.4. Poroelastic parameters of the Los Humeros geothermal field (Mexico).

ρ_f (kg/m ³)	φ (%)	E (GPa)	ν (ad)	ν_U (ad)	G (GPa)	λ (GPa)	λ_U (GPa)	K_B (GPa)	K_U (GPa)	K_s (GPa)	B (ad)	b (ad)	M (GPa)	R (GPa)
2770	3.8	34.8	0.29	0.33	13.5	18.5	25.2	27.5	35.2	50.1	0.49	0.45	38.0	29.6
2500	8.5	35.8	0.31	0.32	13.7	21.7	24.8	30.8	33.9	49.7	0.24	0.38	21.6	19.6
2340	16.3	30.0	0.29	0.31	11.6	16.4	19.0	24.2	26.8	45.2	0.21	0.47	11.9	10.7
2210	20.9	25.3	0.30	0.32	9.70	15.1	17.1	21.5	23.5	40.0	0.19	0.46	9.4	8.64
2210	20.9	25.3	0.30	0.31	9.70	15.1	15.5	21.5	22.0	40.0	0.04	0.46	2.0	1.95

Basic experimental data set used: $\{E, G, \varphi, K_s$ and $K_f\}$. The rocks are andesites. The measured coefficients were obtained under drained conditions, except for K_s . The confining pressure was 25 MPa, the ambient temperature was constant and equal to 25°C. The bulk modulus of water was constant, $K_w = 2.1$ GPa. The last row was computed with a lower bulk modulus of water $K_w = 0.42$ GPa, corresponding to $T = 290^\circ\text{C}$ and $p_f = 11$ MPa. This last example illustrates the influence of the temperature on the poroelastic coefficients. For cold water, the estimated value of $\zeta \approx 2.1 \times 10^{-3}$, while for hot water $\zeta \approx 11.1 \times 10^{-3}$. Therefore, the variation of the fluid content is much higher in geothermal reservoirs than in cold aquifers. The figures in italics were estimated using the poroelastic formulae.

2.2.9 *Tensorial form of Biot's poroelastic theory in 4D*

Let \vec{u}_s, \vec{u}_f be the solid and fluid particles displacements and $\vec{u} = \vec{u}_f - \vec{u}_s$ be the vector displacement of the fluid phase relative to the solid matrix (seepage displacement). Let $\varepsilon_s, \varepsilon_f, \varphi_s, \varphi, V_s$ and V_f be the volumetric dilatations, porosities and volumes of each phase; $-\varepsilon_V$ is the volumetric deformation of the fluid phase relative to the solid phase. The mathematical expressions of these variables are (see eq. 2.24g):

$$\begin{aligned} \frac{\Delta V_s}{V_s} = \varepsilon_s = \vec{\nabla} \cdot \vec{u}_s, \quad \frac{\Delta V_f}{V_f} = \varepsilon_f = \vec{\nabla} \cdot \vec{u}_f, \quad \varepsilon_V = \varepsilon_s - \varepsilon_f, \quad \vec{u} = \vec{u}_f - \vec{u}_s \\ \vec{u} = (u_x, u_y, u_z) \Rightarrow -\varepsilon_V = -\vec{\nabla} \cdot (\vec{u}_s - \vec{u}_f) = \vec{\nabla} \cdot \vec{u} = \frac{\partial u_x}{\partial x} + \frac{\partial u_y}{\partial y} + \frac{\partial u_z}{\partial z} \end{aligned} \quad (2.64)$$

We extend Hookean equations (2.26) and (2.28) to isotropic poroelastic phenomena. Biot and Willis (1957) introduced the strain variable $\zeta(u, t)$, defined in equations (2.35b) and (2.46) to describe the volumetric deformation of the fluid relative to the deformation of the solid:

$$\text{For inhomogeneous rock: } \zeta(\vec{u}, t) = -\vec{\nabla} \cdot (\varphi \vec{u}) = \vec{\nabla} \cdot [\varphi(\vec{u}_s - \vec{u}_f)] \quad (2.65a)$$

$$\text{For homogeneous rock: } \zeta(\vec{u}, t) = \varphi \vec{\nabla} \cdot (\vec{u}_s - \vec{u}_f) = \varphi \varepsilon_s - \varphi \varepsilon_f = \varphi \varepsilon_V \quad (2.65b)$$

The function ζ represents the variation of fluid content in the pore during a poroelastic deformation. Introducing ζ in the same OXYZ frame of reference (Fig. 2.6), we reformulate the theoretical and experimental results of M.A. Biot in tensorial form. The total applied stresses in the porous rock are similar to equations (2.26). However, we need to couple the effect of the fluid in the pores. The linear components of the global stresses, deduced experimentally by Biot (Biot 1941, 1962, Biot and Willis 1957, Wang 2000) are:

$$\lambda_U = \lambda + C b; \quad \text{for } i, j = x, y, z: \sigma_{ij} = \lambda_U \varepsilon_B \delta_{ij} + 2G \varepsilon_{ij} - C \zeta \delta_{ij} \quad (2.66a)$$

The Biot-Willis coefficient b was introduced in equation (2.42a); λ_U is the Lamé bulk modulus of the porous rock measured for undrained conditions, and λ is the drained Lamé modulus defined in equation (2.53c). Note that $\lambda_U > \lambda$, and $\lambda_U = \lambda$ only if there are no pores and $b = 0$.

The global stresses acting in the porous rock cannot be deduced from the relationships in equation (2.50a) because the shear components acting on the skeleton are absent in those formulae. The fluid stress σ_f is equal to the fluid pressure p_f and it is deducible from equation (2.50b):

$$\sigma_f = p_f = \frac{K_B R H^2}{H^2 - K_B R} \left[\frac{\zeta}{K_B} - \frac{\varepsilon_B}{H} \right] = M \zeta - C \varepsilon_B \quad (2.66b)$$

In the poroelastic case, the variables (ε_{ij}) are bulk strains, because they measure the deformation of the skeleton composed of the solid grains in the matrix and pores containing fluid. For the same reason, $\varepsilon_B = \varepsilon_x + \varepsilon_y + \varepsilon_z$ is the bulk volumetric strain. For the shear modulus, it is obvious that $G_B = G$. The stress poroelastic parameters C and M (in [Pa]) were defined in terms of the fundamental poroelastic moduli given by equations (2.47), (2.49a) and (2.55a).

From equations (2.66a) and (2.66b), we can define a symmetric two-order tensor σ_T in four dimensions, represented by a (4×4) matrix, which includes the bulk stress tensor σ_B acting in the porous rock and the fluid stress σ_f acting in the fluid filling up the pores, both influencing

the bulk rock deformation:

$$\begin{aligned}
 \sigma_T = \sigma_B + \sigma_f = (\sigma_{ij}) &= \begin{pmatrix} \sigma_x & \sigma_{xy} & \sigma_{xz} & 0 \\ \sigma_{xy} & \sigma_y & \sigma_{yz} & 0 \\ \sigma_{xz} & \sigma_{yz} & \sigma_z & 0 \\ 0 & 0 & 0 & \sigma_f \end{pmatrix} \\
 &= \varepsilon_B \begin{pmatrix} \lambda_U & 0 & 0 & 0 \\ 0 & \lambda_U & 0 & 0 \\ 0 & 0 & \lambda_U & 0 \\ 0 & 0 & 0 & -C \end{pmatrix} + 2G \begin{pmatrix} \varepsilon_x & \varepsilon_{xy} & \varepsilon_{xz} & 0 \\ \varepsilon_{xy} & \varepsilon_y & \varepsilon_{yz} & 0 \\ \varepsilon_{xz} & \varepsilon_{yz} & \varepsilon_z & 0 \\ 0 & 0 & 0 & 0 \end{pmatrix} - \zeta \begin{pmatrix} C & 0 & 0 & 0 \\ 0 & C & 0 & 0 \\ 0 & 0 & C & 0 \\ 0 & 0 & 0 & -M \end{pmatrix} \quad (2.67) \\
 \leftarrow \qquad \qquad \qquad \sigma_B \qquad \qquad \qquad \rightarrow \quad \leftarrow \qquad \qquad \qquad \sigma_f \qquad \rightarrow
 \end{aligned}$$

Equation (2.67) is analogous to equation (2.26a); they become identical when the rock has zero porosity and $b = 0$. The symmetry of this system occurs for the same reasons explained in the development of equation (2.26a): it is a consequence of the fundamental law of poroelastic dynamics (see subsection 2.2.10.1).

The total stresses in the poroelastic rock are obtained by coupling two tensors, σ_B for the bulk rock and σ_f for the fluid. The inclusion of the fourth dimension is necessary to extend the classical theory of solid elasticity to linear poroelastic rocks, taking into account the effect of the fluid phase.

2.2.9.1 Terzaghi effective stresses in poroelastic rocks

From equation (2.50b), we deduce that:

$$\begin{aligned}
 \zeta = \frac{C}{M} \varepsilon_B + \frac{p_f}{M} \quad \Rightarrow \quad \sigma_{ij} = (\varepsilon_B (\lambda_U - C b) - b p_f) \delta_{ij} + 2G \varepsilon_{ij} \quad (2.68) \\
 \text{thus, } \sigma_{ij} = (\lambda \varepsilon_B \delta_{ij} + 2G \varepsilon_{ij}) - b p_f \delta_{ij}
 \end{aligned}$$

Therefore, we obtain:

$$\sigma_{ij} = \lambda \varepsilon_B \delta_{ij} + 2G \varepsilon_{ij} \quad \Rightarrow \quad \boxed{\sigma_{ij} = \tau_{ij} - b p_f \delta_{ij}} \quad (2.69a)$$

Tensor (τ_{ij}) is called the Terzaghi effective stresses that act only in the solid matrix; $b p_f$ is the pore-fluid pressure. For this reason, b is called the effective stress coefficient. Since there are no shear tensions in the fluid, the pore-fluid pressure affects only the normal strains σ_i ($i = x, y, z$). The functions (σ_{ij}) are the applied stresses acting in the porous rock saturated with fluid. They express that the poroelastic response is controlled by the difference between effective stress and pore pressure. Equation (2.69a) is called the ‘‘law of effective stress’’ (Wang 2000, Terzaghi 1943). This equation illustrates the mechanism of the poroelastic coupling. The solid matrix (τ_{ij}) supports one portion of the total applied tensions in the rock and the fluid in the pores ($b p_f$) supports the other part. This is a maximum for soils, when $b \approx 1$ and is minimum for rocks with very low porosity where $b \approx 0$ (Table 2.3). The matrix form of equation (2.69a) becomes:

$$\begin{aligned}
 \sigma_T = \sigma_B + \sigma_f = (\sigma_{ij}) = \tau - b p_f \\
 \Leftrightarrow \begin{pmatrix} \sigma_x & \sigma_{xy} & \sigma_{xz} & 0 \\ \sigma_{xy} & \sigma_y & \sigma_{yz} & 0 \\ \sigma_{xz} & \sigma_{yz} & \sigma_z & 0 \\ 0 & 0 & 0 & \sigma_f \end{pmatrix} = \begin{pmatrix} \tau_{xx} & \tau_{xy} & \tau_{xz} & 0 \\ \tau_{xy} & \tau_{yy} & \tau_{yz} & 0 \\ \tau_{xz} & \tau_{yz} & \tau_{zz} & 0 \\ 0 & 0 & 0 & 0 \end{pmatrix} - \begin{pmatrix} b & 0 & 0 & 0 \\ 0 & b & 0 & 0 \\ 0 & 0 & b & 0 \\ 0 & 0 & 0 & -1 \end{pmatrix} p_f \quad (2.69b)
 \end{aligned}$$

The simplicity of the 4D poroelastic formulation becomes clear and evident with this last tensor formula.

2.2.9.2 Vectorial formulation of the poroelastic equations

Analogously to equation (2.28), we can make the tensor σ_f equivalent to a seven dimensional stress vector. Using the relation $C = bM$, the matrix of coefficients in equation (2.67) for the fluid becomes:

$$\vec{\sigma}_f = \begin{pmatrix} \sigma_x \\ \sigma_y \\ \sigma_z \\ \sigma_{xy} \\ \sigma_{xz} \\ \sigma_{yz} \\ \sigma_f \end{pmatrix}_f = \begin{pmatrix} 0 & 0 & 0 & 0 & 0 & 0 & -C \\ 0 & 0 & 0 & 0 & 0 & 0 & -C \\ 0 & 0 & 0 & 0 & 0 & 0 & -C \\ 0 & 0 & 0 & 0 & 0 & 0 & 0 \\ 0 & 0 & 0 & 0 & 0 & 0 & 0 \\ 0 & 0 & 0 & 0 & 0 & 0 & 0 \\ -C & -C & -C & 0 & 0 & 0 & M \end{pmatrix} \cdot \begin{pmatrix} \varepsilon_x \\ \varepsilon_y \\ \varepsilon_z \\ 0 \\ 0 \\ 0 \\ \zeta \end{pmatrix}_f \quad (2.70)$$

With this equation, we can construct the total stress vector acting in the porous rock, which includes two components, one for the skeleton and one for the fluid, respectively:

$$\begin{aligned} \sigma_T = \sigma_B + \sigma_f &\Leftrightarrow \vec{\sigma}_T = \mathbf{C}_B \cdot \vec{\varepsilon}_T \Leftrightarrow \vec{\varepsilon}_T = \mathbf{C}_B^{-1} \cdot \vec{\sigma}_T \\ \vec{\sigma}_T = (\sigma_x, \sigma_y, \sigma_z, \sigma_{xy}, \sigma_{xz}, \sigma_{yz}, \sigma_f)^T; &\quad \vec{\varepsilon}_T = (\varepsilon_x, \varepsilon_y, \varepsilon_z, \varepsilon_{xy}, \varepsilon_{xz}, \varepsilon_{yz}, \zeta)^T \end{aligned} \quad (2.71)$$

Equation (2.71) represents the total stresses acting in the rock through σ_B plus the tension force σ_f acting in the pores. It shows the equivalence between two coupled vector-tensorial equations preserving a similar form as the classic elastic equation (2.28). The vector symbols are seventh dimensional transposed vectors with six classic components and extra poroelastic elements. The total poroelastic stress and the total strains are the vectors $\vec{\sigma}_T$ and $\vec{\varepsilon}_T$, respectively. The matrix \mathbf{C}_B for isotropic, isothermal rocks is a seventh order constant tensor obtained by the addition of coefficient matrices in equations (2.28) and (2.70), one for the solid phase and one for the fluid:

$$\mathbf{C}_B = \begin{pmatrix} \lambda_U + 2G & \lambda_U & \lambda_U & 0 & 0 & 0 & -C \\ \lambda_U & \lambda_U + 2G & \lambda_U & 0 & 0 & 0 & -C \\ \lambda_U & \lambda_U & \lambda_U + 2G & 0 & 0 & 0 & -C \\ 0 & 0 & 0 & 2G & 0 & 0 & 0 \\ 0 & 0 & 0 & 0 & 2G & 0 & 0 \\ 0 & 0 & 0 & 0 & 0 & 2G & 0 \\ -C & -C & -C & 0 & 0 & 0 & M \end{pmatrix} \quad (2.72)$$

The determinant of this matrix is:

$$\det(\mathbf{C}_B) = 32G^5[-3C^2 + M(3\lambda_U + 2G)] = 32G^5M(3\lambda + 2G) = 96G^5 K_B M \neq 0$$

Therefore the components of $\vec{\sigma}_T$ are:

$$\vec{\sigma}_T = \begin{pmatrix} \sigma_x \\ \sigma_y \\ \sigma_z \\ \sigma_{xy} \\ \sigma_{xz} \\ \sigma_{yz} \\ \sigma_f \end{pmatrix} = \mathbf{C}_B \cdot \vec{\varepsilon}_T = \mathbf{C}_B \cdot \begin{pmatrix} \varepsilon_x \\ \varepsilon_y \\ \varepsilon_z \\ \varepsilon_{xy} \\ \varepsilon_{xz} \\ \varepsilon_{yz} \\ \zeta \end{pmatrix} = \begin{pmatrix} \lambda_U \varepsilon_B + 2G \varepsilon_x - C \zeta \\ \lambda_U \varepsilon_B + 2G \varepsilon_y - C \zeta \\ \lambda_U \varepsilon_B + 2G \varepsilon_z - C \zeta \\ 2G \varepsilon_{xy} \\ 2G \varepsilon_{xz} \\ 2G \varepsilon_{yz} \\ -C \varepsilon_B + M \zeta \end{pmatrix} \quad (2.73)$$

Using the compact index notation, these components are:

$$\begin{aligned}
 \sigma_i &= \lambda_U \varepsilon_B + 2G \varepsilon_i - bM \zeta = (\lambda \varepsilon_B + 2G \varepsilon_i) - b p_f \\
 \sigma_{ij} &= 2G \varepsilon_{ij}, \quad \forall i, j = x, y, z, i \neq j \\
 \sigma_f &= -C \varepsilon_B + M \zeta = p_f
 \end{aligned} \tag{2.74}$$

Matrix \mathbf{C}_B is always invertible, and its inverse $\mathbf{C}_B^{-1} = (c_{ij})$ is easily calculated:

$$\mathbf{C}_B^{-1} = \begin{pmatrix} c_1 & c_{12} & c_{12} & 0 & 0 & 0 & c_{17} \\ c_{12} & c_1 & c_{12} & 0 & 0 & 0 & c_{17} \\ c_{12} & c_{12} & c_1 & 0 & 0 & 0 & c_{17} \\ 0 & 0 & 0 & c_2 & 0 & 0 & 0 \\ 0 & 0 & 0 & 0 & c_2 & 0 & 0 \\ 0 & 0 & 0 & 0 & 0 & c_2 & 0 \\ c_{17} & c_{17} & c_{17} & 0 & 0 & 0 & c_3 \end{pmatrix} \tag{2.75a}$$

The five non-zero inverse poroelastic coefficients are:

$$\begin{aligned}
 c_1 &= \frac{-C^2 + M(\lambda_U + G)}{G D_B}, \quad c_{12} = \frac{C^2 - M \lambda_U}{2G D_B}, \quad c_3 = \frac{3\lambda_U + 2G}{D_B} \\
 c_2 &= \frac{1}{2G}, \quad c_{17} = \frac{C}{D_B}; \quad D_B = -3C^2 + M(3\lambda_U + 2G) = M(3\lambda + 2G)
 \end{aligned} \tag{2.75b}$$

These coefficients form the exact inverse matrix \mathbf{C}_B^{-1} and the inverted equations are:

$$\begin{aligned}
 \varepsilon_i &= (c_1 - c_{12})\sigma_i + 3\sigma_M c_{12} + c_{17} p_f; \quad i = x, y, z; \quad \varepsilon_{ij} = \frac{\sigma_{ij}}{2G}; \quad i \neq j \\
 \zeta &= 3\sigma_M c_{17} + c_3 p_f; \quad \sigma_M = \frac{\sigma_x + \sigma_y + \sigma_z}{3} = \left(\lambda + \frac{2}{3}G\right)\varepsilon_B - C \zeta
 \end{aligned} \tag{2.76}$$

Note that the shear strains (ε_{ij}) ($i \neq j$) are independent of the fluid pressure. Instead of the constant terms in equation (2.76) of the inverse matrix, we can also use the traditional poroelastic coefficients. Using previous relationships (eq. 2.25) and after doing some algebra we obtain:

$$\begin{aligned}
 c_{12} &= \frac{b^2 M^2 - M\lambda - b^2 M^2}{2GM(3\lambda + 2G)} = \frac{-\lambda}{2G(3\lambda + 2G)} = \frac{-\lambda}{2E(\lambda + G)} = -\frac{\nu}{E} \\
 (c_1 - c_{12}) &= \frac{-3C^2 + M(3\lambda_B + 2G)}{2G[-3C^2 + M(3\lambda_B + 2G)]} = \frac{1}{2G} = c_2 \Rightarrow c_1 = \frac{1}{2G} - \frac{\nu}{E} = \frac{1}{E} \\
 c_3 &= \frac{3\lambda_B + 2G}{M(3\lambda + 2G)} = \frac{3\lambda + 2G + 3b^2 M}{M(3\lambda + 2G)} = \frac{1}{M} + \frac{b^2}{K_B} = \frac{1}{R} - \frac{K_B}{H^2} + \frac{K_B}{H^2} = \frac{1}{R} \\
 c_{17} &= \frac{C}{M(3\lambda + 2G)} = \frac{b}{3\left(\lambda + \frac{2}{3}G\right)} = \frac{b}{3K_B} = \frac{1}{3K_B} \frac{K_B}{H} = \frac{1}{3H}
 \end{aligned}$$

Therefore, the explicit inverse matrix of the elastic coefficients is simply:

$$\mathbf{C}_B^{-1} = \begin{pmatrix} \frac{1}{E} & -\frac{\nu}{E} & -\frac{\nu}{E} & 0 & 0 & 0 & \frac{1}{3H} \\ -\frac{\nu}{E} & \frac{1}{E} & -\frac{\nu}{E} & 0 & 0 & 0 & \frac{1}{3H} \\ -\frac{\nu}{E} & -\frac{\nu}{E} & \frac{1}{E} & 0 & 0 & 0 & \frac{1}{3H} \\ 0 & 0 & 0 & \frac{1}{2G} & 0 & 0 & 0 \\ 0 & 0 & 0 & 0 & \frac{1}{2G} & 0 & 0 \\ 0 & 0 & 0 & 0 & 0 & \frac{1}{2G} & 0 \\ \frac{1}{3H} & \frac{1}{3H} & \frac{1}{3H} & 0 & 0 & 0 & \frac{1}{R} \end{pmatrix} \quad (2.77a)$$

Replacing these coefficients in equation (2.76), we obtain the compact relationships:

$$\begin{aligned} \bar{\varepsilon}_T = \mathbf{C}_B^{-1} \cdot \bar{\sigma}_T &\Leftrightarrow \varepsilon_i = \frac{\sigma_i}{2G} - 3\frac{\nu}{E}\sigma_M + \frac{P_f}{3H}; \\ i, j = x, y, z; \quad \varepsilon_{ij} &= \frac{\sigma_{ij}}{2G} \quad \forall i \neq j \end{aligned} \quad (2.77b)$$

$$\sigma_M = \frac{\sigma_x + \sigma_y + \sigma_z}{3} = \left(\lambda + \frac{2}{3}G\right)\varepsilon_B - bM\zeta; \quad \zeta = \frac{\sigma_M}{H} + \frac{P_f}{R} \quad (2.77c)$$

The Biot strain variable $\zeta(u, t)$ is also expressed in terms of K_U , C , M , average stress and pore fluid pressure. Using equations (2.47), (2.49) and (2.52b) in the last expression for ζ we obtain:

$$\zeta = \frac{C\sigma_M + K_U P_f}{M K_U - C^2} \quad (2.77d)$$

This last equation illustrates, in another way, the coupling of the pore pressure and the global stress acting on the skeleton. There is another useful stresses-strains formulation deduced from equations (2.74) and (2.77b) in terms of the bulk coefficient K_U , the Poisson's modulus ν_U (eq. 2.53d), both undrained, the shear constant G and the Skempton coefficient B (Wang 2000):

$$\text{For } i, j = x, y, z: \sigma_{ij} = 2G \left(\varepsilon_{ij} + \frac{\nu_U \varepsilon_{kk}}{1 - 2\nu_U} \delta_{ij} \right) - B K_U \zeta \delta_{ij} \quad (2.78a)$$

$$\Leftrightarrow \varepsilon_{ij} = \frac{1}{2G} \left(\sigma_{ij} - \frac{\nu_U \sigma_{kk}}{1 + \nu_U} \delta_{ij} + \frac{2}{3} B G \zeta \delta_{ij} \right) \quad (2.78b)$$

Both expressions are deduced from the relations presented in previous sections. The linear theory herein outlined is appropriate for isothermal, isotropic and homogeneous porous rocks. The presence of fluid in the pores adds an extra tension due to the hydrostatic pressure, which is identified with the pore pressure, because it is supposed that all the pores are interconnected. Up to this point, all the fundamental poroelastic concepts for isothermal linear deformations have been introduced and defined.

2.2.10 *Mathematical model of the fluid flow in poroelastic rocks*

The mathematical model of a poroelastic rock volume, fully saturated with a moving fluid, is a group of coupled partial differential equations governing the fluid flow inside the pores of the deformable skeleton. All the coefficients, concepts and relationships developed in previous

sections are sufficient to develop this model. We only need to define the unknowns and arrange methodically the appropriate equations.

There are eleven fundamental unknown variables in poroelasticity. The six stress elements (σ_{ij}) of equation (2.67), the three coordinates (u_x, u_y, u_z) of the relative fluid-solid displacement (eq. 2.64), the variation of the fluid content ζ (eq. 2.44a) and the pore pressure p_f (eq. 2.50b). The six strain components (ε_{ij}) can be computed using either equation (2.77b) or their definition in terms of the vector displacement (eq. 2.27). The corresponding equations are the seven components relating stresses, strains and the pore pressure (eq. 2.71 or 2.73), and four extra partial differential equations; three come from equilibrium conditions in the skeleton and one comes from the conservation of the fluid mass relating ζ with the Darcy's law. This group of equations provides an equilibrated system that can be numerically solved using the techniques described in chapter 5. The four partial differential equations are developed in the next sections.

2.2.10.1 Dynamic and static poroelastic equations for Hookean rocks

The Newton's second law of continuum rock dynamics is a mathematical expression relating the total force acting on the medium Ω and the vectorial acceleration of the rock particles. The integral form of this fundamental law (Duc and Bellet 1976) is:

$$\int_{\Omega} \vec{F}e \, d\Omega + \int_{\partial\Omega} \sigma_B \cdot \vec{n} \, dS = \int_{\Omega} \rho_T \vec{a} \, d\Omega \quad (2.79a)$$

$$\vec{F}e = (F_x, F_y, F_z); \quad \vec{a} = \frac{\partial^2 \vec{u}}{\partial t^2}; \quad \rho_T = \varphi \rho_f + \rho_s \rho_s$$

We define $\vec{F}e$ as the external body force acting on the porous rock; \vec{a} is the vectorial acceleration and ρ_T is the average density, where ρ_f and ρ_s are the fluid and solid phase densities, respectively. Vector \vec{n} is the normal to the surface $\partial\Omega$ wrapping the domain Ω . The term σ_B is the bulk stress tensor of equation (2.67) acting within the rock. This is a (3×3) matrix. The two matrix components of equation (2.67) are (4×4) matrices, one acting in the skeleton and the other one in the fluid both of which give rise to the internal forces acting in the porous rock. The fluid matrix component is going to be treated separately. Applying the divergence theorem to the integral that contains σ_B and using the fact that the volume of integration Ω is arbitrary, we deduce the differential form of the fundamental law of rock mechanics:

$$\vec{F}e + \vec{\nabla} \cdot \sigma_B = \rho_T \vec{a} = \rho_T \frac{\partial^2 \vec{u}}{\partial t^2} \quad (2.79b)$$

$$\text{For } i, j = x, y, z: F_i + \frac{\partial \sigma_{ij}}{\partial x_j} = \rho_T a_i = \rho_T \frac{\partial^2 u_i}{\partial t^2}$$

To include the fluid in the pores, we compute the divergence of the total stress vector in equation (2.73) as follows:

$$\text{div } \vec{\sigma}_T = \mathbf{L}^T \cdot \vec{\sigma}_T; \quad \vec{\sigma}_T = \mathbf{C}_B \cdot \vec{\varepsilon}_T; \quad \vec{\varepsilon}_T = \mathbf{L} \cdot \vec{u} \quad (2.79c)$$

\mathbf{L} is a special tensorial differential operator defined in three dimensions as follows:

$$\mathbf{L} = \begin{pmatrix} \partial_x & 0 & 0 \\ 0 & \partial_y & 0 \\ 0 & 0 & \partial_z \\ \partial_y & \partial_x & 0 \\ \partial_z & 0 & \partial_x \\ 0 & \partial_z & \partial_y \\ -\varphi \partial_x & -\varphi \partial_y & -\varphi \partial_z \end{pmatrix} \Rightarrow \mathbf{L} \cdot \begin{pmatrix} u_x \\ u_y \\ u_z \end{pmatrix} = \begin{pmatrix} \partial_x u_x \\ \partial_y u_y \\ \partial_z u_z \\ \partial_y u_x + \partial_x u_y \\ \partial_z u_x + \partial_x u_z \\ \partial_z u_y + \partial_y u_z \\ -\varphi \vec{\nabla} \cdot \vec{u} \end{pmatrix} = \begin{pmatrix} \varepsilon_x \\ \varepsilon_y \\ \varepsilon_z \\ \varepsilon_{xy} \\ \varepsilon_{xz} \\ \varepsilon_{yz} \\ \zeta \end{pmatrix} = \vec{\varepsilon}_T \quad (2.79d)$$

where $\varepsilon_{ij} = 2\varepsilon_{ij}$. Using this notation, the fundamental law of dynamic poroelasticity is:

$$\vec{div} \vec{\sigma}_T + \vec{F} = \rho_T \vec{a} \quad \Leftrightarrow \quad (\mathbf{L}^T \cdot \mathbf{C}_B \cdot \mathbf{L}) \cdot \vec{u} + \vec{F} = \rho_T \frac{\partial^2 \vec{u}}{\partial t^2} \quad (2.80)$$

This vectorial system provides a solution for the displacement vector $\vec{u} = (u_x, u_y, u_z)$ of the rock particles in equation (2.64). In two dimensions, the fundamental law is written as:

$$\mathbf{L} \cdot \vec{u} = \begin{pmatrix} \partial_x & 0 \\ 0 & \partial_y \\ \partial_y & \partial_x \\ -\varphi \partial_x & -\varphi \partial_y \end{pmatrix} \cdot \begin{pmatrix} u_x \\ u_y \end{pmatrix} = \begin{pmatrix} \partial_x u_x \\ \partial_y u_y \\ \partial_y u_x + \partial_x u_y \\ -\varphi(\partial_x u_x + \partial_y u_y) \end{pmatrix} = \begin{pmatrix} \varepsilon_x \\ \varepsilon_y \\ \varepsilon_{xy} \\ \zeta \end{pmatrix} = \vec{\varepsilon}$$

the matrix of the poroelastic coefficients is: $\mathbf{C}_B = \begin{pmatrix} \lambda_U + 2G & \lambda_U & 0 & -C \\ \lambda_U & \lambda_U + 2G & 0 & -C \\ 0 & 0 & 2G & 0 \\ -C & -C & 0 & M \end{pmatrix}$

Therefore, the fundamental law of dynamic poroelasticity in two dimensions is:

$$(\mathbf{L}^T \cdot \mathbf{C}_B \cdot \mathbf{L}) \cdot \vec{u} + \vec{F} e = \begin{pmatrix} C_0 \frac{\partial^2 u_x}{\partial x^2} + 2G \frac{\partial^2 u_x}{\partial y^2} + C_0 \frac{\partial^2 u_y}{\partial x \partial y} + F_x \\ C_0 \frac{\partial^2 u_y}{\partial y^2} + 2G \frac{\partial^2 u_y}{\partial x^2} + C_0 \frac{\partial^2 u_x}{\partial x \partial y} + F_y \end{pmatrix} = \rho_T \begin{pmatrix} \frac{\partial^2 u_x}{\partial t^2} \\ \frac{\partial^2 u_y}{\partial t^2} \end{pmatrix} \quad (2.81)$$

$$\vec{u}(t) = (u_x, u_y), \quad \frac{\sqrt{u_x^2 + u_y^2}}{L_0} \ll 1, \quad C_0 = \lambda_U + 2G + 2C\varphi + M\varphi^2$$

This model is valid only for small, reversible deformations of Hookean poroelastic rocks, where L_0 is a representative dimension of the porous skeleton (Coussy 2004).

We consider next the important case of static poroelastic equations when the external body force is the vertical gravitational force per unit bulk volume and the acceleration in equation (2.79b) is zero. The governing poroelastostatic equations become:

$$\vec{F} = \begin{pmatrix} 0 \\ 0 \\ -\rho_T g \end{pmatrix} \quad \text{and} \quad \vec{\nabla} \cdot \boldsymbol{\sigma}_B = (\partial_x \quad \partial_y \quad \partial_z) \cdot \begin{pmatrix} \sigma_x & \sigma_{xy} & \sigma_{xz} \\ \sigma_{xy} & \sigma_y & \sigma_{yz} \\ \sigma_{xz} & \sigma_{yz} & \sigma_z \end{pmatrix}; \quad \partial_x = \frac{\partial}{\partial x}, \dots \quad (2.82a)$$

$$\vec{\nabla} \cdot \boldsymbol{\sigma}_B + \vec{F} = \vec{0} \quad \Leftrightarrow \quad F_i + \frac{\partial \sigma_{ij}}{\partial x_j} = 0 \quad \Leftrightarrow \quad \begin{cases} \partial_x \sigma_x + \partial_y \sigma_{xy} + \partial_z \sigma_{xz} + 0 = 0 \\ \partial_x \sigma_{xy} + \partial_y \sigma_y + \partial_z \sigma_{yz} + 0 = 0 \\ \partial_x \sigma_{xz} + \partial_y \sigma_{yz} + \partial_z \sigma_z = \rho_T g \end{cases} \quad (2.82b)$$

These are the three force equilibrium equations governing quasistatic problems. The study of poroelastostatic phenomena assumes that mechanical equilibrium is attained in a very short time or immediately after any change in fluid pressure or in stress occurs in the porous rock. “*In reality, a finite amount of time is required for a dynamic wave to transmit stress changes across the problem domain, but the wave propagation term is ignored in the quasistatic approximation.*” (Wang 2000). To obtain the other three partial differential equations required for the mathematical

model, we replace the stress components of equation (2.74) into equation (2.82b):

$$\begin{aligned} \partial_i \sigma_i &= \partial_i (\lambda \varepsilon_B + 2G \varepsilon_i) - b \partial_i p_f; \quad \partial_{ij} \sigma_{ij} = 2G \partial_{ij} \varepsilon_{ij}; \quad \{i, j = x, y, z\} \\ \varepsilon_B &= \frac{\partial u_x}{\partial x} + \frac{\partial u_y}{\partial y} + \frac{\partial u_z}{\partial z}, \quad \varepsilon_i = \frac{\partial u_i}{\partial i}, \quad \varepsilon_{ij} = \frac{\partial u_i}{\partial j} + \frac{\partial u_j}{\partial i}; \quad \{i, j = x, y, z\} \end{aligned} \quad (2.83)$$

Developing these compact equations and arranging the appropriate factors, we obtain:

$$\begin{aligned} G \left(\frac{\partial^2 u_x}{\partial x^2} + \frac{\partial^2 u_x}{\partial y^2} + \frac{\partial^2 u_x}{\partial z^2} \right) + (\lambda + G) \left(\frac{\partial^2 u_x}{\partial x^2} + \frac{\partial^2 u_y}{\partial x \partial y} + \frac{\partial^2 u_z}{\partial x \partial z} \right) &= b \frac{\partial p_f}{\partial x} \\ G \left(\frac{\partial^2 u_y}{\partial x^2} + \frac{\partial^2 u_y}{\partial y^2} + \frac{\partial^2 u_y}{\partial z^2} \right) + (\lambda + G) \left(\frac{\partial^2 u_x}{\partial x \partial y} + \frac{\partial^2 u_y}{\partial y^2} + \frac{\partial^2 u_z}{\partial y \partial z} \right) &= b \frac{\partial p_f}{\partial y} \\ G \left(\frac{\partial^2 u_z}{\partial x^2} + \frac{\partial^2 u_z}{\partial y^2} + \frac{\partial^2 u_z}{\partial z^2} \right) + (\lambda + G) \left(\frac{\partial^2 u_x}{\partial x \partial z} + \frac{\partial^2 u_y}{\partial y \partial z} + \frac{\partial^2 u_z}{\partial z^2} \right) &= b \frac{\partial p_f}{\partial z} - \rho_T g \end{aligned} \quad (2.84a)$$

In condensed tensorial notation, this system is equivalent to the following formula:

$$G \nabla^2 u_i + (\lambda + G) \frac{\partial^2 u_i}{\partial i \partial j} - b \frac{\partial p_f}{\partial i} + F_i = 0; \quad \{i, j = x, y, z\} \quad (2.84b)$$

Many other expressions of equations (2.84a, b) are easily obtained using the relationships among poroelastic coefficients developed in previous sections. For example, taking the first formula of equation (2.74) with the undrained Lamé modulus and replacing equation (2.66b) in equation (2.84b), the corresponding group of partial differential equations for the variation of the fluid content is:

$$G \nabla^2 u_i + (\lambda_U + G) \frac{\partial^2 u_i}{\partial i \partial j} - C \frac{\partial \zeta}{\partial i} + F_i = 0; \quad \{\forall i, j = x, y, z\} \quad (2.84c)$$

Both equations (2.84b) and (2.84c) are coupling the poroelastic mechanism between the pore pressure or the fluid content, and the displacement of the porous rock particles. Two drained coefficients λ and G emerge in equation (2.84b) because the coupling term is the fluid pressure. The undrained modulus λ_U ($G_U = G$) appears in equation (2.84c) because the coupling term is the variation of the fluid content. Other coupling interpretations can be found in Wang's excellent book (Wang 2000).

To complete the system of eleven equations mentioned at the beginning of this section, we need a last partial differential equation. It is obtained using the function ζ and Darcy's law, which is introduced in chapter 4. From the definition of the variable ζ given by equation (2.65):

$$\zeta(\vec{u}, t) = \varphi \vec{\nabla} \cdot (\vec{u}_s - \vec{u}_f) = -\varphi \vec{\nabla} \cdot \vec{u} \quad \Rightarrow \quad \frac{\partial \zeta}{\partial t} = -\varphi \vec{\nabla} \cdot \frac{\partial \vec{u}}{\partial t} \quad (2.85a)$$

On the other hand, Darcy's velocity is given by equation (4.13), (see section 4.1):

$$\vec{v}_f = \frac{\partial \vec{u}}{\partial t} \quad \text{and} \quad \vec{v}_f = -\frac{k}{\mu_f} (\vec{\nabla} p_f - \rho_f \vec{g}) \quad (2.85b)$$

Equating both equations (2.85a) and (2.85b), neglecting the gravity gradient, we obtain:

$$\varphi \vec{\nabla} \cdot \frac{\partial \vec{u}}{\partial t} = \vec{\nabla} \cdot \vec{v}_f = -\frac{k}{\mu_f} \vec{\nabla} \cdot \vec{\nabla} p_f \quad \Rightarrow \quad \boxed{\frac{\partial \zeta}{\partial t} = \frac{k}{\mu_f} \nabla^2 p_f} \quad (2.86a)$$

This parabolic partial differential equation is a diffusion equation; it characterizes the transient laminar fluid flow in a porous rock as a function of the fluid pressure and the variation of the fluid content. It is worthwhile to express equation (2.86a) solely in terms of ζ or in terms of fluid pressure. Using equations (2.66b) and (2.26b) relating ζ and p_f :

$$\frac{\partial \zeta}{\partial t} = \frac{1}{M} \frac{\partial p_f}{\partial t} + b \frac{\partial \varepsilon_B}{\partial t}; \quad \varepsilon_B = \frac{\sigma_M}{K_B}; \quad \sigma_M = \frac{\sigma_{kk}}{3}; \quad M = \frac{K_U B}{b} \quad \Rightarrow \quad (2.86b)$$

$$\boxed{\frac{C}{M} \frac{\partial \varepsilon_B}{\partial t} + \frac{1}{M} \frac{\partial p_f}{\partial t} = \frac{k}{\mu_f} \nabla^2 p_f} \quad \text{or} \quad \boxed{\frac{b}{K_B} \frac{\partial \sigma_M}{\partial t} + \frac{b}{K_U B} \frac{\partial p_f}{\partial t} = \frac{k}{\mu_f} \nabla^2 p_f} \quad (2.86c)$$

Using the fundamental moduli of equation (2.44a) we obtain:

$$\frac{\partial \zeta}{\partial t} = \frac{1}{H} \frac{\partial \sigma_M}{\partial t} + \frac{1}{R} \frac{\partial p_f}{\partial t} = \frac{k}{\mu_f} \nabla^2 p_f; \quad \frac{1}{H} = \frac{b}{K_B}, \quad \frac{1}{R} = \frac{1}{BH} = \frac{b}{BK_B} \quad (2.86d)$$

$$\Rightarrow \quad \boxed{B \frac{\partial \sigma_M}{\partial t} + \frac{\partial p_f}{\partial t} = \frac{BK_B}{b} \frac{k}{\mu_f} \nabla^2 p_f}$$

Any of the equations (2.86a–d) complete the group of 11 equations required to solve the 11 poroelastic unknowns. They can be solved using the techniques discussed in chapter 5.

2.2.11 Diffusion equations for consolidation

Consolidation is a transient process occurring in porous rocks when “*pore pressure equilibrium is re-established after a change in the stress state. This process involves a flow of the pore fluid through the porous rock*” (Fjaer *et al.* 1992). This fluid flow obeys Darcy’s law, which is detailed in chapter 4. Using the material of previous sections, we illustrate the construction of a simple mathematical model for the coupled process of consolidation. We apply the diffusion equation (2.81) to a vertical column of homogeneous porous rock, in one dimension. We suppose that the lateral strains are negligible, the rock has high permeability, especially at the top of the column, and it is impermeable at the bottom, at a depth equal to z_0 . Using formulae (2.66a) and (2.66b) in the vertical dimension OZ:

$$\sigma_z = (\lambda_U + 2G) \varepsilon_z - C \zeta; \quad p_f = M \zeta - C \varepsilon_z \quad \Rightarrow \quad (2.87a)$$

$$\varepsilon_z = \frac{M \sigma_z + C p_f}{M (\lambda_U + 2G) - C^2} \quad \text{and} \quad \frac{\partial p_f}{\partial t} = M \frac{\partial \zeta}{\partial t} - C \frac{\partial \varepsilon_z}{\partial t}$$

The formula for ε_z in this equation shows that the vertical strain depends on both the vertical stress and the fluid pressure. If p_f changes, ε_z is going to change during the same interval it takes for the pore pressure to reach equilibrium (Fjaer *et al.* 1992). Substituting the last two expressions of equation (2.82) into equation (2.81), we obtain:

$$\frac{\partial \zeta}{\partial t} = \frac{\lambda_U + 2G}{M (\lambda_U + 2G) - C^2} \left(\frac{\partial p_f}{\partial t} + \frac{C}{\lambda_U + 2G} \frac{\partial \sigma_z}{\partial t} \right) = \frac{k}{\mu} \frac{\partial^2 p_f}{\partial z^2} \quad (2.87b)$$

This is a coupled equation, which relates the spatial and temporal changes of the fluid pressure with the vertical stresses acting in the porous rock. It involves the undrained Lamé and shear moduli, the Biot coefficients, the permeability and the dynamic viscosity of the fluid. If the

vertical stress does not change with time, equation (2.83) becomes simpler and we have the following differential model (p_a is the atmospheric pressure in Pa):

$$p_f(z_0, t) = p_a; \quad \frac{\partial p_f}{\partial z}(0, t) = 0; \quad p_f(z, 0) = p_0; \quad \boxed{\frac{\partial p_f}{\partial t} = C_D \frac{\partial^2 p_f}{\partial z^2}} \quad (2.88a)$$

where: $C_D = \frac{M(\lambda_U + 2G) - C^2}{\lambda_U + 2G} \frac{k}{\mu} \left[\frac{\text{m}^2}{\text{s}} \right]; \quad p_f(z, t); z \in [0, z_0]; t \geq 0$

Equation (2.84) is the partial differential equation of consolidation and C_D is the consolidation diffusion coefficient (Ejaer *et al.* 1992). We can deduce another form of equation (2.83), using the initial equations (2.44a):

$$\frac{\partial \zeta}{\partial t} = \frac{1}{H} \frac{\partial \sigma_z}{\partial t} + \frac{1}{R} \frac{\partial p_f}{\partial t} = \frac{1}{R} \left(B \frac{\partial \sigma_z}{\partial t} + \frac{\partial p_f}{\partial t} \right) \Rightarrow B \frac{\partial \sigma_z}{\partial t} + \frac{\partial p_f}{\partial t} = R \frac{k}{\mu} \frac{\partial^2 p_f}{\partial z^2} \quad (2.88b)$$

This is another poroelastic model coupling the changes in vertical stress σ_z to the pore pressure. Constant R is the inverse of the unconstrained storage coefficient (Wang 2000) given in equations (2.45) and $R k/\mu$ is another form of the diffusion coefficient for consolidation.

2.2.12 Basic thermodynamics of porous rocks

General thermodynamics studies the laws that describe the continuous transformations of moving physical systems. Thermostatistics is a branch of thermodynamics that studies the equilibrium states of physical systems during their exchanges of energy and work (Germain 1973, Coussy 2004). Energy, heat, enthalpy, mechanical work, entropy, pressure, density, and temperature are the key concepts in this science. They are called essential variables. A potential is a numeric real function from where other variables derive. The present knowledge in thermostatistics (Coussy 2004) allows us to describe accurately the behavior of porous rocks using one thermodynamic potential and one energy dissipation function. To introduce both concepts, we need the laws of thermodynamics in natural reservoirs or systems formed of porous rocks.

2.2.12.1 The first and second law of thermodynamics for porous rocks

The immediate physical experience shows that the supply or extraction of heat produces deformations in all types of rocks. Any variation of temperature induces a thermo-poroelastic behavior that influences the elastic response of porous rocks. Liquid water has very low compressibility. This property tends to reduce rock elasticity, stiffness and strength. Thus, the presence of hot water in porous rocks affects their geomechanical behavior and always makes them fracture more easily. Let U [J] and S [J/K] be two functions representing the internal energy and the entropy of the reservoir, Q [J] is the heat exchanged between the system and its surroundings, and W [J] is the work done by the system ($W < 0$) or on the system ($W > 0$). The first two laws of thermodynamics (Alonso-Finn 1968) state that:

- *First law*: The change of internal energy of a reservoir is equal to the heat extracted plus the work done by (on) the reservoir system:

$$\Delta U = U - U_0 = W + Q \quad (2.89a)$$

- *Second law*: The most probable processes that may occur in a reservoir are those in which the entropy either increases or remains constant:

$$\Delta S = S - S_0 \geq 0 \quad (2.89b)$$

If the process is reversible and T_0 is a reference temperature then:

$$\Delta Q = T_0 \Delta S \quad (2.89c)$$

To illustrate the use of these functions consider a volume V_B of rock, which is at the initial state (p_0, T_0, ρ_0) . Let $\rho_0 = 1/\nu_0$ be the density of the rock and M_0 be its constant mass. We assume that the rock is subjected to an isothermal compression $\sigma = -p_k < 0$, reaching another state (p_1, T_0, ρ_0) . A heating process under constant pressure follows the compression. The rock goes from the previous state to the final state (p_1, T_1, ρ_0) . We assume that both processes are reversible and that the change of the rock density is negligible. Using the definitions given by equations (2.22a) and (2.40c), we can compute the work done by each process, the entropy change and the change in the internal energy of the system. The differential work done on ΔV_B per unit rock mass is:

$$dW = p_k d\nu = p_k \left(\frac{\partial \nu}{\partial p_k} dp_k + \frac{\partial \nu}{\partial T} dT \right),$$

where: $\left(\frac{\partial \nu}{\partial p_k} \right)_T = - \left(\frac{\partial \nu}{\partial \sigma} \right)_T = C_T \nu_0 = \frac{C_T}{\rho_0}$, and $\left(\frac{\partial \nu}{\partial T} \right)_{p_k} = \gamma_B \nu_0 = \frac{\gamma_B}{\rho_0}$ (2.90a)

hence: $dW = p_k \nu_0 (\gamma_B dT + C_T dp_k) \rightarrow \left[\frac{\text{J}}{\text{kg}} \right]$

For the isothermal compression, we must have $dT = 0$; therefore:

$$\int_0^{W_1} dW = W_1 = \nu_0 C_T \int_{p_0}^{p_1} p_k dp_k = \nu_0 C_T \frac{p_1^2 - p_0^2}{2} \quad (2.90b)$$

For the isobaric heating, we must have $dp_k = 0$, and consequently the work done by the thermal stress is:

$$\int_{W_1}^{W_2} dW = W_2 - W_1 = \frac{p_1}{\rho_0} \gamma_B \int_{T_0}^{T_1} dT = \frac{p_1}{\rho_0} \gamma_B (T_1 - T_0) \quad (2.90c)$$

Therefore, the total work done on the rock is:

$$W_2 = C_T \frac{p_1^2 - p_0^2}{2\rho_0} + \gamma_B \frac{p_1}{\rho_0} (T_1 - T_0) \quad (2.90d)$$

Note that the total work must be positive $W_2 > 0$. The change in the entropy of the system at the end of the second process is:

$$\int_{S_0}^{S_1} dS = \int_{Q_0}^{Q_1} \frac{dQ}{T} = M_0 c_p \int_{T_0}^{T_1} \frac{dT}{T} \Rightarrow \frac{S_1 - S_0}{M_0} = c_p \text{Ln} \left(\frac{T_1}{T_0} \right) \quad (2.90e)$$

Using the numerical values of Table 2.1 for well H-10: $\rho_0 = 2620 \text{ kg/m}^3$, $C_T = 7.3 \times 10^{-11} \text{ Pa}^{-1}$, $c_p = 1088.6 \text{ J/kg/}^\circ\text{C}$, $\gamma_B = 5 \times 10^{-5} \text{ }^\circ\text{C}^{-1}$ and $p_0 = 5 \text{ MPa}$, $p_1 = 35 \text{ MPa}$,

$M_0 = 1.0 \text{ kg}$, $T_0 = 25^\circ\text{C}$, $T_1 = 250^\circ\text{C}$, we obtain:

$$C_T \frac{p_1^2 - p_0^2}{2\rho_0} = 16.72 \frac{\text{J}}{\text{kg}}; \quad \gamma_B \frac{p_1}{\rho_0} (T_1 - T_0) = 150.29 \frac{\text{J}}{\text{kg}}; \quad W_2 = 167.0 \frac{\text{J}}{\text{kg}};$$

$$\frac{S_1 - S_0}{M_0} = 2506.59 \frac{\text{J}}{\text{kg}^\circ\text{C}}; \quad \frac{U - U_0}{M_0} = W_2 + T_0 \frac{\Delta S}{M_0} = 167 + 25 \times 2506.59 = 62832 \frac{\text{J}}{\text{kg}}$$

Note that the thermomechanical specific work done on the rock is relatively small when compared with the change of its specific entropy. This is because the andesitic rock has very small compressibility and expansivity. Consequently, it is hard to change its volume. Nevertheless, the rock internal energy variation is important, reflecting the heat absorption.

2.2.12.2 Differential and integral forms of the first and second law

The first and second law of thermostatics for reversible processes can be written in differential form in a solid REV of volume ΔV_B :

$$d\left(\frac{U}{\Delta V_B}\right) = de = \delta W + \delta Q \rightarrow \left[\frac{\text{J}}{\text{m}^3}\right] \quad (2.91a)$$

$$\frac{Q}{\Delta V_B} = T_0 \frac{S}{\Delta V_B} \Rightarrow \delta Q = T_0 ds \rightarrow \left[\frac{\text{J}}{\text{m}^3}\right] \quad (2.91b)$$

where δW and δQ represent the volumetric work and heat exchanged, respectively, and e and s are the volumetric internal energy and entropy, respectively. The symbol δ means that the differential of both quantities W and Q is not exact. Because e is an equation of state and s is the corresponding entropy, de and ds are total differentials.

Note that if the volumetric work is done at constant volume, then the variation of internal energy is equal to the volumetric heat exchanged (eq. 2.10):

$$\delta W = p \frac{dV}{V_B} = 0 \Rightarrow de = \delta Q \Rightarrow e - e_0 = Q_V = \int_{T_0}^{T_1} C_V dT \quad (2.92a)$$

Note also that if the confining pressure is constant, then heat exchanged is equal to the variation of the volumetric enthalpy (eq. 2.10):

$$\delta W = 0 \Rightarrow de = dh = \delta Q \Rightarrow h - h_0 = Q_p = \int_{T_0}^T C_p dT \quad (2.92b)$$

Note that in both cases, the heat exchanged is independent of intermediate states and the formulae (2.92a) and (2.92b) are valid for any system that receives work only from stresses at constant volume and constant pressure, respectively. In the case of solids and low-enthalpy liquids, their specific volume is very small, consequently $dh \approx de \approx c_p dT$.

It is easy to prove a useful thermodynamic formula relating the difference between specific heats $c_p - c_V$ and volumetric expansivity, density, isothermal compressibility and temperature:

$$C_T = -\frac{1}{V_B} \left(\frac{\partial V_B}{\partial p_k} \right)_T; \quad c_p - c_V = \frac{\gamma_B^2 T}{\rho C_T} \quad (2.92c)$$

For solids and liquids such as oil and water, γ_B is relatively small (10^{-5} K^{-1}), and, therefore, $c_p - c_V$ is small. For this reason, “many tables simply give the specific heat of a solid or a liquid

without designating that it is at constant pressure or volume” (Sonntag and van Wylen 1982). Integrating the rate of change of equation (2.91a) over a rock domain Ω , we obtain the power of the system:

$$\left[\frac{\text{W}}{\text{m}^3} \right] \leftarrow \frac{de}{dt} = \frac{\delta W}{\delta t} + \frac{\delta Q}{\delta t} \Rightarrow \int_{\Omega} \frac{de}{dt} d\Omega = \int_{\Omega} \frac{\delta W}{\delta t} d\Omega + \int_{\Omega} \frac{\delta Q}{\delta t} d\Omega \rightarrow [\text{W}] \quad (2.93)$$

The rate of heat exchanged is computed using the following general integral formula:

$$\int_{\Omega} \frac{\delta Q}{\delta t} d\Omega = - \int_{\partial\Omega} q_n dA = - \int_{\partial\Omega} \vec{q}_T \cdot \vec{n} dA = - \int_{\Omega} \vec{\nabla} \cdot \vec{q}_T d\Omega \quad (2.94a)$$

$$\text{and, therefore: } \frac{\delta Q}{\delta t} = T_0 \frac{\partial s}{\partial t} = - \vec{\nabla} \cdot \vec{q}_T \quad (2.94b)$$

The term q_n is the normal component of the heat flow given by equation (2.9). The application of the divergence theorem in equation (2.91b) completes the integral expression of the rate of heat exchanged by conduction between the domain Ω and its surroundings. All of the relationships introduced up to this point are valid for general thermostatics processes in any continuum medium.

A particular result for the rock solid matrix is that the integral work can be computed using the following classic formula for thermoelastic solids (Germain 1973, Duc and Bellet 1976):

$$\frac{\delta W}{\delta t} = \sigma_{ij} \frac{\partial \varepsilon_{ij}}{\partial t} \quad (2.95)$$

The results given by equations (2.94b) and (2.95), replaced in equation (2.93) lead to the following energy conservation equations for the solid matrix:

$$\int_{\Omega} \left(\frac{\partial e}{\partial t} - \sigma_{ij} \frac{\partial \varepsilon_{ij}}{\partial t} + \vec{\nabla} \cdot \vec{q}_T \right) d\Omega = 0 \Leftrightarrow \frac{\partial e}{\partial t} - \sigma_{ij} \frac{\partial \varepsilon_{ij}}{\partial t} + \vec{\nabla} \cdot \vec{q}_T = 0 \quad (2.96)$$

Both equations (2.96) are equivalent because the integration is performed over an arbitrary domain Ω of the solid matrix. Using Fourier’s law (eq. 2.9) of heat conduction in equation (2.96b) we obtain:

$$\vec{q}_T = -\mathbf{k}_T \cdot \vec{\nabla} T \Rightarrow \frac{\partial e}{\partial t} - \sigma_{ij} \frac{\partial \varepsilon_{ij}}{\partial t} - \vec{\nabla} \cdot (\mathbf{k}_T \cdot \vec{\nabla} T) = 0 \quad (2.97)$$

This formula is a thermoelastic equation coupling the rate of changes of the internal energy, the strains, and the heat transported by conduction.

2.2.12.3 *The Helmholtz free energy: A thermoelastic potential for the matrix*

The Helmholtz free internal energy $F_s(\varepsilon_{ij}, T)$ derives its name from the German physician and physicist, Hermann Ludwig von Helmholtz (Fig. 2.10). This thermodynamic potential is useful to derive the equations of solid non-isothermal elasticity. The function F_s (its units are in Joules and subindex s means solid), establishes mathematical relationships among heat, strains and stresses. Despite the important theoretical character of F_s (Coussy 2004), it is little used in classic thermoelasticity (Mase and Mase 1999). This potential is equal to the algebraic difference of the solid internal energy U_s minus the heat exchanged Q . If we assume that the internal energy dissipation is zero and that the processes involved are reversible, then the heat exchanged is equal

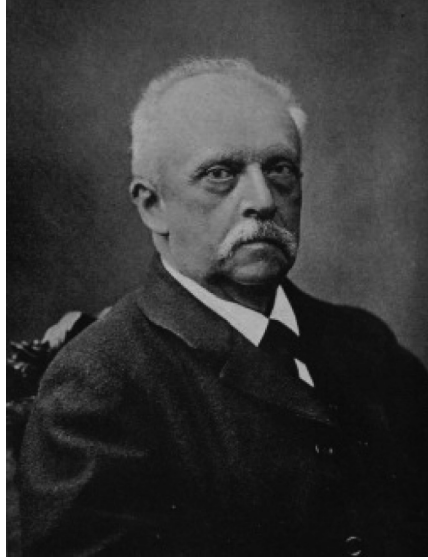


Figure 2.10. Hermann Ludwig von Helmholtz (1821–1894), German scientist, creator of the free energy concept.

to the product of the absolute temperature and the entropy of the system (eq. 2.89c):

$$F_s = U_s - T S_s \quad (2.98a)$$

The Helmholtz potential F_s is an equation of state for the matrix. It is called free energy because in every isothermal compression:

$$\Delta F_s = \Delta U_s - T \Delta S_s \quad (2.98b)$$

The term ΔU_s in this equation is the matrix-stored energy, while the term $T \Delta S_s$ represents the unusable energy. Therefore, ΔF_s acts as a useful energy, able to be totally transformed into work. It is more convenient to formulate equation (2.98a) per unit volume of rock:

$$f_s = \frac{F_s}{\Delta V_B} = \frac{U_s}{\Delta V_B} - T \frac{S_s}{\Delta V_B} \Rightarrow f_s = e_s - T s_s \rightarrow \left[\frac{\text{J}}{\text{m}^3} = \frac{\text{N}}{\text{m}^2} = \text{Pa} \right] \quad (2.98c)$$

The functions f_s , e_s , and s_s , represent the volumetric Helmholtz potential, the volumetric energy and the volumetric entropy, respectively. The potential $f_s(\varepsilon_{ij}, T)$ is the volumetric thermoelastic energy of the matrix [J/m^3]. For small changes in the REV, the total differential of $f_s(\varepsilon_{ij}, T)$ is:

$$\begin{aligned} df_s(\varepsilon_{ij}, T) &= d(e_s - T s_s) = de_s - dT s_s - T ds_s = \sigma_{ij} d\varepsilon_{ij} - s_s dT \\ \Rightarrow df_s &= \frac{\partial f_s}{\partial \varepsilon_{ij}} d\varepsilon_{ij} + \frac{\partial f_s}{\partial T} dT \Rightarrow \sigma_{ij} = \frac{\partial f_s}{\partial \varepsilon_{ij}}, s_s = -\frac{\partial f_s}{\partial T} \end{aligned} \quad (2.98d)$$

Computing the transient derivative of equation (2.98c) and combining with (2.91a), we obtain the rock energy dissipation:

$$\begin{aligned} \frac{\partial f_s}{\partial t} &= \frac{\partial e_s}{\partial t} - T \frac{\partial s_s}{\partial t} - s_s \frac{\partial T}{\partial t} = \sigma_{ij} \frac{\partial \varepsilon_{ij}}{\partial t} - \vec{\nabla} \cdot \vec{\alpha}_{\mathcal{K}T} - s_s \frac{\partial T}{\partial t} + \vec{\nabla} \cdot \vec{\alpha}_{\mathcal{K}T} \\ \Rightarrow -\frac{\partial f_s}{\partial t} + \sigma_{ij} \frac{\partial \varepsilon_{ij}}{\partial t} - s_s \frac{\partial T}{\partial t} &= 0 \end{aligned} \quad (2.98e)$$

We consider the following initial conditions, corresponding to a free strain natural state:

- Zero initial strain: $\varepsilon_{ij}(0) = 0$, and $\sigma_{ij}(0) \ll \sigma_{ij}$.
- Uniform initial temperature: $T(0) = T_0$, consequently: $f_s(0, T_0) = f_s^0$.
- The second condition implies a zero initial thermal gradient.

Under these hypotheses, we can expand $f_s(\varepsilon_{ij}, T)$ using a Taylor development in a neighborhood of the initial state:

$$f_s(\varepsilon_{kl}, T) = \sum_{n=0}^{\infty} \left[\left(\frac{\partial}{\partial \varepsilon_{kl}}, \frac{\partial}{\partial T} \right) \cdot (\varepsilon_{kl}, T - T_0) \right]^n \frac{f_s^0}{n!} = f_s^0 + \varepsilon_{kl} \frac{\partial f_s^0}{\partial \varepsilon_{kl}} + (T - T_0) \frac{\partial f_s^0}{\partial T} + E_{rr}^2$$

E_{rr}^2 represents the error of quadratic order in the approximation. For small deformations, this error is negligible and we obtain a linearization of $f_s(\varepsilon_{kl}, T)$. From the partial derivatives of f_s in equation (2.98d), we deduce the following expressions:

$$\begin{aligned} \sigma_{ij} &\approx \frac{\partial f_s^0}{\partial \varepsilon_{ij}} + \varepsilon_{kl} \frac{\partial^2 f_s^0}{\partial \varepsilon_{ij} \partial \varepsilon_{kl}} + (T - T_0) \frac{\partial^2 f_s^0}{\partial \varepsilon_{ij} \partial T} \\ -s_s &\approx \frac{\partial f_s^0}{\partial T} + (T - T_0) \frac{\partial^2 f_s^0}{\partial T^2} + \varepsilon_{kl} \frac{\partial^2 f_s^0}{\partial \varepsilon_{kl} \partial T} \end{aligned} \quad (2.99a)$$

According to the initial conditions, we deduce the existence of two tensors such that:

$$\begin{aligned} \sigma_{ij} &= \sigma_{ij}^0 + \lambda_{ijkl} \varepsilon_{kl} + \beta_{ij} (T - T_0); \quad s_s = s_0 + C_V \frac{(T - T_0)}{T_0} - \beta_{ij} \varepsilon_{ij} \\ \text{where: } \lambda_{ijkl} &= \frac{\partial^2 f_s^0}{\partial \varepsilon_{ij} \partial \varepsilon_{kl}}, \quad \beta_{ij} = \frac{\partial^2 f_s^0}{\partial \varepsilon_{ij} \partial T}, \quad C_V = -T_0 \frac{\partial^2 f_s^0}{\partial T^2} \end{aligned} \quad (2.99b)$$

The thermoelastic tensors (β_{ij}) and (λ_{ijkl}) are symmetric because (σ_{ij}) is symmetric. There are particular expressions of these tensors for isotropic, homogeneous solids in terms of previously defined coefficients (Duc and Bellet 1976):

$$\begin{aligned} \lambda_{ijkl} &= \lambda \delta_{ij} \delta_{kl} + G (\delta_{ik} \delta_{jl} + \delta_{il} \delta_{jk}) \quad \Rightarrow \quad \lambda_{ijkl} \varepsilon_{kl} = \lambda \varepsilon_B \delta_{ij} + 2G \varepsilon_{ij} \\ \beta_{ij} &= -\frac{3\lambda + 2G}{3} \gamma_B \delta_{ij} = -K_B \gamma_B \delta_{ij}; \quad \gamma_B \cong \frac{1}{V_B} \frac{\Delta V_B}{\Delta T} = \frac{\varepsilon_B}{T - T_0} \end{aligned} \quad (2.99c)$$

The parameter γ_B is the thermal volumetric dilatation defined in equation (2.22a). The group of formulae (2.99a,b,c) relates temperature changes, deformations and tensions within any Hookean solid. The Helmholtz potential leads, in a direct way, to the construction and coupling of the classical thermoelastic linear equations for strains, thermal stresses, temperature and entropy. This thermodynamic potential can be computed explicitly by solving together equations (2.98d) and (2.99b). Using the initial conditions for f_s , starting from a free stress natural state, and integrating twice:

$$\begin{aligned} - \int_{f_s^0}^{f_s} \partial f_s &= \int_{T_0}^T s_s \partial T = \int_{T_0}^T \left(s_0 + \frac{C_V (T - T_0)}{T_0} - \beta_{ij} \varepsilon_{ij} \right) \partial T - \Phi_\varepsilon(\varepsilon_{ij}) \\ \int_{f_s^0}^{f_s} \partial f_s &= \int_0^{\varepsilon_{ij}} \sigma_{ij} \partial \varepsilon_{ij} = \int_0^{\varepsilon_{ij}} (\lambda \varepsilon_B \delta_{ij} + 2G \varepsilon_{ij} + (T - T_0) \beta_{ij}) \partial \varepsilon_{ij} + \Phi_T(T) \\ \Phi_\varepsilon(\varepsilon_{ij}) &= \frac{\lambda}{2} \varepsilon_B^2 + G \varepsilon_{ij}^2; \quad \Phi_T(T) = -s_0(T - T_0) - C_V \frac{(T - T_0)^2}{2T_0} \end{aligned}$$

Φ_ε and Φ_T are arbitrary functions of ε_{ij} and T , respectively; both are fixed during the integrations. Both integrals lead to an analytic formula for the Helmholtz free energy function $f_s(\varepsilon_{ij}, T)$ for Hookean solids:

$$f_s(\varepsilon_{ij}, T) = f_s^0 - s_0(T - T_0) - \frac{C_V}{2} \frac{(T - T_0)^2}{T_0} + \beta_{ij} \varepsilon_{ij}(T - T_0) + \frac{\lambda}{2} \varepsilon_B^2 + G \varepsilon_{ij}^2 \quad (2.100)$$

This potential has practical and theoretical utility; it provides an elegant formulation of non-isothermal processes in elastic solids. Its derivatives are important thermoelastic relationships:

$$\sigma_{ij} = \frac{\partial f_s}{\partial \varepsilon_{ij}} = \lambda \varepsilon_B \delta_{ij} + 2G \varepsilon_{ij} - K_B \gamma_B (T - T_0) \delta_{ij} \quad (2.101a)$$

$$\varepsilon_{ij} = \frac{1 + \nu}{E} \sigma_{ij} - \left(\frac{\nu \sigma_{kk}}{E} + \gamma_B (T - T_0) \right) \delta_{ij} \quad (2.101b)$$

$$s_s = -\frac{\partial f_s}{\partial T} = s_0 + \frac{C_V}{T_0} (T - T_0) + K_B \gamma_B \varepsilon_B \quad (2.101c)$$

Equations (2.101a, b) are known as the Duhamel-Neumann law, which generalizes Hooke's law for non-isothermal processes including thermal stresses. Developing the second term of equation (2.94b) and using equation (2.98c):

$$\begin{aligned} -\vec{\nabla} \cdot \vec{q}_T &= T_0 \frac{\partial s_s}{\partial t} = T_0 \left(\frac{\partial s_s}{\partial \varepsilon_{ij}} \frac{\partial \varepsilon_{ij}}{\partial t} + \frac{\partial s_s}{\partial T} \frac{\partial T}{\partial t} \right) = T_0 \left(-\frac{\partial^2 f_s}{\partial \varepsilon_{ij} \partial T} \frac{\partial \varepsilon_{ij}}{\partial t} - \frac{\partial^2 f_s}{\partial T^2} \frac{\partial T}{\partial t} \right) \\ &= T_0 \left(-\beta_{ij} \frac{\partial \varepsilon_{ij}}{\partial t} + \frac{C_V}{T_0} \frac{\partial T}{\partial t} \right) = T_0 \left(K_B \gamma_B \delta_{ij} \frac{\partial \varepsilon_{ij}}{\partial t} + \frac{C_V}{T_0} \frac{\partial T}{\partial t} \right) = K_B \gamma_B T_0 \frac{\partial \varepsilon_{ii}}{\partial t} + C_V \frac{\partial T}{\partial t} \end{aligned}$$

Finally, introducing the expression of the volumetric heat capacity given by equation (2.10) we deduce the heat equation for the isotropic solid matrix:

$$\boxed{K_B \gamma_B T_0 \frac{\partial \varepsilon_B}{\partial t} + c_p \rho_s \frac{\partial T}{\partial t} = k_T \nabla^2 T} \quad (2.102)$$

Equations (2.101a,b,c) and (2.102) complete the system of linear thermoelasticity, to calculate thermal and mechanical deformations in isotropic, homogeneous elastic solids. We are going to extend this model to non-isothermal poroelastic rocks.

2.2.12.4 The Gibbs free enthalpy: Skeleton thermodynamics with null dissipation

The basic thermodynamical state potentials in a porous rock are the internal energy and the specific enthalpy for the fluid phase. The free energy describes the matrix while for the skeleton the appropriate potential is the free enthalpy (Coussy 2004). The Helmholtz free energy is also used for the thermodynamic properties of water that are described in section 2.3. These potentials, together with other thermodynamic variables such as stresses, strains, entropy, porosity, fluid pressure, density and absolute temperature, completely describe the exchanges of energy in a porous medium. The Gibbs free internal enthalpy G_S derives its name from the American physicist, mathematician and chemist Josiah Willard Gibbs (Fig. 2.11), who founded physical chemistry. The potential G_S (subindex S means skeleton) is useful to derive the equations of the rock skeleton in non-isothermal, reversible processes. The function G_S establishes mathematical relationships among heat, strains, stresses and pore pressure. This potential is equal to the algebraic difference of the skeleton enthalpy H_S minus the heat exchanged Q . If we assume that the internal energy dissipation is zero and that the processes involved are reversible, then the heat exchanged is equal

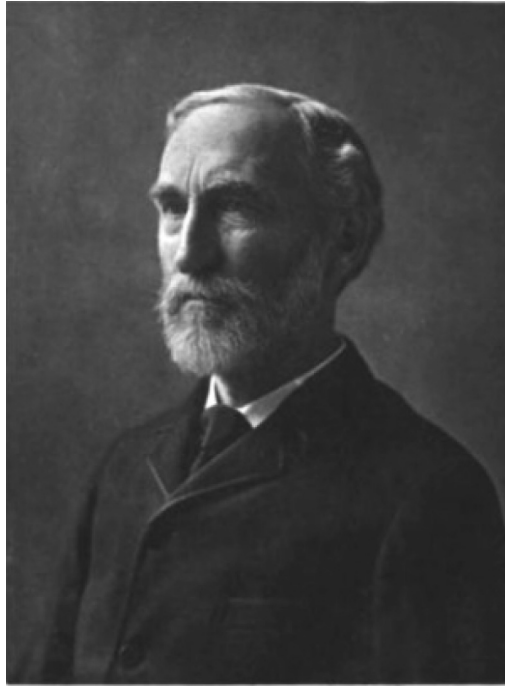


Figure 2.11. Josiah W. Gibbs (1839–1903), founder of chemical thermodynamics.

to the product of the absolute temperature and the entropy of the system (eq. 2.89c):

$$G_S = H_S - TS \rightarrow [\text{J}] \quad (2.103a)$$

The Gibbs potential G_S is an equation of state for the skeleton called free enthalpy because, in every isothermal compression of the form:

$$\Delta G_S = \Delta H_S - T \Delta S \quad (2.103b)$$

The term ΔH_S of this equation is the skeleton-stored enthalpy, while the term $T \Delta S$ represents the unusable energy. Therefore, ΔG_S acts as a useful energy, able to be totally transformed into work. It is more convenient to formulate equation (2.103a) per unit volume of rock:

$$g_S = \frac{G_S}{V_B} = \frac{H_S}{V_B} - T \frac{S}{V_B} \Rightarrow g_S = h_S - TS_S \rightarrow \left[\frac{\text{J}}{\text{m}^3} \right] \quad (2.103c)$$

The functions g_S , h_S , and S_S , represent the volumetric Gibbs potential, the volumetric enthalpy and the volumetric entropy of the skeleton, respectively. $g_S(\varepsilon_{ij}, p, T)$ is the thermoporoelastic available enthalpy per unit volume [J/m^3]. Coussy (2004) deduced the energy dissipation function Ψ_S in the skeleton, using the Gibbs potential, the stresses, the porosity, the pore pressure and the density of entropy per unit volume of porous rock S_S [$\text{J}/\text{m}^3/^\circ\text{C}$] as follows:

$$\frac{d\Psi_S}{dt} = \sigma_{ij} \frac{d\varepsilon_{ij}}{dt} - S_S \frac{dT}{dt} - \varphi \frac{dp}{dt} - \frac{dg_S}{dt} \geq 0 \quad (2.104)$$

Assuming that there is no energy dissipation in the porous rock ($d\Psi_S/dt = 0$) and for small changes in the REV, the Gibbs' potential describes the behavior of the skeleton (Coussy 2004). The total differential of $g_S(\varepsilon_{ij}, p, T)$ is by definition:

$$dg_S = \sigma_{ij} d\varepsilon_{ij} - \varphi dp - S_S dT \Rightarrow \sigma_{ij} = \frac{\partial g_S}{\partial \varepsilon_{ij}}, \quad \varphi = -\frac{\partial g_S}{\partial p}, \quad S_S = -\frac{\partial g_S}{\partial T} \quad (2.105)$$

the respective units are: $g_S \rightarrow \left[\frac{\text{J}}{\text{m}^3} = \text{Pa} \right]$; and $S_S \rightarrow \left[\frac{\text{J}}{\text{m}^3 \text{ } ^\circ\text{C}} \right] = \left[\frac{\text{Pa}}{^\circ\text{C}} \right]$

These partial differential equations are integrated between an initial state g_S^0 , when the strain was zero, ($\varepsilon_{ij}(0) = 0, p = p_0, T = T_0$) and a final state $g_S(\varepsilon_{ij}, p, T)$ as was done in the previous section. Note that we need an initial reference temperature T_0 and an initial pore pressure p_0 , because both thermodynamic variables T and p are going to change in a non-isothermal process. Integrating equations (2.105), Coussy (2004) obtained an exact expression of the Gibbs potential for the skeleton:

$$\begin{aligned} \text{Initial state: } g_S^0 &= g_S(\varepsilon_{ij} = 0, p = p_0, T = T_0); \\ \text{Final state: } g_S &= g_S(\varepsilon_{ij}, p, T) \\ \Rightarrow g_S(\varepsilon_{ij}, p, T) &= \sigma_M^0 \varepsilon_B + \left(\sigma_{ij}^0 - \sigma_M^0 \delta_{ij} \right) \left(\varepsilon_{ij} - \frac{\varepsilon_B}{3} \delta_{ij} \right) - \varphi_0 p - S_S^0 T \\ &+ \frac{K_B}{2} (\varepsilon_B)^2 - b(p - p_0) \varepsilon_B + \alpha_\varphi (p - p_0) (T - T_0) - K_B \gamma_B (T - T_0) \varepsilon_B \\ &- \frac{(p - p_0)^2}{2N} - \frac{C_V (T - T_0)^2}{2T_0} + G \left(\varepsilon_{ij} - \frac{\varepsilon_B}{3} \delta_{ij} \right)^2 \end{aligned} \quad (2.106)$$

The parameters γ_B and $\alpha_\varphi [1/\text{K}]$ are volumetric thermal dilatation coefficients. The first one γ_B (eq. 2.22a) measures the dilatation of the skeleton, while $\alpha_\varphi = -\varphi \gamma_\varphi$ is related to the variation of the porosity when the skeleton temperature changes (eq. 2.22b). C_V is the skeleton volumetric heat capacity coefficient (section 2.1.6) under constant deformations, when strains and pore pressure are held constant. The pore pressure is equal to the fluid pressure ($p = p_f$), which can be measured in the field or calculated using the equation of state for the fluid.

Using the relationships of equations (2.105) and (2.106), we obtain (Coussy 2004):

$$\varphi = -\frac{\partial g_S}{\partial p} = \varphi_0 + b \varepsilon_B - \alpha_\varphi (T - T_0) + \frac{(p - p_0)}{N} \quad (2.107a)$$

$$S_S = -\frac{\partial g_S}{\partial T} = S_S^0 + \gamma_B K_B \varepsilon_B - \alpha_\varphi (p - p_0) + C_V \frac{(T - T_0)}{T_0} \quad (2.107b)$$

$$\sigma_{ij} = \frac{\partial g_S}{\partial \varepsilon_{ij}} = \sigma_{ij}^0 + \lambda \varepsilon_B \delta_{ij} + 2G \varepsilon_{ij} - b(p - p_0) \delta_{ij} - K_B \gamma_B (T - T_0) \delta_{ij} \quad (2.107c)$$

$$\zeta = \varphi \varepsilon_V = -\varepsilon_V \frac{\partial g_S}{\partial p}; \quad b = -\frac{\partial^2 g_S}{\partial \varepsilon_{ij} \partial p}; \quad \frac{1}{N} = -\frac{\partial^2 g_S}{\partial p^2} \quad (2.107d)$$

$$\alpha_\varphi = \frac{\partial^2 g_S}{\partial T \partial p}; \quad \gamma_B = -\frac{1}{K_B} \frac{\partial^2 g_S}{\partial \varepsilon_{ij} \partial T}; \quad C_V = -T_0 \frac{\partial^2 g_S}{\partial T^2} \rightarrow \left[\frac{\text{J}}{\text{m}^3 \text{K}} \right] \quad (2.107e)$$

The Helmholtz free energy f_S of the skeleton, is given by the following expression:

$$f_S(\varepsilon_{ij}, \varphi, T) = g_S(\varepsilon_{ij}, p, T) + p \varphi [\text{Pa}] \quad (2.108)$$

Replacing the average fluid-solid density $\rho = \varphi \rho_f + (1-\varphi) \rho_s$ in equation (2.102) instead of the solid density ρ_s , and using an average specific heat capacity c_p , we complete the set of formulae for the skeleton with the heat equation. To include the reservoir heat production and the effect of the advective transport of energy by the moving fluid in the pores and fractures, it is necessary to add the volumetric heat produced or extracted and a fluid velocity term (Lautrup 2005):

$$\boxed{K_B \gamma_B T_0 \frac{\partial \varepsilon_B}{\partial t} + c_p \rho \left(\frac{\partial T}{\partial t} + \vec{v} \cdot \vec{\nabla} T \right) = k_T \nabla^2 T + \underline{Q}_H} \quad (2.109)$$

where vector \vec{v} represents the Darcy's velocity and \underline{Q}_H [W/m³] is the volumetric thermal energy production. For isothermal processes in rocks with zero porosity $\varphi = 0$, $T = T_0$ and $p = p_0$, the system of equations (2.107) is reduced to Hooke's law for linear elastic solids.

2.2.12.5 Thermodynamics of the fluid mass content

We can obtain an explicit thermodynamic expression for ζ , using equations (2.35a) and (2.35b), which define the fluid mass content m_f and its relationship with ζ :

$$m_f = \rho_f \varphi \quad \Rightarrow \quad dm_f = \varphi d\rho_f + \rho_f d\varphi \quad \Rightarrow \quad d\zeta = \frac{dm_f}{\rho_f} = \varphi \frac{d\rho_f}{\rho_f} + d\varphi \quad (2.110a)$$

On the other hand, the fluid density is a function of both, the fluid pressure and the temperature $\rho_f(p, T)$. Computing its total differential, we obtain:

$$\rho_f(p, T) \quad \Rightarrow \quad \frac{d\rho_f}{\rho_f} = \frac{1}{\rho_f} \frac{\partial \rho_f}{\partial p} dp + \frac{1}{\rho_f} \frac{\partial \rho_f}{\partial T} dT \quad (2.110b)$$

We need to use, in this expression, the definitions of the fluid bulk modulus (eq. 2.54a) and of the fluid thermal expansivity:

$$C_f = \frac{1}{K_f} = \frac{1}{\rho_f} \left(\frac{\partial \rho_f}{\partial p} \right)_T \quad \text{and} \quad \gamma_f = \frac{1}{V_f} \left(\frac{\partial V_f}{\partial T} \right)_{p_f} = -\frac{1}{\rho_f} \left(\frac{\partial \rho_f}{\partial T} \right)_{p_f} \quad (2.110c)$$

Substituting these definitions in equation (2.110a) and setting $p_f = p$:

$$d\zeta = d\varphi + \frac{\varphi}{K_f} dp - \varphi \gamma_f dT \quad (2.110d)$$

Integrating this expression, between the initial and final states, in terms of the porosity differential $d\varphi$ and plugging the result into equation (2.107a), we obtain an equivalent expression for the variation of the fluid content in a linear non-isothermal process:

$$\zeta = \zeta_0 + b \varepsilon_B + \frac{(p - p_0)}{N} + \frac{\varphi}{K_f} (p - p_0) + \varphi \gamma_\varphi (T - T_0) - \varphi \gamma_f (T - T_0) \quad (2.111a)$$

This important equation is simplified using the first expression for the Biot tangent modulus $1/N$ in equation (2.55b):

$$\zeta = \zeta_0 + b \varepsilon_B + \frac{p - p_0}{M} + \varphi (\gamma_\varphi - \gamma_f) (T - T_0) \quad (2.111b)$$

Equation (2.111b) is also written in terms of the relationship between ε_B and $\sigma_{kk} = 3\sigma_M$ in equation (2.25b):

$$\zeta = \zeta_0 + b \frac{\sigma_M}{K_B} + \frac{p - p_0}{M} + \varphi(\gamma_\varphi - \gamma_f)(T - T_0) \quad (2.111c)$$

We can obtain another expression of this equation using the relationships for the moduli M and K_B in terms of the Skempton coefficient, b and K_U , given by equation (2.51):

$$\zeta = \zeta_0 + \frac{B}{R} \sigma_M + \frac{b(p - p_0)}{B K_U} + \varphi(\gamma_\varphi - \gamma_f)(T - T_0) \quad (2.111d)$$

Equations (2.111a–d) express the dependence of the variation of the fluid content in terms of the bulk strain, the average stress, the fluid pressure, the temperature and the corresponding thermal and poroelastic coefficients. It is worthwhile to define another special thermal expansion coefficient γ_m measuring the changes in the fluid mass content when σ_M and p_f are held constant:

$$\gamma_m = \frac{1}{m_f} \left(\frac{\partial m_f}{\partial T} \right)_{p_f} = \frac{1}{\rho_f} \left(\frac{\partial \rho_f}{\partial T} \right)_{p_f} + \frac{1}{\varphi} \left(\frac{\partial \varphi}{\partial T} \right)_{p_f} = -\gamma_f + \gamma_\varphi \quad (2.112)$$

In other words, we find again the thermal coefficients introduced in equation (2.111a), giving them a global physical sense through the thermal change of the fluid mass content. Using the definition of m_f in equation (2.3a,b) we find from equation (2.111c) another expression for $m_f(p, T)$:

$$m_f = m_0 + \frac{b \rho_0}{K_B} \sigma_M + \frac{\rho_0}{M} (p - p_0) + \rho_0 \varphi \gamma_m (T - T_0) \quad (2.113)$$

From equation (2.111b) we deduce the variations of $\zeta(p, T)$ when the volumetric strain remains constant:

$$\left(\frac{\partial \zeta}{\partial p} \right)_{\varepsilon_B} = \frac{1}{M} \quad (2.114a)$$

$$\left(\frac{\partial \zeta}{\partial T} \right)_{\varepsilon_B} = \varphi \gamma_m \quad (2.114b)$$

From expression (2.111c), when p and T are constant, using equations (2.45) and (2.48), we obtain:

$$\left(\frac{\partial \zeta}{\partial \sigma_M} \right)_{p, T} = \frac{b}{K_B} = \frac{B}{R} = \frac{1}{H} \quad (2.114c)$$

From equation (2.111c) or from (2.111e), we deduce an important relationship to compute the fluid pressure variation when the temperature changes and keeping constant the confining pressure σ_M and the fluid content ζ :

$$\left(\frac{\partial p}{\partial T} \right)_{\zeta, \sigma_M} = -M \varphi (\gamma_\varphi - \gamma_f) = -\frac{B K_U}{b} \varphi \gamma_m \quad (2.114d)$$

In the drained experimental regime, any temperature change can produce either a thermal expansion or a contraction of the rock. Consequently, the volumetric strain should contain an

additional thermal deformation, besides the strain produced by the effective pressure p_e :

$$\varepsilon_B = -\frac{p_k - b p}{K_B} + \gamma_B(T - T_0) \quad (2.115)$$

Substituting this equation into formula (2.111b) for $p = p_0$ and including equation (2.112):

$$\zeta = \zeta_0 - \frac{b}{K_B}(p_k - b p) + (\varphi \gamma_m + b \gamma_B)(T - T_0) \quad (2.116a)$$

Guéguen and Boutéca (2004) obtained another expression for equation (2.111c) for drained conditions, when $\sigma_M = -p_k$:

$$\zeta = \zeta_0 + \frac{b}{B K_B}(p - B p_k) + \varphi \gamma_m(T - T_0) \quad (2.116b)$$

Substituting the pressure p_k of equation (2.115) into this formula:

$$\begin{aligned} \zeta &= \zeta_0 + \frac{b p}{B K_B} - \frac{b}{K_B}(-K_B \varepsilon_B + b p + K_B \gamma_B(T - T_0)) + \varphi \gamma_m(T - T_0) \\ &= \zeta_0 + b \varepsilon_B + \frac{b p}{B K_B}(1 - b B) + (\varphi \gamma_m - b \gamma_B)(T - T_0) \end{aligned}$$

Using the first part of equation (2.52a) to simplify the term $(1 - b B)$:

$$\zeta = \zeta_0 + b \varepsilon_B + \frac{b p}{B K_U} + (\varphi \gamma_m - b \gamma_B)(T - T_0) \quad (2.116c)$$

From this equation, we deduce the variation of the fluid mass content when the temperature changes, keeping constant the volumetric strain and the fluid pressure:

$$\left(\frac{\partial \zeta}{\partial T}\right)_{\varepsilon_B, p} = \varphi \gamma_m - b \gamma_B \quad (2.116d)$$

The variation of the fluid pressure when the temperature changes at constant ζ and ε_B :

$$\left(\frac{\partial p}{\partial T}\right)_{\varepsilon_B, \zeta} = -\frac{B K_U}{b}(\varphi \gamma_m - b \gamma_B) \quad (2.116e)$$

The undrained thermal expansivity is (Guéguen and Boutéca 2004):

$$\gamma_U = \gamma_B - B \varphi \gamma_m \quad (2.117)$$

In most cases $\gamma_m < 0$ (see example below) and therefore $\gamma_B < \gamma_U$. In the undrained experimental regime, the additional thermal deformation for the volumetric strain is:

$$\varepsilon_B = -\frac{p_k}{K_U} + \gamma_U(T - T_0) = -\frac{p_k - b p_U}{K_B} + \gamma_B(T - T_0) \quad (2.118)$$

Therefore, the non-isothermal undrained fluid pressure becomes:

$$p_U = \frac{p_k}{b} \left(1 - \frac{K_B}{K_U}\right) + \frac{K_B}{b}(\gamma_U - \gamma_B)(T - T_0) \quad (2.119a)$$

This formula is simplified using equations (2.52a) and (2.117):

$$p_U = B p_k - \frac{B K_B}{b} \varphi \gamma_m (T - T_0) \quad (2.119b)$$

The changes of the undrained fluid pressure when the temperature changes at constant p_k are given by:

$$\left(\frac{\partial p_U}{\partial T} \right)_{p_k} = -\frac{B K_B}{b} \varphi \gamma_m = \frac{K_B}{b} (\gamma_U - \gamma_B) \quad (2.119c)$$

2.2.12.6 Numerical values of the thermal expansivity coefficients

In this section, we give some experimental values of the volumetric thermal dilatation coefficients γ_B , γ_f , γ_φ , γ_m and γ_U [1/K]. As a general trend, thermal expansion increases when temperature rises (see Figs. 2.18 and 2.22 for water). The volumetric thermal expansivity γ_B is about 10^{-5} K^{-1} for solids, 10^{-4} K^{-1} for liquids and 10^{-3} K^{-1} for gases. For the expansivity of the pores in granite we estimated $\gamma_\varphi \approx 1.7 \times 10^{-4} \text{ K}^{-1}$. For water, at 80°C and 10 MPa, $\gamma_f = 6.3 \times 10^{-4} \text{ K}^{-1}$. For low porosity hard volcanic rocks such as granite, having a porosity $\varphi = 0.0018$, $b = 0.3$, and $B = 0.9$, Guéguen and Boutéca (2004) published the values $\gamma_B = 5.0 \times 10^{-5} \text{ K}^{-1}$, $\gamma_m = -46.0 \times 10^{-5} \text{ K}^{-1}$ and $\gamma_U = 5.075 \times 10^{-5} \text{ K}^{-1}$ and the bulk moduli $K_B = 27 \text{ GPa}$ and $K_U = 38 \text{ GPa}$.

Using these data, the corresponding variations of the fluid mass content and of the fluid pressure for drained and undrained conditions are:

$$\begin{aligned} \left(\frac{\partial \zeta}{\partial T} \right)_{\varepsilon_B, p} &= \varphi \gamma_m - b \gamma_B = -1.58 \times 10^{-5} \quad \left[\frac{1}{\text{K}} \right] \\ \left(\frac{\partial p}{\partial T} \right)_{\varepsilon_B, \zeta} &= -\frac{B K_U}{b} (\varphi \gamma_m - b \gamma_B) = 18.04 \times 10^5 \quad \left[\frac{\text{Pa}}{\text{K}} \right] \\ \left(\frac{\partial p_U}{\partial T} \right)_{p_k, \zeta} &= -\frac{B K_B}{b} \varphi \gamma_m = \frac{K_B}{b} (\gamma_U - \gamma_B) = 0.67 \times 10^5 \quad \left[\frac{\text{Pa}}{\text{K}} \right] \end{aligned}$$

These numerical values confirm that in low porosity and low permeability rocks, the thermal variation of the fluid content is very small because of the values of the hydraulic parameters. For the same reason, a significant fluid pressure increase occurs in the presence of thermal stresses, specifically under undrained conditions. This is a common case when cold water is injected into hot dry rock reservoirs.

The last example presented in Table 2.4 illustrates the great sensitivity of poroelastic parameters with regard to temperature changes in non-isothermal processes. The bulk modulus of hot water in the pores is lower in deep geothermal reservoirs compared to cold water, producing larger variations of the fluid content and inducing higher thermoporoelastic deformations. This effect is more important in high porosity sedimentary rocks.

2.2.12.7 Tensorial form of the thermoporoelastic equations

As we did for the isothermal poroelasticity case, we can write in a single four-dimensional tensorial equation the results of thermoporoelasticity relating stresses and strains. We solve first equation (2.111b) in terms of the pore pressure:

$$\sigma_f = p - p_0 = M(\zeta - \zeta_0) - C \varepsilon_B - M\varphi(\gamma_\varphi - \gamma_f)(T - T_0) \quad (2.120)$$

Grouping equation (2.107c) as in equation (2.67), we obtain the thermoporoelastic matrix equations, which include the thermal tensions in the total stress tensor:

$$\begin{aligned} \boldsymbol{\sigma}_T - \boldsymbol{\sigma}_T^0 &= \begin{pmatrix} \sigma_x & \sigma_{xy} & \sigma_{xz} & 0 \\ \sigma_{xy} & \sigma_y & \sigma_{yz} & 0 \\ \sigma_{xz} & \sigma_{yz} & \sigma_z & 0 \\ 0 & 0 & 0 & \sigma_f \end{pmatrix} = \varepsilon_B \begin{pmatrix} \lambda & 0 & 0 & 0 \\ 0 & \lambda & 0 & 0 \\ 0 & 0 & \lambda & 0 \\ 0 & 0 & 0 & -C \end{pmatrix} + 2G \begin{pmatrix} \varepsilon_x & \varepsilon_{xy} & \varepsilon_{xz} & 0 \\ \varepsilon_{xy} & \varepsilon_y & \varepsilon_{yz} & 0 \\ \varepsilon_{xz} & \varepsilon_{yz} & \varepsilon_z & 0 \\ 0 & 0 & 0 & 0 \end{pmatrix} \\ &- (p - p_0) \begin{pmatrix} b & 0 & 0 & 0 \\ 0 & b & 0 & 0 \\ 0 & 0 & b & 0 \\ 0 & 0 & 0 & -M \frac{\zeta - \zeta_0}{p - p_0} \end{pmatrix} - K_B (T - T_0) \begin{pmatrix} \gamma_B & 0 & 0 & 0 \\ 0 & \gamma_B & 0 & 0 \\ 0 & 0 & \gamma_B & 0 \\ 0 & 0 & 0 & \frac{M\varphi}{K_B} (\gamma_\varphi - \gamma_f) \end{pmatrix} \end{aligned} \quad (2.121)$$

Replacing these components in equation (2.73) we obtain the total stress vector $\vec{\sigma}_T$:

$$\vec{\sigma}_T = \begin{pmatrix} \sigma_x \\ \sigma_y \\ \sigma_z \\ \sigma_{xy} \\ \sigma_{xz} \\ \sigma_{yz} \\ \sigma_f \end{pmatrix} = \mathbf{C}_B \cdot \begin{pmatrix} \varepsilon_x \\ \varepsilon_y \\ \varepsilon_z \\ \varepsilon_{xy} \\ \varepsilon_{xz} \\ \varepsilon_{yz} \\ \zeta - \zeta_0 \end{pmatrix} = \begin{pmatrix} \lambda_U \varepsilon_B + 2G \varepsilon_x - C (\zeta - \zeta_0) + \gamma_C (T - T_0) \\ \lambda_U \varepsilon_B + 2G \varepsilon_y - C (\zeta - \zeta_0) + \gamma_C (T - T_0) \\ \lambda_U \varepsilon_B + 2G \varepsilon_z - C (\zeta - \zeta_0) + \gamma_C (T - T_0) \\ 2G \varepsilon_{xy} \\ 2G \varepsilon_{xz} \\ 2G \varepsilon_{yz} \\ M (\zeta - \zeta_0) - C \varepsilon_B - M \varphi \gamma_m (T - T_0) \end{pmatrix} \quad (2.122)$$

where the composed thermal expansivity is $\gamma_C = C\varphi\gamma_m - K_B\gamma_B$, we use the global pore-fluid thermal coefficient $\gamma_m = \gamma_\varphi - \gamma_f$ defined in equation (2.112). Note that the matrix of thermoporoelastic constants \mathbf{C}_B is exactly the same matrix as equation (2.72). Equation (2.122) includes all of the thermal stresses acting in the skeleton and in the fluid contained in the porous rock. It becomes equal to equation (2.73) if the process is isothermal.

The theoretical and numerical results developed in these sections suggest that rock poroelastic deformation is larger at high temperature. This outcome has important consequences on the interpretation of petrophysical data obtained from geothermal reservoirs and from any other experiments involving non-isothermal porous rocks. These results are useful in the study of the deformation of aquifers, in the modeling of enhanced geothermal systems, in deep petroleum reservoirs, in hot dry rock fields and in the interpretation of microseismicity data and in other seismic events.

2.3 MECHANICAL AND THERMODYNAMICAL WATER PROPERTIES

The behavior of water is a complex subject that has been studied since the classical Greek era. Our present scientific knowledge of water is founded upon the works of Carnot, Joule and Kelvin in the 19th century. Two hydrogen atoms and one oxygen atom compose a typical molecule of pure water (H_2O). The three atoms make an angle of approximately 104.5 degrees. Water forms a molecularly stabilized structure in which a hydrogen atom is in line with the oxygen atom of its own molecule and the oxygen atom of a neighbor molecule. These hydrogen bonds, with their extra attractive energy, are the cause of many of the unusual properties of water, including its large heat of vaporization and its expansion upon freezing (<http://www.iapws.org/>). Water reaches its maximum density at approximately 4°C. Below this point, water density declines.

The thermodynamic properties of pure water, under the typical conditions of both aquifers and geothermal reservoirs, are computed accurately using the equations of state described in

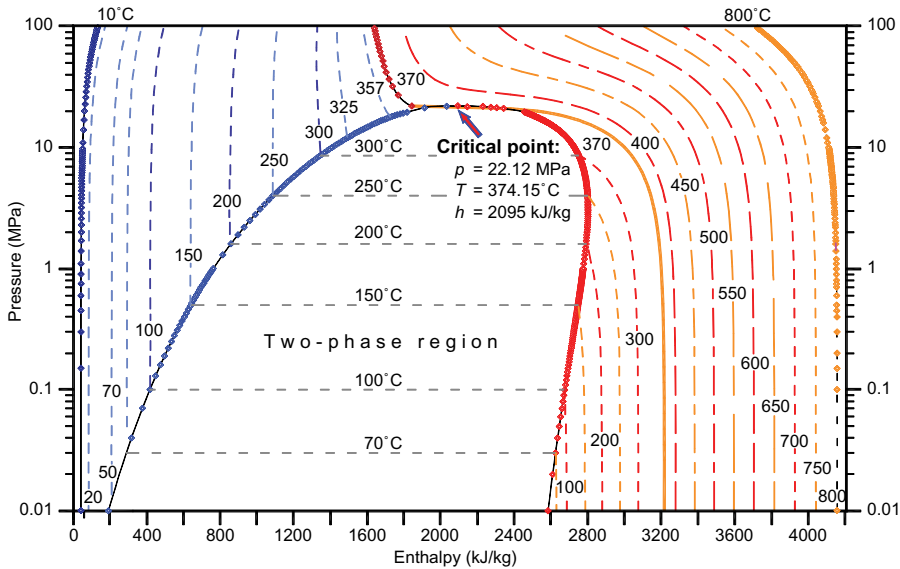


Figure 2.12. The pressure-enthalpy curve of water in the ranges $p \in [0.01, 100]$ MPa, $T \in [0, 800]^\circ\text{C}$ and $h \in [0, 4200]$ kJ/kg (data from Schmidt and Grigull 1979).

section 2.3.3. The general form of the fundamental variables and coefficients are described and shown graphically in this section. Special emphasis on capillarity and relative permeabilities is made. Qualitative descriptions of some fluid parameters for oil and gas are included, because many hydrocarbon reservoirs are closely related to aquifers. The thermodynamic properties of water are given by the following functions and essential variables (*function* [units]): pressure p [MPa], density ρ [kg/m³], temperature T [°C or K], specific enthalpy h [kJ/kg], internal energy e [kJ/kg], Helmholtz free energy f_w [kJ/kg], Gibbs free enthalpy g_w [kJ/kg], viscosity μ [Pa · s], compressibility C_w [Pa⁻¹], isobaric specific heat c_p [J/kg/°C], thermal conductivity k_T [W/m/°C], volumetric thermal expansion γ_w [°C⁻¹], thermal diffusivity δ_w [m²/s], surface tension σ_w [N/m] and salinity concentration (mass fraction) c_m [kg/kg]. All these properties are functions of pressure and temperature in single phase water. In two-phase systems p and T are related in the saturation line (K-function), and another variable must be used, for example steam quality, liquid saturation or fluid enthalpy. Figure 2.12 illustrates the main thermodynamic properties of ordinary water in the whole region of practical interest (0.01 to 100 MPa and from 0 to 800°C).

2.3.1 Practical correlations for aquifers and low-enthalpy geothermal systems

Water in liquid state is almost incompressible over a wide range of pressures. Its simplest equation of state is the mathematical relation between density and pressure at constant temperature. From the definition of water isothermal compressibility:

$$C_w = -\frac{1}{V_w} \left(\frac{\partial V_w}{\partial p} \right)_T = \frac{1}{\rho_w} \left(\frac{\partial \rho_w}{\partial p} \right)_T \Rightarrow \rho_w(p) = \rho_0 e^{C_w(p-p_0)} \quad (2.123)$$

From a practical viewpoint and assuming that the isothermal compressibility C_w is constant, this formula is approximately valid in the interval [0.001, 10] MPa. For example at 20°C, $C_w = 4.590 \times 10^{-10}$ Pa⁻¹, for $p = 0.05$ MPa; and $C_w = 4.474 \times 10^{-10}$ Pa⁻¹ for $p = 10$ MPa. So, $C_w = 4.53 \times 10^{-10}$ Pa⁻¹ is a reasonable average in this range of pressure. Many other correlations can be obtained by interpolation or by using least squares in the same interval of

pressures $p \in [0.001, 10]$ MPa. For example, we constructed the following formulae valid in the range $T \in [0, 150]^\circ\text{C}$, which applies for isothermal aquifers and low-enthalpy geothermal reservoirs (Figs. 2.13 and 2.14). An approximation for the enthalpy of water is (Suárez 1985):

$$h_w(p, T) \cong 0.103703286 + 0.104535515 p + 4.178354567 T - 3.243701 \cdot 10^{-4} p^2 - 2.23906 \cdot 10^{-4} pT + 9.70340 \cdot 10^{-5} T^2 \quad (2.124)$$

The approximations for the specific volume and density of water are (Suárez 1985):

$$\begin{aligned} v_w(p, T) &\cong 999.8427563 \cdot 10^{-6} - 4.4888741 \cdot 10^{-8} p + 4.6382459 \cdot 10^{-8} T \\ &\quad + 6.8717562 \cdot 10^{-10} p^2 - 2.4966892 \cdot 10^{-10} pT + 3.9625548 \cdot 10^{-9} T^2 \\ \rho_w(p, T) &= \frac{1}{v_w(p, T)} \end{aligned} \quad (2.125)$$

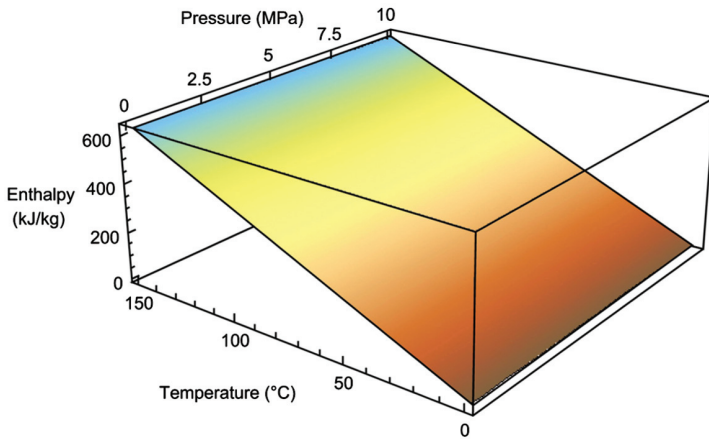


Figure 2.13. Three-dimensional surface of water enthalpy $h_w(p, T)$ [kJ/kg] in the ranges $p \in [0.001, 10]$ MPa and $T \in [0, 150]^\circ\text{C}$. The formula is useful in low-enthalpy geothermal systems.

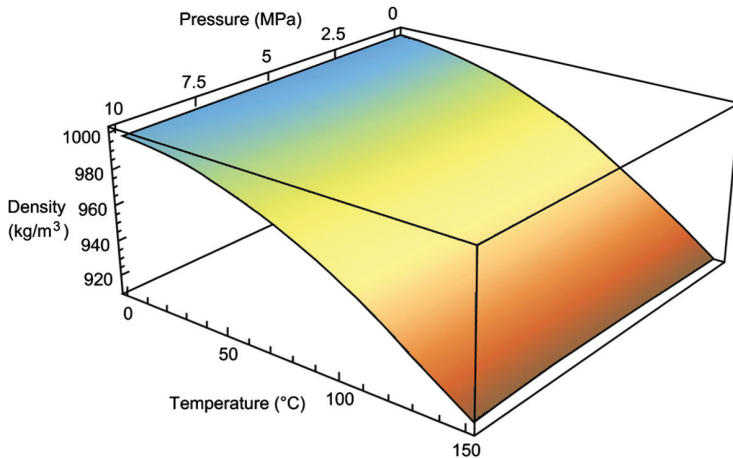


Figure 2.14. Three-dimensional surface of water density $\rho_w(p, T)$ [kg/m³] in the ranges $p \in [0.001, 10]$ MPa and $T \in [0, 150]^\circ\text{C}$. The formula is useful in low-enthalpy geothermal systems.

Under low-enthalpy conditions, the variations of the thermodynamic properties of liquid water are always more important when the temperature changes. Therefore, in this case the properties of water can be assumed to be functions of T only. This approximation is of great practical value in low-enthalpy geothermal reservoirs ($<150^\circ\text{C}$) (Chandrasekharam and Bundschuh 2008). The following correlations are adapted from Holzbecher (1998), some of them are also applicable to high-enthalpy reservoirs ($>150^\circ\text{C}$).

For water density, the following formula can be used in the range $0^\circ\text{C} < T < 20^\circ\text{C}$:

$$\rho_0(T) = 1000.0(1.0 - 8.0 \times 10^{-6}(T - 3.98)^2) \quad (2.126)$$

The density of water in the range $20^\circ\text{C} < T < 300^\circ\text{C}$ is approximated by the equation:

$$\rho_1(T) = 996.9(1 - 3.17 \times 10^{-4}(T - 25.0) - 2.56 \times 10^{-6}(T - 25.0)^2) \quad (2.127)$$

The dynamic viscosity of water can be approximated as a function of temperature only by the equations:

$$\mu_0(T) = 10^{-3}(1 + 0.015512(T - 20.0))^{-1.572}, \quad 0^\circ\text{C} \leq T \leq 100^\circ\text{C} \quad (2.128a)$$

$$\mu_1(T) = 241.4 \times 10^{-7} \times 10^{\frac{247.8}{T+133.15}}, \quad 100^\circ\text{C} \leq T \leq 350^\circ\text{C} \quad (2.128b)$$

The thermal conductivity of water as a function of temperature in low- and high-enthalpy systems can be estimated with this formula (k_T in $10^3 \text{ W/m}^\circ\text{C}$):

$$k_T(T) = -922.47 + 2839.5 \frac{(T + 273.15)}{273.15} - 1800.7 \left(\frac{T + 273.15}{273.15} \right)^2 + 525.77 \left(\frac{T + 273.15}{273.15} \right)^3 - 73.44 \left(\frac{T + 273.15}{273.15} \right)^4; \quad 0^\circ\text{C} \leq T \leq 350^\circ\text{C} \quad (2.129)$$

The isobaric heat capacity of water ($\text{J/kg}^\circ\text{C}$) in the range $0^\circ\text{C} < T < 100^\circ\text{C}$ is approximated by the following polynomial:

$$c_0(T) = -1.3320081 \times 10^{-4}T^3 + 0.0328405 T^2 - 1.9254125 T + 4206.3640128 \quad (2.130)$$

The isobaric heat capacity of water in the range $100^\circ\text{C} < T < 320^\circ\text{C}$ is:

$$\frac{c_1(T)}{4187.6} = 3.3774 - 1.12665 \times 10^{-2}(T + 273.15) + 1.34687 \times 10^{-5}(T + 273.15)^2 \quad (2.131)$$

This formula is valid only in the liquid region. Consequently, for temperatures higher than 250°C , pressures must be $p > 4 \text{ MPa}$. For $T \sim 300^\circ\text{C}$, pressures must be $p > 8.5 \text{ MPa}$. Equation (2.131) can be applied up to 320°C if $p > 13 \text{ MPa}$. All the other formulae on this page are reasonable approximations for all pressures in the range $[0.01, 10] \text{ MPa}$.

It is important to take into account that equations (2.124–2.131) are simply practical approaches to water thermodynamics; they must be used with caution. The exact computation of the thermodynamic properties of water can only be made using the equation of state described in the next section.

2.3.2 *A brief history of the equation of state for water*

In 1921 an International Research Committee on Thermal Properties of Steam was created by the American Society of Mechanical Engineers (ASME). This committee was formed by researchers from the USA, Germany, England and the former Czechoslovakia. The purpose of the committee was to obtain worldwide agreements about the best numerical and experimental values of the properties of pure water. Such agreements provided, for the first time, standard uniform norms for steam. The First International Conference on the Properties of the Steam took place in London, England in 1929. The Sixth Conference took place in New York in 1963. The accepted thermodynamic ranges covered pressures from 0 to 100 MPa and temperatures from 0 to 800°C, extending considerably the previously available charts. To assure the accurate numerical reproduction for interpolation, differentiation and numerical integration of the properties of water, an International Formulation Committee (IFC) was also formed at that time. Its functions would be: “*To develop at the earliest practical date a formulation for use with computers of the properties of steam as they are represented by the International Skeleton Tables of 1963 (IST). This formulation shall provide values that are, at all points, within the tolerances stated in the IST of 1963, and shall be thermodynamically consistent.*” (Schmidt and Grigull 1979).

In March 1966 the IFC met in Glasgow, Scotland and proposed a mathematical formulation of the equations that would satisfy the requirements for the international standardization of the Tables of Water for industrial uses (IFC-67). In spite of the international efforts, it was not possible to build a single equation of state for the whole thermodynamic range covered by all the experimental values known at that time. Hence the thermodynamic range of water was divided into six sub-regions. The boundaries between the sub-domains present discontinuities in the water properties. However, most of them are insignificant from a practical engineering point of view. The representation of the water dynamic viscosity was finished and published in April 1975. In September of the same year, an equation was presented to calculate the surface tension of water. The corresponding correlations for thermal conductivity of each phase of water and the equation for its static dielectric constant were published in December 1977 (Schmidt and Grigull 1979).

In 1989, the International Association for the Properties of Steam became the new International Association for the Properties of Water and Steam (IAPWS; for the historical details see ASME 2005).

The IAPWS approved for scientific use, a new formulation of the thermodynamic properties of water in 1995. It is called the “IAPWS Formulation 1995 for the Thermodynamic Properties of Ordinary Water Substance for General and Scientific Use” (IAPWS-95). This is the present international standard for thermodynamic properties of water and provides the most accurate representation of the thermodynamic properties of the fluid phases of water over a wide range of conditions available at the time this release was prepared. A release was authorized by the IAPWS in September 1997 in Erlangen, Germany, to replace the previous formulation of 1967 (IFC-67). It is called the “IAPWS Industrial Formulation 1997 for Thermodynamic Properties of Water and Steam” (IAPWS-IF97). This is a separate formulation for industrial use because of the special requirements of the steam power industry. Papers describing both formulations were published some years ago (Wagner *et al.* 2000, Wagner and Pruss 2002). Software and computer code implementing the IAPWS-95 formulation, a printed tabulation of properties, compilation of experimental data used to develop the IAPWS-95 formulation, various releases, additional equations, derivatives and many other useful information on the properties of water are available at the IAPWS web site (<http://www.iapws.org/>), updated version September 4, 2007.

The most advanced and up to date correlations for the numeric calculation of the thermodynamic properties of water, are based entirely on the IAPWS-95 and IAPWS-IF97 formulations (NIST - National Institute of Standards and Technology, Harvey *et al.* 2004). These properties are: Gibbs free enthalpy, Helmholtz free energy, pressure, temperature, enthalpy, internal energy, entropy, density, specific volume, dynamic viscosity, compressibility, volume expansivity, thermal conductivity, specific heat capacities, Joule-Thomson and Laplace coefficients, surface tension of two-phase water, dielectric constant, refractive index and speed of sound. The surface tension

and the coefficient of Laplace have an important influence during the evaporation process at the liquid-vapor interface and in the calculation of the capillary pressure.

2.3.3 The IAPWS-95 formulation for the equation of state of water

The basic thermodynamical state potentials in this formulation are the internal energy and the specific enthalpy of the fluid phase. Both potentials, together with the other variables, temperature T , pressure p_f , density ρ_f and entropy s_f , describe the energy exchanges of any fluid contained in the porous rock. The relationships between both potentials and the thermodynamical variables are as follows. Let v_f and e_f be the specific volume and the internal energy of the fluid, respectively:

$$\begin{aligned} v_f = \frac{1}{\rho_f}, e_f(v_f, s_f) &\Rightarrow p = -\frac{\partial e_f}{\partial v_f}, \quad T = \frac{\partial e_f}{\partial s_f} \\ \Leftrightarrow de_f = -p dv_f + T ds_f & \end{aligned} \quad (2.132)$$

The equation for de_f is the first law of thermodynamics written in differential form and valid for any fluid. The term $-p dv_f$ is the mechanical work done by the fluid and $T ds_f$ is the differential heat extracted or received by the differential volume dv_f (eq. 2.89c). Thus, the sum of both quantities is equal to the variation of internal energy. This principle asserts the conservation of energy for the fluid.

We can define a second potential called the specific enthalpy to express the thermodynamic variables in another form. If the thermostatics process is at constant pressure then the change in enthalpy, which includes both the change in internal energy and the work done, is equal to the heat transfer during the isobaric process:

$$\Delta h_f(p, s_f) = \Delta e_f + p \Delta v_f = (\delta Q_p - p \Delta v_f) + p \Delta v_f = \delta Q_p \quad (2.133)$$

That is the main reason why the specific enthalpy is an important function commonly used in geothermal reservoir engineering. The corresponding enthalpy relationships are as follows:

$$h_f(p, s_f) = e_f + \frac{p}{\rho_f} \Rightarrow v_f = \frac{\partial h_f}{\partial p}, \quad T = \frac{\partial h_f}{\partial s_f} \Leftrightarrow dh_f = v_f dp + T ds_f \quad (2.134)$$

A third thermodynamic potential is the Gibbs' specific free enthalpy g_f of the fluid:

$$g_f(p, T) = h_f - Ts_f \Rightarrow dg_f = v_f dp + s_f dT \Rightarrow v_f = \frac{\partial g_f}{\partial p}, \quad s_f = \frac{\partial g_f}{\partial T} \quad (2.135)$$

Another thermodynamic potential is the Helmholtz free energy, which measures the useful work obtainable from a fluid in a closed system at constant temperature and volume. Both potentials are commonly used in the thermodynamical description of the properties of water:

$$\begin{aligned} f_f(v_f, T) = g_f - p v_f = e_f - Ts_f &\Rightarrow df_f = -pdv_f - s_f dT \\ \Rightarrow p = -\frac{\partial f_f}{\partial v_f}, \quad s_f = -\frac{\partial f_f}{\partial T} & \end{aligned} \quad (2.136)$$

The fundamental difference between previous formulations and the IAPWS-95 is the use of the so-called *canonical functions* for water. The IFC-67 used the Gibbs function or specific free enthalpy as the fundamental canonical function $g_w(p, T)$. All other thermodynamic properties are derived directly by partial differentiation of g_w . The IAPWS-95 uses the Helmholtz free energy f_w in its formulation (Fig. 2.15).

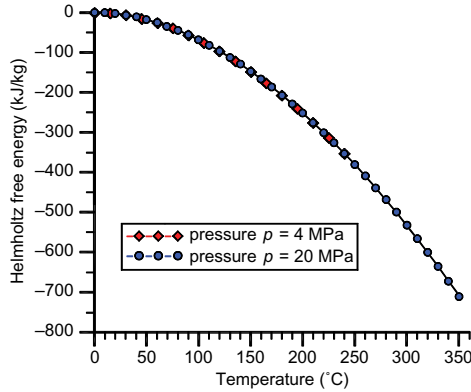


Figure 2.15. Helmholtz free energy for water in the range $p \in [4, 20]$ MPa, $T \in [0, 350]$ °C.

In the NIST/ASME steam properties database (version 2.2), the equilibrium thermodynamic properties for water are calculated from the IAPWS-95 formulation. This formulation is a fundamental equation for the specific Helmholtz free energy per unit mass, defined as $f_w = e_w - Ts_w$, where e_w and s_w are the internal energy and specific entropy of water, respectively. The function $f_w(\rho, T)$ is a function of temperature and density that is made dimensionless by the term $R_g T$; R_g is a mass-based gas constant. The dimensionless form of this equation is called the reduced Helmholtz free energy (Watanabe 1996):

$$\frac{f_w(\rho, T)}{R_g T} = \Phi\left(\frac{\rho}{\rho_C}, \frac{T_C}{T}\right) = \Phi^{\text{ideal-gas}} + \Phi^{\text{residual}} \quad (2.137)$$

where: $\rho_C = 322 \frac{\text{kg}}{\text{m}^3}$, $T_C = 647.096 \text{ K}$, $R_g = 0.46151805 \left[\frac{\text{kJ}}{\text{kgK}} \right]$

The general function Φ is composed of two parts, an ideal-gas part and a residual part. When both functions are combined, a complete Helmholtz energy surface is defined. All other thermodynamic properties are obtained by differentiation of this surface. For example, the water functions pressure p , internal energy e , enthalpy h , entropy s , specific heat capacities c_V , c_p , the Joule-Thomson coefficient J and the speed of sound v_s are constructed as follows:

$$p = \rho^2 \left(\frac{\partial f_w}{\partial \rho} \right)_T, \quad e = f_w - T \left(\frac{\partial f_w}{\partial T} \right)_\rho, \quad h = f - T \left(\frac{\partial f_w}{\partial T} \right)_\rho + \rho \left(\frac{\partial f_w}{\partial \rho} \right)_T$$

$$c_V = \left(\frac{\partial e}{\partial T} \right)_V, \quad c_p = \left(\frac{\partial h}{\partial T} \right)_p, \quad s = - \left(\frac{\partial f_w}{\partial T} \right)_\rho, \quad J = \left(\frac{\partial T}{\partial p} \right)_h, \quad v_s = \sqrt{\left(\frac{\partial p}{\partial \rho} \right)_s} \quad (2.138)$$

A complete description of these functions and all the numerical coefficients involved are in the IAPWS web page. This formulation is valid in the entire stable fluid region of H_2O , from 273.15 K to 1273 K and for all positive $p > 0$ up to 1000 MPa. The absolute limits, beyond which no calculations are made, are $T < 190 \text{ K}$ and $> 5000 \text{ K}$ and $p > 1.0 \times 10^5 \text{ MPa}$. In terms of practical applications, this formulation can certainly be used in the ranges $T \in [0, 1000]$ °C and $p \in [0.001, 100]$ MPa. The graphics of the following sections for the liquid phase of water were obtained using the software developed by the IAPWS-95 (Wagner and Pruss 2002).

2.3.4 Exact properties of low-enthalpy water (0 to 150°C)

The main variables presented in this section are density, enthalpy, isobaric heat capacity, isothermal compressibility, volume expansivity and speed of sound. The temperatures are on the International Temperature Scale of 1990. Each property is correlated as a function of temperature and pressure. Nevertheless, the influence of pressure is insignificant in most variables as can be seen in the following graphics.

2.3.4.1 Density and enthalpy of the liquid

Density of water decreases and enthalpy augments when temperature increases (Fig. 2.16). The zero for the enthalpy is determined by the conventions that the entropy and internal energy are zero for the saturated liquid at the triple point (273.16 K, 611.657 Pa).

2.3.4.2 Isobaric heat capacity and thermal conductivity

The isobaric specific heat of liquid decreases with temperature between 0 and 30°C, then increases up to 150°C. Heat capacity diminishes when pressure increases at constant temperature (Fig. 2.17a). Thermal conductivity varies with temperature: it increases from 0.562 to 0.685 W/m°C between 0 and 130°C, then decreases slightly, reaching 0.664 W/m°C at 150°C (Fig. 2.17b).

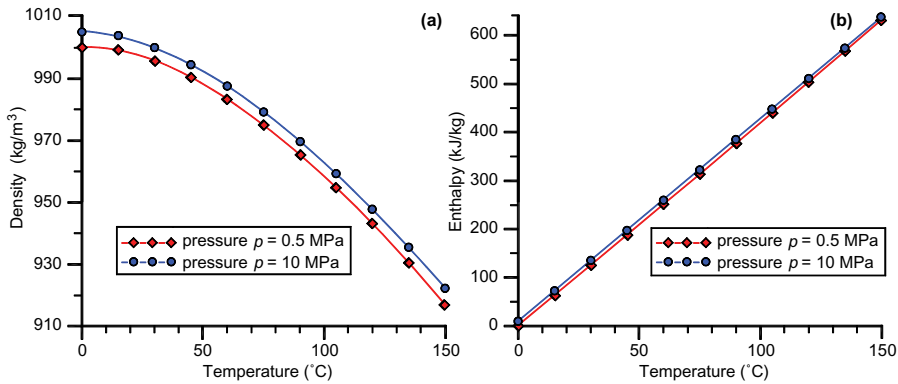


Figure 2.16. Density (a) and enthalpy (b) of water in the range $T \in [0, 150]^\circ\text{C}$, for two different pressures: $p = 0.5$ MPa and 10 MPa (IAPWS-95).

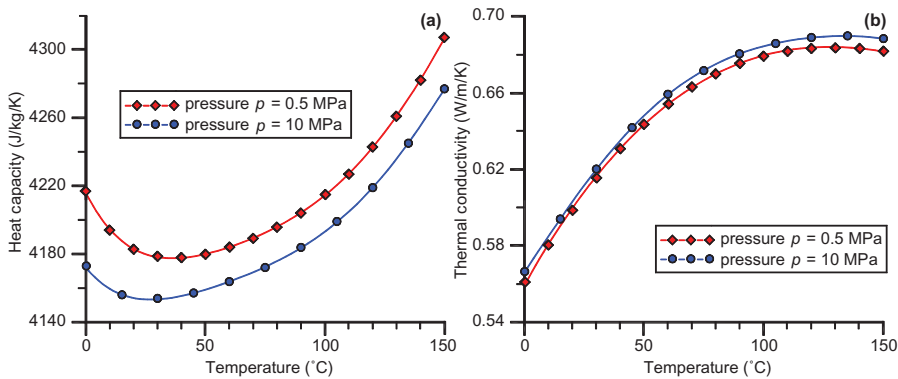


Figure 2.17. Heat capacity at constant pressure (a) and thermal conductivity of water (b) in the range $T \in [0, 150]^\circ\text{C}$, for two different pressures: $p = 0.5$ and 10 MPa.

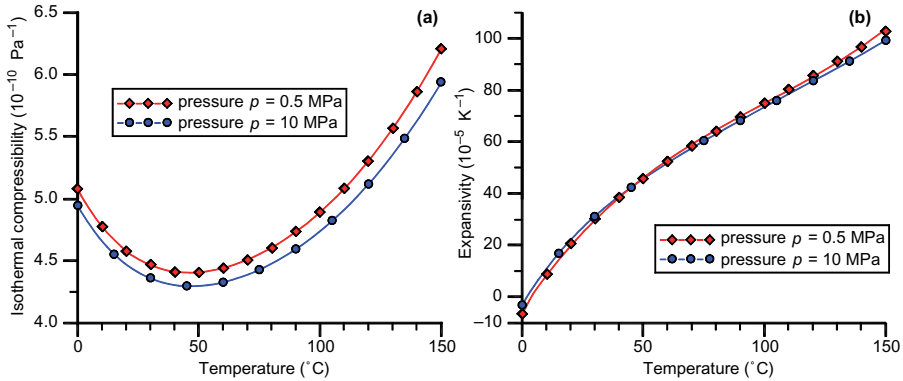


Figure 2.18. Compressibility (a) and expansivity of water (b) in the range $T \in [0, 150]^{\circ}\text{C}$, for two different pressures: $p = 0.5$ and 10 MPa.

2.3.4.3 Compressibility and expansivity

The isothermal compressibility and the volumetric expansivity of water were defined in equation (2.110c). The compressibility of water grows slightly when pressure decreases (Fig. 2.18a). Its variability is larger when the temperature changes; it diminishes from $5.1 \times 10^{-10} \text{ Pa}^{-1}$ to $4.4 \times 10^{-10} \text{ Pa}^{-1}$ between 0 and 50°C , then augments to $6.2 \times 10^{-10} \text{ Pa}^{-1}$ at 150°C . Figure 2.18b shows that the thermal expansion γ_w of liquid water increases in all the intervals considered.

2.3.4.4 Dynamic viscosity and speed of sound

The viscosity of water is a proportionality factor between the amount of advective momentum transferred per unit time across a unit area perpendicular to the direction in which the advective velocity changes. If τ is the shear stress acting on the fluid in the direction of its movement, then:

$$\tau = -\mu \frac{\partial v_x}{\partial y} \quad (2.139a)$$

The negative sign is because the momentum transfer takes place in the direction in which the advective velocity decreases (Alonso and Finn 1967). The units of the dynamic viscosity coefficient are $[\text{kg}/\text{m}/\text{s} \text{ or } \text{Pa} \cdot \text{s}]$. One-tenth of this unit is called Poise. We call $\rho_f v_x$ the convective momentum per unit volume of the fluid. Several experiments showed that the instantaneous change in the momentum of the fluid particles inside a control volume is equal to the viscous force per unit volume plus the gravity acting on the fluid:

$$\frac{\partial}{\partial t}(\rho_f v_x) = -\frac{\partial \tau}{\partial y} + \rho_f g \quad (2.139b)$$

Combining this expression with previous equation (2.139a):

$$\frac{\partial v_x}{\partial t} = \frac{\mu}{\rho_f} \frac{\partial^2 v_x}{\partial y^2} + g \quad (2.139c)$$

This is the equation of motion of the viscous fluid, which represents the conservation of momentum of the moving fluid. Note that the form of this equation is analogous to the heat equation (2.16). For liquid water at constant pressure, the viscosity decreases exponentially from the value $1787 \times 10^{-6} \text{ Pa} \cdot \text{s}$ at 0°C , down to $182.3 \times 10^{-6} \text{ Pa} \cdot \text{s}$ at 150°C (Fig. 2.19a).

The speed of sound is greatly affected by temperature, as shown in Figure 2.19b. It grows when temperature increases from 0 to 80°C; but this effect is less important for temperatures between 60 and 80°C. After 80°C this speed decreases until 150°C.

Fluid viscosity in porous rocks affects the transport of the fluid phases. It is particularly important in the oil displacement mechanisms in thermal processes of petroleum recovery and in the displacement of oil by isothermal water and by geothermal brine (Suárez and Samaniego 2008, Suárez *et al.* 2007, Suárez-Bosche *et al.* 2005). In general, the relative mobility of each phase in the fluid varies with both temperature and pressure. Other studies by Passmore and Archer (1985) on the temperature effects on viscosity and on the oil flow, pointed out that the irreducible saturation of water depends almost linearly upon the oil viscous force, because the viscosity depends mainly on temperature.

2.3.5 Exact properties of high-enthalpy water (150 to 350°C)

The thermodynamic variables presented in this section are density, enthalpy, entropy, Joule-Thomson coefficient, expansivity, isothermal compressibility, isobaric heat capacity, thermal conductivity and speed of sound (Figs. 2.20–2.25). Each property is correlated as function of temperature and pressure. The influence of pressure is insignificant in most variables.

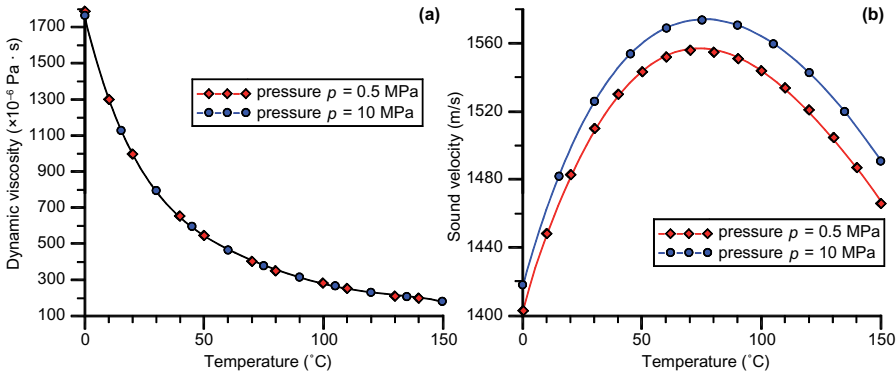


Figure 2.19. Dynamic viscosity (a) and speed of sound (b) in cold water in the range $T \in [0, 150]^{\circ}\text{C}$, for two different pressures: $p = 0.5$ and 10 MPa.

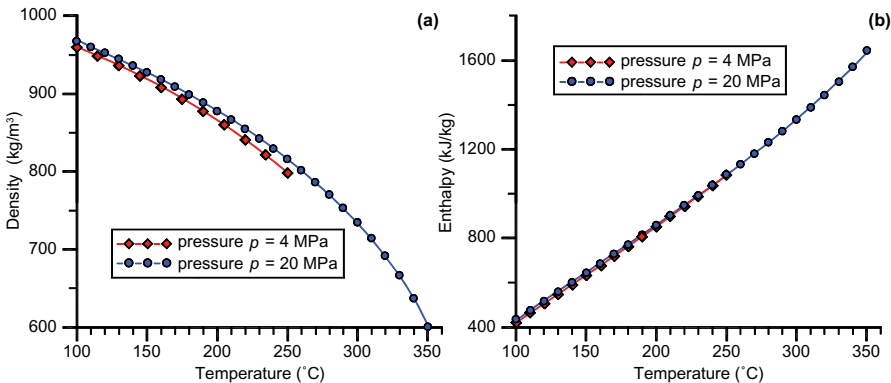


Figure 2.20. Density (a) and enthalpy (b) of water in the range $T \in [100, 350]^{\circ}\text{C}$, for two different pressures: $p = 4$ and 20 MPa.

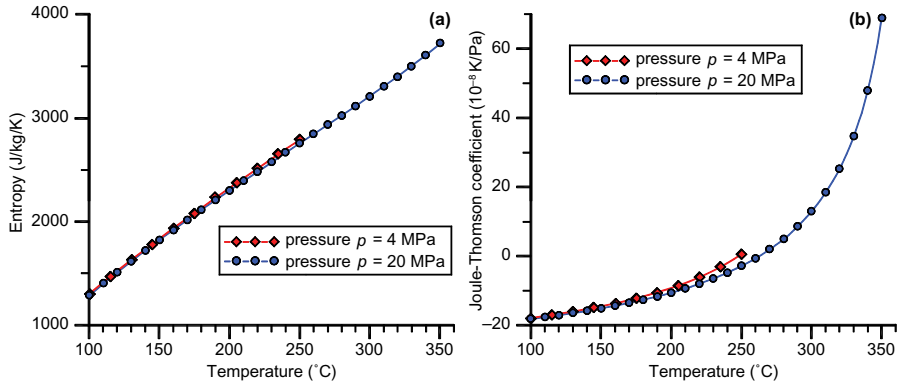


Figure 2.21. Entropy (a) and Joule-Thomson coefficient (b) of water in the range $T \in [100, 350]^{\circ}\text{C}$, for two different pressures: $p = 4$ and 20 MPa.

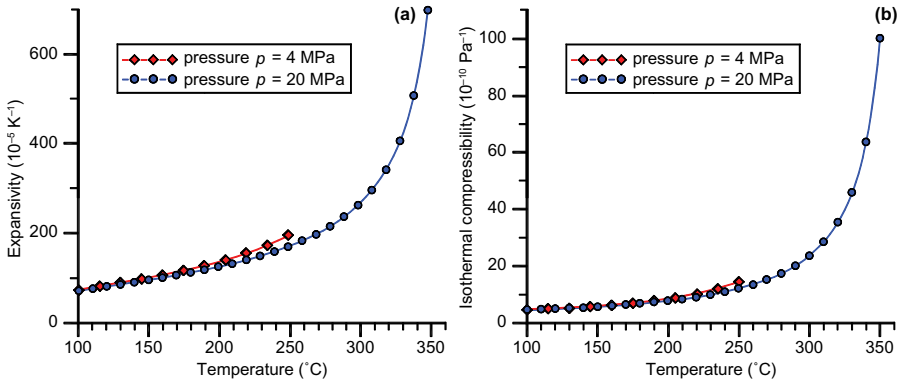


Figure 2.22. Expansivity (a) and isothermal compressibility (b) of water in the range $T \in [100, 350]^{\circ}\text{C}$, for two different pressures: $p = 4$ and 20 MPa.

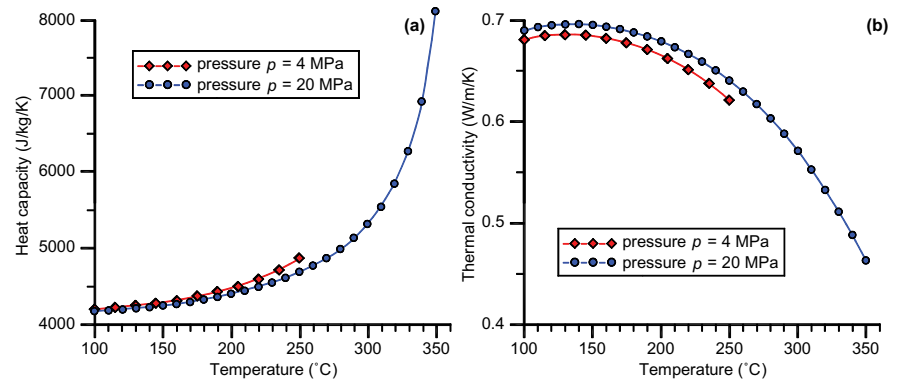


Figure 2.23. Heat capacity (a) and thermal conductivity (b) of water in the range $T \in [100, 350]^{\circ}\text{C}$, for two different pressures: $p = 4$ and 20 MPa.

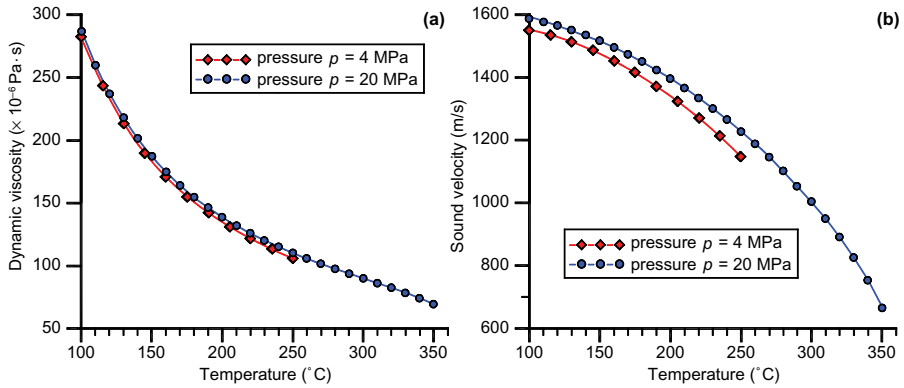


Figure 2.24. Dynamic viscosity (a) and speed of sound (b) in water in the range $T \in [100, 350]^{\circ}\text{C}$, for two different pressures: $p = 4$ and 20 MPa.

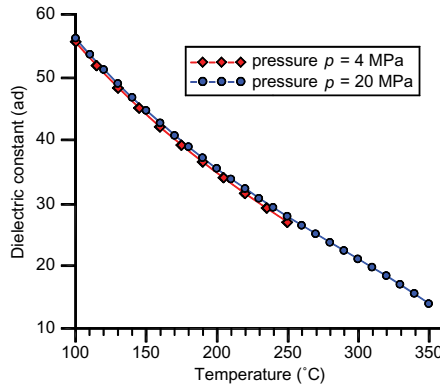


Figure 2.25. Dielectric constant of water in the range $T \in [100, 350]^{\circ}\text{C}$, for two different pressures: $p = 4$ and 20 MPa.

2.3.6 Properties of two-phase geothermal water (100 to 370 $^{\circ}$ C)

Based entirely on the formulation and data published by Schmidt and Grigull (1979), we programmed in FORTRAN 77 language the code AquaG370.for, containing an equation of state of pure water for geothermal uses. All correlations are included in the code, which is freely available on the Internet (<http://www.fismat.umich.mx/~marioc/>). The programmed equations are valid for pressures between 0.1 and 22 MPa, and for temperatures between 5 and 370 $^{\circ}$ C. Above the critical point of water, both phases melt in one single phase and it is no longer possible to distinguish the separated properties of the liquid or of the steam. In the single-phase regions, the basic variables are pressure and temperature. The other thermodynamic properties of water can be calculated as functions of these two variables, because pressure and temperature are naturally independent in single-phase water. The corresponding functions for liquid were presented in previous sections.

In the two-phase region, the temperature T_{sat} depends on the saturation pressure p_{sat} through the Clapeyron relationship $T_{\text{sat}} = T(p_{\text{sat}})$. For that reason, in a two-phase system it is necessary to have another variable that determines the quantity of thermal energy or enthalpy *in situ* or the relative quantity of steam or of liquid present in each phase. The second variable adapted in this case is specific enthalpy, or steam quality or liquid saturation. For a two-phase condition, steam

quality X_v is defined as the mass of water in the vapor phase divided by the total mass of water. Liquid saturation S_l is defined as the volume of water in the liquid phase divided by the total volume of water. For the saturated liquid and saturated vapor, the steam quality is 0.0 and 1.0, respectively.

2.3.6.1 Thermodynamic range of validity of the code AquaG370.For

(p, T) , (p, h) , (p, S_l) , (p, X_v) , (T, S_l) , (T, X_v) the first two couples are for steam or vapor. The last four couples of variables are for two-phase flow.

Liquid phase: $20.0 \leq h \leq 1842$ kJ/kg ; $0.1 \leq p \leq 22$ MPa ; $5^\circ\text{C} \leq T \leq 370^\circ\text{C}$

Steam phase: $2675.5 \leq h \leq 3488$ kJ/kg; $0.1 \leq p \leq 21$ MPa; $99.7^\circ\text{C} \leq T \leq 800^\circ\text{C}$

Two-phase: $20.0 \leq h \leq 1800$ kJ/kg ; $0.1 \leq p \leq 20$ MPa; $99.5^\circ\text{C} \leq T \leq 360^\circ\text{C}$

Enthalpies of each phase: $21 \leq h_l \leq 1818$ kJ/kg , $2510 \leq h_v \leq 2428$ kJ/kg.

The following relationships are valid and useful in the two-phase region:

$$\begin{aligned} p_{\text{steam}} < p_{\text{saturation}} < p_{\text{liquid}}; \quad T_{\text{liquid}} < T_{\text{saturation}} < T_{\text{steam}} \\ h_{\text{liquid}} < h_{\text{saturation}} < h_{\text{steam}}; \quad 0 \leq X_l, X_v, S_l, S_v \leq 1 \end{aligned}$$

2.3.6.2 Temperature of saturation (subroutine T_{sat})

This subroutine calculates approximately the saturation temperature corresponding to a fixed saturation pressure (Fig. 2.26). The iterations start from a given pressure p_X using one of the empiric correlations given by the following formulae:

$$\begin{aligned} p_1 &= \text{Exp} \left(24.02 \frac{4606.0}{T_0 + 273.15} \right) \quad ! \text{ Pruess (1988)} \\ p_2 &= \text{Exp} \left(12.598330 \frac{4667.07504}{T_0 + 273.15} \right) \quad ! \text{ Ramey (1974)} \\ p_3 &= \left(\frac{T_0 + 17.778}{116.744444} \right), \quad 1 < p_3 < 200 \text{ bar} \quad ! \text{ Ramey (1974)} \end{aligned} \quad (2.140)$$

2.3.6.3 Saturation pressure (subroutine P_{sat})

The saturation pressure p_{sat} corresponding to a given temperature T_{sat} is calculated exactly with the K-function (Fig. 2.26).

2.3.6.4 Density and enthalpy of liquid and steam (subroutines L_{ikid} and V_{apor})

The properties of each phase, liquid and steam, are calculated separately as functions of temperature and pressure; density and enthalpy are shown in Figure 2.27.

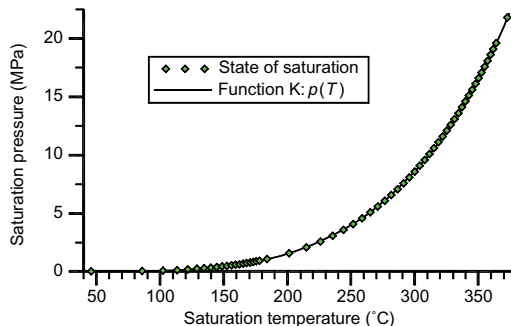


Figure 2.26. State of saturation of two-phase water, or K-line.

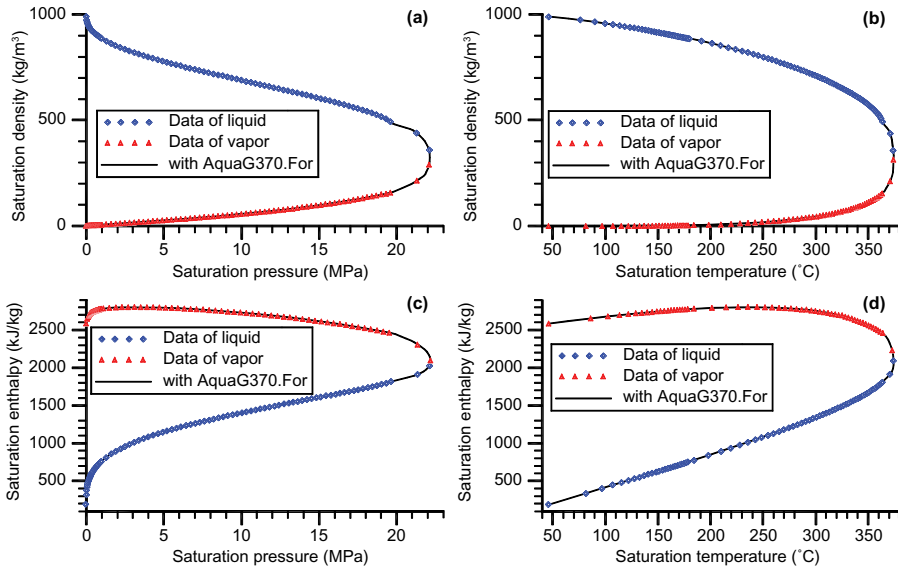


Figure 2.27. Properties of liquid and steam phase of water as functions of saturation temperature and saturation pressure: (a, b) density, (c, d) enthalpy.

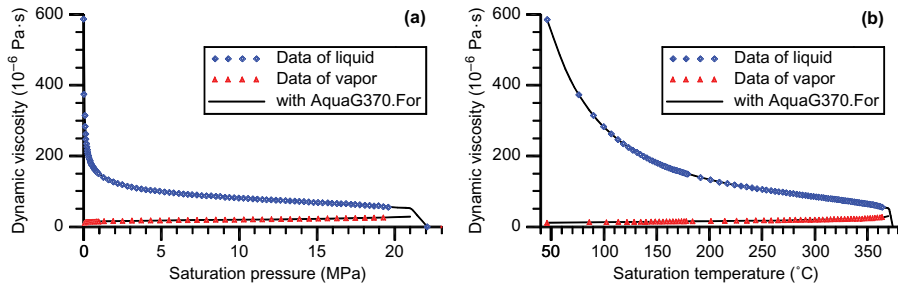


Figure 2.28. Dynamic viscosity of liquid and steam phase of water as functions of saturation pressure (a) and saturation temperature (b).

2.3.6.5 Dynamic viscosity of two-phase water (subroutine *Visf*)

This subroutine calculates the dynamic viscosity of the liquid and steam phase in [kg/m/s], as functions of the absolute temperature of the corresponding phase and of its specific volume. The general formula is based on the equation of Alexandrov (Schmidt and Grigull 1979). For the liquid phase, at 200°C, the viscosity grows slightly from 133.7×10^{-6} Pa · s at 2 MPa, up to 138.2×10^{-6} Pa · s at 20 MPa. For the vapor phase the relationships are inverted, the viscosity of steam increases from 18.14×10^{-6} Pa · s at 264°C, up to 24.38×10^{-6} Pa · s at 400°C at a constant pressure of 5 MPa. For two-phase water, the viscosities depend mainly on the saturation temperature (Fig. 2.28).

2.3.6.6 Thermal conductivity of two-phase water (subroutine *Terk*)

The thermal conductivity of water $k_w(T, \rho)$ is calculated as a function of both temperature and density. This equation is valid between 5 and 800°C. The thermal conductivity of the steam increases slightly when temperature increases and grows faster when pressure increases. The relationship for the liquid is inverse because its heat capacity decreases continuously with temperature from

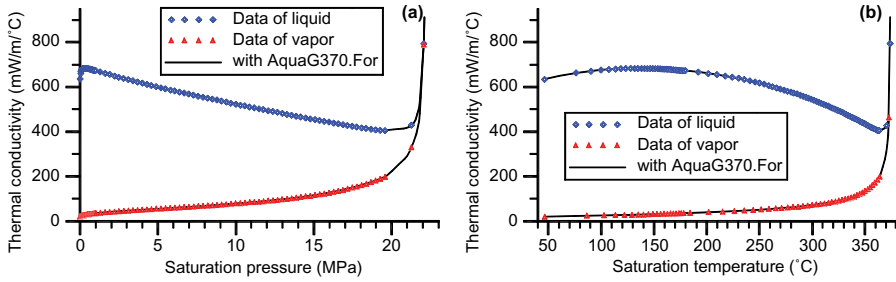


Figure 2.29. Thermal conductivity of liquid and steam phase of water as functions of saturation pressure (a) and saturation temperature (b).

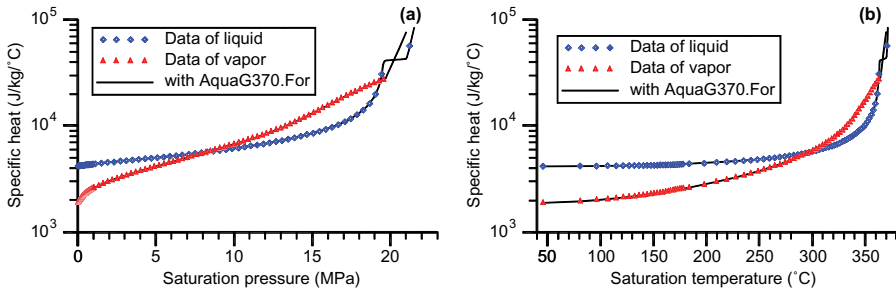


Figure 2.30. Specific heat of liquid and steam phase of water as functions of saturation pressure (a) and saturation temperature (b).

0 up to 380°C approximately (Fig. 2.29). Crude oil shows a similar behavior as liquid water; density decrements and thermal conductivity increments when temperature increases.

2.3.6.7 Specific heat of two-phase water (subroutines CPliq and CPvap)

The specific heat capacity of water $c_p(T, p)$ (isobaric specific heat) is calculated as a function of temperature and pressure. The specific heat capacity of vapor phase $c_v(T, p)$ is calculated as a function of pressure and temperature. The formulae are valid between 1 and 800°C (Fig. 2.30).

2.3.6.8 Surface tension of two-phase water (subroutine Tensa)

The surface tension of two-phase water is the stress existing at the common interface of steam and liquid. This tension originates from the different types of molecular attraction in each one of the phases. The surface tension of water σ [N/m] is calculated as a function of temperature (Fig. 2.31).

2.3.6.9 Practical correlations for two-phase flow

The following exact correlations are useful in two-phase water computations. Definitions of liquid quality X_l , steam quality X_v , liquid saturation S_l and steam saturation S_v , h_f and e_f are the average enthalpy and energy of the two-phase water:

$$X_l = \frac{dM_l}{dM_f}, \quad X_v = \frac{dM_v}{dM_f}, \quad X_l + X_v = 1, \quad S_l = \frac{dV_l}{dV_f}, \quad S_v = \frac{dV_v}{dV_f}, \quad S_l + S_v = 1 \quad (2.141)$$

$$\text{Fluid density-saturations: } \rho_f = \rho_l S_l + \rho_v S_v \quad \Leftrightarrow \quad S_l = \frac{\rho_f - \rho_v}{\rho_l - \rho_v} \quad (2.142)$$

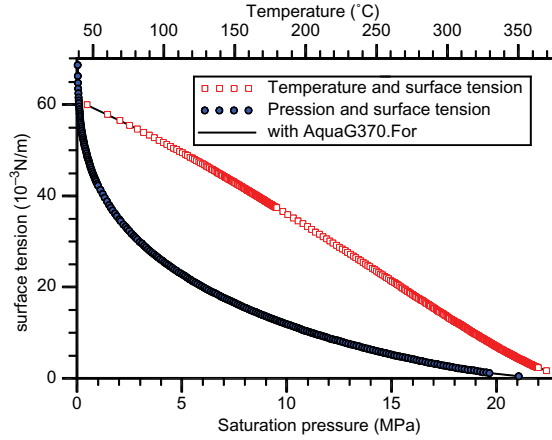


Figure 2.31. Surface tension of liquid and steam phase of water as functions of saturation pressure and saturation temperature.

Quality-enthalpy:

$$h_f(p, X_v) = X_l h_l + X_v h_v = h_l + X_v (h_v - h_l) \quad \Leftrightarrow \quad X_v = \frac{h_f - h_l}{h_v - h_l} \quad (2.143)$$

Enthalpies, densities, internal energies and saturations of the two-phase fluid:

$$\begin{aligned} \rho_f h_f &= S_l \rho_l h_l + S_v \rho_v h_v = \rho_f e_f + p \\ \rho_f e_f &= S_l \rho_l e_l + S_v \rho_v e_v = \rho_f h_f - p \end{aligned} \quad (2.144)$$

Liquid saturation, enthalpies and densities of the two-phase fluid:

$$S_l = \frac{\rho_v (h_v - h_f)}{h_f (\rho_l - \rho_v) - \rho_l h_l + \rho_v h_v} \quad (2.145)$$

Liquid saturation, densities and steam quality of the two-phase fluid:

$$\frac{1}{S_l} = 1 - \frac{\rho_l (h_f - h_l)}{\rho_v (h_f - h_v)} = 1 + \frac{\rho_l}{\rho_v} \frac{X_v}{(1 - X_v)} \quad (2.146)$$

Saturations, densities and qualities of the two-phase fluid:

$$\begin{aligned} X_v &= \frac{\rho_v (1 - S_l)}{\rho_f} = \frac{\rho_v}{\rho_f} S_v, \quad \rho_l S_l X_v = \rho_v S_v X_l \\ \rho_f X_v &= \rho_v S_v; \quad \rho_f X_l = \rho_l S_l \end{aligned} \quad (2.147)$$

2.3.7 Capillary pressure

Different fluids and two or more fluid phases may be contained in the pores of a rock. This phenomenon involves concepts such as capillarity, interfacial tension, wettability and relative permeability to characterize the fluid behavior. Two different immiscible fluids in contact, for example liquid and gas, are separated by a thin skin or stretched surface of infinitesimal thickness.

The stretching of the membrane is due to an interfacial tension between both fluids. A discontinuity in pressure emerges, which depends on the curvature of this surface separating both fluids in the pores and fractures. The capillarity originates from those forces of superficial stress. AGAT laboratories (<http://www.agatlabs.com/>) describe capillarity as follows:

- The combination of surface tension and curvature due to the capillaries causes the two phases to experience different pressures. As the relative saturations of the phases change, it has been found that these pressure differences also change. The difference between the pressures of any two phases is referred to as the capillary pressure. Capillary pressures can be determined for any two fluid phases; of interest to the oil industry are those for gas-brine, gas-oil and oil-brine systems. Capillary pressure data is used directly in numerical simulation programs and to calculate fluid distributions in reservoirs. The residual and irreducible fluid saturations, determined when measuring capillary pressures, can be used to help estimate the amount of recoverable oil and the expected connate water saturations. In any porous material with two fluid phases present, the wetting phase will always have the lower pressure. Therefore, capillary pressure curves can also be used to determine the wetting characteristics of reservoir rocks.

The capillary pressure p_C in a porous medium is defined as the difference of pressures at the interface of the two immiscible fluids at rest. One of the fluids wets the internal surface of the pores more than the other. Let p_{nw} and p_w be the corresponding pressures of the non-wetting and wetting phases, respectively, the capillary pressure is:

$$p_C = p_{nw} - p_w \quad (2.148)$$

If the fluid phases are liquid and vapor $p_C = p_v - p_l$; for oil and water, $p_C = p_o - p_w$; for oil and gas $p_C = p_g - p_o$. The phenomenon of capillarity also involves the solid in contact with the fluid and plays an important role in the process of displacement of one fluid by another in porous rocks. The static properties of two different fluids coexistent in a rock depend on the intramolecular distribution of the phases inside the pores, which is controlled by the wettability of the porous rock. This is a key parameter affecting capillary pressure, relative permeabilities and liquid distribution (Dandekar 2006). The wettability measures the preference degree of the pore's internal surface to be wetted by one of the phases. It is also defined as the relative ability of a fluid to spread or adhere to a solid surface in the presence of another fluid.

The capillary pressure in a reservoir is also a function of the history and distribution of the saturation of the fluids in the pores and fractures. To clarify this dependency, it is necessary to understand the saturation mechanisms of drainage and imbibition. Both processes are dependent on the wetting characteristics of fluid phases. A drainage process occurs when the wetting phase decreases. An imbibition process occurs when the wetting phase increases. Drainage in porous rock refers to a decrement in the saturation of the wetting phase by discharge or removal of this phase inside the pores. The term imbibition refers to an increment in the saturation of the wetting phase originated by the trend of the porous rock to absorb this phase, under the sole action of the attractive capillary force and in the absence of any other pressure. In geothermal reservoirs, the liquid is the wetting phase and the steam is the non-wetting phase. In oil reservoirs, the water can be the wetting phase and the oil the non-wetting phase. When water displaces oil from a water-wet rock, the process is imbibition. But if water displaces oil from an oil-wet rock, the process is drainage. On the other hand, when steam displaces liquid water or gas displaces oil, the process is always drainage because gas and steam are always the non-wetting phases.

Diverse experiments show that the two capillary pressure-saturation curves, obtained during a drainage-imbibition process, are always different. This phenomenon is called capillary hysteresis. In general, a physical system with hysteresis has memory and exhibits path-dependence. This means that there is no way to predict the output of the system without knowing the history of the system's input. Therefore, it is necessary to know the path that the input followed before it reached its current value. The drainage and imbibition curves present hysteresis, which is attributed to

wettability (Dandekar 2006). The capillary pressure depends upon the history of the saturation process and therefore presents hysteresis.

The vapor pressure on the surface of a liquid is a function of the curvature of the liquid surface. The same dependence is valid for the capillary pressure. For two-phase water, the liquid is the wetting phase, and the equilibrium pressure is larger than the vapor pressure $p_E > p_v$. Therefore, the liquid pressure is smaller than the equilibrium pressure $p_l < p_E$. Since the capillary pressure is a function of the liquid saturation, the decline of vapor pressure should also be a function of the liquid saturation in the porous rock. There are three different geometrical classes of liquid-vapor interfaces: convex, plane and concave. In the convex interface, the steam equilibrium pressure is larger than the pressure in a liquid-vapor flat interface. On the other hand, in the concave interface, the steam equilibrium pressure is smaller than the pressure at the flat interface. The vapor pressure at the interfacial surface is given by the famous Laplace capillarity equation:

$$\frac{1}{r_M} = \frac{1}{R_1} + \frac{1}{R_2} \Rightarrow p_C = \frac{\sigma_0}{r_M} \tag{2.149}$$

where σ_0 is the surface tension in the liquid and r_M is the average radius of curvature of the interface and R_1 and R_2 are the radii of two separate points of the curved interfacial surface. The equation of Laplace postulates that the surface tension existent at the separation surface between two different fluids at different pressures, maintains both fluids in mechanical equilibrium. As long as $p_C > 0$, the pressure in the concave side of the surface is greater than the pressure in the convex side. In porous rocks, if the liquid saturation is small, the liquid-vapor interface is concave. If the radius $r_M \rightarrow \infty$ then $p_C \rightarrow 0$, and therefore, the interfacial surface is flat only if both pressures are the same.

In geothermal reservoirs the capillary pressure is obtained by subtracting the liquid pressure from the steam equilibrium pressure. However, the exact value of p_v is not known and it should be obtained from other thermodynamic variables, for example, using the Kelvin equation:

$$\text{Ln} \left(\frac{p_{sv}}{p_v} \right) = \frac{2\sigma_0 v_M}{RT} \frac{1}{r_M} \tag{2.150}$$

where p_{sv} is the vapor saturation pressure for a flat interface, p_v is the vapor saturation pressure for a curved interface of average radius r_M , v_M is the liquid phase molar volume, R (8.314472 J/K/mol) is the ideal gas constant and T the absolute temperature.

The same surface tension between two immiscible fluids also exists between fluids and solids. The law of Young-Dupre expresses that a non-zero resulting force cannot exist in the contact among three media in equilibrium with different molecular compositions (De Wiest 1969). Figure 2.32 illustrates this law. The phenomenon described for water (l), gas (g) and solid (s) or for oil (l), gas (g) and solid (s), is expressed by the following equation:

$$\sigma_{sg} = \sigma_{sl} + \sigma_{lg} \text{Cos } \theta \Rightarrow \text{Cos } \theta = \left| \frac{\sigma_{sg} - \sigma_{sl}}{\sigma_{lg}} \right| \leq 1 \tag{2.151}$$

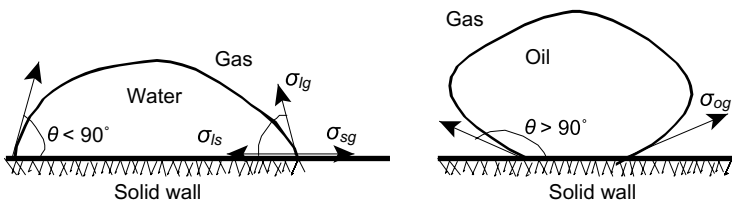


Figure 2.32. Capillarity in the law of Young-Dupre (De Wiest 1969).

This equation presupposes that the three phases coexist in equilibrium. However, the preferential wettability of one of the phases can produce movement without the presence of any pressure gradient in the fluid. Such a movement by capillarity of one of the phases can displace the previous phase present in the porous medium. This phenomenon is the imbibition of the wetting phase. Passmore and Archer (1985) reported that the time necessary to reach the saturation of equilibrium decreases when the pressure increases and that the hysteresis among the drainage curves and the imbibition curves decreases when the temperature increases. The imbibition model of Naar and Henderson (Passmore and Archer 1985), also indicates a decrement of the hysteresis. This model relates the saturations of water imbibition and of water drainage, at a fixed capillary pressure, with the irreducible water saturation S_{wi} :

$$S_w^{\text{drainage}} - S_w^{\text{imbibition}} = \frac{S_w^{\text{drainage}} - S_{wi}}{2(1 - S_{wi})} \quad (2.152)$$

The term S_{wi} represents the minimum water saturation that is present in the pores of a rock. It is also called the interstitial saturation of water. For example, the irreducible water saturation of the reservoir rocks of The Geysers geothermal field is around 15%. The irreducible gas saturation is 20%; porosity of the core is 4.3% (Habana 2002). The general normalized wetting-phase saturation S_{nw} in the drainage case is expressed as follows:

$$S_{nw} = \frac{S_w - S_{rw}}{1 - S_{nwi} - S_{rw}} \quad (2.153)$$

where S_{nwi} is the initial saturation of the non-wetting phase and S_{rw} is the residual saturation of the wetting phase. The normalized saturation is needed in next sections.

Adsorption is the adhesion of fluid molecules to the walls of solid bodies in contact with the fluid. In porous media, this phenomenon results from the interaction between particles of the solid rock and the fluid molecules in the pore space. This mechanism originates forces of attraction between the fluid and the solid surface (Dullien 1979). The phenomenon of adsorption, together with capillarity, produces a descent in the steam equilibrium pressure in two-phase flows. The classic relationship of Clapeyron in the thermodynamics of two-phase water becomes dependent on other factors. The presence of other phases such as non-condensable gases (NCG) and dissolved chemical compounds species such as ions also produces a pressure drop. This effect is particularly important in geothermal reservoirs with superheated vapor because a certain quantity of residual liquid remains in the pores influencing the mass balance of the system. Capillarity tends to keep the vapor phase in the fractures and the liquid phase in the pores. In this manner, the fractures are not fully saturated with liquid and the possibility of having a heat pipe is increased.

Capillarity is an important phenomenon in both geothermal and hydrocarbon reservoir engineering. Capillary pressure is an useful parameter in the numerical simulation and evaluation of the reservoir. Several practical correlations to calculate the capillary pressure are given in the next section.

2.3.8 *Practical correlations for capillary pressures*

Capillary pressure is the algebraic difference between two pressures of different phases, gas-liquid or between two liquids (oil-water), occupying the pores of the rock. Capillary forces play an important role in determining the natural state of fractured reservoirs and have a significant effect on fluid distribution, water injection, liquid transfer between fractures and pores, and in production from geothermal reservoirs (Li and Horne 2007).

2.3.8.1 *Correlation of Van Genuchten*

Van Genuchten (1980) adopted an implicit capillary pressure function to predict the relative hydraulic conductivity of unsaturated soils containing water and air. The original equation was

developed for the soil-water content-pressure head curve:

$$(1 + (apC)^n) = \left(\frac{S_w - S_{rw}}{1 - S_{rw}} \right)^c \quad (2.154)$$

where a , c , and n are parameters to be determined experimentally. The initial saturation of the non-wetting phase S_{nwi} (eq. 2.153) was set equal to zero in this model. This correlation is the most frequently used for unconsolidated porous rocks.

2.3.8.2 Correlation of Schulz and Kehrwald

Schulz *et al.* (2005) obtained the following correlation for the capillary pressure as a function of water saturation:

$$p_C(S_w) = \frac{1}{\alpha} \left(S_w^{-\frac{n}{n-1}} - 1 \right)^{\frac{1}{n}} \quad (2.155)$$

where: $\alpha = 0.137 \text{ kPa}^{-1}$, $n = 4.387$

The values of the parameters α and n fitted the Van Genuchten (1980) equation with the experiments reported by Schulz *et al.* (2005). The experimental curve for the capillary pressure is shown in Figure 2.33. It was obtained directly from data of surface tension, curvature, and contact angle.

2.3.8.3 Correlation of Li and Horne

Li and Horne (2000) proposed two correlations for a porous reservoir with fractures. For porous blocks, the capillary pressure curves are similar to those derived from a typical The Geysers isotherm (Satik 1998), as described by the Van Genuchten equation. For fractures, the relation is linear:

$$\begin{aligned} \text{porous blocks: } S_e = \frac{S_w - S_{rw}}{1 - S_{rw}} \quad \Rightarrow \quad p_C(S_w) = p_0 \left((S_e)^{-\frac{1}{\lambda_\varphi}} - 1 \right)^{1-\lambda_\varphi} \quad (2.156) \\ \text{in the fractures: } p_{Cf}(S_w) = p_{F \max}(1 - S_w) \end{aligned}$$

where p_0 (initial pressure) and λ_φ (pore size distribution coefficient) are constants, S_e is the effective liquid saturation and S_{rw} is the residual water saturation, $p_{F \max}$ is the maximum fracture capillary pressure (Pruess and O'Sullivan 1992, Li and Horne 2000). For example, Noel *et al.* (1998) used model (2.156) and the values $p_0 = 100 \text{ kPa}$, $\lambda_\varphi = 0.6$ and $p_{F \max} = 0, 50, 100 \text{ kPa}$ to investigate how capillary forces affect the stability of a water saturated region overlying a liquid-dominated, two-phase zone.

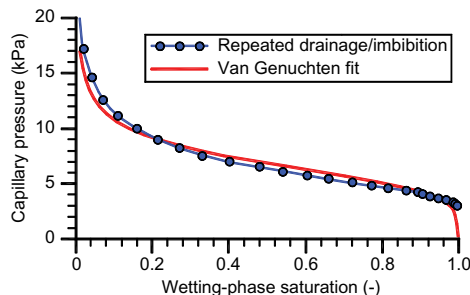


Figure 2.33. Capillary pressure-saturation curves (modified from Schulz *et al.* 2005).

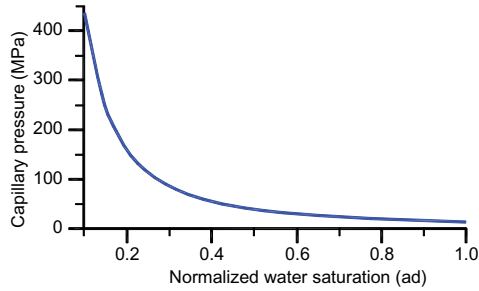


Figure 2.34. Brooks-Corey (1964) capillary pressure curve (modified from Li and Horne 2000).

2.3.8.4 Correlation of Brooks-Corey

The function of Brooks-Corey (1964) is often used to model the capillary pressure curve. This formula is the most frequently used for consolidated porous rocks and the most appropriate to the drainage case in geothermal reservoir engineering (Li and Horne 2006). The formula is given by:

$$p_C(S_w) = p_{Ce} \left(\frac{S_w - S_{rw}}{1 - S_{rw}} \right)^{-\frac{1}{\lambda_\varphi}} \quad (2.157)$$

where p_{Ce} is the entry capillary pressure and λ_φ is the pore size distribution coefficient; both are assumed constants. Using the coefficients from a rock of The Geysers (Nevada, USA) geothermal field: $p_{Ce} = 13.96$ MPa, $\lambda_\varphi = 0.669$, $S_{rw} = 0.2$, Li and Horne (2000) obtained the following graphic (Fig. 2.34):

In Brooks-Corey case, S_{rw} was the residual oil saturation and S_{nwi} was equal to zero.

2.3.8.5 Correlation of Li and Horne for geothermal reservoirs

Li and Horne (2007) developed a method to calculate the steam-water capillary pressure using experimental data from steady-state, two-phase flow experiments. They derived an empirical model to compute p_C directly. The resulting mathematical model is useful to calculate the steam-water capillary pressure in rocks of geothermal reservoirs. The proposed steam-water capillary pressure model based on experimental data for the drainage case is expressed by:

$$p_C(S_w) = 4.012\sigma_0 \left(\frac{k_0}{\varphi} \right)^{-\frac{1}{2}} (S_{nw})^{-1.843} \quad (2.158)$$

$$\text{where: } p_C \text{ [MPa], } \sigma_0 \left[\frac{\text{mN}}{\text{m}} \right], k_0 \text{ [} 10^{-6}\text{mD]}$$

The initial saturation S_{nwi} in this model is set equal to zero in the normalized wetting-phase saturation S_{nw} (eq. 2.153). The model described by this equation is suitable for drainage processes and is based on the assumption that the contact angle does not change with permeability and temperature (Li and Horne 2007).

Figure 2.35 shows theoretical data of steam-water capillary pressures calculated using equation (1.158) for rock samples with permeability ranging from 1.3 to 500×10^{-9} D (a typical range for The Geysers reservoir rocks). The porosity used in the calculation was 1.9%. The surface tension at a temperature of 240°C is 28.41×10^{-3} N/m.

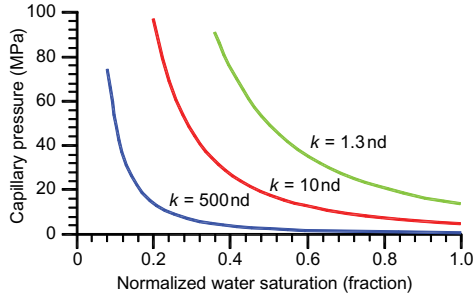


Figure 2.35. Drainage steam-water capillary pressure curves at 240°C for rocks of different permeability (modified from Powell and Li 2003).

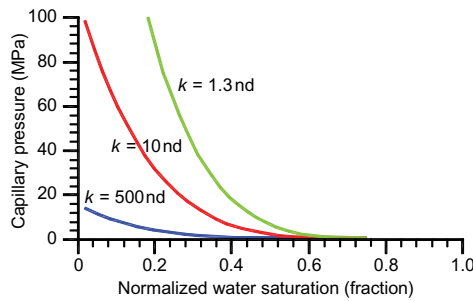


Figure 2.36. Imbibition steam-water capillary pressure curves at 240°C for rocks of different permeability (modified from Li and Horne 2007).

For the imbibition steam-water capillary pressure curve, the proposed empirical model (i.e., the “imbibition model”) is expressed as follows:

$$p_C(S_w) = 88.86 \sigma_0 \left(\frac{k_0}{\varphi} \right)^{-\frac{1}{2}} (S_{nwimb})^{5.539} \tag{2.159}$$

$$\text{where: } S_{nwimb} = \frac{S_w - S_{wi}}{1 - S_{wi} - S_{rs}}, \quad p_C \text{ [MPa]}, \quad \sigma_0 \left[10^{-3} \frac{\text{N}}{\text{m}} \right], \quad k_0 \text{ [} 10^{-6} \text{ mD]}$$

Both models only need to know the reservoir porosity φ , the permeability k_0 , the surface tension σ , the initial water saturation S_{wi} , the normalized water saturation S_{nwimb} and the residual steam saturation S_{rs} by imbibition. The model in equation (2.159) is suitable for imbibition processes (water injection) in which water saturation increases and is based on the same assumptions as the drainage model (Li and Horne 2007).

Example data of steam-water capillary pressure in the imbibition case were calculated using equation (2.159) for rock samples with permeability ranging from 1.3 to 500×10^{-9} D. The results are plotted in Figure 2.36. The porosity, surface tension, and temperature are the same as in the experiments whose results are depicted in Figure 2.35. These models are simple, the only parameters required being reservoir temperature, pressure, porosity and permeability. Despite their simplicity, these models could prove useful for geothermal reservoir engineers as they will help to reduce the uncertainty in numerical simulation and other calculations. Imbibition capillary pressure is, as we have already mentioned, usually less than that for the drainage case (Figs. 2.35 and 2.36).

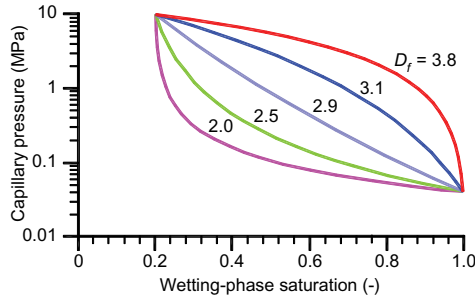


Figure 2.37. Typical capillary pressure curves calculated using the new generalized model assuming different fractal dimension values (modified from Li and Horne 2006).

2.3.8.6 The Li-Horne general fractal capillary pressure model

Li and Horne (2004, 2006, and 2007) proposed and developed a generalized fractal model to represent capillary pressure functions in porous rocks. This model includes the frequently used Brooks-Corey (1964) formula (2.157) and other correlations as well. Their initial work focused on obtaining a model for rock samples (greywacke) of The Geysers geothermal reservoir. Nevertheless, (Li and Horne 2007) found that:

- fractal curves inferred from capillary pressure data were good straight lines for both the Berea sandstone, for which the Brooks-Corey model works and The Geysers rock samples, for which this model does not work. This finding implies that a more general capillary pressure model may exist to represent both rocks.

The model is expressed as follows:

$$p_C(S_w) = P_{C\max}(1 - b_0 S_{Nw})^{-\frac{1}{\lambda_\phi}}; \quad b_0 = 1 - \left(\frac{p_e}{P_{C\max}}\right)^{-\lambda_\phi} \quad (2.160)$$

where S_w is the wetting-phase saturation, S_{wr} the residual saturation of S_w and S_{nw} is again the normalized saturation of the wetting phase (eq. 2.153), with $S_{nwi} = 0$; $p_{C\max}$ is the maximum capillary pressure at the residual non-wetting phase saturation in the imbibition case, or the capillary pressure at the residual wetting phase saturation in the drainage case. p_e is the entry capillary pressure; $\lambda_\phi = 3 - D_f$ is the pore size distribution index and D_f is the fractal dimension.

The fractal dimension determines the heterogeneity of the rock sample; the greater D_f , the greater the heterogeneity. In equation (2.160), b_0 is a constant parameter associated with the rock pore size. If $p_{C\max} \rightarrow \infty$ and the fractal dimension $D_f < 3$ then equation (2.160) becomes equal to the empirical Brooks-Corey equation (2.157). According to these authors, “one can see that the Brooks-Corey capillary pressure model has a solid theoretical basis. This may be why the Brooks-Corey model can be a good fit to capillary pressure curves of many rock samples”.

This new fractal model is “universal” in the sense that it can represent both the capillary pressure and the relative permeability of rocks of very different nature. The model could be applied in both complex structured porous rock and in a single capillary tube as well as in both drainage and imbibitions cases (Li and Horne 2004, 2007). Figure 2.37 shows theoretical capillary pressure data calculated using the generalized model (eq. 2.160) with different fractal dimensions. The maximum capillary pressure and entry capillary pressure assumed were 10 and 0.04 MPa, respectively. The residual wetting-phase saturation was 20%.

2.3.9 Relative permeabilities

When the porous medium contains more than one fluid phase (oil and water; liquid and vapor; oil, water and gas), the permeability of the rock with respect to one of the phases is called effective

hydraulic permeability. This permeability depends on the volumetric fraction of each phase in the porous space (saturation) and on the characteristics of the wettability of the rock. The concept of relative permeability k_{ri} is dimensionless and refers to the quotient of the effective permeability k_e divided by the absolute rock permeability k . Its mathematical expression is expressed as:

$$k_{ri} = \frac{k_e}{k} \quad (2.161)$$

where subindex ri refers to the particular fluid phase under consideration: i = water, oil, gas, liquid or steam. The corresponding relative permeabilities for these phases are denoted by k_{rw} , k_{ro} , k_{rg} , k_{rl} and k_{rv} , respectively. This concept originated when extending Darcy's law to a two-phase fluid. The Oilfield Glossary defines relative permeability as (Schlumberger 2009):

- *Relative permeability is the ratio of effective permeability of a particular fluid at a particular saturation to absolute permeability of that fluid at total saturation. If a single fluid is present in a rock, its relative permeability is one. Calculation of relative permeability allows comparison of the different abilities of fluids to flow in the presence of each other, since the presence of more than one fluid generally inhibits flow.*

Relative permeability is a dimensionless variable conceived to adapt Darcy's law to multiphase flow conditions. There is evidence that relative permeability may be a function of many more parameters than solely fluid saturation. AGAT Laboratories (<http://www.agatlabs.com/>) describe it like this:

- Temperature, flow velocity, saturation history, wettability changes and the mechanical and chemical behavior of the matrix material may all play roles in changing the functional dependence of the relative permeability on saturation. The best defined of these dependences is the variation of relative permeability with saturation history; relative permeability curves show hysteresis between drainage processes (wetting phase decreasing) and imbibition processes (wetting phase increasing).

In 1937, Muskat *et al.* published relative permeability curves for gases and liquids in unconsolidated sands, showing that the curves k_{rg} and k_{rl} are independent of the nature of the sand. This result is exceptional because in all the other cases studied later in diverse experiments reported in the literature, the relative permeability curves depend on both the type of porous rock and on the nature of the fluid. Consequently, there does not exist a valid general correlation for these functions for any fluid in any porous medium. The models to calculate relative permeabilities are determined experimentally in each particular case. For example, laboratory measurements indicate that the relative permeability of the wetting phase depends on the square of the saturation of the corresponding phase, or on the saturation elevated to a higher power.

Diverse experiments show that the addition of relative permeabilities is always inferior to one ($k_{rw} + k_{rmw} < 1$). This indicates that in two-phase flows, the total capacity of the fluid to flow inside the porous rock is reduced, in other words, there is phase interference. The lower is the sum $k_{rw} + k_{rmw} < 1$, the greater is the phase interference. The sum ($k_{rw} + k_{rmw} = 1$) could indicate the absence of phase interference. Physically, this result would imply that each phase flows in its own path without impeding the flow of the other. The real effects of the sum of relative permeabilities can also be interpreted assuming that the movement of each individual phase is slowed by the presence of the other phase, and that the grade of interference depends on the volumetric proportion of each phase. This fact is an obvious consequence of the molecular interactions between both phases.

Since the phases movement depends on the relative permeability functions, it was suggested (Bodvarsson *et al.* 1980) that the two-phase fluid behaves as a fluid with a kinematic effective

viscosity ν_f given by:

$$\frac{1}{\nu_f} = \frac{k_{rl}}{\nu_l} + \frac{k_{rv}}{\nu_v} \quad (2.162)$$

Similarly, the enthalpy transported by the mixture depends on k_{rl} and on k_{rv} , and is different from the static enthalpy (*in situ*). The enthalpy of the two-phase fluid in movement is:

$$h_f = \nu_f \left(h_l \frac{k_{rl}}{\nu_l} + h_v \frac{k_{rv}}{\nu_v} \right) \quad (2.163)$$

The transport of mass and energy in geothermal reservoirs are then strongly influenced by the magnitude of the dynamic effective viscosity and by the enthalpy of the fluid in movement. The relative permeability also depends on other important factors such as temperature, pressure and liquid saturation. It has been found that the mineralogy of the rock also plays a role in its characterization and, if there is a multiphase fluid, the geometry of pores and fractures also has an influence.

Several petroleum and water studies, reported by Passmore and Archer (1985), indicated that the relative permeability of both oil and water increases when temperature increases. Apparently, this effect is larger for oil than for water. However, other experiments reported that the results are confusing. Ramey *et al.* (1974) reported studies of capillary pressure in consolidated sandstones and in calcareous rocks with oil and water; the range of temperatures was between 24 and 163°C. These results showed that the irreducible saturation of water is increased, while the saturation of residual oil comes down when temperature increases. In the specialized literature on petroleum engineering it is accepted that the residual saturation of oil is reduced (especially in heavy oils), while the irreducible saturation of water increases when the temperature increases. The relative permeability also presents hysteresis. The relative permeability of the wetting phase changes slightly when its saturation varies. On the other hand, the relative permeability of the non-wetting phase is clearly lower during imbibition than during drainage.

2.3.10 Practical correlations for relative permeabilities

In this section several practical formulae for the effective calculation of relative permeabilities are described. Relative permeability functions usually depend on phase saturation. The two most commonly used expressions for relative permeability for homogeneous porous media are the X-curves and Corey curves. The X-curves describe relative permeability as a linear function of saturation: $k_{rl} = S_l$, $k_{rv} = S_v$ where S_l and S_g are the liquid and gas saturation, respectively. The Corey curves relate relative permeability to the irreducible or residual liquid and gas saturation, S_{rl} and S_{rg} .

2.3.10.1 Constant functions for perfectly mobile phases

The relative permeabilities are constant in the whole range [0, 1] for any saturation:

$$k_{rw} = 1 \quad \text{and} \quad k_{rmw} = 1 \quad (2.164)$$

2.3.10.2 Linear functions

Both relative permeabilities k_{rw} and k_{rmw} increase linearly with liquid saturation in the range [0, 1]:

$$k_{rw} = a_1 + b_1 S_w, \quad k_{rmw} = a_2 + b_2 S_w \quad (2.165)$$

The four constants in both linear relationships need to be estimated experimentally.

2.3.10.3 Functions of Purcel

The original Purcel's (1949) work was done to estimate absolute permeability by using experimental values of capillary pressure. This formula was extended later to compute the relative permeabilities in two-phase flow (Li and Horne 2002):

$$k_{rw} = (S_{Nw})^{\frac{2+\lambda_\varphi}{\lambda_\varphi}} \quad (2.166a)$$

$$k_{rmw} = (1 - S_{Nw})^2(1 - k_{rw}) \quad (2.166b)$$

where S_{Nw} is the normalized saturation of the wetting phase given in equation (2.153) and λ_φ is the pore size distribution index. A practical way of using these correlations is to compute first k_{rw} with the formula: $k_{rw} = S_{Nw} / R_I$, where R_I is the resistivity index that can be calculated from experimental data (Li and Horne 2002). Archie (1942) showed a relationship between electrical resistivity and saturation of the form $R_I = (S_w)^{-2}$. After k_{rw} is obtained, the value of λ_φ is estimated inverting equation (2.166a):

$$\lambda_\varphi = \frac{2\text{Log}(S_{Nw})}{\text{Log}(k_{rw}) - \text{Log}(S_{Nw})} \quad (2.166c)$$

Note that λ_φ can also be estimated from capillary pressure data. Once both values λ_φ and S_{Nw} are computed, the relative permeability of the non-wetting phase is calculated using equation (2.166b) (Li and Horne 2002).

2.3.10.4 Functions of Corey

On the basis of oil-gas capillary pressure data Corey (1954) developed the following empirical correlations:

$$k_{rw} = S_{Nw}^4; \quad k_{rmw} = (1 - S_{Nw})^2(1 - S_{Nw}^2) \quad (2.167)$$

where: $S_{Nw} = \frac{S_w - S_{rw}}{1 - S_{rw}}$ (drainage), $S_{Nw} = \frac{S_w - S_{rw}}{1 - S_{rw} - S_{rmw}}$ (imbibition)

2.3.10.5 Functions of Brooks-Corey

Because of severe limitations of Corey's functions, Brooks and Corey (1966) developed a couple of correlations that have become famous, to estimate the relative permeability of the wetting and non-wetting phases:

$$k_{rw}(S_w) = (S_{Nw})^{\frac{2+3\lambda_\varphi}{\lambda_\varphi}} \quad (2.168a)$$

$$k_{rmw}(S_w) = (1 - S_{Nw})^2 \left(1 - (S_{Nw})^{\frac{2+\lambda_\varphi}{\lambda_\varphi}} \right) \quad (2.168b)$$

Note that Corey's formulae (2.167) are special cases of equations (2.168a,b) when $\lambda_\varphi = 2$.

Several experiments realized by Li and Horne (2002) with steam-water flows, demonstrated that the Purcel model was the best fit for the experimental data of the liquid phase relative permeability for both drainage and imbibitions processes. However, this correlation is not a good fit for the steam phase. The Brooks-Corey (1966) model was the best fit for the steam phase.

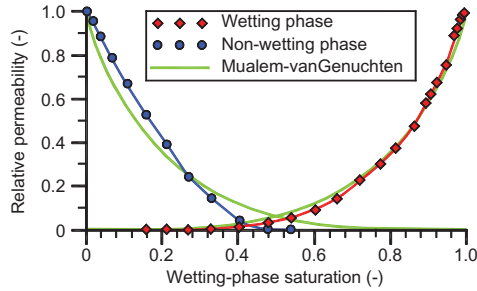


Figure 2.38. Relative permeabilities-saturation curves of Schulz *et al.* (2005).

2.3.10.6 Functions of Schulz-Kehrwald

Schulz *et al.* (2005) performed drainage experiments and obtained the following correlation for the relative permeability functions:

$$\frac{k_{ri}(S_i)}{k_{abs}} = (S_i)^a \left(1 - \left(1 - S_i^{\frac{n}{n-1}} \right)^{1 - \frac{1}{n}} \right)^2 \quad (2.169)$$

where: $a = 0.844$, $n = 4.387$, $i = w, nw$

These curves of relative permeability were obtained by one-phase CFD simulation (Fig. 2.38).

2.3.10.7 Functions for three-phase relative permeabilities

Cunha *et al.* (1999) developed an experimental and analytical method to calculate the relative permeabilities for a three-phase flow process involving water, oil and gas. The experiments were conducted in a Berea sandstone core (permeability 1.8 D, porosity 0.22) at 22°C of laboratory temperature. The relative permeabilities for oil and water are the Brooks-Corey (1964) correlations that were verified experimentally with the following numerical values (Cunha *et al.* 1999):

$$k_{rw}(S_w) = 0.0525 \left(\frac{S_w - 0.363}{0.326} \right)^{2.714} ; \quad k_{ro}(S_w) = 1.318 \left(\frac{0.689 - S_w}{0.326} \right)^{1.193} \quad (2.170a)$$

The relative permeabilities for oil and gas were obtained only for the drainage process (Cunha *et al.* 1999). The analytic expressions of these correlations are as follows:

$$k_{rg}(S_g) = 0.324 \left(\frac{S_g - 0.0528}{0.5842} \right)^{2.307} ; \quad k_{ro}(S_o) = 1.318 \left(\frac{S_o - 0.480}{0.326} \right)^{2.16} \quad (2.170b)$$

In both formulae, the numbers inside the parentheses were measured experimentally, while the values outside the parentheses, coefficients, and exponents were obtained by least squares fitting (Cunha *et al.* 1999).

2.3.10.8 Li-Horne universal relative permeability functions based on fractal modeling of porous rocks

Li and Horne (2004, 2007) found that fractal functions “inferred from capillary pressure curves were good straight lines for all the rock samples, both those with and those without fractures . . .”. These authors developed a generalized model based on fractal modeling of a porous rock to estimate the curves of relative permeability. The fractal dimension is a manifestation of the rock

heterogeneity and is represented by the parameter λ_φ of the pore size distribution. The analytic expressions of these correlations are as follows:

$$k_{rw}(S_{Nw}) = \frac{(P_{Cmax}^{-\lambda_\varphi} - (P_{Cmax}^{-\lambda_\varphi} - p_e^{-\lambda_\varphi}) S_{Nw})^{\frac{(2+\lambda_\varphi)}{\lambda_\varphi}} - (P_{Cmax})^{-(2+\lambda_\varphi)}}{p_e^{-(2+\lambda_\varphi)} - (P_{Cmax})^{-(2+\lambda_\varphi)}} \quad (2.171a)$$

$$k_{rmw}(S_{Nw}) = \frac{p_e^{-(2+\lambda_\varphi)} - (P_{Cmax}^{-\lambda_\varphi} - (P_{Cmax}^{-\lambda_\varphi} - p_e^{-\lambda_\varphi}) S_{Nw})^{\frac{2+\lambda_\varphi}{\lambda_\varphi}}}{p_e^{-(2+\lambda_\varphi)} - (P_{Cmax})^{-(2+\lambda_\varphi)}} \quad (2.171b)$$

where p_{Cmax} is the capillary pressure at residual wetting phase saturation in the drainage case. Note that at the end-points in this model, $k_{rw}(1) = k_{rmw}(0) = 1$ and $k_{rw}(0) = k_{rmw}(1) = 0$. Both functions (2.171a,b) depend upon the heterogeneity of the porous rock, the pore size distribution and the maximum capillary pressure. This model includes the frequently used Brooks-Corey model (Li and Horne 2007).

2.3.10.9 Linear X-functions for relative permeability in fractures

The so called X-curves are typically assumed for fracture flows and are modeled by the equations:

$$k_{rl}(S_w) = \frac{S_w - S_{rl}}{S_{rg} - S_{rl}}, \quad k_{rv}(S_w) = 1 - k_{rl} \quad (2.172)$$

$$k_{rl}, k_{rv} < 1$$

where k_{rl} is the relative permeability of the liquid and k_{rv} is the relative permeability of the steam. S_{rl} is the irreducible water saturation and S_{rg} is the water saturation at irreducible gas saturation (air or steam).

2.3.10.10 Relative permeabilities in fractures: The Honarpour-Diomampo model

Diomampo *et al.* (2002) studied in their experiments the mechanism of two-phase flow through fractures, using nitrogen-liquid water and steam-liquid water on both smooth and rough parallel plates to determine the governing flow mechanisms. For both smooth-and rough-walled fractures, a clear relationship between relative permeability and saturation was observed. There is considerable phase interference in flow through fractures because the sum of the relative permeabilities of gas and liquid is lower than one. The experiments revealed the unsteady nature of flow through fractures. This is consistent with the observed flow mechanism where the gas and water compete in establishing pathways through the fracture (Li and Horne 2005). The calculated relative permeability curves follow Corey-type behavior. The data for both imbibition and drainage experiments were fitted separately with the Honarpour *et al.* (1982) expression:

$$k_{rw} = k_{rw0} \left(\frac{S_w - S_{rw}}{1 - S_{rw} - S_{rg}} \right)^{n_w}, \quad k_{rg} = k_{rg0} \left(\frac{1 - S_w - S_{rg}}{1 - S_{rw} - S_{rg}} \right)^{n_g} \quad (2.173)$$

where: $k_{rw0} = k_{rw}(S_{wi})$, $k_{rg0} = k_{rg}(S_{rw})$ for drainage
 $k_{rw0} = k_{rw}(S_{rg})$, $k_{rg0} = k_{rg}(S_{wi})$ for imbibition

The term S_{wi} is the initial water saturation for drainage. In both functions, the fitted Honarpour curves give good representation of the trend of relative permeability data with saturation. The fitted curves have different exponents for the Honarpour expression for imbibition and drainage (Table 2.5).

Steam-water relative permeability can be calculated from capillary pressure. However this technique still requires measurement of capillary pressure. In this study, a semi-analytical model

Table 2.5. Honarpour fit parameters for smooth-walled (*s*) and for rough-walled (*r*) fracture experiments (data adapted from Diomampo *et al.* 2002).

Parameter	Drainage (<i>s</i>)	Imbibition (<i>s</i>)	Drainage (<i>r</i>)	Imbibition (<i>r</i>)
S_{rw}	0.81	0.81	0.132	0.141
S_{rg}	0	0.321	0	0.51
k_{rw0}	1	0.564	1	0.27
k_{rg0}	0.509	0.509	0.274	0.1
n_w	2.27	4.57	1.75	1.2
n_g	3.59	1.92	2.53	0.52

was developed to infer relative permeability from resistivity data. Although it would still be necessary to conduct experimental measurements of resistivity, these are easier than measuring capillary pressure (Li and Horne 2005). Gas and water relative permeability can be effectively modeled in many porous media using the modified Corey (1954) equations (Byrnes 2003):

$$k_{rg} = \left(1 - \frac{(S_w - S_{wgc})}{(1 - S_{gc} - S_{wgc})}\right)^p \left(1 - \frac{(S_w - S_{wgc})}{(1 - S_{wgc})}\right)^q, \quad k_{rw} = \left(\frac{S_w - S_{wc}}{1 - S_{wc}}\right)^r$$

for $k = 1$ mD: $S_{gc} = 0.15$, $S_{wgc} = 0.16$, $S_{gc} = 0.1$, $p = 1.7$, $q = 2$, $r \approx p$ (2.174)

where S_w is water saturation, S_{gc} is the critical gas saturation (expressed as fraction gas saturation), S_{wgc} is the critical water saturation for gas (expressed as fraction water saturation), S_{wc} is the critical water saturation, and p , q , and r are exponents reflecting topology and size distribution of pores. Byrnes (2003) describes it like this:

- Critical water saturation can be operationally defined as the saturation at which water is immobile or water flow is negligible on the time scale of importance for the evaluation of flow properties. Critical water saturation is also often experimentally defined as the saturation at which the ratio of the non-wetting phase flow to water (wetting phase) flow is greater than 1000 (i.e., water flow represents less than 0.001 of total flow). Critical gas saturation (S_{gc}) represents the saturation below which the gas phase is discontinuous and therefore does not flow. Experimentally this is defined as the saturation at which a threshold pressure achieves first detectable gas flow.

In rocks with permeability $k > 10$ mD the measurement and operational definitions of S_{gc} and S_{wc} can be clearly defined within a range of 1%. However, as permeability decreases and rocks move more into the transition zone interval of the capillary pressure curve, the nature of both becomes more complex with implications for modeling using relative permeability. Further details and figures for several cases using equation (2.174) can be found in Byrnes (2003).

2.3.11 *Observed effects of dissolved salts (NaCl) and non-condensable gases (CO₂)*

We must consider that in nature, real geothermal systems or cold aquifers are multi-component systems formed by water, and numerous dissolved chemical species such as dissolved salts and gases. The concentrations of these chemical species can be very variable in different aquifers and may vary strongly between different geothermal reservoirs or even within the same reservoir. As an example, Tables 2.6 and 2.7 show the main chemical species in the extracted fluid from the Los Azufres geothermal reservoir (Mexico).

The main effect of salts dissolved in water is to increase its density. Seawater, geothermal brine and aquifer water are denser than freshwater, which reaches a maximum density of 1000 kg/m³ at a temperature of 4°C. The concentration of dissolved salts in water is usually given in physical

Table 2.6. Chemical composition of the extracted fluid of the Los Azufres geothermal field (Mexico).

	Cl	Na	HCO ₃	SiO ₂	SO ₄	B	NH ₄	K	Li	Rb	Cs	Ca	As
mg/kg	2581	1500	74.3	1008	520	237	580	4188	260	50	20	186	200

units relating mass of salt to volume of fluid, for example milligrams per liter (mg/L), or grams per cubic meter (g/m^3). Mass fractions are also commonly used in reservoir engineering, relating mass of dissolved salt to mass of fluid. In this case the units are dimensionless [ad]: for example parts per hundred (% by weight), parts per thousand (‰ by weight), parts per million (ppm or mg/kg if we use SI units) or parts per billion (ppb or $\mu\text{g/kg}$ if we use SI units). The density of fresh water is a reference value equal to 1000 kg/m^3 ; in this case $1 \text{ mg/L} = 1 \text{ ppm}$ (or $= 1 \text{ mg/kg}$), otherwise we must use the relation $C [\text{mg/kg}] = C [\text{mg/L}] \times 1/\rho_f [\text{l/kg}]$ for converting the mass and volume related concentration units.

There is a classification of water, which depends on the concentration on dissolved chemical species, e.g. salts: fresh water ($< 1000 \text{ mg/L}$), brackish water ($1000\text{--}10,000 \text{ mg/L}$), saline water ($\approx 10,000\text{--}100,000 \text{ mg/L}$), brine ($> 100,000 \text{ mg/L}$) (Holzbecher 1998). At the surface of the ocean, seawater has an average density of 1025 kg/m^3 and a salinity of about 3.5% by weight or 35 g/kg or $35,000 \text{ mg/kg}$.

In the following, we will reduce this complex chemical spectrum to only two representative compounds, CO_2 and dissolved NaCl. For the fluid density dependence on salinity, we consider the following correlations, which are appropriate for aquifers at 20°C but may also be applicable approximately to low-enthalpy geothermal systems (adapted from Holzbecher 1998).

The water density as a function of the concentration of dissolved salts is:

$$\rho = \rho_0 e^{0.6923C_m} \quad (2.175)$$

where ρ_0 is the density of fresh water and C_m is the mass fraction of dissolved NaCl in [kg/kg]. For example, using this formula, the corresponding average concentration of seawater is $C_m = 0.0357$ [kg/kg]. The density of a mixture of two fluids with respective densities ρ_0 and ρ_1 is approximated by the following formula:

$$\rho(C_m) = \rho_0 \left(\frac{\rho_1}{\rho_0} \right)^{C_m} \quad (2.176)$$

where C_m is the mass fraction of NaCl [kg/kg] of equation (2.175) dissolved in the fluid ρ_1 . This correlation is valid in the interval $0 \leq C_m \leq 0.26$, which is the solubility limit of NaCl at temperature of 20°C and is valid for a large interval of pressures [0.1, 10] MPa.

A correlation of water density in terms of temperature [$^\circ\text{C}$] and C_m [kg/kg] is given by the following equation (Holzbecher 1998):

$$\rho(T, C_m) = \rho_0(1.0 + 0.805 C_m - (T + 220.0 C_m - 4.0)^2 \cdot 6.5 \times 10^{-6}) \quad (2.177)$$

The steam phase at volcanic reservoirs has a heterogeneous composition, showing a wide range of NCG concentrations. For example, the steam phase of the fluids from Los Azufres geothermal field, which is influenced by volcanic processes, contain 1–9% of total gas (by weight). Principal gases are CO_2 , H_2S , NH_3 , CH_4 , O_2 , H_2 , N_2 , He and Ar (Table 2.7). Carbon dioxide is the major gas constituent found in the field, representing between 70% and 99% of total NCG weight (Suárez and Samaniego 2003). H_2S is the second most important gas, varying between 0.2 and 13% in the total weight.

Table 2.7. Extracted gases (% in weight) at the Los Azufres geothermal field.

	CO ₂	H ₂ S	NH ₃	He	H ₂	Ar	N ₂	O ₂	CH ₄
Weight%	96.83	2.279	0.189	0.0002	0.0102	0.01	0.0654	0	0.0254

To take into account the non-condensable gases in the mass and energy-balance equations it is necessary to include extra components in equations (4.95) and (4.101) described in chapter 4. The main effect of CO₂ is that its partial pressure augments the total pressure of the geothermal fluid because it is present in both the liquid and the steam phases. It is well known that NCG diminish the efficiency of the turbine in geothermal power plants, reducing notably both the condensation and the global heat transfer coefficients. This combined effect causes the efficiency of the geothermal power cycle to decrease. Therefore, the effect of non-condensable gases in geothermal reservoirs is an important subject. However, its detailed discussion goes beyond the introductory scope of this book. The interested reader may consult other sources in the specialized literature (e.g., Kestin 1980, Pruess 2003).

CHAPTER 3

Special properties of heterogeneous aquifers

“Unfortunately, soils [and rocks] are made by nature and not by man, and the products of nature are always complex... As soon as we pass from steel and concrete to earth, the omnipotence of theory ceases to exist. Natural soil [rock] is never uniform. Its properties change from point to point while our knowledge of its properties are limited to those few spots at which the samples have been collected. In soil [rock] mechanics the accuracy of computed results never exceeds that of a crude estimate, and the principal function of theory consists in teaching us what and how to observe in the field.”

Karl Terzaghi (1883–1963)*

3.1 THE PROBLEM OF HETEROGENEITY IN AQUIFERS

The thermal, mechanical, electrical and transport properties of rocks are determined by their mineralogical composition, chemistry and texture. Several experimental studies have demonstrated correlations between the simple petrology and chemical composition of rocks and some of their petrophysical properties (Contreras *et al.* 1994, Viggiano and Gutiérrez 1988). The interrelationships between chemical characteristics and petrophysical properties of rocks are extremely complex, poorly understood and hard to model, from both a theoretical and practical point of view. Heterogeneities in the fractured matrix allow us to consider the mechanisms of interaction among different matrix blocks, fractures, microfractures and faults with different porosities and permeabilities. The effective treatment of heterogeneities is achieved using special averages at the contact interfaces.

During the geological development of a reservoir, the primary parameters acquired initial values at different moments in its formation. Later, unpredictable and aleatory physical processes altered these primary values. In this way porosity, permeability, modules of elasticity, thermal conductivity, density and mobility of the fluid became heterogeneous. The numerical simulation of the coupled heat and mass flow in multiple porosity systems that we call $M\varphi-Nk$ reservoirs (M -porosities, N -permeabilities), needs to average highly variable physical parameters, at the boundaries between different media. A crucial decision is which type of averaging formula should be used to represent the global transport processes inside heterogeneous matrix blocks with fractures and microfractures. This heterogeneity affects the mass and energy flow and the thermodynamic evolution of the system. The averaging process should represent the fluid crossing different geologic areas of the reservoir, so the averages have a decisive influence on the numeric results of reservoir simulation. In this section, several formulae for calculating the averages of petrophysical parameters are introduced. These formulae are useful in all techniques of reservoir simulation by any numerical method. The choice of a particular average is dependent on experience, combining the findings of laboratory tests and studies in the field (Suárez and Samaniego 1999, Suárez 2002).

* Source: D. Goodman: *Karl Terzaghi, the Engineer as an Artist*. ASCE Press, 1999.

3.2 THE CONCEPT OF MULTIPLE POROSITY IN HETEROGENEOUS AQUIFERS

Any medium exhibiting finite discontinuities in the distribution of its porosities should be considered as a multiple porosity or *multiporous* system. Microscopic observation of thin core sheets demonstrates the existence of microfractures connected to the matrix and to the fractured net (Fig. 2.1). These microfractures form another continuum, with intermediate permeabilities, overlapping the previous ones (Fig. 3.1). In this way the notion of multiple porosity-permeability in heterogeneous reservoirs arises ($M\varphi-Nk$ reservoirs). For example, when two different types of matrix blocks are detected in a fractured, faulted medium, the transfer would be: matrix 1 \rightarrow matrix 2 \rightarrow microfractures \rightarrow fracture \rightarrow fault. Under the concept of multiple porosity $M(>2)$ porous continuous media interact with each other. Each medium has its own parameters and its own interporosity flow, which can be stationary, pseudo-stationary or transitory. The saturating fluid may be non-isothermic, two-phase or multiphase and can contain multiple components. The classic models of double porosity can be classified as special cases of this general theoretical concept.

A complex system is one whose properties and behavior cannot be totally explained by the separate understanding of each of its components. The non-isothermal multiporosity idea is a more general concept applicable to all class reservoirs, forming the highest degree of complex systems in geothermal and petroleum reservoir engineering. The multiple porosity concept describes a global interconnected phenomenon that also produces multiple effects on other interdependent phenomena on a larger scale. However, it is not possible to define multiporosity in a unique way. Specific models of single, double, triple and multiple porosity-permeability are described below.

The simplest porous medium possesses a continuous distribution of a single type of empty space with only one permeability. This is a *single porous-single permeability* medium ($M = N = 1$). When the medium is fractured, the net of fractures adds a secondary porosity to the original porosity, breaking the porous medium into blocks. If the system is highly fractured with a high permeability matrix, its behavior is equivalent to that of a medium with a single permeability but two different porosities. If it is not possible to distinguish the permeability between the fractures and the matrix, this is a *double porosity-single permeability* medium ($M = 2, N = 1$). A fractured reservoir with low permeability but with high global storage, fits this model. The classical pattern where the matrix has high porosity and low permeability while the fractures have low porosity and high permeability corresponds to a *double porosity-double permeability* ($M = 2, N = 2$) medium.

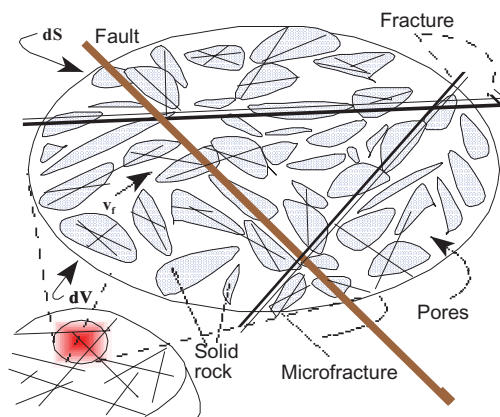


Figure 3.1. Differential volume dV and surface dS of a heterogeneous rock with different permeabilities: fault (10^{-11} m^2), matrix (10^{-18} m^2), fractures (10^{-13} m^2) and microfractures (10^{-15} m^2).

An immediate extension of the concept of double porosity is triple porosity. A reservoir that has fractures with homogeneous properties interacting with two types of separated matrix blocks, each with a different porosity but similar permeability, is a medium of *triple porosity–double permeability* ($M = 3, N = 2$). This model occurs when a system with dominant fractures intercepts a less permeable net of fissures, nested inside a matrix with a different porosity. In this case the mechanism of flow is matrix \rightarrow fissures towards the fracture. The *triple porosity–triple permeability* model ($M = 3, N = 3$) is found when the rock has three different porosities and three different permeabilities. The case of volcanic geothermal reservoirs with matrix-microfracture-fracture-fault flow, corresponds to a *tetra porosity–tetra permeability* model ($M = 4, N = 4$). Finally, if the matrix is so heterogeneous that four or more porosities and permeabilities can be clearly distinguished, then five, six or more porosities and permeabilities may be identified in the same medium. To denote the characteristics of reservoirs in compact form, we use the notation $M\varphi-Nk$ (M -porosities, N -permeabilities).

3.3 THE TRIPLE POROSITY-PERMEABILITY CONCEPT IN GEOTHERMICS

The main characteristic of the classical double porosity (DP) model is the clear distinction between two types of flow: along the fractures and intergranularly inside the matrix. The DP model also supposes the existence of a transfer function describing the fluid exchange between both continua. Its general formulation allows the treatment of flow through the matrix blocks, along the fractures and at the contact boundaries between both media. However, the DP concept is insufficient to explain the behavior of volcanic geothermal reservoirs, traversed by large, open faults. Experimental observations show that the intensity of fracturing is higher near the fault than in the distal fractured net. There is a remarkable contrast in permeabilities between the matrix blocks, the fractures and the fault (Fig. 3.1).

The concept of *triple porosity-permeability* in geothermics (Suárez and Samaniego 1995), considers that the diffusivity of the geothermal fluid is larger in the conductive fault than in the fractured net, and larger in the fractures than in the matrix. The flow towards the exploitation wells occurs in such a way that the initial response in the extraction area is detected immediately in the fault, and then becomes apparent in the fractures and much later in the matrix blocks. The global permeability depends inversely on the distance from the fault. According to this concept, the three media: matrix, net of fractures and fault are considered as three interacting continua related through special interporosity transport functions, which depend on the form and size of the blocks, the intensity of fracturing, the distance to the fault and on their mutual communication.

3.4 AVERAGES OF PARAMETERS AT DIFFERENT INTERFACES

3.4.1 Permeability and thermal conductivity

To illustrate the averaging process we consider the discretization of Darcy's law using the finite volume method, described in section 5.4.1, where k is the absolute permeability of the porous rock in the X direction. Neglecting gravity and because of the continuity of the flowing mass when crossing the boundary S_{ni} (Fig. 5.11), the flow at each side of the interface between two finite volumes with nodal distance $d_{ni}(= d_n + d_i)$ is the same, but the density ρ , viscosity μ and pressure p are different. From equation (5.141) in the steady state case:

$$F_{ni} = \frac{Q_{ni}}{S_{ni}} = \rho_{ni} v_{ni} = -\frac{k\rho}{\mu} \frac{dp}{dx} \Rightarrow \frac{Q_{ni} d_{ni}}{k_{ni}} = -S_{ni} \int_{p_n}^{p_i} \frac{\rho}{\mu} dp = \int_0^{d_{ni}} \frac{Q_{ni}}{k} dx \quad (3.1)$$

We deduce that:

$$\begin{aligned} \int_0^{d_{ni}} \frac{Q_{ni}}{k} dx &= \int_0^{d_n} \frac{Q_{ni}}{k} dx + \int_{d_n}^{d_{ni}} \frac{Q_{ni}}{k} dx = Q_{ni} \left(\frac{1}{k_n} \int_0^{d_n} dx + \frac{1}{k_i} \int_{d_n}^{d_{ni}} dx \right) \\ &= Q_{ni} \left(\frac{d_n}{k_n} + \frac{d_i}{k_i} \right) = \frac{Q_{ni} d_{ni}}{k_{ni}} \Rightarrow k_{ni} = (d_n + d_i) \cdot \left(\frac{d_n}{k_n} + \frac{d_i}{k_i} \right)^{-1} \end{aligned} \quad (3.2)$$

where k_{ni} is the averaged permeability of the medium at the interface S_{ni} . Similarly, if k_{Tni} is the thermal conductivity at the same interface, the flow of heat is:

$$\begin{aligned} \frac{Q_{Tni}}{S_{ni}} = -k_{Tni} \frac{dT}{dx} &\Rightarrow \frac{Q_{Tni} d_{ni}}{k_{Tni}} = \int_0^{d_{ni}} \frac{Q_{Tni}}{k_T} dx = Q_{Tni} \left(\frac{d_n}{k_{Tn}} + \frac{d_i}{k_{Ti}} \right) \\ &\Rightarrow \frac{d_{ni}}{k_{Tni}} = \frac{d_n}{k_{Tn}} + \frac{d_i}{k_{Ti}} \end{aligned} \quad (3.3)$$

where k_{ni} and k_{Tni} are the effective permeability and effective thermal conductivity at the common interface S_{ni} separating the elements V_n and V_i . Both averages are based on the continuity hypothesis of the mass flow and of the heat flow when crossing that interface.

3.4.2 Special average for thermal conductivity in dry rock

Zierfuss and Van der Vliet (1956) measured the thermal conductivity of 50 samples from different rocks. They found that as porosity increases, thermal conductivity decreases. However, this tendency is altered by the influence of different permeabilities and densities of rocks with the same porosity. Anand *et al.* (1973), applying multiple regression analysis to 38 data sets, established the following relationships to predict the thermal conductivity of rocks using other properties:

$$F_e = \frac{1}{\varphi^c}, \quad k_{Ts} = 0.34\rho_r - 3.2\varphi + 0.53k^{0.1} + 0.013F_e - 0.031 \quad (a)$$

$$\text{Log}_{10}(F_e k_T)_{\text{water}} = 3.874 - 15.29\varphi + 31.84\varphi^2 - 27.00\varphi^3 \quad (b) \quad (3.4)$$

$$\text{Log}_{10}(F_e k_T)_{\text{oil}} = 3.840 - 15.75\varphi + 32.37\varphi^2 - 27.79\varphi^3 \quad (c)$$

where F_e is the electrical resistivity factor of the formation, which decreases when the size of the pores increases, and c is a cementation factor (≈ 2 in sandstones). The first correlation of (3.4) is valid for dry rock. The second and third correlations are valid for sandstones saturated with water and oil, respectively. Among the samples analyzed by the aforementioned authors, the thermal conductivity of 31 samples (82%) is reproduced by equations (3.4), with a margin of error of 15%. Porosity is the parameter that has the largest effect on these correlations.

3.4.3 Heat capacity of the rock-fluid system

The heat capacity per unit volume of porous rock saturated with two-phase fluid is evaluated by means of the specific heat coefficient at constant pressure. The following formula was adapted from Passmore and Archer (1985):

$$c_p = (1 - \varphi)\rho_r c_r + \varphi(S_l \rho_l c_l + S_v \rho_v c_v) \quad (3.5)$$

A useful formula for saturated rock with three components, i.e. oil, water and gas, is:

$$c_p = (1 - \varphi)\rho_r C_r + \varphi(S_o \rho_o c_o + S_l \rho_l c_l) + \varphi S_g \left(f_v S_g \rho_g + \frac{(1 - f_v)\rho_v L_v}{\Delta T} + \rho_v c_l \right) \quad (3.6)$$

This equation is valid for five components: rock (*r*), oil (*o*), liquid water (*l*), vapor (*v*) and non-condensable gas (*g*), where L_v is the latent heat of vaporization and f_v is the volumetric fraction of incondensable gas referred to the whole gaseous phase.

3.4.4 Linear Lagrange interpolation for densities

Using the classical formula of linear Lagrange interpolation, the interfacial average of the fluid density is:

$$\begin{aligned} \rho(x) &= \frac{\rho_0 x_1 - \rho_1 x_0}{x_1 - x_0} + \frac{\rho_1 - \rho_0}{x_1 - x_0} x \\ \Rightarrow \rho_{ni} &= \frac{\rho_n(d_n + d_i) - \rho_i \cdot 0 + (\rho_i - \rho_n)d_n}{d_n + d_i - 0} = \frac{\rho_n d_i + \rho_i d_n}{d_n + d_i} \end{aligned} \quad (3.7)$$

In general, any interpolation formula of higher order is a more sophisticated average that requires a larger number of data points around the interface S_{ni} .

3.5 AVERAGES FOR SYSTEMS WITH TWO AND THREE COMPONENTS: GENERAL MODELS OF MIXTURES

The rock-fluid system with two-phase flow is a compound of three components: solid, liquid and gas. A key question is how do parameters such as thermal conductivity act in these types of mixtures? For example, the effective thermal conductivity of rock depends on the relative amounts, distribution and geometric form of their constituents. Different types of minerals can form the matrix or rock solid phase, varying in grain size, and containing cracks and pores that can be saturated with liquid or gas (Contreras *et al.* 1994).

Some models for mixtures have strong physical and conceptual bases. Others are merely empirical relationships. Some expressions are mathematical analogies of particular models of mixtures with very wide application, adapted to estimate properties of multicomponent systems. The problem is complex and there is no unique form for solving it. The following models are proven averages for performing effective calculations in numerical modeling. Here, K_m represents any average physical property; the subindices *f*, *r*, *l* and *v* are for fluid, rock, liquid and vapor, respectively.

3.5.1 Parallel and serial models

$$\begin{aligned} \text{Parallel:} \quad & \text{1-Phase: } K_m = \varphi K_f + (1 - \varphi)K_r \\ & \text{2-Phases: } K_m = S_l \varphi K_l + S_v \varphi K_v + (1 - \varphi)K_r \end{aligned} \quad (3.8)$$

$$\begin{aligned} \text{Serial:} \quad & \text{1-Phase: } \frac{1}{K_m} = \frac{\varphi}{K_f} + \frac{(1 - \varphi)}{K_r} \\ & \text{2-Phases: } \frac{1}{K_m} = \frac{S_l \varphi}{K_l} + \frac{S_v \varphi}{K_v} + \frac{(1 - \varphi)}{K_r} \end{aligned} \quad (3.9)$$

3.5.2 *Geometrical model*

$$K_m = K_r^{(1-\varphi)} \cdot K_l^{S_l \varphi} \cdot K_v^{S_v \varphi} \quad (3.10)$$

3.5.3 *Model of Griethe*

$$K_m = K_l^\varphi \cdot K_r^{1-\varphi} \quad (3.11)$$

3.5.4 *Model of Budiansky*

$$\begin{aligned} \text{1-Phase: } \frac{1}{K_m} &= \frac{\varphi}{\frac{2K_m}{3} + \frac{K_f}{3}} + \frac{(1-\varphi)}{\frac{2K_m}{3} + \frac{K_r}{3}} \\ \text{2-Phases: } \frac{1}{K_m} &= \frac{S_l \varphi}{\frac{2K_m}{3} + \frac{K_l}{3}} + \frac{S_v \varphi}{\frac{2K_m}{3} + \frac{K_v}{3}} + \frac{(1-\varphi)}{\frac{2K_m}{3} + \frac{K_r}{3}} \end{aligned} \quad (3.12)$$

In both cases Budiansky's model can be solved exactly. For a single phase:

$$\begin{aligned} 2K_m^2 + [(3(1-\varphi) - 2)K_f + (3\varphi - 2)K_r]K_m - K_r K_f &= 0 \\ \Rightarrow K_m = \frac{-b \pm \sqrt{b^2 + 8K_r K_f}}{4}; \quad b = (3(1-\varphi) - 2)K_f + (3\varphi - 2)K_r \end{aligned} \quad (3.13)$$

The parameter b is usually a negative quantity ($K_r > K_f$) and one should only take the positive sign of the square root. For two phases and three components, the algebra provides a cubic equation for the implicit correlation of Budiansky whose solution is also classic:

$$\begin{aligned} K_m^3 + b K_m^2 + c K_m + d &= 0; \quad d = \frac{K_r K_l K_v}{4} \\ b &= \frac{6(1-\varphi)(K_l + K_v) + 6\varphi(S_l K_v + S_v K_l) + (6\varphi - 4)K_r - 4(K_l + K_v)}{4} \end{aligned} \quad (3.14)$$

$$4c = (1 - 3\varphi)K_l K_v + 3\varphi K_r (S_l K_v + S_v K_l) - 2K_r (K_l + K_v)$$

The root is given by:

$$\begin{aligned} K_m = X_2 &= -2\sqrt{Q} \cos\left(\frac{\theta + 2\pi}{3}\right) - \frac{b}{3} \\ Q &= \frac{b^2 - 3c}{9}, \quad R = \frac{2b^3 - 9bc + 27d}{54}, \quad \text{and: } \theta = \text{ArcCos}\left(\frac{R}{\sqrt{Q^3}}\right) \end{aligned} \quad (3.15)$$

3.5.5 *Model of Hashin-Shtrikman*

This very important model results from averaging the maximum and minimum thermal conductivities given by the following correlations:

$$\begin{aligned} \text{1-Phase: } K_{\max} &= K_r + \varphi \left[(K_f - K_r)^{-1} + \frac{1-\varphi}{3K_r} \right]^{-1} \\ K_{\min} &= K_f + (1-\varphi) \left[(K_r - K_f)^{-1} + \frac{\varphi}{3K_f} \right]^{-1} \end{aligned} \quad (3.16)$$

For two-phases:

$$\begin{aligned}
 K_{\max} &= K_r + \varphi \left[\left(S_l \left[(K_l - K_r)^{-1} + \frac{1}{3K_r} \right]^{-1} \right. \right. \\
 &\quad \left. \left. + S_v \left[(K_v - K_r)^{-1} + \frac{1}{3K_r} \right]^{-1} \right)^{-1} - \frac{\varphi}{3K_r} \right]^{-1} \\
 K_{\min} &= K_v + (1 - \varphi) \left[\left(\frac{\varphi S_l}{1 - \varphi} \left[(K_l - K_v)^{-1} + \frac{1}{3K_v} \right]^{-1} \right. \right. \\
 &\quad \left. \left. + \left[(K_r - K_v)^{-1} + \frac{1}{3K_v} \right]^{-1} \right)^{-1} - \frac{1 - \varphi}{3K_v} \right]^{-1}
 \end{aligned} \tag{3.17}$$

In both cases the average conductivity is:

$$K_m = \frac{K_{\max} + K_{\min}}{2} \tag{3.18}$$

3.5.6 Model of Brailsford-Major

$$A = (3\varphi_S - 1)K_r + (3\varphi - 1)K_f \Rightarrow K_m = \frac{1}{4} \left(A + \sqrt{A^2 + 8K_f K_r} \right) \tag{3.19}$$

3.5.7 Model of Waff

$$K_m = \frac{K_f K_r (1 - \varphi)^{\frac{2}{3}}}{K_r \sqrt{(1 - \varphi)} + K_f \varphi^{1/3}} + K_f \varphi^{\frac{2}{3}} \tag{3.20}$$

3.5.8 Model of Walsh-Decker

$$K_m = \frac{K_r K_f (3 + \varphi)}{\varphi K_r + 3K_f} \tag{3.21}$$

3.5.9 Model of Maxwell

$$K_m = K_l \frac{2\varphi K_l + (3 - 2\varphi)K_r}{(3 - \varphi)K_l + \varphi K_r} \tag{3.22}$$

3.5.10 Maxwell's dispersive model

$$K_m = K_r \left[\frac{2 \frac{K_r}{K_f} + 1 - 2\varphi \left(\frac{K_r}{K_f} - 1 \right)}{2 \frac{K_r}{K_f} + 1 + \varphi \left(\frac{K_r}{K_f} - 1 \right)} \right] \tag{3.23}$$

3.5.11 Model of Russel

$$K_m = K_l \frac{(1 - \varphi)^{\frac{2}{3}} + \frac{K_l}{K_r} (1 - (1 - \varphi)^{\frac{2}{3}})}{(1 - \varphi)^{\frac{2}{3}} - (1 - \varphi) + \frac{K_l}{K_r} (2 - \varphi - (1 - \varphi)^{\frac{2}{3}})} \quad (3.24)$$

3.6 SOME APPLICATIONS TO FIELD DATA

3.6.1 Application to data from rocks of the Los Azufres and Los Humeros geothermal fields (Mexico)

All of the previously described correlations may be applied for the creation of a database of averaged parameters (Table 3.1). The decision as to which type of average is best suited to tackle each particular problem depends on the subjective opinion of the user. This decision should be firmly supported by data from laboratory experiments and field studies. The series, parallel,

Table 3.1. Useful averages in a fractured reservoirs with multicomponent fluid¹⁾.

Averages for two components		Averages for 3 or more components	
Name	Formula	Name	Formula
Simple arithmetic average	$P_A = \frac{K_i + K_j}{2}$	General arithmetic average	$P_{gA} = \frac{1}{N} \sum_{j=1}^N K_j$
Simple geometric average	$P_G = \sqrt{K_i \times K_j}$	General geometric average	$P_{gG} = \frac{1}{N} \prod_{j=1}^N K_j$
Logarithmic average	$P_L = \frac{K_i - K_j}{\text{Ln } K_i - \text{Ln } K_j}$	Weighted geometric average	$P_{wG} = K_r^{\varphi_S} K_l^{S_l \varphi} K_v^{S_v \varphi}$ $\varphi_S = 1 - \varphi$
Continuity average	$\frac{d_i + d_j}{P_C} = \frac{d_i}{K_i} + \frac{d_j}{K_j}$	Parallel average	$P_p = \varphi_S K_r + S_l \varphi K_l + S_v \varphi K_v$
Linear Lagrange average	$P_{L1} = \frac{d_j K_i + d_i K_j}{d_i + d_j}$	Serial average	$\frac{1}{P_S} = \frac{\varphi_S}{K_r} + \frac{\varphi S_l}{K_l} + \frac{\varphi S_v}{K_v}$
Simple weighted average $0 \leq \theta_i \leq 1$	$P_w = (1 - \theta) K_i + \theta K_j$	General weighted average $0 \leq \theta_i \leq 1$	$P_{wA} = \sum_{i=1}^N \theta_i K_i; \quad \sum_{i=1}^N \theta_i = 1$
Budiansky's average 2D ²⁾	$P_{B1} = \frac{-b + \sqrt{b^2 + 8K_i K_j}}{4}$	Budiansky's average 3D ²⁾	$P_{B2} = K_m$
2D Hashin-Shtrikman ²⁾	$P_{HS} = \frac{K_{\max} + K_{\min}}{2}$	3D Hashin-Shtrikman ²⁾	$P_{HS2} = \frac{K_{\max} + K_{\min}}{2}$

¹⁾ Letter *K* represents any parameter of the reservoir, *S* is saturation, φ is porosity (the volumetric fraction of the component). Subindices *i, j*, represent two different zones (Fig. 5.11); (*d_i + d_j*) is the distance between the centers of *V_i* and *V_j*.

²⁾ The formulae of Budiansky (Pritchett 1995) are given by the equations (3.12)–(3.15); those of Hashin and Shtrikman (1962) are given by the equations (3.16)–(3.18).

harmonic and arithmetic averages provide the general form of the equations to calculate any average in these systems. The probability that the phases are in series or in parallel is the same in most of the systems studied. The weighted geometric average gives intermediate values of the effective parameter. For any value of the involved parameters, the following inequality is always valid between geometric (P_G), linear (P_L) and arithmetic (P_A) averages: $P_G < P_L < P_A$. If the distances d_i and d_j are similar, then the continuity average $P_C < P_G < P_L < P_A$ (Table 3.1).

We show results with different averages using data from the Los Azufres, Mexico geothermal reservoir. This fractured reservoir contains three-component fluid: two-phase water, liquid with dissolved salts and vapor with carbon dioxide. The numerical examples illustrate that the correct computation of the parameters at the interfaces V_n/V_i is critical to obtain precision in modeling with any numerical method. This influence can be as decisive as the relative permeabilities or the capillary pressure correlations. The general theory is illustrated with simple averages and some generalizations from Table 3.1. In some cases, the general relationships among different media depend on the distances between both regions (Figs. 3.1 and 5.11) and on the numeric values of the petrophysical parameters.

In 1985, several petrophysical parameters were measured in 24 cores from 17 wells of the Los Azufres, Mexico geothermal field (Table 3.2). Measurements of thermal and mechanical

Table 3.2. Primary parameters of the reservoir for the mass and energy flows.

Parameter ¹⁾	Rock (1-phase, liquid)	Fractured zone (2-phases liquid + vapor)	Component type	k_T (W/m ² /°C)
Distance (m)	10	2	Rock	3
Permeability (m ²)	1.0×10^{-15}	1.0×10^{-12}	Liquid	0.67
Fluid density (kg/m ³)	780	400	Steam	0.043
Mobility (m · s/kg)	503	5600	Gas (carbon dioxide)	0.02
Pressure (MPa)	6.0	5.0	Gas saturation	50%
Temperature (°C)	264	263.9	Liquid saturation	50%

¹⁾ The primary numerical values for mobility $\eta = k_r/\mu$, are: $k_{rl} = 0.0504$, $\mu_l = 99.85 \times 10^{-6}$ kg/m/s for the liquid phase, and $k_{rvl} = 0.1939$, $\mu_s = 18.13 \times 10^{-6}$ kg/m/s for the vapor phase. k_r is relative permeability, μ is fluid dynamic viscosity.

Table 3.3. Calculated averages for some parameters at the boundary between two zones.

Parameter	Average					
	P_C	P_G	P_L	P_A	P_{L1}	P_W
Permeability (m ²)	1.2×10^{-15}	3.2×10^{-14}	1.5×10^{-13}	5.0×10^{-13}	8.3×10^{-13}	1.0×10^{-12}
Fluid density (kg/m ³)	673	559	569	590	463	527
Mobility (m · s/kg)	593	1678	2115	3052	4750	3901
Porosity (ad)	0.06	0.11	0.12	0.15	0.22	0.23
Thermal cond. (W/m ² /°C)	P_{gA}	P_{gG}	P_{wG}	P_p	P_s	P_{wA}
Two components	1.84	1.42	2.22	2.53	1.77	2.74
Three components	1.24	0.44	1.69	2.47	0.37	2.41

Table 3.4. Some petrophysical properties of a $M\varphi-N_k$ reservoir¹⁾.

Well	Depth (m)	φ (%)	ρ (kg/m ³)	k (mD)	k_T (W/m ² °C)	c_p (J/kg/°C)
H-18	1750–1753	14.7	2340	0.005	2.42	921.1
H-02	616–619	19.7	2160	0.02	1.54	1046.7
H-19	1769–1771	11.5	2460	0.15	1.91	1172.3
H-26	1810–1813	4.5	2670	1.87	1.95	1004.8
H-24	2844–2847	12.7	2450	3.83	1.62	1046.7
Az-33	1350	12	2355	247.6	1.93	1165
H-28	1200	12.3	2430	101.3×10^3	1.99	1069

¹⁾ The petrophysical data were measured in liquid saturated cores ($p = 10$ MPa, $T = 25^\circ\text{C}$) using a Terra-Tek device in the rock mechanics laboratory of the Mexican Institute of Electrical Research—IEE (Contreras *et al.* 1990). The permeabilities in the last two rows of the table come from pressure tests. The letter H-* denotes wells of the Los Humeros, while well Az-33 is in the Los Azufres reservoir.

properties were reported (Contreras *et al.* 1988): rock density, porosity (total and effective), absolute permeability, rock compressibility, Young and Poisson modules, specific heat, diffusivity and thermal conductivity. Table 3.3 contains the primary measurements and Table 3.4 shows some averages calculated using these field data.

In Table 3.3 the parameter θ is equal to 1 for permeability, 2/3 for density and mobility, and 8/9 for porosity and thermal conductivity with 2 components, rock and liquid. The three components are rock, gas and liquid; the units are the same as those used in Table 3.2. It is noteworthy that each formula gives very different results using the same data. For example, the permeability varies from 1 mD for porous simple rock to 1 Darcy for completely fractured rock.

3.7 DISCONTINUITIES OF PARAMETERS WHEN CROSSING HETEROGENEOUS INTERFACES

In multiporosity and multipermeability media, quantification of the fluid passing from one medium to another, e.g. from the matrix to fractures, is a highly complex problem. To simplify this analysis we assume a stationary flow of an isothermic liquid between medium V_i and medium V_j through their common interface S_{ij} (Fig. 5.11). The parameter used to represent the interaction between both media is q_{ij} , the mass of fluid crossing each second, per unit volume of fractured rock. Darcy's law without gravity becomes:

$$v_x = -\frac{k_{ij}}{\mu_{ij}} \frac{dp_{ij}}{dx} \Rightarrow \frac{\rho_{ij} v_x}{\Delta x} \cong -\frac{\rho_{ij} k_{ij}}{\mu_{ij} \Delta x} \frac{\Delta p}{\Delta x} \quad (3.25)$$

$$\text{if: } \alpha_{ij} = \frac{k_{ij}}{(\Delta x)^2} \Rightarrow q_{ij} = \alpha_{ij} \frac{\rho_{ij}(p_i - p_j)}{\mu_{ij}}$$

where ρ_{ij} is the fluid density and μ_{ij} viscosity, both functions can be constant when crossing S_{ij} , or they can represent averages between both media. $\Delta x = d_i + d_j$ represents the distance between one point inside the medium i at pressure p_i and another point in medium j at pressure p_j . This distance is a critical unknown variable, because a very small value can lead to discontinuities in the flow parameters. In general α_{ij} is a dimensionless constant that only depends on the geometry of the boundary S_{ij} . For example if medium i is a matrix block and medium j is a fracture, then the effective permeability k_{ij} should be interpreted as an average at the block-fracture boundary. Equation (3.25) is the basic model of Barenblatt *et al.* (1960) and also implicitly contains the discretization of the finite volume method for stationary flow (see chapter 5). If there is no pressure difference, there is no flow and $q_{ij} = 0$. If $q_{ij} > 0$ is constant, then we can calculate the

pressure in either of the two media. For example, if p_i is known:

$$p_j = p_i - \frac{\mu_{ij} q_{ij}}{\rho_{ij} \alpha_{ij}} \quad (3.26)$$

Let us examine what happens when k_{ij} is obtained from different averages in a tetra porosity medium using real data from the Los Humeros geothermal field (Suárez 1995, Table 3.3).

If the fluid is homogeneous and independent of pressure, then ρ_{ij} and μ_{ij} are constants. If the fluid suffers thermodynamic changes from one medium to the next, then the same parameters are discontinuous when crossing the interface and equation (3.26) is no longer valid. Let us compare k_{ij} values obtained with different averages. Typical data from the Los Humeros geothermal field are: $p_i = 12$ MPa, $T = 320^\circ\text{C}$, $\rho_i = 669.3$ kg/m³, $\mu_i = 78.7 \times 10^{-6}$ Pa · s, and the enthalpy corresponds to compressed liquid: $h_i = 1460.9$ kJ/kg; $q_{ij} = 0.03$ kg/s/m³ (Suárez 1995). Let $\Delta x = 1$ m be the distance previously defined. In this case, medium i is a matrix block with microfractures, with $k_i \approx 10^{-15}$ m²; medium j is an intensely fractured zone close to a fault, with $k_j \approx 10^{-12}$ m². Using equation (3.26) and the formulae from Table 3.1, we obtain the results shown in Table 3.5.

Table 3.5. Values of the interporosity flow at the interface S_{ni} .

Formula	k_{ni} (m ²)	β_F/k_{ni} (MPa)	p_i (MPa)
P _{BI} ¹⁾	1.03×10^{-15}	3.422	8.58
P _C	2.00×10^{-15}	1.764	10.24
P _{HS}	4.36×10^{-15}	0.809	11.19
P _G	3.16×10^{-14}	0.112	11.89
P _L	1.45×10^{-13}	0.024	11.98
P _W	6.67×10^{-13}	0.005	11.995

¹⁾ Note: With Budiansky's formula we assume a volumetric fraction of fractures equal to 1%, $\beta_F = q_{ni} \mu / \rho$.

Table 3.6. Some petrophysical parameters from the Cerritos Colorados (La Primavera) geothermal field (adapted from data of JICA 1989 and from García *et al.* 1991¹⁾).

Well	Depth (m)	φ (%)	ρ (kg/m ³)	k_T (W/m/°C)	c_p (J/kg/°C)	δ_T (10 ⁻⁶ m ² /s)
Pr-01	93	19.2	<u>2170</u> /1980	1.28	—	—
Pr-01	912	21.1	<u>2120</u> /1910	1.09	—	—
Pr-02	351	3.6	<u>2340</u> /2300	2.03	—	—
Pr-02	670	19.4	<u>1840</u> /1650	0.64	—	—
Pr-02	902	25.8	<u>2120</u> /1860	0.89	—	—
Pr-02	1361	14.7	<u>2260</u> /2110	1.37	—	—
Pr-02 ¹⁾	1358	13.7	<u>2056</u> /2218	<u>2.37</u> /1.53	<u>1.25</u> /0.97	<u>0.92</u> /0.71
Pr-04	301	8.3	<u>2300</u> /2220	1.78	—	—
Pr-05	201	5.1	<u>2260</u> /2210	1.87	—	—
Pr-05	431	3.2	<u>2210</u> /2170	1.74	—	—
Pr-11 ¹⁾	1717	5.6	<u>2605</u> /2712	<u>2.77</u> /1.98	<u>1.00</u> /0.73	<u>1.06</u> /1.00
Pr-12 ¹⁾	2300	5.6	<u>2562</u> /2647	<u>2.97</u> /2.51	<u>1.09</u> /1.03	<u>1.06</u> /0.92
Pr-13 ¹⁾	2000	5.6	<u>2477</u> /2554	<u>2.34</u> /1.85	<u>1.11</u> /0.88	<u>1.11</u> /0.82
RC-1	1717	23.1	<u>2230</u> /2000	1.08	—	—
RC-1	2300	12.4	<u>2540</u> /2410	1.38	—	—
RC-1	1502	14.8	<u>2280</u> /2140	1.35	—	—

k_T is thermal conductivity, c_p is rock specific heat, δ_T is thermal diffusivity. The underlined numbers indicate that they were obtained in saturated rock.

From Table 3.5 it becomes clear that the thermodynamic conditions of volume V_j are extremely sensitive to the type of average used to calculate the pressure p_j . Assuming isothermal flow when the fluid is crossing the interface, the first and second pressure falloffs correspond to an abrupt phase change. The liquid becomes 100% steam with an enthalpy $h_j = 2710$ kJ/kg and $\rho_j = 63.6$ kg/m³, its viscosity $\mu_j = 20.9 \times 10^{-6}$ Pa · s. If the flow is non-isothermal, the Hashin-Shtrikman formula shows that only a slight decrement in the fluid temperature ($\sim 0.6^\circ\text{C}$) is required to obtain two-phase conditions, because at 11.2 MPa, the saturation temperature is 319.4°C. Both thermodynamic states are frequently observed at Los Humeros geothermal field (Suárez 1995).

As previously mentioned, if the fluid is homogeneous then ρ_{ij} and μ_{ij} are constants. However, if the fluid pressure suffers a sharp falloff when crossing the interface between media then both parameters become discontinuous at the common boundary S_{ij} . In this case, equation (3.26) is only valid if appropriate averages are included for ρ_{ij} and μ_{ij} . Equation (3.25) also needs to incorporate a different expression for the discontinuous permeability, which is a function of a very small distance $(x - x_0)$, where x_0 is the exact position of the common interface S_{ij} . In terms of distributions or generalized functions, its mathematical representation in one dimension is:

$$\begin{aligned} k_{ij}(x) &= (k_j - k_i)H(x - x_0) + k_i \\ H(x - x_0) &= 1, \quad \text{if } x \geq x_0; \quad H(x - x_0) = 0, \quad \text{if } x < x_0 \\ \text{its derivative is: } \frac{dH(x_0)}{dx} &= \delta(x_0) \end{aligned} \quad (3.27)$$

where $H(x)$ is the Heaviside distribution. The data presented in Table 3.4 are an example of the discontinuous nature of permeability in a $M\varphi-N_k$ real reservoir. In the case where the basic equations require the derivation of a discontinuous permeability, it becomes necessary to explicitly use the Dirac distribution $\delta(x)$ each time the permeability changes. This description proves that the multiple porosity and permeability model provides flexibility and a solid theoretical-practical framework to improve both, the analysis of pressure tests and the numerical simulation of heterogeneous reservoirs.

3.8 EXAMPLES OF HETEROGENEOUS NON-ISOTHERMAL AQUIFERS—PETROPHYSICAL PROPERTIES IN MEXICAN GEOTHERMAL FIELDS

Over a number of years, measurements have been made of the petrophysical properties of cores extracted from wells of the Los Azufres (Michoacán), Los Humeros (Puebla) and Cerritos Colorados (formerly La Primavera, Jalisco) geothermal reservoirs in Mexico. A number of parameters were measured: rock density, effective porosity, thermal conductivity, compressibility and specific heat. To illustrate the physical parameters described above, these data are presented in Tables 3.6, 3.7 and 3.8 following descriptions of cores from these non-isothermal aquifers (for more details about these geothermal reservoirs see section 9.1).

3.8.1 *Cerritos Colorados (La Primavera), Jalisco*

The cores in this geothermal field were collected from seven wells. The effective porosity of the cores was variable, but most had high values for this parameter. Thermal conductivity is proportional to density. Thus highly dense rocks with low porosity have high thermal conductivity. In general, high porosity ($>10\%$) was observed in rocks located above a depth of 1000 m, with few exceptions. Below a depth of 1500 m the measured effective porosities were generally lower with an average value of 6%.

Diffusivity, thermal conductivity and specific heat were measured in four different cores (Table 3.6). Measurements were made in both, dry and water-saturated rock at pressure and

temperature at atmospheric conditions (0.1 MPa and 25°C). The higher values of thermal conductivity were recorded in cores from deeper parts of the reservoir, exhibiting larger rock compactation and smaller porosity. The rock thermal diffusivity values, in dry and saturated rock, were very close to 10^{-6} m²/s; rock specific heat values were around 1 J/kg/°C (Table 3.6).

General characteristics of Cerritos Colorados (La Primavera) geothermal reservoir:

Average reservoir pressure = 12.0 MPa	Average temperature = 304°C
Initial natural state = compressed liquid	Maximum temperature = 355°C
Electric capacity = 125 MW _e	Minimum volume = 6 km ³

3.8.2 Los Humeros, Puebla

In 1988 the petrophysical properties of cores taken from wells of the Los Humeros, Puebla geothermal field were examined (Contreras *et al.* 1990). Eighteen cores from 15 wells were divided into 39 fragments for analysis. The range of depth was 616 to 2848 m. The measured parameters were rock density, porosity, absolute permeability, compressibility, module of elasticity, specific heat, thermal conductivity and thermal diffusivity. These properties were measured in dry rock and in water-saturated rock at the ambient temperature of 25°C. The confining pressures were 10.0, 25.0 and 40.0 MPa. An important conclusion from these data is that the big problem at Los Humeros is not permeability nor porosity, but perhaps insufficient water which, for unknown reasons, the system was unable to retain in its geological past. From the geochemical data, it may be deduced that there is no longer a significant entrance of liquid. This system can be classified as a one with relatively little stored water.

Table 3.7 shows the measurements reported for saturated rock. Additionally, arithmetic averages of the effective measured values in the different fragments composing each core are given. The averaged absolute permeability is given separately for matrix blocks and fractures, respectively. The values correspond to arithmetic averages of the effective measured values in the different fragments composing each core.

Table 3.7. Some petrophysical parameters from the Los Humeros geothermal field (data adapted from Contreras *et al.* 1990).

Well	Depth (m)	φ (%)	ρ (kg/m ³)	k (mD)	k_T (W/m/°C)	c_p (J/kg/°C)
H-2	616–619	19.7	2160	0.019	1.54	1046.7
H-4	907–910	19.4	2240	0.086	1.96	1046.7
H-10	1469–1473	6.1	2620	0.026	1.61	1088.6
H-10	1825–1830	6.5	2550	0.008	2.29	963.0
H-15	1410–1412	5.2	2520	0.001	–	–
H-17	2227–2230	20.5	2600	–	2.74	1214.2
H-18	1750–1753	14.7	2340	0.005	2.42	921.1
H-19	1769–1771	11.5	2460	0.147	1.91	1172.3
H-20	1403–1406	15.8	2270	0.059	2.19	1046.7
H-22	663–666	18.1	2250	0.096	1.96	1088.6
H-22	1110–1113	9.1	2460	0.001	–	–
H-23	1924–1927	13.9	2370	1.252	1.82	1088.6
H-24	2297–2300	11.6	2370	0.070	2.14	1130.4
H-24	2844–2847	12.7	2450	3.829	1.62	1046.7
H-25	1710–1713	4.1	2760	0.001	–	–
H-26	1810–1813	4.5	2670	1.873	1.95	1004.8
H-27	1500–1503	10.1	2400	0.145	1.89	1130.4
H-29	1200–1203	18.4	2250	0.334	1.86	1046.7
Averages	–	12.3	2430	0.071 ^{m)} 2.318 ^{f)}	1.99	1069.0

^{m)} in matrix blocks.

^{f)} in fractures.

General characteristics of the Los Humeros geothermal reservoir:

Average reservoir pressure = 12.5 MPa	Average temperature = 310°C
Initial natural state = compressed liquid	Maximum temperature = 400°C
Estimated electric capacity = 75 MW _e	Minimum volume = 19 km ³

3.8.3 *Los Azufres, Michoacán*

Examination of the petrophysical properties of cores from the Los Azufres reservoir was performed in 1988. Data were collected for 24 cores from 18 wells. A single measurement of diffusivity and specific heat was made at well Az-19: thermal diffusivity is $0.66 \times 10^{-6} \text{ m}^2/\text{s}$, and specific heat = 1165 J/kg°C, at 250°C and 8.0 MPa. The measurements were performed in the Terra Tek laboratory of rock mechanics (Contreras *et al.* 1988). The petrophysical data are presented in Table 3.8.

General characteristics of Los Azufres geothermal reservoir:

Average reservoir pressure = 9.2 MPa (N), 10.0 MPa (S)
Average temperature = 301°C (N), 311°C (S)
Initial natural state = liquid (N), two-phase (S)
Maximum temperature = 360°C (S)
Estimated electric capacity = 300 MW _e (N), 200 MW _e (S)
Minimum volume = 49 km ³ (N), 23 km ³ (S)
(N and S stand for northern and southern part of Los Azufres geothermal field, respectively).

Table 3.8. Some petrophysical parameters from the Los Azufres geothermal field (data adapted from Contreras *et al.* 1988).

Well	Depth (m)	φ (%)	ρ (kg/m ³)	k (mD)	k_T (W/m/°C)	c_p (J/kg/°C)
Az-01	1825.0–1829.6	2.6	2720	0.0010	–	–
Az-03	600.0–605.5	14.8	2300	0.0035	1.68	–
Az-03	1874.0–1880.0	13.2	2560	0.1773	1.84	–
Az-03	2117.0–2119.7	2.1	2740	0.0013	1.99	–
Az-04	1000.0–1000.5	12.6	2430	0.0018	1.56	–
Az-05	600.0–600.5	23.2	2080	0.0017	1.17	–
Az-05	1160.0–1165.0	11.9	2380	0.1513	–	–
Az-08	800.0–804.0	7.8	2590	0.1235	2.34	–
Az-09	1705.0–1710.0	2.6	2660	2.224	–	–
Az-10	1004.0–1005.0	4.7	2660	0.0013	–	–
Az-19	1000.0–1005.0	15.5	2290	0.015	1.97	1165
Az-20	650.0–654.5	13.1	2260	0.0018	1.58	–
Az-20	1600.0–1603.0	4.7	2660	0.0015	1.71	–
Az-22	800.0–805.0	9.9	2450	0.0017	2.17	–
Az-25	671.0–675.0	14.5	2300	0.0018	1.75	–
Az-26	596.0–601.0	2.6	2610	0.0020	2.20	–
Az-26	1002.0–1007.0	10.4	2410	0.4010	1.55	–
Az-29	400.0–402.0	20.1	2070	0.0410	1.05	–
Az-29	2496.0–2496.2	0.7	2810	–	–	–
Az-41	600.0–605.0	16.3	2360	0.0013	–	–
Az-46	802.0–805.0	7.4	2510	–	–	–
Az-47	2962.0–2964.0	2.1	2760	0.0020	1.89	–
Az-48	2678.5–2684.5	1.0	2840	–	–	–
Az-50	1133.0–1136.0	8.9	2470	0.0100	1.52	–
Averages	–	9.3	2500	–	1.75	1165

CHAPTER 4

Fluid flow, heat and solute transport

“My first attempt to get at the transient problem was to take Thiem’s equation for confined conditions, apply it to the ground-water body with a free surface, and imagine that the water withdrawn from storage was miraculously conveyed to the outer rim of the Thiem’s cone and percolated from there to the well. I could then compute the volume of this Thiem’s cone, multiply it by the specific yield as I then called it, equate this to the rate of pumpage times the time and, of course, get an equation for the external radius of the Thiem’s cone in terms of time. This can be then substituted for the value of the external radius in Thiem’s equation. What you get is a transient equation which is the same as the present non-equilibrium equation, excepting that the well function of u contained only the log term. The constant and the long power series were missing.”

Henry Darcy (1803–1856)*

4.1 THE CONSERVATION OF MASS FOR FLUIDS

The total fluid mass in a porous volume can be computed using its density distribution, as it was done in section 2.1.3; in any differential porous volume dV_Φ :

$$\text{fluid mass in } dV_\Phi: dM_f = \rho_f dV_\Phi = \varphi \rho_f dV \quad \Rightarrow \quad M_f = \int_{V_B} \varphi \rho_f(\vec{r}, t) dV \quad (4.1)$$

$\vec{r} = (x, y, z)$ is the position vector of a fluid particle in $V_\Phi = \varphi V_B$; $t \geq 0$.

This equation presupposes that the pore fluid density depends on both space and time. If the mass of the fluid is conserved, it must remain constant under motion. Thus, the advective or total derivative (eq. 2.4) of the previous integral (4.1) is zero (eq. 2.6a):

$$\frac{DM_f}{Dt} = \frac{D}{Dt} \int_{V_B} \varphi \rho_f(\vec{r}, t) dV = \int_{V_B} \left(\frac{\partial(\varphi \rho_f)}{\partial t} + \vec{\nabla} \cdot (\varphi \rho_f \vec{v}_f) \right) dV = 0 \quad (4.2)$$

This equation is the integral form of the *principle of conservation of fluid mass* in a porous rock, valid for any part of the rock continuum. Vector $\vec{v}_f = (v_x, v_y, v_z)$ is the field velocity of the fluid particles. Figure 4.1 shows a schematic representation of a differential porous rock volume with bulk modulus V_B and pore volume V_Φ . The volume V_B can be any arbitrary portion of the porous rock. For example let V_B be a differential volume (REV) $V_B \approx dV$, consequently the continuous integrand of equation (4.2) must be identical to zero:

$$\frac{\partial(\varphi \rho_f)}{\partial t} + \vec{\nabla} \cdot (\varphi \rho_f \vec{v}_f) = \frac{D(\varphi \rho_f)}{Dt} + (\varphi \rho_f) \vec{\nabla} \cdot \vec{v}_f = 0 \quad (4.3)$$

* Source: Robert R. White and Alfred Clebsch: C.V. Theis: The Man and his Contributions to Hydrogeology. In: Selected Contributions to Ground-Water Hydrology by C.V. Theis, and a Review of his Life and Work, US Geological Survey, Water-Supply Paper 2415, 1994.

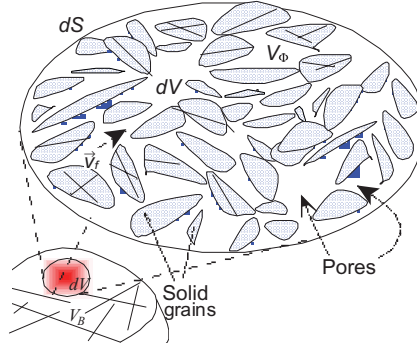


Figure 4.1. Differential volume dV and surface dS of a simplified porous rock; \vec{v}_f is the field velocity of the fluid particles.

Formula (4.3) is also known as the *continuity equation* for the fluid, which expresses the same *principle of conservation of mass* in the form of a partial differential equation. Under appropriate conditions, this law can be related directly to the volumetric deformation of the fluid (see section 2.1.3 for further details):

$$\begin{aligned} \frac{D(\varphi \rho_f)}{Dt} &= -(\varphi \rho_f) \vec{\nabla} \cdot \vec{v}_f \Rightarrow \vec{\nabla} \cdot \vec{v}_f = \frac{-1}{\varphi \rho_f} \frac{D(\varphi \rho_f)}{Dt}; \quad \text{but } V_f \rho_f = M_f \\ \Rightarrow \frac{-V_f}{\varphi M_f} \frac{D}{Dt} \left(\frac{\varphi M_f}{V_f} \right) &= -V_f \frac{D}{Dt} (V_f)^{-1} = V_f \left(V_f^{-2} \frac{D V_f}{Dt} \right) = \frac{1}{V_f} \left(\frac{D V_f}{Dt} \right) \end{aligned}$$

Therefore:

$$\text{with: } \varepsilon_f = \frac{\Delta V_f}{V_f} = \vec{\nabla} \cdot \vec{u}_f, \quad \vec{v}_f = \frac{\partial \vec{u}_f}{\partial t} \Rightarrow \vec{\nabla} \cdot \vec{v}_f = \frac{1}{V_f} \left(\frac{D V_f}{Dt} \right) = \frac{D \varepsilon_f}{Dt} \quad (4.4)$$

Hence, the divergence of the fluid velocity is equal to the rate of change of the fluid volume V_f . The variable ε_f is defined as the volumetric deformation (dilatation or compaction) of the fluid phase. If the fluid and the porosity do not change with time:

$$\frac{\partial(\varphi \rho_f)}{\partial t} = 0 \Rightarrow \vec{\nabla} \cdot (\varphi \rho_f \vec{v}_f) = 0 \quad (4.5)$$

If the fluid is incompressible and the porosity is constant:

$$\varphi \rho_f \vec{\nabla} \cdot (\vec{v}_f) = 0 \Rightarrow \vec{\nabla} \cdot \vec{v}_f = 0 \quad (4.6)$$

All previous equations are different forms of the same principle of conservation of fluid mass. The last formula (4.6) is the simplest form of the continuity equation. If there is extraction or injection (q_f) of fluid mass in one or more parts of the reservoir:

$$\begin{aligned} \int_{V_B} \left(\frac{\partial(\varphi \rho_f)}{\partial t} + \vec{\nabla} \cdot (\varphi \rho_f \vec{v}_f) \right) dV &= \int_{V_B} q_f(\vec{r}, t) dV \\ \Leftrightarrow \frac{\partial(\varphi \rho_f)}{\partial t} + \vec{\nabla} \cdot (\varphi \rho_f \vec{v}_f) &= q_f \quad \left[\frac{\text{kg}}{\text{m}^3 \text{s}} \right] \end{aligned} \quad (4.7)$$

where q_f represents the volumetric extraction of fluid from the reservoir (sink or well: $q_f < 0$) or the injection of fluid into the reservoir (source: $q_f > 0$) at the specific locations where the wells are drilled.

4.2 GENERAL MODEL OF FLUID FLOW: THE NAVIER-STOKES EQUATIONS

In 1822, Claude Louis Navier, a great French mathematician and engineer, introduced the influence of viscosity in fluid flow equations. In 1845, the British mathematician and physicist George Gabriel Stokes (Fig. 4.2) derived the same equations in a form similar to what we use today. Since then, the Navier-Stokes equations have been used to solve fluid flow problems in many branches of science and engineering. These equations have proven to be among “*the most challenging of all the partial differential equations that arise from physics*” (Brodkey 1967). They incorporate friction effects inside the fluid, so they are physically more realistic than the Euler equations used before 1822.

The Navier-Stokes equations describe the general flow of real, viscous fluids. They originate from the combination of the *fundamental law of fluid dynamics* and the *viscous forces in Newtonian fluids*. They are constructed in the following way. We first define the main functions and coefficients acting on the fluid: σ is the stress tensor, λ_f and μ_f are the coefficients of fluid viscosity, p is fluid pressure and \mathbf{D}_v is the symmetrical tensor of spatial changes of fluid velocity. The behavior of a Newtonian fluid is defined by the following equations (Germain 1973):

$$\begin{aligned} \text{tensorial form: } \sigma &= -p\mathbf{I} + \lambda_f D_{v_{kk}}\mathbf{I} + 2\mu_f \mathbf{D}_v \\ \text{components form: } \sigma_{ij} &= (-p + \lambda_f D_{v_{kk}})\delta_{ij} + 2\mu_f D_{v_{ij}} \\ D_{v_{ij}} &= \frac{1}{2} \left(\frac{\partial v_i}{\partial x_j} + \frac{\partial v_j}{\partial x_i} \right), \quad D_{v_{kk}} = \frac{\partial v_x}{\partial x} + \frac{\partial v_y}{\partial y} + \frac{\partial v_z}{\partial z} = \vec{\nabla} \cdot \vec{v}_f \end{aligned} \tag{4.8}$$

where λ_f is the viscosity of dilatation (or compression) and μ_f is the shear fluid dynamic viscosity. The composed coefficient $K_f = \lambda_f + 2\mu_f/3$ is the bulk modulus of the fluid or volumetric dynamic viscosity. The three coefficients have units of [1 Pa · s = 1 kg/m/s = 1 g/cm/s = 1 Poise]. The *fundamental law of fluid dynamics* is:

$$\rho_f \vec{a} = \vec{\nabla} \cdot \sigma + \vec{F} \tag{4.9}$$

where vector \vec{a} is the acceleration of fluid particles and \vec{F} is the external vectorial force applied to the fluid (see section 2.2.10). Computing the divergence of the tensor σ in equation (4.8) and

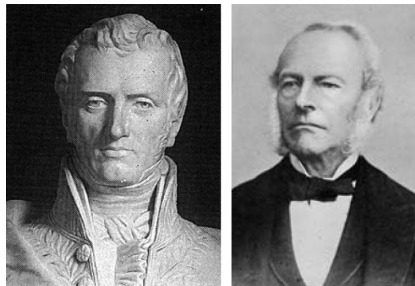


Figure 4.2. Left: scientist and engineer C. Navier (2/10/1785–8/21/1836). Right: Sir G. Stokes (8/13/1819–2/01/1903).

replacing the result in equation (4.9) we obtain:

$$\begin{aligned}
 &\text{tensorial form: } \rho_f \vec{a} = \vec{F} - \vec{\nabla} p + (\lambda_f + \mu_f) \vec{\nabla} (\vec{\nabla} \cdot \vec{v}_f) + \mu_f \Delta \vec{v}_f \\
 &\text{components form: } \rho_f a_i = F_i - \frac{\partial p}{\partial x_i} + (\lambda_f + \mu_f) \frac{\partial D_{vkk}}{\partial x_i} + \mu_f \frac{\partial^2 v_i}{\partial x_j^2} \quad (4.10) \\
 &\text{where the vector of the Laplacian operator is: } \Delta \vec{v}_f = \vec{\nabla} \cdot \vec{\nabla} \vec{v}_f = \nabla^2 \vec{v}_f
 \end{aligned}$$

This tensorial form is equivalent to a group of three scalar equations in component form ($i = 1, 2, 3$) and are known as the Navier-Stokes equations. They can be applied to the description of flow of any viscous fluid, in any medium, including the pores network of reservoir rocks. The shear dynamic viscosity μ_f measures the fluid resistance to flow. The dynamic viscosity of liquids decreases with pressure at constant temperature, but it depends less on pressure and much more on fluid temperature. For example, for water at 250°C and 15.0 MPa, $\mu_f = 109 \times 10^{-6}$ Pa · s; at the same temperature and 4.0 MPa, $\mu_f = 106 \times 10^{-6}$ Pa · s; while for the same fixed pressure of 4.0 MPa and at 50°C, $\mu_f = 548 \times 10^{-6}$ Pa · s (Fig. 4.3). The dependence of μ_f on pressure is noticeable only when p reaches large values, for example in reservoirs at more than 2000 m depth.

The bulk dynamic viscosity λ_f measures the resistance of the fluid to be compressed or dilated. Experimentally it was found that for different fluids $\lambda_f \geq 0$ is always true (Truesdell 1963); $\lambda_f = 0$ only if the fluid compressibility is completely negligible, as is the case of cold water. In general $\lambda_f \geq \mu_f$ and the quotient λ_f/μ_f is larger in gases and lower in dense liquids. For water the experimental range is $1 \leq \lambda_f/\mu_f \leq 3$. For gases this quotient is much larger; for example $\lambda_f/\mu_f \approx 10^3$ for CO₂ at atmospheric conditions (Truesdell 1963). For the case of water in cold aquifers, at 25°C and 2.0 MPa, $\mu_f = 890 \times 10^{-6}$ Pa · s and $\lambda_f \approx 2600 \times 10^{-6}$ Pa · s. For the case of geothermal systems, at 250°C and 20 MPa the shear viscosity of liquid water is $\mu_f = 110.4 \times 10^{-6}$ Pa · s. At these conditions the corresponding value of its bulk dynamic viscosity is $\lambda_f \approx 330 \times 10^{-6}$ Pa · s. For the steam phase at 300°C and 1.0 MPa, the shear viscosity of vapor is $\mu_f = 20.2 \times 10^{-6}$ Pa · s; and at the same temperature and 8.5 MPa, $\mu_f = 19.7 \times 10^{-6}$ Pa · s. Figure 4.3 shows the dependence on temperature of the shear viscosity of both phases of water. Notice that close to the critical point of water (374.15°C, 22.12 MPa) the viscosity of both phases tends to collapse to the common value of 47×10^{-6} Pa · s. The Euler equations are for non-viscous fluids, because they neglect the effects of fluid viscosity. These classic equations are included in the Navier-Stokes system as a special case ($\lambda_f = \mu_f = 0$). Therefore, a solution of the Euler equations is only a coarse approximation of the real fluid flow problem.

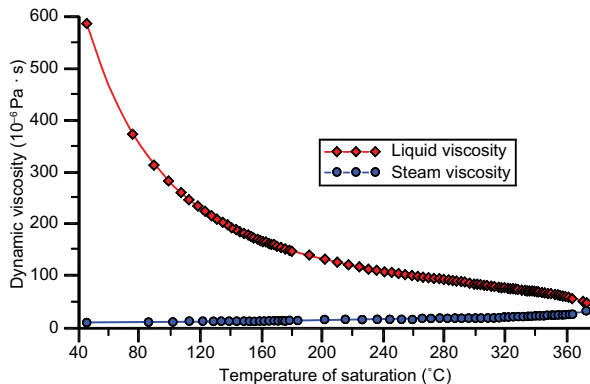


Figure 4.3. Shear dynamic viscosity μ_f for two-phase water.

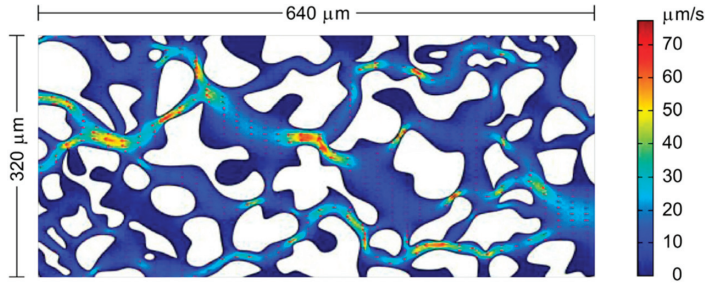


Figure 4.4. Groundwater flow at porous scale using Navier-Stokes equation. The velocity field plot shows the velocities relative to the inlet velocity within the studied section. The modeling is based on the data provided by COMSOL-Multiphysics[®] software model library (COMSOL 2008c; courtesy COMSOL AB).

4.2.1 Flow of fluids at the scale of the pores

Average approximations of porous flow produce estimates that are sufficient when considering flow over large areas (macroscopic approach on field scale). However, the approximations miss the microscopic flow details between grains and pores. These details can be very important to understand several phenomena, such as permeability reduction, plastic deformations, or testing the best correlations for relative permeabilities and capillary pressure. These nuances are modeled with equations (4.10). Recent experiments have been made to model the real flow at the scale of the pores (Fig. 4.4) using the Navier-Stokes equations (e.g., Auset and Keller 2004, Auset *et al.* 2005, Keller and Auset 2007). To illustrate this procedure, we present the graphical results of a numerical model solved with finite elements using COMSOL-Multiphysics[®] software (Version 3.5; Comsol 2008a). This numerical technique will be introduced in chapter 5 (section 5.2). This non-conventional model of porous flow uses a simplified form of the Navier-Stokes equations (4.10) in two dimensions. This model results from pore-scale flow experiments conducted by Auset and Keller (2004). This type of modeling with finite elements is shedding new light on the movement of real fluids through variable-pore geometries. To produce the model geometry, the authors scanned electron microscopic images of thinly sliced rock sections (Fig. 4.4). The entire model covers $640 \times 320 \mu\text{m}$ ($\approx 0.2 \times 10^{-6} \text{ m}^2$). The mesh representing this microscopic region contains 15,130 triangular elements. Incompressible, isothermal water moves from right to left across the geometry of the pores. Flow is laminar in the pores and does not enter the grains. The inlet and outlet fluid pressures are known. The flow is symmetrical at the top and bottom boundaries. The water has constant density in the pore spaces and the corresponding continuity (4.6) and Navier-Stokes (4.10) equations are applied. Because of the dimensions of this small scale example, micro-units are used: dynamic viscosity μ_f ($\mu\text{g}/(\mu\text{m} \cdot \text{s})$), fluid velocity ($\mu\text{m}/\text{s}$), fluid density ($\mu\text{g}/\mu\text{m}^3$) and pressure ($\mu\text{g}/\mu\text{m} \cdot \text{s}$). The model does not include gravity effects. Velocities are zero at the grain boundaries, which have a non-slip condition. Figure 4.4 shows the obtained solution predicted with a Navier-Stokes analysis for relative velocities in the pore spaces of a micro-scale porous medium. The water velocities are higher (50–70 $\mu\text{m}/\text{s}$) in the narrow pores with high-pressure drops. The fluid velocities tend to decrease (0–30 $\mu\text{m}/\text{s}$) in wider sectional areas and close to grain boundaries.

4.3 DARCY'S LAW: PRESSURE AND HEAD

In porous rocks, the real flow of fluids occurs at a microscopic level, through a tortuous trajectory and complex mesh of interconnected pores and fissures of different dimensions (Fig. 4.4).

To apply the Navier-Stokes equations at the microscopic scale of the pores in all problems of underground flow is neither appropriate nor practical. The main problem is the amount of calculus involved and the lack of corresponding data. For example, if we use 15,130 elements to represent $0.2 \times 10^{-6} \text{ m}^2$ of rock, we will need a mesh composed of $75,650 \times 10^6$ triangles to simulate only one m^2 of microscopic porous material. In most practical situations, it is preferable to use a simpler classical equation describing the effective average speed of flow in the porous rock. This macroscopic approach does not take into account the real geometry of the pores as in the previous section (Bear and Bachmat 1984).

It is typical to represent fluid flow in the pores as a continuum process using average volumetric properties rather than detailing the geometry of the solid particles in the porous medium. When inserting the adequate bulk parameters into an appropriate equation, it is possible to obtain average flow properties to understand the global phenomenon. Between 1855 and 1856 the French engineer Henry Philibert Gaspard Darcy (Fig. 4.5) made the first specific porous-flow studies and conducted experiments of water flow in a vertical homogeneous sand filter. Darcy's law is an experimentally derived equation that describes the flow of fluids through a porous medium. With his experiments, Darcy (1856) estimated the average velocity of the underground flow of the fountains of the city of Dijon in France. This law can be also derived from the Navier-Stokes equations. Darcy's law along with the equation of conservation of mass forms the main groundwater flow equation, one of the basic relationships of hydrogeology. It is analogous to Fourier's law in heat conduction, or Fick's law in diffusion theory. Darcy's law is commonly used to describe the flow of water, oil and gases in aquifers, in petroleum and in geothermal reservoirs. Darcy's law contains the scientific definition of permeability k used in reservoir engineering. It is a proportional relationship between the instantaneous discharge rate Q_V through the flow cross-sectional area A [m^2] of a porous medium, the viscosity of the fluid and the pressure drop ($p_2 - p_1$) over a given distance L :

$$Q_V = -\frac{k_x}{\mu_f} \frac{p_2 - p_1}{x_2 - x_1} A \left[\frac{\text{m}^3}{\text{s}} \right] \quad (4.11)$$

where Q_V is the volumetric discharge (volume of water per second) and $L = x_2 - x_1$ is the length of space over which the pressure drop is taking place. The negative sign is because water always flows from high pressure zones to low pressure regions. Dividing both sides of equation (4.11) by the area and using a compact notation equals:

$$\frac{Q_V}{A} = v_f = -\frac{k_x}{\mu_f} \frac{\Delta p}{\Delta x} = -\frac{k_x}{\mu_f} \frac{\partial p}{\partial x} \left[\frac{\text{m}}{\text{s}} \right] \quad (4.12)$$



Figure 4.5. French scientist Henry Darcy (06/10/1803–01/3/1858).

where v_f is called the Darcy flux, or volumetric discharge per unit area, or Darcy velocity, or seepage velocity; and $\Delta p/\Delta x = \vec{\nabla}_x p$ is the pressure gradient vector in one dimension. This flux is not equal to the microscopic velocity of water traveling through the pores. The real microscopic velocity is given by the Navier-Stokes equations (4.10). The Darcy flux is an average flow velocity that occurs only through one portion of the cross sectional area A of the porous column. The solid grains occupy the remaining part of A . The portion of the area effectively available to flow is φA (Bear 1979). Thus, the relation between the average pore velocity v_A of the fluid through the porous column and the apparent discharge is $v_f = \varphi v_A$. The Darcy flux is divided by porosity to account for the fact that only a fraction of the total formation volume is available for flow. Darcy's law is an expression of conservation of momentum when the kinetic energy of the fluid is neglected. In three-dimensional space, gravity must be accounted for, because the vertical pressure drop caused by gravity affects the flow. In this case Darcy's law for a single-phase fluid in an anisotropic porous medium of permeability tensor \mathbf{K} is:

$$\vec{v}_f = -\frac{1}{\mu_f} \mathbf{K} \cdot (\vec{\nabla} p - \rho_f \vec{g})$$

$$\vec{v}_f = \begin{pmatrix} v_x \\ v_y \\ v_z \end{pmatrix} = -\frac{1}{\mu_f} \begin{pmatrix} k_x & 0 & 0 \\ 0 & k_y & 0 \\ 0 & 0 & k_z \end{pmatrix} \cdot \begin{pmatrix} \partial_x p \\ \partial_y p \\ \partial_z p - \rho_f g \end{pmatrix} \tag{4.13}$$

The symbol \mathbf{K} is the tensor of absolute permeability at any point (x, y, z) of the porous medium, \vec{g} is the acceleration of gravity in the same direction of the Earth's radius. The validity of Darcy's law has been tested in many experiments and has shown itself to be accurate for a wide domain of flows (Scheidegger 1974).

Equation (4.13) is also valid for two-phase flow; for example, in the case of water, subindex f represents the liquid phase ($f = l$) or the vapor phase ($f = v$). It is useful to define the vectorial flow of fluid at each point (x, y, z) flowing through a differential area dS surrounding a differential volume dV_B of any fractured porous reservoir (Fig. 4.6). This flow vector is equal to the quantity of mass passing every second through the unit area and is valid also for non-Darcian flows:

$$\vec{F}_{M1} = \rho_f \vec{v}_f \left[\frac{\text{kg}}{\text{m}^2 \text{s}} \right] \tag{4.14}$$

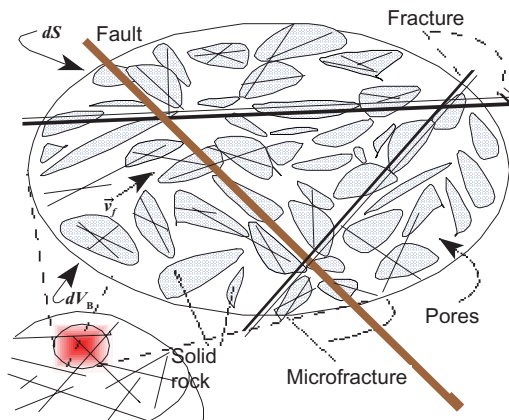


Figure 4.6. A differential volume dV_B of a porous fractured rock.

4.3.1 Pressure formulation of the general groundwater flow equation

In porous rocks, the real flow of fluids occurs at a microscopic level through tortuous paths. Equation (4.14) defines the momentum of the fluid, per unit volume of porous rock. The principle of conservation of the fluid mass (section 4.1) is:

- The instantaneous rate of change of the fluid mass flowing in a differential volume dV_B of porous rock is equal to the total flow of mass through the differential surface dS surrounding dV , plus the extracted or injected rate of fluid in dV_B .

This principle is expressed symbolically as the continuity equation (4.7) for the fluid inside each differential porous volume (REV) dV_B :

$$\frac{\partial}{\partial t}(\varphi \rho_f) = -\vec{\nabla} \cdot \vec{F}_{M1} + q_f \quad (4.15)$$

where q_f [$\text{kg}/\text{m}^3/\text{s}$] is the volumetric fluid production (<0) or injection (>0) rate in dV_B . Each term in equation (4.15) has units of [$\text{kg}/\text{s}/\text{m}^3$]. The continuity equation, including Darcy's law, is:

$$\begin{aligned} \left[\frac{\text{kg}}{\text{m}^3\text{s}} \right] \rightarrow \frac{\partial}{\partial t}(\varphi \rho_f) - q_f &= \vec{\nabla} \cdot \left(\frac{\rho_f}{\mu_f} \mathbf{K}(\vec{\nabla}p - \rho_f \vec{g}) \right) \\ &= \frac{\partial}{\partial x} \left(\frac{\rho_f k_x}{\mu_f} \frac{\partial p}{\partial x} \right) + \frac{\partial}{\partial y} \left(\frac{\rho_f k_y}{\mu_f} \frac{\partial p}{\partial y} \right) + \frac{\partial}{\partial z} \left(\frac{\rho_f k_z}{\mu_f} \left(\frac{\partial p}{\partial z} - \rho_f g \right) \right) \end{aligned} \quad (4.16)$$

This partial differential equation is called the groundwater flow equation; it is the pressure formulation of the fluid flow because p is the only variable. The fluid density is computed as a function of p and T (see section 2.3). Equation (4.16) is used in hydrogeology, in petroleum and in geothermal reservoir engineering to describe groundwater flow through aquifers and the flow of oil and gas in hydrocarbon systems. Its mathematical form is similar to the heat diffusion equation.

4.3.2 Darcy's law in terms of hydraulic head and conductivity

The original form of Darcy's law was published for the first time in 1856 in terms of hydraulic head difference and hydraulic conductivity \mathbf{K}_H . This rock property describes the ease with which a fluid can move through pore spaces or fractures. It depends on the intrinsic permeability of the material and on the physical properties of the fluid.

Darcy's law in terms of hydraulic head is a simple proportional relationship between the instantaneous discharge rate through the porous medium, its hydraulic conductivity and the head difference ($h_2 - h_1$) over a given distance $L = z_2 - z_1$ where the head drop occurs (Fig. 4.7); h is also called the piezometric head:

$$Q_V = -K_H \frac{h_2 - h_1}{z_2 - z_1} A \quad \left[\frac{\text{m}^3}{\text{s}} \right] \Leftrightarrow \frac{Q_V}{A} = v_z = -K_H \frac{\Delta h}{\Delta z} \quad \left[\frac{\text{m}}{\text{s}} \right] \quad (4.17)$$

where Q_V is the water total discharge (volume of water per second), A is the cross-sectional area to flow, $L = z_2 - z_1$ is the length and v_z is the Darcy's velocity. The negative sign indicates that, under the action of gravity, water always flows from the high head to the low head. Expressed in words equation (4.17) simply states that v_z is proportional to the hydraulic gradient $\Delta h/\Delta z$. Hydraulic conductivity K_H is the proportionality constant in Darcy's law, which relates the amount of water that will flow through a unit cross-sectional area of an aquifer under a unit gradient of hydraulic head. It is analogous to the thermal conductivity of materials in heat conduction (eq. 2.9). The hydraulic conductivity K_H is specific to each fluid, water, oil, air or other gases. Intrinsic

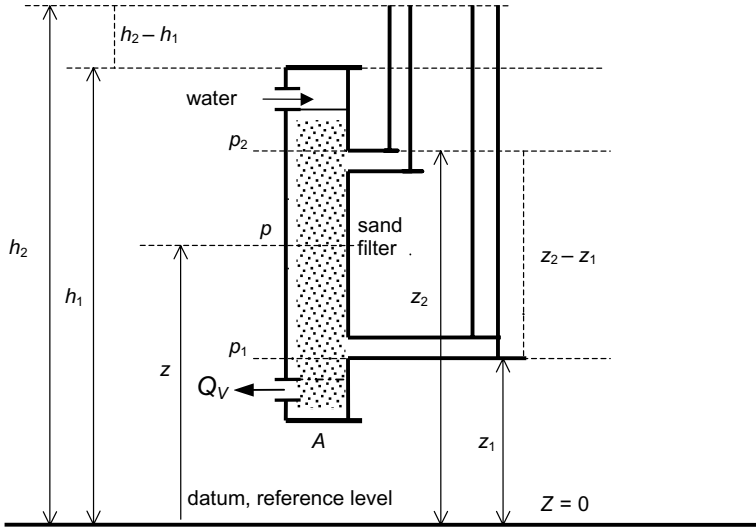


Figure 4.7. Simplified scheme of the original Darcy's experiment using water flowing inside a vertical sand filter in a column maquette.

permeability k is a parameter of the porous rock, which is independent of the fluid. These two parameters are related through the following equation deduced from Darcy's law:

$$\begin{aligned}
 \text{hydraulic conductivity: } Q_V &= -K_H A \frac{\Delta h}{\Delta z}, \quad K_H \left[\frac{\text{m}}{\text{s}} \right], \quad Q_V \left[\frac{\text{m}^3}{\text{s}} \right], \\
 \text{permeability: } Q_V &= -\frac{kA}{\mu_f} \frac{\Delta p}{\Delta z}, \quad k \left[\text{mD} \cong 10^{-15} \text{m}^2 \right], \quad p = \rho_f g h \\
 \Rightarrow \Delta p &= \rho_f g \Delta h \quad \Rightarrow \quad \frac{Q_V}{Q_V} = 1 = \frac{K_H \lambda \Delta h \mu_f \Delta x}{k \lambda \Delta x \rho_f g \Delta h} \\
 \Rightarrow \boxed{K_H = \frac{\rho_f g}{\mu_f} k} & \quad \text{in tensorial form:} \quad \boxed{\mathbf{K}_H = \frac{\rho_f g}{\mu_f} \mathbf{K}} \quad (4.18)
 \end{aligned}$$

For example, K_H will rise if the water in a porous medium is heated because this reduces the water viscosity (the related decrease of fluid density, which contributes to an K_H decrease, is lower than the effect of viscosity decrease), but k will remain constant. Permeabilities can be calculated from hydraulic permeability for any condition using equation (4.18). Let us take for example $K_H \approx 10^{-10}$ m/s for massive igneous and metamorphic rocks, and $K_H \approx 10^{-2}$ m/s for clean sand and gravel. Then, using formula (4.18) the corresponding values of k for water at 30°C ($\rho_f = 997.8$ kg/m³, $\mu_f = 796.9 \times 10^{-6}$ Pa · s), are $k \approx 10^{-17}$ m² (0.01 mD) and $k \approx 10^{-9}$ m² (10⁶ mD), respectively. There is a large range of values for hydraulic conductivity and permeability in different rocks, some examples for principal rocks are listed in Table 4.1.

Bernoulli's theorem expresses the conservation of mechanical energy in incompressible moving fluids. Hydraulic head and fluid pressure are related through the total mechanical fluid energy equation when the fluid kinetic energy is neglected in the aquifer and the groundwater velocity is very low:

$$\begin{aligned}
 \frac{1}{2} \rho_f v_f^2 + p - \rho_f g z &= \rho_f g h; \quad \text{if } \frac{v_f^2}{2g} \approx 0 \\
 \Rightarrow \rho_f g h &= p - \rho_f g z, \quad \text{and: } \vec{\nabla} h = \vec{\nabla} \left(\frac{p}{\rho_f g} \right) - \vec{e}_z \quad (4.19a)
 \end{aligned}$$

Table 4.1. Ranges of hydraulic conductivity K_H and permeability k for principal rocks and organic materials. The values are valid for cold freshwater with values of viscosity and density of groundwater at 20°C and 0.1 MPa (modified from Bear 1972).

K_H (m/s)	10^0	10^{-1}	10^{-2}	10^{-3}	10^{-4}	10^{-5}	10^{-6}	10^{-7}	10^{-8}	10^{-9}	10^{-10}	10^{-11}	10^{-12}
Relative permeability	pervious				semi-pervious				impervious				
Unconsolidated gravel sand	well sorted gravel	well sorted sand or sand & gravel			very fine sand, silt, loess, loam								
Unsolidated clay, organic materials					peat		layered clay			fat/unweathered clay			
Consolidated rocks	highly fractured rocks				oil reservoirs, convective geother. systems			fresh sandstone		fresh limestone, dolomite		fresh granite	
k (millidarcy) \approx	10^8	10^7	10^6	10^5	10^4	10^3	10^2	10^1	10^0	10^{-1}	10^{-2}	10^{-3}	10^{-4}
k (m ²)	10^{-7}	10^{-8}	10^{-9}	10^{-10}	10^{-11}	10^{-12}	10^{-13}	10^{-14}	10^{-15}	10^{-16}	10^{-17}	10^{-18}	10^{-19}

The coordinate z is positive downwards (e_z) and therefore $-z$ is the elevation above the reference level or datum (Fig. 4.7); p is the fluid pressure at that point. Therefore, the hydraulic head, as a function of space and time, is defined as:

$$h(x, y, z, t) = \frac{p}{\rho_f g} - z \quad (4.19b)$$

Darcy's law can be written in terms of hydraulic head and hydraulic conductivity using equation (4.19b). We assume that the vertical coordinate z is positive in the direction of gravity. Suppose first that the fluid density is constant; combining equations (4.18) and (4.19b) and replacing both in equation (4.13):

$$\begin{aligned} \mathbf{K} = \frac{\mu_f}{\rho_f g} \mathbf{K}_H &\Rightarrow \vec{v}_f = -\frac{1}{\mu_f} \frac{\mu_f}{\rho_f g} \mathbf{K}_H \cdot (\vec{\nabla} p - \rho_f g \vec{e}_z), \quad \text{and} \quad \frac{\vec{\nabla} p - \rho_f g \vec{e}_z}{\rho_f g} = \vec{\nabla} h \\ &\Rightarrow \boxed{\vec{v}_f = -\mathbf{K}_H \cdot \vec{\nabla} h} \end{aligned} \quad (4.20a)$$

In one (vertical) dimension, equation (4.20a) is the original relationship published by the engineer Henry Darcy in 1856. However, this formula is not valid when the fluid density is variable. The general form of Darcy's law in terms of hydraulic head and hydraulic conductivity for variable fluid density is deduced directly replacing equation (4.19) into equation (4.13):

$$\begin{aligned} \vec{v}_f &= -\frac{\mathbf{K}}{\mu_f} \cdot (\vec{\nabla}[\rho_f g (h+z)] - \rho_f g \vec{e}_z) = -\rho_f g \frac{\mathbf{K}}{\mu_f} \cdot \vec{\nabla}(h+z) - (h+z)g \frac{\mathbf{K}}{\mu_f} \cdot \vec{\nabla} \rho_f \\ &\quad + \frac{\mathbf{K}}{\mu_f} \cdot \rho_f g \vec{e}_z = -\mathbf{K}_H \cdot \vec{\nabla} h - (h+z) \frac{g}{\mu_f} \mathbf{K} \cdot \vec{\nabla} \rho_f \\ &\Rightarrow \boxed{\vec{v}_f = -\mathbf{K}_H \cdot \vec{\nabla} h - \frac{h+z}{\rho_f} \mathbf{K}_H \cdot \vec{\nabla} \rho_f} \end{aligned} \quad (4.20b)$$

4.3.3 The hydraulic head governing equation of groundwater flow

A groundwater flow equation similar to (4.16) for the hydraulic head h can be deduced introducing two other hydraulic variables: storativity (or storage coefficient) S [ad] and transmissivity

T_v [m^2/s] (see next subsection). In order to interpret and implement these concepts it is necessary to understand the different types of existing aquifers.

Aquifers may be classified as confined or unconfined reservoirs, depending upon the absence or presence of a free water table (Bear 1979):

- A confined aquifer, also known as a pressure aquifer, is one bounded from above and from below by impervious formations. A unconfined aquifer, also called phreatic aquifer or water table aquifer is one in which the upper boundary is the phreatic surface or free water table. A phreatic aquifer can be directly recharged from the ground surface above it. An artesian aquifer is a confined aquifer where the elevations of the piezometric surface is above ground surface. A well in such an aquifer will flow freely without pumping. Aquifers, whether confined or unconfined, that can lose or gain water through either or both of the semi-permeable rock layers bounding them from above or below, are called leaky or semiconfined aquifers.

4.3.3.1 *Storativity and transmissivity*

The storativity is the volume of water V_w of an aquifer released from or taken into storage, per unit area A , per unit change in the hydraulic head h :

$$S = \frac{d}{dh} \left(\frac{V_w}{A} \right) \Leftrightarrow \Delta V_w = SA(h_2 - h_1) \quad (4.21a)$$

The storage coefficient S [ad] is a concept that can have different meanings depending on the nature of the reservoir. In an unconfined aquifer, assuming that neither the water nor the rocks are compressible, the storativity is equal to the effective porosity of the rock (Scheidegger 1974, Bear 1979) and is equal to the rock specific yield, which is the storage or release of water without retention, representing the effective pore volume that supplies water to the wells. Unconfined aquifers have storativity or specific yield, greater than 0.01. Typical values of S for phreatic aquifers are between 0.05 and 0.3 (Kresic 2007). This type of aquifers release water from storage by the mechanism of actually draining the pores of the aquifer, releasing relatively large amounts of water.

In confined aquifers, the storativity depends entirely on the elastic properties (compressibility and expansivity) of the fluid-rock system (section 2.2.6). Confined aquifers have very low storativity values, lower than 0.01. Their typical values are between 10^{-5} and 10^{-3} (Kresic 2007). These small values indicate that the skeleton expansion and the compressibility of water are the main mechanisms of storing water in the reservoir. Both coefficients have typically quite small values. The value of storativity obtained for example from an aquifer test (section 4.5; see also chapter 6.7.2.4) can be used to determine if an aquifer is confined or unconfined.

Transmissivity [m^2/s] is the horizontal water flow rate per unit width through the entire average thickness b_a [m] of the aquifer per unit hydraulic gradient (Bear 1979). In mathematical terms:

$$T_v(x, y) = \int_{b_1}^{b_2} K_H(x, y) db = K_H b_a \Leftrightarrow \Delta T_v = K_H(b_2 - b_1) \quad (4.21b)$$

where $K_H b_a$ is an average product defining the average transmissivity. Transmissivity measures the amount of water that can be transmitted horizontally, such as to a pumping well; it appears only when the flow through the entire aquifer average thickness b_a is considered. For a confined aquifer, transmissivity remains constant in time at a specific point (x, y) , as the water-saturated thickness remains constant. The aquifer thickness of an unconfined aquifer extends from the base of the aquifer to the water table. The water table can fluctuate as a function of time, changing the transmissivity of the aquifer. This concept is valid only in two-dimensional (horizontal) flows where it is generally applied to confined aquifers; in three-dimensional aquifers, the transmissivity

concept is useless. If the aquifer is anisotropic, the transmissivity \mathbf{T}_v is a tensor corresponding to the tensorial nature of the hydraulic conductivity \mathbf{K}_H (see eq. 4.23a).

Another useful related concept is the specific storage (or specific storage coefficient) S_{sp} [m^{-1}] of confined aquifers, defined as the volume of water released or stored by unit volume of porous rock per unit area. The specific storage is due to the unit change in the component of hydraulic head normal to the aquifer surface (Kresic 2007). In more simple terms, S_{sp} is the storativity per unit aquifer thickness. We give two mathematical expressions:

$$S = S_{sp} b_a, \quad \text{and} \quad S_{sp} = \rho_f g (C_B + \varphi C_f) \quad (4.21c)$$

where C_B is the aquifer compressibility (eq. 2.24d) and C_f is the water compressibility given by equation (2.40b). We assume that the aquifer porosity is constant, and that the fluid density depends only on pressure. Using the definition of fluid compressibility, equation (4.15) becomes:

$$\varphi \frac{\partial}{\partial t} \rho_f (p) = \varphi \frac{\partial \rho_f}{\partial p} \frac{\partial p}{\partial t} = \varphi \rho_f C_f \frac{\partial p}{\partial t} = -\rho_f \vec{\nabla} \cdot \vec{v}_f + q_f \quad (4.22a)$$

We assume negligible both the changes in the fluid density and the aquifer elastic storativity term ($\rho_f g C_B$) of S_{sp} in equation (4.21c). From the relationship (4.19b) between pressure and hydraulic head and from Darcy's law (eq. 4.20a), we obtain:

$$\begin{aligned} \varphi \rho_f C_f \frac{\partial p}{\partial t} &= (\varphi \rho_f C_f g) \rho_f \frac{\partial h}{\partial t} = S_{sp} \rho_f \frac{\partial h}{\partial t} = -\rho_f \vec{\nabla} \cdot \vec{v}_f + q_f \\ \Rightarrow S_{sp} \frac{\partial h}{\partial t} &= \frac{\lambda_f}{\rho_f} \vec{\nabla} \cdot (\mathbf{K}_H \cdot \vec{\nabla} h) + \frac{q_f}{\rho_f}, \quad q_V = \frac{q_f}{\rho_f} \left[\frac{m^3}{s} \frac{1}{m^3} \right] \end{aligned} \quad (4.22b)$$

In this way, we can build another general equation that controls the transitory groundwater flow in porous, anisotropic and heterogeneous rocks:

$$\mathbf{K}_H = \begin{pmatrix} K_{Hx} & 0 & 0 \\ 0 & K_{Hy} & 0 \\ 0 & 0 & K_{Hz} \end{pmatrix}, \quad \begin{array}{l} \text{tensorial form: } \vec{\nabla} \cdot (\mathbf{K}_H \cdot \vec{\nabla} h) = S_{sp} \frac{\partial h}{\partial t} - q_V \\ \text{components form: } \frac{\partial}{\partial x_i} \left(K_{Hj} \frac{\partial h}{\partial x_j} \right) = S_{sp} \frac{\partial h}{\partial t} - q_V \end{array} \quad (4.23a)$$

Considering all the hypotheses we have set, the three-dimensional partial-differential equation (4.23a) of groundwater flow becomes:

$$\frac{\partial}{\partial x} \left(K_{Hx} \frac{\partial h}{\partial x} \right) + \frac{\partial}{\partial y} \left(K_{Hy} \frac{\partial h}{\partial y} \right) + \frac{\partial}{\partial z} \left(K_{Hz} \frac{\partial h}{\partial z} \right) + q_V = S_{sp} \frac{\partial h}{\partial t} \quad (4.23b)$$

This equation, when combined with boundary and initial conditions, describes transient three-dimensional groundwater flow in an isothermal, heterogeneous, and anisotropic aquifer. Function $h(x, y, z, t)$ is the hydraulic head in meters. The matrix coefficients K_{Hx} , K_{Hy} , K_{Hz} [m/s] are the principal values of the hydraulic conductivity tensor \mathbf{K}_H , related to the permeability tensor \mathbf{K} as indicated in equation (4.18). The principal axes of hydraulic conductivity must be aligned with the corresponding aquifer's coordinate directions. The term q_V [$m^3/s/m^3 = 1/s$] is the volumetric flow rate per unit volume of the sources or sinks of water in the porous rock; $q_V < 0$ for flow out of the aquifer, and $q_V > 0$ for fluid injection, natural recharge or water accretion.

4.3.3.2 Two-dimensional groundwater flow—The Boussinesq approximation

Mathematical models represented by equations (4.16) and (4.23a,b) are general groundwater flow equations that can be used to predict the flow in porous rocks in two or three dimensions. Often it

is advantageous to simplify such models treating the groundwater flow in a horizontal plane in two dimensions. In this case, the governing partial differential equations are simplified accordingly. The modified forms of the equations are different for confined, phreatic, and leaky aquifers. They are special cases for equation (4.23b) and were discussed in detail by Bear (1979). In this subsection, we present deductions of the main results.

The groundwater flow in a confined, inhomogeneous and anisotropic aquifer in two dimensions can be modeled by replacing the definitions of transmissivity (eq. 4.21b) and storativity (eq. 4.21c) in equation (4.23b):

$$\begin{aligned} K_{Hx} &= \frac{T_{vx}}{b_a}, \quad S = S_{sp} b_a, \quad q_N = q_V b_a \\ \Rightarrow \quad \frac{\partial}{\partial x} \left(T_{vx} \frac{\partial h}{\partial x} \right) + \frac{\partial}{\partial y} \left(T_{vy} \frac{\partial h}{\partial y} \right) + q_N &= S \frac{\partial h}{\partial t} \end{aligned} \quad (4.24a)$$

where the term q_N [m/s] represents the rate of recharge/extraction in the reservoir. This model is further simplified if the confined aquifer is homogeneous and isotropic:

$$\frac{\partial^2 h}{\partial x^2} + \frac{\partial^2 h}{\partial y^2} + \frac{q_N}{T_v} = \frac{S}{T_v} \frac{\partial h}{\partial t} \quad (4.24b)$$

The groundwater flow in a phreatic aquifer is comparatively more complicated than in a confined aquifer. Unconfined reservoirs can replenish from areal recharge such as percolation and precipitation. The saturated total thickness of these aquifers changes for the reason that the water table changes because of the recharge and discharge they receive (Kresic 2007). Neglecting the elastic storativity, replacing the variable h in the aquifer thickness, and using again equation (4.21c), the model of the phreatic, inhomogeneous, anisotropic aquifer is:

$$S_{sp} = \frac{S}{b_a}, \quad b_a \rightarrow h \quad \Rightarrow \quad \frac{\partial}{\partial x} \left(K_{Hx} h \frac{\partial h}{\partial x} \right) + \frac{\partial}{\partial y} \left(K_{Hy} h \frac{\partial h}{\partial y} \right) + q_N = S \frac{\partial h}{\partial t} \quad (4.25a)$$

This model is called the Boussinesq equation (1903), in honor of the great French mathematician and physicist Joseph Valentin Boussinesq (1842–1929). The term q_N [m/s] contains the gain of water due to infiltration (positive sign) or the loss of water due to evapotranspiration or pumping (negative sign). The hypotheses Boussinesq introduced to develop his model were: the aquifer has a horizontal impermeable base, which is the reference level; the average thickness of the aquifer can be considered equal to the hydraulic head, and the changes of h are small (Kresic 2007). Boussinesq also developed linear approximations for homogeneous and isotropic unconfined aquifers:

$$\frac{\partial}{\partial x} \left(h \frac{\partial h}{\partial x} \right) + \frac{\partial}{\partial y} \left(h \frac{\partial h}{\partial y} \right) + \frac{q_N}{K_H} = \frac{S}{K_H} \frac{\partial h}{\partial t} \quad (4.25b)$$

This equation becomes linear with respect to h^2 assuming that $\frac{\partial h}{\partial t} \approx \frac{1}{h} \frac{\partial}{\partial t} \left(\frac{h^2}{2} \right)$:

$$\begin{aligned} \frac{1}{2} \frac{\partial}{\partial x} \left(\frac{\partial h^2}{\partial x} \right) + \frac{1}{2} \frac{\partial}{\partial y} \left(\frac{\partial h^2}{\partial y} \right) + \frac{q_N}{K_H} &\approx \frac{S}{K_H} \frac{1}{h} \frac{\partial}{\partial t} \left(\frac{h^2}{2} \right) \\ T_v \approx K_H h \quad \Rightarrow \quad \frac{\partial^2 h^2}{\partial x^2} + \frac{\partial^2 h^2}{\partial y^2} + 2 \frac{q_N}{K_H} &= \frac{S}{T_v} \frac{\partial h^2}{\partial t} \end{aligned} \quad (4.25c)$$

Making the same approximation for the average transmissivity T_{va} in equation (4.24a) and defining the hydraulic diffusivity δ_H , we obtain a linear equation with respect to h :

$$\delta_H = \frac{K_H b_a}{S} \approx \frac{K_H h}{S} = \frac{T_{va}}{S} \Rightarrow \frac{\partial^2 h}{\partial x^2} + \frac{\partial^2 h}{\partial y^2} + \frac{q_N}{T_{va}} = \frac{1}{\delta_H} \frac{\partial h}{\partial t} \quad (4.25d)$$

This equation is commonly used to model the unsteady groundwater flow in unconfined aquifers. Coefficients T_v and S_S will be defined analytically in section 4.5, showing how they can be determined with pumping tests.

4.3.4 Reservoir anisotropy in two dimensions

If the aquifer is anisotropic, the three components of the symmetric permeability tensor ($k_{xy} = k_{yx}$) depend on the spatial coordinates. In two dimensions, Darcy's law is:

$$\vec{v} = -\frac{\mathbf{K}}{\mu_f} \vec{\nabla} p \Rightarrow \begin{pmatrix} v_x \\ v_y \end{pmatrix} = -\frac{1}{\mu_f} \begin{pmatrix} k_{xx} & k_{xy} \\ k_{yx} & k_{yy} \end{pmatrix} \begin{pmatrix} \partial_x p \\ \partial_y p \end{pmatrix} = \begin{pmatrix} -\frac{k_{xx}}{\mu_f} \frac{\partial p}{\partial x} - \frac{k_{xy}}{\mu_f} \frac{\partial p}{\partial y} \\ -\frac{k_{yx}}{\mu_f} \frac{\partial p}{\partial x} - \frac{k_{yy}}{\mu_f} \frac{\partial p}{\partial y} \end{pmatrix} \quad (4.26)$$

Tensor \mathbf{K} is symmetric, therefore it is always possible to find two orthogonal principal flow directions k_X and k_Y , which are called the permeability eigenvalues. The respective velocity components are simplified in these principal directions:

$$v_X = -\frac{k_X}{\mu_f} \frac{\partial p}{\partial x}, \quad v_Y = -\frac{k_Y}{\mu_f} \frac{\partial p}{\partial y} \quad (4.27)$$

This is a general result from linear algebra (Lang 1969), also valid in three dimensions. From Figure 4.8 we deduce the following relationships that are useful to transform any flow directions into the principal directions and *vice versa*:

$$\begin{aligned} k_{xx} &= \frac{k_X + k_Y}{2} + \frac{k_X - k_Y}{2} \cos 2\theta, & k_{yy} &= \frac{k_X + k_Y}{2} - \frac{k_X - k_Y}{2} \cos 2\theta \\ k_{xy} = k_{yx} &= -\frac{k_X - k_Y}{2} \sin 2\theta \Rightarrow \tan 2\theta = \frac{2k_{xy}}{k_{xx} - k_{yy}} \end{aligned} \quad (4.28)$$

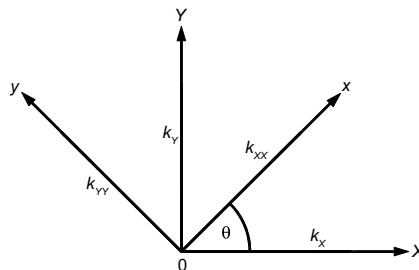


Figure 4.8. Permeability eigenvalues.

These relations are inverted to determine the main permeability directions or eigenvalues of \mathbf{K} . The formulae are also valid for both tensors \mathbf{K}_H and \mathbf{T}_V (Bear 1979):

$$k_X = \frac{k_{xx} + k_{yy}}{2} + \sqrt{\left(\frac{k_{xx} - k_{yy}}{2}\right)^2 + k_{xy}^2}, \quad k_Y = \frac{k_{xx} + k_{yy}}{2} - \sqrt{\left(\frac{k_{xx} - k_{yy}}{2}\right)^2 + k_{xy}^2} \quad (4.29)$$

These formulae are useful tools for making field measurements of permeability.

4.4 FLOW TO WELLS IN HOMOGENEOUS ISOTROPIC AQUIFERS

4.4.1 Simple geometries for isothermal stationary groundwater flow

In the following section, we derive some useful equations for simple geometries of isothermal groundwater flow. The first case is radial horizontal flow (Fig. 4.9a), which describes groundwater flow towards a well. In this case, flow is distributed uniformly along the entire well axis. This situation is valid for fully penetrating wells (with filter sections all along) and is an important approach when the near flow field around a well is considered. Linear horizontal flow (Fig. 4.9b) to a well is of interest when considering the impact of groundwater extraction by a well on the far groundwater flow field. Spherical flow (Fig. 4.9c) considers groundwater flow towards a point, making it applicable to partially penetrating wells or wells with filter sections not extending over the entire well axis.

4.4.1.1 Radial flow

In the case of steady state radial flow, the gravity is neglected in the aquifer (Fig. 4.9a) and the fluid discharge per unit porous area is assumed constant (eq. 4.12):

$$v = \frac{Q_V}{A}, \quad A = 2\pi r b_a \Rightarrow Q_V = -\frac{k}{\mu_f} \frac{dp}{dr} \quad (4.30)$$

Integrating from $p(r_w) = p_w$ to $p(r)$:

$$\int_{p_w}^p dp = -\int_{r_w}^r \frac{\mu_f Q_V}{k A} dr = -\frac{\mu_f Q_V}{2\pi b_a k} \int_{r_w}^r \frac{dr}{r} = -\frac{\mu_f Q_V}{2\pi b_a k} \text{Ln} \left(\frac{r}{r_w} \right) \quad (4.31)$$

The pressure at a distance r from the well r_w is:

$$\int_{p_w}^p dp = p - p_w \Rightarrow p(r) = p_w - \frac{\mu_f Q_V}{2\pi b_a k} \text{Ln} \left(\frac{r}{r_w} \right) \quad (4.32)$$

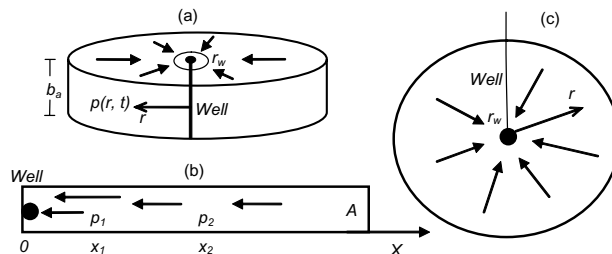


Figure 4.9. (a) Radial horizontal, (b) linear horizontal and (c) spherical flow to a well.

If the pressure at some radial distance $r_e > r_w$, $p(r_e) = p_e$ is known, then the volumetric extraction or injection rate can be computed:

$$Q_V = -\frac{2\pi b_a k}{\mu_f} \frac{p_e - p_w}{\text{Ln}(r_e) - \text{Ln}(r_w)} \left[\frac{\text{m}^3}{\text{s}} \right] \quad (4.33)$$

The radial flow pressure is:

$$p(r) = p_w + \frac{p_e - p_w}{\text{Ln}(r_e/r_w)} \text{Ln} \left(\frac{r}{r_w} \right) \quad (4.34)$$

To estimate the average reservoir pressure we compute:

$$\bar{p} = \frac{1}{\int_V dV} \int_V p(r) dV = \frac{1}{V} \int_{r_w}^r \left[p_w - \frac{\mu_f Q_V}{2\pi b_a k} \text{Ln} \left(\frac{r}{r_w} \right) \right] dr \quad (4.35)$$

The average reservoir pressure in a homogeneous reservoir of radial geometry is:

$$\bar{p} = p_w + \frac{\mu_f Q_V}{2\pi b_a k} \left[\text{Ln} \left(\frac{r_e}{r_w} \right) - \frac{1}{2} \right] \quad (4.36)$$

4.4.1.2 *Linear flow*

In the case of steady state linear flow, gravity is not considered. Knowing the pressure at two different points x_1 and x_2 (Fig. 4.9b), we have:

$$\begin{aligned} \frac{\partial^2 p}{\partial x^2} = 0 &\Rightarrow p(x) = cx + c_0, \quad \begin{cases} p_1 = cx_1 + c_0 \\ p_2 = cx_2 + c_0 \end{cases} \\ &\Rightarrow p(x) = p_1 + \frac{p_2 - p_1}{x_2 - x_1} (x - x_1), \quad Q_V = \frac{kA}{\mu_f} \left(\frac{dp}{dx} \right)_{x=0} \end{aligned} \quad (4.37)$$

4.4.1.3 *Spherical flow*

In a reservoir with steady state spherical flow (Fig. 4.9c), the flow equation is:

$$\frac{d}{dx} \left(r^2 \frac{dp}{dx} \right) = 0 \Rightarrow p(r) = \frac{c}{r} + c_0, \quad \text{with } p_e = p(r_e), \quad p_w = p(r_w)$$

Replacing the known values of the pressure at two different points we obtain the fluid pressure at any radial distance from the center of the sphere:

$$p(r) = p_w + \frac{p_e - p_w}{\frac{1}{r_e} - \frac{1}{r_w}} \left(\frac{1}{r} - \frac{1}{r_w} \right) = \frac{r_w p_w (r_e - r) + r_e p_e (r - r_w)}{r(r_e - r_w)} \quad (4.38a)$$

The constant volumetric rate can be computed, integrating as follows:

$$Q_V dr = -\frac{k}{\mu_f} 4\pi r^2 dp \Rightarrow Q_V = \frac{4\pi k}{\mu_f} \frac{p_e - p_w}{\frac{1}{r_e} - \frac{1}{r_w}} = \frac{4\pi k}{\mu_f} \frac{p_e - p_w}{r_w - r_e} r_e r_w \quad (4.38b)$$

4.4.2 Darcy's law and the equation of state of slightly compressible water

As in previous examples, again we neglect gravity. We suppose that a single-phase fluid flows in the reservoir and has a slight and constant compressibility, such as water or oil for example, and that the pressure gradients are relatively small. We also assume that the physical properties of the system are approximately constant. The mass conservation and Darcy's laws are in this case:

$$\frac{\partial}{\partial t}(\rho_f \varphi) + \text{div}(\rho_f \vec{v}) = 0, \quad \vec{v} = -\frac{k}{\mu_f} \vec{\nabla} p \quad (4.39)$$

The compressibility of isothermal water (eq. 2.40b) implies that:

$$C_f = -\frac{1}{V_f} \left(\frac{\partial V_f}{\partial p} \right)_T = \frac{1}{\rho_f} \frac{d\rho_f}{dp} \Rightarrow V_f = V_0 e^{-C_f(p-p_0)}, \quad \rho_f = \rho_0 e^{C_f(p-p_0)} \quad (4.40)$$

The fluid mass is $M_f = \rho_f V_f$, $\rho_0 = \rho_f(p_0)$, performing a Taylor series expansion of its density:

$$\rho_f(p) = \rho_0 e^{C_f(p-p_0)} = \rho_0 \left(1 + C_f(p-p_0) + \frac{C_f^2}{2!} (p-p_0)^2 + \dots \right) \quad (4.41)$$

Assuming that C_f is small, we can neglect the terms beyond the quadratic expression to obtain the equation of state for slight compressible isothermal water:

$$\rho_f(p) \cong \rho_0(1 + C_f(p-p_0)) \quad (4.42)$$

This equation of state can be combined with previous equations (4.39) to obtain:

$$\begin{aligned} \frac{\partial}{\partial t}(\varphi \rho_0 e^{C_f(p-p_0)}) &= \vec{\nabla} \cdot \left(\rho_0 e^{C_f(p-p_0)} \frac{k}{\mu_f} \vec{\nabla} p \right) \\ \Rightarrow C_f \varphi \rho_0 e^{C_f(p-p_0)} \frac{\partial p}{\partial t} &= \frac{k \rho_0}{\mu_f} \vec{\nabla} (e^{C_f(p-p_0)}) \cdot \vec{\nabla} p + \frac{k \rho_0}{\mu_f} e^{C_f(p-p_0)} \nabla^2 p \\ \Rightarrow \frac{\partial p}{\partial t} &= \frac{k}{\varphi \mu_f} \|\vec{\nabla} p\|^2 + \frac{k}{\varphi \mu_f C_f} \nabla^2 p \end{aligned} \quad (4.43)$$

By hypothesis, the pressure gradient is small; for that reason, the square of its module was canceled. Thus if we assume constant rock parameters and a small constant C_f , we obtain the classic hydraulic diffusion equation:

$$\eta_H = \frac{k}{\varphi \mu_f C_f}, \quad \vec{\nabla} \cdot \vec{\nabla} p = \boxed{\nabla^2 p = \frac{1}{\eta_H} \frac{\partial p}{\partial t}} \quad (4.44)$$

where η_H is the hydraulic diffusion coefficient. It is interesting to compare numerically both fluid diffusivities, hydraulic and thermal. Using the following data for water at 5.0 MPa and 250°C: $k = 24 \times 10^{-15} \text{ m}^2$, $\varphi = 0.1$, $\mu_f \approx 10^{-4} \text{ Pa}\cdot\text{s}$, $C_f \approx 0.1 \times 10^{-8} \text{ Pa}^{-1}$, we obtain $\eta_H \approx 1.6 \text{ m}^2/\text{s}$. The coefficient of thermal diffusion is: $\delta_T = k_T / \rho_f c_p$. Using $k_T \approx 0.623 \text{ W/m}^\circ\text{C}$, $\rho_f \approx 800 \text{ kg/m}^3$, $c_p \approx 4856 \text{ J/kg}^\circ\text{C}$, we obtain $\delta_T \approx 1.6 \times 10^{-7} \text{ m}^2/\text{s}$. Hence the relation between both coefficients is $\eta_H \approx 10^7 \delta_T$. This means that thermal disturbances spread much more slowly than pressure waves. In other words, in a porous rock the fluid pressure signal can travel thousands of times faster than the thermal signal.

If the rock is anisotropic in the principal directions (X, Y), equation (4.44) becomes:

$$\frac{\partial}{\partial X} \left(k_X \frac{\partial p}{\partial X} \right) + \frac{\partial}{\partial Y} \left(k_Y \frac{\partial p}{\partial Y} \right) = \varphi \mu_f C_f \frac{\partial p}{\partial t} \quad (4.45)$$

4.4.3 Transient flow of slight compressible fluids, This solution

We suppose that the fluid is slightly compressible, the homogeneous, confined reservoir is a cylinder, the flow is radial and the pressure gradients are relatively small. We also assume that the physical properties of the aquifer are approximately constant. Therefore, we can apply the hydraulic diffusion equation (4.44) in cylindrical coordinates (Fig. 4.10):

$$\frac{\partial p}{\partial t} = \eta_H \Delta p \Rightarrow \Delta p = \frac{1}{r} \frac{\partial}{\partial r} \left(r \frac{\partial p}{\partial r} \right) + \frac{1}{r^2} \frac{\partial^2 p}{\partial \theta^2} + \frac{\partial^2 p}{\partial z^2} \quad (4.46)$$

Assuming radial symmetry for the whole reservoir, the angular and vertical components θ and z have no influence in pressure; thus, the corresponding partial derivatives are zero. The reservoir has a very large radius; the extraction/injection takes place at its center. The velocity, given by Darcy's law, must equal the extraction/injection rate at the center. That means: $A_r v_r = Q_V$ [m^3/s], where $A_r = 2\pi r b_a$ is the flow area; p_i represents the initial constant pressure of the aquifer. The simplified mathematical model, with internal and external boundaries and initial conditions, is:

$$\begin{aligned} \frac{\partial p}{\partial t} &= \eta_H \frac{\partial^2 p}{\partial r^2} + \frac{\eta_H}{r} \frac{\partial p}{\partial r}, \quad p(r, t) > 0 \\ \text{initial condition: } &p(r, 0) = p_i, \quad \forall r \geq 0 \\ \text{external boundary: } &\lim_{r \rightarrow \infty} p(r, t) = p_i, \quad \forall t > 0 \\ \text{internal boundary: } &\lim_{r \rightarrow 0} \left(r \frac{\partial p}{\partial r} \right) = -\frac{Q_V \mu_f}{2\pi b_a k} \end{aligned} \quad (4.47)$$

To solve this model we use a Boltzmann transformation:

$$\omega(r, t) = \frac{r^2}{4\eta_H t} > 0 \Rightarrow \frac{\partial \omega}{\partial r} = \frac{2\omega}{r}; \quad \frac{\partial^2 \omega}{\partial r^2} = \frac{2\omega}{r^2} \quad \text{and} \quad \frac{\partial \omega}{\partial t} = -\frac{\omega}{t} \quad (4.48)$$

Replacing this new variable, equation (4.47) is transformed into:

$$\frac{1}{\eta_H} \frac{\partial p}{\partial \omega} \frac{\partial \omega}{\partial t} = \frac{\partial}{\partial r} \left(\frac{\partial p}{\partial \omega} \frac{\partial \omega}{\partial r} \right) + \frac{1}{r} \frac{\partial p}{\partial \omega} \frac{\partial \omega}{\partial r} \Rightarrow -\frac{\omega}{\eta_H t} \frac{dp}{d\omega} = \frac{d^2 p}{d\omega^2} \frac{4\omega^2}{r^2} + \frac{dp}{d\omega} \frac{4\omega}{r^2} \quad (4.49)$$

Finally, in terms of $\omega(p)$ $\Rightarrow \omega \frac{d^2 p}{d\omega^2} + (\omega + 1) \frac{dp}{d\omega} = 0$

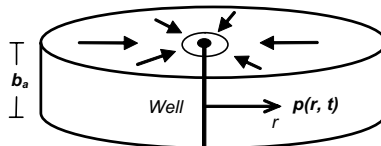


Figure 4.10. This solution with radial flow to the well.

This ordinary differential equation can be solved exactly. Let P' be equal to $dp/d\omega$, then:

$$\begin{aligned} \omega \frac{dP'}{d\omega} &= -(\omega + 1)P' \Rightarrow \int \frac{dP'}{P'} = - \int \frac{(\omega + 1)}{\omega} d\omega + c_0 \\ \Rightarrow \text{Ln } P' &= -\omega - \text{Ln } \omega + c_0 \Rightarrow \omega \frac{dp}{d\omega} = c_1 e^{-\omega} \end{aligned} \tag{4.50}$$

The internal boundary condition for the new variable ω is:

$$\begin{aligned} \lim_{r \rightarrow 0} \left(r \frac{\partial p}{\partial r} \right) &= \lim_{\omega \rightarrow 0} \left(r \frac{dp}{d\omega} \frac{\partial \omega}{\partial r} \right) = \lim_{\omega \rightarrow 0} \left(2\omega \frac{dp}{d\omega} \right) = 2c_0 = -\frac{Q_V \mu_f}{2\pi b_a k} \\ \Rightarrow \omega \frac{dp}{d\omega} &= -\frac{Q_V \mu_f}{4\pi b_a k} e^{-\omega} \end{aligned} \tag{4.51}$$

The corresponding integral solution for the Boltzmann variable is:

$$\int_p^{P_i} dp = p_i - p = - \int_{\omega}^{\infty} \frac{Q_V \mu_f}{4\pi b_a k} \frac{e^{-\omega}}{\omega} d\omega \Rightarrow p(\omega) = p_i + \frac{Q_V \mu_f}{4\pi b_a k} \int_{\omega}^{\infty} \frac{e^{-u}}{u} du \tag{4.52}$$

The semi-infinite integral appearing in this solution is a special mathematical function called the “exponential integral” defined by:

$$-E_i(-\omega) = E_1(\omega) = \int_{\omega}^{\infty} \frac{e^{-u}}{u} du \tag{4.53}$$

This special function can be easily approximated using the following formulae (for a distinction between E_i and E_1 , see Abramowitz and Stegun 1965):

$$\begin{aligned} \text{if } 0 < \omega < 0.01 \Rightarrow E_1(\omega) &\cong \text{Ln} \left(\frac{1}{\omega} \right) - 0.5772 \\ E_1(\omega) &\cong -0.57721566 + \omega - 0.24991055 \omega^2 + 0.05519968 \omega^3 \\ &\quad - 976.004 \times 10^{-5} \omega^4 + 107.857 \times 10^{-5} \omega^5 - \text{Ln}(\omega); \quad \forall \omega \in [0, 1] \\ E_1(\omega) &\cong \frac{\omega^2 + 2.334733 \omega + 0.250621}{\omega^2 + 3.330657 \omega + 1.681534} \times \frac{e^{-\omega}}{\omega}; \quad \forall \omega \in [1, \infty] \end{aligned} \tag{4.54}$$

For a complete reference to the approximation given by equation (4.54), see Abramowitz and Stegun (1972).

Replacing the value of ω , the final solution of model (4.47), satisfying the boundary and initial conditions, is:

$$p(r, t) = p_i + \frac{Q_V \mu_f}{4\pi b k} E_1 \left(\frac{r^2}{4\eta_H t} \right) \tag{4.55}$$

If $Q_V > 0$, then the fluid is entering the reservoir (injection). If $Q_V < 0$, the fluid is being extracted from the reservoir (well production). This formula, practical and elegant, is known as the Theis (1935) solution, after Charles Vernon Theis (1900–1987), an American hydrogeologist who

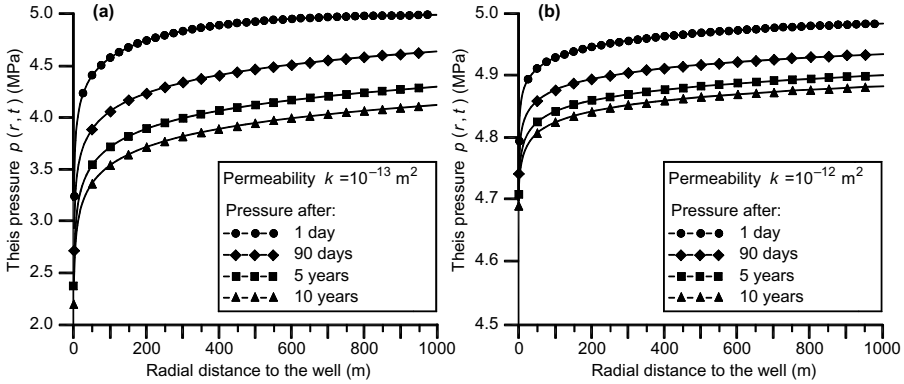


Figure 4.11. Theis solutions for an aquifer with the following parameters: $p_i = 5.0 \text{ MPa}$, $T = 30^\circ\text{C}$, $C_f = 0.442 \times 10^{-9} \text{ Pa}^{-1}$, $b_a = 1000 \text{ m}$, $Q_V = -0.2 \text{ m}^3/\text{s}$, $\mu_f = 7.97 \times 10^{-4} \text{ Pa} \cdot \text{s}$: (a) corresponds to an aquifer evolution with $k = 100 \times 10^{-15} \text{ m}^2$, $\eta_H = 62.7 \times 10^{-3} \text{ m}^2/\text{s}$; (b) corresponds to a permeability $k = 1000 \times 10^{-15} \text{ m}^2$, $\eta_H = 6.27 \times 10^{-3} \text{ m}^2/\text{s}$.

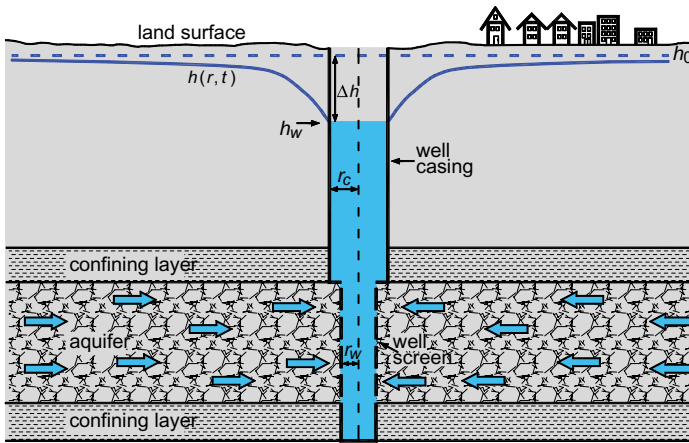


Figure 4.12. Radial flow to a finite diameter well in a confined homogeneous isotropic aquifer with uniform thickness b_a where the Theis solution (eq. 4.55), which assumes a zero radius (line source) well is no further valid. The total volumetric pumping rate $Q_V = \text{constant}$, $r_c =$ the inner radius of well casing in the interval over which the water level declines, $r_w =$ effective radius of well screen, $r =$ distance from the center of the well, $h(r, t) =$ hydraulic head of the confined aquifer with pumping conditions at a distance r and time t , $h_0 =$ hydraulic head without pumping and $\Delta h = h_0 - h_{well} =$ drawdown in the well.

was the first to develop this mathematical expression capable of determining the characteristics of an aquifer and predicting how water levels change during pumping. The Theis equation is useful for simple, fast computations in groundwater flow. The formula is used often by petroleum engineers and hydrogeologists and is the foundation of pressure analysis techniques. The Theis solution is for flow to a point well and has several practical applications: it is used to calculate pressure drawdown in aquifers (Figs. 4.11 and 4.12) and oil reservoirs, and to explore the inverse modeling of aquifer properties (porosity, permeability, reservoir dimensions). It is very useful as a first analytical approach to aquifer tests (see section 4.5.2 for more details).

4.4.4 Flow to a well of finite radius, wellbore storage

Wellbore storage is an important example of fluid flow to wells; its effects have been the subject of many studies in hydrogeology, geothermal and petroleum engineering:

- Pumping from a completed well removes the fluids, in the borehole and the casing (e.g. pipes, liners, etc.), before fluids from the reservoir enter the well. The magnitude and duration of the wellbore storage's impact depends on the size of the well and casing. These effects are important particularly at early times, typically when engineers assess the viability of reservoirs. For large-scale projects with big wells, these “early time” effects can linger for many months and significantly inhibit production (COMSOL 2008d).

Wellbore storage can be modeled by adding a time-dependent ordinary differential equation to the well boundary (Fig. 4.12). The equation governing the flow is Darcy's law included in the continuity equation (4.16), in terms of pressure and specific storativity. The term $\rho_f g C_B$ is neglected as we did in equation (4.22a):

$$\begin{aligned} \varphi \rho_f C_f g \frac{\partial p}{\partial t} &= \vec{\nabla} \cdot \left[\frac{\rho_f g}{\mu_f} k (\vec{\nabla} p - \rho_f g \vec{e}_z) \right] + g q_f \\ \Leftrightarrow \frac{S_{sp}}{\rho_f g} \frac{\partial p}{\partial t} &= \frac{K_H}{\rho_f g} \vec{\nabla} \cdot (\vec{\nabla} p - \rho_f g \vec{e}_z) + \frac{g q_f}{\rho_f g} \end{aligned} \quad (4.56a)$$

Defining S_p [m²/kg] as the specific storage for pressure and neglecting gravity in Darcy's law:

$$S_p = \frac{S_{sp}}{\rho_f g} \quad \Rightarrow \quad S_p \frac{\partial p}{\partial t} = \frac{K_H}{\rho_f g} \nabla^2 p + \frac{q_f}{\rho_f} \quad (4.56b)$$

We apply this mathematical model to the flow at a well of finite radius (Fig. 4.12), employing radial coordinates in the Laplacian of the pressure (eq. 4.47). We assume that the fluid from the aquifer moves into the well obeying Darcy's law:

$$v_r = -\frac{K_H}{\rho_f g} \frac{\partial p}{\partial r} = -\frac{Q_V}{2\pi r_w b_a} \quad (4.57)$$

where v_r is the radial flow velocity and r_w the effective radius of well screen. The model can account for wellbore storage by including a second drawdown pressure when $r = r_w$, as follows (COMSOL 2008d):

$$Q_V = -\frac{K_H}{\rho_f g} 2\pi b_a r_w \frac{\partial p}{\partial r}(r_w) + \frac{\pi r_c^2}{\rho_f g} \frac{dp_w}{dt} \rightarrow \left[\frac{\text{m}^3}{\text{s}} \right] \quad (4.58)$$

where Q_V is the total volumetric pumping rate [m³/s], b_a is the production interval (in our case the thickness of the confined aquifer), r_c is the radius of the well casing, $p_w(t)$ and dp_w/dt are the pressure and the pressure drawdown in the well, respectively. This equation states that withdrawals from the well consist of two parts: the first part is the flux into the well from the aquifer; the second part is the water coming from the wellbore itself. The main hypothesis is that the pressure just inside the well equals the pressure just outside of it $p_w(t) = p(r_w, t)$. This is a continuity hypothesis for the pressure at the interior well's boundary.

The model represented by equations (4.57) and (4.58) can be readily solved using the techniques developed in chapter 5. In order to illustrate the practical consequences of including the wellbore storage in the analysis of the fluid flow to wells, we present graphics of this model with the following data and results from COMSOL (2008d). The zone of interest has a diameter of 1 km; the effective radius of well screen is $r_w = 0.1$ m; the well casing radius $r_c = 0.15$ m; the hydraulic conductivity $K_H = 10^{-4}$ m/s; the aquifer thickness $b_a = 50$ m; the specific storage

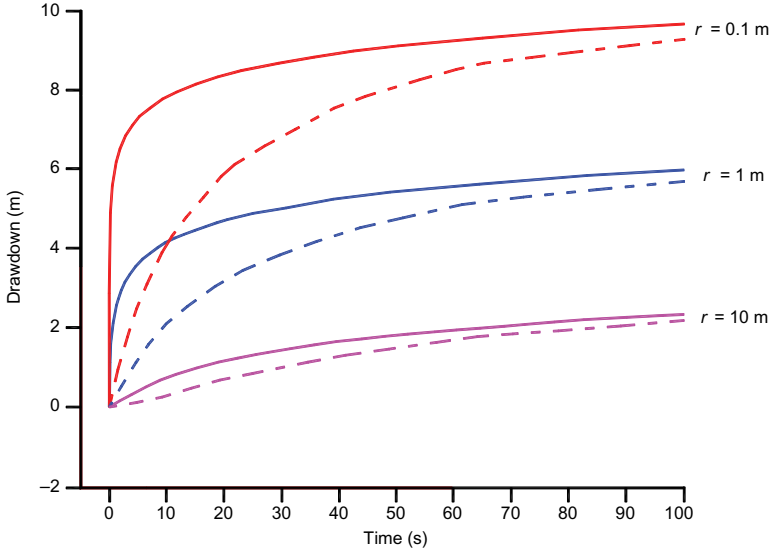


Figure 4.13. Hydraulic head drawdown calculated with (dashed lines) and without (solid lines) considering wellbore storage. Results are shown for the well boundary ($r = 0.1$ m) and two points at a distance of $r = 1$ and 10 m from the well axis (modified from COMSOL 2008d).

$S_S = 10^{-5}$ 1/m; density is 1000 kg/m³; $g = 9.81$ m/s²; the pumping constant volumetric rate $Q_V = 0.05$ m³/s; the initial pressure is $p_0 = 9.82 \times 10^5$ Pa.

Figure 4.13 shows the solution obtained with COMSOL-Multiphysics[®] software (Version 3.5; COMSOL 2008a) for drawdown (dp_w/dt) as a function of time ($0 \leq t \leq 100$ s), for the well boundary itself and two observation points near the well with wellbore storage impacts. For comparison, the figure also provides results for the case without considering wellbore storage. The difference in the two solutions is the reduction in reservoir withdrawals owing to fluids present in the wellbore. This impact diminishes with distance from the well and time.

4.4.5 The Brinkman equation and the coupled flow to wells

Understanding what happens during the transition from slow flow in porous media to fast flow in fractures, faults, and wells is critical in many practical situations. The modeling of transitioning flows requires coupling different mathematical expressions of flow laws. The Brinkman equation (introduced by Brinkman in 1947) is used to account for transitional fluid flow between boundaries in porous heterogeneous media with more than one porosity, such as micro-porous rocks with fractures, or rocks with two, three, or more different, contrasting porosities. In these cases, the global structure of the porous medium is at different length scales. Sometimes it is possible to divide the porous medium into two regions: one for larger porosity and another one for smaller pores. In the first region, the Navier-Stokes equation for incompressible flow holds. In the second region, Darcy's law describes the flow. The two boundary conditions to be satisfied at the common interface are continuity of the fluid velocity and the shear stress. Darcy's law alone is not sufficient to satisfy these boundary conditions. The Brinkman equation is an extension of the traditional form of Darcy's law created to match boundary conditions at an interface between two regions with very different porosity and permeability (see section 3.2).

Brinkman's original equation is semi-empirical in nature and defined as:

$$\mu_e \nabla^2 \vec{v}_B + \vec{v}_B = -K_H \vec{\nabla} h \quad (4.59a)$$

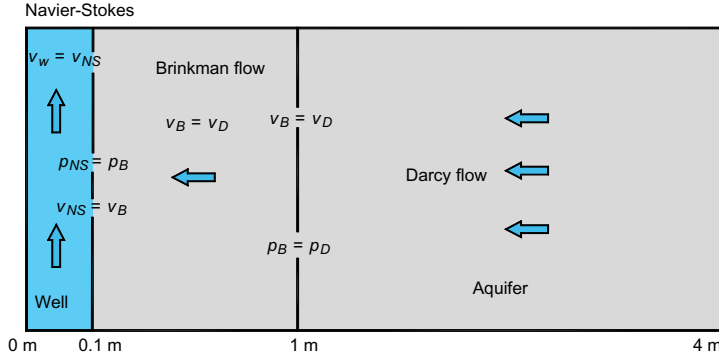


Figure 4.14. Model geometry showing zones and boundary conditions for coupling Darcy's law ($1 \text{ m} < r < 4 \text{ m}$), Brinkman equations ($0.1 \text{ m} < r < 1 \text{ m}$) and the Navier-Stokes equations inside the well ($r < 0.1 \text{ m}$). Water flows from the right side of the model area to the well and enters through a perforation in the well casing. Illustration modified from COMSOL (2008e).

The correction term is defined by the Laplacian of the Brinkman fluid velocity \vec{v}_B . The term μ_e is an effective viscosity parameter that accounts for flow through both media, it is not the real fluid viscosity. The effective viscosity is only a parameter that allows for matching the shear stress boundary condition across the free-fluid/porous medium interface. We are going to set equation (4.59a) in terms of fluid pressure coupling a transitional zone between two different flow regimes (Fig. 4.14).

In this discussion, we recapitulate the general description of the Darcy-Brinkman model published by COMSOL (2008e). A fluid moves slowly through a thin porous layer towards a perforation in a well casing and moves into the well (Fig. 4.14). The coordinate r represents the radial flow from the well to the reservoir. The fluid flow follows Darcy's law (eq. 4.13) in the far field ($1 \text{ m} < r < 4 \text{ m}$) and the Brinkman equations near the well opening ($0.1 \text{ m} < r < 1 \text{ m}$). The permeable layer is 0.875 m thick and confined at its top and bottom by impermeable materials. For simplicity, it shall be assumed that the reservoir is homogeneous and has isotropic hydraulic properties, and that the fluid has constant density and viscosity. The fluid flux at the inlet at the right side and the pressure at the perforations at the well casing are known. The flow field is stationary. In terms of fluid pressure the Brinkman equations for steady state flow are:

$$-\vec{\nabla} \cdot \mu_f / \varphi \left(\vec{\nabla} \vec{v}_B + (\vec{\nabla} \vec{v}_B)^T \right) = \frac{\mu_f}{k} \vec{v}_B + \vec{\nabla} p_B; \quad \vec{\nabla} \cdot \vec{v}_B = 0 \quad (4.59b)$$

where μ_f is the dynamic viscosity ($\text{Pa} \cdot \text{s}$), \vec{v}_B equals the velocity vector (m/s), p_B is pressure (Pa), both in the Brinkman region, and k (m^2) denotes the permeability, which is assumed to be the same in both flow zones.

The Brinkman equations allow the description of fluid flow in those porous media where flow velocities are high enough so that momentum transport by shear stress becomes significant. From the Brinkman side of the Darcy-Brinkman interface the fluid velocity is constrained since the boundary condition on the Darcy side fixes the pressure. The velocity constraint on the Brinkman side of the interface reflects that velocities are dependent variables in the Brinkman equations but not in Darcy's law for \vec{v}_f . The boundary condition on velocities is:

$$\vec{v}_B = \vec{v}_f \quad (4.59c)$$

Since the confining layers and the well casing are impermeable to flow, \vec{v}_B equals zero to eliminate all components of the velocity at the boundary. Obtaining a unique solution to this problem requires the definition of the pressure at the well since the model prescribes fluid flux

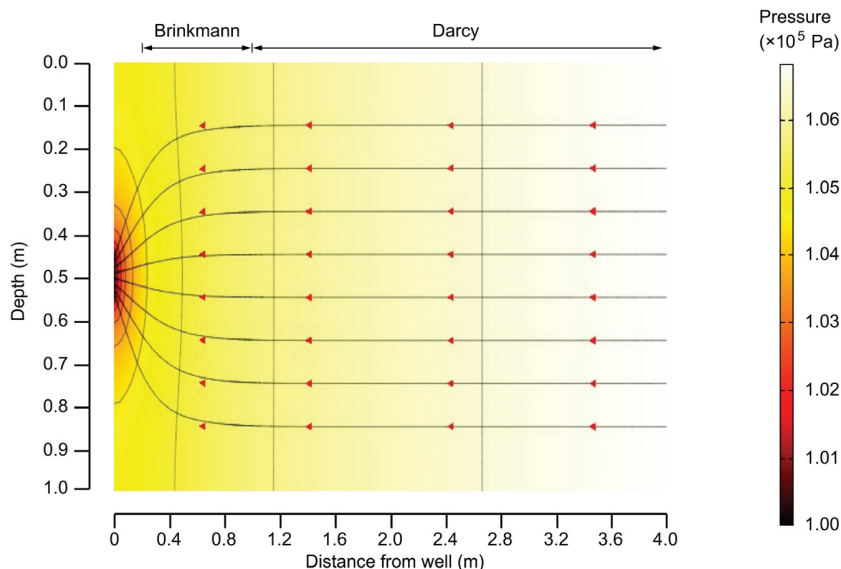


Figure 4.15. COMSOL Multiphysics[®] solution for fluids following Darcy's law ($1 \text{ m} < r < 4 \text{ m}$) and the Brinkman equations ($0.1 \text{ m} < r < 1 \text{ m}$). The results shown are pressure (surface plot and contours) and velocities (streamlines). Note that the vertical axis is expanded. The modeling is based on the data provided by COMSOL-Multiphysics[®] software model library (COMSOL 2008e; courtesy of COMSOL AB).

conditions for all other boundaries. The constraint on pressure is $p_B = p_w$. To solve equation (4.59b) the following data were used: layer thickness $b_a = 1 \text{ m}$; reservoir radius $r_C = 4 \text{ m}$; well radius $r_w = 0.1 \text{ m}$; fluid density (water) 990.2 kg/m^3 ; $g = 9.82 \text{ m/s}^2$; fluid viscosity $\mu_f = 0.0005477 \text{ Pa} \cdot \text{s}$; permeability $k = 10^{-10} \text{ m}^2$ porosity $\varphi = 0.40$; pumping rate $Q_V = 0.001 \text{ m}^3/\text{s}$; well pressure $p_w = 10^5 \text{ Pa}$. The Darcy-Brinkman problem, with these data and boundary conditions, was numerically solved using finite elements (chapter 5) with the COMSOL-Multiphysics[®] software (Version 3.5, COMSOL 2008a). Figure 4.15 shows the solution to this Darcy-Brinkman problem where Darcy's law governs slow flow far from the well, Brinkman equations apply near it. The impacts of the transition between both flow laws occur at $r = 1 \text{ m}$. The streamlines show the fluid moving from the inlet at the right to the well on the left. The streamlines funnel because the flow is moving into a perforation in the well casing.

4.4.5.1 Coupling the Darcy-Brinkman-Navier-Stokes equations in the flow to wells

We have shown how Darcy's law describes slow flow velocities in porous rocks at a distance from the well; closer to the well the Brinkman equations apply when the fluid moves in porous media but shear is non-negligible. On the other hand, the Navier-Stokes equations (4.10) describe movement of fluid inside the well and in open faults (Fig. 4.14). More generally, the Navier-Stokes equations govern open-channel flows.

As another interesting example, we present a transition in three flow regimes: slow flow in porous media quickens to a perforation in a well casing and ultimately moves into and up the well. This example couples Darcy's law with the Brinkman equations and with the Navier-Stokes equations, which model the flow within the wellbore at a radius $r < 0.1 \text{ m}$, producing a fully coupled simulation for three different flow laws (Fig. 4.14). The interface between the Brinkman and Navier-Stokes flow zones is the perforation at the midpoint of the casing. The coupling problem requires the fluid velocity in the well to be equal to the Navier-Stokes velocity. At the Navier-Stokes/Brinkman boundary the conditions are $p_{NS} = p_B$ and $v_{NS} = v_B$. At the

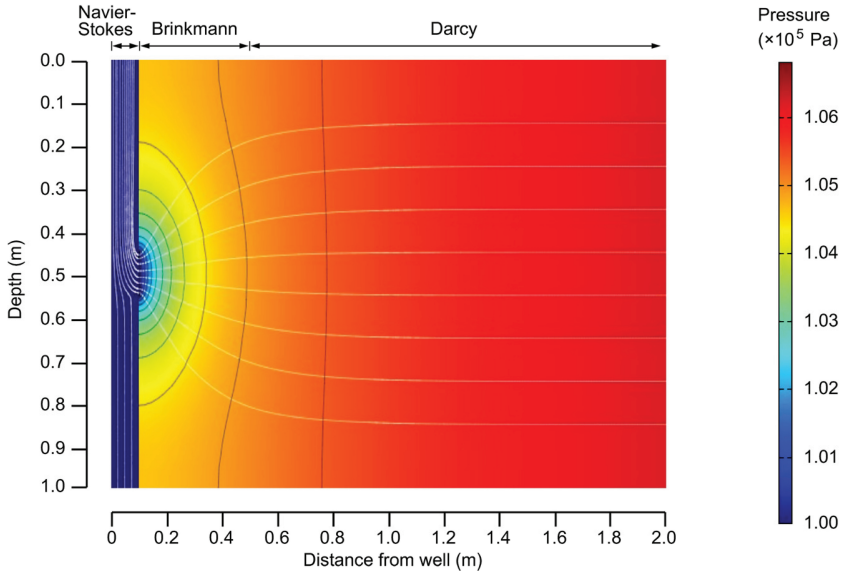


Figure 4.16. COMSOL Multiphysics[®] solution for fluids following Darcy's law ($1 \text{ m} < r < 4 \text{ m}$), the Brinkman equations ($0.1 \text{ m} < r < 1 \text{ m}$), and the Navier-Stokes equations ($r < 0.1 \text{ m}$). The results shown are pressure (surface plot and contours) and velocities (streamlines). The vertical axis is expanded for clarity. The modeling is based on the data provided by COMSOL-Multiphysics[®] software model library (COMSOL 2008e; courtesy COMSOL AB).

Brinkman/Darcy boundary the conditions are $p_B = p_D$ and $v_B = v_D$ (Fig. 4.14). Using the same data, a simulation of this Darcy-Brinkman-Navier-Stokes coupled problem was performed. Figure 4.16 shows the solution to the COMSOL (2008e) model for flow that transitions from Darcy's law in the far field ($r > 1 \text{ m}$), to the Brinkman equations in the intermediate zone ($0.1 \text{ m} < r < 1 \text{ m}$) and to the Navier-Stokes equation in the well ($r < 0.1 \text{ m}$). The pressure distribution (surface plot and contours) and velocities (streamlines) vary smoothly with no disruption at either the Darcy-Brinkman interface ($r = 1$) or the Brinkman-Navier-Stokes interface ($r = 0.1 \text{ m}$). The streamlines show fluid moving through the perforation and up the well.

4.5 PUMPING TEST FUNDAMENTALS

Aquifer tests, which comprise pumping, slug and bail tests are a common tool for hydrogeologists and groundwater engineers, to evaluate an aquifer (for more details see section 6.7.2.4). Their results allow the characterization of aquifers, aquitards and flow system boundaries. Aquifer tests are conducted to evaluate an aquifer by 'stimulating' the aquifer and observing the aquifer's 'response' such as water level changes in nearby observation wells or the stimulated well itself. Stimulation can be done through: (1) pumping in the well (pumping test), (2) changing the stagnant groundwater level in a borehole or well either by instantaneous addition, or withdrawal of a measured volume of water (slug test) and (3) withdrawal of a defined water volume using a bailer or pump (bail test). Aquifer tests are typically interpreted using an analytical aquifer flow model to match the data observed in the real world, then assuming that the matching hydrologic parameters from the idealized model correspond to the real-world aquifer (Theis 1935, Ferris *et al.* 1962, Stallman 1971, Reed 1980, Franke *et al.* 1987, Boonstra 1989, Hall 1996, Kruseman and Ridder 1991, Dawson and Istok 1991, Raghavan 1993, Day-Lewis 1995, Walton 1996, Batu 1998, Brassington 1998, Weight and Sonderegger 2001, Moore 2002, Kresic 2007). In more

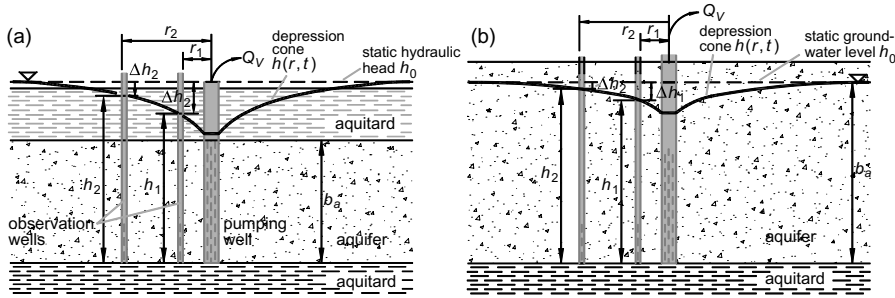


Figure 4.17. Representation of a depression cone with Dupuit-Thiem equations: the static hydraulic head is $h_0 = h(r, t = 0)$ and $\Delta h = h(r, t) - h_0$ is the drawdown or change in hydraulic head at a point (r, t) of the aquifer due to pumping at the well site $r = 0$: (a) confined aquifer; $Q_V = 2\pi T_V (h_2 - h_1)/\text{Ln}(r_2/r_1)$; (b) free aquifer; $Q_V = \pi K_H (h_2^2 - h_1^2)/\text{Ln}(r_2/r_1)$.

complex cases, a numerical model may be used to analyze the results of an aquifer test, but adding complexity does not ensure better results (Wikipedia 2009a).

The aquifer characteristics evaluated by aquifer tests are: hydraulic conductivity, transmissivity, storativity, specific yield or drainable porosity, leakage coefficient, aquifer boundaries and their distances from pumped wells. Transmissivity T_V is the reservoir's ability to transmit fluid. Storativity S is the water volume that a confined aquifer will discharge for a determined change in hydraulic head. Specific yield is a measure of the amount of water an unconfined aquifer will give up when completely drained. The leakage coefficient is necessary when the aquifer is bounded by an aquitard that allows a slow exchange of water. If the aquitard gives up water to the aquifer, then the drawdown during the pumping test is reduced, if the aquifer releases water to the aquitard, the drawdown in the pumping well will be increased). An appropriate model to the groundwater flow equation must be chosen to fit the observed data. Many solutions to aquifer tests are based on the Theis formula (eq. 4.55), built upon the simplifying assumptions previously detailed.

The basic measurements carried out during pumping tests are variations in water levels in both time and space. The depression of the water table or the change in hydraulic head is generally measured in observation wells located close (distance r) from the pumping well referred to the initial reference level h_0 (at $t = 0$) given as $\Delta h = h(r, t) - h_0$ (Fig. 4.17). Reason is that the pumping well is affected by construction factors that are hard to assess.

In general, there is no need to wait for equilibrium conditions to be reached, but the determination of initial levels (before pumping) cannot be omitted. On the other hand, the recovery process always should be recorded, especially if only the pumping well is available for measurement. Assessing the recovery process does not allow establishing the storage coefficient, because discharge and recharge contributions are balanced. It is essential that a constant pumping flow be kept during a given period.

There are a great number of assessment methods for different types of aquifers and external conditions (Krusemann and De Ridder 1991). Around the year 1900, Dupuit and Thiem developed the basic equations for the stationary regime based on Darcy's law (eq. 4.23b). Theis, in 1935, presented the general equation for non-stationary wells (eq. 4.56). A series of analytical methods has been developed on this basis (for more details see section 6.7.2.4).

4.5.1 Stationary flow towards a well—Dupuit and Thiem well equations

4.5.1.1 Confined aquifer

For the radial flow of groundwater towards a well, the following holds:

$$Q_V = v_r A \tag{4.60}$$

where A = area; v_r = radial velocity of groundwater. For the area receiving the flow, the following holds (only for confined aquifers):

$$A = 2\pi r b_a \quad (4.61)$$

where b_a = aquifer thickness; r = radial distance from the vertical axis of the well. In accordance with Darcy's law, we have for velocity:

$$v_r = -K_H dh/dr \quad (4.62)$$

By replacing (4.61) and (4.62) in (4.60), the following expression is obtained for the volumetric flow Q_V of the well:

$$Q_V = -2\pi r b_a K_H \frac{dh}{dr} \quad (4.63)$$

$$\text{or: } \frac{\partial h}{\partial r} = -\frac{1}{r} \frac{Q_V}{2\pi b_a K_H} \quad (4.64)$$

By integrating, we obtain:

$$h = -\frac{Q_V}{2\pi b_a K_H} \text{Ln } r + C_0 \quad (4.65)$$

This is the general solution for the groundwater flow equation for a homogeneous, isotropic and confined aquifer under stationary conditions. The constant C_0 results from the boundary values with $h = h_{well}$ and $r = r_w$ in the well:

$$Q_V = -2\pi b_a K_H \frac{(h - h_{well})}{\text{Ln } (r/r_w)} \quad (4.66)$$

where r_w is the radius of the well and h_{well} is the water level in the well.

Consequently, in the vicinity of the well, transmissivity $T_v = b_a K_H$ can be determined by observing levels h_1 and h_2 in two observation wells located at distances r_1 and r_2 from the pumping well:

$$T_v = b_a K_H = \frac{Q_V \text{Ln } (r_2/r_1)}{2\pi (h_2 - h_1)} \quad (4.67)$$

4.5.1.2 Unconfined aquifer

With Dupuit's equation for wells and applying Darcy's law for radial flow, the following holds for a free, homogeneous, isotropic and horizontal aquifer (eq. 4.25b):

$$Q_V = -2\pi K_H h \frac{dh}{dr}; \quad h dh = -\frac{dr}{2\pi K_H} \quad (4.68)$$

The integration with levels h_1 and h_2 in two observation wells located at distances r_1 and r_2 from the pumping well results in:

$$Q_V = \pi K_H \frac{(h_2^2 - h_1^2)}{\text{Ln } (r_2/r_1)} \quad (4.69)$$

Solving for K_H we obtain:

$$K_H = \frac{Q_V \text{Ln}(r_2/r_1)}{\pi (h_2^2 - h_1^2)} \quad (4.70)$$

where h_1 and h_2 are the piezometric heads of the observation wells located at distances r_1 and r_2 from the pumping well.

4.5.2 Transient flow—explicit Theis equation for confined aquifers

The Theis equation was adopted from heat transfer literature, for two-dimensional radial flow (Figs. 4.12, 4.17a) to a point source in an infinite, homogeneous aquifer (Kresic 2007). Introducing previous definitions (eq. 4.55), the Theis solution in terms of hydraulic head is obtained as follows.

Using previous relationships:

$$T_v = K_H b_a \left[\frac{\text{m}^2}{\text{s}} \right], \quad S = \frac{1}{A} \frac{\Delta V_w}{\Delta h} \quad [\text{ad}], \quad S_S = \frac{S}{b_a} = \rho_f g C_B + \varphi \rho_f g C_f \left[\frac{1}{\text{m}} \right],$$

$$p = \rho_f g h + \rho_f g z, \quad K_H = \frac{\rho_f g}{\mu_f} k$$

we obtain by direct substitution:

$$p(r, t) = p_i + \frac{Q_V \mu_f}{4\pi b_a k} E_1 \left(\frac{r^2}{4\eta_H t} \right)$$

$$\Rightarrow \rho_f g h(r, t) + \rho_f g z_0 = \rho_f g h_0 + \rho_f g h z_0 + \frac{Q_V \mu_f}{4\pi b_a k} E_1 \left(\frac{r^2}{4\eta_H t} \right)$$

$$\eta_H = \frac{k}{\varphi \mu_f C_f}$$

$$\Rightarrow \rho_f g h(r, t) = \rho_f g h_0 + \frac{Q_V \mu_f}{4\pi b_a k} E_1 \left(\frac{r^2}{4\eta_H t} \right)$$

$$= \rho_f g h_0 + \frac{Q_V \mu_f}{4\pi b_a K_H} \frac{\rho_f g}{\mu_f} E_1 \left(\frac{r^2 \varphi \mu_f C_f}{4t k} \right)$$

Eliminating redundant terms:

$$h(r, t) = h_0 + \frac{Q_V}{4\pi b_a K_H} E_1 \left(\frac{r^2 \varphi \mu_f C_f \rho_f g}{4t K_H \mu_f} \right) = h_0 + \frac{Q_V}{4\pi T_v} E_1 \left(\frac{r^2 \varphi C_f \rho_f g}{4t K_H} \right)$$

$$= h_0 + \frac{Q_V}{4\pi T_v} E_1 \left(\frac{r^2 S_S}{4t K_H} \right)$$

therefore:

$$h(r, t) = h_0 + \frac{Q_V}{4\pi T_v} E_1 \left(\frac{r^2 S}{4t b_a K_H} \right)$$

and finally:

$$\boxed{h(r, t) = h_0 + \frac{Q_V}{4\pi T_v} E_1 \left(\frac{r^2 S}{4T_v t} \right)} \quad (4.71)$$

where $h_0 = h(r, 0)$ and $\Delta h = h(r, t) - h_0$ is the drawdown or change in hydraulic head at a point (r, t) of the aquifer since the beginning of the test, when $t = 0$. $E_1(\omega)$ is the “Theis well function” previously defined as the exponential integral in equations (4.53) and (4.54). Classically $E_1(\omega)$ function values are tabulated for being used with this formula to evaluate the pumping test (Table 4.2). The term $w = r^2 S / 4 T_v t$ is a dimensionless variable; Q_V is the discharge or pumping rate of the well (m^3/s), T_v and S are the transmissivity and storativity of the aquifer around the well, r is the distance from the pumping well to the point where the drawdown was observed and t is the time since pumping began.

The hypotheses required by the Theis solution in terms of hydraulic head are the same as those assumed in the development of the equation (4.55). It should be noted that the Theis equation is valid only under these conditions:

- Confined aquifers with horizontal basis.
- Infinite, homogeneous and isotropic aquifers with constant thickness.
- Horizontal level of hydraulic head at rest.
- Complete pumping well.
- Horizontal laminar viscous flow of groundwater exclusively.
- Constant flow from the pumping well as a function of time.
- For a non-stationary regime, the following is assumed:
 - The aquifer is emptied with no delays.
 - The storage capacity of the well itself is negligible.

This has the following consequences:

- Rotation symmetry of the depression cone.
- Infinite growth of the depression cone.
- Extraction purely from the storage of the aquifer.
- The first and last sections of the time/depression curve cannot be used.

Even though these assumptions oversimplify the problem, still the Theis solution is very useful for many practical applications.

Equation (4.71) is used to find the average T_v and S values near the pumping well, from drawdown data collected during a pumping test. This is a very simple form of inverse modeling (see chapter 7), since the final adopted values of T_v and S are those which best reproduce the measured data. Several values of T_v and S are put into equation (4.71) until a best fit is found between the observed data and the analytic solution. Essentially, field data of drawdown Δh versus time t are plotted separately for each observation well on field data graphs with the same log-log scale as the Theis function graph. Once a satisfactory match is found, a match point $(\Delta h, E_1(\omega))$ is selected on the overlapping graphs. Afterwards, the transmissivity of the aquifer is calculated using equation (4.71):

$$T_v = \frac{Q_V}{4\pi \Delta h} E_1(\omega) \tag{4.72a}$$

The storage coefficient is calculated using this transmissivity value:

$$S = \frac{4 T_v \omega}{r^2} t \tag{4.72b}$$

For example, in a real well pumping test, performed during 24 hours in a confined aquifer, the following data were obtained (Kresic 2007): $Q_V = 8 \times 10^{-3} \text{ m}^3/\text{s}$, $\omega = 0.054$, $E_1(\omega) = 2.35$, $\Delta h = 1 \text{ m}$, $b_a = 18 \text{ m}$, $t = 2250 \text{ s}$. The computed hydrogeologic parameters were $T_v = 1.5 \times 10^{-3} \text{ m}^2/\text{s}$, storativity $S = 5.2 \times 10^{-5}$ [ad], and hydraulic conductivity $K_H = T_v/b_a = 8.33 \times 10^{-3} \text{ m/s}$.

Table 4.2. $E_1(\omega)$ function values according to Wenzel (1942): $n(y) = n \times 10^y$ (for example: for $1/\omega = 0.833 \times 10^6 = 0.833 n(6)$ we obtain $E_1(\omega) = 1.306(1) = 13.06$).

$1/\omega =$	n	$n(1)$	$n(2)$	$n(3)$	$n(4)$	$n(5)$	
$\omega =$	N	$N(-1)$	$N(-2)$	$N(-3)$	$N(-4)$	$N(-5)$	
$n = 1.000$	$N = 1.0$	2.194(-1)	1.823	4.038	6.332	8.633	1.094(1)
0.833	1.2	1.584(-1)	1.660	3.858	6.149	8.451	1.075(1)
0.714	1.4	1.162(-1)	1.524	3.705	5.996	8.297	1.060(1)
0.625	1.6	8.361(-2)	1.409	3.574	5.862	8.163	1.047(1)
0.556	1.8	6.471(-2)	1.310	3.458	5.745	8.046	1.035(1)
0.500	2.0	4.890(-2)	1.223	3.355	5.639	7.940	1.024(1)
0.455	2.2	3.719(-2)	1.145	3.261	5.544	7.845	1.015(1)
0.417	2.4	2.844(-2)	1.076	3.176	5.458	7.758	1.006(1)
0.385	2.6	2.185(-2)	1.014	3.098	5.378	7.678	9.980
0.357	2.8	1.686(-2)	9.573(-1)	3.026	5.303	7.604	9.906
0.333	3.0	1.305(-2)	9.057(-1)	2.959	5.235	7.535	9.837
0.286	3.5	6.970(-3)	7.942(-1)	2.810	5.081	7.381	9.683
0.250	4.0	3.779(-3)	7.024(-1)	2.681	4.948	7.247	9.550
0.222	4.5	2.073(-3)	6.253(-1)	2.568	4.831	7.130	9.432
0.200	5.0	1.148(-3)	5.598(-1)	2.468	4.726	7.024	9.326
0.182	5.5	6.409(-4)	5.034(-1)	2.378	4.631	6.929	9.231
0.166	6.0	3.601(-4)	4.544(-1)	2.295	4.545	6.842	9.144
0.154	6.5	2.034(-4)	4.115(-1)	2.220	4.465	6.762	9.064
0.142	7.0	1.155(-4)	3.738(-1)	2.151	4.392	6.688	8.990
0.133	7.5	6.583(-5)	3.403(-1)	2.087	4.323	6.619	8.921
0.125	8.0	3.767(-5)	3.106(-1)	2.027	4.259	6.555	8.856
0.118	8.5	2.162(-5)	2.840(-1)	1.971	4.199	6.494	8.796
0.111	9.0	1.245(-5)	2.602(-1)	1.919	4.142	6.437	8.739
0.105	9.5	7.185(-6)	2.387(-1)	1.870	4.089	6.383	8.685

$1/\omega =$	n	$n(6)$	$n(7)$	$n(8)$	$n(9)$	$n(10)$	
$\omega =$	N	$N(-6)$	$N(-7)$	$N(-8)$	$N(-9)$	$N(-10)$	
$n = 1.000$	$N = 1.0$	2.194(-1)	1.324(1)	1.554(1)	1.784(1)	2.015(1)	2.245(1)
0.833	1.2	1.584(-1)	1.306(1)	1.536(1)	1.766(1)	1.996(1)	2.227(1)
0.714	1.4	1.162(-1)	1.290(1)	1.520(1)	1.751(1)	1.981(1)	2.211(1)
0.625	1.6	8.361(-2)	1.277(1)	1.507(1)	1.737(1)	1.968(1)	2.198(1)
0.556	1.8	6.471(-2)	1.265(1)	1.495(1)	1.726(1)	1.956(1)	2.186(1)
0.500	2.0	4.890(-2)	1.255(1)	1.485(1)	1.715(1)	1.945(1)	2.176(1)
0.455	2.2	3.719(-2)	1.245(1)	1.475(1)	1.701(1)	1.936(1)	2.166(1)
0.417	2.4	2.844(-2)	1.236(1)	1.467(1)	1.697(1)	1.927(1)	2.157(1)
0.385	2.6	2.185(-2)	1.228(1)	1.459(1)	1.689(1)	1.919(1)	2.149(1)
0.357	2.8	1.686(-2)	1.221(1)	1.451(1)	1.681(1)	1.912(1)	2.142(1)
0.333	3.0	1.305(-2)	1.214(1)	1.444(1)	1.674(1)	1.905(1)	2.135(1)
0.286	3.5	6.970(-3)	1.199(1)	1.429(1)	1.659(1)	1.889(1)	2.120(1)
0.250	4.0	3.779(-3)	1.185(1)	1.415(1)	1.646(1)	1.876(1)	2.106(1)
0.222	4.5	2.073(-3)	1.173(1)	1.404(1)	1.634(1)	1.864(1)	2.094(1)
0.200	5.0	1.148(-3)	1.163(1)	1.393(1)	1.623(1)	1.854(1)	2.084(1)
0.182	5.5	6.409(-4)	1.153(1)	1.384(1)	1.614(1)	1.844(1)	2.074(1)
0.166	6.0	3.601(-4)	1.145(1)	1.375(1)	1.605(1)	1.835(1)	2.066(1)
0.154	6.5	2.034(-4)	1.137(1)	1.367(1)	1.597(1)	1.827(1)	2.058(1)
0.142	7.0	1.155(-4)	1.129(1)	1.360(1)	1.590(1)	1.820(1)	2.050(1)
0.133	7.5	6.583(-5)	1.122(1)	1.353(1)	1.583(1)	1.813(1)	2.043(1)
0.125	8.0	3.767(-5)	1.116(1)	1.346(1)	1.576(1)	1.807(1)	2.037(1)
0.118	8.5	2.162(-5)	1.110(1)	1.340(1)	1.570(1)	1.801(1)	2.031(1)
0.111	9.0	1.245(-5)	1.104(1)	1.334(1)	1.565(1)	1.795(1)	2.025(1)
0.105	9.5	7.185(-6)	1.099(1)	1.329(1)	1.559(1)	1.789(1)	2.020(1)

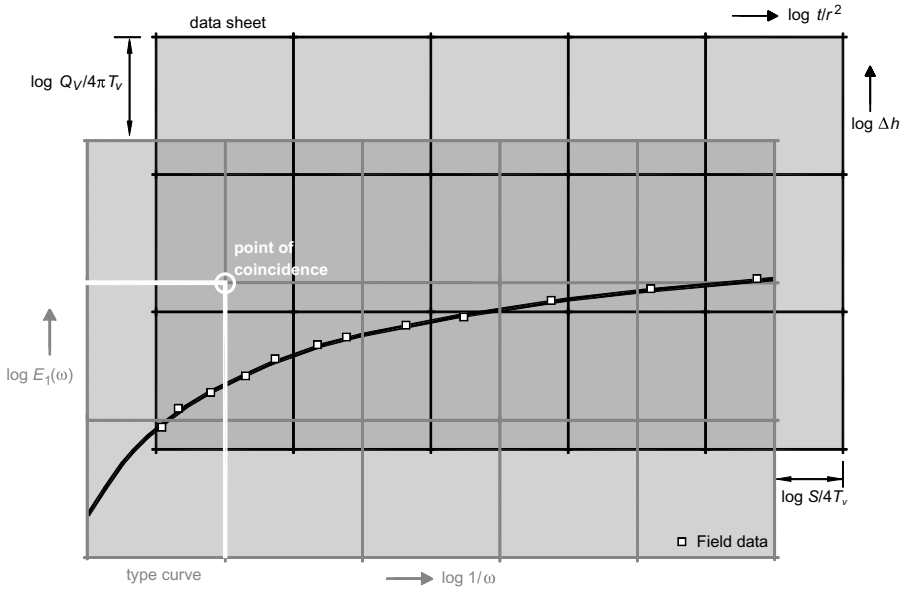


Figure 4.18. Principle of the Theis method for non-stationary groundwater flow regimes in a confined aquifer.

In practice, $1/\omega$ is used instead of ω , and the overlaid point is chosen so that $E_1(\omega)$ and $1/\omega$ are easily readable values (Fig. 4.18).

The displacement needed to achieve overlay is somewhat subjective and is hindered when the previously mentioned conditions required by the Theis equation are not fulfilled in all pairs of t and r values, for example at the beginning or at the end of the pumping test, when storage in the well itself is significant (see also section 4.4.4). For some of these special cases there are other suitable methods (see section 6.7.2.4).

The issue of subjectivity when overlaying cannot be solved by calculation; there is danger of interference that may go unnoticed. It is therefore best to make a graphic representation to be able to visually control the quality of the curve.

4.5.3 Transient flow—Hantush equation (semiconfined aquifer)

The following equation describes the incoming groundwater flow to a well in a semi-confined (leaky) homogeneous, isotropic aquifer (main aquifer), which may exchange water through its top or bottom with other aquifers in the polar coordinates plane:

$$\frac{\partial^2 h}{\partial r^2} + \frac{1}{r} \frac{\partial h}{\partial r} + \frac{h_0 - h}{\lambda_D^2} = \frac{S}{T_v} \frac{\partial h}{\partial t} \quad (4.73)$$

r = radial distance from the pumping well

T_v = transmissivity of the main aquifer

S = storage coefficient of the main aquifer

h_0 = hydraulic head of the upper or lower aquifer and initial piezometric level of the main aquifer

λ_D = leakage coefficient (dripping coefficient)

L = leakage factor (dripping factor)

b_s = thickness of the semiconfining layer

K_{HL} = vertical hydraulic conductivity of the semiconfining layer

$$\text{with: } \lambda_D = \sqrt{\frac{T_v}{L}} \quad \text{where: } \lambda_D = \sqrt{\frac{b_s T_v}{K_{HL}}} \quad \text{with: } L = \frac{K_{HL}}{b_s}$$

For the same initial and boundary values considered in the derivation of the Theis equation, Hantush (1956) obtained the following solution for the flow equation in a semi-confined aquifer, describing the piezometric levels $h(r, t)$ as a function of the radial distance r from the pumping well and time t since the beginning of the pumping process:

$$\Delta h = h_0 - h(r, t) = -\frac{Q_v}{4\pi T_v} E_1(\omega, r/\lambda_D)$$

$$\text{with: } \omega = \frac{r^2 S}{4T_v t} \quad \text{and: } E_1(\omega) = \int_{\omega}^{\infty} \frac{1}{u} e^{-u - \frac{r^2}{4\lambda_D^2} u} du$$

4.5.4 Turbulence and the Forchheimer's law

Since its formulation in 1856, Darcy's law has been accepted as the fundamental equation of the flow of fluids in porous media. Nevertheless, very early on it was observed that this basic law is valid only for slow, laminar, viscous flows. The domain of validity for Darcy's law is called the *seepage velocity domain* (Scheidegger 1974). Fortunately, most groundwater flow cases fall in this category. Bear (1979) states: "Practically all evidence indicates that Darcy's law is valid as long as the Reynolds number does not exceed some value between 1 and 10". Any flow with a Reynolds number below 10 is clearly laminar, and it would be valid to apply Darcy's law. Reynolds number is a dimensionless parameter; for porous media flow, it is expressed as:

$$Re = \frac{\rho_f v d_g}{\mu_f} \quad (4.74)$$

where v is the specific discharge and d_g is a representative grain diameter for the porous medium, or the fracture aperture in fissured rocks. Sometimes d_g is taken such that 10% or 30% by weight of the grains are smaller than that diameter. Other authors suggest $d_g = (k/\phi)^{1/2}$ to be the representative length (Bear 1979). The resistance to flow inside the porous rock is computed by a friction factor defined by Scheidegger (1974):

$$f_{\phi} = \frac{2d_g}{v^2 \rho_f} \frac{dp}{dx} \quad (4.75a)$$

Multiplying this factor by Re we obtain a dimensionless condition for the validity of Darcy's law (eq. 2.0):

$$Re f_{\phi} = \frac{\rho_f d_g}{\mu_f} \frac{2d_g}{v \rho_f} \frac{dp}{dx} = \frac{2d_g^2}{k} \quad (4.75b)$$

The flow in a porous rock obeys Darcy's law if the product $Re f_{\phi}$ is constant. This constant depends on both permeability and diameter d_g . Experimental tests have shown that for flow regimes with Reynolds number values up to 10 are Darcyan. However, experimental values reported by Scheidegger (1974) indicate that for the interval $0.1 < Re < 75$, the flow may still be Darcyan. Bear (1979) mentioned the value of $Re = 100$, as the upper limit of the transition region in which Darcy's law is no longer valid. At higher values, the flow becomes completely turbulent (Bear 1979). We assume that when the Reynolds number $Re > 100$, the porous flow

is turbulent; in these cases, instead of using equation (4.13), the classic formula of Forchheimer (1901) or another generalization of this equation must be applied:

$$\begin{aligned} -\vec{\nabla}p &= \frac{\mu_f}{k} \vec{v} + \rho_f \beta_f |\vec{v}| \vec{v} \dots \quad (\text{a}) \\ -\frac{dp}{dx_i} &= \frac{\mu_f}{k} v_i + \rho_f \beta_f v_i^{n_\beta} \dots \quad (\text{b}) \end{aligned} \quad (4.76)$$

where β_f is an experimental factor and v_i is the velocity component in the direction of the turbulence. The exponent n_β can be a whole number or a fractional number, although 2 is a common value (Bear 1979). Forchheimer himself established in 1930 an interval for this parameter, $1.6 < n_\beta < 2$. Other authors found $n_\beta = 1.8, 2.23$ and 2.49 for air flowing in porous media (Bear 1972). Experiments by Thauvin and Mohanty (1997) found that the coefficient β_f in the original equation of Forchheimer depends closely on the morphology of the porous medium. If the average opening of the pores is increased, porosity and permeability increase, but β_f falls abruptly. On the other hand, if the pores reduce their size or tend to collapse, the coefficient β_f is increased. The experimental measured values are $2.7 \times 10^4 < \beta_f < 5.5 \times 10^6$.

Using nitrogen as a natural tracer, Suárez and Mañón (1990), estimated that the average velocity of the fluid displacement in a region of the Los Azufres, Mexico, reservoir with faults and fractures varies between 2.6×10^{-4} and 0.53×10^{-5} m/s. Applying this information to a traverse section of a water saturated fault with an aperture of 0.01 m, we could estimate the value of the Reynolds number in the fault:

$$Re = \frac{\rho_f d_g v}{\mu_f \varphi} = \frac{412.6 \times 0.01}{6.3 \times 10^{-5} \times 0.2} v = 327460.3 v \leq 10 \quad \Leftrightarrow \quad v \leq 3.05 \times 10^{-5} \frac{\text{m}}{\text{s}} \quad (4.77)$$

Combining these parameters with field data, we found that $v \approx 10^{-5}$ m/s; thus the coefficient in the Forchheimer equation is:

$$\begin{aligned} -\frac{dp}{dx} &= 1.7 \times 10^4 \frac{\text{Pa}}{\text{m}} = \frac{\mu_f}{k} v + \rho_f \beta_f v^2 \quad \Rightarrow \quad \beta_f = \left(-\frac{dp}{dx} - \frac{\mu_f}{k} v \right) \frac{1}{\rho_f v^2} \\ &= \frac{\left(1.7 \times 10^4 - \frac{6.3 \times 10^{-5} \times 2.6 \times 10^{-4}}{10^{-12}} \right)}{412.6 \times (2.6 \times 10^{-4})^2} = 2.22 \times 10^7 \text{ m}^{-1} \end{aligned} \quad (4.78)$$

Now the non-Darcy part of the pressure gradient is around $\rho_f \beta_f v^2 = 0.0006$ MPa, which represents 3.7% of the estimated total pressure gradient. At larger flow velocities in the fault, we expect a larger pressure drawdown and consequently higher non-Darcyan coefficients.

4.6 HEAT TRANSPORT EQUATIONS

The transfer of thermal energy from a hot region of a porous rock to a colder zone of the same rock is called heat transport. The transfer always originates from the different temperatures existing in the rock/fluid system. This phenomenon is a very intuitive matter and its experimental perception (section 2.1) is at the foundations of porous rock thermodynamics. Heat transport occurs through three mechanisms: conduction, which is the energy transferred by molecular vibration through a rock or fluid; convection, which is the energy transferred by the fluid in motion; radiation, which is the energy transferred through electromagnetic waves, or any combination of these modes. In this book, we consider only the first two forms of heat transport.



Figure 4.19. Joseph Fourier (1768–1830).

4.6.1 Heat conduction

The *fundamental law of heat conduction* is an experimental result stating that heat flow in a continuous rock occurs because of temperature differences existing in the medium. The transfer of energy occurs from the zones of higher temperature to the zones of lower temperature. The French mathematician and physicist Jean Baptiste Joseph Fourier (Fig. 4.19), who was the first scientist to experiment with heat conduction, formulated an accurate model for this type of energy transfer and solved his model using for the first time the Fourier series technique (chapter 5). His doctoral advisor was Joseph Lagrange and Fourier was the teacher of Gustav Dirichlet and of Claude Louis Navier (Fig. 4.2). Joseph Fourier discovered also the greenhouse effect on Earth in 1824, stating that “. . . an atmosphere serves to warm a planet . . . gases in the atmosphere might increase the surface temperature of the Earth.” (Wikipedia 2009b).

Energy flow is equal to the thermal conductivity multiplied by the temperature gradient within the rock. The statement of the heat conduction is expressed mathematically as the Fourier’s law introduced in equation (2.9):

$$\vec{q}_T = -\mathbf{k}_T \cdot \vec{\nabla} T \quad (4.79)$$

The vectorial flow of heat has units of $[\text{W}/\text{m}^2]$, the components of \mathbf{k}_T , which is the thermal conductivity tensor of the porous rock, have units of $[\text{W}/\text{m}/^\circ\text{C}]$ and their properties were discussed in section 2.1.4. Let Ω be the domain of a conductive porous rock and let $\Gamma = \partial\Omega$ be its boundary. Let Q_E [J] be the thermal energy of Ω that can be exchanged with its environment. Then the instantaneous energy flow going in/out of Ω is (eq. 2.94a):

$$\frac{dQ_E}{dt} = - \int_{\Gamma} \vec{q}_T \cdot \vec{n} \, dS = - \int_{\Omega} \vec{\nabla} \cdot \vec{q}_T \, d\Omega, \quad \left[\frac{\text{J}}{\text{s}} = \text{W} \right] \quad (4.80)$$

We used the divergence theorem to transform the first integral in this equation. There is a basic thermodynamic relationship connecting Q_E to the thermal rock properties and with the volumetric heat generation $Q_H(x, y, z) = q_H/V_B$ (eq. 2.13):

$$\frac{dQ_E}{dt} = \int_{\Omega} \frac{\partial}{\partial t} (c_p \rho_r T) d\Omega = \int_{\Omega} \vec{\nabla} \cdot (\mathbf{k}_T \cdot \vec{\nabla} T) d\Omega + \int_{\Omega} Q_H \, d\Omega \quad (4.81)$$

As long as equation (4.81) is valid for an arbitrary domain Ω , from this integral rock property, we deduce the mathematical model for heat transfer in porous rocks:

$$\frac{\partial}{\partial t}(c_p \rho_r T) = \vec{\nabla} \cdot (\mathbf{k}_T \cdot \vec{\nabla} T) + Q_H \quad \left[\frac{\text{W}}{\text{m}^3} \right] \quad (4.82)$$

Model (4.82) is a partial differential equation that describes the spatial distribution and variation of temperature in the domain Ω . Note that if T is constant, both sides of equation (4.82) become nulls and $Q_H = 0$. Due to the thermodynamic relations used to derive it, this equation also describes the heat distribution in the region occupied by the porous rock. The thermal conductivity tensor \mathbf{k}_T is specific of Ω ; it can depend on the spatial coordinates at any point $(x, y, z) \in \Omega$ and usually has the form of a diagonal matrix, with non-zero components (k_{Tx}, k_{Ty}, k_{Tz}) in the main diagonal. In three dimensions, equation (4.82) develops into the following system:

$$\begin{aligned} \frac{\partial}{\partial t}(c_p \rho_r T) - Q_H &= \vec{\nabla} \cdot \begin{pmatrix} k_{Tx} & 0 & 0 \\ 0 & k_{Ty} & 0 \\ 0 & 0 & k_{Tz} \end{pmatrix} \cdot \vec{\nabla} T = \vec{\nabla} \cdot \begin{pmatrix} k_{Tx} \partial_x T \\ k_{Ty} \partial_y T \\ k_{Tz} \partial_z T \end{pmatrix} \\ &= \frac{\partial}{\partial x} \left(k_{Tx} \frac{\partial T}{\partial x} \right) + \frac{\partial}{\partial y} \left(k_{Ty} \frac{\partial T}{\partial y} \right) + \frac{\partial}{\partial z} \left(k_{Tz} \frac{\partial T}{\partial z} \right) \end{aligned} \quad (4.83)$$

Under some circumstances the porous rock is more or less homogeneous and isotropic, its density and specific heat are constants and $\mathbf{k}_T = k_T \mathbf{I}$ (\mathbf{I} is the unit matrix) and the heat equation is simplified:

$$\begin{aligned} \frac{\partial T}{\partial t} &= \frac{k_T}{\rho c_p} \vec{\nabla} \cdot \vec{\nabla} T + \frac{Q_H}{\rho c_p}, \quad \delta_T = \frac{k_T}{\rho c_p}, \quad \left[\frac{\text{m}^2}{\text{s}} \right] \\ \Rightarrow \quad \boxed{\frac{\partial T}{\partial t} = \delta_T \nabla^2 T + \frac{\delta_T}{k_T} Q_H}, \quad \left[\frac{^\circ\text{C}}{\text{s}} \right] \end{aligned} \quad (4.84)$$

The coefficient δ_T is the thermal diffusion coefficient of the domain Ω discussed in section 2.1.8 of chapter 2. Conduction always decreases with density. Liquid water and steam are less conductive than solid rock. At 200°C, volcanic rock k_T is about 1.8 W/m°C; at the same conditions, k_T of liquid water is 0.65 W/m°C and k_T of steam is 0.05 W/m°C. The pure mathematical form of the heat equation is analogous to other phenomena appearing in cold aquifers and geothermal systems such as the groundwater flow and the solute transport equations. Fourier's law of heat conduction is analogous to Darcy's law and to Fick's law of diffusion. Several examples and fundamental solutions of (4.84) for simple domains are found at Wikipedia (2009c). Complete references on general heat transfer are found in the free electronic book of Lienhard IV and Lienhard V (2008).

4.6.2 Heat convection

Thermal energy transported by convection is a fundamental mechanism in geothermal systems. This type of heat transfer is associated with the circulation of hot fluids in the reservoir. We can distinguish between two mechanisms of convection: free convection (=natural convection) and forced convection. Forces convection occurs if heat is transported with a fluid, which moves as result of a hydraulic gradient. At free convection, the heat is carried by the movement originating out of fluid density changes (due to variable temperature in space and time) and the buoyancy for example produced by fluid heating in deeper regions of the reservoir itself. The buoyancy results from the lower density of the deep warmed fluid, which ascends forming convection cells. Boiling and condensation are convection transfers associated with the heat carriage during phase

change of the fluid. For example, when the liquid evaporates, it gains condensation heat; when steam condenses, it releases the latent heat of vaporization. Boiling is a very efficient energy transfer mechanism. The amount of heat released is the same as the amount of heat absorbed during evaporation. The basic equation for convection is Newton's law of cooling:

$$\frac{dQ_E}{dt} = h_T A(T - T_f) \quad \left[\frac{\text{J}}{\text{s}} \right] \quad (4.85)$$

The term h_T [$\text{J/s/m}^2/^\circ\text{C}$] is the heat transfer coefficient, Q_E is the thermal energy transfer by convection, A is the rock surface area of the heat being transferred, T is the temperature of the rock and T_f is the average temperature of the moving fluid in the porous environment. If there is thermal equilibrium in the fluid-rock system, $T \approx T_f$ and the rate of heat transfer by convection is zero. This classic formula of cooling applies only under laboratory conditions and is not very useful in real geothermal systems because it is very difficult to measure all the parameters included in the formula. Very often, the hypothesis of thermal equilibrium between the porous rock and the fluid is made in numerical simulations. Therefore, it is necessary to simplify the solution of the equations involved. The formula normally used for the study of convection in geothermal reservoirs is:

$$\text{convective fluid energy: } \vec{Q}_f = \rho_f \vec{v}_f h_f, \quad \left[\frac{\text{kg} \cdot \text{m} \cdot \text{kJ}}{\text{m}^3 \cdot \text{s} \cdot \text{kg}} \right] = \left[\frac{\text{kW}}{\text{m}^2} \right] \quad (4.86)$$

where \vec{Q}_f is the vectorial flow of convective energy related to the fluid movement, \vec{v}_f is the Darcy's velocity, ρ_f is the fluid density and h_f its specific enthalpy. Convection in porous media can only occur in the fluids during the transport of heat by fluid circulation combined with conduction into the fluid and between the rock and the fluid. The total flow of heat combined in the rock/fluid system is convection plus conduction:

$$\text{total flow of fluid energy: } \vec{E}_f = \rho_f \vec{v}_f h_f - k_{Tf} \cdot \vec{\nabla} T \quad (4.87)$$

The coefficient k_{Tf} is the fluid thermal conductivity. This formula is used in the next section to develop the flow equations in single and two-phase geothermal reservoirs. In chapter 5 the same expression will be used to build the numerical approximations of these two flow models.

4.7 FLOW OF MASS AND ENERGY IN TWO-PHASE RESERVOIRS

4.7.1 Darcy's law for two-phase systems

Under appropriate thermodynamic conditions (Fig. 2.12), vapor and liquid can coexist simultaneously in high-enthalpy geothermal reservoirs. The geothermal reservoir can naturally contain water in vapor and liquid phase or the reservoir may initially contain only liquid and the fluid extraction diminishes the pressure producing a steam phase. Then it is said that the reservoir is a two-phase system. This situation introduces several thermodynamic complications in the fluid because each phase has its own variables: density, viscosity, enthalpy, specific heat, and thermal conductivity. In section 2.3 the thermodynamic properties of two-phase water are shown in a wide range. The main useful relationships for two-phase fluids are listed in subsection 2.3.6.9. The vectorial flow of a two-phase fluid through a differential area dS wrapping a differential volume dV_B of the porous reservoir is the mass of fluid passing per unit area, per second [$\text{kg/m}^2/\text{s}$]:

$$\begin{aligned} \text{flow of liquid: } \vec{F}_l &= \rho_l \vec{v}_l - \vec{e}_v \dots \quad (\text{a}) \\ \text{flow of steam: } \vec{F}_v &= \rho_v \vec{v}_v - \vec{e}_l \dots \quad (\text{b}) \\ \text{two-phase flow: } \vec{F}_{M2} &= \vec{F}_l + \vec{F}_v \dots \quad (\text{c}) \end{aligned} \quad (4.88)$$

where subindices l, v represent liquid and vapor; the terms ε_v and ε_l are the evaporation and condensation rates of each phase, respectively. In each closed differential volume dV_B , we have $\varepsilon_l + \varepsilon_v = 0$. For laminar flow, the average vectorial velocity of each phase is given by Darcy's law, generalized by Muskat (1937) for two-phase flows. The specific discharges of each phase through the differential element of surface dS are:

$$\text{a) } \vec{v}_l = -\frac{\mathbf{K} k_{rl}}{\mu_l} (\vec{\nabla} p_l - \rho_l \vec{g}), \quad \text{b) } \vec{v}_v = -\frac{\mathbf{K} k_{rv}}{\mu_v} (\vec{\nabla} p_v - \rho_v \vec{g}) \quad (4.89)$$

where \mathbf{K} is the rock absolute permeability tensor at each point (x, y, z) , k_{rl} and k_{rv} are the relative permeabilities of each phase. The two-phase continuity equation is:

$$\begin{aligned} \frac{\partial}{\partial t} (\varphi \rho_f) &= -\vec{\nabla} \cdot \vec{F}_{M2} + q_f; & q_f &= q_l + q_v \\ \rho_f &= \rho_l S_l + \rho_v S_v; & S_l + S_v &= 1; & p_C &= p_v - p_l \end{aligned} \quad (4.90)$$

The phase pressures are related through the capillary pressure p_C and the two phases are coupled through the mixture density and by the relationship among saturations.

4.7.2 Flow of energy in reservoirs with single-phase fluid

The vectorial flow of thermal energy at each point (x, y, z) through a differential area dS of a porous volume dV_B of the reservoir (Fig. 4.1), is the total amount of heat by convection plus the total amount of heat by conduction that passes every second, per unit area [$\text{J/m}^2/\text{s}$] in the rock-fluid system:

$$\begin{aligned} \text{fluid energy: } \vec{E}_f &= \vec{F}_{M1} h_f - \mathbf{k}_{Tf} \cdot \vec{\nabla} T \dots \quad (\text{a}) \\ \text{rock energy: } \vec{E}_r &= \vec{F}_r h_r - \mathbf{k}_{Tr} \cdot \vec{\nabla} T \dots \quad (\text{b}) \\ \text{total energy flow: } \vec{F}_{E1} &= \vec{E}_f + \vec{E}_r \dots \quad (\text{c}) \end{aligned} \quad (4.91)$$

The first term in the second member of equations (4.91a) and (4.91b) represents convection while the second term is the heat conduction. \mathbf{k}_{Tf} and \mathbf{k}_{Tr} are the thermal conductivity tensors for the fluid and for the rock, respectively. We assume that the rock mass flow is negligible ($F_r \approx 0$) under practical geothermal conditions. Then the total energy flow in the differential volume dV_B (Fig. 4.6) is:

$$\vec{F}_{E1} = \vec{F}_{M1} h_f - \mathbf{k}_T \cdot \vec{\nabla} T, \quad \mathbf{k}_T = (1 - \varphi) \mathbf{k}_{Tr} + \varphi \mathbf{k}_{Tf} \quad (4.92)$$

where h_f [J/kg] is the specific enthalpy of the fluid; \vec{F}_{M1} is the fluid mass flow (eq. 4.14) and \mathbf{k}_T is the effective or average thermal conductivity of the rock-fluid system. This parameter can be used as a tensor or a number, depending on the availability of measured field data. The total internal energy in the REV or differential volume dV_B is:

$$\frac{\text{fluid energy} + \text{rock energy}}{\text{volume}} = U_T = \varphi \rho_f e_f + (1 - \varphi) \rho_r e_r \quad \left[\frac{\text{J}}{\text{m}^3} \right] \quad (4.93)$$

The rock energy is approximated through its specific enthalpy. Using the definition of the rock specific heat at constant pressure (see chapter 2):

$$c_r = \left(\frac{\partial h_r}{\partial T} \right)_p \Rightarrow de_r \approx dh_r \approx c_r dT \quad (4.94)$$

The conservation of energy states that:

- The instantaneous change of thermal energy in a differential volume dV_B of porous rock is equal to the total flow of heat through the differential surface dS surrounding dV_B , plus the rate of heat extracted or produced in dV_B .

$$\frac{\partial U_T}{\partial t} = -\vec{\nabla} \cdot \vec{F}_{E1} + Q_H \quad \left[\frac{\text{J}}{\text{s m}^3} = \frac{\text{W}}{\text{m}^3} \right] \quad (4.95)$$

The model defined by equation (4.95) is applicable to complex porous media with simultaneous heat and mass flows in single-phase or in two-phase fluids, as shown in the next section.

4.7.3 *Flow of energy in reservoirs with two-phase fluid*

The vectorial flow of thermal energy at each point (x, y, z) through a differential area dS of a porous volume dV_B of the reservoir is the total amount of heat by convection plus the total amount of heat by conduction that passes per unit area in every second [$\text{J}/\text{m}^2/\text{s}$] in the two-phase fluid-rock system:

$$\begin{aligned} \text{liquid energy flow: } \vec{E}_l &= \vec{F}_l h_l - \mathbf{k}_{Tl} \cdot \vec{\nabla} T_l \dots \quad (\text{a}) \\ \text{steam energy flow: } \vec{E}_v &= \vec{F}_v h_v - \mathbf{k}_{Tv} \cdot \vec{\nabla} T_v \dots \quad (\text{b}) \\ \text{rock energy flow: } \vec{E}_r &= \vec{F}_r h_r - \mathbf{k}_{Tr} \cdot \vec{\nabla} T_r \dots \quad (\text{c}) \end{aligned} \quad (4.96)$$

The total heat flow is:

$$F_{E2} = \vec{E}_l + \vec{E}_v + \vec{E}_r = \vec{F}_l h_l + \vec{F}_v h_v - \mathbf{k}_T \cdot \vec{\nabla} T \quad (4.97)$$

The effective porous rock thermal conductivity is:

$$\mathbf{k}_T = (1 - \varphi) \mathbf{k}_{Tr} + \varphi S_l \mathbf{k}_{Tl} + \varphi S_v \mathbf{k}_{Tv} \quad (4.98)$$

where \mathbf{k}_{Tr} , \mathbf{k}_{Tl} and \mathbf{k}_{Tv} are the thermal conductivity tensors of the rock, liquid and steam, respectively. The equation for the flow of thermal energy in the volume dV_B has the same form as in equation (4.95), with the total flow of thermal energy given by equation (4.97). We also assume that the temperature of both phases is the same as the temperature of the surface of the rock in contact with the fluid. That means, there is an instantaneous thermal equilibrium in the rock-fluid system and $T_l \approx T_v \approx T_r = T$. The variation of the total thermal energy is:

$$\begin{aligned} \frac{\partial U_T}{\partial t} &= -\vec{\nabla} \cdot \vec{F}_{E2} + Q_H \\ U_T &= \frac{\text{fluid energy} + \text{rock energy}}{\text{volume}} = \varphi \rho_f e_f + (1 - \varphi) \rho_r e_r \end{aligned} \quad (4.99\text{a})$$

The reciprocal relation between internal energy and specific enthalpy is:

$$\begin{aligned} \rho_f e_f &= S_l \rho_l e_l + S_v \rho_v e_v = \rho_f h_f - p \\ \rho_f h_f &= S_l \rho_l h_l + S_v \rho_v h_v = \rho_f e_f + p \end{aligned} \quad (4.99\text{b})$$

In chapter 5 we present the solution of all these equations for the flow of mass and energy in porous media using different numerical methods.

4.7.3.1 The Garg's model for two-phase fluid

Garg (1980) derived a simple diffusivity equation for the two-phase flow of water in geothermal systems. This model is valid for reservoirs of radial geometry, assuming a fully penetrating well in a very large homogeneous, isotropic reservoir of thickness b_a . The main hypothesis is that the reservoir is initially a two-phase system with uniform pressure and temperature everywhere. The resulting partial differential equation is completely analogous to (eq. 4.47) developed in section 4.4.3. The simplified mathematical model (Garg 1980) is:

$$\frac{\partial p}{\partial t} = \eta_H \frac{\partial^2 p}{\partial r^2} + \frac{\eta_H}{r} \frac{\partial p}{\partial r}; \quad \eta_H = \frac{1}{\varphi \rho_f C_T} \left(\frac{k}{v_f} \right)_T \quad (4.100)$$

In this model, C_T is the total compressibility, v_f is the kinematic viscosity, and equation (4.90) gives the fluid density. The hydraulic diffusivity η_H depends on the total kinematic mobility $(k/v)_T = (k/v)_l + (k/v)_v$, which depends on temperature. The internal and external boundaries and initial conditions are:

$$\begin{aligned} \text{initial condition: } & p(r, 0) = p_i, \quad \forall r \geq 0 \\ \text{external boundary: } & \lim_{r \rightarrow \infty} p(r, t) = p_i, \quad \forall t > 0 \\ \text{internal boundary: } & \lim_{r \rightarrow 0} \left(r \frac{\partial p}{\partial r} \right) = -\frac{Q_M}{2\pi b_a} \left(\frac{v_f}{k} \right)_T \end{aligned} \quad (4.101)$$

To solve this model we use the same Boltzmann transformation of section (4.4.3). Replacing the corresponding values, the final solution of the model (eqs. 4.100 and 4.101), satisfying the boundary and initial conditions, is:

$$p(r, t) = p_i + \frac{Q_M}{4\pi b_a} \left(\frac{v_f}{k} \right)_T E_1 \left(\frac{r^2}{4\eta_H t} \right) \quad (4.102)$$

If Q_M [kg/s] > 0 the fluid is entering the reservoir (injection). If Q_M < 0 the fluid is being extracted from the reservoir (production). The flowing enthalpy is given by the following formula:

$$h = \left(\frac{k}{v_l} h_l + \frac{k}{v_v} h_v \right) \left(\frac{v_f}{k} \right)_T \quad (4.103)$$

4.7.4 Heat pipe transfer in two-phase reservoirs

A heat pipe is a simple device, natural or artificial, that can quickly transfer large amounts of heat from one point to another. Heat pipes are like heat superconductors because they possess an extraordinary heat transfer capacity with almost no energy loss. R.S. Gaugler first suggested the idea of heat pipes in 1942. In two-phase geothermal reservoirs, the heat pipe steam-liquid counterflow mechanism explains the heat transfer when the system is in its natural state. To understand natural heat pipes in reservoirs we briefly describe how an artificial one works (Wikipedia 2009d):

- A typical heat pipe consists of a sealed pipe made of a material with high thermal conductivity. Inside the container is a liquid under its own pressure that enters the pores of the capillary material of the heat pipe, wetting all the internal surfaces. Applying heat at any point along the surface of the heat pipe causes the liquid at that point to boil and enter a vapor state. When this happens, the liquid picks up the latent heat of vaporization. The high-pressure gas moves inside the sealed container to a colder location where it condenses. Thus, the gas gives up the latent heat of vaporization and moves heat from the input to the output end of the heat pipe. The main reason for the effectiveness of heat pipes is the evaporation and condensation of the

working fluid. Almost all of that energy is rapidly transferred to the “cold” end, at the point where the fluid condenses, making a very effective heat transfer system with no moving parts. Heat pipes have an effective thermal conductivity many thousands of times that of copper. The heat transfer or transport capacity of a heat pipe is specified by its “axial power rating (APR)”. It is the energy moving axially along the pipe. The larger the heat pipe diameter, the greater is the APR. Similarly, the longer the heat pipe, the lesser is the APR.

Natural heat pipes occur very often in two-phase reservoirs. The corresponding conceptual model of such systems can be simplified with a vertical section of porous, fractured rock in which thermal energy is transported from depth by ascending steam. This steam condenses at the top of the aquifer releasing its heat of vaporization. The condensed liquid descends to the bottom of the permeable reservoir, where the temperature is higher. The liquid is heated and it evaporates again. For example, this type of effective heat transfer drives the Los Azufres, Mexico geothermal system (Suarez *et al.* 1989). The numerical simulation of a natural heat pipe mechanism in this two-phase reservoir is described in example 9.6.7.

4.7.5 *The general heat flow equation*

The general heat flow equation in geothermal reservoirs includes conduction and convection through an advective term related to the transport of energy by the moving fluid in the pores (Lautrup 2005). These combined energy transfer processes are modeled by the following partial differential equation:

$$c_p \rho \frac{\partial T}{\partial t} - \vec{\nabla} \cdot (\mathbf{k}_T \cdot \vec{\nabla} T) + \vec{\nabla} \cdot (c_p \rho T \vec{v}) = Q_H \quad (4.104a)$$

where vector \vec{v} represents the Darcy’s fluid velocity and Q_H [W/m³] is the volumetric thermal energy production. The other parameters were introduced in chapter 2. This equation is valid not only for heterogeneous, anisotropic porous rocks, but also for moving viscous fluids governed by the Navier-Stokes equations, at the micro-scale of the pores or for the wellbore for example.

To include convection in the heat flow vector (eq. 2.9) it is necessary to add the corresponding effect of advection related to the fluid velocity in the reservoir (see eq. 4.87):

$$\vec{q}_T = -\mathbf{k}_T \cdot \vec{\nabla} T + c_p \rho T \vec{v} \quad (4.104b)$$

These two equations complete our discussion of the heat transfer phenomena in porous rocks.

4.8 SOLUTE TRANSPORT EQUATIONS

Diffusion is a common molecular phenomenon in porous rocks that occurs because of the presence of different concentrations of a substance in the fluid. Diffusion is the mechanism by which particles of a fluid mixture are transported from regions of high concentration to regions of lower concentration. The diffusion phenomenon is the macroscopic effect of a molecular random motion. Diffusion can occur in gases, liquids, and solids. The dissolved substance is the solute and the substance in which the solute is dissolved is called the solvent. Solutes diffuse at different speeds, the fastest in gases, and the slowest in solids. In aquifers and in geothermal systems, the solvent is the water and the solutes are salts, gases, organic or inorganic constituents. The non-homogeneous distribution of gases and salts in the reservoir fluid starts the diffusion process. The transport of an artificial tracer injected into a porous system also occurs by diffusion. The substance dissemination occurs in the same direction in which its concentration decreases. The resulting flux is proportional to the concentration gradient of the solute. In this section, we introduce the general solute transport equations.

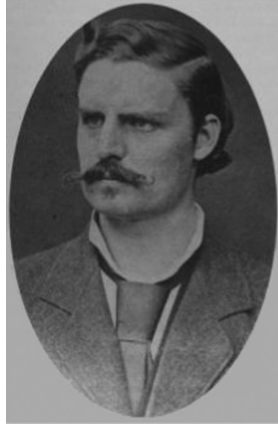


Figure 4.20. Adolf E. Fick (1829–1901), German physiologist.

4.8.1 Fick's law of diffusion

In 1855, Adolf Eugen Fick (Fig. 4.20) introduced his Fick's law to describe the diffusion of a gas across a fluid membrane. This law was first devised as a technique for measuring cardiac output. Later it was applied equally to physiology and physics. Fick considered the concentration of oxygen as a marker substance to calculate the blood flow to the different organs inside the human body. Fick noticed the physical analogy between heat conduction and diffusion. The concentration $N^*(x)$ of the diffusive substance is the number of molecules of the solute existing per unit volume of solvent [N_M/m^3]. We define the concentration flux q^* as the number N_M of molecules of the substance passing through the unit area of the medium in each time t in the direction of diffusion. Fick discovered a relationship between flow and concentration of the substance that can be expressed in one-dimensional flow as:

$$q^* = -D^* \frac{dN^*(x)}{dx} \quad \left[\frac{N_M}{m^2s} \right] \quad (4.105)$$

The molecular diffusivity D^* [m^2/s] is a parameter that describes how fast or slow the molecules of the solute diffuse. For diffusion in porous rocks, this equation is modified to take into account the presence of both the pores and the solid grains. The first form of Fick's law in porous media is a steady state equation (Batu 2006):

$$\begin{aligned} \text{in one dimension: } q_D &= -\varphi D \frac{\partial C}{\partial x}(x) \\ \text{in 3D: } \vec{q}_D &= -\varphi \mathbf{D} \cdot \vec{\nabla} C(x, y, z) = -\varphi \left(D_x \frac{\partial C}{\partial x} + D_y \frac{\partial C}{\partial y} + D_z \frac{\partial C}{\partial z} \right) \\ \vec{x} &= (x, y, z), \vec{q}_D = (q_{Dx}, q_{Dy}, q_{Dz}) \quad \left[\frac{\text{mol}}{m^2s} \right] \text{ is the diffusion flux} \end{aligned} \quad (4.106)$$

The negative sign in equation (4.106) indicates that the diffusing mass flows in the direction of decreasing concentration. This principle states that a substance put into solution will tend to diffuse towards constant concentration throughout the solution. The absence of a velocity term in (eq. 4.106) indicates that diffusive transport of solutes can occur in fluids at rest. If the solution is flowing, diffusive transport can still occur and becomes part of hydrodynamic dispersion (Bear 1979, Bear and Bachmat 1984, Batu 2006).

The main function $C(x)$ is the molecular concentration of the substance in $[\text{mol}/\text{m}^3]$, which is the number of molecules of solute per unit volume of the solution; however, other units can be used (see subsection 2.3.11). For example, grams per liter $[\text{g}/\text{L}]$ or $[\text{kg}/\text{m}^3]$, if C is defined as the mass of solute dissolved per unit volume of the solvent. In aquifers and in geothermal reservoirs, the most common units for $C(x)$ are milligrams per liter $[\text{mg}/\text{L}]$ and parts per million [ppm or mg/kg if we use SI units], which equals the number of grams of solute per million grams of solution $[\text{g solute}/10^6 \text{g solution}]$.

The parameter D $[\text{m}^2/\text{s}]$ is called the diffusivity or coefficient of molecular diffusion in the porous rock and depends on the substances contained in the fluid. It can be a constant number in one dimension, or a tensor in two or three dimensions. It also depends on the spatial coordinates and on time. In general, D grows with temperature and decreases with pressure. Diffusivity is proportional to the velocity of the particles of solute and this velocity depends on both fluid temperature and viscosity. In two and three dimensions, the diffusion flux becomes a vector, but because of the tortuous pathway and the presence of the interface between the fluid and the solid grains (Figs. 2.2 and 4.1), the coefficient D in porous rocks is lower than the diffusivity D_0 in pure aqueous solutions (Batu 2006, Bear 1972):

$$D = D_0 \tau_f, \quad 0.0 < \tau_f < 1.0 \quad (4.107)$$

The tortuosity factor τ_f ranges between 0.3 and 0.7, for most soils; $\tau_f \approx 0.707$ for unconsolidated granular media and $\tau_f \approx 0.67$ for consolidated porous rock. The major ions in groundwater (Na^+ , K^+ , Mg^{2+} , Ca^{2+} , Cl^- , HCO_3^- , and SO_4^{2-}) have diffusion coefficients in the range $[1.0, 2.0] \times 10^{-9} \text{ m}^2/\text{s}$ at 25°C . Considering water as the solvent substance, there are different values of D_0 for the following solutes (data from Batu 2006): $D_0 = 1.46 \times 10^{-9} \text{ m}^2/\text{s}$ for CO_2 at 10°C ; $D_0 = 1.77 \times 10^{-9} \text{ m}^2/\text{s}$ for CO_2 at 20°C ; $D_0 = 1.26 \times 10^{-9} \text{ m}^2/\text{s}$ for NaCl at 18°C and $0.05 \text{ kmol}/\text{m}^3$ of solute concentration; $D_0 = 1.54 \times 10^{-9} \text{ m}^2/\text{s}$ for NaCl at 18°C and $5.4 \text{ kmol}/\text{m}^3$ of concentration; $D_0 = 0.83 \times 10^{-9} \text{ m}^2/\text{s}$ for ethanol at 10°C and $0.05 \text{ kmol}/\text{m}^3$ of solute concentration.

The difference in concentration between two regions of the porous rock is called the concentration gradient. No mechanical mixing or stirring is involved. For instance, if C represents an artificial contaminant, a drop of contaminant added to water will diffuse down the concentration gradient until evenly mixed. Diffusion occurs more rapidly across a higher concentration gradient and at higher temperatures. Diffusion is quite different from the movement of molecules when a fluid is flowing. In the last case, movement is not random; all molecules are moving together and in the direction of groundwater flow. The coefficient D is closely related to the thermodynamic state of the porous medium and on the diffusing substance.

The second form or non-steady-state of Fick's law takes into account the change in concentration of the substance with respect to time. Combining the Fick's law with the principle of conservation of mass for the spreading molecules, we obtain the following partial differential equation:

$$\begin{aligned} \text{in one dimension:} \quad & -\frac{\partial q_D}{\partial x} = \frac{\partial C(x, t)}{\partial t} = D \frac{\partial^2 C}{\partial x^2} \\ \text{in two or three dimensions:} \quad & -\vec{\nabla} \cdot \vec{q}_D = \frac{\partial C(\vec{x}, t)}{\partial t} = \vec{\nabla} \cdot (\mathbf{D} \cdot \vec{\nabla} C) \end{aligned} \quad (4.108)$$

This is the diffusion equation; except for the units and the physical meaning of the parameters involved, its mathematical form is completely analogous to the groundwater flow equation (4.23a), deduced from Darcy's law or to the heat equation, deduced from Fourier's law of heat conduction (eqs. 2.16 and 4.82).

Typically, a compound's diffusion coefficient is about 10,000 times greater in gases than in liquids. Carbon dioxide in air has a diffusion coefficient of $16 \text{ mm}^2/\text{s}$, and in water, its coefficient

is $0.0016 \text{ mm}^2/\text{s}$. In a two-component mixture, if species 1 diffuses to the left, species 2 must diffuse to the right. In this case, D becomes the “binary diffusivity”.

4.8.2 Fick's law with advection and dispersion

The general solute flux in porous rocks with fluid movement has three components: diffusion, advection and mechanical dispersion. Advection occurs because groundwater's natural movement can transport the solutes. Dispersion occurs because there is a mixing process produced by local velocity variations, which is macroscopically similar to molecular diffusion (Bear 1972, Batu 2006). This generalization of Fick's law is expressed as follows:

$$\begin{aligned} \text{diffusive flux} &= -\varphi D \frac{\partial C}{\partial x}(x, t), & \text{dispersive flux} &= -\varphi D_m \frac{\partial C}{\partial x}(x, t) \\ \text{advective flux} &= \varphi u_x C(x, t); & \text{with: } D_x &= D + D_m \quad \text{and} \quad v_x = \varphi u_x \\ \text{in one dimension: } q_{D_x} &= v_x C(x, t) - \varphi D_x \frac{\partial C}{\partial x}(x, t) \end{aligned} \quad (4.109)$$

The term u_x is the pore fluid velocity and v_x is the Darcy velocity. The new parameter D_m is the mechanical or hydrodynamic dispersion coefficient (Bear 1972) which, together with the previous diffusion coefficient D , defines a longitudinal dispersion coefficient D_x acting in the direction of the groundwater flow. In three dimensions, the total flux of the solute concentration is defined as a tensorial equation:

$$\begin{aligned} \text{components form: } q_{Di} &= v_i C(x_i, t) - \varphi D_{ij} \frac{\partial C}{\partial x_j}(x_i, t) \\ \text{matrix form: } \vec{q}_D &= \vec{v} C(\vec{x}, t) - \varphi \mathbf{D} \cdot \vec{\nabla} C(\vec{x}, t) \\ \text{where: } \mathbf{D} = (D_{ij}) &= \begin{pmatrix} D_{xx} & D_{xy} & D_{xz} \\ D_{yx} & D_{yy} & D_{yz} \\ D_{zx} & D_{zy} & D_{zz} \end{pmatrix}, \quad \vec{x} = (x, y, z); i, j = x, y, z \end{aligned} \quad (4.110)$$

The vector \vec{q}_D defined by this equation is the advective-dispersive flux of the solute dissolved in the fluid contained in the porous rock. If the flow velocity is zero, this vector becomes identical to the diffusive flux term of equation (4.106). Figure 4.21 shows the schematic representation of mechanical dispersion in a 2-dimensional aquifer with uni-directional groundwater flow. If the porous reservoir is homogeneous and anisotropic the tensor \mathbf{D} has a simpler form, only the coefficients in the main diagonal are non zero: $D_{ii} \neq 0$ and $D_{ij} = 0$ for $i, j = x, y, z, i \neq j$.

Figure 4.22 illustrates the effect of dispersion in a 1-dimensional homogeneous isotropic sediment column with stationary water flow. If a solute is added at one end of the column (initial solute concentration C_0), either continuously (Fig. 4.22a) or instantaneously, it travels through the column. If solute transport is only by advection, all solute particles released at the same time at the source will travel with the same velocity and reach the exit boundary of the column at the same time; there the solute concentration is $C = C_0$ ($C/C_0 = 1$) (Fig. 4.22b shows the case of a continuous solute source). However, laboratory studies have shown, that the solute concentration is not exactly C_0 , when the solute reaches the exit boundary since the flow velocities along the different parallel flow lines of the water in the column are not exactly the same through a cross section of the column (Rehfeldt *et al.* 2004). So generally solute along flow lines in the middle of the cross section, have a different propagation velocity compared to those closer to the wall. Therefore, the contaminant particles do not reach exactly the exit boundary at the same time. The measured concentration of the outflowing water corresponds to a value averaged over the entire cross-sectional area. For a short time interval, the measured average concentration appears to be smaller than C_0 . However, for a long enough time interval, as the solute from all the flowpaths arrive at the exit, the average concentration increases to C_0 .

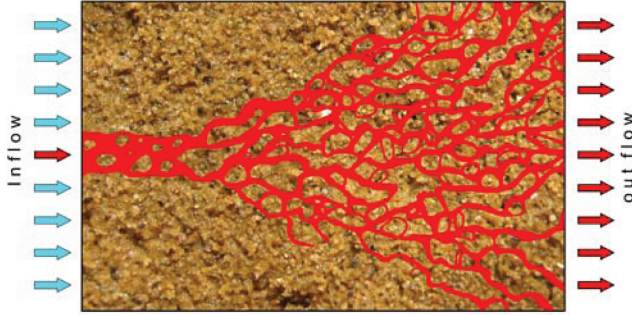


Figure 4.21. Schematic representation of mechanical dispersion in a 2-dimensional sand aquifer section with uni-directional stationary groundwater flow from left to right. A solute (red) is injected continuously at the left (red arrow) and is transported by advection (groundwater flow) from left to right. The advective transport component is overlain by the transport process of longitudinal (parallel to groundwater flow) and transversal (perpendicular to groundwater flow) mechanical dispersion, resulting in longitudinal and transversal spreading of the solute plume.

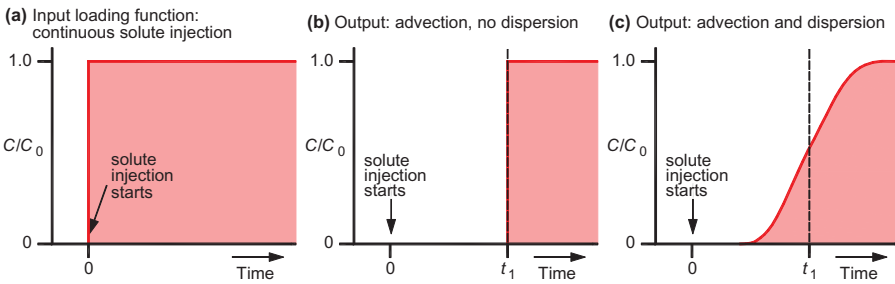


Figure 4.22. Solute propagation in a 1-dimensional homogeneous isotropic aquifer column with continuous solute injection at one side of the column (a). Solute concentrations at the exit boundary of the column when the solute is solely transported by advective movement of the groundwater are given in (b), and when additional mechanical dispersion occurs are given in (c). For further explanations see the text.

If in addition to the advective transport, we consider also the mechanical dispersion, then in our simple 1-dimensional case, the solute can only spread in the direction of water flow. The size of the spreading zone depends on D , and lies between the regions where $C/C_0 < 1$ and $C/C_0 > 0$ (Fig. 4.22c). In the case of a continuous solute source, the concentration behind the spreading zone is $C = C_0$ (constant; $C/C_0 = 1$) (Fig. 4.22c). In case of instantaneous solute source, where a pulse of solute mass is injected at $t = t_0$ (Fig. 2.23a for $t = t_0$), the maximum solute concentration along the center line of propagation decreases with increasing distance from the solute source since the concentration spreading zone becomes wider due to the increasing effect of the mechanical dispersion. Figure 2.23a shows the distributions at two different times t_1 and t_2 after solute injection.

If we consider 2- and 3-dimensional transport, dispersion also causes transversal spreading. This causes a reduction of the solute concentration behind the longitudinal zone of spreading, since mass spreads laterally. Figure 4.23b shows an example for the 2-dimensional case for both, instantaneous and continuous solute injection. In case of instantaneous injection at $t = t_0$, the contamination zone spreads symmetrically around the site of solute concentration maximum as shown in Figure 4.23b for two times t_1 and t_2 . Spreading increases with time and distance from the solute source and correspondingly the peak concentration decreases along the flowpath.

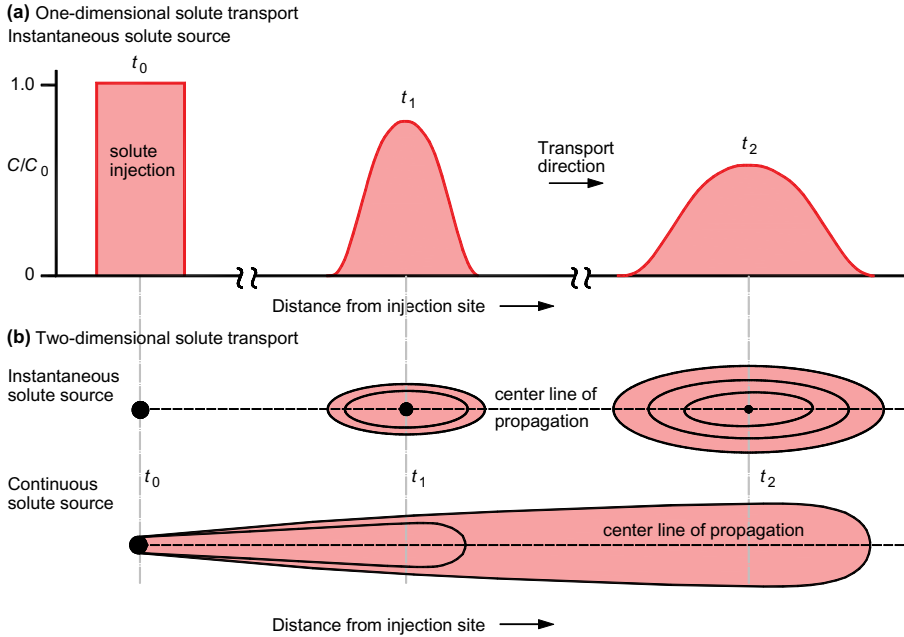


Figure 4.23. (a) Solute propagation in a 1-dimensional homogeneous and isotropic aquifer with instantaneous injection at one side of the column. Solute concentrations are shown for two different distances from the solute source corresponding to two different times t_1 and t_2 ; (b) In the 2-dimensional case, the dispersion effect is shown for a pulse obtained from an instantaneous solute injection and for a solute plume resulting from continuous solute injection. Solute pulses and solute plumes are given for two times t_1 and t_2 , which correspond to two different distances from the solute source. For further explanations see text. Modified from Rehfeldt *et al.* (2004).

Since the spreading of the pulse is higher in the direction of water flow compared to those in perpendicular direction, the longitudinal dispersive flux is greater than the transversal one. The reason for this behavior is that the center of solute mass moves at the average linear velocity of the groundwater.

In case of continuous solute injection, the front of the concentration plume at t_1 , has traveled as far as in the case of instantaneous injection (Fig. 4.23b). The solute concentrations in the zone behind the front of the plume remain high increasing towards the source along the center line of plume. At t_2 , the plume has become longer and wider than at earlier times. In contrast to the example of instantaneous solute injection, the concentration gradients are low in the longitudinal direction, with the exception is at the front of the plume. This indicates that longitudinal dispersion occurs predominantly at the front of the solute plume. In the transversal direction, the gradient of the solute concentration is high along the entire length of the plume. Domenico and Schwartz (1990) expresses that transverse dispersion leads to decreased concentrations ($C/C_0 < 1$) everywhere, with exception of the solute injection site itself, while longitudinal dispersion only results in spreading at the front of the plume. We have already observed this behavior in our 1-dimensional example (Fig. 4.22c).

4.8.3 General solute transport equations

Assuming there is no production or removal of solute by reaction in the reservoir, the governing partial differential equations describing solute transport in porous rocks are generalizations of the

second form of Fick's law:

$$\text{with: } \mathbf{D} = \begin{pmatrix} D_X & 0 & 0 \\ 0 & D_Y & 0 \\ 0 & 0 & D_Z \end{pmatrix}$$

$$\Rightarrow \text{Tensorial form: } \vec{\nabla} \cdot (\varphi \mathbf{D} \cdot \vec{\nabla} C) - \vec{\nabla} \cdot (C \vec{v}) = \varphi \frac{\partial C}{\partial t} + C_{\text{sol}} q_V \quad (4.111)$$

$$\text{Components form: } \frac{\partial}{\partial x_i} \left(\varphi D_j \frac{\partial C}{\partial x_j} \right) - \frac{\partial}{\partial x_i} (C v_i) = \varphi \frac{\partial C}{\partial t} + C_{\text{sol}} q_V$$

The scalar function $C(x, y, z, t)$ is the solute concentration in moles per m^3 ; the matrix \mathbf{D} contains the eigenvalues D_X, D_Y, D_Z [m^2/s] of the dispersion coefficients or principal values of the dispersion tensor \mathbf{D} ; v_i is the cartesian component of Darcy's velocity. The term C_{sol} is the solute concentration in the source fluid, q_V [$\text{m}^3/\text{s}/\text{m}^3$] is the volume flow rate per unit volume of the source or sink in the aquifer (eq. 4.22b), and φ is the effective porosity as usual.

The most general partial differential equation governing solute transport is:

$$\text{in one dimension: } \frac{\partial}{\partial x} \left(\varphi D_x \frac{\partial C}{\partial x} \right) - \frac{\partial}{\partial x} (v_x C) - C_S q_V + \varphi \sum_{j=1}^{N_R} R_j = \varphi \frac{\partial C(x, t)}{\partial t} \quad (4.112)$$

$$\text{in 2D or 3D: } \vec{\nabla} \cdot (\varphi \mathbf{D} \cdot \vec{\nabla} C) - \vec{\nabla} \cdot (C \vec{v}) - C_S q_V + \sum_{j=1}^{N_R} \varphi R_j = \varphi \frac{\partial C(\vec{x}, t)}{\partial t}$$

where R_j is the rate of solute production in the reaction number j of a total of N_R different reactions. For equilibrium-controlled reactions (e.g. sorption and ion exchange processes between solid and fluid) if they can be described by linear processes (no time-dependence of processes), with radioactive decay (Javandel *et al.* 1987), the summation of the terms R_j is:

$$\sum_{j=1}^{N_R} R_j = -\lambda_R C R_d - \frac{\rho_B K_d}{\varphi} \frac{\partial C(\vec{x}, t)}{\partial t} \quad (4.113)$$

In this case equation (4.112) can be written as:

$$\vec{\nabla} \cdot (\varphi \mathbf{D} \cdot \vec{\nabla} C) - \vec{\nabla} \cdot (C \vec{v}) - C_S q_V - \varphi \lambda_R C R_d = \varphi R_d \frac{\partial C(\vec{x}, t)}{\partial t} \quad (4.114)$$

$$\text{where: } \lambda_R = \frac{0.693}{t_{0.5}} \quad \text{and} \quad R_d = 1 + \frac{\rho_B K_d}{\varphi} \approx \frac{v_i}{v_C}$$

where R_d is called the retardation factor, K_d is the distribution coefficient, ρ_B is the bulk density of the rock, and λ_R is the radioactive decay constant; $t_{0.5}$ represents the value of half-life for the radioactive substance. For example, $\lambda_R = 2.71 \times 10^{-12}$ 1/day for ^{235}U (Batu 2006).

The retardation factor R_d is the ratio between the velocities of the fluid v_i and the solute v_C . $R_d = 1$ if no retardation occurs and the solute moves with the same velocity as the transporting fluid; this is valid e.g. for ideal tracers. Retardation is caused by physical, chemical or biological interactions between the solute and other chemical species present in the fluid, or interactions between the solute and the solid aquifer material such as adsorption/desorption and ion exchange processes (see e.g., de Marsily 1986 for more details).

If the velocity v_C of the contaminant is known, and for a one-dimensional flow in the direction x_i , $R_d \sim v_i/v_C$ (Javandel *et al.* 1987). For unconsolidated rocks an interval of values for R_d was found to be: $1 + (3.98 \text{ g/cm}^3) K_d \leq R_d \leq 1 + (10.60 \text{ g/cm}^3) K_d$. Using the experimental value of $K_d = 0.2 \text{ cm}^3/\text{g}$ for tetrachloroethylene, a halogenated organic compound (Batu 2006), we deduce that $1.80 \leq R_d \leq 3.12$.

In a two dimensional homogeneous and isotropic porous rock without solute sources, equation (4.114) can be simplified to:

$$\varphi \left(D_X \frac{\partial^2 C}{\partial x^2} + D_Y \frac{\partial^2 C}{\partial y^2} \right) - v_X \frac{\partial C}{\partial x} - \varphi \lambda_R R_d C = \varphi R_d \frac{\partial C}{\partial t} \quad (4.115)$$

where D_X and D_Y are the hydrodynamic dispersion coefficients, parallel and perpendicular respectively to the velocity v_X in the flow direction OX. They are measures of the extent to which the solute spreads in the specified direction.

Since the dispersion coefficient D is based on microscopic pore-scale movement of the fluid, which cannot be measured in the field, we introduce the parameter dispersivity α [m]. Dispersivity is an empirical field-scale parameter, which indicates how much a solute strays away from the macroscopic field-scale velocity of the groundwater. Longitudinal dispersivity (α_L), describes the spreading of the solute particles behind or in front of the fluid motion (in macroscopic flow direction), whereas the transversal dispersivity (α_T) quantifies the spreading of the solute particles perpendicular to the macroscopic groundwater flow direction.

However, dispersivity is not really a measurable parameter for field problems. It can only be determined in small areas, e.g. in the direct vicinity of a well or in very well-defined simple aquifer fabric, such as it is found in some experimental test sites. For real problems, dispersivity is merely a fitting parameter that covers our lack of knowledge of the true flow patterns. It is not a real aquifer property. It is considered as an aquifer adjustment for the lack of information about the modeled system and the error of our assumptions, such as averaging when using a macroscopic field scale description. So, there are different aquifer characteristics that determine dispersivity. There may be small-scale inhomogeneities in the aquifer as well as larger-scale heterogeneities, such as beds or lentils of gravel or clay in an aquifer that we have assumed as a sand aquifer. So, in the same aquifer, the dispersivity may be different if we consider a volume of e.g. 1 m^3 composed by sand compared with the value considering a larger volume, where the presence of layers or lentils of gravel or clay determine dispersivity. In consequence, dispersivity is often spatial-scale-dependent and so a time-dependent variable in the modeling. Thus, a single constant value does not often well-describe what we measure or wish to predict in the field. In consequence, both the concept and the methods of its determination are topics of many studies and an issue of controversy.

Many studies were performed on the scale-dependency of dispersivity, both at the column scale (Han *et al.* 1985, Porro *et al.* 1993, Zhang 1995) and at the field scale (Gelhar *et al.* 1992, Yasuda *et al.* 1994, Ellsworth *et al.* 1996). Wheatcraft and Tyler (1988) applied fractal theory to explain the scale effect on dispersivity, whereas Pachepsky *et al.* (2002) used the fractional advection-dispersion equation. Other approaches used stochastic methods (Gelhar and Axness 1983, Dagan 1984, Schwarze *et al.* 2001). Wang *et al.* (2006) specified five ways to define dispersivity. They designated dispersivity as dependant on local time, average time, apparent time, local distance, or apparent distance in a numerical scheme and tested numerically how these different ways affected the calculated break through curves. They used generalized linear and power scale-dependent dispersivity functions for a one-dimensional problem. These authors found that differences decreased with increasing apparent Peclet number.

The dispersivities α_L and α_T are related to the dispersion coefficients D_L and D_T (which correspond to D_X and D_Y in the simplified 2-dimensional case of equation 4.111) by $D_L = \alpha_L v_C$ and $D_T = \alpha_T v_C$. Dispersivities can be estimated e.g. by tracer tests (see section 6.7.2.5 and 6.7.3.4 for tracer tests in cold and geothermal aquifers, respectively). There are also methods, which allow the determination of α_L using the geometric data of a contaminant's contamination

plume. So, Xu and Eckstein (1995) give the following formula, which relates α_L to the measured plume length L :

$$\alpha_L = 0.83(\text{Log}_{10} L)^{2.414} \quad (4.116)$$

In practical applications, and in absence of further data, the transversal dispersivities are often deduced from the longitudinal dispersivity. Depending whether the transversal dispersion occurs in horizontal or vertical direction, Gelhar *et al.* 1992 recommends to calculate α_T as 1/10th and 1/100th of the value of α_L , respectively.

In the following discussion we resume the findings of Gelhar *et al.* (1992) who discussed extensively the issue of dispersivities in various geologic formations. These authors summarized literature data of α_L values for different scales of individual studies (scale value is defined as distance between site of originating solute e.g. the point of contaminant release or tracer injection and the site of observation), the type of rock (sediment or hard rock) and the reliability of the data (Fig. 4.24). This approach means that α_L data points do not present real α_L values at a particular location (a certain distance from the source), but correspond to apparent dispersivity that has evolved to that particular scale. In reality, α_L values will change along the pathway of the solute traveling from the source point to the point of observation (for examples of multiple snapshots of the variation of α_L along the pathway at a single site; see e.g., Freyberg 1986, Garabedian *et al.* 1991). Gelhar *et al.* (1992) found no significant difference in dispersivities determined in fractured and porous rocks. Their most important findings are:

- Not considering the reliability of the data, α_L increases continuously with scale.
- Most of the large-scale data are derived from numerical models. However, the reliability of dispersivities from numerical models is considered as low. Reasons are: (1) Undocumented numerical dispersion, may lead to wrong estimates of dispersivity and (2) in other modeling applications, unrealistic α_L were used, which do not correspond to the real field values, but were introduced into the model either for numerical stability reasons, or to use dispersivity as merely a fitting parameter that covers the lack of knowledge of the true flow patterns as we have already mentioned earlier.

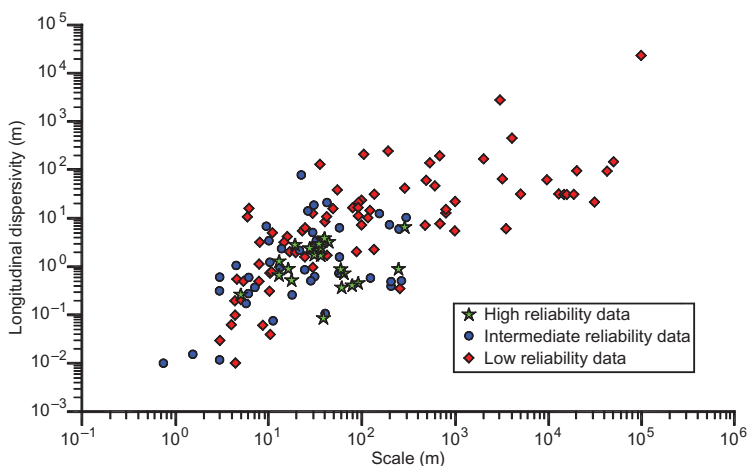


Figure 4.24. Scale dependency of α_L . Scale is considered as distance from origin of solute (e.g., site of tracer injection) to the observation point. Note that the data points are apparent α_L values, and do not correspond to real values corresponding to α_L at a specific point. Modified from Gelhar *et al.* (1992).

- Considering only the most reliable data, a positive correlation between α_L and scale data is still present. However, no clear extrapolation to large scales is possible, since the largest high reliability data point is ($\alpha_L = 7$; scale = 300 m) (Fig. 4.24).
- Independent on scale, α_L values vary by 2–3 orders of magnitude.

In consequence, the previous equations describing hydrodynamic dispersion require to be modified, and require the inclusion of terms that include scale-dependent functions of the dispersion coefficient and/or dispersivity, which results in a time-dependency of these values. However, this is behind the scope of our introductory book and we refer the reader to specialized literature (see e.g. Wang *et al.* 2006).

Solving the general partial differential equations herein presented is a difficult task. Some analytical methods can handle some simplified aspects of solute transport in porous media. Nevertheless, because of the complexity of the equations involved, the analytical solutions are restricted to uniform velocities and to radial flow geometries. Readers interested in modeling and predicting groundwater contamination can find a more detailed discussion, together with various analytical and numerical models of different levels of depth and complexity in the excellent monograph of Batu (2006) and in the handbook by Javandel *et al.* (1987). In chapter 5 of this book, we describe powerful numerical tools able to solve all the equations introduced in this chapter.

CHAPTER 5

Principal numerical methods

“Mathematics is a language for describing Nature, it is a language of scientific knowledge of the world. If you wish to speak to Nature, you need to have the mathematical language. If you wish to comprehend Nature, you need to have the mathematical language.”

Juri I. Neimark (2003)*

The description of groundwater flow and the transport of solutes and heat requires the use of differential equations, with their initial and boundary conditions. Research on reservoir topics requires the solution of these equations for the hydrogeological or geothermal problem in question. Unlike a few special idealized cases with very simple geometry, finding analytical solutions for regions of arbitrary shape is impossible. In real reservoir problems, numerical mathematical methods must be used to obtain approximate results. Numerical techniques allow finding solutions in irregularly bounded areas or when boundary conditions vary in time as for instance, in aquifers whose space, solute, source, and sink parameters vary as fluid is extracted or injected, and in cases where energy transport varies in time. Logically, an essential condition is the availability of data describing the system. The characteristic shared by the numerical methods used is, generally speaking, the substitution of partial differential equations by systems of algebraic equations or by ordinary differential equations that can be solved by means of different algorithms. The availability of small and low-cost computers such as PCs or workstations has led to the use of powerful numerical methods to solve complex hydrogeological or geothermal problems.

Knowledge on how to solve differential equations using numerical methods and algorithms is essential not only for programming tasks, but also for the use of commercially available modeling programs that are commonly employed. This knowledge will be useful in detecting weaknesses in the software and determining program sensitivity. It also gives the user the ability, to a certain degree, to diagnose computing problems. This chapter provides a general overview of the major numerical methods currently used for modeling hydrogeological or geothermal problems. This chapter is by no means a complete compilation of all modeling techniques, since the field of study is extremely broad and its development has resulted in a significant specialization. With the exception of the finite difference and finite element method, detailed mathematical derivations are left aside, since they are described in detail by specialized literature. It would have been impossible to do so within the scope of this book. Smith (1978), Kinzelbach (1987), Bear and Verruijt (1987), Bear and Bachmat (1990), Zienkiewicz and Taylor (2000), Katsikadelis (2002), Pruess (2006), Fish and Belytschko (2007), contain full descriptions, including practical examples of the different classical numerical methods. However, we have included some methods in connection to hydrogeological, petroleum and geothermal systems. Users of commercially available programs should obtain information about the numerical algorithms used and the structure of the program through the corresponding manual. This book will briefly describe only the principles of the most important methods, and their benefits and drawbacks will be compared.

* Juri I. Neimark: *Mathematical Models in Natural Science and Engineering*. Springer-Verlag, Berlin, 2003.

5.1 THE FINITE DIFFERENCE METHOD

5.1.1 Fundamentals

The finite difference method is a classic numerical solution technique, which despite its limitations is still widely used in modeling groundwater and geothermal systems due to its simplicity and consequent easiness in programming. The basis of the finite difference method consists of replacing differential expressions by quotients of differences. The numerators of those quotients are the differences that include the values of the unknowns. Thus, the solution of partial differential equations is performed by means of a system of algebraic equations that can be solved using different techniques.

To create a finite difference model the area to be modeled should first be spatially discretized. This is done by dividing the domain under consideration (model area) into a finite number of cells to which hydrogeological properties are attributed. At the center of each cell there is a node, denoted (i, j, k) , where i represents the cell indice in the x -direction and j represents the cell indice in the y -direction. Time is also discretized into a finite number of intervals, and represented by k . At a given node (i, j) and given time k , the hydraulic head is represented by the value $h(i, j, k)$, the concentration of dissolved solutes by $C(i, j, k)$ and temperature by $T(i, j, k)$. For each cell, a water and solute balance is carried out for each time interval, e.g., by applying Darcy's law. Figure 5.1 shows a two-dimensional example where the study area (e.g. domain) has been divided into eight cells in the x -direction ($i = 1$ to 9) and eleven cells in the y -direction ($j = 1$ to 12). The total number of nodes is $n = i \times j$ and for each of these nodes the hydraulic head h and the substance concentration C can be described by means of an algebraic equation. Thus, we obtain a system of equations with n unknowns.

On each given node, the following can be determined:

- hydraulic heads,
- flow velocity (Darcy's flux),
- solute concentration or temperature (heat content) at each node.

The principle of the finite difference method is presented below in a simplified way for two specific examples, through the derivation of flow and transport equations. In order to show these examples, we must first construct partial derivatives that can be used for our various models. We begin by considering the partial derivative with respect to x of the hydraulic head $h(x, y)$.

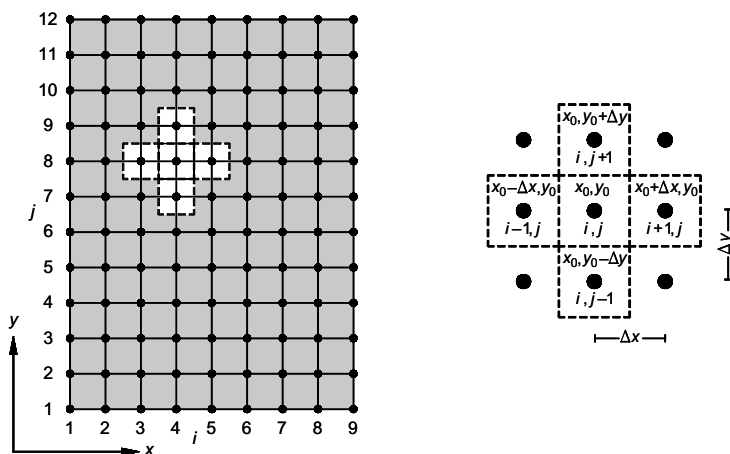


Figure 5.1. Network of nodes centered on the cells for the construction of a two-dimensional groundwater flow model, in accordance with the finite difference method: ● node; dashed: examples of cells; i and j are the indices in the directions x and y for the classification of the network nodes.

According to the definition of the first partial derivative of the function $h(x, y)$ with respect to x , the following holds:

$$\frac{\partial h}{\partial x} = \lim_{\Delta x \rightarrow 0} \frac{h(x + \Delta x, y) - h(x, y)}{\Delta x} \quad (5.1)$$

However, in opposition to classical differential calculus, digital computers do not allow calculating limits that approach zero. Therefore, Δx is replaced by a finite value that describes the distances of the lines of the difference grid. We can further illustrate this idea by considering the Taylor series expansion. Using this idea, we know that for each coordinate of the grid with $y = y_0$, function $h(x, y_0)$ can be written as a Taylor series centered around the coordinate (x_0, y_0) :

$$h(x, y_0) = h(x_0, y_0) + (x - x_0) \frac{\partial h}{\partial x}(x_0, y_0) + \frac{(x - x_0)^2}{2} \frac{\partial^2 h}{\partial x^2}(x_0, y_0) + \dots \quad (5.2)$$

If the terms of order greater than one are neglected, we can then obtain the following approximation for $\partial h / \partial x$:

$$\frac{\partial h}{\partial x}(x_0, y_0) = \frac{h(x, y_0) - h(x_0, y_0)}{x - x_0} \quad (5.3)$$

Depending upon the method implemented, the following substitutions of x can be used in equation (5.3):

$$x = x_0 + \Delta x \quad \text{for the forward difference method} \quad (5.4)$$

$$x = x_0 - \Delta x \quad \text{for the backward difference method} \quad (5.5)$$

$$x = x_0 \pm \frac{1}{2} \Delta x \quad \text{for the centered difference method} \quad (5.6)$$

$$x = x_0 \pm \frac{i}{2} \Delta x \quad i = 3, 4, \dots \quad \text{for higher orders}$$

To write the forward difference formula in terms of the given nodes, we would have for the forward differences:

$$\frac{\partial h}{\partial x}(x_i, y_j) \approx \frac{h(x_{i+1}, y_j) - h(x_i, y_j)}{\Delta x} \quad (5.7)$$

Note that this forward difference can also be approximated by using the slope of the secant defined by the coordinates (x_i, y_j) and (x_{i+1}, y_j) as demonstrated in Figure 5.2a.

For the backward finite differences, the derivative is approximated by means of the slope of the secant corresponding to the cell to the left of x_i (Fig. 5.2b):

$$\frac{\partial h}{\partial x}(x_i, y_j) \approx \frac{h(x_i, y_j) - h(x_{i-1}, y_j)}{\Delta x} \quad (5.8)$$

With the central finite difference method (5.6), a greater accuracy in the approximation is achieved by taking advantage of the symmetry when considering the immediate neighboring cells, both to the right and to the left, since the secant defined by the coordinates $(x_{i-1/2}, y_j)$ and $(x_{i+1/2}, y_j)$ is almost parallel to the tangent of the function curve $h(x, y_i)$ (Fig. 5.2c):

$$\frac{\partial h}{\partial x}(x_i, y_j) \approx \frac{h(x_{i-1/2}, y_j) - h(x_{i+1/2}, y_j)}{\Delta x} \quad (5.9)$$

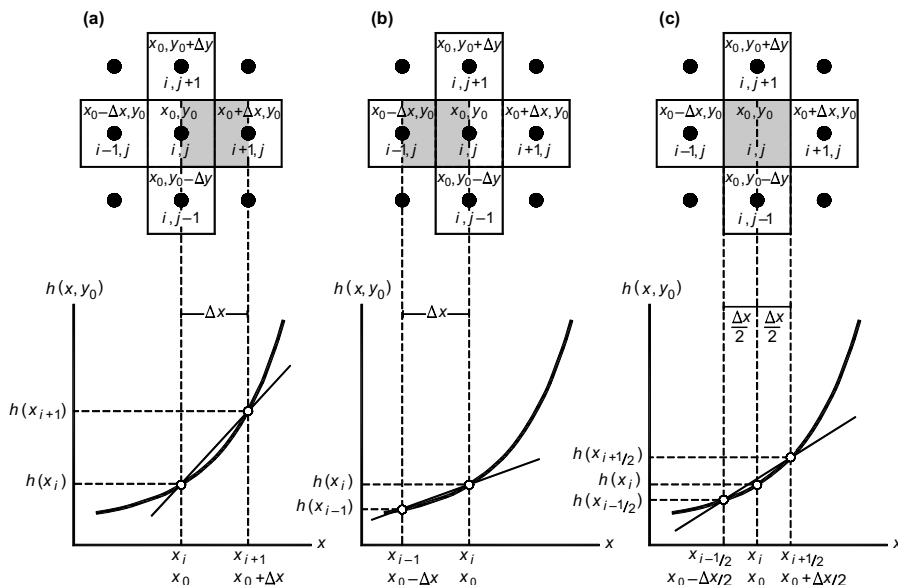


Figure 5.2. Use of the different adjacent cells or nodes in the different finite difference methods for the example of the calculation of the first derivation of the hydraulic head: (a) forward, (b) backward, and (c) centered. The curves corresponding to function $h(x, y_0)$ have also been represented with the secants corresponding to the slope of the derivative $\partial h(x_0, y_0)/\partial x$ at point (x_0, y_0) .

To further illustrate the principle of the finite difference method, that is, the replacement of partial derivatives by quotients of differences, two examples are presented below. From the flow equation, difference methods are formulated for the calculation of hydraulic head h in the study area for these two special cases. One example is an isotropic and homogeneous aquifer with stationary, two-dimensional groundwater flow; the other example is an anisotropic and heterogeneous aquifer with non-stationary two-dimensional groundwater flow. Both examples do not incorporate sink/source terms. Derivations will first be carried out for the inner nodes of the model. Then, h will be calculated for the outer nodes on the contour of the model, for different types of boundary values.

5.1.2 Stationary two-dimensional groundwater flow

5.1.2.1 Difference method for model nodes and centers

The continuity equation for a two-dimensional groundwater flow in a homogeneous and isotropic aquifer is expressed by means of Laplace's equation:

$$\frac{\partial^2 h}{\partial x^2} + \frac{\partial^2 h}{\partial y^2} = 0 \quad (5.10)$$

To discretize this partial differential equation for each inner node of the model in the finite difference grid, the second order partial derivatives $\partial^2 h/\partial x^2$ and $\partial^2 h/\partial y^2$ should be replaced by finite differences. This is done separately, following the same techniques as in the case of first partial derivatives. We discuss below the three methods (forward, backward, and centered differences) for approximating the second partial derivatives.

5.1.2.1.1 Forward difference method

Using the forward difference, we replace x in equation (5.3) by (5.4) and obtain:

$$\frac{\partial h}{\partial x}(x_0, y_0) = \frac{h(x_0 + \Delta x, y_0) - h(x_0, y_0)}{\Delta x} \quad (5.11)$$

The desired second partial derivative is obtained through the difference of the first derivative at $x_0 + \Delta x$ and x_0 combined with division by Δx :

$$\frac{\partial^2 h}{\partial x^2}(x_0, y_0) = \frac{\frac{\partial h}{\partial x}(x_0 + \Delta x, y_0) - \frac{\partial h}{\partial x}(x_0, y_0)}{\Delta x} \quad (5.12)$$

where the first derivative $\frac{\partial h(x_0 + \Delta x, y)}{\partial x}$ in the coordinate of $(x + \Delta x, y)$ is obtained by replacing x_0 by $x_0 + \Delta x$ in (5.11):

$$\frac{\partial h}{\partial x}(x_0 + \Delta x, y_0) = \frac{h(x_0 + 2\Delta x, y_0) - h(x_0 + \Delta x, y_0)}{\Delta x} \quad (5.13)$$

Using equations (5.11) and (5.13) in equation (5.12), the following expression is obtained for the second partial derivative with respect to x :

$$\frac{\partial^2 h}{\partial x^2}(x_0, y_0) = \frac{h(x_0 + \Delta x, y_0) - 2h(x_0, y_0) + h(x_0 - \Delta x, y_0)}{(\Delta x)^2} \quad (5.14)$$

Equation (5.14) and the similarly derived term corresponding to $\partial^2 h / \partial y^2$ introduced in Laplace's equation (5.9) yields the necessary finite difference equation. This allows for calculating the hydraulic head of any point (x_0, y_0) within the model and is given by:

$$\begin{aligned} & \frac{h(x_0 + \Delta x, y_0) - 2h(x_0, y_0) + h(x_0 - \Delta x, y_0)}{(\Delta x)^2} \\ & + \frac{h(x_0, y_0 + \Delta y) - 2h(x_0, y_0) + h(x_0, y_0 - \Delta y)}{(\Delta y)^2} = 0 \end{aligned} \quad (5.15)$$

In the special case in which the model is composed of squares, $\Delta x = \Delta y$, equation (5.15) simplifies to:

$$\begin{aligned} & \frac{1}{(\Delta x)^2} (h(x_0 + \Delta x, y_0) + h(x_0 - \Delta x, y_0) + h(x_0, y_0 + \Delta y) \\ & + h(x_0, y_0 - \Delta y) - 4h(x_0, y_0)) = 0 \end{aligned} \quad (5.16)$$

If indices i, j are used to describe the nodes of the model and coordinate (x_0, y_0) is used as the (i, j) node, equation (5.16) can then be written as:

$$h_{ij} = \frac{1}{4} (h_{i+1,j} + h_{i-1,j} + h_{i,j+1} + h_{i,j-1}) \quad (5.17)$$

5.1.2.1.2 Centered difference method

If instead of using the forward difference we choose to use central differences, we then have the following expression for the first partial derivative:

$$\frac{\partial h}{\partial x}(x_0, y_0) = \frac{h\left(x_0 + \frac{1}{2}\Delta x, y_0\right) - h\left(x_0 - \frac{1}{2}\Delta x, y_0\right)}{\Delta x} \quad (5.18)$$

The second partial derivative necessary for Laplace's equation is obtained through the creation of differences of the first derivative at $(x_0 + \frac{1}{2}\Delta x)$ and $(x_0 - \frac{1}{2}\Delta x)$ as well as division by Δx :

$$\frac{\partial^2 h}{\partial x^2}(x_0, y_0) = \frac{\frac{\partial h}{\partial x}\left(x_0 + \frac{1}{2}\Delta x, y_0\right) - \frac{\partial h}{\partial x}\left(x_0 - \frac{1}{2}\Delta x, y_0\right)}{\Delta x} \quad (5.19)$$

Notice that for the derivative $\partial h(x_0 + \frac{1}{2}\Delta x, y_0)/\partial x$ we replace x_0 by $(x_0 + \frac{1}{2}\Delta x)$ in equation (5.18) and this gives us:

$$\frac{\partial h}{\partial x}\left(x_0 + \frac{1}{2}\Delta x, y_0\right) = \frac{h(x_0 + \Delta x, y_0) - h(x_0, y_0)}{\Delta x} \quad (5.20)$$

and for the first derivative $\frac{\partial h}{\partial x}(x_0 - \frac{1}{2}\Delta x, y_0)$ we replace x_0 with $(x_0 - \frac{1}{2}\Delta x)$ in equation (5.18) to obtain:

$$\frac{\partial h}{\partial x}\left(x_0 - \frac{1}{2}\Delta x, y_0\right) = \frac{h(x_0, y_0) - h(x_0 - \Delta x, y_0)}{\Delta x} \quad (5.21)$$

Using equations (5.20) and (5.21) in equation (5.19) we then have:

$$\frac{\partial^2 h}{\partial x^2}(x_0, y_0) = \frac{\frac{\partial h}{\partial x}\left(x_0 + \frac{1}{2}\Delta x, y_0\right) - \frac{\partial h}{\partial x}\left(x_0 - \frac{1}{2}\Delta x, y_0\right)}{\Delta x} \quad (5.22) = (5.14)$$

This procedure continues and the same result is obtained as in the forward finite difference method (equation 5.11).

5.1.2.1.3 Backward difference method

Lastly, we briefly mention the result using the backward difference method. For this method, we use equation (5.5) in equation (5.3) to obtain:

$$\frac{\partial h}{\partial x}(x_0, y_0) = \frac{h(x_0, y_0) - h(x_0 - \Delta x, y_0)}{\Delta x} \quad (5.23)$$

The procedure continues as in sections 5.1.2.1.1 and 5.1.2.1.2 and also leads to equation (5.14) for the second partial derivative with respect to x .

We conclude by noting that regardless of the method used, the same equation (5.15 or 5.16) is obtained for calculating the hydraulic head at the inner nodes of a square model area. Equation (5.17) means that in a homogeneous and isotropic aquifer with stationary groundwater flow, the hydraulic head at each inner node of a grid with constant inter-node distances is equal to the arithmetic mean of the 4 neighboring nodes. The derivatives of the nodes located on the boundaries of the model area can be determined in a similar way, so as to obtain the difference method for calculating head h for each of the boundary nodes.

5.1.2.2 *Difference method for boundary nodes*

The difference method for the calculation of the hydraulic heads of the nodes located on the boundaries of the model area can also be derived from equation (5.17) for an equidistant grid. In the following, impermeable boundaries (Neumann type boundary conditions) and boundaries with a fixed (prescribed) hydraulic head (Dirichlet type boundary conditions) will be considered.

An impermeable boundary does not allow for the flow of groundwater through the boundary. As a consequence, hydraulic heads outside the boundary of the cell will be equal to that of the boundary cell. The hydraulic head h for a node of a boundary cell is equal to that of a fictitious neighboring cell located outside the model area. Depending upon which boundary the model nodes (i, j) are located, different conditions hold. Figure 5.3 represents a grid with $i = 1$ to n and $j = 1$ to m nodes. We have the following conditions along the boundaries:

- for the upper and lower boundaries,

$$h_{i,j-1} = h_{i,j+1} \tag{5.24}$$

- for the right and left boundaries,

$$h_{i-1,j} = h_{i+1,j} \tag{5.25}$$

- for the corners,

$$h_{i-1,j} = h_{i+1,j} \quad \text{and} \quad h_{i,j-1} = h_{i,j+1} \tag{5.26}$$

The conditions (5.24)–(5.26) give the hydraulic head of the nodes located on the boundaries as a result for the different types of boundaries used in (5.17). For example, for the lower boundary of the model, the expression $h_{i,j-1}$ is replaced in (5.17), according to condition (5.24), by $h_{i,j+1}$ (on the other hand, for the upper boundary of the model, $h_{i,j+1}$ was replaced by $h_{i,j-1}$). The difference equation therefore only shows indices of real nodes:

$$h_{ij} = \frac{1}{4}(h_{i+1,j} + h_{i-1,j} + 2h_{i,j+1}) \tag{5.27}$$

and for the left lower corner of the model we have:

$$h_{ij} = \frac{1}{4}(2h_{i+1,j} + 2h_{i,j+1}) \tag{5.28}$$

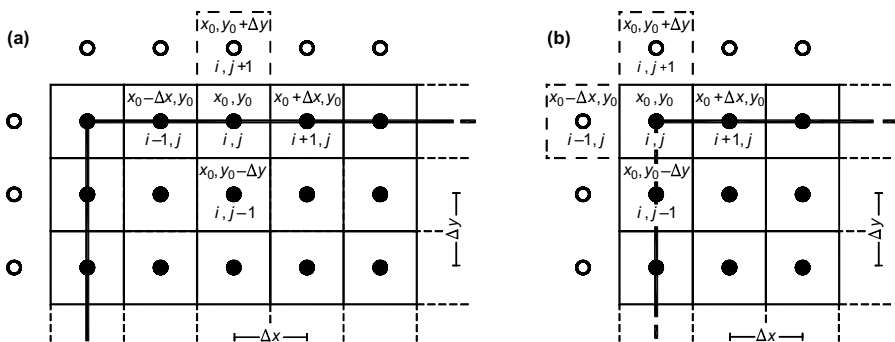


Figure 5.3. Detail of the finite difference model grid shown in Figure 5.2. Derivation of the conditions for calculating hydraulic head at nodes located on the boundary of the model (—•—) using fictitious nodes (o) located outside the model area.

If there is irregular spacing between the nodes of the grid, conditions (5.24)–(5.26) should be used in equation (5.15). We note that with Dirichlet type boundary values, the hydraulic head, h , at the boundaries of the model is preset to fixed values. Thus, the system of equations described in (5.6) or (5.17) can be solved and the hydraulic head at each inner node (i, j) can be calculated.

5.1.3 Transient groundwater flow

5.1.3.1 Time discretization

The following sections will show how to carry out the discretization in time and space of a horizontal, isotropic and homogeneous aquifer. As in the previous example, the discretization is done on a finite number of cells with individual aquifer properties (Fig. 5.4). The nodes are located in the center of the cells whose hydraulic heads define those of the respective cells. The thickness, b_a , of the aquifer is expressed using the thickness of the cells, which is constant for all cells in the following example (see section 4.3.3 and eq. 4.23b):

$$K_{Hx} \frac{\partial^2 h}{\partial x^2} + K_{Hy} \frac{\partial^2 h}{\partial y^2} = S_{sp} \frac{\partial h}{\partial t} \tag{5.29}$$

Note that in this case time t must be discretized as well.

For a horizontal confined aquifer with constant thickness b_a , transmissivity T_v is equal to the hydraulic conductivity K_H multiplied by the aquifer thickness. That is, $T_v = K_H b_a$. This gives us the following relations:

$$K_{Hx} = \frac{T_{vx}}{b_a} \tag{5.30}$$

$$K_{Hy} = \frac{T_{vy}}{b_a} \tag{5.31}$$

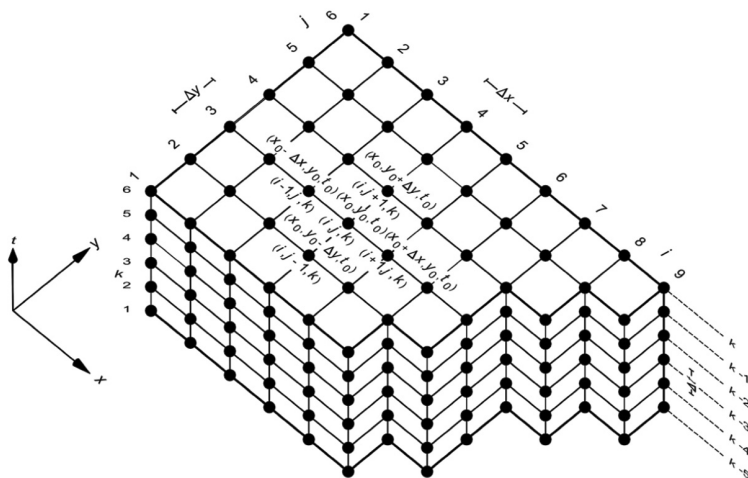


Figure 5.4. Detail of the finite difference model grid in a two-dimensional confined aquifer (x - y plane) and the discretization of time t in intervals of time with an increment of Δt . Indices i, j, k are used to identify the corresponding nodes and cells in directions x and y , as well as in the time axis t . The discretization of the aquifer is carried out by the centered finite difference method, whereas to discretize time, the forward method is used.

For the storage coefficient, S , we have:

$$S_{sp} = \frac{S}{b_a} \quad (5.32)$$

Using relations (5.30)–(5.32) in (5.29) as well as considering that in the case of a homogeneous isotropic aquifer with $b_a = \text{constant}$, $T_{v_x} = T_{v_y} = T_v$ and we have:

$$T_v \frac{\partial^2 h}{\partial x^2} + T_v \frac{\partial^2 h}{\partial y^2} = S \frac{\partial h}{\partial t} \quad (5.33)$$

If we use the centered method, the second partial derivatives with respect to x and y can be replaced in equation (5.33), in accordance with condition (5.14). The time discretization is done by subdividing the total duration of the simulation t_{\max} into a finite number of chronological steps of length Δt ; the index used for these time steps is k . By using the indices i, j and the time discretization, we have:

$$T_v \frac{h_{i+1,j} - 2h_{i,j} + h_{i-1,j}}{\Delta x^2} + T_v \frac{h_{i,j+1} - 2h_{i,j} + h_{i,j-1}}{\Delta y^2} = S \frac{h_{i,j,k+1} - h_{i,j,k}}{\Delta t} \quad (5.34)$$

The spatial derivatives of the continuity equation are first approximated by difference quotients. However, the specific moment within the time interval at which the spatial difference quotients are taken, or the hydraulic heads that appear in the left term of (5.34), should be defined. In principle, these quantities can be selected at any moment within the time interval $[k, k + 1]$. A simple formulation for the description of the corresponding terms for hydraulic head $h_{i,j}$ for each moment within the time interval consists of using time weighting between the hydraulic head at the beginning ($h_{i,j,k}$) and at the end ($h_{i,j,k+1}$) of each time step. That is,

$$h_{i,j} = \varepsilon h_{i,j,k} + (1 - \varepsilon) h_{i,j,k+1} \quad \text{with } 0 \leq \varepsilon \leq 1 \quad (5.35)$$

Three special cases will be represented for the selection of the weighting factor ε :

- $\varepsilon = 1$ explicit difference method
(differences forwarded in time),
- $\varepsilon = 0$ implicit difference method
(differences backwarded in time),
- $\varepsilon = 0.5$ Crank-Nicholson difference method
(differences centered in time).

5.1.3.2 Explicit difference method ($\varepsilon = 1$)

By introducing $\varepsilon = 1$ in equation (5.35), hydraulic heads $h_{i,j}$ are obtained for the lower end of the time interval and we use:

$$h_{i,j} = h_{i,j,k} \quad (5.36)$$

These values for the hydraulic heads are then introduced on the left side of equation (5.34). Combining this with the forward difference model, we have that:

$$T_v \frac{h_{i+1,j,k} - 2h_{i,j,k} + h_{i-1,j,k}}{\Delta x^2} + T_v \frac{h_{i,j+1,k} - 2h_{i,j,k} + h_{i,j-1,k}}{\Delta y^2} = S \frac{h_{i,j,k+1} - h_{i,j,k}}{\Delta t} \quad (5.37)$$

Solving for the hydraulic head value at the upper time interval, $h_{i,j,k+1}$, gives us:

$$h_{i,j,k+1} = h_{i,j,k} + \frac{T_v \Delta t}{S \Delta x^2} (h_{i+1,j,k} - 2h_{i,j,k} + h_{i-1,j,k}) + \frac{T_v \Delta t}{S \Delta y^2} (h_{i,j+1,k} - 2h_{i,j,k} + h_{i,j-1,k}) \quad (5.38)$$

The consequence of equation (5.38) is at each node (i, j) inside the model, the hydraulic head for the new time interval $k + 1$ can be calculated based upon the hydraulic head corresponding to the previous interval, using the same node (i, j) as well as the four neighboring nodes. Since the hydraulic heads of the latter are known and there is only one unknown, the method is fully explicit. However, one disadvantage of this method is that the selection of the magnitude for the time interval is restricted by various stability criteria that frequently lead to an excessively refined discretization compared to the physical model. This results in unnecessary calculations. For example, in a simulation it is possible to increase the magnitude of the time interval. This then slows down the transformations of the processes described by the method or they reach a stationary state in a manner that differs from the physical reality.

5.1.3.3 *Implicit difference method* ($\varepsilon = 0$)

Introducing ($\varepsilon = 0$) in equation (5.35) hydraulic head $h_{i,j}$ is obtained for the upper end of the time interval:

$$h_{i,j} = h_{i,j,k+1} \quad (5.39)$$

Using these values for the hydraulic heads in the left side of equation (5.34) we then have:

$$\begin{aligned} T_v \frac{h_{i+1,j,k+1} - 2h_{i,j,k+1} + h_{i-1,j,k+1}}{\Delta x^2} \\ + T_v \frac{h_{i,j+1,k+1} - 2h_{i,j,k+1} + h_{i,j-1,k+1}}{\Delta y^2} = S \frac{h_{i,j,k+1} - h_{i,j,k}}{\Delta t} \end{aligned} \quad (5.40)$$

Solving this for $h_{i,j,k+1}$:

$$\begin{aligned} h_{i,j,k+1} = h_{i,j,k} + \frac{T_v \Delta t}{S \Delta x^2} (h_{i+1,j,k+1} - 2h_{i,j,k+1} + h_{i-1,j,k+1}) \\ + \frac{T_v \Delta t}{S \Delta y^2} (h_{i,j+1,k+1} - 2h_{i,j,k+1} + h_{i,j-1,k+1}) \end{aligned} \quad (5.41)$$

In accordance with (5.41), for each node (i, j) inside the model, the hydraulic head for the new time interval $k + 1$ is calculated. This calculation is carried out using the hydraulic head of node (i, j) of the previous time interval k , which is known, and the unknown hydraulic head of the new time interval, $k + 1$, corresponding to the four neighboring nodes. Since the latter are unknown, a system of n equations with n unknowns must be simultaneously solved; the method is therefore referred to as an implicit method. Comparing this implicit method ($\varepsilon = 0$) with the previous explicit method ($\varepsilon = 1$), we note that the implicit difference approximation is more stable and does not present limitations regarding the time interval selection. It is therefore versatile and can be adapted to the requirements of the described example problem. The resolution of the system of equations can be performed by direct calculations (e.g., Brebbia and Ferrante 1978) or through iterative methods. Among the latter, ADI (alternating direction implicit methods) and IADI (iterative alternating direction implicit methods) are the classical methods that are most widely used (e.g., Peaceman and Rachford 1955, D'Yakonov 1961, Fairweather *et al.* 1967, Hadjidimos 1969). Pinder and Bredehoft (1968) adapted this methodology to hydrogeological

problems, whereas Pinder and Grey (1977) produced a detailed and systematic review of different methods.

5.1.3.4 Crank-Nicholson difference method ($\varepsilon = 0.5$)

A similar algorithm that will only be briefly mentioned in this book uses $\varepsilon = 0.5$, which causes the hydraulic head on the left side of equation (5.34) to be taken at the center of the time interval, $k + 1/2$. This method is more accurate than purely explicit or fully implicit schemes and is stable. The Crank-Nicolson method represents a semi-implicit approach and leads accordingly to stable and precise solutions (Crank and Nicholson 1947). For this method, the obtained system of equations has to be solved similar to a fully implicit method.

5.1.3.5 Difference method for an inhomogeneous, anisotropic, confined aquifer

In this sub-section, the previous example is modified to obtain an implicit difference method that allows for calculating the hydraulic head of an anisotropic and inhomogeneous aquifer. The inner nodes of the model are considered; groundwater can be extracted from or injected into any of the cells. The discretization of the aquifer is performed in a finite number of cells (i, j) with hydraulic conductivities $K_{H_{i,j}}$, transmissivities $T_{v_{i,j}}$, aquifer thicknesses $b_{a_{i,j}}$, and storage coefficients $S_{i,j}$. The nodes are located in the center of these cells, and the hydraulic heads define those of the corresponding cells. The thickness of the aquifer is expressed using thickness of the cell, which is assumed to be constant.

The transient flow equation derived in chapter 4 (eq. 4.23b) for an inhomogeneous and anisotropic aquifer can be expressed in its three-dimensional form according to:

$$\frac{\partial}{\partial x} \left(K_{H_x} \frac{\partial h}{\partial x} \right) + \frac{\partial}{\partial y} \left(K_{H_y} \frac{\partial h}{\partial y} \right) + \frac{\partial}{\partial z} \left(K_{H_z} \frac{\partial h}{\partial z} \right) = S_{sp} \frac{\partial h}{\partial t} \quad (5.42)$$

For the two-dimensional case, since the aquifer, as in the previous example, has a constant thickness b_a , and is horizontal and confined, (5.42) can be written as follows:

$$\frac{\partial}{\partial x} \left(T_{v_x} \frac{\partial h}{\partial x} \right) + \frac{\partial}{\partial y} \left(T_{v_y} \frac{\partial h}{\partial y} \right) = S_{sp} \frac{\partial h}{\partial t} \quad (5.43)$$

where (5.30), (5.31) and (5.32) were used.

To derive the finite difference equation for the hydraulic head of each inner node (i, j), the partial derivatives must be replaced by the difference quotients, as in the previous example.

The formulation of (5.18) with indices (i, j), using the centered difference method (see section 5.1.2.1.2), yields the following for the first partial derivative with respect to x :

$$\left(\frac{\partial h}{\partial x} \right)_{i,j} = \frac{h_{i+1/2,j} - h_{i-1/2,j}}{\Delta x} \quad (5.44)$$

Next, we need to formulate the second derivatives given in (5.43). That is,

$$\frac{\partial}{\partial x} \left(T_{v_x} \frac{\partial h}{\partial x} \right) \quad (5.45)$$

and:

$$\frac{\partial}{\partial y} \left(T_{v_y} \frac{\partial h}{\partial y} \right) \quad (5.46)$$

Using (5.44), (5.45) can be written as:

$$\frac{\partial}{\partial x} \left(T_{v_x} \frac{\partial h}{\partial x} \right) = \frac{\left(T_{v_x} \frac{\partial h}{\partial x} \right)_{i+1/2,j} - \left(T_{v_x} \frac{\partial h}{\partial x} \right)_{i-1/2,j}}{\Delta x} \quad (5.47)$$

Similarly, the remaining derivatives can be approximated by means of difference quotients using (5.44). In accordance with (5.44), for $(i + \frac{1}{2}, j)$ we have that:

$$\left(\frac{\partial h}{\partial x} \right)_{i+1/2,j} = \frac{(h)_{i+1,j} - (h)_{i,j}}{\Delta x} \quad (5.48)$$

and for $(i - \frac{1}{2}, j)$ we have:

$$\left(\frac{\partial h}{\partial x} \right)_{i-1/2,j} = \frac{(h)_{i,j} - (h)_{i-1,j}}{\Delta x} \quad (5.49)$$

Using equations (5.48) and (5.49) in equation (5.47) we have that:

$$\frac{\partial}{\partial x} \left(T_{v_x} \frac{\partial h}{\partial x} \right) = (T_{v_x})_{i+1/2,j} \frac{(h)_{i+1,j} - (h)_{i,j}}{(\Delta x)^2} - (T_{v_x})_{i-1/2,j} \frac{(h)_{i,j} - (h)_{i-1,j}}{(\Delta x)^2} \quad (5.50)$$

The transmissivities that appear at $(i + \frac{1}{2})$ and $(i - \frac{1}{2})$ must be replaced by those corresponding to the nodes in the center of the cells. $(T_{v_x})_{i+1/2,j}$ and $(T_{v_x})_{i-1/2,j}$ are determined, for example, by applying the arithmetical mean of the transmissivities either between (i) and $(i - 1)$, or between $(i + 1)$ and (i) :

$$(T_{v_x})_{i+1/2,j} = \frac{(T_{v_x})_{i+1,j} + (T_{v_x})_{i,j}}{2} \quad (5.51)$$

$$(T_{v_x})_{i-1/2,j} = \frac{(T_{v_x})_{i,j} + (T_{v_x})_{i-1,j}}{2} \quad (5.52)$$

Inserting equations (5.51) and (5.52) in equation (5.50), the following expression is obtained:

$$\begin{aligned} \frac{\partial}{\partial x} \left(T_{v_x} \frac{\partial h}{\partial x} \right) = & \partial \frac{1}{2(\Delta x)^2} \left(((T_{v_x})_{i+1,j} + (T_{v_x})_{i,j}) ((h)_{i,j+1} - (h)_{i,j}) \right. \\ & \left. - ((T_{v_x})_{i,j} + (T_{v_x})_{i-1,j}) ((h)_{i,j} - (h)_{i-1,j}) \right) \end{aligned} \quad (5.53)$$

Alternatively, after ordering we have:

$$\begin{aligned} \frac{\partial}{\partial x} \left(T_{v_x} \frac{\partial h}{\partial x} \right) = & \frac{1}{2(\Delta x)^2} \left(((T_{v_x})_{i+1,j} + (T_{v_x})_{i,j}) ((h)_{i,j+1}) \right. \\ & - ((T_{v_x})_{i+1,j} + 2(T_{v_x})_{i,j} + (T_{v_x})_{i-1,j}) ((h)_{i,j}) \\ & \left. + ((T_{v_x})_{i,j} + (T_{v_x})_{i-1,j}) ((h)_{i-1,j}) \right) \end{aligned} \quad (5.54)$$

The second partial derivative with respect to y in equation (5.46) is obtained in a similar fashion:

$$\begin{aligned} \frac{\partial}{\partial y} \left(T_{v_y} \frac{\partial h}{\partial y} \right) &= \frac{1}{2(\Delta y)^2} \left((T_{v_y})_{i,j+1} + (T_{v_y})_{i,j} \right) ((h)_{i,j+1}) \\ &\quad - \left((T_{v_y})_{i,j+1} + 2(T_{v_y})_{i,j} + (T_{v_y})_{i,j-1} \right) ((h)_{i,j}) \\ &\quad + \left((T_{v_y})_{i,j} + (T_{v_y})_{i,j-1} \right) ((h)_{i,j-1}) \end{aligned} \quad (5.55)$$

Thus, the spatial derivatives of continuity equation (5.32) are presented as difference quotients. The temporal term $S(\partial h/\partial t)$ still needs to be approximated. This can only be done by applying the backward difference method, with the time interval index being $(k-1, k)$:

$$S \frac{\partial h}{\partial t} = S_{i,j} \frac{(h)_{i,j,k} - (h)_{i,j,k-1}}{\Delta t} \quad (5.56)$$

Previously, the spatial derivatives of the continuity equation were approximated by difference quotients. For this process it is important to define a specific moment in time from the time interval when either the difference quotients or hydraulic heads are used. To obtain the implicit difference equation, hydraulic head should be taken at the upper end of the time interval $(k-1, k)$, and therefore receives the index k .

We can now replace all derivatives by the difference quotients. By inserting equations (5.54), (5.55) and (5.56) in equation (5.43), the difference equation for calculating the hydraulic heads for each inner node of the model is obtained. To summarize the expression of hydraulic heads of equal indices, we have:

$$\begin{aligned} &\underbrace{\frac{1}{2(\Delta x)^2} \left((T_{v_x})_{i+1,j} + 2(T_{v_x})_{i,j} + (T_{v_x})_{i-1,j} \right)}_{A_1} \\ &\quad + \underbrace{\frac{1}{2(\Delta y)^2} \left((T_{v_y})_{i,j+1} + 2(T_{v_y})_{i,j} + (T_{v_y})_{i,j-1} \right)}_{A_2} + \underbrace{\frac{S_{i,j}}{\Delta t}}_{A_3} ((h)_{i,j,k}) \\ &= \underbrace{\frac{1}{2(\Delta y)^2} \left((T_{v_y})_{i,j} + (T_{v_y})_{i,j-1} \right)}_B ((h)_{i,j-1,j,k}) + \underbrace{\frac{1}{2(\Delta x)^2} \left((T_{v_x})_{i+1,j} + (T_{v_x})_{i,j} \right)}_C ((h)_{i+1,j,k}) \\ &\quad + \underbrace{\frac{1}{2(\Delta y)^2} \left((T_{v_y})_{i,j+1} + (T_{v_y})_{i,j} \right)}_D ((h)_{i,j+1,k}) + \underbrace{\frac{1}{2(\Delta x)^2} \left((T_x)_{i,j} + (T_x)_{i-1,j} \right)}_E ((h)_{i-1,j,k}) \\ &\quad + \underbrace{\frac{S_{i,j}}{\Delta t} ((h)_{i,j,k-1})}_F, \quad \text{with } A = A_1 + A_2 + A_3 \end{aligned} \quad (5.57)$$

A more readable expression of the difference method is obtained by summarizing the transmissivity and storage coefficient parameters in terms of A to F :

$$\begin{aligned}
 h_{i,j,k} &= \frac{1}{A} (B(h)_{i,j-1,k} + C(h)_{i+1,j,k} + D(h)_{i,j+1,k} + E(h)_{i-1,j,k} + F); \quad \text{with:} \\
 A &= \frac{1}{2(\Delta x)^2} ((T_{v_x})_{i+1,j} + 2(T_{v_x})_{i,j} + (T_{v_x})_{i-1,j}) \\
 &\quad + \frac{1}{2(\Delta y)^2} ((T_{v_y})_{i,j+1} + 2(T_{v_y})_{i,j} + (T_{v_y})_{i,j-1}) + \frac{S_{i,j}}{\Delta t} \\
 B &= \frac{1}{2(\Delta y)^2} ((T_{v_y})_{i,j} + (T_{v_y})_{i,j-1}) \\
 C &= \frac{1}{2(\Delta x)^2} ((T_{v_x})_{i+1,j} + (T_{v_x})_{i,j}) \\
 D &= \frac{1}{2(\Delta y)^2} ((T_{v_y})_{i,j+1} + (T_{v_y})_{i,j}) \\
 E &= \frac{1}{2(\Delta x)^2} ((T_{v_x})_{i,j} + (T_{v_x})_{i-1,j}) \\
 F &= \frac{S_{i,j}}{\Delta t} ((h)_{i,j,k-1})
 \end{aligned} \tag{5.58}$$

This equation is valid for calculating the hydraulic head at the inner nodes of the model.

The nodes where water is injected into or extracted from the aquifer have still not been considered. For these nodes, equation (5.58) also holds, with the only difference being that a term $W_{i,j,k}$ must be added to the term F . This allows for taking into account a water source or water sink, respectively:

$$F = \frac{S_{i,j}}{\Delta t} ((h)_{i,j,k-1}) + W_{i,j,k} \tag{5.59}$$

where $W_{i,j,k}$ can be expressed by a pumping or infiltration flow $Q_{v_{i,j,k}}$:

$$W_{i,j,k} = \frac{Q_{v_{i,j,k}}}{(\Delta x)^2} \tag{5.60}$$

The corresponding equations used for calculating the hydraulic head at nodes located on the boundaries of the model are derived in a similar way.

5.1.4 *Calculating the groundwater flow velocity (average pore velocity)*

In section 5.1.2, the hydraulic heads for the cell centers, which are the nodes of the finite difference model grid, were determined. Using these hydraulic heads and applying Darcy's law as well as the effective porosity value, the average pore velocity, v_A , of groundwater at the boundary between two cells can be determined.

The concentration of a solute (or heat content) in a cell is described through its value on the corresponding node. Instead of establishing a water balance for the continuity equation, we now establish a solute mass or thermal energy balance for the interval $(t, t + \Delta t)$.

That is,

$$\begin{aligned} \text{storage} &= \text{convective contribution} + \text{dispersive contribution} \\ &+ \text{contribution from sources/sinks} - \text{destruction and disintegration.} \end{aligned}$$

This gives n explicit equations with n unknown concentration $C_{i,j}(t + \Delta t)$ of solutes (or heat content, respectively) at the n nodes of the grid. These equations can be solved using the solute concentration $C_{i,j}(t)$ (or heat content) of the previous time interval as well as the boundary conditions. By repeating this step for each time interval starting at the initial time t_0 of the simulation up to the stipulated simulation time t_{\max} , the spatial distribution of concentration for each time interval is obtained. Similar to the case of the continuity equation, the difference method can be explicit, fully implicit, or it can make use of the semi-implicit Crank-Nicholson method. Some of these classical methods are briefly described by Kinzelbach (1987); a more detailed description is included in Ortega and Reinholdt (1970).

In the following, we derive the difference method for the transport equation in the simple one-dimensional case with a constant dispersion coefficient, D . The two- and three-dimensional difference methods will not be derived because of the great calculation effort demanded, particularly in the description of dispersive tensor flows. Kinzelbach (1987) discusses this topic and considers different boundary value types.

The transport equation can be simplified if only one dimension is considered, combined with a constant dispersion tensor D and a constant flow average pore velocity v_A (stationary groundwater model, see eq. 4.111):

$$\frac{\partial C}{\partial t} = -\bar{v}_A \frac{\partial C}{\partial x} + D \frac{\partial^2 C}{\partial x^2} \quad (5.65)$$

There are several possibilities for approximating the solution to this partial equation. They differ in the approximation of the first derivative. If the centered difference method (section 5.1.2.1.2) is used for the spatial discretization (in this case only for the x axis) and the forward difference method (section 5.1.2.1.1) is used for the temporal discretization, the so-called centered explicit approximation is obtained for (5.65):

$$\frac{C_{x,t+\Delta t} - C_{x,t}}{\Delta t} = -(v_A)_x \frac{C_{x+\Delta x,t} - C_{x-\Delta x,t}}{2\Delta x} + D \frac{C_{x+\Delta x,t} - 2C_{x,t} + C_{x-\Delta x,t}}{(\Delta x)^2} \quad (5.66)$$

Note that each equation for a node contains an expression of the unknown concentration $C_{x,t+\Delta t}$ and can therefore be solved as a function of concentration. Assuming that concentration values for all the nodes at the previous time are known, the concentrations can be calculated for each node separately (explicitly) for each time interval.

5.1.6 *Stability and accuracy criteria*

The finite difference method, as with other numerical methods, provides an approximation of the exact solution of differential equations. Numerical calculations must comply with certain convergence and stability criteria for the results to be reliable. The convergence condition in a numerical calculation for an approximation is fulfilled if the numerical solution is equal to the solution of the differential equation on which it is based when the size of the finite intervals in space and time tend to zero. This condition can be corroborated only with simple examples, since it is only in these cases that analytical solutions can be obtained. For this reason, the convergence of a

numerical method is tested in practice with several analytically solvable examples. If the numeric results obtained match the exact solution within some tolerance, the method is considered to be convergent.

To obtain the stability of the explicit finite difference method, different stability criteria that are related to the selection of time intervals and grid spacing are considered. The correct stability criteria must be used when implementing the model.

The following sections will describe the principal stability criteria for two-dimensional transport problems, but their derivations will not be included. Other stability criteria, including those corresponding to linear and non-linear adsorption and reaction processes, can be found, e.g. in Kinzelbach (1977), whereas Forsythe and Wasnow (1960) and Fox (1962) mainly deal with the mathematical derivations.

5.1.6.1 Courant criterion

Applied to explicit approximation, the Courant criterion (Courant *et al.* 1928) requires using Courant's magnitude, Co , for spatial centered differences:

$$Co_x = \left| \frac{\Delta t v_{ax}}{\Delta x} \right| \leq 1 \quad (5.67)$$

$$Co_y = \left| \frac{\Delta t v_{ay}}{\Delta y} \right| \leq 1 \quad (5.68)$$

or alternatively:

$$\Delta t \leq \left| \frac{\Delta x}{v_{Ax}} \right| \quad (5.69)$$

$$\Delta t \leq \left| \frac{\Delta y}{v_{Ay}} \right| \quad (5.70)$$

For the dispersion process, this means that velocities greater than the average pore velocity, v_A , cannot occur. Alternatively, as expressed by Kinzelbach (1987), the concentration in a cell during a given time interval cannot be higher than the concentrations received from the advective contributions. In other words, during a time interval, it is not possible for a cell to release more substance than it had at the beginning of the time interval (Kinzelbach 1987).

5.1.6.2 Neumann criterion

The Neumann criterion (Richtmyer and Morton 1967) for a two-dimensional transport equation with groundwater flow parallel to either x or y (diagonal dispersion tensor \mathbf{D}) can be expressed as follows for explicit approximations (Reddel and Sunada 1970):

$$\left(\frac{D_{xx}}{(\Delta x)^2} + \frac{D_{yy}}{(\Delta y)^2} \right) \Delta t \leq 0.5 \quad (5.71)$$

This can be simplified, in the case of a one-dimensional transport equation (5.66), to the expression:

$$\left(\frac{D}{(\Delta x)^2} \right) \Delta t \leq 0.5 \quad (5.72)$$

This criterion requires that during a given time interval, concentration gradients are not inverted by dispersive mass flows alone (Kinzelbach 1987).

5.2 INTRODUCTION TO THE FINITE ELEMENT METHOD (FEM)

Modeling of groundwater flow and the transport of mass and heat in reservoirs require solving differential equations or systems of differential equations, with initial and boundary conditions. These equations were developed in chapters two and four. The finite element method (FEM) is the most used numerical technique to solve approximately mathematical models expressed as partial differential equations (PDE). The *CRC Concise Encyclopedia of Mathematics* (Weisstein 2003) defines the FEM as follows:

- The FEM is a method for solving an equation by approximating continuous quantities as a set of quantities at discrete points, often regularly spaced into a so-called *grid* or *mesh*. Because finite element methods can be adapted to problems of great complexity and unusual geometry, they are an extremely powerful tool in the solution of important problems in heat transfer, fluid mechanics, and mechanical systems. Furthermore, the availability of fast and inexpensive computers allows problems which are intractable using analytic or mechanical methods to be solved in a straightforward manner using finite element methods.

The mathematical background of the method has existed since the first half of the twentieth century. The main ideas spread throughout the works of people working on mechanical problems. Rayleigh (1896) and Ritz (1909) solved variational problems; Galerkin (1915) found direct approximate solutions to boundary value problems, without using variational formulations; Courant (1943), solved vibration problems using the variational Ritz method and Sobolev (1950) developed tools of functional analysis. These references can be classified as the basis of finite element analysis from the mathematical standpoint, without being the method itself. In the 1950s, engineers of the aviation industry, developed, used and published the first coherent ideas regarding the FEM when seeking approximate simple solutions to simulate aircrafts as two-dimensional structures (Turner *et al.* 1956). By late 1950s, the key concepts of stiffness matrix and element assembly existed, for the most part, as they do today. Clough (1960, 1965) used the name “finite element” for the first time in his famous paper: “*The Finite Element in Plane Stress Analysis*”. Later Zienkiewicz (1965) extended its applications to other engineering areas. NASA issued a request for proposals on the development of the general-purpose finite element software NAS-TRAN in 1965. In the next decade, mathematicians in different countries coupled functional analysis tools to the FEM and made a first theory based on variational techniques (Zienkiewicz 1973). Strang and Fix (1973) wrote the first book on the mathematical foundation of the FEM. Pinder and Gray (1977) synthesized the first applications of the FEM to hydrogeology. Presently the FEM is the most commonly used numerical simulation tool in engineering and in virtually all areas of applied sciences (Zienkiewicz and Taylor 2000, Reddy and Gartling 2001, COMSOL 2008a).

The basic physical concept in FEM is the subdivision of the domain of the mathematical model into disjointed, non-overlapping components of simple geometry, such as triangles or rectangles, called *finite elements*. This mental picture assumes that the system is formed from simpler components. In this way, a geometrically similar model of discrete elements on a structured or unstructured grid represents the real object. The response of each element is expressed in terms of a finite number of degrees of freedom characterized by the value of an unknown function at a set of nodal points. Equations of equilibrium and physical considerations are applied to each element using simple interpolators, and a system of simultaneous linear equations is constructed. This system is solved for the unknown values in the nodal points. The response of the mathematical model is then considered to be approximated by that of the discrete model obtained by connecting or assembling the collection of all elements (Zienkiewicz and Taylor 2000). While being an approximate method, the accuracy of the FEM can be improved in two ways: by refining the mesh in the model using more elements and nodes and by employing better interpolators. The FEM is the dominant discretization technique in structural mechanics for the determination of stresses and displacements in mechanical systems (Liu and Quek 2003). However, it is also routinely used in the analysis of many other types of problems, including those in heat transfer,

solid state diffusion and reactions with moving boundaries, fluid dynamics, electromagnetism and flow of mass and heat in porous media. In the following sections, we present a brief, simplified introduction to the FEM that can be useful in hydrogeology, including aquifers, hydrocarbon reservoirs, and geothermal systems. Further information can be found online (COMSOL 2009, Wikipedia 2009e, Felippa 2007, 2009a, b).

5.2.1 Brief description of the method fundamentals

The FEM is used in hydrogeology to approximately calculate the distribution of unknown functions (pressure, temperature, velocity) in the spatial domain occupied by the aquifer. The FEM can be understood easily as a specifically sophisticated interpolation technique. The domain of the reservoir is subdivided into a finite number of subdomains or elements of very simple geometry (Fig. 5.6). The physical laws of the problem are applied to each element. The unknown variable, assumed to be a continuous function, can be approximated by interpolation functions in each element. For each one of these elements a matrix is obtained, which approaches the behavior of the corresponding region. The accuracy of this matrix approach depends upon the size and complexity of the finite elements. The unknowns are the discrete values of the variable in the nodes linking the elements; all the elements are bound together to obtain a global matrix that represents the whole domain. In the stationary case, this process leads to a set of simultaneous linear algebraic equations, or to a system of ordinary differential equations in the transient case. In both cases, the solutions to these equations allows for approximating the unknown variable. The same basic procedure can be applied to an immense variety of problems.

Let us consider for example the reservoir pressure $p(x, y, z, t)$, which is distributed in space and time. This variable is mathematically defined in a space E that is continuous and, therefore, of infinite dimension. The technique of finite elements seeks a simpler, approximate solution p^e that comes close to p , by defining a similar problem in another space E_h of finite dimension, in such a way that $p \approx p^e \in E_h$. It is said that p^e is the discrete solution that approximates the continuous function p .

This brief discussion of FEM's nature shows that the finite element is composed of two parts: a geometric part, given by the form of the subdomains and an analytical part given by the interpolation function. In this section, we introduce the mathematical foundations of the FEM in a simple, practical and useful way. The approach we use is called the *Galerkin finite element method*. The reader will find examples here that can be solved by hand, using a pocket calculator. However, when applied to real complex problems, the FEM requires a large volume of computing. Therefore, the systematic use of computers and programming languages such as Visual Fortran, or C++, and high-level software like *Matlab*, *Mathematica* or even better, COMSOL-Multiphysics to accomplish the calculations is recommended.

5.2.2 Finite elements using linear Lagrange interpolation polynomials

In this section we illustrate how finite elements are built using linear Lagrange polynomials (see Appendix for details). Let $f(x)$ be a real function defined in the interval $\Omega = [a, b]$. We partition

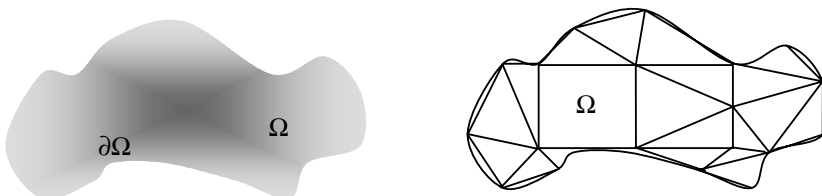


Figure 5.6. Discretization of a domain using the FEM. Left: real object; right: simplified object.

this domain into N subintervals (Fig. 5.7):

$$a = x_0 < x_1 < x_2 < \dots < x_{k-1} < x_k < x_{k+1} < \dots < x_{N-1} < x_N = b \quad (5.73)$$

Let $I_k = [x_{k-1}, x_k]$ be the k -subinterval and let $h_k = x_k - x_{k-1}$ be its size. All the $I_k \{k = 1, N\}$ are non-overlapping subintervals of $[a, b]$ (Fig. 5.7). Each segment I_k is the geometric part of the k -finite element. The assembly consisting of the union of all the intervals is called the mesh \mathcal{M}_1 of the domain Ω , which is the solution domain in one dimension:

$$\mathcal{M}_1 = \bigcup_{k=1}^N I_k \quad (5.74)$$

In one dimension, the mesh \mathcal{M}_1 is the same as Ω . In two or three dimensions, the mesh is only a geometric approximation to the real domain, due to the presence of curvatures at the boundary of Ω (Fig. 5.6). Let \mathbf{E}_1 be the vector space of continuous piecewise linear functions defined on the mesh \mathcal{M}_1 . Any function $p_1 \in \mathbf{E}_1$ is linear over each interval I_k and continuous in $\Omega = [a, b]$. Let us assume that $p_1(x) = m_1 x + b_1$, using the known values of the function $f(x)$ at the nodes of the interval I_1 (Fig. 5.7) we obtain:

$$\begin{aligned} \forall x \in I_1 = [x_0, x_1], \quad f(x) \approx p_1(x) = m_1 x + b_1, \quad \text{therefore:} \\ \left. \begin{aligned} p_1(x_0) = f_0 = m_1 x_0 + b_1 \\ p_1(x_1) = f_1 = m_1 x_1 + b_1 \end{aligned} \right\} \Rightarrow p_1(x) = \frac{f_1 - f_0}{x_1 - x_0} x + \frac{x_1 f_0 - x_0 f_1}{x_1 - x_0} \quad (5.75a) \end{aligned}$$

Arranging algebraically this expression, we obtain the same interpolation deduced in the Appendix A for the function $f(x)$, which could be interpolated in the interval $[x_0, x_1]$ using

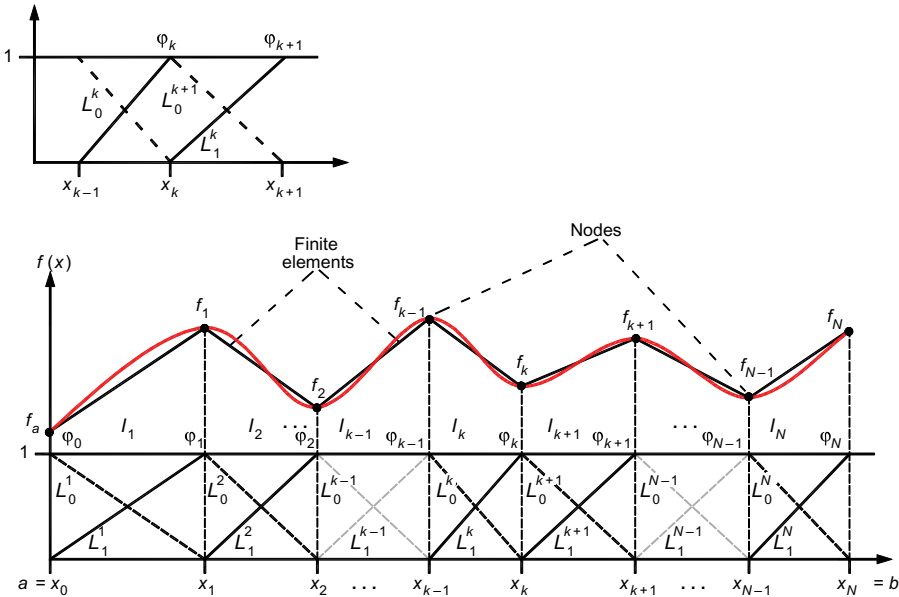


Figure 5.7. Construction of the interpolation of a continuous function $f(x)$, using linear Lagrange polynomials. The union of the intervals forms a mesh with $N + 1$ nodes and N finite elements. L is the generic name for the Lagrange polynomials.

two linear Lagrange polynomials:

$$p_1(x) = \frac{x - x_1}{x_0 - x_1} f_0 + \frac{x - x_0}{x_1 - x_0} f_1 = L_0(x) f_0 + L_1(x) f_1 = \sum_{j=0}^1 L_j(x) f(x_j) \quad (5.75b)$$

$$\Rightarrow f(x) \approx p_1(x), \quad \forall x \in [x_0, x_1]$$

The function $f(x)$ can be interpolated in the interval $[x_0, x_2] = I_1 \cap I_2$ using the same Lagrange technique (see Appendix):

$$f(x) \approx \frac{x - x_1}{x_0 - x_1} f_0 + \frac{x - x_0}{x_1 - x_0} f_1 + \frac{x - x_2}{x_1 - x_2} f_1 + \frac{x - x_1}{x_2 - x_1} f_2 \quad (5.76)$$

$$= L_0^1(x) f_0 + (L_1^1(x) + L_0^2(x)) f_1 + L_1^2(x) f_2, \quad \forall x \in [x_0, x_2]$$

L_0^1 and L_1^1 are the linear Lagrange polynomials in the interval $I_1 = [x_0, x_1]$

L_0^2 and L_1^2 are the linear Lagrange polynomials in the interval $I_2 = [x_1, x_2]$

In a very similar way, we can interpolate the function $f(x)$ throughout the whole interval $[x_0, x_N]$ using only the two corresponding linear Lagrange polynomials in each subinterval $I_k (k = 1, N)$:

$$\begin{aligned} f(x) &\approx \frac{x - x_1}{x_0 - x_1} f_0 + \frac{x - x_0}{x_1 - x_0} f_1 + \frac{x - x_2}{x_1 - x_2} f_1 + \frac{x - x_1}{x_2 - x_1} f_2 + \dots + \frac{x - x_{k-1}}{x_k - x_{k-1}} f_k \\ &+ \frac{x - x_{k+1}}{x_k - x_{k+1}} f_k + \dots + \frac{x - x_{N-2}}{x_{N-1} - x_{N-2}} f_{N-1} + \frac{x - x_{N-1}}{x_N - x_{N-1}} f_N \\ &= L_0^1 f_0 + (L_1^1 + L_0^2) f_1 + (L_1^2 + L_0^3) f_2 + \dots + (L_1^k + L_0^{k+1}) f_k + \dots + L_1^N f_N \end{aligned} \quad (5.77)$$

This technique is known as the piecewise linear interpolation of $f(x)$; its correct use requires that each one of the unknown values x one wishes to interpolate should be placed in the appropriate subinterval I_k . The problem with equation (5.77) is that the Lagrange polynomials L_0 and L_1 are non-continuous functions in every subinterval. For example, $L_0^1(x_1) = 0 \neq L_1^1(x_1) = 1$. To overcome this difficulty we can build a continuous piecewise linear function in formula (5.77) by defining the following linear splines or unitary interpolators $\varphi_k(x)$ (see Fig. 5.7):

$$\begin{aligned} \varphi_k(x) &= L_1^k \cup L_0^{k+1}, \quad \forall k = 1, N - 1; \quad \varphi_0(x) = L_0^1(x), \quad \varphi_N(x) = L_1^N(x) \\ \varphi_k(x) &= \left\{ \begin{array}{ll} L_1^k(x), & \text{if } x \in I_k = [x_{k-1}, x_k] \\ L_0^{k+1}(x), & \text{if } x \in I_{k+1} = [x_k, x_{k+1}] \\ 0, & \text{if } x \notin \Omega_k \end{array} \right\}, \quad \begin{array}{l} \Omega_k = I_k \cup I_{k+1} \\ \text{and } \varphi_k(x_j) = \delta_{kj} \\ \forall k = 1, N - 1 \end{array} \end{aligned} \quad (5.78a)$$

Another equivalent, more explicit form of constructing these functions is as follows:

$$\begin{aligned} \varphi_0(x) &= \frac{x_1 - x}{x_1 - x_0}, \quad \varphi_N(x) = \frac{x - x_{N-1}}{x_N - x_{N-1}} \\ \varphi_k(x) &= \left\{ \begin{array}{ll} \frac{x - x_{k-1}}{x_k - x_{k-1}}, & \text{if } x \in [x_{k-1}, x_k] \\ \frac{x_{k+1} - x}{x_{k+1} - x_k}, & \text{if } x \in [x_k, x_{k+1}] \\ 0, & \text{if } x \notin [x_{k-1}, x_{k+1}] \end{array} \right\} \quad \begin{array}{l} \forall k = 1, N - 1 \\ \varphi_k(x_k) = 1 \\ \varphi_k(x_j) = 0 \\ \forall j \neq k = 0, N \end{array} \end{aligned} \quad (5.78b)$$

The continuous interpolation of $f(x)$ using only unitary functions becomes:

$$f(x) \approx \sum_{k=0}^N \varphi_k(x) f(x_k), \quad \forall x \in \Omega = [a, b] \quad (5.79)$$

The $N + 1$ functions $\{\varphi_k(x), k = 0, N\}$, defined explicitly in terms of the Lagrange linear functions are all continuous in $[a, b]$ and satisfy the properties: $\varphi_k(x_k) = 1$, $\varphi_k(x_j) = 0$ if $k \neq j$. This is the analytic part of the finite element k . Each interpolator $\varphi_k(x)$ is called *nodal function* or *shape function* or *hat function* (Fig. 5.7) and is defined on the whole domain $[a, b]$, but vanishes outside the corresponding interval $[x_{k-1}, x_{k+1}]$. The first interval of the mesh is $[a, x_1]$, the last interval is $[x_{N-1}, b]$. Functions $\varphi_0(x)$ and $\varphi_N(x)$ are associated with the boundary points 0 and N . Therefore, the total number of interpolators is $N + 1$ for this mesh \mathcal{M}_1 . We deduce that the dimension of \mathbf{E}_1 is $\dim(\mathbf{E}_1) = N + 1$. Note that $f(x)$ is approximated by a combination of N straight lines $p_k(x)$ (Fig. 5.7) passing through the points (x_{k-1}, f_{k-1}) and (x_k, f_k) :

$$f(x) = \bigcup_{k=1}^N \frac{f_k - f_{k-1}}{x_k - x_{k-1}} x + \frac{x_k f_{k-1} - f_k x_{k-1}}{x_k - x_{k-1}} = \bigcup_{k=1, N} m_k x + b_k \quad (5.80)$$

The finite elements of this numerical technique (FEM) are formed by a geometric part and by an analytic part. This fact can be symbolized as $EF_k = (I_k, \varphi_k)$. The functions $\varphi_k(x)$ ($k = 0, N$) form a special basis of \mathbf{E}_1 which is called the unitary basis. The use of these linear functions as the interpolation basis is just one choice among many other possible choices. We could take the quadratic and cubic Lagrange polynomials or the Hermite or the Tchebyshev functions as other types of higher degree interpolators (Eriksson *et al.* 1996, Zienkiewicz and Taylor 2000; see also Appendix). In general, any continuous function u of the space \mathbf{E}_1 can be represented as a linear combination of the φ_k functions:

$$\forall u \in E_1 \Rightarrow u(x) = \sum_{k=0}^N u(x_k) \varphi_k(x) = u_0 \varphi_0(x) + \dots + u_N \varphi_N(x) \quad (5.81)$$

This last property is due to the fact that $u(x_k) = u_k \varphi_k(x_k) = u_k$. All the remaining terms with subindex $\neq k$ are equal to zero because of the previous property (5.78a). We say that (u_0, u_1, \dots, u_N) are the coordinates of $u(x)$ in the vector space \mathbf{E}_1 . Let $u(x)$ be the linear interpolator of $f(x)$ in the nodes $x_k : f(x) \approx u(x)$ and $f(x_k) = u(x_k) = u_k, k = 0, N$. Therefore:

$$f(x) \approx u(x) = \sum_{k=0}^N u_k \varphi_k(x), \quad \forall x \in \Omega \quad (5.82)$$

Equation (5.82) expresses that the function f , continuous in $[x_0, x_N]$, is approximated by a piecewise continuous linear polynomial (linear splines) in the space \mathbf{E}_1 . We just demonstrated that any continuous function could be interpolated by a combination of linear nodal functions. This is a consequence of the postulate of the Weierstrass theorem enunciated in the Appendix.

5.2.3 Numerical solution of the Poisson's equation with the FEM—Galerkin method

In this section, we show how to build an approximate solution of the Poisson's equation. This differential equation appears in previous chapters representing different steady state phenomena ($\partial/\partial t = 0$): the heat equation (2.16, 2.109, 4.83), the groundwater flow equation (4.16, 4.23b and 4.25a), and the diffusion equation (4.111). To illustrate the method with a specific example, we use FEM in a one-dimensional flow problem in a homogeneous isothermal aquifer. We employ two types of interpolators: trigonometric functions and linear Lagrange polynomials. The flow

domain is $[a, b]$, and the unknown is the steady state water pressure $p(x)$ with the following boundary conditions (eq. 4.16, in one dimension):

$$\begin{aligned} \frac{\rho_f k_x}{\mu_f} \frac{d^2 p}{dx^2} = -q_f(x) &\Rightarrow \frac{d^2 p}{dx^2} = \frac{\mu_f}{\rho_f k_x} q_f(x) = q(x) \\ \forall x \in \langle a, b \rangle; \quad p(a) = p_a, \quad p(b) = p_b \end{aligned} \quad (5.83)$$

We assume first that the permeability k_x is constant. To solve this general non-homogeneous equation, an idea is to make this problem homogeneous through a simple change of function $y(x) + u(x)$, where $u(x)$ belongs to the vector space E_1 :

$$\begin{aligned} u(x) &= \frac{b-x}{b-a} p_a + \frac{x-a}{b-a} p_b, \quad \text{and} \quad y(x) = p(x) - u(x) \\ \Rightarrow \quad u(a) &= p_a, \quad \text{and} \quad u(b) = p_b \quad \Rightarrow \quad y(a) = y(b) = 0 \end{aligned} \quad (5.84)$$

Therefore, the differential problem (5.83) becomes:

$$-\frac{d^2 y}{dx^2} = q(x), \quad \forall x \in \langle a, b \rangle, \quad y(a) = 0, \quad y(b) = 0 \quad (5.85)$$

In order to clarify fully the FEM, we solve this problem in two ways: the first one consists of approximating $y(x)$ using general test functions $v_i(x)$, which can be linear or not. The second form uses directly the piecewise linear polynomial of the previous section to approximate $y(x)$ in each one of the subintervals of the mesh. In both cases, the technique used to approximate the solution is known as the Galerkin method, in honor to Boris Grigoryevich Galerkin, a Russian mathematician, engineer and professor of structural mechanics (Fig. 5.8). In 1915, Galerkin published his technique as a way to approximate the solutions of differential equations in plate analysis problems. By exploiting the fact that function $y(x)$ vanishes at the end-points ($x_0 = a, x_{N+1} = b$), we make a slightly different partition of this domain into $N - 1$ subintervals: $x_1 < x_2 < \dots < x_k \dots < x_{N-1} < x_N$ (Fig. 5.7). Let $v(x)$ be a test function, derivable for all $x \in [a, b]$, and such that it satisfies the homogeneous boundary conditions: $v(a) = v(b) = 0$. The Galerkin method consists of multiplying both terms of equation (5.85) by $v(x)$, then integrating both sides of the equality and transforming through integration by parts the resulting equation



Figure 5.8. Boris Galerkin (1871–1945).

in the interval $[a, b]$:

$$\begin{aligned}
 - \int_a^b \frac{d^2y}{dx^2} v(x) dx &= \int_a^b q(x) v(x) dx \\
 \Leftrightarrow - \frac{dy(x)}{dx} v(x) \Big|_a^b + \int_a^b \frac{dy}{dx} \frac{dv}{dx} dx &= \int_a^b q(x) v(x) dx
 \end{aligned}
 \tag{5.86}$$

The first term in the second line of equation (5.86) is zero because we assume that $v(x)$ disappears in both extrema of the interval, a and b . This integral equation implicitly contains the boundary conditions and is equivalent to the original differential problem (5.85), which now becomes an integral-differential equation, equivalent to the abstract formulation:

$$\int_a^b \frac{dy}{dx} \frac{dv}{dx} dx = \int_a^b q(x) v(x) dx \quad \Leftrightarrow \quad \langle y', v' \rangle = \langle q, v \rangle
 \tag{5.87}$$

Equation (5.87) is the integral form of model (5.85) and is called the “weak formulation” of the original differential problem. This name originates in the fact that equation (5.87) does not require $y(x)$ or $v(x)$ to have continuous second derivatives. In the integral formulation, it is sufficient that both functions are derivable just once. Thus, the condition is weaker than the original one, which is called the strong form of the differential problem. It is important to note that the Galerkin method is not associated to any variational method. The variational approach in these problems is known as the Ritz method (Zienkiewicz and Taylor 2000).

5.2.3.1 Numerical method 1: General test functions

We assume that the test functions $\{v_i(x), i = 1, N\}$, also known as trial functions, form a basis of the space E_h where we are seeking the solution of equation (5.87). The interpolation of the unknown function $y(x)$ in terms of test functions is $y_e(x)$:

$$y(x) \approx y_e(x) = \sum_{j=1}^N y_j v_j(x) = y_1 v_1(x) + y_2 v_2(x) + \dots + y_N v_N(x)
 \tag{5.88}$$

where the $y_j = y(x_j)$, $\{j = 1, N\}$ are unknown constants, equal to the values of $y(x)$ at each one of the nodes x_j of the partition of the interval $[x_1, x_2, \dots, x_N]$. Replacing the interpolation (5.88) into the weak formulation (5.87):

$$\begin{aligned}
 \int_a^b \frac{dy_e}{dx} \frac{dv_i}{dx} dx &= \int_a^b \sum_{j=1}^N y_j \frac{dv_j}{dx} \frac{dv_i}{dx} dx = \int_a^b q(x) v_i(x) dx \\
 \Leftrightarrow \sum_{j=1}^N y_j \int_a^b \frac{dv_j}{dx} \frac{dv_i}{dx} dx &= \int_a^b q(x) v_i(x) dx = q_i, \quad \text{for } i = 1, N
 \end{aligned}
 \tag{5.89a}$$

For each numerical integral we define: $k_{ji} = \int_a^b \frac{dv_j}{dx} \frac{dv_i}{dx} dx = k_{ij}$. Therefore:

$$\sum_{j=1}^N y_j k_{ji} = q_i, \quad \text{for } i = 1, N \quad \Rightarrow \quad k_{1i} y_1 + k_{2i} y_2 + \dots + k_{Ni} y_N = q_i
 \tag{5.89b}$$

In this way, a linear system of algebraic equations in matrix form is obtained; its inverse provides the approximated solution of the differential equation (5.85):

$$\begin{bmatrix} k_{11} & k_{12} & \cdot & \cdot & \cdot & k_{1N} \\ k_{12} & k_{22} & \cdot & \cdot & \cdot & k_{2N} \\ \cdot & \cdot & \cdot & \cdot & \cdot & \cdot \\ \cdot & \cdot & \cdot & \cdot & \cdot & \cdot \\ \cdot & \cdot & \cdot & \cdot & \cdot & \cdot \\ k_{1N} & k_{2N} & \cdot & \cdot & \cdot & k_{NN} \end{bmatrix} \cdot \begin{bmatrix} y_1 \\ y_2 \\ \cdot \\ \cdot \\ \cdot \\ y_N \end{bmatrix} = \begin{bmatrix} q_1 \\ q_2 \\ \cdot \\ \cdot \\ \cdot \\ q_N \end{bmatrix} \Leftrightarrow \begin{cases} \mathbf{K}^e \cdot \vec{y}_e = \vec{q}_e \\ \vec{y}_e = \mathbf{K}^{e-1} \cdot \vec{q}_e \end{cases} \quad (5.90)$$

In this groundwater flow context, matrix \mathbf{K}^e is called the conductivity matrix and vector \vec{q}_e is the flux vector. In structural mechanics, they are called the stiffness matrix and load vector, respectively. Note that the symmetry of this matrix is due to the commutativity of the product of derivatives in equation (5.89a). The interpolation coefficients y_j are known after solving the system (5.90). Then they are replaced in equation (5.88) to obtain the approximate solution of $y(x)$. The final approximation of the water pressure is simply $p(x) = y(x) + u(x)$, which satisfies the original non-homogeneous boundary conditions. To complete this problem we present a simple numerical example adapted from Gockenbach (2002). We use the following data estimated from an aquifer in Mexico: $p_a = 3.5$ MPa, $p_b = 3.0$ MPa, $\rho_f = 999.6$ kg/m³, $\mu_f = 891 \times 10^{-6}$, Pa · s, $k_x = 8.91 \times 10^{-10}$ m², $q_f(x) = 10^{-3}x$ kg/s/m³. Consequently, we obtain for $q(x)$:

$$q(x) = \frac{\mu_f}{\rho_f k_x} q_f(x) = \frac{891 \times 10^{-6} \times 10^{-3}}{999.6 \times 8.91 \times 10^{-10}} x = 1.0x, \quad \forall x \in \llbracket a, b \rrbracket$$

We consider the trigonometric basis $\{\sin \pi x, \sin 2\pi x, \dots, \sin j\pi x, \dots, \sin N\pi x\}$ of test functions defined in the interval $[a = 0, b = 1]$ km. Computing the elements of the matrix in equation (5.90):

$$\begin{aligned} k_{ij} &= \int_0^1 \frac{dv_i}{dx} \frac{dv_j}{dx} dx = \int_0^1 i\pi \cos(i\pi x) \cdot j\pi \cos(j\pi x) dx = i\pi \sin(j\pi x) \cos(i\pi x) \Big|_0^1 \\ &+ i^2 \pi^2 \int_0^1 \sin(i\pi x) \sin(j\pi x) dx = 0 + 0 = 0 \quad \Rightarrow \quad k_{ij} = 0 \quad \text{if } i \neq j \end{aligned}$$

When $i = j$ we obtain a different result:

$$\begin{aligned} k_{ii} &= i^2 \pi^2 \int_0^1 \cos(i\pi x) \cos(i\pi x) dx = i\pi \sin(i\pi x) \cos(i\pi x) \Big|_0^1 + i^2 \pi^2 \int_0^1 \sin^2(i\pi x) dx \\ &= i^2 \pi^2 \left(\int_0^1 dx - \int_0^1 \cos^2(i\pi x) dx \right) \Rightarrow 2i^2 \pi^2 \int_0^1 \cos^2(i\pi x) dx = i^2 \pi^2, \end{aligned}$$

$$\text{then } k_{ii} = \frac{i^2 \pi^2}{2}$$

In this case, the matrix \mathbf{K}^e is diagonal. For all $i \neq 0$ we have:

$$q_i = \int_0^1 q(x)v_i(x)dx = \int_0^1 x \sin(i \pi x)dx = \frac{-x}{i\pi} \cos(i \pi x) \Big|_0^1 + \frac{1}{i \pi} \int_0^1 \cos(i \pi x)dx$$

$$= (-1) \frac{\cos(i \pi)}{i \pi} = \frac{(-1)(-1)^i}{i \pi} = \frac{(-1)^{i+1}}{i \pi}$$

The resulting linear system is:

$$\frac{\pi^2}{2} \begin{pmatrix} 1 & 0 & 0 & . & \dots & 0 \\ 0 & 4 & 0 & . & \dots & 0 \\ 0 & 0 & 9 & . & \dots & 0 \\ 0 & 0 & 0 & . & \dots & 0 \\ 0 & 0 & 0 & . & \dots & 0 \\ 0 & 0 & 0 & . & \dots & 0 \\ 0 & 0 & 0 & . & \dots & N^2 \end{pmatrix} \cdot \begin{pmatrix} y_1 \\ y_2 \\ y_3 \\ \dots \\ \dots \\ y_N \end{pmatrix} = \frac{1}{\pi} \begin{pmatrix} 1 \\ -1/2 \\ 1/3 \\ \vdots \\ (-1)^{N+1}/N \end{pmatrix}$$

The approximate Galerkin finite element solutions of problems (5.85) and (5.83) are:

$$y(x) \approx y_e(x) = \sum_{i=1}^N (-1)^{i+1} \frac{2 \sin(i \pi x)}{i^3 \pi^3}$$

$$\Rightarrow p(x) \approx \sum_{i=1}^N (-1)^{i+1} \frac{2 \sin(i \pi x)}{i^3 \pi^3} + (1-x)p_a + x p_b$$

Problem (5.85) for $q(x) = x$, and homogeneous boundary conditions in the interval $[0,1]$ has the exact solution $y(x) = (x - x^3)/6$. Table 5.1 shows both values $y(x_k)$ and $y_e(x_k)$ for $N = 8$.

5.2.3.2 Numerical method 2: Linear polynomials

We return to the original problem (5.83) with inhomogeneous boundary conditions. The interpolation of the unknown pressure in terms of unitary $\varphi_i(x)$ is $p(x) \approx p^e(x)$:

$$p^e(x) = \sum_{j=0}^{N+1} y_j \varphi_j(x) = y_0 \varphi_0(x) + y_1 \varphi_1(x) + \dots + y_N \varphi_N(x) + y_{N+1} \varphi_{N+1}(x) \quad (5.91)$$

Table 5.1. Comparison of the numerical results $y_e(x_k)$ obtained with finite elements and the exact solution $y(x_k)$ of the differential equation (5.85).

x_k	0.1	0.2	0.4	0.5	0.6	0.7	0.8	1.0
$y(x_k)$	0.0165	0.032	0.056	0.0625	0.064	0.0595	0.048	0.0
$y_e(x_k)$	0.01648	0.03204	0.05606	0.06244	0.06404	0.05948	0.04797	1.2×10^{-17}

By applying the piecewise linear polynomials defined by equation (5.78b) in each interval $[x_{i-1}, x_i]$ of the interior mesh ($i = 1, N$), one obtains:

$$\begin{aligned}
 x \in [x_0, x_1] &\rightarrow p_1^e(x) = y_0 \frac{x - x_1}{x_0 - x_1} + y_1 \frac{x - x_0}{x_1 - x_0} = y_0 \varphi_0(x) + y_1 \varphi_1(x) \\
 x \in [x_1, x_2] &\rightarrow p_2^e(x) = y_1 \frac{x - x_2}{x_1 - x_2} + y_2 \frac{x - x_1}{x_2 - x_1} = y_1 \varphi_1(x) + y_2 \varphi_2(x) \\
 &\dots \\
 x \in [x_{i-1}, x_i] &\rightarrow p_i^e(x) = y_{i-1} \frac{x - x_i}{x_{i-1} - x_i} + y_i \frac{x - x_{i-1}}{x_i - x_{i-1}} = y_{i-1} \varphi_{i-1}(x) + y_i \varphi_i(x) \\
 x \in [x_i, x_{i+1}] &\rightarrow p_{i+1}^e(x) = y_i \frac{x - x_{i+1}}{x_i - x_{i+1}} + y_{i+1} \frac{x - x_i}{x_{i+1} - x_i} = y_i \varphi_i(x) + y_{i+1} \varphi_{i+1}(x) \\
 &\dots \\
 [x_{N-1}, x_N] &\rightarrow p_N^e(x) = y_{N-1} \frac{x - x_N}{x_{N-1} - x_N} + y_N \frac{x - x_{N-1}}{x_N - x_{N-1}} = y_{N-1} \varphi_{N-1}(x) + y_N \varphi_N(x)
 \end{aligned} \tag{5.92}$$

At the nodes of the end-points, where the boundary conditions are known we have:

$$p_0^e(x) = \frac{x_1 - x}{x_1 - x_0} p_a = p_a \varphi_0(x), \quad p_{N+1}^e(x) = \frac{x - x_N}{x_{N+1} - x_N} p_b = p_b \varphi_{N+1}(x) \tag{5.93}$$

It is clear now that the basis of unitary functions $\varphi_i(x)$, built from the linear Lagrange polynomials, is just a particular case of trial functions $v_i(x)$. Galerkin method is part of a general class of methods used in converting a continuous operator problem (a differential equation) to a discrete problem. The aim of Galerkin's method is the production of a linear system of equations that represents approximately the original operator. We approximate the solution of problem (5.83) using the same previous data with $q(x) = x$ and the weak formulation in each subinterval for ($j = i - 1, i$) (eqs. 5.92):

$$\begin{aligned}
 p_i^e(x) = y_{i-1} \varphi_{i-1}(x) + y_i \varphi_i(x) &\Rightarrow \int_{x_{i-1}}^{x_i} \frac{dp_i^e}{dx} \frac{d\varphi_j}{dx} dx = \int_{x_{i-1}}^{x_i} x \varphi_j dx \\
 \Rightarrow \int_{x_{i-1}}^{x_i} [y_{i-1} \varphi'_{i-1}(x) + y_i \varphi'_i(x)] \varphi'_j(x) dx &= \int_{x_{i-1}}^{x_i} x \varphi_j(x) dx = q_j
 \end{aligned} \tag{5.94a}$$

In every interval $[x_{i-1}, x_i]$ we obtain a coupled set of linear equations that can be solved directly:

$$\begin{aligned}
 j = i - 1 &\rightarrow y_{i-1} \int_{x_{i-1}}^{x_i} \varphi'_{i-1}(x) \varphi'_{i-1}(x) dx + y_i \int_{x_{i-1}}^{x_i} \varphi'_i(x) \varphi'_{i-1}(x) dx = \int_{x_{i-1}}^{x_i} x \varphi_{i-1} dx \\
 j = i &\rightarrow y_{i-1} \int_{x_{i-1}}^{x_i} \varphi'_{i-1}(x) \varphi'_i(x) dx + y_i \int_{x_{i-1}}^{x_i} \varphi'_i(x) \varphi'_i(x) dx = \int_{x_{i-1}}^{x_i} x \varphi_i dx
 \end{aligned}$$

This formula generates a local linear system in every subinterval for each FE. By defining the integrals as the elements of a local matrix, we obtain:

$$\left. \begin{aligned} y_{i-1} k_{i-1,i-1} + y_i k_{i,i-1} &= \int_{x_{i-1}}^{x_i} x \varphi_{i-1} dx = q_{i-1} \\ y_{i-1} k_{i-1,i} + y_i k_{i,i} &= \int_{x_{i-1}}^{x_i} x \varphi_i dx = q_i \end{aligned} \right\} \Rightarrow \begin{aligned} k_{ij} &= \int_{x_{i-1}}^{x_i} \frac{d\varphi_i}{dx} \frac{d\varphi_j}{dx} dx, \quad i, j = 1, N \\ \begin{pmatrix} k_{i-1,i-1} & k_{i,i-1} \\ k_{i-1,i} & k_{i,i} \end{pmatrix} \cdot \begin{pmatrix} y_{i-1} \\ y_i \end{pmatrix} &= \begin{pmatrix} q_{i-1} \\ q_i \end{pmatrix} \end{aligned} \quad (5.94b)$$

This linear system is repeated at every subinterval and represents the solution over each finite element. At each pair of consecutive FE $(i-1, i)$, $(i, i+1)$, the coefficient y_i appears as a common unknown in two successive matrix equations (5.94b). This is the coupling term between two successive FE. The assembly of all these solutions forms the global conductivity matrix, which approximates the solution of the differential equation (5.83). The computation of the derivatives of each $\varphi_i(x)$ is a very simple task:

$$\begin{aligned} x \in [x_1, x_2] &\rightarrow \varphi_1(x) = \frac{x_2 - x}{x_2 - x_1} \Rightarrow \frac{d\varphi_1}{dx}(x) = \frac{-1}{x_2 - x_1} \\ &\dots \\ x \in [x_{i-1}, x_i] &\rightarrow \varphi_i(x) = \frac{x - x_{i-1}}{x_i - x_{i-1}} \Rightarrow \frac{d\varphi_i}{dx}(x) = \frac{1}{x_i - x_{i-1}} \\ x \in [x_i, x_{i+1}] &\rightarrow \varphi_i(x) = \frac{x_{i+1} - x}{x_{i+1} - x_i} \Rightarrow \frac{d\varphi_i}{dx}(x) = \frac{-1}{x_{i+1} - x_i} \\ &\dots \\ x \in [x_{N-1}, x_N] &\rightarrow \varphi_N(x) = \frac{x - x_{N-1}}{x_N - x_{N-1}} \Rightarrow \frac{d\varphi_N}{dx}(x) = \frac{1}{x_N - x_{N-1}} \end{aligned} \quad (5.95)$$

It is obvious that $\varphi_i(x)$ is zero except on the interval $[x_{i-1}, x_{i+1}]$ (eq. 5.78b), therefore, most of the elements of the global matrix are zero because they are computed with the product of derivatives of $\varphi_i(x)$ (eq. 5.95). The diagonal matrix elements k_{ii} ($i = 1, N$) are:

$$k_{ii} = \int_{x_{i-1}}^{x_{i+1}} \frac{d\varphi_i}{dx} \frac{d\varphi_i}{dx} dx = \int_{x_{i-1}}^{x_i} \left(\frac{d\varphi_i}{dx} \right)^2 dx + \int_{x_i}^{x_{i+1}} \left(\frac{d\varphi_i}{dx} \right)^2 dx \quad (5.96a)$$

Substituting the values of the derivatives from (eq. 5.95):

$$k_{ii} = \int_{x_{i-1}}^{x_i} \left(\frac{1}{x_i - x_{i-1}} \right)^2 dx + \int_{x_i}^{x_{i+1}} \left(\frac{-1}{x_{i+1} - x_i} \right)^2 dx = \frac{1}{x_i - x_{i-1}} + \frac{1}{x_{i+1} - x_i} = \frac{1}{h_{ii}} \quad (5.96b)$$

The off-diagonal matrix elements k_{ij} ($i \neq j = 2, N - 1$) are:

$$\begin{aligned}
 k_{i-1, i} &= \int_a^b \frac{d\varphi_{i-1}}{dx} \frac{d\varphi_i}{dx} dx = \int_{x_{i-1}}^{x_i} \frac{-1}{x_i - x_{i-1}} \frac{1}{x_i - x_{i-1}} dx = \frac{-1}{x_i - x_{i-1}} = \frac{-1}{\Delta x_i} = \frac{-1}{h_i} \\
 k_{i, i+1} &= \int_a^b \frac{d\varphi_i}{dx} \frac{d\varphi_{i+1}}{dx} dx = \int_{x_i}^{x_{i+1}} \frac{-1}{x_{i+1} - x_i} \frac{1}{x_{i+1} - x_i} dx = \frac{-1}{x_{i+1} - x_i} = \frac{-1}{\Delta x_{i+1}} = \frac{-1}{h_{i+1}} \\
 k_{ij} = k_{ji} &= \int_{x_i}^{x_j} \frac{d\varphi_i}{dx} \frac{d\varphi_j}{dx} dx = 0, \quad \text{if } j > i + 1, \quad \text{or } j < i - 1, \quad \text{and } h_i = x_i - x_{i-1}
 \end{aligned} \tag{5.96c}$$

Therefore, the global conductivity matrix \mathbf{K}^e for ($N = 5$) is:

$$\mathbf{k}^e = \begin{bmatrix} \left(\frac{1}{h_1} + \frac{1}{h_2}\right) & -\frac{1}{h_2} & 0 & 0 & 0 \\ -\frac{1}{h_2} & \left(\frac{1}{h_2} + \frac{1}{h_3}\right) & -\frac{1}{h_3} & 0 & 0 \\ 0 & -\frac{1}{h_3} & \left(\frac{1}{h_3} + \frac{1}{h_4}\right) & -\frac{1}{h_4} & 0 \\ 0 & 0 & -\frac{1}{h_4} & \left(\frac{1}{h_4} + \frac{1}{h_5}\right) & -\frac{1}{h_5} \\ 0 & 0 & 0 & -\frac{1}{h_5} & \left(\frac{1}{h_5} + \frac{1}{h_6}\right) \end{bmatrix} \tag{5.96d}$$

$$\text{If all the intervals have the same size } h = h_i, \quad \forall i \Rightarrow \mathbf{k}^e = \frac{1}{h} \begin{bmatrix} 2 & -1 & 0 & 0 & 0 \\ -1 & 2 & -1 & 0 & 0 \\ 0 & -1 & 2 & -1 & 0 \\ 0 & 0 & -1 & 2 & -1 \\ 0 & 0 & 0 & -1 & 2 \end{bmatrix}$$

Inverting the matrix (5.96d) we deduce the numerical values of the coefficients y_i with the purpose of completing the interpolation (5.91):

$$\mathbf{K}^e \cdot \vec{p}^e = \vec{q}^e \Leftrightarrow \vec{p}^e = \mathbf{K}^{e^{-1}} \cdot \vec{q}^e = (y_1, y_2, \dots, y_N) \tag{5.97}$$

The final approximation of the linear finite element solution for the differential problem (5.83) has the form:

$$p(x) \approx p^e(x) = \sum_{i=1}^N y_i \varphi_i(x) + p_a \varphi_0(x) + p_b \varphi_{N+1}(x) \tag{5.98}$$

This approximated numerical solution includes the boundary conditions of the problem, because at the two boundary points of the domain $\Omega = [a, b]$:

$$p(a) = p_a \varphi_0(x_0) = p_a, \quad p(b) = p_b \varphi_{N+1}(x_{N+1}) = p_b \tag{5.99}$$

5.2.3.3 *Variable permeability in the weak form of the Galerkin method*

Let us assume that the aquifer permeability $k_x(x)$ is variable, and depends on the coordinate $x \in \Omega$. The differential equation of problem (5.83) now becomes:

$$-\frac{d}{dx} \left(k_x(x) \frac{dp}{dx} \right) = q(x), \quad \forall x \in \langle a, b \rangle, \quad p(a) = p_a, \quad p(b) = p_b \quad (5.100)$$

where: $q(x) = \frac{\mu_f}{\rho_f} q_f(x)$

The abstract formulation of this boundary value problem is almost the same weak form of the differential equation already developed in equations (5.87, 5.94a). The difference here is that the variable permeability must be explicitly included in the first integration:

$$\text{Find } p^e \in E_1 \text{ such that: } p(x) \approx p^e(x) \text{ in } [a, b], \quad \text{and } \forall j = 1, N:$$

$$\Omega_j = [x_{j-1}, x_{j+1}], \quad \int_{\Omega_j} k_x(x) \frac{dp^e}{dx} \frac{d\varphi_j}{dx} dx = \int_{\Omega_j} q(x) \varphi_j(x) dx \quad (5.101)$$

By replacing the interpolation (5.91) in equation (5.101), we obtain a similar abstract expression to obtain the unknown coefficients y_i of the polynomial $p^e(x)$:

$$\sum_{i=1}^N y_i \int_{\Omega_j} k_x \frac{d\varphi_i}{dx} \frac{d\varphi_j}{dx} dx + p_a \int_{I_0} k_x \frac{d\varphi_0}{dx} \frac{d\varphi_j}{dx} dx + p_b \int_{I_N} k_x \frac{d\varphi_{N+1}}{dx} \frac{d\varphi_j}{dx} dx \quad (5.102)$$

$$= \int_{\Omega_j} q(x) \varphi_j(x) dx, \quad \forall j = 1, N; \quad I_0 = [x_0, x_1], \quad I_N = [x_N, x_{N+1}]$$

The derivatives of the functions of the unitary basis were computed already in equations (5.96a,b,c). At the boundaries we define:

$$-a_j = p_a \int_{I_0} k_x \frac{d\varphi_0}{dx} \frac{d\varphi_1}{dx} dx = \frac{p_a k_a}{x_1 - a}, \quad a_j = 0 \quad \text{if } x \notin I_0 \quad (5.103)$$

$$-b_j = p_b \int_{I_N} k_x \frac{d\varphi_{N+1}}{dx} \frac{d\varphi_N}{dx} dx = \frac{p_b k_b}{b - x_N}, \quad b_j = 0 \quad \text{if } x \notin I_N$$

By replacing the integrals with the corresponding matrix components k_{ij} as was previously done, for all $j = 1, N$ the total sum of integrals in equation (5.102) is reduced to a tridiagonal system of linear algebraic equations:

$$k_{j,j-1} y_{j-1} + k_{jj} y_j + k_{j,j+1} y_{j+1} = -\frac{y_{j-1}}{h_j} + \frac{y_j}{h_{jj}} - \frac{y_{j+1}}{h_{j+1}} = q_j \quad (5.104)$$

$$q_j = \int_{\Omega_j} q(x) \varphi_j(x) dx + a_j + b_j, \quad \forall j = 1, N$$

5.2.3.4 *The general diffusion equation in the weak form of the Galerkin method*

In this subsection, we show how to formulate in the FEM the general diffusion equation appearing in the conduction-convection formula (4.104a) and in the general solute transport

equation (4.111). The conditions are for a steady state process in one dimension. Both equations are reformulated as abstract boundary value problems with generic variable coefficients and inhomogeneous conditions:

$$\begin{aligned} \frac{d}{dx} \left(a_x(x) \frac{df}{dx} \right) + b_x(x) \frac{df}{dx} + c_x(x) f(x) &= q(x) \\ \forall x \in \langle a, b \rangle, \quad f(a) = f_a, \quad f(b) = f_b \end{aligned} \quad (5.105)$$

Let us make the same change of function we did in equation (5.84), $f(x) = y(x) + u(x)$, where $u(x)$ belongs to the vector space \mathbf{E}_1 :

$$\begin{aligned} u(x) &= \frac{b-x}{b-a} f_a + \frac{x-a}{b-a} f_b, \quad \text{and} \quad y(x) = f(x) - u(x) \\ \Rightarrow \quad u(a) &= f_a, \quad \text{and} \quad u(b) = f_b \quad \Rightarrow \quad y(a) = y(b) = 0 \end{aligned}$$

Therefore, the differential problem (5.105) becomes:

$$\begin{aligned} \frac{d}{dx} \left(a_x(x) \frac{dy}{dx} \right) + b_x(x) \frac{dy}{dx} + c_x(x) y(x) &= Y(x) \\ \forall x \in \langle a, b \rangle, \quad \text{and} \quad y(a) = 0, \quad y(b) = 0 \end{aligned} \quad (5.106)$$

where:

$$Y(x) = q(x) - \left(\frac{f_b - f_a}{b-a} \right) \left(\frac{da_x}{dx} + b_x \right) - c_x u(x) \quad (5.107)$$

The interpolation of the unknown function $y(x)$ in terms of hat functions is again $y_e(x)$:

$$y(x) \approx y_e(x) = \sum_{j=1}^N y_j \varphi_j(x) = y_1 \varphi_1(x) + y_2 \varphi_2(x) + \cdots + y_N \varphi_N(x) \quad (5.108)$$

The weak formulation of equation (5.105) is similar to the differential equation already developed in equation (5.87). The difference is that there are more functions to be included in the integrations. Integrating by parts the first term of equation (5.106):

$$\begin{aligned} \int_a^b \frac{d}{dx} \left(a_x \frac{dy}{dx} \right) \varphi_i dx + \int_a^b b_x \frac{dy}{dx} \varphi_i dx + \int_a^b c_x y(x) \varphi_i dx &= \int_a^b Y(x) \varphi_i dx \\ \Rightarrow \quad a_x \frac{dy}{dx} \varphi_i \Big|_a^b - \int_a^b a_x \frac{dy}{dx} \frac{d\varphi_i}{dx} dx + \int_a^b b_x \frac{dy}{dx} \varphi_i dx + \int_a^b c_x y \varphi_i dx &= \int_a^b Y \varphi_i dx \end{aligned} \quad (5.109)$$

This is the weak form of equation (5.106). By replacing the interpolation formula (5.108) of $y(x)$ into equation (5.109) we find the final linear system:

$$\sum_{j=1}^N y_j \left(- \int_a^b a_x \frac{d\varphi_j}{dx} \frac{d\varphi_i}{dx} dx + \int_a^b b_x \frac{d\varphi_j}{dx} \varphi_i dx + \int_a^b c_x \varphi_j \varphi_i dx \right) = \int_a^b Y \varphi_i dx$$

$$K_{ji} = \int_a^b a_x \frac{d\varphi_j}{dx} \frac{d\varphi_i}{dx} dx, \quad L_{ji} = \int_a^b b_x \frac{d\varphi_j}{dx} \varphi_i dx, \quad M_{ji} = \int_a^b c_x \varphi_j \varphi_i dx \quad (5.110)$$

$$\Rightarrow \sum_{j=1}^N y_j (-K_{ji} + L_{ji} + M_{ji}) = Y_i \quad \Leftrightarrow \quad \sum_{j=1}^N N_{ji} y_j = Y_i \quad \Leftrightarrow \quad \boxed{\mathbf{N} \cdot \vec{y}_e = \vec{Y}}$$

where: $\mathbf{N} = -\mathbf{K} + \mathbf{L} + \mathbf{M}$

This final matrix equation approaches the solution of the homogeneous problem (5.106). The finite element solution of the general inhomogeneous diffusion equation (5.105) is:

$$f_e(x) = y_e(x) + \frac{b-x}{b-a} f_a + \frac{x-a}{b-a} f_b \quad (5.111)$$

Note that the particular form of the tridiagonal matrix in equations (5.96d) and (5.104) comes from the fact that we used linear basis functions. When using different bases the shape matrix changes (Fish and Belytschko 2007). The interested reader will find himself the matrix specific form of equation (5.110).

The Galerkin method allows increasing the accuracy of the approximation in two ways:

- By augmenting the order of the interpolation polynomials,
- by increasing the size of the space \mathbf{E}_1 .

The latter form implies the simultaneous increase of the number of linear polynomials in $[a, b]$ and the reduction of the size of the elements in the mesh. Both techniques are applied in two- and three-dimensional finite elements.

5.2.4 Galerkin weighted residuals method; weak formulation of the heat equation for a stationary temperature in two dimensions

To illustrate the finite element technique in two dimensions we consider the following classic differential problem (Poisson's equation), which is a simplification of the general heat equation (4.104a), introduced in section 4.7.5. The boundary conditions are mixed:

$$-\vec{\nabla} \cdot (\mathbf{k}_T \cdot \vec{\nabla} T) = - \frac{\partial}{\partial x} \left(k_{T_x} \frac{\partial T}{\partial x} \right) - \frac{\partial}{\partial x} \left(k_{T_y} \frac{\partial T}{\partial y} \right) = Q_H \quad (5.112)$$

$$\left\{ \begin{array}{l} T(x, y) = \bar{T}(s) \quad \text{on } \Gamma_T = \partial\Omega_1 \\ \mathbf{k}_T \cdot \vec{\nabla} T \cdot \vec{n} = q_n \quad \text{on } \Gamma_n = \partial\Omega_2 \end{array} \right\} \quad \forall (x, y) \in \Omega \subset \mathbb{R}^2$$

$$\Gamma_T + \Gamma_n = \partial\Omega = \Gamma$$

Let $w(x, y) \in \mathbf{E}_h$ be a weight (trial) function which we assume is differentiable and integrable in the domain Ω where we seek the solution. Let $u^e(x, y)$ be a function that approximates the unknown temperature T . We suppose that the thermal conductivity tensor is constant and equal

to k_T . The error or residual term of this approximation is defined as:

$$R^e(x, y) = T(x, y) - u^e(x, y) \neq 0 \quad (5.113)$$

We replace this expression in equation (5.112) then, multiplying both sides of the same equation by the test function w and integrating the result in Ω , we obtain an integro-differential equation for the Laplacian of the residual, which we equate to zero:

$$0 = k_T \int_{\Omega} w \nabla^2 R^e d\Omega = - \int_{\Omega} w Q_H d\Omega - \int_{\Omega} k_T w \nabla^2 u^e d\Omega \quad (5.114)$$

The assumption that this integral is equal to zero is equivalent to assuming that the Laplacian of the residual and the weight function are orthogonal in Ω . We obtain in this way the weighted residuals formulation or weak form of the heat model (5.112):

$$- \int_{\Omega} \left[w \frac{\partial}{\partial x} \left(k_T \frac{\partial u^e}{\partial x} \right) + w \frac{\partial}{\partial y} \left(k_T \frac{\partial u^e}{\partial y} \right) \right] d\Omega = \int_{\Omega} w Q_H d\Omega \quad (5.115)$$

The Green's theorem (see Appendix) is useful for simplifying this type of integrals:

$$\int_{\Omega} w \nabla^2 u^e d\Omega = \int_{\partial\Omega} w \frac{\partial u^e}{\partial n} ds - \int_{\Omega} \vec{\nabla} w \cdot \vec{\nabla} u^e d\Omega$$

Applying Green's theorem to equation (5.115) we obtain the final weak form of the original PDE problem:

$$\int_{\Omega} k_T \vec{\nabla} w \cdot \vec{\nabla} u^e d\Omega = \int_{\Omega} w Q_H d\Omega + \int_{\Gamma} w q_n ds \quad (5.116)$$

where the second boundary condition is included:

$$\int_{\Gamma} k_T w \frac{\partial u^e}{\partial n} ds = \int_{\Gamma} w k_T \vec{\nabla} u^e \cdot \vec{n} ds = \int_{\Gamma} w q_n ds$$

The weak form concept has the same meaning as in section 5.2.7; equation (5.116) does not contain second order partial derivatives. In this two-dimensional integral formulation, it is sufficient that functions w and u^e have continuous first derivatives. On the other hand, in the original equation (5.112) the second partial derivatives of T should be continuous so that the function is integrable. This is a strong continuity condition for T .

5.2.5 Finite elements using bilinear Lagrange interpolation polynomials over triangles

The domain of the PDE problem is discretized with triangles of arbitrary form. We consider a triangle (Fig. 5.9) defined by the coordinates of its vertexes P_1, P_2, P_3 , with respect to an arbitrary origin \mathbf{O} .

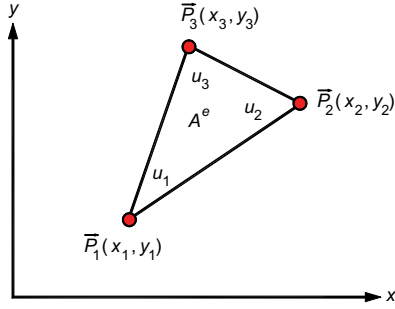


Figure 5.9. A triangle of the FEM.

The area of the triangle is calculated as follows:

$$A^e(x, y) = \frac{\text{base} \times \text{height}}{2} = \|\vec{P}_2 - \vec{P}_1\| \cdot \|\vec{P}_3 - \vec{P}_1\| \frac{\sin \theta}{2}, \quad \text{or equivalently:}$$

$$A^e = \frac{\|(\vec{P}_2 - \vec{P}_1) \times \vec{P}_3 - \vec{P}_1\|}{2} = \frac{1}{2} \begin{vmatrix} 1 & x_1 & y_1 \\ 1 & x_2 & y_2 \\ 1 & x_3 & y_3 \end{vmatrix} = \frac{(x_2 - x_1)(y_3 - y_1) - (x_3 - x_1)(y_2 - y_1)}{2} \quad (5.117a)$$

A bilinear interpolation is done on the finite element represented by the triangle. This is the most simple interpolation in two dimensions:

$$u^e(x, y) = a_1 + a_2 x + a_3 y$$

$$\Rightarrow \begin{cases} u^e(x_1, y_1) = a_1 + a_2 x_1 + a_3 y_1 = u_1 \\ u^e(x_2, y_2) = a_1 + a_2 x_2 + a_3 y_2 = u_2 \\ u^e(x_3, y_3) = a_1 + a_2 x_3 + a_3 y_3 = u_3 \end{cases} \Leftrightarrow \begin{pmatrix} 1 & x_1 & y_1 \\ 1 & x_2 & y_2 \\ 1 & x_3 & y_3 \end{pmatrix} \cdot \begin{pmatrix} a_1 \\ a_2 \\ a_3 \end{pmatrix} = \begin{pmatrix} u_1 \\ u_2 \\ u_3 \end{pmatrix} \quad (5.117b)$$

The interpolation coefficients a_1, a_2, a_3 are found by inverting this matrix:

$$\begin{pmatrix} a_1 \\ a_2 \\ a_3 \end{pmatrix} = \frac{1}{2A^e} \begin{pmatrix} x_2 y_3 - x_3 y_2 & x_3 y_1 - x_1 y_3 & x_1 y_2 - x_2 y_1 \\ y_2 - y_3 & y_3 - y_1 & y_1 - y_2 \\ x_3 - x_2 & x_1 - x_3 & x_2 - x_1 \end{pmatrix} \cdot \begin{pmatrix} u_1 \\ u_2 \\ u_3 \end{pmatrix} \quad (5.117c)$$

The interpolation function or interpolator in two dimensions is defined as:

$$u^e(x, y) = \sum_{i=1}^3 u_i \varphi_i(x, y) = u_1 \varphi_1(x, y) + u_2 \varphi_2(x, y) + u_3 \varphi_3(x, y) \quad (5.118)$$

From equation (5.117c), we deduce that every interpolator has the following form:

$$\begin{aligned} \varphi_1(x, y) &= \frac{1}{2A^e} [(x_2 y_3 - x_3 y_2) + (y_2 - y_3)x + (x_3 - x_2)y] \\ \varphi_2(x, y) &= \frac{1}{2A^e} [(x_3 y_1 - x_1 y_3) + (y_3 - y_1)x + (x_1 - x_3)y] \\ \varphi_3(x, y) &= \frac{1}{2A^e} [(x_1 y_2 - x_2 y_1) + (y_1 - y_2)x + (x_2 - x_1)y] \end{aligned} \quad (5.119)$$

Each one of these three functions has the following properties:

$$\varphi_i(x_j, y_j) = \delta_{ij}, \quad \sum_{i=1}^3 \varphi_i(x, y) = 1 \quad (5.120)$$

The Galerkin method is accomplished by setting the test functions equal to the interpolators given by equation (5.119), $w_j = \varphi_j$. In this manner the weak form of Poisson's equation (5.112) in each triangle becomes:

$$\int_{\Omega^e} \sum_{i=1}^3 k_T u_i \vec{\nabla} \varphi_i \cdot \vec{\nabla} \varphi_j d\Omega = \int_{\Omega^e} \varphi_j Q_H d\Omega + \int_{\Gamma_n^e} \varphi_j q_n^e ds, \quad \forall j = 1, 2, 3 \quad (5.121a)$$

$$\sum_{i=1}^3 k_{ij} u_i = q_j \quad \Leftrightarrow \quad \mathbf{K}^e \cdot \vec{u}^e = \vec{q}^e$$

The integral coefficients are defined as:

$$k_{ij} = \int_{\Omega^e} k_T \vec{\nabla} \varphi_i \cdot \vec{\nabla} \varphi_j d\Omega, \quad q_j = \int_{\Omega^e} \varphi_j Q_H d\Omega + \int_{\Gamma_n^e} \varphi_j q_n^e ds, \quad \forall j = 1, 2, 3 \quad (5.121b)$$

$$k_{11} = \frac{1}{4A^e} [(x_3 - x_2)^2 + (y_2 - y_3)^2]$$

$$k_{22} = \frac{1}{4A^e} [(x_1 - x_3)^2 + (y_3 - y_1)^2]$$

$$k_{33} = \frac{1}{4A^e} [(x_2 - x_1)^2 + (y_1 - y_2)^2] \quad (5.121c)$$

$$k_{12} = [(x_3 - x_2)(x_1 - x_3) + (y_2 - y_3)(y_3 - y_1)]/4A^e = k_{21}$$

$$k_{13} = [(x_3 - x_2)(x_2 - x_1) + (y_2 - y_3)(y_1 - y_2)]/4A^e = k_{31}$$

$$k_{23} = [(x_1 - x_3)(x_2 - x_1) + (y_3 - y_1)(y_1 - y_2)]/4A^e = k_{32}$$

Depending on the nature of the two-dimensional physical problem, \mathbf{k}^e is called the matrix of rigidity, of thermal conductivity, or of hydraulic conductivity, etc. For the same reason, \vec{q}^e is called the load vector, or the heat flow vector, etc. The elements of \mathbf{k}^e are computed explicitly in the corresponding program used to solve the problem.

5.2.6 Finite elements using bilinear Lagrange interpolation polynomials over rectangles

In this case, the domain of the PDE problem is discretized with rectangles. The coordinates of the vertices $u_1(-b, -c), u_2(b, -c), u_3(b, c), u_4(-b, c)$ (Fig. 5.10) define one rectangle with respect to the origin \mathbf{O} . The bilinear approximation function is:

$$u^e(x, y) = a_1 + a_2 x + a_3 y + a_4 xy \quad (5.122)$$

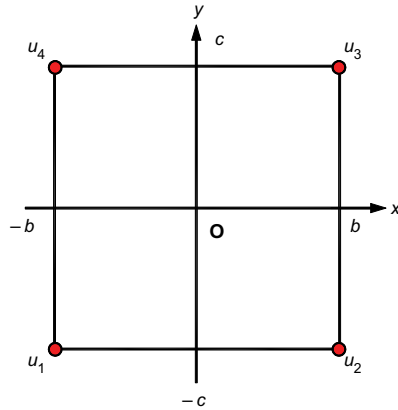


Figure 5.10. A FEM rectangle.

In terms of the coordinates of the nodes, we obtain:

$$u^e(x_i, y_i) = u_i = a_1 + a_2 x_i + a_3 y_i + a_4 x_i y_i; \quad i = 1, 4$$

$$\Leftrightarrow \begin{pmatrix} 1 & x_1 & y_1 & x_1 y_1 \\ 1 & x_2 & y_2 & x_2 y_2 \\ 1 & x_3 & y_3 & x_3 y_3 \\ 1 & x_4 & y_4 & x_4 y_4 \end{pmatrix} \cdot \begin{pmatrix} a_1 \\ a_2 \\ a_3 \\ a_4 \end{pmatrix} = \begin{pmatrix} u_1 \\ u_2 \\ u_3 \\ u_4 \end{pmatrix} = \begin{pmatrix} 1 & -b & -c & bc \\ 1 & b & -c & -bc \\ 1 & b & c & bc \\ 1 & -b & c & -bc \end{pmatrix} \cdot \begin{pmatrix} a_1 \\ a_2 \\ a_3 \\ a_4 \end{pmatrix} \quad (5.123)$$

The determinant of the second matrix is $\det(*) = -16 b^2 c^2 < 0$. Therefore we can compute the corresponding inverse matrix:

$$\begin{pmatrix} a_1 \\ a_2 \\ a_3 \\ a_4 \end{pmatrix} = \frac{1}{4} \begin{pmatrix} 1 & 1 & 1 & 1 \\ -b^{-1} & b^{-1} & b^{-1} & -b^{-1} \\ -c^{-1} & -c^{-1} & c^{-1} & c^{-1} \\ (bc)^{-1} & (-bc)^{-1} & (bc)^{-1} & (-bc)^{-1} \end{pmatrix} \cdot \begin{pmatrix} u_1 \\ u_2 \\ u_3 \\ u_4 \end{pmatrix} \quad (5.124)$$

The approximation of u^e can be written as:

$$u^e(x, y) = \sum_{i=1}^4 u_i N_i(x, y), \quad \text{where: } \sum_{i=1}^4 N_i(x, y) = 1, \quad N_i(x_j, y_j) = \delta_{ij} \quad (5.125)$$

Explicitly the functions N_i are:

$$N_1 = \frac{(b-x)(c-y)}{2b \cdot 2c} = \varphi_1(x) \psi_1(y); \quad N_2 = \frac{(b+x)(c-y)}{2b \cdot 2c} = \varphi_2(x) \psi_1(y)$$

$$N_3 = \frac{(b+x)(c+y)}{2b \cdot 2c} = \varphi_2(x) \psi_2(y); \quad N_4 = \frac{(b-x)(c+y)}{2b \cdot 2c} = \varphi_1(x) \psi_2(y) \quad (5.126)$$

Each one of these functions is a bilinear Lagrange interpolator. The original Poisson equation in terms of the finite element discretization becomes:

$$K_{ij} = \int_{\Omega^e} \vec{\nabla} N_i \cdot \vec{\nabla} N_j d\Omega = K_{ji} \Rightarrow \sum_{i=1}^4 K_{ij} u_i = \int_{\Omega^e} N_j Q_H d\Omega + \int_{\Gamma_n^e} N_j q_n^e ds = f_j$$

$$\Leftrightarrow \mathbf{K}^e \cdot \vec{u}^e = \vec{f}^e \tag{5.127}$$

The integral coefficients of the hydraulic conductivity matrix are:

$$\mathbf{K}^e = \frac{1}{6bc} \begin{pmatrix} 2(b^2 + c^2) & (b^2 - 2c^2) & -(b^2 + c^2) & -(2b^2 - c^2) \\ (b^2 - 2c^2) & 2(b^2 + c^2) & -(2b^2 - c^2) & -(b^2 + c^2) \\ -(b^2 + c^2) & -(2b^2 - c^2) & 2(b^2 + c^2) & (b^2 - 2c^2) \\ -(2b^2 - c^2) & -(b^2 + c^2) & (b^2 - 2c^2) & 2(b^2 + c^2) \end{pmatrix} \tag{5.128}$$

while the flow vector \vec{f}^e is computed with the following integrals:

$$\vec{f}^e = \int_{-b-c}^{+b+c} \int_{-b-c}^{+b+c} \begin{pmatrix} N_1 \\ N_2 \\ N_3 \\ N_4 \end{pmatrix} Q_H(x, y) dy dx + \int_{-b-c}^{+b+c} \int_{-b-c}^{+b+c} \begin{pmatrix} N_1 \\ N_2 \\ N_3 \\ N_4 \end{pmatrix} q_n^e ds \tag{5.129}$$

Depending on the form of the source term $Q_H(x, y)$ and on the flow itself, these integrals may be easy or difficult to calculate. In general, a numerical method is used to evaluate them. Some of these methods are mentioned in the literature (e.g. Liu and Quek 2003). The interpolation functions and the matrices in both types of elements, triangles and rectangles, are similar for every domain discretized with finite elements. The matrices only differ on size and coordinates of the nodes.

5.2.7 Solution of the transient heat equation using finite elements in 1D

Let us consider the following one-dimensional differential problem:

$$\rho c_p \frac{\partial T}{\partial t} - k_T \frac{\partial^2 T}{\partial x^2} = Q_H(x, t), \quad \forall 0 < x < L, \quad t > t_0 > 0$$

$$T(x, t_0) = \psi_0(x), \quad \frac{dT}{dt}(0, t) = \frac{dT}{dt}(L, t) = 0 \tag{5.130}$$

$$\delta_T = \frac{k_T}{\rho c_p} \text{ is the thermal diffusivity.}$$

The weak formulation of this problem is obtained by integrating by parts over the interval $[0, L]$ with respect to a weighted arbitrary function $w(x)$:

$$\int_0^L \frac{\partial T}{\partial t} w dx + \int_0^L \delta_T \frac{\partial T}{\partial x} \frac{\partial w}{\partial x} dx = w \frac{\partial T}{\partial x} \Big|_0^L + \int_0^L Q_H(x) w(x) dx \tag{5.131}$$

Using the same interpolation of previous section:

$$T(x, t) \approx u^e(x, t) = \sum_{i=1}^N u_i(t) \varphi_i(x) \tag{5.132}$$

Functions $\{\varphi_i; i = 1, N\}$ are the interpolators already defined. The Galerkin technique consists of taking $w(x) = \varphi_j(x)$ for $j = 1, N$. Replacing this interpolation in the weak formulation (5.131):

$$\sum_{i=1}^N \int_0^L \frac{du_i}{dt} \varphi_i \varphi_j dx + \sum_{i=1}^N \delta_T \int_0^L u_i(t) \frac{\partial \varphi_i}{\partial x} \frac{\partial \varphi_j}{\partial x} dx = \int_0^L Q_H(x) \varphi_j(x) dx \quad (5.133)$$

The same equation (5.133) is repeated for all weighted functions $\varphi_j(x), j = 1, N$. In this manner the following linear system is obtained:

$$\begin{aligned} \sum_{i=1}^N M_{ij} \frac{du_i}{dt}(t) + \sum_{i=1}^N K_{ij} u_i(t) &= f_j \\ \Leftrightarrow \mathbf{M} \cdot \vec{u}'(t) + \mathbf{K} \cdot \vec{u}(t) &= \vec{f} \quad \Leftrightarrow \frac{d\vec{u}}{dt} = \mathbf{A} \cdot \vec{u} + \vec{F} \end{aligned} \quad (5.134)$$

where: $\mathbf{A} = -\mathbf{M}^{-1} \cdot \mathbf{K}$, $\vec{F} = \mathbf{M}^{-1} \cdot \vec{f}$

Therefore, the finite element formulation of the heat transient conduction problem is equivalent to solving a system of ordinary differential equations.

5.3 THE FINITE VOLUME METHOD (FVM)

The finite volume method, also known as integrated finite differences or surface integrated finite differences (Narasimhan and Witherspoon 1976, Narasimhan 1982, Pruess 2006), is a numerical technique used to approximately evaluate partial differential equations. “Similar to the finite difference method, values are calculated at discrete places on a meshed geometry. Finite volume refers to the small volumes surrounding each node point on a mesh. In the finite volume method, volume integrals in a partial differential equation that contain a divergence term are converted to surface integrals, using the divergence theorem. These terms are then evaluated as fluxes at the surfaces of each finite volume. Because the flux entering a given volume is identical to that leaving the adjacent volume, these methods are conservative. Another advantage of the finite volume method is that it is easily formulated to allow for unstructured meshes. The method is used in many computational fluid dynamics packages”, (Wikipedia 2009f).

The FVM estimates flow variables, pressure or temperature, averaged across a volume; it can work in either structured (with regular distribution of nodes) or unstructured meshes of domains with highly irregular geometries. One of the main advantages of the FVM in groundwater flow is that it is a conservative method in the sense that it can conserve hydraulic head, pressure, temperature or solute concentration on coarse meshes easily. In problems demanding high resolution schemes, the method of *monotone upstream-centered schemes for conservation laws*, (Wikipedia 2008f) can be used to obtain high accuracy in the numerical solution of models involving discontinuities, shocks or large gradients.

5.3.1 The FVM in the solution of single-phase mass flow

The FVM is used in hydrogeology and in geothermal reservoir engineering to calculate the distribution of field functions (Pruess 1988, 2006). We consider a reservoir Ω of volume V_B discretized by N_V finite volumes $\{V_n, n = 1, N_V\}$, as shown in Figure 5.11.

To illustrate the use of this method we specifically solve the continuity equation (4.15) for a single phase fluid inside a differential porous volume dV . The FVM consists of directly integrating

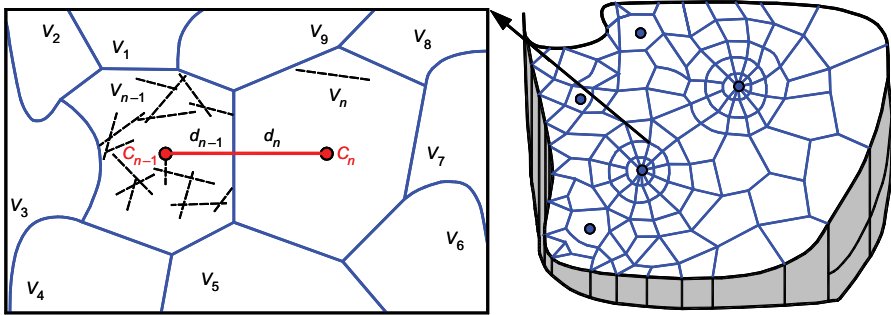


Figure 5.11. Unstructured mesh: Finite volume method in a 2-dimensional region showing its main parts. C_n is the center of each volume V_n ; d_n is the orthogonal distance between this center and the corresponding boundary. Volume V_n is surrounded by boundaries of areas S_{ni} , $i = 1, M$; where M is the number of these local boundaries.

this equation over each finite volume $V_n \{n = 1, N_V\}$:

$$\frac{\partial}{\partial t} \int_{V_n} (\varphi \rho_f) dV = - \int_{V_n} \vec{\nabla} \cdot \vec{F}_{M1} dV + \int_{V_n} q_f dV = - \int_{S_n} \vec{F}_{M1} \cdot \vec{n} dS + q_n \int_{V_n} dV \quad (5.135)$$

To obtain the last part of equation (5.135) we apply the divergence theorem of integral calculus. The global boundary S_n of every V_n is composed of three or more surfaces connecting each V_n with the boundaries of other volumes in the neighborhood:

$$\partial V_n = S_n = \bigcup_{i=1}^{M_n} S_i; \quad S_i \cap S_j = \Phi \quad \text{if } i \neq j \quad \text{and} \quad S_{ni} = S_n \cup S_i \quad (5.136)$$

The *mean value theorem* for integrals (Weisstein 2003) states that for any integrable function f defined in V_n or in S_n , its average value f_n is:

$$\int_{V_n} f dV = V_n f_n, \quad \text{and:} \quad \int_{S_n} f dS = S_n f_n \quad (5.137)$$

We use the mean value theorem for all the terms of the integro-differential equation (5.135):

$$\begin{aligned} \int_{S_n} \vec{F}_{M1} \cdot \vec{n} dS &= \sum_{i=1}^{M_n} \int_{S_i} \vec{F}_{M1} \cdot \vec{n} dS = \sum_{i=1}^{M_n} F_{ni} \int_{S_i} dS \\ &\Rightarrow \frac{\partial}{\partial t} (\varphi_n \rho_n) V_n + \sum_{i=1}^{M_n} F_{ni} S_{ni} = q_n V_n = Q_n \end{aligned} \quad (5.138)$$

Note that Q_n is the flow rate in [kg/s]. Subindex n indicates that the corresponding integrated variable is an averaged quantity in each V_n . The passage from equation (5.135) to formula (5.138) is the key step in the FVM formulation. The accuracy of the method depends on both the size and geometry of the volumes in the mesh, as well as the precision of the integral mean value theorem. The FVM is dependent neither on a coordinate system nor on the region's dimensions.

This equation is valid in 1, 2 or 3 dimensions. The averaged flux F_{ni} is computed at every interface S_{ni} assuming that Darcy's law is valid (Forchheimer's law and Navier-Stokes can also be used):

$$-K_{ni} \frac{\rho_{ni}}{\mu_{ni}} \int_{S_{ni}} (\vec{\nabla} p \cdot \vec{n} - \rho_{ni} \vec{g} \cdot \vec{n}) dS = -K_{ni} \frac{\rho_{ni}}{\mu_{ni}} \left[\frac{\partial p_n}{\partial n_i} - \rho_{ni} g \cos \theta_{ni} \right] S_{ni} = F_{ni} S_{ni} \quad (5.139)$$

where θ_{ni} is the angle between gravity and the vector orthogonal to the corresponding boundary S_{ni} . Here we have used the fact that the scalar product between the pressure gradient and the normal vector is equal to the directional derivative of pressure. Given that porosity and fluid density depend on (p, T) at every V_n :

$$(\varphi_n \rho_n)(p, T) \Rightarrow \frac{\partial}{\partial t}(\varphi_n \rho_n) = \frac{\partial(\varphi_n \rho_n)}{\partial p} \frac{\partial p_n}{\partial t} + \frac{\partial(\varphi_n \rho_n)}{\partial T} \frac{\partial T_n}{\partial t} \quad (5.140)$$

In this equation the fluid flow is implicitly coupled to the rock deformation through the variation of porosity. In non deformable rocks φ_n becomes constant. In equation (5.139) we approximate the normal derivative of pressure by a simple finite difference:

$$F_{ni} S_{ni} \approx -\frac{K_{ni} \rho_{ni} S_{ni}}{\mu_{ni}} \left[\frac{p_i - p_n}{d_n + d_i} - \rho_{ni} g \cos \theta_{ni} \right] \quad (5.141)$$

All terms with subindex ni represent computed average values at every interface S_{ni} . Several averaging techniques were introduced in chapter 3. Grouping all developments herein presented in equation (5.138) we finally obtain a fully discretized partial differential equation for each finite volume V_n :

$$\frac{\partial(\varphi_n \rho_n)}{\partial p} \frac{\partial p_n}{\partial t} + \frac{\partial(\varphi_n \rho_n)}{\partial T} \frac{\partial T_n}{\partial t} = \sum_{i=1}^{M_n} \frac{K_{ni} \rho_{ni} S_{ni}}{V_n \mu_{ni}} \left[\frac{p_i - p_n}{d_n + d_i} - \rho_{ni} g \cos \theta_{ni} \right] + \frac{Q_n}{V_n} \quad (5.142)$$

The partial derivatives of fluid density are calculated with the equation of state of water introduced in chapter 2. A simple approximation to estimate the porosity variation can be done employing a linear Taylor expansion:

$$\begin{aligned} \varphi_n(p, T) &= \varphi_0 + (p - p_0) \frac{\partial \varphi_0}{\partial p} + (T - T_0) \frac{\partial \varphi_0}{\partial T} + \text{term} \left(\frac{\partial^2 \varphi_0}{\partial p^2}, \frac{\partial^2 \varphi_0}{\partial T^2} \right) \dots \\ \Rightarrow \varphi_n(p, T) &\approx \varphi_0 \left[1 + C_\varphi(p - p_0) + \gamma_\varphi(T - T_0) \right] \end{aligned} \quad (5.143)$$

where C_φ is the compressibility of the pore volume at constant p_d (eq. 2.40a) and γ_φ is the thermal expansion of the pores at constant p_k and constant p (eq. 2.22b):

$$C_\varphi = -\frac{1}{\varphi_0} \frac{\partial \varphi_0}{\partial p_k} \text{ (compressibility); } \quad \gamma_\varphi = \frac{1}{\varphi_0} \frac{\partial \varphi_0}{\partial T} \text{ (expansivity)} \quad (5.144)$$

To simplify the final expression of the model, we define the following functional coefficients:

$$\begin{aligned} A_{1n}(p, T) &= \frac{\partial(\varphi_n \rho_n)}{\partial p}, & B_{1n}(p, T) &= \frac{\partial(\varphi_n \rho_n)}{\partial T} \\ C_{1ni}(p, T) &= \frac{K_{ni} \rho_{ni} S_{ni}}{V_n \mu_{ni}}, & D_{1ni}(p, T) &= \frac{K_{ni} \rho_{ni} S_{ni}}{V_n \mu_{ni}} \rho_{ni} g \cos \theta_{ni} \end{aligned} \quad (5.145)$$

where subscript ni represents an average value computed at the interface S_{ni} , while the subscript l means that the fluid is single phase. Finally, equation (5.142) can be written as follows:

$$A_{1n} \frac{\partial p_n}{\partial t} + B_{1n} \frac{\partial T_n}{\partial t} = \sum_{i=1}^{M_n} \left[C_{1ni} \frac{p_i - p_n}{d_n + d_i} - D_{1ni} \right] + \frac{Q_n}{V_n} = \Psi_{1M} \quad (5.146)$$

The last term Ψ_{1M} of this differential equation represents the total volumetric flow rate [kg/s/m³] exchanged between the finite volume V_n $\{n = 1, N_V\}$ and its surroundings formed by all the other volumes V_i $\{i = 1, M_n\}$. Equation (5.146) is a non-linear discretized model, with all its coefficients dependent on the unknown variables (p, T). These coefficients also contain the geometric information of each element of the mesh: volume V_n , areas S_{ni} , and nodal distances d_n, d_i . Notice also that the internodal distance $d_n + d_i$ is different at every interface, it measures the pressure gradient strength in the orthogonal direction to S_{ni} . The internodal distances will be similar or equal only if the mesh is regular and structured, formed by rectangles or squares.

5.3.2 The FVM in the numerical solution of single-phase energy flow

The FVM can be also used in geothermal reservoirs where the flow processes are non isothermal. The integral equation of the thermal energy flow in every volume V_n of the mesh is as follows (see equation 4.95 with $q_U = Q_H$):

$$\int_{V_n} \frac{\partial U}{\partial t} dV = \frac{\partial}{\partial t} \int_{V_n} [\varphi \rho_f e_f + (1 - \varphi) \rho_r h_r] dV = - \int_{V_n} \vec{\nabla} \cdot \vec{F}_{E1} dV + \int_{V_n} q_U dV \quad (5.147a)$$

Using the mean value theorem in all the terms of this integro-differential equation:

$$\frac{\partial}{\partial t} (\varphi_n \rho_n e_n) V_n + \rho_{rn} \frac{\partial}{\partial t} [(1 - \varphi_n) h_{rn}] V_n = - \int_{S_n} \vec{F}_{E1} \cdot \vec{n} dS + q_{Un} V_n \quad (5.147b)$$

Developing the right term of equation (5.147a): using the same methodology of previous section we obtain:

$$\begin{aligned} - \int_{S_n} \vec{F}_{E1} \cdot \vec{n} dS &= - \int_{S_n} (h_f \vec{F}_{M1} \cdot \vec{n} + k_T \vec{\nabla} T \cdot \vec{n}) dS \\ &= - \sum_{i=1}^{M_n} \left(h_{ni} F_{ni} S_{ni} + K_{Tni} \frac{\partial T_n}{\partial n_i} S_{ni} \right) \\ &= \sum_{i=1}^{M_n} \left(\frac{K_{ni} \rho_{ni} h_{ni} S_{ni}}{\mu_{ni}} \left[\frac{p_i - p_n}{d_n + d_i} - \rho_{ni} g \cos \theta_{ni} \right] + K_{Tni} S_{ni} \frac{T_i - T_n}{d_n + d_i} \right) \end{aligned} \quad (5.148)$$

The temporal derivative of averaged internal energy is:

$$\begin{aligned} \frac{\partial}{\partial t} [U_{Tn}] &= \left[e_n \frac{\partial}{\partial p} (\varphi_n \rho_n) + \varphi_n \rho_n \frac{\partial e_n}{\partial p} - \rho_{rn} h_{rn} \frac{\partial \varphi_n}{\partial p} \right] \frac{\partial p_n}{\partial t} \\ &+ \left[e_n \frac{\partial}{\partial T} (\varphi_n \rho_n) + \varphi_n \rho_n \frac{\partial e_n}{\partial T} + (1 - \varphi_n) \rho_{rn} C_{rn} - \rho_{rn} h_{rn} \frac{\partial \varphi_n}{\partial T} \right] \frac{\partial T_n}{\partial t} \end{aligned} \quad (5.149)$$

To obtain a compact expression for the energy model we define the following functional coefficients:

$$\begin{aligned}
 E_{1n}(p, T) &= e_n \frac{\partial}{\partial p}(\varphi_n \rho_n) + \varphi_n \rho_n \frac{\partial e_n}{\partial p} - \rho_{rn} h_{rn} \frac{\partial \varphi_n}{\partial p} \\
 F_{1n}(p, T) &= e_n \frac{\partial}{\partial T}(\varphi_n \rho_n) + \varphi_n \rho_n \frac{\partial e_n}{\partial T} - \rho_{rn} h_{rn} \frac{\partial \varphi_n}{\partial T} + (1 - \varphi_n) \rho_{rn} C_{rn} \\
 G_{1ni}(p, T) &= \frac{K_{Tni} S_{ni}}{V_n}, \quad Q_{Un} = q_{Un} V_n
 \end{aligned} \tag{5.150}$$

Replacing these coefficients and the previous expressions in equation (5.147b):

$$E_{1n} \frac{\partial p_n}{\partial t} + F_{1n} \frac{\partial T_n}{\partial t} = \sum_{i=1}^{M_n} \left[C_{1ni} h_{ni} \frac{p_i - p_n}{d_n + d_i} + G_{1ni} \frac{T_i - T_n}{d_n + d_i} - D_{1ni} h_{ni} \right] + \frac{Q_{Un}}{V_n} = \Psi_{1E} \tag{5.151}$$

The last term of this partial differential equation represents the total volumetric heat flow rate [J/s/m³] exchanged between the finite volume V_n and all the other volumes V_i $\{i = 1, M_n\}$, plus the volumetric energy Q_{Un}/V_n which is extracted or injected in V_n . This equation is a strongly non-linear discretized model, with all its coefficients dependent on the unknown variables (p, T). These coefficients contain thermodynamic and geometric information of each element of the mesh. Both equations (5.146) and (5.151) are coupled through p_n and T_n .

5.3.3 The FVM in the numerical solution of two-phase mass flow

When the water of geothermal systems is in a state of saturation, both phases, liquid and steam, can coexist. The boundary of this two-phase thermodynamic region is called the K-line; here, the temperature of the fluid depends on the saturation pressure (Fig. 2.31) through the Clapeyron relationship $T_{\text{sat}} = T(p_{\text{sat}})$. In a two-phase system it is necessary to have another variable that determines the quantity of thermal energy or enthalpy *in situ* or the relative quantity of steam or liquid present in each phase. The thermodynamic state of the two-phase fluid in the reservoir depends on the relative composition of each phase. The second variable adapted in this case can be the specific enthalpy, the steam quality or the liquid saturation. To simplify the model for two-phase flow systems we assume that the capillary pressure between liquid and vapor is negligible. Practical correlations to compute this pressure are found in section 2.3.8; a complete finite element model using capillary pressure is developed in section 9.4. The integral equation for two-phase flow is:

$$\frac{\partial}{\partial t} \int_{V_n} (\varphi \rho_l S_l + \varphi \rho_v S_v) dV + \int_{V_n} (\vec{\nabla} \cdot \vec{F}_l + \vec{\nabla} \cdot \vec{F}_v) dV = \int_{V_n} (q_l + q_v) dV = \int_{V_n} q_f dV \tag{5.152}$$

Applying the FVM to this integral equation, the corresponding averaged partial differential equation is:

$$\frac{\partial(\varphi_n \rho_n)}{\partial t} V_n = \frac{\partial}{\partial t} (\varphi \rho_l S_l + \varphi \rho_v S_v) v_n = - \sum_{i=1}^{M_n} (F_l + F_v)_{ni} S_{ni} + q_n V_n \tag{5.153}$$

Using the fact that the porosity is a function of (p, T) and $T(p)$, the temporal derivative of $(\varphi_n \rho_n)$ is:

$$(\varphi_n \rho_n)(p, h) \Rightarrow \frac{\partial}{\partial t}(\varphi_n \rho_n) = \left[\left(\frac{\partial \varphi_n}{\partial p_n} + \frac{\partial \varphi_n}{\partial T_n} \frac{\partial T_n}{\partial p_n} \right) \rho_n + \varphi_n \frac{\partial \rho_n}{\partial p_n} \right] \frac{\partial p_n}{\partial t} + \varphi_n \frac{\partial \rho_n}{\partial h_n} \frac{\partial h_n}{\partial t} \quad (5.154)$$

Replacing the fluxes of both phases given by equation (4.88) in equation (5.154):

$$\begin{aligned} (F_l + F_v)_{ni} &= - \sum_{i=1}^{M_n} \sum_{f=l}^v \frac{K_{ni} \rho_{fni} k_{fni}}{\mu_{fni}} \left[\frac{p_i - p_n}{d_n + d_i} - \rho_{fni} g \cos \theta_{ni} \right] \quad (5.155) \\ \Rightarrow \left[\left(\frac{\partial \varphi_n}{\partial p_n} + \frac{\partial \varphi_n}{\partial T_n} \frac{\partial T_n}{\partial p_n} \right) \rho_n + \varphi_n \frac{\partial \rho_n}{\partial p_n} \right] \frac{\partial p_n}{\partial t} + \varphi_n \frac{\partial \rho_n}{\partial h_n} \frac{\partial h_n}{\partial t} &= \frac{q_n V_n}{V_n} + \sum_{i=1}^{M_n} \frac{K_{ni} S_{ni}}{V_n} \\ &\times \left[\left(\frac{k_{lni} \rho_{lni}}{\mu_{lni}} + \frac{k_{vni} \rho_{vni}}{\mu_{vni}} \right) \left(\frac{p_i - p_n}{d_n + d_i} \right) - \left(\frac{k_{lni} \rho_{lni}^2}{\mu_{lni}} + \frac{k_{vni} \rho_{vni}^2}{\mu_{vni}} \right) g \cos \theta_{ni} \right] \quad (5.156) \end{aligned}$$

To obtain a compact expression for the two-phase flow model we define the following functional coefficients:

$$\begin{aligned} A_{2n}(p, h) &= \left(\frac{\partial \varphi_n}{\partial p_n} + \frac{\partial \varphi_n}{\partial T_n} \frac{\partial T_n}{\partial p_n} \right) \rho_n + \varphi_n \frac{\partial \rho_n}{\partial p_n} \\ B_{2n}(p, h) &= \varphi_n \frac{\partial \rho_n}{\partial h_n} \\ C_{2ni}(p, h) &= \frac{K_{ni} S_{ni}}{V_n} \left(\frac{\rho_{lni} k_{lni}}{\mu_{lni}} + \frac{\rho_{vni} k_{vni}}{\mu_{vni}} \right) \\ D_{2ni}(p, h) &= \frac{K_{ni} S_{ni}}{V_n} \left(\frac{k_{lni} \rho_{lni}^2}{\mu_{lni}} + \frac{k_{vni} \rho_{vni}^2}{\mu_{vni}} \right) g \cos \theta_{ni} \quad (5.157) \end{aligned}$$

Replacing these coefficients in the corresponding equation (5.146):

$$A_{2n} \frac{\partial p_n}{\partial t} + B_{2n} \frac{\partial h_n}{\partial t} = \sum_{i=1}^{M_n} \left[C_{2ni} \frac{p_i - p_n}{d_n + d_i} - D_{2ni} \right] + \frac{Q_n}{V_n} = \Psi_{2M} \quad (5.158)$$

The last term of partial differential equation (5.158), Ψ_{2M} represents the total volumetric two-phase flow rate [kg/s/m³] exchanged between the finite volume V_n and its surroundings formed by all the other volumes $V_i \{i = 1, M_n\}$. This is also a non-linear discretized model, with all its coefficients dependent on the unknown variables (p, h) .

5.3.4 The FVM in the numerical solution of two-phase energy flow

The total heat flow in a two-phase geothermal system is given by equation (4.97):

$$\begin{aligned} \vec{F}_{E2} &= \vec{F}_l h_l + \vec{F}_v h_v - k_T \vec{\nabla} T \\ k_T &= (1 - \varphi) k_{Tl} + \varphi S_l k_{Tl} + \varphi S_v k_{Tv} \end{aligned}$$

The integral equation of the thermal energy flow in every volume V_n is:

$$\int_{V_n} \frac{\partial U}{\partial t} dV = \frac{\partial}{\partial t} \int_{V_n} [\varphi \rho_f e_f + (1 - \varphi) \rho_r h_r] dV = - \int_{V_n} \vec{\nabla} \cdot \vec{F}_{E2} dV + \int_{V_n} q_U dV \quad (5.159)$$

Applying the FVM to the two-phase energy flow:

$$\begin{aligned} \int_{S_n} \vec{F}_{E2} \cdot \vec{n} dS &= \int_{S_n} \left[(h_l \vec{F}_l + h_v \vec{F}_v) \cdot \vec{n} - k_T \vec{\nabla} T \cdot \vec{n} \right] dS \\ &\approx \sum_{i=1}^{M_n} S_{ni} \left(K_{ni} \frac{k_{lni} \rho_{lni} h_{lni}}{\mu_{lni}} \left(\frac{p_i - p_n}{d_n + d_i} - \rho_{lni} g \cos \theta_{ni} \right) + k_{Tni} \frac{T_i - T_n}{d_n + d_i} \right) \\ &\quad + \sum_{i=1}^{M_n} S_{ni} \left(K_{ni} \frac{k_{vni} \rho_{vni} h_{vni}}{\mu_{vni}} \left(\frac{p_i - p_n}{d_n + d_i} - \rho_{vni} g \cos \theta_{ni} \right) \right) \end{aligned} \quad (5.160)$$

The calculus and algebra for this equation is completely analogous to the single phase energy flow; the only difference is the number of terms involved, because here there are two phases. Developing the temporal derivative of equation (5.159) using the corresponding methodology of the previous section and factorizing we obtain:

$$\begin{aligned} &\left[(\rho_n h_n - p_n - \rho_{rn} h_{rn}) \left(\frac{\partial \varphi_n}{\partial p_n} + \frac{\partial \varphi_n}{\partial T_n} \frac{\partial T_n}{\partial p_n} \right) + \varphi_n h_n \frac{\partial \rho_n}{\partial p_n} - \varphi_n + (1 - \varphi_n) \rho_{rn} C_{rn} \frac{\partial T_n}{\partial p_n} \right] \frac{\partial p_n}{\partial t} \\ &+ \left(\varphi_n \rho_n + \varphi_n h_n \frac{\partial \rho_n}{\partial h_n} \right) \frac{\partial h_n}{\partial t} = \sum_{i=1}^{M_n} \frac{K_{ni} S_{ni}}{V_n} \left(\frac{k_{lni} \rho_{lni} h_{lni}}{\mu_{lni}} + \frac{k_{vni} \rho_{vni} h_{vni}}{\mu_{vni}} \right) \left(\frac{p_i - p_n}{d_n + d_i} \right) \\ &- \sum_{i=1}^{M_n} \frac{K_{ni} S_{ni}}{V_n} \left(\frac{k_{lni} \rho_{lni}^2 h_{lni}}{\mu_{lni}} + \frac{k_{vni} \rho_{vni}^2 h_{vni}}{\mu_{vni}} \right) g \cos \theta_{ni} + \sum_{i=1}^{M_n} \frac{k_{Tni} S_{ni}}{V_n} \frac{T_i - T_n}{d_n + d_i} \\ &+ \frac{(q_{ln} h_{ln} + q_{vn} h_{vn} + q_{rn}) V_n}{V_n} \end{aligned} \quad (5.161)$$

To obtain a compact expression for the energy model we define the following functional coefficients:

$$\begin{aligned} E_{2n}(p, h) &= [*]; \quad F_{2n}(p, h) = \left(\varphi_n \rho_n + \varphi_n h_n \frac{\partial \rho_n}{\partial h_n} \right) \\ G_{2ni}(p, h) &= \frac{K_{ni} S_{ni}}{V_n} \left(\frac{k_{lni} \rho_{lni} h_{lni}}{\mu_{lni}} + \frac{k_{vni} \rho_{vni} h_{vni}}{\mu_{vni}} \right) \\ H_{2ni}(p, h) &= \frac{K_{ni} S_{ni}}{V_n} \left(\frac{k_{lni} \rho_{lni}^2 h_{lni}}{\mu_{lni}} + \frac{k_{vni} \rho_{vni}^2 h_{vni}}{\mu_{vni}} \right) g \cos \theta_{ni} \\ Q_{2Un} &= (q_{ln} h_{ln} + q_{vn} h_{vn} + q_{rn}) V_n \end{aligned} \quad (5.162)$$

where the symbol [*] in the first line of equation (5.162) means that the coefficient E_{2n} is equal to the whole expression of the first line of equation (5.161), which is a factor of the partial derivative

$\partial p_n / \partial t$. Finally, we obtain a condensed expression for the energy flow:

$$E_{2n} \frac{\partial p_n}{\partial t} + F_{2n} \frac{\partial h_n}{\partial t} = \sum_{i=1}^{M_n} \left[G_{2ni} \frac{p_i - p_n}{d_n + d_i} + \frac{k_{Tni} S_{ni}}{V_n} \frac{T_i - T_n}{d_n + d_i} - H_{2ni} \right] + \frac{Q_{Un}}{V_n} = \Psi_{2E} \quad (5.163)$$

The last term of this partial differential equation represents the total volumetric heat flow rate [W/m³] of the two-phase flow of fluid exchanged between the finite volume V_n and all the other volumes V_i $\{i = 1, M_n\}$, plus the volumetric energy Q_{Un}/V_n which is extracted or injected in V_n . This equation is a strongly non-linear discretized model, with all its coefficients dependent on the unknown variables (p , T). The discretized equation and its coefficients contain thermodynamic and geometric information of each element of the mesh. Both equations (5.158) and (5.163) are coupled through p_n and h_n .

5.3.5 Numerical approximations of the time-level

The parabolic-type differential equations (5.146), (5.151), (5.158) and (5.163) are numerical approximations of the total energy and mass flows in single-phase and two-phase geothermal systems. Those expressions are based on the finite volume method; the following general non-linear model represents all of them:

$$\alpha_{jn}(p, X_j) \frac{\partial p_n}{\partial t} + \beta_{jn}(p, X_j) \frac{\partial X_{jn}}{\partial t} = \Psi_{jk}(\vec{\nabla} p_n, \vec{\nabla} X_{jn}) \quad (5.164)$$

The functional coefficients α_{jn} , β_{jn} and Ψ_{jk} can be recognized by comparison with the coefficients of the respective previous equations, for ($j = 1, 2$) and ($k = M, E$). The variable X_j represents temperature T ($j = 1$) in single-phase flows, or enthalpy h ($j = 2$) in two-phase flows. To complete the solution of these equations it is necessary to use time-level schemes in order to estimate the evolution of pressure, temperature and enthalpy. Two or three time-level schemes can be constructed to approximate these parabolic equations using finite-differences (see section 5.1). The non-linear system of coupled equations (5.164) is equivalent to the following matrix equation, which is valid in either single or two-phase flows:

$$\begin{pmatrix} A_{jn} & B_{jn} \\ E_{jn} & F_{jn} \end{pmatrix} \cdot \begin{pmatrix} \frac{\partial p_n}{\partial t} \\ \frac{\partial X_{jn}}{\partial t} \end{pmatrix} = \begin{pmatrix} \Psi_{jM} \\ \Psi_{jE} \end{pmatrix}_n \Leftrightarrow \Lambda_n \frac{\partial \vec{\tau}_n}{\partial t} = \vec{\Psi}_n \Leftrightarrow \frac{\partial \vec{\tau}_n}{\partial t} = \Lambda_n^{-1} \cdot \vec{\Psi}_n \quad (5.165a)$$

$$\text{where : } \Lambda_n = \begin{pmatrix} A_{jn} & B_{jn} \\ E_{jn} & F_{jn} \end{pmatrix}, \quad \frac{\partial \vec{\tau}_n}{\partial t} = \frac{\partial}{\partial t} \begin{pmatrix} p_n \\ X_{jn} \end{pmatrix} \quad \text{and} \quad \vec{\Psi}_n(t) = \begin{pmatrix} \Psi_{jM} \\ \Psi_{jE} \end{pmatrix}_n \quad (5.165b)$$

This matrix system should be solved for each finite volume V_n ($n = 1, N_V$), it includes the mutual flows between V_n and its surroundings within the mesh (Fig. 5.11).

5.3.5.1 Explicit numerical approximation of the time-level

The inverse of the matrix in equation (5.165a) is:

$$\Lambda_n^{-1} = \frac{1}{\Delta \Lambda_n} \begin{pmatrix} F_{jn} & -B_{jn} \\ -E_{jn} & A_{jn} \end{pmatrix}; \quad \Delta \Lambda_n = A_{jn} F_{jn} - B_{jn} E_{jn} \neq 0 \quad (5.165c)$$

The finite-difference explicit approximation of equation (5.165b) is done using either a forward-difference formula or a backward-difference formula. The truncation error in both formulae is

linear and of the same order as the time step $O(\Delta t)$. Using the forward-difference formula, we obtain a very simple scheme to advance in time:

$$\left\{ \begin{array}{l} \frac{\partial p_n}{\partial t} \approx \frac{p_n^{t+\Delta t} - p_n^t}{\Delta t} = \frac{F_{jn} \Psi_{jM} - B_{jn} \Psi_{jE}}{\Delta \Lambda_n} \\ \frac{\partial X_{jn}}{\partial t} \approx \frac{X_{jn}^{t+\Delta t} - X_{jn}^t}{\Delta t} = \frac{A_{jn} \Psi_{jE} - E_{jn} \Psi_{jM}}{\Delta \Lambda_n} \end{array} \right\} \quad (5.166a)$$

Therefore:

$$\begin{aligned} p_n^{t+\Delta t} &= p_n^t + \Delta t \left(\frac{F_{jn} \Psi_{jM} - B_{jn} \Psi_{jE}}{\Delta \Lambda_n} \right)^t \\ X_{jn}^{t+\Delta t} &= X_{jn}^t + \Delta t \left(\frac{A_{jn} \Psi_{jE} - E_{jn} \Psi_{jM}}{\Delta \Lambda_n} \right)^t \end{aligned} \quad (5.166b)$$

where t represents the present time and $t + \Delta t$ the future time. The time iteration ranges from the initial condition ($t = 0$) up to the maximum time ($t = t_{\max}$) the user wants to reach in the simulation. Equations (5.166b) give simple explicit formulae for the unknown pressure and temperature or enthalpy in each volume V_n at the time ($t + \Delta t$) in terms of known variables along the time axis t .

It is important to note that all non-linear terms included in the functional coefficients only depend on the present time t at each iteration. They are explicitly updated with equations (5.166b). Therefore, the numerical representation of the simultaneous heat and mass flow in geothermal reservoirs is quite straightforward using this scheme in the FVM. In spite of its simplicity the time-level explicit approximation is useful only when the changes in the reservoir variables are smooth and at slow speed. Otherwise, this scheme has one serious drawback. The size of the time step Δt becomes necessarily very small because the process is valid only for $\Delta t \leq 0.5 \Delta d^2$ (Smith 1978), where d is a representative diameter of V_n . Under this condition, the size of each V_n must be kept small to attain reasonable accuracy. If the flow speed is high as it occurs close to wells, the simulation becomes overwhelmingly slow.

5.3.5.2 *Implicit numerical approximation of the time-level*

A more general finite-difference approximation of the time-level consists in averaging the dependence on time of the functions in equation (5.165a) between two consecutive time steps t^{k+1} (future) and t^k (present) as follows:

$$\begin{aligned} \Lambda_n(p_n, X_{jn}, t) \cdot \frac{\partial \bar{\tau}_n}{\partial t} &= \bar{\Psi}_n(p_n, X_{jn}, t) \cdot \quad \text{With: } \delta t = t^{k+1} - t^k \\ \Rightarrow \Lambda_n^k \cdot \frac{(\bar{\tau}_n^{k+1} - \bar{\tau}_n^k)}{\delta t} &= [\theta \bar{\Psi}_n^{k+1} + (1 - \theta) \bar{\Psi}_n^k], \quad \theta \in [0, 1] \end{aligned} \quad (5.167)$$

Coefficient θ determines the nature of the weighted average. If $\theta = 0$ we obtain the explicit scheme; if $\theta = 1$ we obtain a fully implicit scheme, which must be solved as a linear system of equations. If $0 < \theta < 1$ the time-level approximation is mixed, implicit-explicit. The truncation error in this case is of the order $O(\Delta t^2)$ (e.g., Smith 1978).

5.3.5.3 *Three time-level numerical approximations*

Generally speaking, three time-level schemes are used to achieve more advantages over two time-level schemes, such as smaller local truncation errors, larger numerical stability, or the transformation of a non-linear problem to a linear one (Smith 1978, Richtmyer and Morton 1967).

For example the following approximation of equation (5.165b) is a three time-level finite-difference equation where the time steps are t^{k+1} (future), t^k (present) and t^{k-1} (past):

$$\Lambda_n^k \cdot \left[\frac{3}{2} \frac{(\bar{\tau}_n^{k+1} - \bar{\tau}_n^k)}{\delta t} - \frac{1}{2} \frac{(\bar{\tau}_n^k - \bar{\tau}_n^{k-1})}{\delta t} \right] = \left[\theta \bar{\Psi}_n^{k+1} + (1 - \theta) \bar{\Psi}_n^k \right], \quad \theta \in [0,1] \quad (5.168)$$

The truncation error in this scheme is of the same order $O(\Delta t^2)$ as in the previous mixed, implicit-explicit algorithm, but this time-level approximation is the better one to use when the initial data are discontinuous or varies very rapidly with the spatial dimensions (Smith 1978). The implicit two time-level scheme should be used when the initial data and its derivatives are continuous.

5.4 THE BOUNDARY ELEMENT METHOD FOR ELLIPTIC PROBLEMS

During the numerical estimation of the initial state of a reservoir it is clear that, after a great number of time steps, the transient term in equation (5.130) becomes practically zero. Thus, in this case, the transient equation becomes a PDE of elliptic type. The *boundary element method* (BEM) is specifically intended for linear elliptic PDE in homogeneous media. In this type of physical problems, the BEM is clearly superior to FD, FV and FE methods in both accuracy and efficiency. Mainly, because all these methods demand the discretization of the whole solution domain Ω . The key feature of the BEM is that only the surface boundary of the porous medium needs to be discretized. The field variable can be calculated with high precision at any point in the interior of the domain using only the known values of the function at the boundary of Ω . The BEM provides an effective reduction of the dimension of the PDE solution space. As a result, improved numerical accuracy is obtained and the use of computational resources is reduced.

Using BEM, differential problems can be solved quite adequately on a notebook type PC. Other methods would undoubtedly require the use of cluster or a workstation, or even a supercomputer, to obtain the same level of accuracy when dealing with the degree of geometric complexity of certain reservoir boundaries (Cruse and Rizzo 1975, Ameen 2001, Pozrikidis 2002). To illustrate the method, we solve an elliptic problem representing a stationary temperature (or pressure) distribution, described by Poisson's equation with mixed boundary conditions (Fig. 5.12):

$$\left. \begin{aligned} \nabla^2 T &= f(\vec{P}), \quad \forall \vec{P} = (x, y) \in \Omega \subset \mathbb{R}^2, \\ T(\vec{P}) &= u_T(\vec{P}), \quad \forall \vec{P} \in \Gamma_T, \\ \frac{\partial T}{\partial n}(\vec{P}) &= u_n(\vec{P}), \quad \forall \vec{P} \in \Gamma_N \end{aligned} \right\} \partial\Omega = \Gamma = \Gamma_T \cup \Gamma_N \quad (5.169)$$

Let's assume first that $f = 0$ (Laplace PDE). Applying Green's theorem and the fundamental solution to the integral form of equation (5.169) (see Appendix) we obtain:

$$\left. \begin{aligned} T(\vec{P}) &= -\frac{1}{2\pi} \int_{\Gamma} \left[\text{Ln} \|\vec{P} - \vec{q}\| \frac{\partial T(\vec{q})}{\partial n} - \frac{T(\vec{q})}{\|\vec{P} - \vec{q}\|} \text{Cos} \theta \right] ds \\ \forall \vec{P} \in \Omega, \quad \vec{q} \in \partial\Omega, \quad \theta &= \angle(\vec{r}_{Pq}, \vec{n}), \quad \vec{n} = \text{normal to } \Gamma \text{ at } \vec{q} \end{aligned} \right\} \quad (5.170)$$

The boundary $\partial\Omega$ is discretized into $\Gamma_j (j = 1, N_b)$ boundary elements which can be linear, parabolic, or cubic splines in 2D. In the 3D case, the boundary elements can be triangles, rectangles, shells, etc.

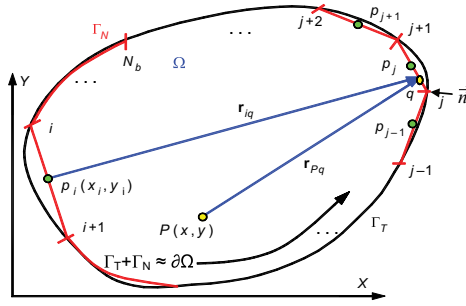


Figure 5.12. Boundary discretization of the domain Ω , for the 2D solution of the PDE (5.169).

The main fundamental theorem supporting the BEM is the general form of Stoke's theorem (Pita 1995):

$$\int_{\Omega} d\omega = \int_{\Gamma} \omega, \Gamma = \partial\Omega, \Omega \subset \mathbb{R}^n, \Gamma \subset \mathbb{R}^{n-1} \tag{5.171}$$

$n = 1, 2, 3; \quad \Gamma = \partial\Omega$ is the boundary of Ω

where Ω is an open subset of \mathbb{R}^n and ω is any differential form defined in Ω . This simple and elegant theorem has many significant consequences. Let's define $\omega(x, y) = f(x, y) + g(x, y)$; Stoke's theorem implies that:

$$\int_{\Omega} \left(\frac{\partial f}{\partial x} + \frac{\partial g}{\partial y} \right) dx dy = \int_{\Gamma} (f dy - g dx) \tag{5.172}$$

Assuming that (f, g) are the components of a gradient and defining a vector normal to the curve Γ , then

$$\vec{\nabla}F = \left(\frac{\partial F}{\partial x}, \frac{\partial F}{\partial y} \right) = (f, g); \quad \vec{n} = (n_x, n_y) = (dy - dx)$$

$$\Rightarrow \int_{\Omega} (\Delta F) dx dy = \int_{\Gamma} \vec{\nabla}F \cdot \vec{n} ds = \int_{\Gamma} \frac{\partial F}{\partial n} ds \tag{5.173}$$

where: $\Delta F = \vec{\nabla} \cdot (\vec{\nabla}F) = \left(\frac{\partial^2 F}{\partial x^2} + \frac{\partial^2 F}{\partial y^2} \right)$

This result implies the first form of Green's theorem:

$$f = u \frac{\partial v}{\partial x}, g = v \frac{\partial u}{\partial y}, u, v : \Omega \rightarrow \mathbb{R}, u, v \in C^2_{\Omega} \tag{5.174}$$

$$\int_{\Omega} (u \Delta v + \vec{\nabla}u \cdot \vec{\nabla}v) dx dy = \int_{\partial\Omega} u \frac{\partial v}{\partial n} ds$$

Interchanging the roles of u and v in this formula and subtracting both results we finally arrive at the full expression of the general Green's theorem:

$$\int_{\Omega} (u \Delta v - v \Delta u) d\Omega = \int_{\partial\Omega} \left(u \frac{\partial v}{\partial n} - v \frac{\partial u}{\partial n} \right) ds \quad (5.175)$$

$$\Omega \subset \mathbb{R}^n \quad \text{and} \quad \partial\Omega \subset \mathbb{R}^{n-1}, \quad n = 1, 2, 3$$

5.4.1 The Dirac distribution (a generalized function)

Another fundamental result that supports the theory of the BEM concerns Dirac's delta distribution (Pozrikidis 2002, Katsikadelis 2002). It can be defined in 1, 2 or 3 dimensions and interpreted as a forced Laplace's equation for a field around a singular point. Let \vec{P} and $\vec{P}_0 \in \mathbb{R}^n$, be two points in the n -dimensional space ($n = 1, 2, 3$), where \vec{P}_0 is the location of a fixed singular point, \vec{P} is any variable point of the field. The distribution of Dirac $\delta_n(\vec{P} - \vec{P}_0)$ is a generalized function such that:

$$\delta_n(\vec{P} - \vec{P}_0) = \lim_{\beta \rightarrow \infty} \frac{\beta}{\pi} \exp(-\beta \|\vec{P} - \vec{P}_0\|^2) \quad (5.176)$$

$$\|\vec{P} - \vec{P}_0\| = \sqrt{\sum_{k=1}^n (x_k - x_{0k})^2} \quad \text{for } n = 1, 2, 3$$

where β is a real positive parameter related to an arbitrary length. The following properties are easily demonstrated:

- 1) $\delta_2(\vec{P} - \vec{P}_0) = \delta_1(x - x_0)\delta_1(y - y_0)$
- 2) $\delta_3(\vec{P} - \vec{P}_0) = \delta_1(x - x_0)\delta_1(y - y_0)\delta_1(z - z_0)$
- 3) $\delta_n(\vec{P} - \vec{P}_0) = 0 \quad \forall \vec{P} \neq \vec{P}_0$
- 4) $\delta_n(\vec{P} - \vec{P}_0) = \infty \quad \text{if } \vec{P} = \vec{P}_0$ (5.177)
- 5) $\int_{\Omega} \delta_n(\vec{P} - \vec{P}_0) d\Omega = 1 \quad \forall \Omega \ni \vec{P}_0$
- 6) $\int_{\Omega} \delta_n(\vec{P} - \vec{P}_0) f(\vec{P}) d\Omega = f(\vec{P}_0) \quad \forall \Omega \ni \vec{P}_0$

This last property shows that the integral of the product of δ_n and an arbitrary function over a domain Ω containing the singular point \vec{P}_0 is equal to $f(\vec{P}_0)$, the value of the function at the singular point. Thus, if Ω does not contain \vec{P}_0 this integral is equal to zero.

5.4.2 The fundamental solution in free space

Let \vec{P} be any point, and \vec{P}_0 a heat point source located somewhere in the plane R^2 . The influence of the heat source is described by the Dirac's delta distribution $f(\vec{P}) = \delta(\vec{P} - \vec{P}_0)$.

The temperature field is described by the fundamental PDE (Pozrikidis 2002) in polar (see Appendix) coordinates:

$$\Delta v = \frac{d^2 v}{dr^2} + \frac{1}{r} \frac{dv}{dr} = \delta(\vec{P} - \vec{P}_0), \quad (5.178)$$

$$r = \|\vec{P} - \vec{P}_0\| = \sqrt{(x - x_0)^2 + (y - y_0)^2}$$

The solution of this PDE plays a very important role in the BEM and is called the singular or fundamental solution or Green's free space function. Its expression is:

$$v(\vec{P} - \vec{P}_0) = \frac{\text{Ln}(r)}{2\pi} \quad (5.179)$$

Applying results (5.175) and (5.178) to the Laplace PDE (5.169) with $f(P) = 0$ we obtain:

$$\int_{\Omega} (v \Delta T - T \Delta v) d\Omega = \int_{\Omega} (0 - T(\vec{P}_0) \delta(\vec{P} - \vec{P}_0)) d\Omega$$

$$\Rightarrow T(\vec{P}) = \int_{\Gamma = \Gamma_T + \Gamma_N} \left(T(\vec{q}) \frac{\partial v(\vec{q}, \vec{P})}{\partial n} - v(\vec{q}, \vec{P}) \frac{\partial T(\vec{q})}{\partial n} \right) ds \quad (5.180)$$

$$\forall \vec{P}, \vec{P}_0 \in \Omega \subset \mathbb{R}^n \quad \text{and} \quad \vec{q} \in \partial\Omega \subset \mathbb{R}^{n-1}, \quad n = 1, 2, 3$$

This is the main solution of the classical BEM. The method has been extended to more complex problems, including transient PDE of parabolic type in heterogeneous media (Archer 2000, Archer *et al.* 1999, Sato 1992).

5.4.3 BEM solution of the Poisson's equation

Let us assume now that $f \neq 0$ (Poisson PDE 5.169), applying the same methodology proposed by Katsikadelis (2002) we obtain:

$$\forall \vec{P}, \vec{Q} \in \Omega: T(\vec{P}) = \int_{\Omega} v(\vec{P}, \vec{Q}) f(\vec{P}) d\Omega$$

$$- \int_{\Gamma} \left[v(\vec{P}, \vec{q}) \frac{\partial T(\vec{q})}{\partial n} - T(\vec{q}) \frac{\partial v(\vec{P}, \vec{q})}{\partial n} \right] ds \quad (5.181)$$

$$\text{where } \vec{q} \in \Gamma \quad \text{and} \quad v(\vec{P}, \vec{q}) = \frac{\text{Ln}(\|\vec{P} - \vec{q}\|)}{2\pi}$$

The auxiliary function v is the fundamental solution of the singular form of Laplace equation (Appendix) and plays a crucial role in the classical BEM. For time-dependent problems of parabolic type the BEM can also be applied using two subsidiary techniques:

- Solving first the PDE in time using FD, then applying the BEM to the time-discretized equations.
- Removing the time dependence of the PDE using the Laplace transform.

5.4.4 The BEM numerical implementation: An example

Let us assume that each Γ_j is a constant linear segment. The discretization of the boundary Γ (Fig. 5.12) in equation (171) implies that:

$$\Gamma_T \cup \Gamma_N = \Gamma \approx \bigcup_{j=1}^{N_b} \Gamma_j \quad (5.182)$$

Consequently equation (5.180) can be discretized as:

$$\frac{T^i}{2} = - \sum_{j=1}^{N_b} \int_{\Gamma_j} v(\vec{p}_i, \vec{q}) \frac{\partial T(\vec{q})}{\partial n_j} ds + \sum_{j=1}^{N_b} \int_{\Gamma_j} T(\vec{q}) \frac{\partial v(\vec{p}_i, \vec{q})}{\partial n_j} \quad (5.183)$$

or equivalently as:

$$\sum_{j=1}^{N_b} H_{ij} T^j = \sum_{j=1}^{N_b} G_{ij} \frac{\partial T^j}{\partial n} \quad (5.184)$$

The influence coefficients H_{ij} and G_{ij} are integral forms equal to:

$$H_{ij} = \int_{\Gamma_j} \left(\frac{\partial v}{\partial n_j} ds \right) - \frac{\delta_{ij}}{2}; \quad G_{ij} = \int_{\Gamma_j} v(\vec{p}_i, \vec{q}) ds \quad (5.185)$$

From equation (5.184) we finally obtain the linear system:

$$\mathbf{H} \cdot \vec{T} = \mathbf{G} \cdot \vec{T}_n \quad (5.186)$$

$$T^j = (u^j); \quad T_n^j = \frac{\partial T^j}{\partial n} = (u_n^j)$$

Because of the assumed mixed boundary conditions, u_T in Γ_T and u_n in Γ_N , there are unknown quantities in both sides of equation (5.186). Consequently, we need to separate the identified u 's from the unknown u 's in order to obtain a consistent system of linear equations. As an example, the system for $N_b = 4$ is:

$$\begin{pmatrix} H_{11} & H_{12} & H_{13} & H_{14} \\ H_{21} & H_{22} & H_{23} & H_{24} \\ H_{31} & H_{32} & H_{33} & H_{34} \\ H_{41} & H_{42} & H_{43} & H_{44} \end{pmatrix} \cdot \begin{pmatrix} u^1 \\ u^2 \\ T^3 \\ T^4 \end{pmatrix} = \begin{pmatrix} G_{11} & G_{12} & G_{13} & G_{14} \\ G_{21} & G_{22} & G_{23} & G_{24} \\ G_{31} & G_{32} & G_{33} & G_{34} \\ G_{41} & G_{42} & G_{43} & G_{44} \end{pmatrix} \cdot \begin{pmatrix} T_n^1 \\ T_n^2 \\ u_n^3 \\ u_n^4 \end{pmatrix} \quad (5.187)$$

Let us suppose that the u^j are the known quantities and the T^j are the unknown variables. Moving all the unknowns to the left hand side of equation (5.187) we obtain the

final linear system:

$$\mathbf{A} \cdot \vec{\mathbf{T}} = \mathbf{B} \Leftrightarrow \begin{pmatrix} -H_{13} & -H_{14} & G_{11} & G_{12} \\ -H_{23} & -H_{24} & G_{21} & G_{22} \\ -H_{33} & -H_{34} & G_{31} & G_{32} \\ -H_{43} & -H_{44} & G_{41} & G_{42} \end{pmatrix} \cdot \begin{pmatrix} T^3 \\ T^4 \\ T_n^1 \\ T_n^2 \end{pmatrix} = \begin{pmatrix} B^1 \\ B^2 \\ B^3 \\ B^4 \end{pmatrix} \quad (5.188)$$
$$B^i = H_{i1} u^1 + H_{i2} u^2 - G_{i3} u_n^3 - G_{i4} u_n^4$$

The matrix in this system is full and non symmetric, but is at least four times smaller than the equivalent matrix obtained by FD, FE or FV. This result can be easily generalized for any $N_b > 4$. We will apply the BEM to submarine reservoirs in chapter 9.

CHAPTER 6

Procedure of a numerical model elaboration

“We should not overlook the importance of simplicity combined with depth of understanding, not only for its cultural value, but as a technological tool. It leads to quantitative predictions without laborious and costly calculations; it suggests new inventions and simple solutions of engineering problems.”

Maurice A. Biot (1962)*

6.1 INTRODUCTION

Establishing a numerical model can be described as the representation of a conceptual model of a natural system using numerical algorithms, such as an aquifer or a system of interacting aquifers. In this chapter, we will distinguish between two groups: cold (non-geothermal) and geothermal aquifers. Numerical models can be used to simulate responses due to perturbations of the system in order to evaluate the dominating influences on the more complex real-world systems. Using the basic laws of physics and chemistry that govern groundwater flow, and solute and heat transport, the conceptual model is mathematically represented. The conceptual model considers all the information available on geological setting, geometrical properties, hydraulic parameters, solid phase properties, including homogeneity and isotropy, fluid properties, boundary condition, both sources and sinks of fluids, solutes and heat, and their spatial time-dependent distributions within the study area and its boundaries. The purpose of the numerical model is to solve the differential equations either at steady state conditions for the unperturbed system, or to model the behavior of the domain over time.

The development of an accurate numerical model for simulating groundwater flow and solute and heat transport requires the processing of a large amount of information regarding the domain area, and is generally comprised of the following seven steps (see Fig. 6.1).

- Defining the specific objectives of the model.
- Developing a conceptual model of the aquifer or the geothermal reservoir that includes all available information about the geology and existing databases for the physical and chemical properties of the system that are relevant for the explicit description of the system. These are the properties that describe groundwater flow and solute and heat transfer.
- Constructing a mathematical model, where all the concepts from the conceptual model are expressed in mathematical equations. Assumptions about the boundary conditions and other properties of the conceptual model are included here.
- Elaborating the numerical model by (1) discretizing the domain creating a numerical mesh or grid of the area to be modeled (or use other discretization methods as e.g., meshless methods); (2) Discretizing the mathematical equations of the mathematical model (if you write your own modeling computer program), or selecting a computer program that can solve the mathematical equations of the mathematical model. The computer program should be verified against known analytical solutions or previously solved problems to determine whether the computer code is correct and functioning as intended. Input to the program are the assigned values of hydraulic

* Speech of Maurice A. Biot during the Acceptance speech of Timoshenko Award. American Society of Mechanical Engineers, *Applied Mechanics Reviews* 16:2, 1963.

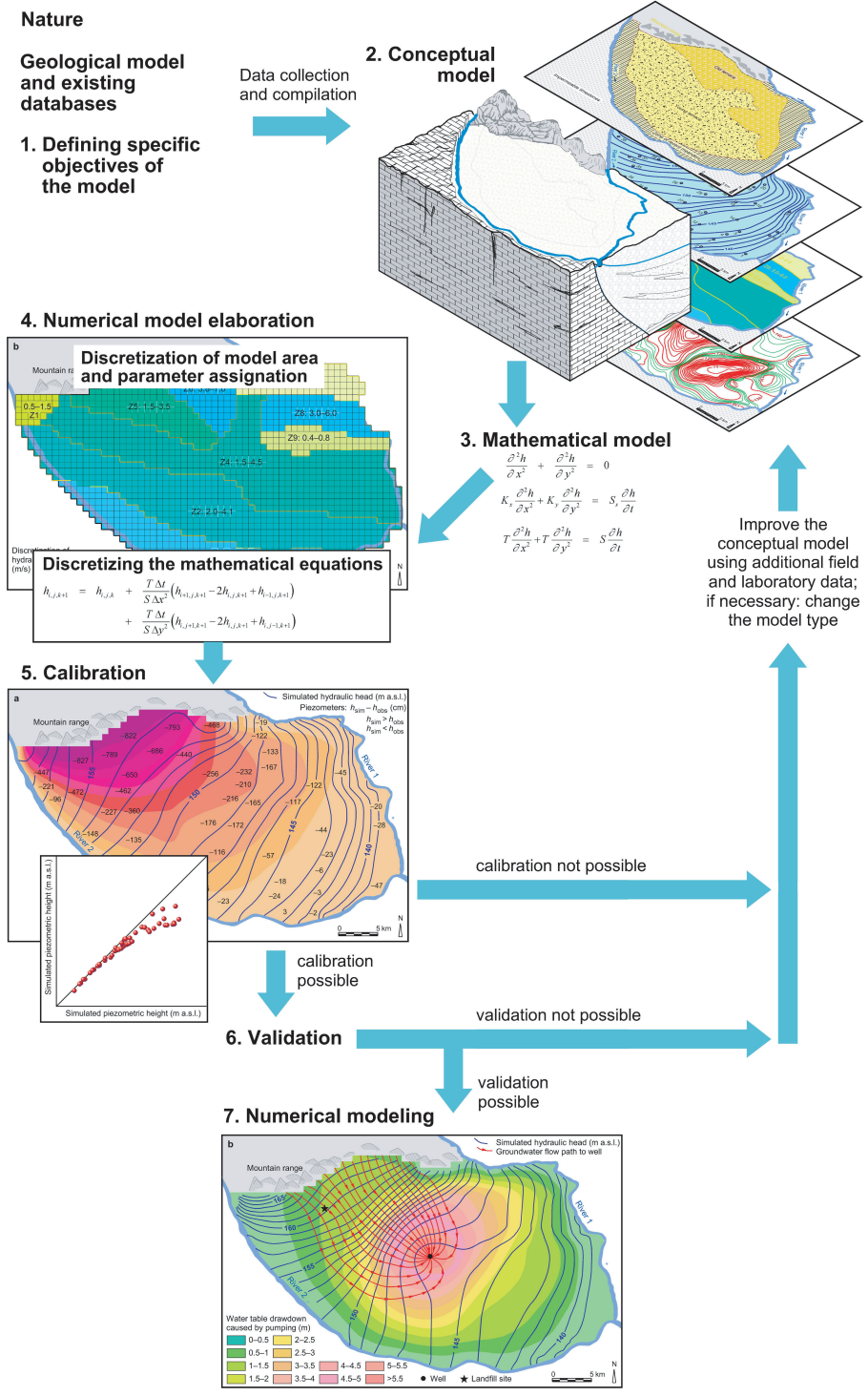


Figure 6.1. Schematic representation of the elaboration of a numerical model.

parameters, fluid and material properties, etc., to each cell or element; (3) Assigning boundary conditions to the mesh or grid (external and internal ones).

- Calibration of the numerical model, where the values of the numerical or physical modeling parameters in the computational model are optimized so that a good fit between simulated and measured field data is achieved, and the derived results are plausible. Model calibration is done using field data collected in the past and compared with the numerical results.
- Validation of the numerical model is used to determine the degree to which a model is an accurate representation of the real world from the perspective of the intended uses of the model (AIAA 1998). It is performed using field data that have not been used for model calibration.
- After model calibration and validation, a sensitivity analysis is done to determine the most important parameters affecting the behavior of the system. If the model uncertainty is low (comparison between numerical results and experimental data), the numerical model can be considered suitable to perform the numerical simulations according to the specific tasks for which it was developed (e.g., to make predictions).

In this chapter, we will learn, step by step, how to construct and use a numerical model. The main steps for constructing a conceptual model to be used in the development of the numerical model and the simulations are explained in a general form. A simplified example illustrates the different steps. In this example, a regional stationary groundwater flow model is developed.

6.2 DEFINING THE OBJECTIVES OF THE NUMERICAL MODEL

Numerical models are used for performing simulations to reconstruct processes which occurred in the past, and to forecast processes of complex real subsurface systems, such as aquifers or geothermal reservoirs, in which numerous coupled processes with interacting parameters and parameter functions drive groundwater and steam movement, as well as the transport of solutes, gases, and heat.

Numerical groundwater-flow and transport models can be used as tools for feasibility studies and planning in the areas of water supply for drinking water, agriculture, industry, mining, energy production, and civil engineering. Numerical simulations allow the investigation of a wide range of subsurface conditions. The objectives of the simulations could be: (1) Optimizing groundwater resources management and interpreting the results of groundwater monitoring, (2) prediction of groundwater influxes during execution of engineering foundation works, tunnels, and hydraulic engineering projects, (3) predicting the fate and transport of anthropogenic and natural contaminants to evaluate the risk of contamination for aquifers, and design remediation and protection measures, (4) designing projects for nuclear waste storage underground, (5) designing projects for seasonal heat storage in the subsurface, and (6) studying the possibility of geothermal energy exploitation and the evolution of geothermal fields under exploitation.

The type of simulation model constructed depends on the questions considered. Due to the wide range of possible applications (see Tables 6.1 and 6.2), the model constructed can be very different, even for similar situations, depending on the specific characteristics of the problem and questions being addressed. This can be easily recognized when we consider an example in which an aquifer that is used as a drinking water supply was anthropogenically contaminated by an accident in an industrial plant. Here, depending on the goals of the questioner, such as the contaminating agent, legislator, victims, insurance companies, citizen associations, communities, political parties, mass-media, etc., the aims of the numerical model and the resulting simulation will be different. For the evaluation of groundwater contaminations, the DVWK (1989) created a questionnaire:

- Is contamination accidental?
- Which are the major substances causing the contamination?
- What is the extent of the damage?
- Who caused the contamination?
- Can contamination be demonstrated/proven?
- To what degree is the person/organization that caused the damage accountable for it?

Table 6.1. Overview of principal applications of numerical groundwater flow models.

Groundwater exploration and decision-making tool for groundwater management

- (1) Modeling an aquifer response (e.g., changes of the groundwater level, changes of groundwater quality, propagation of contaminant fronts, changes of temperature) caused by a natural or anthropogenic stimulation (stress; e.g., a certain water or energy withdrawal/entrance or contaminant input) on the aquifer, in evaluations of past processes and future forecasts
- (2) Establishing groundwater balances
- (3) Delimitation of groundwater protection zones around water works, wellhead protection area delineation
- (4) Optimization of groundwater withdrawal by selecting the most appropriate design of the exploitation method (e.g., single well, group of wells, horizontal well, filter gallery), and optimizing the exploitation rate(s)
- (5) Evaluation of aquifer tests (pumping, slug and bail tests)
- (6) Regional numerical models for evaluation of regional groundwater resources and balancing regional groundwater recharge; forecast of the effect of future groundwater exploitation on groundwater levels
- (7) Modeling the infiltration of river water into an aquifer (bank filtration) to assess contamination hazard of aquifers by contaminated surface waters

Soil and rock excavation and foundation work; tunneling projects

- (1) Forecasting of the water influx and optimization of drainage measures in excavation pits (e.g., pumping rates needed for proper removal of groundwater entering excavation pits, decision about the need of closed pits or sheet pile walls)
- (2) Determination of the pumping rate needed to lower the water table at the required level, and estimation of pump discharge for reduction of the lifting force on a building to decide if other counter measures are needed (e.g., increasing the weight of the foundation of the building, etc.)
- (3) Estimation of groundwater influx into tunnels during and after the construction phase, in order to define the specifications of the construction plan, and to determine tunnel casing needs

Hydroelectric projects and hydraulic engineering

- (1) Optimization of the construction requirements for storage dams: Estimation of water percolation through, below, and around storage dams, to design proper measures to reduce flow rates, e.g., use of low permeability bottom layers or liners, or inject special slurries (e.g., cement) to reduce the aquifer permeability
- (2) Modeling changes of the natural groundwater flow field during construction of a dam and changes caused by the filling of the storage lake, and assessment of the resulting environmental impact
- (3) Evaluation of groundwater flow around weirs and below sluices

Mining projects

- (1) Estimation of groundwater infiltration in subsurface mining constructions (e.g., galleries)
- (2) Estimating groundwater influx in open pits and optimization of remediation methods

Agriculture

- (1) Modeling as tool to optimize groundwater management (see under: Groundwater exploration, water management)
-

- Is the person/organization that caused the contamination still continuing the polluting activity?
- What is the chronological evolution of the contamination?
- How would contamination evolve if no measures to counteract it are taken?
- What urgent measures have to be taken?
- What preventive measures can be taken to avoid future damages?
- What are the collateral actions of certain measures?
- Is it possible to prove the effectiveness and safety of the measures?
- How long will the decontamination take?

Corresponding questionnaires can be developed for other cases, e.g., evaluation of geothermal resources, or the prediction of geothermal field responses using numerical modeling. In any case, the accuracy and reliability of the answers depend on the level of knowledge available and on the complexity of the system to be modeled.

Table 6.2. Overview on principal applications of numerical groundwater flow, solute and heat transport models.

Solute transport modeling

Natural and anthropogenic contamination, protection, and remediation

- (1) Modeling and forecast of the fate and migration of contaminants in aquifers for risk evaluation, to define remediation methods and their design, and to establish protective measures (including reactive and multiphase transport modeling; bioremediation modeling)
- (2) Delineation of water protection zones around water works, recharge areas, etc.
- (3) Groundwater contamination hazard assessment (deep and shallow aquifers) and definition of protection needs
- (4) Evaluation of landfill leaching and its influence on groundwater quality
- (5) Evaluation of the impact of injecting waste water into deep aquifers
- (6) Modeling of seawater intrusions into freshwater aquifers in coastal areas, uprising deep saline groundwater in overlying freshwater aquifers (e.g., due to increased stress on the freshwater aquifers caused by increased exploitation), and definition of sustainable maximal yields

Tracer test evaluation

Immiscible flow of oil and water in hydrocarbon reservoirs

Mining projects

- (1) Environmental impact study of mining activities on the chemical quality of groundwater resources

Agriculture

- (1) Environmental impact study of agricultural activities on the chemical quality of groundwater resources

Heat transport modeling

Non-geothermal systems (cold aquifers)

- (1) Evaluation of groundwater system heat storage: assessment of recharge and discharge areas (water volumes), heat discharge fluxes, available energy, and evaluation of possible efficiency
- (2) Heat pump optimization regarding site selection and design
- (3) Evaluation of heat production at radioactive waste storage sites to optimize storage

Geothermal systems

- (1) Modeling convective geothermal systems (water-dominated systems, steam-dominated systems, two-phase systems) during the exploration stage, and during exploitation in order to optimize exploitation (and to avoid cooling of the reservoir due to unsuitable re-injection of residual fluids and/or over-exploitation)
 - (2) Modeling of Enhanced Geothermal Systems (EGS); Simulation of artificial stimulation, to achieve optimal rock deformation for increasing porosity and permeability of the geothermal reservoir.
 - (3) Modeling radial and vertical heat flow in geothermal wells to optimize exploitation and to determine the most suitable well field design, number and location of production and re-injection wells, production rates, and re-injection rates
 - (4) Analysis of pressure and injection tests in geothermal wells and slim holes
 - (5) Evaluation of submarine geothermal systems by modeling
-

6.3 CONCEPTUAL MODEL

Before selecting commercial software or constructing a custom-built code for establishing a numerical model, a conceptual model of the problem domain needs to be created. The conceptual model is our idealization of a hydrogeological system, as described by a mathematical and numerical model. It is a virtual representation of a geological system, drawing on maps, cross-sections and existing databases, such as physical and chemical properties, which allows an explicit description of the most important properties that drive groundwater flow, solute, and heat transfer. The conceptual model includes assumptions on (1) governing processes related to groundwater, solute, and heat transfer, (2) transport at the boundaries of the domain, (3) dimensionality, (4) hydrostratigraphy, (5) flow directionality, (6) material properties, and (7) heterogeneity patterns. In other words, a conceptual model is a simplified and systematized high-level representation of the domain containing a set of assumptions. This model constitutes the best understanding of the processes that naturally occur in an aquifer.

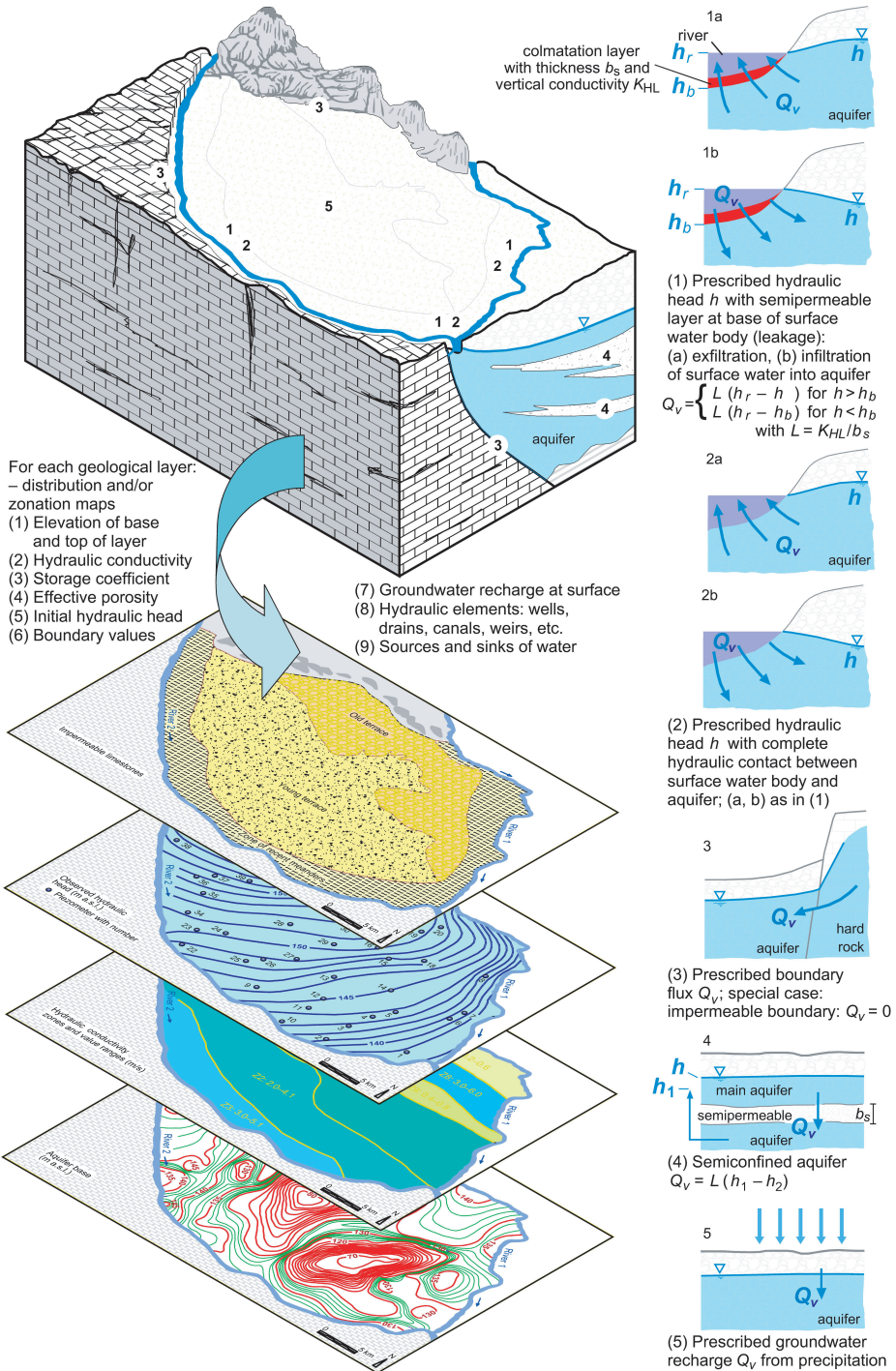


Figure 6.2. Construction of a conceptual stationary regional groundwater flow model by field data integration (left) and principal boundary condition types (right).

Identifying physical, chemical, and biological processes that are relevant to a particular problem and establishing an accurate conceptual model are the most critical issues in the development of a successful numerical model. All pertinent geological, hydrogeological, hydrogeochemical, and other processes and factors that control and drive groundwater flow in aquifers and leakage through semipermeable layers, need to be described and represented mathematically. If the purpose is to model the transport of solutes or heat, then all processes and factors influencing the movement and the chemical alteration of solutes as they are transferred by groundwater should be considered. These processes include the mass and/or heat exchange with the solid aquifer matrix (e.g., sorption and desorption processes, physical and chemical reactions, biological processes, decay), advective, diffusive and dispersive solute transport, and convective and conductive heat transport.

If the conceptual model is not a faithful representation of the real-world system, the numerical model will make incorrect and/or meaningless predictions. Much care is therefore required for this modeling step. Careful evaluation of the information, factors, and parameters that are genuinely necessary for the conceptual model, as well as those that can be excluded is necessary in order to fulfill the special objectives for which the model will be used. The available field data, the available time frame, and the monetary resources, should also be taken into account. In addition, this step should determine whether new field data have to be collected, and which computer codes are appropriate for using as the basis of the model. The accuracy demands must be considered, e.g., it should be determined whether or not field data can be averaged over space (or space zones) and time (or time intervals). An oversimplification may result in inaccurate simulation results. An undersimplification may exact unreasonable demands for labor, computer resources, and/or field data collection.

The construction of the conceptual model requires the compilation of detailed information on geology (geometry of geological layers and matrix properties), hydrogeology (flow regime, hydraulic parameters, sinks and sources of fluids and solutes), fluid properties, hydrochemistry, geothermics (sinks and sources of heat, water phases present), and respective boundary values, which all may be functions of time.

A simple example of a stationary groundwater flow model, which we will use throughout this chapter, is shown in Figure 6.2. In this example, as well as in most other examples in chapter 8, we have selected a two- rather than three-dimensional model, since it exhibits the same principles as a three-dimensional approach, but has the advantage of reduced geometric complexity which may distract the reader from the important issues that we want to address.

The established conceptual model contains all existing information to fully describe the problem domain. After the discretization of the domain and the definition of initial and boundary conditions, the properties of the model (e.g., elevation of the layers, hydraulic conductivity) will be imported into a mathematical model as base for the numerical model. These conditions are needed to initialize the numerical simulations.

In practice, it is often not sufficient to work with only one conceptual model. Often, different conceptual models need to be set up before proper calibration can be obtained. That means that after running the numerical model, the assumptions of the original conceptual model may be reexamined, changed, extended by inclusion of newly obtained field data, or otherwise improved, until the numerical model can be calibrated and validated. This is especially true if the real systems are complex or if the initial field data are poor.

6.4 TYPES OF CONCEPTUAL MODELS

Previously, we defined a conceptual model as a set of assumptions which are used to make a simplified model of a real-world system. However, the word “real-world” may be confusing, since we do not want to model something as detailed as the groundwater flow around each grain of an aquifer matrix (microscale), which has an irregular form and is surrounded by irregular flux. We want a simplified version of the real-world system, which represents only the essential points

of interest needed to solve the tasks according to the defined objectives. So, as in the case of a groundwater flow model, we want to use a field-scale flow analysis approach that can effectively describe the groundwater flow in a porous or fractured aquifer.

Generally for the conceptual model of a porous granular aquifer, the continuum approach is used. Fractured cold (non-geothermal) aquifers and geothermal reservoirs are generally described by extending the continuum approach to ‘single equivalent continuum formulation’ or ‘dual’ (or multiple)-continuum formulation, ‘explicit discrete fracture formulation’, or ‘discrete-fracture network’, and other alternative conceptual models or combinations. These will be discussed in the following overview; for details we refer to the manifold available literature.

6.4.1 *The porous medium continuum model (granular medium)*

Since a microscale approach to solve practical modeling tasks is not practical and the necessary field data for calibrating and validating such models is not available, a suitable macroscale, or field-scale, conceptual model must be found.

The basic assumption is that the domain of interest is a porous granular medium that can be regarded as a continuum (e.g., Bear 1972). The continuum assumption ignores the fact that a medium is comprised of discrete molecules. Instead, properties such as temperature and pressure are assumed to be well-defined at infinitely small scale, and that they vary continuously from point to point.

Rocks, including granular and fractured aquifers, and oil and geothermal reservoirs, are domains of porous media, either granular or fractured, and are composed of a solid matrix and void space that may be filled by one or more fluid phases, such as water, non-aqueous liquids, vapor, gas, or air. When considering groundwater flow and solute transport in non-deformable media, only the interconnected pore space needs to be considered, whereas the solid matrix can participate in heat transport and solute-fluid interactions such as sorption and ion-exchange reactions.

The description of the aquifer domain as a continuum greatly simplifies the mathematical description. However, we must also recognize porous medium domains are not continua, strictly speaking. By definition, a domain may only be regarded as a continuum with respect to any variable if that variable can be defined at every point within the domain. This is not possible for a porous medium since it is composed of at least two phases, characterized by different variables. For example, the variable “solute concentration” cannot be defined in points within the solid matrix (point P_1 in Fig. 6.3), and the variable “solid matrix compressibility” cannot be defined in points within the fluid phase (point P_2 in Fig. 6.3).

On a micro-scale, the fluid flow in the interconnected void space of the porous medium can be described using the state variable fluid velocity obtained from the solution of the momentum balance equation, which is given by the Navier-Stokes equation for water (see chapter 4). However, the solution of this partial differential equation would require knowledge of the exact geometry of the boundary surfaces of the irregular solid-fluid interphases, to formulate the boundary conditions. However, due to the inhomogeneity of the media, this information is unknown. Fortunately, we do not need this level of knowledge in order to find good solutions to real-world problems.

To overcome the problem of heterogeneities of the porous media, an equivalent continuum that smoothes these micro-scale heterogeneities is needed. Therefore, the concept of the “representative elementary volume (REV)” will be used (Bear 1972). The REV is the minimum volume at which a given parameter measurement becomes independent of the size of the sample. In other words, the REV corresponds to the minimum volume of the porous media in which volumes of the solid and liquid phase can be considered large enough to obtain non-random estimates of the parameters describing the solid, the void space, and fluid phases at any point in the porous medium domain. At this scale, the estimated parameters behave as the parameters of a homogeneous medium or continuum. The REV must be much larger than the microscopic scale of

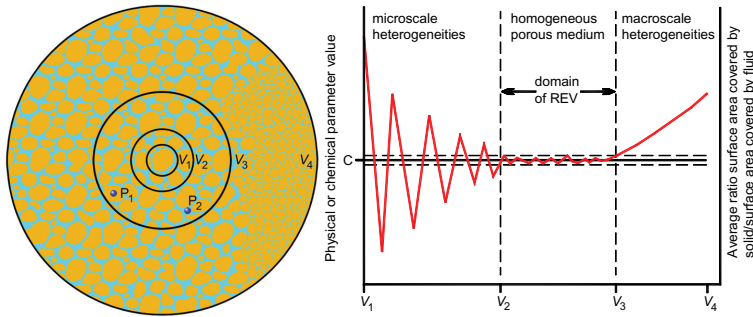


Figure 6.3. Representative elementary volume (REV) approach: The medium becomes homogeneous beyond V_2 (constant value C), where microscale heterogeneities have no more impact being in the lower REV range limit. Above V_4 , macroscopic aquifer heterogeneity becomes important being the upper limit of the REV range, where a continuum exists. The surface area covered by the solid refers to the solid areas present in the cross-section and similarly to the fluid phase.

heterogeneity related to the distribution of solid and void spaces, but much smaller than the size of the considered model domain (Bear 1972).

The principle of the REV concept is shown in Figure 6.3, where in a porous medium composed of one solid and one fluid phase, different-sized volumes are shown around a point. This figure shows the minimal REV for which the physical and chemical parameters of solid and fluid phases are uniform within a certain range of error, and this means the volume beyond which the corresponding, macroscopic, property shows little change.

The next step is to determine the range of volumes for which the porous medium can be considered as homogeneous. We therefore need to search the range to find the volumes that are large enough so that microscale heterogeneity and its effects on variables are negligible, and small enough so that it avoids impacts caused by macroscale heterogeneity. This homogeneity concept corresponds to the definition of a continuum. The volume range in which the physical and chemical properties of a porous media can be represented as homogeneous corresponds to the volume range in which REV's exist (*representative*: structure contained in the volume represents the porous media; *elemental*: because we can represent the entire model domain and all its variables within that volume). This principle is illustrated in Figure 6.3 where for a solid-liquid phase mixture, the solid to fluid ratio compared to the average value (surface fraction in 2D or volume fraction in 3D) of the REV is shown. A region, or volume, can be considered homogeneous if within each cross-section the ratio of areas covered by the solid and the liquid phase is constant, or independent of V , and within a small range of error (dashed horizontal lines in Figure 6.3). The volume range (REV range, V_2 to V_3 in Figure 6.3) for which this applies can be considered a homogeneous porous medium or continuum.

It can be observed that with increasing volume the influence of the microscopic heterogeneities decreases. Consequently, the fluctuation of the ratio of the areas covered by solid and fluid phase decreases and within a small range of error approach (dashed horizontal lines in Fig. 6.3) a constant value. During a further increase of the volume, this value remains constant until V becomes so large that macroscopic inhomogeneities have some influence. In the example within this REV range, the porous medium can be considered a continuum with homogenous behavior in terms of the property surface or volume fraction of solid and fluid.

Properties within each REV can now be defined as the volume-averaged value of any macroscopic variable, thus transforming microscale properties to effective macroscale quantities.

Considering again the two points which previously could not be assigned a value of solute concentration (P_1 in Fig. 6.3, which is located in a solid phase particle), these points can now use the REV centered at P_1 . Take the average value of solute concentration over that REV is assigned at P_1 . This means that now, in each point of the porous medium domain, any macroscopic variable exists, expressed as averages of fluid and solid properties for the fluids or solids contained within the REV. In this conceptualization, if we have a real porous medium, composed of a solid and several fluid phases, each is a continuum which fills up the entire REV, resulting in several overlapping and generally interacting continua. At any point in the domain, chemical and physical parameters are single-valued functions pinned to geometric coordinates, generating a continuous field of the specific macroscopic state variable.

Now, after we have developed continuous fields of macroscopic variables, the microscopic models need to be replaced or scaled up by averaging the microscopic description and microscopic variables over the respective REV to a macroscopic level at which one value for each macroscopic variable is obtained. This process is then repeated for all the REV's in the entire model domain. In this way, the complex and unknown geometry of the microscale void-solid interface will be expressed by different macroscale parameters, such as porosity, hydraulic permeability, and dispersivity. These macroscale parameters can now be used as input parameters for the numerical model.

Next, the governing equations at the macroscale must be considered. If the multiple phases (solid, fluids, gases) are now represented as continua, or intrinsic phases, we can separately write for each continuum mass-, momentum-, and heat-balance equations, and later link them to constitutive relations such as Darcy's law. The set of governing equations for multiphase fluid flow can be coupled to the equations for multicomponent fluid transport and heat transfer to generate the set of simultaneous equations needed to solve the problem. Again, each REV is represented as a continuous entity. Within each REV in a porous or fractured medium, unique and well-defined properties for each constituent of each phase exist spatially everywhere (e.g., groundwater flow velocity and temperature field).

However, there are some limitations to the REV concept. For example, some micro-scale phenomena cannot be described in macro-scale, such as interfacial properties in multiphase porous medium systems. For this reason, coupled pore-scale and simulation-scale models were developed (see e.g., Balhoff 2007). Another issue is that in some coupled problems, the size of the cells or elements required to obtain stable solutions and convergence of the numerical models, is too small for practical solutions. In other words, the necessary size of the cells or elements are smaller than the REV, making it difficult to assign proper values to the properties of the cells or elements. In most cases the grid/mesh is defined intuitively because the effect and distribution of the heterogeneities are unknown (see e.g., Bear 1972).

6.4.2 *Conceptual models of fracture flow*

Due to their importance in many applications of representing field-scale problems in hydrogeology and in geothermal and petroleum reservoir exploration and exploitation, fractured rock conceptual models and their numerical implementations have obtained increasing attention the last two decades. Different conceptual approaches for fracture flow were developed according to:

- The complexity of the hydraulic conduits and highly variable irregular geometry of fractured rocks. These conduits are responsible for the rock storage and flow capabilities.
- The rock type (e.g., crystalline rocks, volcanic rocks, carbonate rocks, or clastic formations), because each type has different hydraulic properties.

Additionally, the selection of the approach depends on the objectives, availability of field data, and the spatial and temporal scale in which the flow and transport in the fracture system shall be described. The definition of the scale is of particular importance because it determines whether temporal or spatial averaging of the flow regime, e.g., over a number of fissures, can be

applied using a continuum approach, whether all or some fissures need to be treated individually in the model (non-continuum or discrete approach), or whether a model with a mixture of both methods is required. The following scales of flows in fractured media are distinguished by Bear and Berkowitz (1987): (1) the ‘very near field’, with water flow in one single fracture which can be described by solely porous medium fluid flow, (2) the ‘near field’, with individual flows to be described individually for each fracture, (3) the ‘far field’, with two coupled flow regimes corresponding to two overlapping continua describing the flows in the porous domain and the fracture domain, and (4) the ‘very far field’, where fracture flow can be described similarly to those of a granular porous medium.

According to these highly variable and different requirements for field-scale fluid flow solutions in fractured systems of different scales, a variety of conceptual models have been developed. These models range from the explicit discrete fracture approach used in ‘near field’ applications, to the single equivalent porous medium model used in ‘far field’ applications. The dual, or multiple, continuum approach covers ‘middle field’ to ‘far field’. Finally, the discrete fracture network approach, which originally was used for intermediate to small-scale applications, is increasingly being used for complex large-scale models.

In the following sections we will introduce only the principal conceptual models used to describe fracture flow. We will address the key points which need to be considered to select a model appropriate to fulfill the objectives of the modeling task. For further details on fractured rocks flow we refer to the resumes in the books of Bear *et al.* (1993), National Research Council (1996), Singhal and Gupta (1999), Dietrich *et al.* (2005), Krasny and Sharp (2007), and the references therein.

6.4.2.1 *Equivalent porous medium (EPM) approach*

The equivalent porous medium (EPM) flow model is the simplest conceptual model to describe fluid flow and transport in fractured porous media. It describes the fractured bedrock as a homogeneous region with effective properties, and assumes that the scale is large enough that the fractured bedrock can be considered a porous medium (see e.g., Pankow *et al.* 1986, Neuman 1987). Since the fractured bedrock is approximated as a single aquifer or reservoir system, the continuum approach can be used. Using this approach, the groundwater flow is laminar at this scale and can be described by Darcy’s law. Criteria for using an EPM approach for fractured rocks are (Long *et al.* 1992): (1) the fracture density is high enough, (2) the fracture orientations are distributed rather randomly instead of limited to a few distinct orientations, (3) the fracture apertures have a constant width instead of randomly distributed widths, and (4) the domain of interest is large (regional extension of model domain).

Due to its simplicity, this approach has been widely used for a gross description of regional flow systems in fractured rocks, in cases where their permeability can be approximated by an equivalent permeability that considers the flow throughout the fracture and porous-media matrix. Regional-scale models are much more likely to be successful compared to intermediate or small-scale models (Huntoon 1995).

However, this approach becomes unsuitable when short-term temporal predictions are made, when fractures are irregularly distributed in the model domain, if fracture spacings are too large, flow velocities too high, and the permeability of the rock matrix too low (see e.g., Pruess *et al.* 1990a,b).

Although an accurate simulation of transport processes is still problematic in many field-scale applications, the EPM approach is often adequate to describe and quickly model hydraulic heads, water fluxes, and general flow direction in the aquifers.

6.4.2.2 *Dual and multiple continuum approach*

Dual and multiple continuum models are classical and widely used approaches for dealing with flow and transport in fractured porous media. These models were introduced in the special form of the double porosity model half a century ago (Barenblatt *et al.* 1960, Warren and Root 1963), and were later extended to the multi-porosity, the dual permeability, and the more general multiple interacting continua (MINC) model (Pruess and Narasimhan 1985, Pruess 1991).

They are based on the fact that we have two domains: (1) unfractured rock masses (rock matrix) which account for much of the porous space (storage) and have low permeability (slow fluid flow), and (2) fractures that have low storage capacity, but high permeability or fast fluid flow (Diodato 1994).

In the dual, or multiple, porosity model the features and properties of fractures and rock matrix are represented as two (or more) separate overlapping and interconnected domains. In the case of a classical dual porosity model we have a primary domain formed by the lower porosity and permeability rock matrix, and a secondary domain with high permeability formed by the fractures.

In the multi-continuum approach two or more continua, representing matrix and fracture systems with their respective specific porosities or permeabilities, share the same model domain. Flow and transport processes can be described for each continuum separately.

The multiporosity/multipermeability approach of Bai *et al.* (1993), which corresponds to a multi-continuum approach, shows that single porosity/single permeability, dual porosity/single permeability, dual porosity/dual permeability, dual porosity/triple permeability, and triple porosity/triple permeability models are all special cases of the multi-continuum approach.

For each continuum we obtain for our mathematical model parallel sets of coupled constitutive equations, which can be solved together with the momentum, energy, and/or species balances. Fluid, solute, and heat exchange, or cross flow between the distinct continua are described by equations with appropriate exchange coefficients (see e.g., Huyakorn *et al.* 1983).

Compared to other approaches, especially models that consider individual fractures, the dual continuum approach does not require as much input data. This approach reduces the effort of establishing the conceptual, mathematical, and numerical model, as well as running the simulations. On the other hand, it is a much more powerful approach for field scale modeling compared to EPM approaches. For these reasons, it can be considered the most widely used model to describe fractured groundwater, geothermal, and petroleum systems.

The use of multiple or dual continuum models which average the transient hydraulic behavior of rock matrix and fractures are often appropriate for describing large fractured rock units. However, they often fail to describe local-scale features.

6.4.2.3 *Explicit discrete fracture approach*

This approach incorporates fractures as explicit discrete elements. In simple approaches, the orientation of the fractures can only exist along the principal axes of the Cartesian coordinate system. In some cases, this simplification well describes the field situation. It has the advantage of reduced need for empirical data, and simplifies construction of the conceptual and numerical models.

The explicit discrete-fracture models have the significant advantage of an explicit description of single fractures (and additionally, conduits and other elements in the case of karst) while allowing the reliable representation of hydraulic head gradients and fluxes between fractures and rock matrix. However, it requires a great deal of information on all single fractures in the model domain (location, geometry, fracture matrix, hydraulic properties), whose collection becomes especially difficult and time-consuming when the number of fractures is high and when fractures are not planar surfaces, but rather tortuous irregular surfaces. One important and useful application of this kind of model is the solution of fluid flow, heat transfer, and solute transport equations at fault zones. Faults can be represented as single fractures. The data describing faults is more easily obtained than data describing smaller fractures in the domain.

For domains with small multiple fractures, the field data requirements reduce the possible application of these models, and they are generally applied for *near-field* applications (see e.g., modeling of conduit systems by Halihan and Wicks 1998, Jeannin 2001). The dual-continuum method, which is conceptually simpler, requires much less computational effort, and similarly to the discrete-fracture approach can describe fracture matrix interaction. This kind of model is preferentially applied to the *intermediate* and *far field* scale (see e.g., Wu and Pruess 2005).

Another suitable simplification of fractured aquifers is to describe them by a two-domain flow model, with one domain comprising the dominant fractures (where, if needed, also non-Darcy

flow laws can be used) and one domain with a network of numerous smaller fractures (using Darcy's law). For the former, an explicit discrete fracture approach can be used. For the latter a continuum medium approach can be used in which the numerous smaller fractures are treated as a porous medium. These approaches can describe the groundwater flows in both systems, coupling them through suitable parameters, e.g., hydraulic head, or water and solute/heat fluxes. This combination allows the simulation of individual groundwater fluxes in the major fractures as well as the fluxes in the fractured rock aquifer, allowing the modeling of large domains.

Another way to reduce the need for highly resolved empirical data is to substitute the deterministic description of each fracture by the statistical attributes of the fractures. The realization of multiple solutions to the problem using the statistical attributes of the fractures obtains the statistical distribution of heads, concentrations, or temperatures in the different elements of the domain. In this case, a unique solution is not obtained, but a range of possible values for the different parameters can be realized.

The accurate description of solute and heat transport in fractured/karstic media in the numerical model, and later in the numerical modeling phase, is very complex due to the difficulty to predict *a priori*, the flow direction, and solute/heat fluxes. These are essential in elaborating on the physical model and defining the boundary conditions of the model. Over the last two decades, investigations of transport processes in fractured media and their numerical modeling have become an important task in the problem solving of hydrogeological, and geothermal reservoir objectives (see e.g., Bear *et al.* 1993, National Research Council 1996, Rausch *et al.* 2005).

6.4.2.4 Discrete-fracture network (DFN) approach

Discrete-fracture-network models describe flow and transport using a class of dual-continuum models, where each fracture is treated as a continuous medium which is surrounded by an impermeable matrix. In contrast to previously described models, the DFN approach does not consider the porous medium (rock matrix), and all flow is restricted to the fractures. This significantly reduces the model complexity and the high computational resources needed for more sophisticated numerical simulations, such as explicit discrete fracture approach discussed in the previous section. However, the complexity remains high compared to continua approaches. The description of each fracture in the model domain makes the DFN approach a powerful solution in cases where models based on continua approaches can not be applied, e.g., when working either in the near or intermediate field, when temporal fast changes are happening, or when fracture distributions are highly irregular. Although the DFN can also be applied in far field to model flow and transport on a regional scale, in domains with thousands of fractures, we need to consider that this modeling approach generally requires a huge volume of empirical data (since we need to describe each individual fracture) and results in high computational expense. The potential for simplification of the fracture network should always be considered. The data requirement and the model construction can be significantly simplified if the fractures can be approximated by lines (in 2-dimensional models) or by planes (in 3-dimensional models).

6.4.3 Simplification by using 2-dimensional horizontal models

In many cases, 2-dimensional horizontal models can be used to describe 3-dimensional groundwater flow and transport problems. Such simplification has significant advantages because it requires much less field data, less time, and fewer efforts in constructing the model.

This simplification is based on the assumption that groundwater flow is practically horizontal. This occurs when the horizontal velocity is much larger than the vertical velocity. This situation often appears when the horizontal extension of the aquifer or geothermal reservoir is much larger than its vertical extension. This is the situation in regional models where horizontal extensions are typically in the range of tens to hundreds of kilometers, whereas the vertical extension ranges from tens to hundreds of meters (e.g., our example).

Using this simplification, in each point of the model, the value of a variable (e.g., hydraulic conductivity, porosity, velocity, solute concentration, temperature, etc.) is obtained by integrating

it over the vertical thickness of the aquifer, and hence, it corresponds to a depth-averaged value (so called hydraulic approach; Bear *et al.* 1992). This makes them functions of the horizontal coordinates only, which then requires much less field data for establishing the model.

It must be noted that such horizontal flow simplification is not valid in special areas of regional models where the vertical flow component could be significant, such as near pumping wells. This is especially true if they are only partially penetrating the aquifer along temporary streams and other surface water bodies that are in hydraulic contact with the aquifer, or at springs. However, the horizontal assumption becomes valid again at a certain distance from these elements. According to Bear (1979), horizontal flow can be assumed at distances larger than 1.5 to 2 times the thickness of the aquifer from the point of vertical flow disturbance.

The horizontal flow assumption is also valid for leaky aquifers. If the hydraulic conductivity of the aquifer is much larger (by many orders of magnitude) than that of the semipermeable layer, and if the aquifer thickness exceeds the thickness of the leaky aquitard, then groundwater flow can be assumed as horizontal in the aquifer and vertical in the semipermeable layer. This can easily be described with a quasi-2-dimensional model in which a vertical leakage in, or outflux, is defined. The validity of this assumption can be easily checked by a modeler through establishing a 2-dimensional vertical cross-section flow model (chapter 8.6 shows some examples of these models).

If solute or heat transport is considered, it must be taken into account that solute concentrations and heat energy are often not equally distributed over the aquifer thickness, and that concentration or temperature values obtained by this kind of model are values averaged over the thickness of the aquifer. However, 2-dimensional cross-section models can be used in many practical cases to solve the modeling tasks according to the objectives without the need to generate a 3-dimensional model with all its complexity. Decades ago, computer resources were not powerful enough to model aquifers in three dimensions. At the present time, 3-dimensional modeling may still not be feasible due to the lack of enough data with regard to the vertical distribution of the parameters. In these cases, 2-dimensional models are still useful.

6.5 FIELD DATA REQUIRED FOR CONSTRUCTING THE CONCEPTUAL MODEL

6.5.1 *General evaluation of sufficiency of available field data*

Before constructing a numerical model and choosing an appropriate commercial simulation program, or writing a custom-designed code, the extent of the experimental data needed for the model must be explained. Table 6.3 shows different data availability scenarios and the corresponding possibilities and restrictions of model elaboration for evaluating the contamination of an aquifer due to an accidental release of contaminants. If existing field data are not sufficiently resolved to elaborate a model capable of predicting the behavior of the contaminant plume, the acquisition of additional information should be planned. Finally, the objectives and goals of the problem statement can be used to guide the modeler to an appropriate formulation. Due to the diversity of objectives and to the fact that each case has its own characteristics, it is impossible to provide a standard recipe for specifying the field data needs in a generic fashion. As an example of an accidental contamination of an aquifer, a scheme of the DVWK (1989) that represents the possible research phases is given in Figure 6.4.

There is significant difficulty in obtaining the necessary field data to elaborate a model at the required resolution in space and time. In transport models of low salinity or low temperature systems, special attention should be paid to the use of pre-calibrated groundwater flow models since such calibration is a precondition for an accurate modeling of solute and heat transport. In these systems, fluid density and temperature are approximately constant. This applies to many groundwater systems, such as most of the aquifers used for drinking water supply. If this condition is not fulfilled (e.g. high temperature variability or variable salinity systems), then the groundwater flow equation must be solved in conjunction with the solute and/or heat transport equations

Table 6.3. Possible use of models depending on various field data available for the example of an accidental groundwater contamination problem (modified from DVWK 1989).

Case	Data situation			Use of numerical models
	Groundwater flow	Solute propagation	Chemical reactions	
I	Information is not available about hydraulic heads and flow boundaries of the contaminated area	Data on total areal extent of contamination is not available	Chemical analyses are available for a few selected points	Impossible
II	Only a few hydraulic head data are available that allow a gross approximation of the flow field	Few solute concentration measurements are available from some wells	Limited knowledge of characteristic components and reaction behaviors	With simple models, it is possible to assess the risk and to plan protective measures; The measurement network must be completed to improve the modeling work
III	The groundwater flow field is well known because there are many wells and hydraulic head measurements at different times	Solute concentrations at wells have been measured allowing the estimation of dispersion parameters	Knowledge of exchange reactions between the solute and the rocks, but the distribution coefficients have not been measured	Calibrated groundwater flow model is available (flow time calculation); Dispersion coefficients can be estimated; Sensitivity analysis can be done; Limited prognosis possible since retardation factor and contaminant influx rate are unsure
IV	Extensive data available for hydraulic heads; Existence of a calibrated numerical groundwater flow model	Concentrations of contaminant in the liquid and solid phase have been determined. The magnitude of contaminant source and its location have been estimated.	Quantitative description of chemical reactions (e.g., retardation factor well known). Distribution coefficient between solid and liquid phase is known.	Prognosis calculations; Reliability range determination; Selection of the optimal protection alternative

because density and viscosity are functions of solute concentration and temperature. This becomes especially important if we consider water with high salinity, such as geothermal brines, where the salinity and temperature have substantial impact on fluid viscosity and density. In these cases, the groundwater flow equation must be simultaneously solved with the solute and heat transport equation.

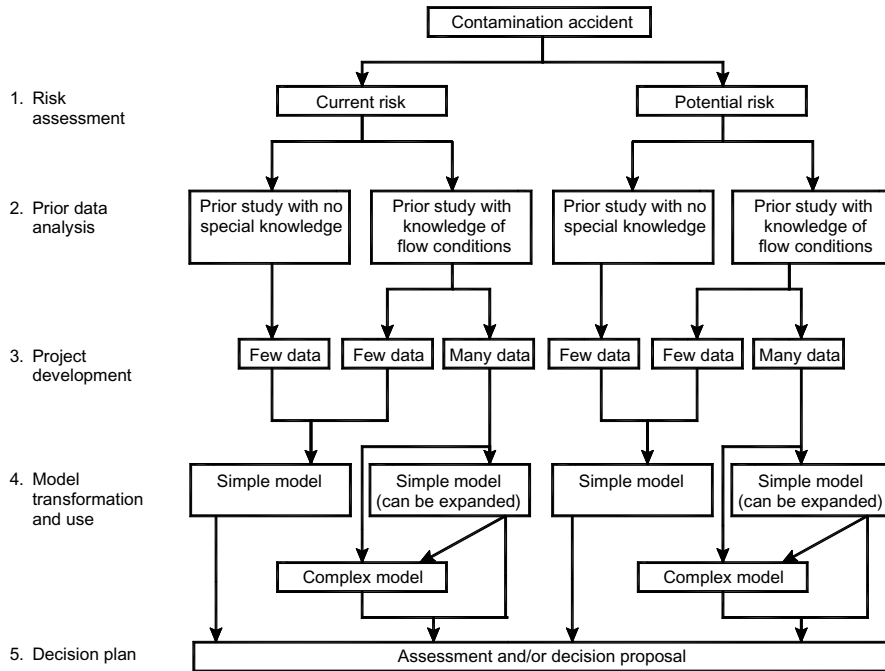


Figure 6.4. Possible research phases in the use of transport models to study a contamination accident (modified from DVWK 1989).

6.5.2 Types of model boundaries and boundary values

Hydrogeological boundaries could be defined as the natural limits of normal regional groundwater flow/transport. They could be large faults, zones of lithological changes, anticlinorium axes, large rivers, seashore, etc. Springs, drains, small rivers, and pumping/injection wells represent internal boundaries. Other internal boundaries can be contacts between different rock layers or rock units and structural-tectonic elements.

There are first order (Dirichlet), second order (Neuman), and third order boundaries, the last being a combination of the first two, and all may be functions of time.

First order boundaries describe the borders of the model where hydraulic head, the concentration of dissolved substances, or temperature is known. Rivers and lakes in complete hydraulic contact with the groundwater body form important examples of the implementation of this boundary type. Here it is assumed that the hydraulic heads of the water tables measured in the field can be considered as fixed, or are changing in a known way, during a simulation. Springs are characterized by points with fixed hydraulic head, corresponding to the topographic height of the spring outlet in the field. At first order boundaries with prescribed hydraulic head, substance concentration or temperature, the respective prescribed values are kept fixed during the simulation by adding the necessary heat, solute, or water input (Fig. 6.2).

Second order boundaries (Neumann) describe model margins for which there is a known flux e.g. of groundwater, solutes, or heat. Impermeable boundaries are a special case within this group. Contacts of the aquifer with impermeable rock units and areas where the groundwater flow lines diverge (e.g. at ridges) are the most important implementations of this boundary type.

When using second order boundaries, the prescribed fluxes are kept fixed by adapting the hydraulic head, solute concentration, or temperature (Fig. 6.2).

In our example, the model area is limited to the SW, S, E and NE directions, by rivers with known water levels. These wide rivers could be considered as first order boundaries (Fig. 6.5).

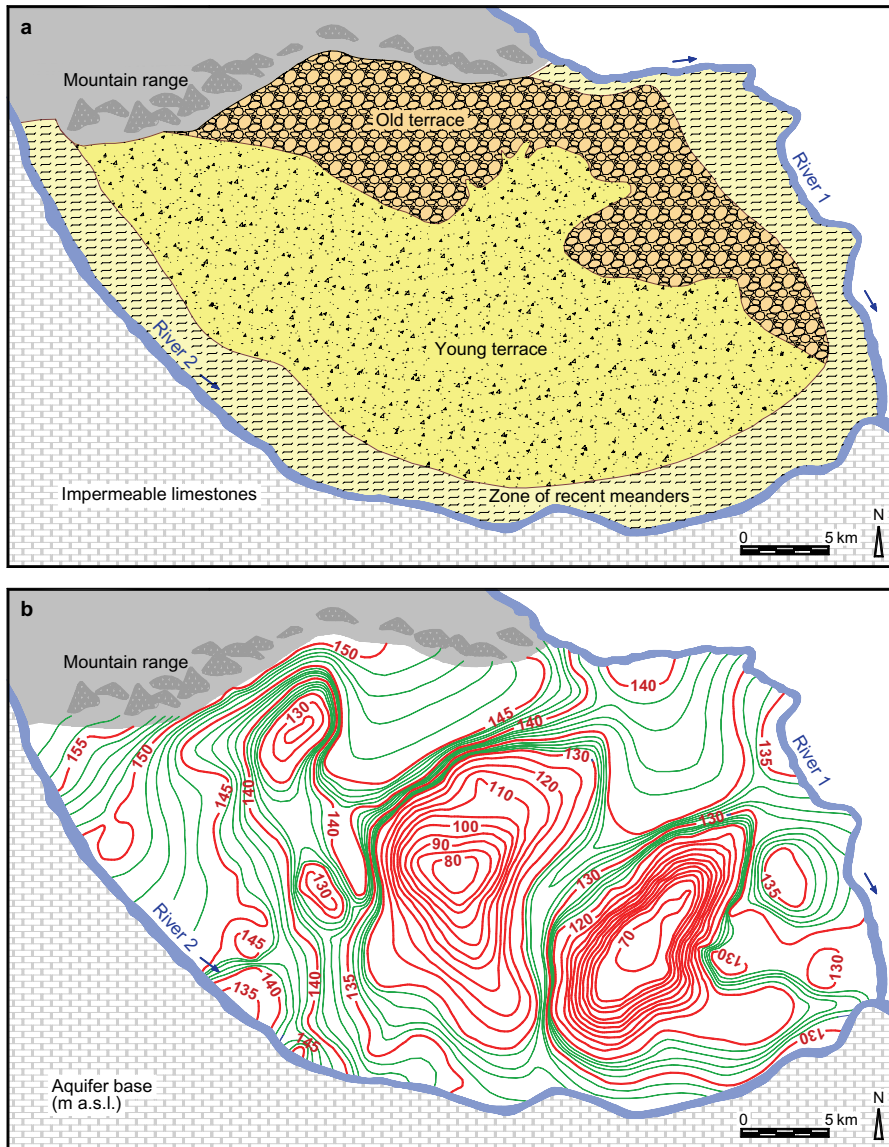


Figure 6.5. Example of model area of regional groundwater flow delimited by the rivers 1 and 2 in the SW, S, E and NE and by a mountain range to the N and NW: (a) Morphology; (b) Location of the aquifer base showing three NW–SW directed depressions.

Along the boundaries to the N and NW, a groundwater inflow into the model area from the mountain range constitutes a second order boundary. The existence of this influx is supposed to exist since the mountain range is composed of strongly fractured metamorphic rocks.

6.5.3 Aquifer geometry, type, solid and fluid properties

The structure and geometry of the different geological layers or units of the model domain comprising aquifers, aquitards, and semipermeable layers, have to be determined because they form the inner and outer boundary values of the model. The aquifer materials that make up each

geological unit and their relevant aquifer, solid and fluid properties, including compressibility, and density, with their spatial variation, homogeneity or heterogeneity, and isotropy or anisotropy, must be evaluated in horizontal and vertical directions. For a list of respective properties which can be a function of temperature, pressure and salinity, see Table 6.4. Spatial variation can be considered by establishing zones, each with the same representative value. Information on the aquifer type is a primary need, whether it is a purely porous granular, a purely fractured aquifer, or a combination of both. The principal groundwater flow directions must be evaluated in order to define whether the flow is preferentially 1, 2 or 3-dimensional. This information, together with the modeling objectives, helps in selecting the dimensionality of the conceptual and the numerical model code.

Depending on model type (stationary or transient flow/transport) different hydraulically relevant parameters with their horizontal and vertical spatial distributions need to be determined. Only hydraulic conductivity, K_H , is required to describe stationary flow. When transient flow is considered, in the case of 3-dimensional flow the specific storage coefficient, S_{sp} (see section 2.1), and in the 2-dimensional vertical case the storage coefficient, $S = S_{sp} \times b_a$ of the porous medium, is needed (b_a : aquifer thickness). In the case of a two-dimensional horizontal groundwater flow in a confined aquifer, the transmissivity $T_v = K_H \times b_a$ (see section 2.1) can be used instead of K_H . The hydraulic conductivity is a function of fluid viscosity, μ_f , which is highly dependent on temperature and to a lesser extent on solute concentration. Hence, in cases where fluid density or viscosity are not constant (in time or space) hydraulic permeability, k , which is independent of temperature and solute concentration should be used as the fundamental parameter instead of hydraulic conductivity, $K_H = (k \times \rho_w \times |g|) / \mu_f$.

When transport is modeled, boundary conditions and initial values of solute concentrations, or temperature distributions need to be specified. Additionally, for the description of the dispersive solute fluxes, J^* , and the diffusive solute flux, J , the longitudinal and transversal dispersivities, α_L and α_T , the coefficient of molecular diffusion, γ_a , and, the effective porosity, φ_{eff} , must be known. Heterogeneity of the aquifers must be evaluated and smoothed out by defining zones with uniform values. Information is required whether there is only one fluid or more, and whether they are miscible or not. The system must be evaluated to see if the solute concentration or temperature

Table 6.4. Overview on required hydraulic, fluid and aquifer matrix properties.

Aquifer (fluid + solid matrix)		
Hydraulic conductivity (or permeability)	$K_H, (k)$	[m/s], [m ²]
Specific storage coefficient, storage coefficient ¹⁾	S_{sp}, S	[1/m], [-]
Aquifer thickness	b_a	[m]
Longitudinal dispersivity	α_L	[m]
Transversal dispersivity	α_T	[m]
Coefficient of molecular diffusion	γ_a	[m ² /s]
Distribution coefficient, retardation factor	K_d, R_d	[ad], [ad]
Fluid		
Compressibility	C_w	[1/Pa]
Specific heat capacity	c_{pw}	[J/kg/K or J/kg/°C]
Thermal conductivity	k_{Tw}	[W/m/K or W/m/°C]
Dynamic viscosity	μ	[Pa·s]
Mass density	ρ_w	[kg/m ³]
Aquifer matrix		
Compressibility	C_s	[1/Pa]
Specific heat capacity	c_{ps}	[J/kg/K or J/kg/°C]
Thermal conductivity	k_{Ts}	[W/m/K or W/m/°C]
Mass density	ρ_s	[kg/m ³]

¹⁾ $S = S_{sp} \times b_a$.

(and their spatial or temporal changes) have a considerable effect on the fluid density, ρ_w , and/or viscosity, μ , and the manner in which the corresponding functions can be quantitatively expressed. Depending on expected fluid flow velocities, the fluid flow may be laminar or turbulent, and may correlate best to differing constitutive relations for conserved quantities or fluxes (e.g., Darcy's law, Brinkman's law, Dupuit-Forchheimer equation, Fick's law). Flow regime may be different at different parts of the model domain. So, Darcy's law may be valid for most of the aquifer, whereas Brinkman's law is needed near a pumping well to properly characterize the flow velocity, which tends to be much higher and may also be turbulent.

The description of adsorption processes requires knowledge of the corresponding adsorption functions. The distribution coefficient, K_d , relates the adsorbed concentration of a solute to the concentration in water and describes the manner in which a solute sorbs to the solid matrix in which it is located. It is an important parameter for calculating the retardation coefficient, R_d , which expresses the degree to which solute propagation is retarded, compared to the groundwater flow. Substance production, chemical reactions, chemical decay, degradation, and decomposition may require specific terms which describe these processes quantitatively. To describe heat transport, the thermal properties of the system must be known, including heat capacity, c_p , and thermal conductivity, k_T , for both the solid matrix and the fluid.

In the case of fractured systems, we need information on the fractures consisting of detailed information on location, geometry, aperture, filling, hydraulic properties, and information on exchange coefficients between the fracture and surrounding rock matrix. For details see e.g., Bear *et al.* (1993), National Research Council (1996), Singhal and Gupta (1999), Krasny and Sharp (2007) and the references therein.

What information is necessary and what can be neglected depends to a large degree on the objectives of the numerical model and hence, must be envisioned individually by the modeler.

In our simple example of a stationary regional groundwater flow, the model area and the aquifer geometry are shown in Figure 6.5. The model area boundaries from the SW, S, E and NE directions are rivers. From the N and NW, the domain is limited by a mountain range composed of fractured metamorphic rocks of low hydraulic permeability compared to the quaternary aquifers of the basin. The model area covers approximately 1000 km². With respect to the morphology of the area, the following units can be differentiated: old terrace, young terrace, and recent meanders (Fig. 6.5a).

Geometry of the aquifer: A single unconfined aquifer is located above Tertiary sediments delimiting its base. The location of this base was determined by geoelectrical mapping and is shown in Figure 6.5b. Three depressions oriented in a NW–SW direction can be distinguished. They were originated by tectonic processes during the Pleistocene age. The thickness of the aquifer increases from its average value of 10 to 30 m, and up to 80 m at the location of the depressions.

Aquifer parameters: The aquifer is mainly composed of gravel with different percentages of sand and has an average hydraulic conductivity of approximately $K_H = 1 \times 10^{-4}$ m/s. Figure 6.6a shows the distribution of hydraulic permeability values for the aquifer as obtained by pumping tests. Effective porosity, φ_{eff} , was determined for aquifer sediments at 20–25% for sandy gravels, and 15–20% for gravel-laden sands using general references for these sediments (Scheffer and Schachtschabel 1989).

The measured piezometric level of the aquifer is shown in Figure 6.6b. The regional distribution of the piezometric level indicates a general flow of groundwater towards the east and the southeast.

6.5.4 Sources and sinks within the model area

This group of field data includes all in- and out fluxes of water, dissolved solutes, and heat that occur within the modeled area and on its inner boundaries. If these quantities vary in time, this must also be prescribed.

- groundwater recharge/discharge through pumping/injection wells,
- groundwater discharge at springs,
- areal groundwater recharge by rainfall or irrigation (infiltration minus evapotranspiration),

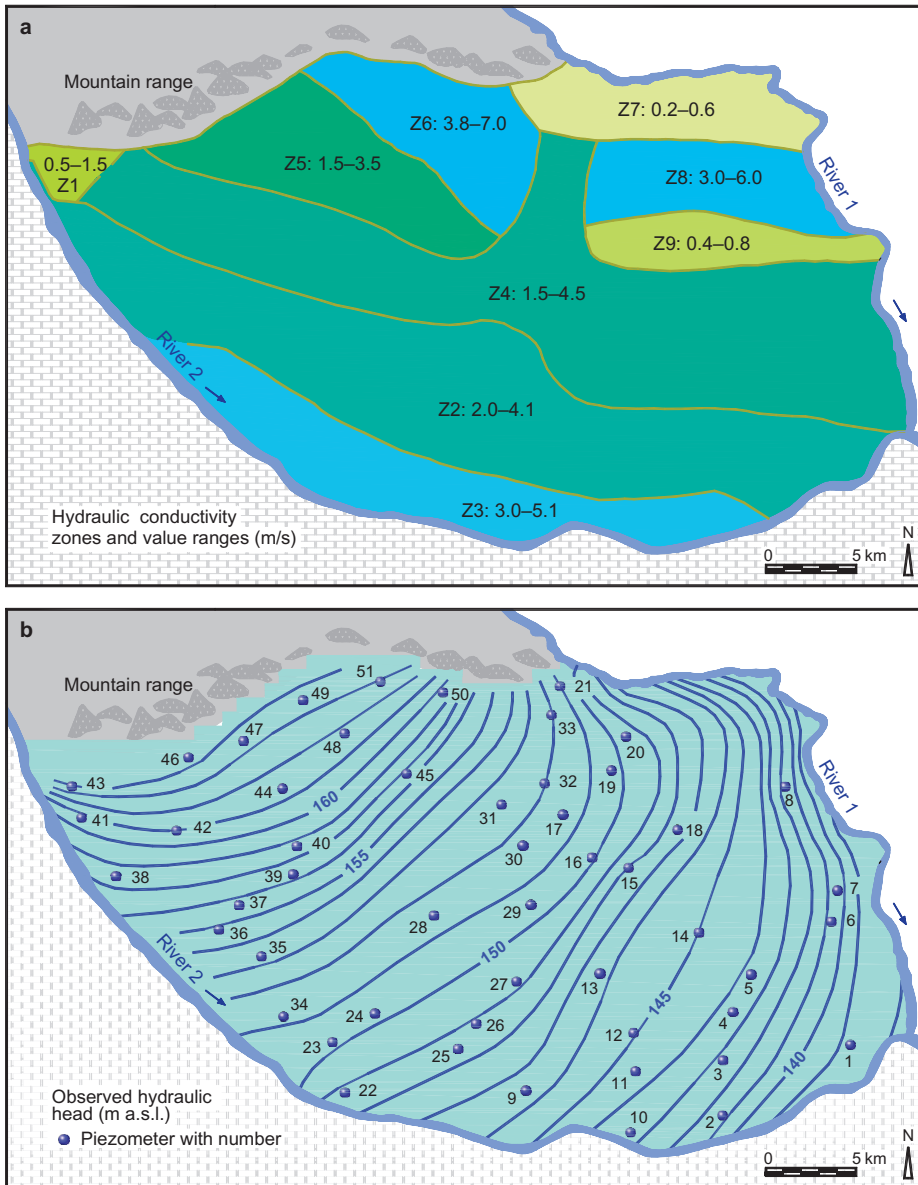


Figure 6.6. Model area example: (a) Zones and value ranges of hydraulic conductivity K_H ; (b) Measured hydraulic heads and location of piezometers 1 to 51.

- groundwater recharge/discharge by infiltration/exfiltration from surface water bodies (rivers, lakes, canals),
- leakage to or from semipermeable layers or from surface water bodies,
- heat inputs,
- heat storage/withdrawal,
- solutes inputs/outputs,
- production/degradation of solutes or heat,
- radioactive decay/production of new substances.

In the case of anthropogenic groundwater contamination, it must be noted that these are generally detected after they appear in the aquifer. This frequently poses a problem, because sources of contamination are usually unknown, both regarding the amount of contaminating solute released into the aquifer, and the chronological development of the event. However, the sources can often be determined with reasonable precision by backwards tracing as long as the groundwater flow field and the current distribution of contaminants are known.

In our example, numerical simulations indicate that aquifer recharge from rainfall is practically uniform in the entire model area, corresponding to about 7% of annual rainfall amounting in 500 mm/year.

6.6 NUMERICAL FORMULATION OF THE CONCEPTUAL MODEL

6.6.1 *From the conceptual to the mathematical and numerical model*

Once the conceptual model is constructed, all the information included in it needs to be converted into a set of mathematical expressions expressing the mass, solute and energy balance and flow equations (including the respective boundary conditions) as addressed in chapter 4 (mathematical model). Then, the numerical model is constructed by discretizing these mathematical equations in space, using a control volume approach, and in time. The resulting matrices of discrete numerical equations and the input data arrays with the boundary and initial conditions are then used to numerically simulate the responses of the real-world system. The values of the input variables can be changed to produce different simulation scenarios.

The control-volume approach uses a mesh, i.e., a field of discrete cells, which covers the model domain in one, two, or three dimensions. For the control volume of each element an individual averaging (or interpolation) of flow, transport, and thermodynamic properties or variables is performed. The control-volume approach includes the following widely used discretization schemes: the conventional finite difference method (see chapter 5.1), different finite element methods, e.g., the classical Galerkin finite element methods (see chapter 5.2.3), as well as boundary element and meshless methods (see chapter 5.2.7), which were developed recently and used for modeling groundwater and geothermal systems.

In most cases, the user can develop numerical models using existing public domain or commercial codes (an overview of the principal codes is given in section 6.8) and only in a few cases does s/he write his/her own computer code.

6.6.2 *Discretizing the model domain of an aquifer*

Numerical solution of flow/transport equations requires discretization of the model area or volume. The mesh is a web of intersecting lines that are embedded within the domain and on its boundaries. The cells are defined by the regions within the intersecting lines, and the intersecting points are denoted as nodes. The cells, or elements, can be triangular, rectangular or of polygonal shape in two dimensions. The corresponding elements in three dimensions are tetrahedral, quadrilateral or prismatic in shape. Volumetric quantities such as temperature or pressure are defined at the centroids of the elements. Rectangular grids can be rotated if necessary to achieve the best fit with the conceptual model area. Wells and drains should be located in centers of grid cells or at nodes of a mesh. For accuracy, a grid or a mesh is refined around important wells or other points where large gradient in hydraulic heads, temperature, concentration, or rock properties are observed.

In the example, the grid constructed for the model area and the boundary cells with respective boundary conditions (prescribed hydraulic head, constant groundwater influx) are shown in Figure 6.7a.

In the next step, hydrogeologic data and parameters of the studied area must be discretized. Rivers, wells, drains, generally with defined hydraulic heads, recharge zones, hydraulic conductivity zones, etc., are assigned to the grid cells or nodes of the mesh.

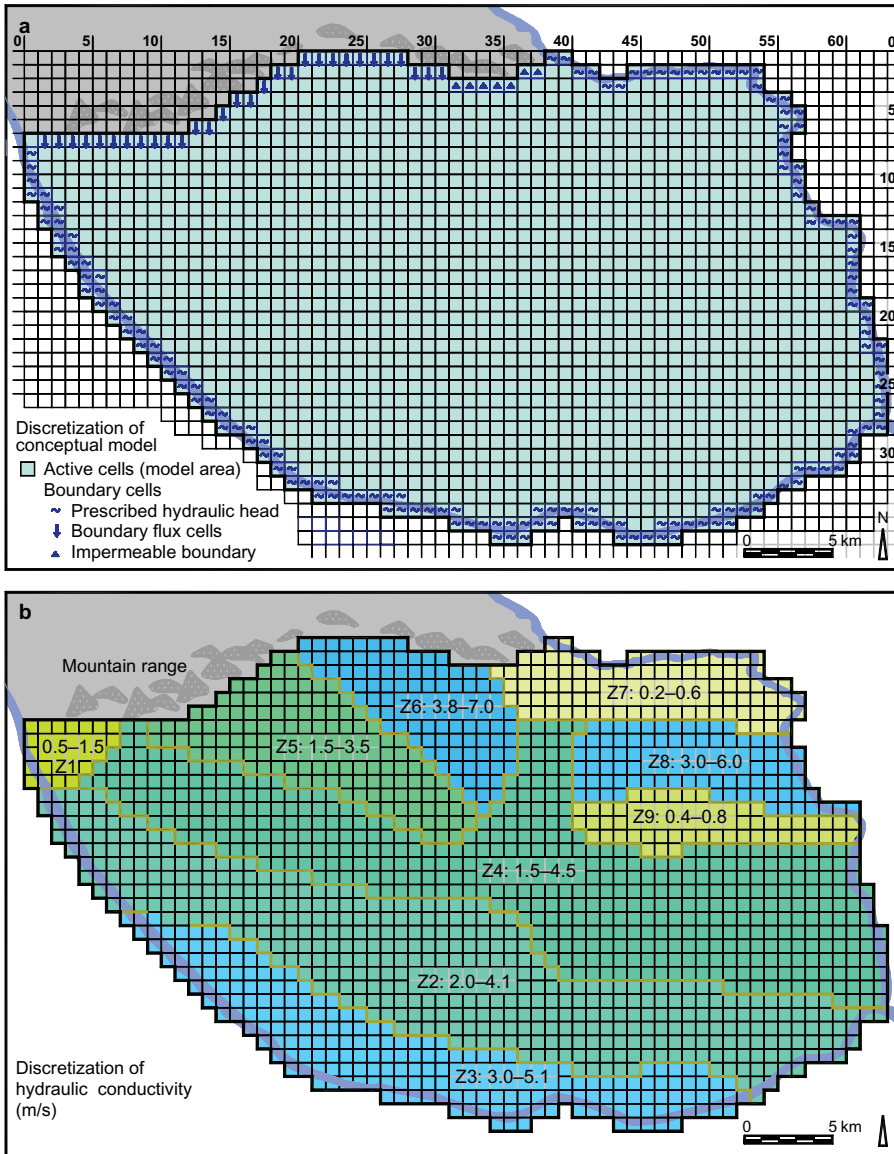


Figure 6.7. Discretization of the conceptual model: (a) Grid (cell size 782.6×782.6 m). The cells outside of the physical model area, which delimit the study area, are neglected in the numerical model by setting their hydraulic conductivity K_H to zero (impermeable); (b) Discretization of the hydraulic conductivity to the model grid.

In the example, the discretization of the hydraulic conductivity zones (Fig. 6.6a) to the model grid is shown in Figure 6.7b. For each zone, the arithmetic mean of the upper and lower value of the K_H range is assigned. The height of the aquifer base from Figure 6.6b is accordingly discretized (not shown). Only cells within the area delimited by the two rivers and the mountain range are active, cells outside are specified as non-active cells.

For the boundary cells, numerical values of the respective parameters (prescribed hydraulic head values or water influx values) are prescribed. The hydraulic heads in boundary cells corresponding to rivers (prescribed hydraulic heads) correspond to the measured surface-water

levels. Since the groundwater flow model for this particular problem is stationary, the storage coefficient need not be considered. The northeastern border of the model area is initially set up as a non-flow boundary, but flow later is specified during the model calibration.

6.6.3 *Initial values*

At the beginning of any numerical transient simulation, a suitable distribution of hydraulic heads, and/or concentrations must be set for the entire modeled area. In order to avoid unrealistic values at the first time steps, these values should be as near as possible to the expected real values. Suitable initial values for transient models can be obtained using the results of the respective stationary model, e.g., the obtained steady-state hydraulic head distribution.

In the stationary simulation example, the initial hydraulic head of the entire model area is set to 147 m a.s.l., corresponding to an average obtained from groundwater level measurements (Fig. 6.6). Exceptions are the boundary cells where the real hydraulic heads corresponding to the measured surface water levels in the rivers were used.

6.6.4 *Ready for numerical simulations*

After all the relative information, including parameters, boundary conditions, and initial values, from the conceptual model, is translated into the discretized numerical model, and after setting all the dynamic values in function of space and time, the numerical model can be run. However, before using it for real problem solving, it needs to be calibrated as described in section 6.9.

6.7 PARAMETER ESTIMATION

There are three principal experimental ways to estimate the hydrogeological parameters needed to construct a conceptual model of a groundwater system or the special case of a geothermal reservoir: (1) remote sensing, (2) field investigations, and (3) laboratory tests and experiments. However, the values of the parameters determined from these three methods often do not correspond to the best values needed to construct and to calibrate the model. As discrete measurements are taken in a continuous, heterogeneous, and often anisotropic medium, the values obtained through experimental methods often do not represent the real distribution of the parameter. The values of the parameters and their spatial distribution are better determined through forward modeling or inverse modeling. The values for the model are refined until a good match between observed and calculated values of parameters, such as hydraulic heads, solute concentrations, or temperatures, is found. This method, which is often used as the method for automatic calibration of numerical models, indirectly determines the parameters (this will be addressed in more detail in section 6.10). It should be noted that the experimental values of the parameters represent the starting values that can be used in simulations. They are used to restrict the values of the parameters that can vary in many orders of magnitude (e.g. hydraulic conductivity). Only a short overview of the first three types of experimental parameter determination methods will be addressed in this section. Examples of parameter estimation and some selected bibliographical references will be given to allow the reader access to the appropriate information.

In the following section, a short overview will be given on remote sensing techniques, followed by a short description of the principal field methods for parameter estimation. Separate methods for cold (non-geothermal) groundwater systems and geothermal systems will be presented. They include geological, hydrogeological, geophysical, and geochemical surface surveys as well as different subsurface measurements, which are performed in boreholes.

6.7.1 *Remote sensing*

The analysis of geomorphological and geological patterns and processes can be facilitated by observing the earth's surface from the air or space. Remote sensing technologies include aerial

photography, multi-spectral, and hyper-spectral satellite imagery, which are used to identify regional and local scale land cover and geological structures such as faults. These features are difficult to recognize from the surface and the use of remote sensing can speed up surface geological mapping by identifying the extension of geological stratigraphic units and structures. After comparison, these can be used to compile regional geological maps using a few points at the earth's surface. Interferometric and polarimetric synthetic aperture radar (SAR) can be used for mapping topography and electrical properties of the earth's surface. From these properties soil water content and salinity can be assessed. Light detection and ranging (Lidar) and interferometric SAR can be applied to map geomorphological changes.

Remote sensing images can be used to identify surface characteristics related to groundwater movement and storage. These characteristics include land morphology, soils, faults, fractures, shear zones, recharge and discharge zones, vegetation, and drainage patterns (Wolski 1998). Several authors highlight the importance of defining lineaments using remote sensing images with special emphasis on identifying interconnected lineaments and their areal extent, lineament length, and associated springs (e.g., Teeuw 1995, Shaban *et al.* 2004, Kresic 1995, Sree Devi *et al.* 2001, Smith *et al.* 1997). For this purpose, airborne photos and Landsat Thematic Mapper images are used (Teeuw 1995).

The different hydrogeological features identified by remote sensing may be combined into the concept of "hydrotopes" (Engelen and Vennecker 1990, Wolski 1998), or units that combine water balance and internal flow regime. Hydrotopes are delineated using lithology, geology, geomorphology, permeability, land use, and vegetation. Hydrotopes are units that transform rainfall into evaporation, surface runoff, and groundwater flow. Advances in remote sensing have generated the concept of 'megawatersheds' (Bisson 1994). In megawatersheds, groundwater flow throughout large permeable regional faults and fracture zones is recognized as critical for exploration, groundwater mapping, and modeling. Some of the fracture and fault systems act as continuous zones where large fluxes of water circulate. The length scales of these systems can be hundreds of kilometers. Bisson (1994) describes the broadest possible three-dimensional catchment areas with multiple recharge zones, primary permeability in the rock matrix, and secondary permeability along the fault and fracture zones.

Remote sensing methods have been used to detect variations in vegetation coverage that can be interpreted as functions of water table depth (Ringrose *et al.* 1998). These authors used two vegetative criteria: dense woody cover and abundance of deep-rooting species as indicative of near-surface groundwater. These two vegetation classes mapped from the Thematic Mapper Imagery were combined in a GIS environment with other hydrogeological features such as geomorphic units and bedrock geology to determine the degree of coincidence with known aquifers. Deep rooting species tend to occur in low-lying aquifers (fossil valleys) and dense woody cover vegetation occurs in topographically higher aquifers. It seems that this technique combined with other studies of remote sensing of geological structures for groundwater flow can provide important information and constraints for conceptual models of groundwater systems.

Other applications of remote sensing to groundwater problems include the investigation of seasonal groundwater fluctuations produced by variations in groundwater recharge in Taiwan (Chang *et al.* 2004). These fluctuations in the water table generate ground deformation due to the dewatering of sediments. In another study, suitable areas for artificial recharge of aquifers in India were identified using remote sensing methods for groundwater exploration (Krishnamurty *et al.* 2000).

For the investigation of geothermal reservoirs, airborne investigations have obtained increased importance in the last few years. Airborne electromagnetics, magnetics, and radiometrics such as the Forward Looking Infrared Radiometry (FLIR), an airborne imaging technique that compiles high-resolution temperature maps (see e.g. survey in Chena, Alaska: Yourownpower 2007 and in New Zealand: Mongillo 2002), allows information on geologic structures to be obtained. This information is important because fluid flow and discharges are structurally controlled in the majority of geothermal systems.

6.7.2 Field surveys of cold (non-geothermal) aquifer systems

Geological, hydrogeological, geophysical, geochemical surface and subsurface field techniques, their appropriate selection, including the choice of instruments and the correct use, and the interpretation of the obtained results, are discussed in detail in Brassington (1998), Weight and Sonderegger (2001), and Moore (2002). Special needs and methods of hydrogeological, geophysical, and hydrochemical investigations in fractured rocks are described by Singhal and Gupta (1999). Goldscheider and Drew (2007) and focus on evaluation methods which are suitable for use in karst areas including hydraulic investigations, geophysics, hydro(geo)chemistry (including isotope chemistry), and water tracing.

6.7.2.1 Geological and hydrogeological studies

Obtaining the field data listed in 6.5.1, which are needed to formulate a conceptual model of a groundwater system, requires detailed knowledge of the rock formations in the area, their stratigraphic and structural interrelationships, and their hydraulic properties. Additional information on sources and sinks of fluids, solutes and heat in the model domain, and on its boundaries is also needed. The availability or the collection of reliable field data is a prerequisite for the construction of an accurate model.

A generalized program to obtain hydrogeological data for modeling is comprised of the following steps: (1) collection and compilation of available existing information, identification of the gaps in the available information, and, depending on the gaps, planning a field program to collect the missing field data needed to establish an accurate conceptual model of the domain, and (2) field work to complement the missing information. First, surface methods are used to characterize geological and hydrogeological surface manifestations of a three-dimensional domain. After these investigations, direct measurements and sampling of rocks and fluids in boreholes allow a correlation between the subsurface properties and the surface observations. In this way an understanding of the stratigraphic interrelation of the rock units, the hydrogeological flow systems, and their flow pattern is obtained.

Standard surface and subsurface methods comprise geomorphological, geological, hydrogeological, and hydrochemical investigations as well as groundwater vulnerability mapping, measurements of surface and groundwater levels, discharges of springs and rivers, rainfall, estimation of infiltration into the underground, and location of surface and groundwater divides. These are used to delimit groundwater recharge and discharge zones, and to calculate or estimate their respective hydrological water balances. The methods comprise direct or indirect measurements (e.g., isotope or non-isotope tracers or empirical methods). For the areal groundwater recharge estimation by rainfall, several methods are used. Brassington (1998), Lerner *et al.* (1990), and Seiler (2007) use hydrochemical methods (e.g., chloride method, isotope tracers), infiltration tests, measurements of the vertical water movement in the unsaturated zone, and the more accurate but more complicated lysimeter experiments. Both hydrogeological surface, and subsurface field techniques, are treated by Brassington (1998), Weight and Sonderegger (2001), and Moore (2002). A compilation of hydrogeological and hydrochemical maps is given in Struckmeier and Margat (1995). Mapping groundwater vulnerability is described in Vrba and Zaporozec (1994) and in Witkowski *et al.* (2007).

6.7.2.2 Hydro(geo)chemical surveys

Analysis of hydrochemical data obtained from springs, piezometers, wells, and surface waters allows insight into hydro(geo)chemical processes in the subsurface and on groundwater-surface water interactions, and may give information on the propagation of solute contaminants in aquifers. Hydrochemical data comprises physico-chemical parameters (color, odor, taste, smell, turbidity, pH value, redox potential, dissolved oxygen, electrical conductivity, density), major ions (Ca^{2+} , Mg^{2+} , K^+ , Na^+ , HCO_3^- , Cl^- , SO_4^{2-} , NO_3^-), inorganic minor elements (e.g., phosphate, fluoride, boron), inorganic trace elements (e.g., heavy metals, metalloids, rare earth elements), isotopes, and organic compounds. Hydrochemical data, graphically displayed, can provide information on

natural geochemical environments related to distinct stratigraphic units with specific material composition (hydrochemical facies), giving important insights into subsurface processes. Mapping of soil gases on the surface can sometimes be used as indicators for fractures, which cannot be recognized by other methods. Gases, such as CO₂ or radon, upraise especially along fracture zones from deeper layers allowing the identification of high permeability vertical pathways (e.g., Padrón *et al.* 2003, Magaña *et al.* 2004). However, to obtain reliable accurate hydrochemical data requires an adequate sampling protocol, conservation and storage, and proper analysis in the laboratory or directly in the field after sampling for those parameters which can change quickly in time such as pH, temperature, redox potential, bicarbonate concentration, etc. Sampling and analysis guidelines include the following points: (1) elaboration and execution of a detailed sampling program that corresponds to the objectives of the investigation and problem to solve. This includes adequate selection of parameters to measure, sampling equipment, additives to preserve the sample (if required), and type of sample bottles, and (2) during fieldwork the elaboration of a detailed sampling protocol with a detailed description of the sampling site (geomorphology, geology, sampling devices, sample preservation, evaluation of possible anthropogenic contamination at the sampling site, e.g., presence of cattle near a sampling well, and peculiarities of the sampling water (turbidity, color, odor etc).

Isotope techniques: Natural or anthropogenic, and stable or radioactive isotopes can be used to trace and identify subsurface processes and are characterized by isotope fractionation and changes in radioactivity levels of decay isotopes. These include groundwater-surface water interactions, evaporation trends, and water-rock exchange processes. Isotope techniques can be useful in the determination of groundwater recharge (areas and quantity), mixing of waters from different aquifers, determining groundwater flow velocity, detecting injected tracers in wells or boreholes (absolute value and direction of velocity), effective porosity of the aquifer, and dispersivity (see section 6.7.2.5.2). Isotope techniques can also be used to derive information about groundwater circulation systems on a large scale and over large time periods which cannot be obtained through direct measurements. Overviews on isotope applications in the field of hydrogeology can be found e.g. in IAEA (1984a, 1984b, 1988), Clark and Fritz (1997), Brassington (1998), Moore (2002), and Mook (2005).

The most commonly used isotopes are those from hydrogen and oxygen, normally given as isotope concentration ratios which are much easier to determine as compared to absolute concentrations. ²H/¹H and ¹⁸O/¹⁶O concentration ratios are used for deriving information on water evaporation/condensation, delineation of recharge areas, and mixing of different waters types. The radioactive isotopes ³H (half-life 12.4 yr), ⁸⁵Kr (half-life 10.76 yr), and ¹⁴C (half-life 5730 yr) can be used to obtain information on the source of water and its mean age, or average residence time in the saturated zone (see e.g. Mook 2005). Due to the very different half-lives, the isotopes used for groundwater age determination depend on the expected order of age which ranges from days, up to millions of years. The age obtained is a “mean” age because the sampled waters are a mixture of water with different residence times.

Groundwater age determination using tritium (³H): Tritium is produced naturally by cosmic radiation, although a much greater production accompanied the atmospheric testing of thermonuclear bombs between 1951 and 1980. Most of this “bomb”-tritium has been washed from the atmosphere by ~1990 (Clark and Fritz 1997). The continuously decreasing concentration of tritium in recharging rainwater due to radioactive decay and due to dilution effects can be used to determine groundwater age. The lack of ³H in groundwater samples indicates a minimum residence time of 60 years and a lack of mixing with recently recharged water. The detection of any ³H in the groundwater indicates a young water component, which is of special interest for the origin and circulation of deep groundwater or geothermal systems (see e.g., Clark and Fritz 1997, Mook 2005).

Oxygen-18/deuterium (¹⁸O/²H) applications: The principal process affecting the ¹⁸O/²H concentration ratio is isotope fractionation during phase transformations as evaporation/boiling or condensation (see e.g., Mook 2005). This temperature dependency makes this method suitable for

the research of geothermal systems. In low-temperature groundwater systems, the isotope fractionation has three principal effects and applications: (1) the *altitude effect*, which is caused by a relative decrease of heavy isotopes in rainwater in comparison to lighter isotopes with increasing topographic height. This makes the $^{18}\text{O}/^{2}\text{H}$ method suitable to estimate the average altitudes of a groundwater recharge area, (2) the *seasonal change* of the $^{18}\text{O}/^{2}\text{H}$ concentration ratio in rainwater, which is caused by temperature changes resulting in lower $^{18}\text{O}/^{2}\text{H}$ concentration ratios in winter and higher $^{18}\text{O}/^{2}\text{H}$ concentration ratios in summer. This allows use of the $^{18}\text{O}/^{2}\text{H}$ method to identify and quantify seasonal groundwater recharge components in groundwater, (3) temperature related changes of the $^{18}\text{O}/^{2}\text{H}$ concentration ratio in recharged groundwater, which are caused by long-term climate changes (cold periods, warm periods). This effect can be used to determine the surface temperature during recharge time, or using additional isotopes for groundwater age determination, to determine air temperature at a certain time (e.g. age determined with the ^{14}C method) (see e.g., Mook 2005).

Another anthropogenic tracer is krypton-85 which is released predominantly by nuclear plants. Its atmospheric concentration has continuously increased since the installation of the first nuclear power plants in the 1950s. Consequently, the ^{85}Kr input into aquifers via their recharge by rainfall started at this time and can be used to determine the mean groundwater residence time for waters that were recharged after the 1950s (see e.g., Clark and Fritz 1997). Using the ^3H and the ^{85}Kr method together, the young water component of an aquifer can be determined.

^{14}C originates from cosmic radiation in the atmosphere and reaches the groundwater through the biosphere where it is measured in the inorganic C compounds. It can be used to determine mean groundwater ages over the last 30,000 years (Clark and Fritz, 1997). ^{14}C analysis should be combined with ^{13}C measurements.

Other isotope techniques used for special applications are: (1) the stable isotope ^{15}N (which is determined in groundwater nitrate) is used to trace and forecast anthropogenic groundwater contamination sources releasing nitrate, (2) the stable isotopes ^{11}B , ^{34}S , ^{87}Sr , and (3) the radioactive isotopes ^{32}Si , ^{39}Ar , ^{222}Rn , ^{223}Ra , ^{224}Ra , ^{226}Ra , ^{228}R , ^{210}Pb , ^{210}Po , ^{238}U , ^{234}U , ^{235}U , and ^{40}K (for special applications of these isotopes see e.g., Clark and Fritz, 1997).

6.7.2.3 Geophysical survey

Geophysical methods can be used to provide a three-dimensional map of the subsurface conditions, such as delimitation of geological layers, their hydraulic properties, faults, fractures, and to give information on groundwater quality. Geophysical methods can be divided into two groups, surface and borehole geophysics. These methods and their application in the field of hydrogeology are described in detail in Kirsch (2006), whereas Repsold *et al.* (1989) give an overview of well logging.

Surface geophysical methods: The main surface geophysical methods used to obtain information on groundwater systems include: seismic reflection and refraction, seismic electrical imaging, electromagnetic (ground-penetrating radar, GPR, in the frequency domain and in the time domain), direct current (DC), resistivity, and magnetic methods (e.g., magnetotellurics).

Seismic, electromagnetics, DC-resistivity, and ground-penetrating radar techniques all provide information about the subsurface structure and the properties of different geological layers under differing physical site constraints. They are used to locate and delimit the distinct geological layers, faults, and fractures in order to obtain the geometric properties and stratigraphy of the bedrock.

Geoelectric soundings (DC-resistivity) are cheap techniques that are widely used to distinguish zones of high and low electrical conductivity. They can be used to determine the limits of geological layers characterized by different materials and electrical conductivities, as well as to determine the limit between the water unsaturated and saturated zones, and the depth to the groundwater table of an unconfined aquifer. Additionally, this DC-resistivity application can delimit confining layers and can be used to distinguish aquifer zones of low (potable) from

high mineralized (non-potable) groundwater, which show contrasting electrical conductivity in aquifers. However, this last application can only be used if the aquifer material is uniform, in order to ensure that conductivity changes are only related to the changes of the water's electrical conductivity, and not to changes of the solid matrix of the aquifer. The intrusion of saltwater in coastal areas is an example of this application. Resistivity methods can additionally be used to distinguish and delineate clay or mineral rich zones.

Borehole geophysical methods: The principal geophysical borehole logging methods used for hydrogeological investigations are comprised of temperature, resistance, natural gamma, resistivity, spontaneous potential, flowmeter, video, gamma, magnetic susceptibility, and caliper logs.

The logs, performed along the entire borehole, provide diverse information on the geological layers of the underground, their solid phase, and fluid properties, as well as information on faults and fractures. This information from direct measurements can be compared and correlated with the results obtained from the surface geophysical surveys in order to calibrate the indirect measurements and to establish a three-dimensional model of the investigated domain.

Spontaneous potential logs provide information on boundaries between different lithologic units, whereas electrical resistivity measurements provide information on the porosity, and natural γ -log on the clay content of the rocks. Both temperature and flow meter logs can be used to delimit water-bearing zones. Caliper logs can be used to identify fracture zones, and together with video logs allow measurement of strike, dip, and aperture of fractures. This information on the fracture properties is important. Additionally, physico-chemical and hydrochemical data on the groundwater (e.g., pH, Eh, electrical conductivity, dissolved oxygen) can be measured along the borehole profile, and together with the other well logging results can be used to distinguish between different sections or aquifers composed of different water types.

6.7.2.4 *Aquifer tests*

Establishing an accurate conceptual and numerical model to describe and simulate groundwater flow and transport in aquifers requires detailed knowledge of the values and spatial distribution of the parameters that are responsible for the hydraulic behavior in the system. These are primarily hydraulic conductivity, storage coefficient, and effective porosity. Additionally, for transport processes, the dispersivity, α , is determined on a field scale by aquifer and tracer test.

Aquifer tests such as pumping tests, and slug and bail tests, are predominantly used to obtain values for the hydraulic conductivity, K_H (or transmissivity, T_v), the storage coefficient (storativity), S , and sometimes the leakage coefficient, L . Tracer tests provide additional information about flow directions and dispersivities, longitudinal and vertical.

Detailed treatment of most analytical methods for aquifer tests or the background theory can be found in Theis (1935), Ferris *et al.* (1962), Stallman (1971), Reed (1980), and Franke *et al.* (1987). Analytical aquifer test method and their interpretations are treated by Boonstra (1989), Kruseman and Ridder (1991), Dawson and Istok (1991), Raghavan (1993), Day-Lewis (1995), Hall (1996), Walton (1996), Batu (1998), Brassington (1998), Weight and Sonderegger (2001), Moore (2002) and Kresic (2007). Butler (1998) addresses slug tests, and Singhal and Gupta (1999) include an overview of pumping tests and slug tests for fractured rocks. Different commercial and public domain software were developed for evaluating aquifer and tracer tests using analytical methods (e.g., Aquifer^{win32}, Aquifer Test, and Aqtesolv). An overview can be found at the International Groundwater Modeling Center (<http://typhoon.mines.edu/software/igwmcsoft/>).

Pumping tests: Among the most common techniques to determine hydraulic aquifer properties are pumping tests. In this test, water is pumped from one well at a steady or step-by-step variable rate, while measuring the piezometric water levels in nearby monitoring wells and/or in the well itself. The response of an aquifer (drawdown characteristics) to the perturbation caused by pumping is measured by the depression of water level as a function of time and the radial distance between the pumping well and the observation well. The drawdown of the observation well can therefore be used to determine the hydraulic aquifer properties (K_H or T_v in confined aquifers) and S values. The steady-state drawdown at the observation well is a function of the aquifer transmissivity alone, and the transient drawdown depends on both transmissivity and storativity.

Pumping tests under steady state and transient conditions are used to obtain information on these two important aquifer parameters. Additionally, the subsequent rise of the water level after terminating the pumping can be interpreted by recovery tests. If there is no observation well available at a suitable distance from the pumping well, then the decline of the water table in the pumping well itself can be used for the estimation of hydraulic aquifer parameters.

Based on Darcy's law, Dupuit and Thiem developed the basic formula for stationary groundwater flow at the end of the 19th century. In 1935, Theis presented a general equation to evaluate non-stationary pumping tests. On this basis, a series of analytical methods were developed for confined, unconfined, and semiconfined aquifers which often require time-consuming graphical solutions (e.g., matching a type curve with the analytical solution on the measured field data). Additionally, the analytical solutions evaluated using this method are restricted to following special boundary conditions: (1) the aquifer has an unlimited horizontal extension, (2) the aquifer is homogeneous and isotropic, (3) the aquifer has a constant thickness and its base is horizontal, and (4) the pumping rate is constant, and the well extraction interval comprises the entire aquifer.

In the last four decades, sophisticated analytical methods were developed incorporating more complex and realistic boundary conditions such as leaky aquifers, spatial limited aquifer (e.g., limited by boundaries of prescribed hydraulic head or an impermeable margin), variable thickness of the aquifer, inclined aquifer base, inclined groundwater table (or hydraulic head level), incomplete well, presence of more than one pumping well, partial penetration of the pumping and monitoring wells, multilayer aquifer systems, anisotropic and heterogeneous aquifers, horizontal filter well, and fractured aquifers (see e.g. Boonstra 1989, Hall 1996, Kruseman and Ridder 1991, Dawson and Istok 1991, Raghavan 1993, Day-Lewis 1995, Walton 1996, Batu 1998, Brassington 1998, Weight and Sonderegger 2001, Moore 2002, and Singhal and Gupta 1999). However, the analytical solutions for these problems often become difficult, require large calculation efforts, and often do not allow the consideration of combinations of several of these special conditions. Also, it is impossible to solve these problems if a greater number of pumping wells and irregular or time-dependent boundary conditions are present. In other words, even when these new analytical solutions are available, they still fail to represent the complex problems that are usually found in real aquifers. For many real aquifers, computer-aided evaluation, based on analytical solutions, or numerical evaluation of pumping tests, is needed.

Slug and bail tests: During a slug test, the stagnant groundwater level in a borehole or well is changed either by instantaneous addition, or withdrawal of a measured volume of water. In a bail test, withdrawal of a defined water volume is performed using a bailer or pump which is technically more difficult since instantaneous water removal must be fast and since the equipment disturbs the water level measurements.

The characteristics and duration of water level restoration to the initial, before the test, quasi-steady state depends on the hydraulic conductivity of the system. Therefore, the registered groundwater level versus time curve can be used to derive values for the hydraulic conductivity.

Compared to pumping tests, which normally require measurements in observation wells, slug tests are easier to perform and do not require pumping, but they lead to less accurate and less representative results. The results of pumping tests with measurements in surrounding observation wells are more accurate. The values obtained from slug tests correspond exclusively to a small area around the borehole itself. It is a very useful method if a large number of wells must be tested, if no pumps can be used, or if the purpose is to obtain preliminary estimates.

There are many different analytical solutions for the evaluation of slug tests. Classical methods are the Hvorslev approximation, which approximates the transient water flow by a simple exponential function, and which is valid for confined aquifers and partially for unconfined aquifers (Hvorslev 1951). The Bouwer-Rice method has been applied for confined and unconfined aquifers (Bower and Rice 1976, Bower 1989), and the Cooper-Bredehoeft-Papadopulos method is suitable for large diameter wells (Cooper *et al.* 1967).

Although slug tests are generally conducted as single-well tests, multi-well slug tests are also done. In multi-well slug tests, one well is used for the injection or withdrawal of water, and the others are used as observation wells.

6.7.2.5 *Tracer tests*

Tracer techniques comprise marking the groundwater or surface water with substances that can be sampled and analyzed along the flow path, and trace the hydraulic behavior of the water. Tracer techniques are the only methods that allow a direct observation of the flow paths and dynamic behavior of the water. On a field scale, groundwater flow can be traced in a porous or fractured medium. The discharge of rivers can be determined by tracers, which is especially important for conditions with a highly torrential flow regime (e.g., mountain rivers) with restricted applications for other techniques. Tracer tests are an essential tool to derive information for complex transport processes which are controlled by numerous factors of heterogeneous geologic and geochemical environments with physical-chemical interactions between the flowing groundwater, dissolved solutes, immiscible substances (e.g., organic contaminants), and the solid phase (adsorption, retardation). On a laboratory scale, tracer techniques can be used in column experiments (see 6.7.4). Tracer tests and their evaluation are described by Terry (1981), Käss (1992), Weight and Sonderegger (2001) and Singhal and Gupta (1999).

6.7.2.5.1 Overview on principal artificial tracers and their applications

The type of tracer applied depends on the local situation, the available equipment, and the objectives. There are chemical substances (reactive or non-reactive; inorganic or organic; ionic and non-ionic; volatile and non-volatile), isotopes (stable or radioactive), and particle tracers.

Regarding the method of measuring tracer concentrations in observation wells, we can distinguish the following types:

1. *Non fluorescent dyes*, which can be detected qualitatively by visual methods (color) or quantitatively by measuring the concentration of fuchsine acid, basic fuchsine, malachite green (aniline green), erythrosine, amaranth, carmoisine, Ponceau 4 R, methylenblue, or potassium permanganate (brilliant blue) with a field photometer.
2. *Fluorescent dyes*, for which concentrations are measured using their fluorescent properties by fluorimetry; e.g., uranine, eosine, naphthionate, pyranine, rhodamine (B, WT, and WTS), sulforhodamine (B, G, WT, WTS), lissamine, fluorescent micro- and nano-particles.
3. *Salts*, the concentration of which can be determined either by measuring the electrical conductivity (NaCl), using ion-sensitive electrodes, or analyzing specific salts: Cl^- (in form of NaCl), Br^- (in form of KBr), difluorobenzoate, Li^+ (lithium in form of LiCl), $\text{Na}_2\text{B}_4\text{O}_7 \cdot 10 \text{H}_2\text{O}$ (borax), In^{3+} (indium in form of indium-ethylenediamine tetraacetic acid complex; In-EDTA), and iodide.
4. *Radioactive tracers*, which are quantified by measuring the radioactivity of the water sample, e.g.: ^3H , ^{51}Cr , ^{82}Br , ^{127}I .
5. *Particle tracers*, e.g., spores, bacteria, phages, fluorescent micro-particles.

According to Wernli (2003), uranine, eosine, and rhodamine are suitable for karst aquifers, and naphthionate and pyranine for short distances. Uranine and eosine are appropriate for tracer experiments in granular porous aquifers, whereas for short distances (less than 200–300 m) naphthionate is applicable. If the aquifer is very permeable and if only half-quantitative tracer tests are needed, then sulforhodamine B can be used as a tracer. For small-scale tracer tests, such as in laboratory column experiments of mini-aquifers (e.g., testfields), uranine, eosine, naphthionate, bromide, halite (NaCl), difluorobenzoate, partly nitrate, sulfate, and fluorescent micro-particles are suitable tracer substances. Halite, sulforhodamine B (in waters with low content of suspended load), uranine, and rhodamine WTS (it is not approved in turbid waters), are suitable for discharge measurements in surface waters.

6.7.2.5.2 Field-scale tracer tests performed in boreholes (wells)

Field-scale tracer tests performed in boreholes, or wells, are used to monitor groundwater movement by tracing the path of the moving water and obtaining information on transport parameters controlling the dispersive transport and behavior of solutes in the groundwater. These parameters are: effective porosity, dispersivities (longitudinal dispersivity along, and transversal dispersivity

perpendicular to the flow direction) and retardation factors. The determination of these parameters becomes especially important for heterogeneous media, such as alluvial sediments and fractured rocks in karst terrains. The first quantitative tracer test in karst terrains was performed in 1877 in southern Germany (Käss 1992).

Different types of tracer test designs can be found: (1) a single-well, injection-withdrawal tests, in which the tracer is injected into a well, transported through the aquifer, and then pumped up again; (2) multiwell tests in which a known amount of a tracer is injected into one well or borehole and monitoring its propagation within the aquifer by measuring the tracer concentration versus time (break-through curves) in one (or better more) downgradient located monitoring well(s); (3) multilevel tracer injection and recovery tests, in which vertical variability in transport characteristics is assessed. Multiwell tests can be performed either as (1) forced-gradient tracer test where groundwater is pumped from the observation well (radial flow) or (2) as natural-gradient tracer test, in which the injected tracer propagates according to the natural groundwater flow field (in the simplest case linear flow with a uniform flow velocity in one direction), and is measured in an unpumped observation well.

When performing single well tracer tests, it must be considered that only a small area around the injection well is tested, so that the measured aquifer properties are only representative of this small area, and may highly depend on local heterogeneities. In contrast, if a two, or more, well constellation is used, then the resulting parameter values correspond to an average velocity along the distance between the tracer source and the observation well. In addition, the determination of the longitudinal dispersivity, α_L , from forced-gradient tracer tests can significantly underestimate the real, α_L , if the distance between the injection and the observation pumping well is not large enough (Tiedeman and Hsieh 2004). Hence, to obtain accurate dispersivities for description of solute dispersion under natural-aquifer conditions, either a natural-gradient tracer test, or a two-well tracer test with a large well separation, must be performed.

To investigate the groundwater flow pattern of a domain, conservative, non-reactive, tracers are used, since these are supposed to propagate with the same velocity as the water itself. In this case, the only solute transport processes are advection and dispersion. Advective movement of the dissolved tracer is due to groundwater flow with average water velocity. Dispersion is caused by the variability of pore-water velocities within an aquifer due to heterogeneities and the tortuosity of the porous media. Some solute particles move slower and others faster than the mean velocity, resulting in a broadening of the solute plume and a concentration decrease. If the response of the aquifer to tracer injection is known in a form of the registered break-through curves, then the parameters describing advection (mean pore-water velocity) and dispersion (longitudinal and transversal dispersivities) can be determined by analytical or numerical methods using solute transport models.

Different tracers can be used during the same test (multi-species tracer test, e.g., a combination of a color tracer, and a salt tracer). Nonreactive tracers which describe dispersive transport can be combined with reactive tracers to detect and delimit geochemical aquifer conditions such as dilution, sorption, and reduction reactions as demonstrated in the following example. The reactive tracer represented by nickel, complexed with an organic ligand, e.g., NiEDTA, reacts with the aquifer material. The reaction is a function of pH, adsorption of NiEDTA on Fe and Mn oxyhydroxides that form the solid aquifer matrix, and results in a loss of a part of the injected tracer mass from the water. By comparing the breakthrough curves of the ideal, non-reactive, and the reactive Ni-tracer, the retardation factor of the reactive tracer, defined as the quotient of groundwater flow velocity and the propagation velocity of the reactive tracer, can be determined. Comparison with data on retardation factors as a function of pH, obtained from the literature or in the laboratory, can then be used to reconstruct the pH of the aquifer system.

6.7.3 Field survey of geothermal systems

Similar methods as those used for the determination of hydrogeological parameters describing cold (non-geothermal) groundwater systems, such as hydrogeological, geophysical, and geochemical

techniques, are used to obtain knowledge on the structure and properties of deep geothermal systems.

6.7.3.1 *Geological and hydrogeological surface studies*

Geological and hydrogeological studies for geothermal reservoir characterization involve the same basic geological and hydrogeological investigations as low-temperature groundwater systems (see 6.7.2.1) with some additional studies to assess the particular properties of geothermal reservoirs. These studies comprise geologic mapping of the area of interest, identification of tectonic elements, such as active and inactive fractures and fracture zones, caldera structures, and geothermal surface manifestations, such as hot springs or fumaroles. Together with the results of the other studies (remote sensing, surface geophysics, and hydrogeochemistry), these studies allow the construction of a preliminary conceptual model of the geothermal system and the chemical and physical processes occurring within the system. This model is used in decision-making regarding further steps to investigate and locate gradient wells and slim holes. These results will allow further refinement of the conceptual model and the selection of sites for the production wells.

6.7.3.2 *Hydro(geo)chemical surveys*

Hydrogeochemical surveys, including isotope techniques, are used as a low-cost tool, in comparison to the more expensive geophysical surveys. These less expensive surveys are applied to determine whether the geothermal system is water- or vapor-dominated, evaluate the expected composition and variability of the reservoir fluids, obtain information on the sources of water and heat, and locate the recharge area and estimate the respective recharge rate. This information is needed to simulate the response of the reservoir to exploitation. The chemical composition of waters and gases is used to estimate the temperatures expected in the reservoir (geothermometry) assuming equilibrium with respect to some known chemical reactions that are common in geothermal systems (Chandrasekharam and Bundschuh 2008).

The geochemical survey comprises mapping of geothermal surface manifestations, such as hot springs, fumaroles, solfatares, etc., sampling of water and gases, and the chemical and/or isotope analyses of the water and gas samples. The gas samples are obtained from gas vents or stripped under vacuum from the fluid sample. When drilling has already been performed, water and gas samples are taken from wells. In addition to the applications of chemical and isotopic methods described previously for low temperature systems, in geothermal systems the applications of chemical methods are predominantly based on two principles: (1) to use different water and gas geothermometers to estimate the expected reservoir temperature, and (2) to use natural markers that indicate the magmatic component of the fluid compared to the meteoric component, such as $^4\text{He}/^3\text{He}$ ratios in the gas phase and $^{11}\text{B}/^{10}\text{B}$ ratios in the water phase. The evolution of the geothermal fluids as the magmatic fluids mix with groundwater and react with the surrounding rocks, can also be investigated (e.g., Giggenbach 1988) allowing the assessment of the degree of water-rock interactions for the system. In addition to water and gas samples from wells and thermal manifestations, the gases released by the geothermal aquifer and diffused throughout the unsaturated zone to the atmosphere, are also investigated. Examples are soil radon and mercury, and their areal distribution, and more recently, carbon dioxide fluxes and concentrations of soil gases, such as He and CO_2 (e.g., Padrón *et al.* 2003, Magaña *et al.* 2004). The purpose of the soil gases studies is the determination of vertical permeability pathways or fractures close to the surface. Descriptions of geochemical methods, including isotope techniques to obtain information on geothermal reservoirs, can be found in Nickolson (1993), IAEA (2001), Chandrasekharam and Bundschuh (2002, 2008). These methods are generally used in geothermal reservoir exploration, but the chemical composition of the geothermal fluids is monitored during the exploitation of the reservoirs.

6.7.3.3 *Geophysical surveys*

In the case of a geothermal aquifer, parameters to describe the reservoir are obtained through the same surface geophysical methods used for exploration of deep non-geothermal aquifers

(see 6.7.2.3). Some geophysical methods have been adopted directly from the oil industry and hence, are not adapted to investigate the more complex and irregular shapes found in geothermal reservoirs, as compared to the simpler shapes that are typical of oil reservoirs. However, well logging equipment is generally unsuitable for the high temperatures found in geothermal reservoirs.

Geophysical surveys, which are described in a detailed overview by Manzella (2000), are included in the first study phase of the site carried out at the earth's surface or from the air. Later, if drilling is possible, borehole geophysics can be applied.

Surface geophysical methods: In a first approximation, without having deep perforations, these are used to determine the physical parameters of deep geological layers and structures and their geometry (shape, size, depth), temperatures, and other characteristics of the geothermal reservoir from the earth's surface or from depths close to the earth's surface. The following parameters can be investigated for this purpose: (1) magnetic susceptibility (magnetic survey), (2) electrical conductivity (electrical and electromagnetic methods), (3) propagation velocity of elastic waves (seismic survey), (4) rock density (gravimetric survey), and (5) temperature (thermal survey: determination of geothermal gradients and terrestrial heat flow using temperatures measured at the surface, in sediment columns, or in gradient wells). Knowledge of the geothermal gradient can provide a good approximation of the temperature at the top of the reservoir. Seismic, gravity, and magnetic methods can give information on the geometry of the deep structures (shape, size, depth) of a geothermal reservoir, but they do not provide information about the presence of geothermal fluids in the structure considered a geothermal reservoir. To obtain information on the presence of geothermal fluids in the investigated structure, electrical and electromagnetic surveys are used. The presence of water and dissolved ions decreases the electrical resistivity, allowing the detection of the conductive layer. The magnetotelluric survey can define deeper structures better than electric and other electromagnetic methods.

Borehole geophysical methods: Compared to well logging in low-temperature aquifers or in oil reservoirs, the use of borehole geophysics is limited in geothermal reservoirs since high temperatures and, in some cases, strong corrosion caused by very acidic geothermal fluids, affect not only the sensors of the equipment but also the measuring results because precise instruments cannot be used at these high temperatures. Nevertheless, direct measurements in boreholes remain an important tool, since they allow a comparison of directly measured properties with the results of surface geophysical surveys and allow the calibration of these methods.

Well logging is used predominantly to determine: (1) the stratigraphy of the underground, (2) the permeability of rocks and individual principal fractures, (3) the fluid characteristics, and (4) the subsurface temperature distribution. For the application in geothermal reservoirs, various special methods were developed (see e.g., Manzella 2000), which are predominantly based on resistivity, γ -ray, seismic wave velocity (acoustic and sonic), and density logs. In recent years multi-frequency electromagnetic logging and tomography methods have found increasing application (Manzella 2000).

6.7.3.4 Tests performed in drillings

The hydraulic permeability of geothermal reservoirs is generally attributed to (1) fractured rocks or to (2) large scale fracture systems within otherwise low permeability bedrock. Spontaneous flow occurs within these fractures when wells, slim holes or large diameter production wells, are exploited. To characterize the hydraulic properties of the reservoir, two parameters are used, the injectivity index (isothermal and non-isothermal injectivity index) derived from a steady state injection test, and the hydraulic transmissivity obtained from pressure transient injection tests. Numerous modifications and adaptations of these tests to special situations have been developed. Geothermal tracer tests are another important tool for parameter estimation in geothermal reservoirs.

Injection tests: During a steady state injection test, cold water is injected into a borehole, while pressure and temperature downhole are recorded simultaneously. The injectivity index corresponds to the mass injection rate multiplied by the pressure difference between the flowing

well at the gauge depth during the cold water injection, and the shut-in pressure at the gauge depth, or the pressure difference between the well and the reservoir. For the pressure transient injection test, the injection rate is a function of time and allows for the calculation of the transmissivity values. However, conventional geothermal pressure transient testing methods for characterizing fractured bedrocks were adapted from the oil industry, provide only general indicators of permeability, and are unable to estimate fracture distribution, orientation, and reservoir permeability. Therefore, special modifications of pressure transient testing methods have been developed.

Geothermal tracer tests can be used following the same procedures as described for low-temperature groundwater systems, and additionally allow the consideration of the effects caused by the high temperatures, which influence certain variables. They can be used to determine the mean residence time, the swept pore volume, and the flow-storage geometry. However, most of the tracer tests, which were performed world-wide in over 100 geothermal sites, were interpreted only qualitatively without considering the tracer breakthrough curve quantitatively, resulting in gross test interpretations (Shook and Forsman 2005). Few investigators applied tracer tests to estimate heat transfer parameters (e.g., Robinson and Tester 1984, Axelsson *et al.* 2001), to constrain reservoir-scale numerical models (e.g., Gunderson *et al.* 2002, Bloomfield and Moore 2003), or to estimate the flow geometry. Shook and Forsmann (2005) present a series of Excel macros written in Visual Basic for quantitative interpretation of the tracer results.

6.7.4 *Laboratory tests and experiments*

Different methods are available to determine hydraulic conductivity, storage coefficient, effective porosity, and longitudinal and transversal dispersivities in the laboratory. However, when using these values on a field scale for numerical modeling, it must be taken into consideration that these values were determined on a laboratory small-scale, and probably do not fit the corresponding field-scale values. Other values obtained normally in the laboratory comprise material and fluid properties, such as thermal properties, compressibility, viscosity and density as function of temperature, and solute concentration. Additionally, rock/fluid interactions are determined predominantly on a laboratory scale by using batch and column experiments to identify and quantify processes, such as sorption (adsorption, absorption), ion exchange, and reaction kinetics of chemical compounds which determine solute concentrations in the water. Sequential extraction experiments are used to determine on which mineral phase or organic fraction of the solid matrix the chemical compounds or contaminant are sorbed or precipitated. This information is important in identifying the hydrogeochemical processes occurring between the solid and fluid phase and further, to quantify these processes during the numerical modeling. Applications in geothermal reservoirs, steam quality measurements, and fluid compositions are additionally important.

6.8 SELECTION OF MODEL TYPE AND CODE

After the acquisition of information and field data on the aquifer system or geothermal reservoir of interest, a conceptual model is established in which all relevant transport processes occurring in the subsurface have been identified and expressed by their governing equations. Next, the potentially choices for modeling codes must be evaluated. An evaluation of the suitability of each individual program according to the available field data and the objectives of the modeling effort is needed before the selection of the final code.

It is impossible to provide a full description of all existing public domain and commercial modeling programs. The large number of programs already available and numerous new programs that are under development prevent the compilation of a completely comprehensive list here. Good, periodically updated references can be found in the USGS (United States Geological Survey; http://water.usgs.gov/software/ground_water.html) and IGWMC (International Groundwater Modeling Center; <http://typhoon.mines.edu/software/igwmcsoft/>) catalogues. The latter gives

an excellent continuously updated overview of most public-domain and commercial modeling software. A compendium of fracture flow models is given by Diodato (1994).

In this chapter, we provide only a brief summary of the different types of models and their application possibilities (Table 6.5). In addition, some of the programs that are used in this book in the modeling examples are presented.

6.8.1 Model types

Based on the objectives, the questions to be solved and the nature and quantity of field data, a numerical model can be selected. Models can be classified according to (1) their physical-chemical options, (2) their dimensionality, and (3) the numerical algorithms (see chapter 5) used for discretizing the mathematical equations.

Table 6.5. Overview on principal public domain and commercial software for numerical modeling groundwater flow, solute and heat transport with specific properties, and possible applications. FE: finite element method; FD: finite differences method; RW: random walk. Compiled from USGS (http://water.usgs.gov/software/ground_water.html) and IGWMC (<http://typhoon.mines.edu/software/igwmcsoft/>) catalogues.

Application

Groundwater flow (single phase)

Porous granular aquifers

3-dimensional

MicroFEM (transient hybrid FE/FD flow)

MODFLOW96, 98, 2000, 2005 (transient FD flow)

PMWIN platform (integrates MODFLOW, PMPATH, MT3D/MT3DMS, MOC3D, PEST2000 and UCODE)

2-dimensional

FLOWPATH II (steady-state FD flow)

JDB2D/3D (transient FD flow)

MODFE (transient FE flow)

PLASM (transient FD flow; IGWMC version)

RADFLOW (radial transient FD flow)

Fractured aquifers

FRACFLOW (2-dimensional transient flow, dual continuum approach)

Groundwater flow, solute and heat transport (1 fluid, and solute and/or heat transport)

3-dimensional

COMSOL Multiphysics (transient FE flow and solute and heat transport)

FTWORK (transient FD flow and transport)

HOTWTR (3-dimensional steady-state FD flow and heat transport)

HST3D (transient FD flow and solute and heat transport)

MOC3D (flow and transport; integrated with Modflow and considers advection, dispersion, mixing from other fluid sources, linear sorption, and radioactive decay)

MODFLOWT (FD solute transport module for MODFLOW)

MT3DMS (FD solute transport module for MODFLOW)

MULAT (steady-state FE flow and transport)

PMWIN platform (integrates MODFLOW, PMPATH, MT3D/MT3DMS, MOC3D, PEST2000 and UCODE) allows multispecies solute transport modeling through MT3D module

RAND3D (RW solute transport module for MODFLOW)

SUTRA3D (transient hybrid FE/FD variable density fluid flow and solute and heat transport)

SWICHA (FE variable density fluid flow and solute transport)

SWIFT-98 (coupled transient FD flow and solute and heat transport)

TARGET (series of 2- and 3-dimensional integral FD flow and transport models)

(Continued)

Table 6.5. (Continued)

2-dimensional
ABCSEM (transient FE flow and RW transport)
ASM (transient FD flow and FD/RW solute transport)
BEAVERSOF (set of educational programs: transient FD/FE flow and RW transport)
FLONET/TRANS (steady-state FE flow and transport)
HYDRUS-1D/-2D (1/2-dimensional FE flow and solute and heat transport)
MOC (FD model for the simulation of non-conservative solute transport in aquifers)
PHREEQM-2D (multi-component mass transport model consisting of two coupled simulation programs: HST2D and PHREEQE)
SUTRA (transient hybrid FE/FD variable density fluid flow and solute and heat transport)
<i>Porous granular and fractured aquifers</i>
Comsol Multiphysics (transient FE flow and solute and heat transport)
FEFLOW (3-dimensional transient density dependent FE flow and solute and heat transport in porous aquifers with additional discrete fractures)
SWIFT-98 (coupled transient FD flow and solute and heat transport; explicit discrete fracture and dual continuum approaches)
<i>Fractured aquifers</i>
3-dimensional
FRAC3DVS (transient fluid flow, solute, and radionuclides transport, explicit discrete fracture approach)
FracMan (transient fluid flow, solute, heat and radionuclides transport, dual continuum approach for discrete fracture network)
MOTIF (transient fluid flow, solute, heat and radionuclides transport, dual continuum and explicit discrete fracture approaches)
NETFLO/NETTRANS (steady-state flow in fracture networks and solute transport, discrete fracture network approach)
STAFF3D (transient fluid flow, solute, and radionuclides transport, dual continuum and explicit discrete fracture approaches)
TRAFRAP-WT (transient FE flow and solute and radionuclides transport, explicit discrete fracture and dual continuum approaches)
2-dimensional
FRACSTRAN (steady state fluid flow, solute, and radionuclides transport, explicit discrete fracture approach)
SEFSTRAN (transient fluid flow, solute, and radionuclides transport, explicit discrete fracture approach)
STAFF2D (transient fluid flow, solute, and radionuclides transport, dual continuum and explicit discrete fracture approaches)
TRAFRAP-WT (transient FE flow and solute and radionuclides transport, explicit discrete fracture and dual continuum approaches)
<i>Multiphase flow</i>
Comsol Multiphysics (transient FE flow and solute and heat transport)
FEHM (transient multiphase fluid flow, solute, heat and radionuclides transport, dual continuum and explicit discrete fracture approaches)
MOTRANS (FE model to simulate flow of water, dense or light nonaqueous phase liquid [NAPL] and air, and transport of up to five partitionable species in two-dimensional vertical sections)
PMWIN platform (integrates MODFLOW, PMPATH, MT3D/MT3DMS, MOC3D, PEST2000 and UCODE) allows multispecies solute transport modeling through MT3D module
PORFLOW (2–3 D transient multiphase fluid flow, solute, heat and radionuclides transport, explicit discrete fracture and equivalent porous medium approaches)
STAR (3-dimensional multiphase flow; energy transport in 2-phase, liquid-steam geothermal systems)
SWANFLOW (3-dimensional FD flow of water and an immiscible nonaqueous phase)
TOUGH2 (transient multiphase fluid flow, solute, and heat transport, dual continuum approach; with module TOUGHREACT additionally modeling of chemical reactive flows)
TRACR3D (transient multiphase fluid flow, solute, heat and radionuclides transport, biokinetics, dual continuum and explicit discrete fracture approaches)

(Continued)

Table 6.5. (Continued)

Salt water intrusions	
	Comsol Multiphysics (transient FE flow and solute and heat transport)
	FEFLOW (3-dimensional, transient FE variable density fluid flow and solute and heat transport in porous aquifers with additional distinct fractures)
	HST3D (3-dimensional transient FD variable density fluid flow and solute and heat transport)
	MOCDENSE (2-dimensional 2-constituent FD solute transport for groundwater of variable density)
	SHARP (quasi-three dimensional FD model for simulating freshwater and saltwater flow)
	SUTRA3D (transient hybrid FE/FD variable density fluid flow and solute and heat transport)
	SWICHA (3-dimensional FE variable density fluid flow and solute transport)
Virus transport	
	CANVAS (2-dimensional, composite analytical/numerical (FE) model for virus transport and fate in groundwater)
	VIRALT (modular semi-analytical/numerical model for virus transport and fate in groundwater, transient)
Bioremediation	
	BIO1D (1-dimensional FD model for simulation of biodegradation and sorption of a degradable hydrocarbon assuming an uniform flow field in the aquifer)
	BIOF&T (2-D/3-D) (3/2-dimensional FE model for flow of water and multi-component aqueous phase transport in variably-saturated porous and in fractured media)
	BIOPLUME III (2-dimensional FD model for simulating the natural attenuation of organic contaminants in groundwater)

The physical-chemical options classification indicates the aquifer properties that can be simulated with the model that is under consideration. This classification indicates (1) whether a system can be modeled as a porous grain or fractured aquifer, or a combination of both, (2) whether fluid density and viscosity must be considered as variable (e.g. variable temperature and/or salinity within the domain) or if they can be approximated by constant values, (3) whether the compressibility of the fluid and the granular structure must be considered or not, (4) whether only groundwater flow or additionally the propagation of dissolved solutes and heat will be considered, (5) whether flow and transport is in one or several phases of fluid (water, steam) and whether solutes (miscible fluids or immiscible solutes) occur, and (6) in case of solute transport, whether physical, chemical and/or biogeochemical reactions and interactions occur between the solutes or between solutes and solid phase.

Regarding the dimensionality of models, we can select 1, 2, or 3 dimensions. One-dimensional models can often be used for small-scale cases, e.g., column experiments in the laboratory, or when special chemical or biogeochemical processes along a groundwater flow line are studied. Many tracer tests are often evaluated using one-dimensional approaches. In addition, one-dimensional flow and transport models are suitable for initial assessments (when no details on aquifer geometry and properties are available) and the results of these assessments can be used for defining a field data collection campaign.

Two-dimensional models are much easier to construct and require much less data compared to three-dimensional models, and often approach the real problem with sufficient accuracy. Two-dimensional horizontal models are most useful for describing the regional groundwater flow (also including transport processes in a limited way) if the vertical extension of the aquifer is much smaller compared to the horizontal extension of the model domain, and if only one principal aquifer is present. However, water influxes from over- or underlying the principal semiconfined aquifers can be considered using leakage terms. In these models, fluid density must be considered as constant. This allows neglecting the vertical flow components on a regional scale. Small-scale vertical flows (e.g., at partially penetrating wells, or at sites where water exchange between groundwater and surface water bodies occurs) can be neglected if regional modeling results are considered. A two-dimensional vertical model is suitable if vertical flow components cannot be

neglected, e.g. if various aquifers are present and if changes (hydraulic heads, aquifer properties) in the horizontal direction are low, so that the model plain is parallel to groundwater flow lines. The combination of a horizontal model with vertical models as orthogonal cross-sections of the domain is another option to 3-dimensional models. So, e.g., a regional flow model can be elaborated and in selected areas (e.g., around well fields) a vertical model can be constructed to consider vertical flow components. Two-dimensional models can also be used to describe special 3-dimensional problems if cylinder coordinates can be used to describe these as in the case of radial flow problems, such as when the groundwater flows towards a well.

If the foregoing simplifications are not practical or meaningful, then a fully three-dimensional model must be developed, especially if regional groundwater models with multiple aquifers need be constructed and in situations in which the vertical groundwater flow component is significant or variable density flow is considered. However, this choice requires that the hydrogeological conditions are well known in three dimensions.

6.8.2 *Public domain and commercial software for numerical modeling*

An overview of the principal computer codes used for modeling aquifer systems and their specific application features is given in Table 6.4. The most well known numerical software for modeling groundwater systems with a broad application range comprise MODFLOW for groundwater flow modeling with its different modules developed for solute transport modeling. Most of the codes for groundwater flow, solute and/or heat transport modeling can model 1, 2 or 3-dimensional models, as, e.g., COMSOL Multiphysics, FEFLOW, MOC, SUTRA3D, SWIFT and HST3D for modeling of porous grain aquifers. Some of them (e.g., FEFLOW, COMSOL Multiphysics, and SWIFT) additionally include dual continuum or other approaches, which make them suitable for modeling fractured systems, where the one-continuum approach used by most other programs is not accurate. However, special programs were developed for modeling complex fractured aquifers (including geothermal reservoirs) such as FRACMAN, FRAC3DVS, FRACTRAN for single phase and PORFLOW, TOUGH2, and TRACR3D for multiphase modeling (see Table 6.4), which apply different model approaches described in section 6.4. Then there exist programs for special applications, such as the modeling of multi-phase flow, bioremediation in aquifers, vapor transport, virus transport, etc. (Table 6.4). In addition, there are platforms such as GMS, a groundwater modeling system with interfaces to many programs: MODFLOW, MODPATH, MT3D, SEAM3D, FEMWATER, SEEP2D, and to different parameter estimation modules, such as PEST and UCODE and to stochastic and geostatistic modules. GMS is a GIS (Geographic Information System)-based platform for data in- and output making it a very powerful comprehensive modeling tool. The multi-task GIS-based Windows interface ARGUS ONE works using models such as MODFLOW, MT3D, MT3DMS, MF2K-GWT, MODPATH, HST3D, MOC3D, SUTRA3D, NAPL, PTC, and FEMWATER. Plug-In extensions (PIEs) for this interface are constantly improving by the USGS. ARGUS ONE probably provides the widest possibilities for performing both logical and mathematical operations with GIS layers. Other powerful and well-known platforms are PMWIN and VISUAL MODFLOW software, graphic interfaces for MODFLOW/MT3D/MODPATH. In the following, only those programs used in this book and some few of the frequently used modeling codes will be presented shortly. These comprise ASM, SUTRA, MODFLOW, PMWIN, TOUGH, STAR and COMSOL-Multiphysics. For more details refer to the vendor websites or the program manuals.

6.8.3 *ASM (Aquifer Simulation Model)*

The DOS-version of ASM with its highly didactic structure was published by Kinzelbach and Rausch in 1989 (Kinzelbach and Rausch 1989, 1995). However, the MS-Windowstm-version (Chiang *et al.* 1997, 1998), is much improved and nowadays ASM can be used not only for academic purposes, for which it was originally developed, but is also suitable for many professional

applications in hydrogeology, civil and environmental engineering. This program, compared to many other modeling software, is easy to use for a beginner, which makes it an ideal program to get familiar with the construction and the use of numerical groundwater and transport models. In addition, it can be used free of charge for academic purposes.

ASM is a finite differences model with a friendly graphical user-interface for data input and output, the last allowing direct output in maps or diagrams or alternatively in data files. These data files can be used in other software programs for further processing. ASM allows the simulation of stationary or transient groundwater flow in two dimensions with advective and dispersive solute transport. Aquifers can be confined (vertical and horizontal plane models) or unconfined (horizontal plane models only). ASM allows the construction of a model of up to 150×150 cells and 1000 time periods with different pumping rates for wells. A time-dependent groundwater recharge can be implemented. Additionally, a leakage option allows the modeling of leaky aquifers as well as the interaction between surface waters and aquifers, whose contact is limited, e.g., by a colmation layer.

ASM comprises a finite-difference flow model including a tool for its automatic calibration (steady state model), a random walk particle tracking model (based on Ito-Fokker-Planck theory), and a finite differences transport model, which can be used alternatively for transport modeling. The finite differences flow equations are solved by the PCG (preconditioned conjugate gradient) method using alternatively diagonal or Cholesky preconditioning. Particle tracking (forward and backward particle tracking) uses different velocity interpolation methods and applies Euler-integration to calculate flow paths and travel times.

Additional tools include (1) a *result extractor* to extract simulation results (e.g., hydraulic heads, drawdowns, Darcy velocities, leakage terms and concentrations) from any period to a spread sheet, (2) a *field interpolator* to create contour maps or solid fill plots of input data and simulation results, (3) a *field generator* using Mejía's algorithm, can be used to generate fields of heterogeneously distributed hydraulic conductivity or transmissivity values in order to statistically simulate the influence of unknown small-scale heterogeneities, (4) a *water budget calculator*, which can be used to calculate the water budget of user-defined zones and the corresponding exchanged water volumes between these zones, and (5) a *graph viewer* for output of temporal changes of hydraulic heads, drawdowns, and concentrations in previously defined observation points.

Several of the examples presented in this book were solved by using ASM. However, they can be easily solved using the same data and other modeling software.

6.8.4 SUTRA

The classical public domain modeling program SUTRA (Saturated Unsaturated TRANsport), is applied using its 2-dimensional modeling code in several examples of the book, which are complex and require the simulation of groundwater flow coupled with solute and heat transport considering varying fluid density and viscosity. SUTRA, which can also be used in a 3-dimensional mode (SUTRA3D; Voss and Provost 2002), has been used because of its clear structure and its worldwide use in many applications since its publication in 1984. It exhibits high efficiency, and the clear structure of the program code makes modifications easy.

SUTRA was developed by Voss (1984) from the US Air Force Engineering and Services Center and the US Geological Survey. It can be used to simulate water movement in the saturated and the unsaturated porous matrix with a coupled transport of solutes or heat.

The independent flow and transport equations are solved by a combination of a two-dimensional hybrid finite-element and integrated-finite-difference method. In the flow equation, it is considered that fluid density and viscosity are functions of temperature, pressure, and solute concentration. The parameter functions of these dependencies can be programmed by the user. Boundary conditions, sources, and sinks may be time-dependent.

Solute transport is limited to a single reacting species and accounts for solute sorption (linear, Freundlich or Langmuir equilibrium isotherm), zero- and first-order decay, and zero-order production, dispersion, and molecular diffusion.

The heat transport comprises: (1) conductive heat transport in both the solid and fluid, and (2) advective heat transport in the fluid, which can be divided in free convection (due to temperature dependent fluid-density differences) and forced convection (due to water flow). Heat fluxes through the model boundaries can be advective by groundwater flow or by pure conduction.

SUTRA uses quadrilateral finite elements, in cartesian or cylinder coordinates, which allows great flexibility in covering highly irregular model areas. Pinch nodes can be inserted for local refinement of the mesh. Anisotropy of permeability and heterogeneity with respect to most flow and transport parameters is considered. Areal and cross-sectional models of both confined and phreatic aquifers can be constructed.

Storage coefficient, effective porosity, extension of the elements in the third dimension (perpendicular to the model area), and hydraulic permeability can vary in each element or node. If needed, the time-dependent parameters such as pressure, temperature, solute concentration, in- and outflux of fluid, sources and sinks of heat and solutes may be programmed by the user as a function of time.

A graphical post-processor, SUTRA-PLOT, is distributed by IGWMC with SUTRA. SUTRA-PLOT uses SUTRA input and output files and can be used to draw the finite element mesh with the model boundary, fluid velocity vectors, and contours of pressure, saturation, concentration, and temperature. Other commercial contouring programs are also available to display the simulation results.

6.8.5 *Visual MODFLOW*

Visual MODFLOW is a professional computer program that numerically solves the three-dimensional groundwater flow equation for a porous medium and solute transport modeling. MODFLOW is the most complete and easy-to-use modeling environment for practical applications in three-dimensional groundwater flow and contaminant transport simulations. MODFLOW was originally developed by the U.S. Geological Survey and released to the public domain in 1983. This code was eventually updated to conform to the Fortran 77 programming language. As with most computer programs that are used over a long time period, MODFLOW underwent several overall updates. The first commercial version of MODFLOW was originally documented and released in 1984. The second revised version of MODFLOW was referred to as MODFLOW-88 and released to the public domain in 1988. The third version was called MODFLOW-96. MODFLOW-2000, 2001 and 2002 were developed to facilitate the addition of multiple types of equations. When writing this book, the newest version is Visual MODFLOW 2009.1 and is a product of Schlumberger Water Services (Schlumberger 2009a). Ease of understanding continues to be included as an objective of the design of the code.

The partial-differential equation of groundwater flow described in chapter 4 is solved in MODFLOW by using the finite-difference method (chapter 5). This equation, when combined with boundary and initial conditions, describes transient three-dimensional groundwater flow in heterogeneous and anisotropic aquifers, provided that the principal axes of hydraulic conductivity are aligned with the coordinate directions. The groundwater flow system is divided into a grid of cells. For each cell, there is a single point, called a node, at which head is calculated. The finite-difference equation for a cell is solved using the concept of hydraulic conductance.

Visual MODFLOW 2009.1 is a suite of environmental software applications engineered for aquifer data management and analysis, modeling and simulation, visualization, and reporting, maximizing productivity and minimizing the complexities associated with groundwater and environmental projects. Applications include well head capture zone delineation, pumping well optimization, aquifer storage and recovery, groundwater remediation design, simulating natural attenuation, and saltwater intrusion. Visual MODFLOW is a complete, and user-friendly, modeling environment for practical applications in three-dimensional groundwater flow and contaminant transport simulation. This fully integrated package combines powerful analytical tools with a logical menu structure and easy-to-use graphical tools making possible to:

- Quickly dimension the model domain and select units.
- Conveniently assign model properties and boundary conditions.
- Run model simulations for flow and contaminant transport.
- Calibrate the model using manual or automated techniques.
- Optimize pumping and remediation well rates and locations, and visualize the results using 2D or 3D graphics.
- Simulate the effect of fluid viscosity variations and simulate fluid density as a function of temperature.
- Specify non-linear equations to represent the dependence of viscosity on temperature.

The model input parameters and results can be visualized in 2D (cross-section and plan view) or 3D at any time during the development of the model or the displaying of the results. A temperature species can now be added when defining a new transport variant, allowing simulating heat and solute transport simultaneously. In previous versions of Visual MODFLOW, simulation of pumpage by wells was limited to withdrawal at specified rates from individual cells. With the new version it is possible to simulate intraborehole flow in wells with screens that span multiple layers. The following features have been implemented for this version:

- Head loss is defined with skin parameters for the well screen.
- Linear and nonlinear head loss.
- Different options for each well, including partially penetrating wells, pumping and observation wells.
- Import concentrations from a text file.
- Pumping well optimization.
- Minimizing the mass removal and the pumping/treatment cost of a pump-and-treat groundwater remediation system while maintaining capture of a contaminant plume.
- Minimizing pumping costs of a dewatering system while maintaining head levels below excavated areas.
- Maximizing mass removal rates; maximizing the pumping rate at one or more water supply wells while maintaining a minimum drawdown level in the aquifer or the concentration of an identified pollutant below a specified level.

For numerical solution of the advection-dispersion transport equation, the transport engines provide the following solution methods:

- The particle-tracking based Eulerian-Lagrangian methods: method of characteristics (MOC), modified method of characteristics (MMOC) and hybrid MOC/MMOC (HMOC).
- Standard finite-difference methods: upstream finite difference (UFD), central finite difference (CFD).
- The higher-order finite-volume TVD method.

No single solution method has been shown to be effective for all transport conditions. The combination of these solution methods, each having its own strengths and limitations, is believed to offer the best approach for solving the most wide-ranging transport problems with desired efficiency and accuracy. A brief description of all the above solution methods, and their advantages and disadvantages is found in the user's manual of this software (Schlumberger 2009a). It provides an introduction to all these solution methods, and a discussion and comparison of their relative strengths and limitations with emphasis on their implications in solving practical problems.

6.8.6 Processing MODFLOW for Windows (PMWIN)

PMWIN (Processing Modflow for Windows) is a very powerful freely available platform for modeling groundwater flow and solute transport which integrates the public domain programs MODFLOW, PMPATH, MT3D and MT3DMS, MOC3D, PEST2000 and UCODE (Chiang

and Kinzelbach 1998a, Chiang 2005, Chiang and Kinzelbach 2006, <http://www.pmwin.net>). It was developed by Kinzelbach and Chiang and can be downloaded for free from <http://www.ifu.ethz.ch/publications/software/pmwin>. It includes a detailed manual (Chiang and Kinzelbach 1998a) and there are about 3000 pages of reference material available.

The PMWIN software package combines PMWIN code and all the supported models (i.e., MODFLOW, MT3D, MT3DMS, MOC3D, PMPATH for Windows, PEST2000, and UCODE).

PMWIN integrates the 3D finite differences groundwater-flow model MODFLOW (see section 6.8.5) with its alone-standing modules whose principal capacities are resumed in the following (for details see Chiang and Kinzelbach 1998a, Chiang 2005, Chiang and Kinzelbach 2006):

- PMPATH (Chiang and Kinzelbach, 1994, 1998b) can be used to model the advective transport by using a semi-analytical particle tracking scheme (Pollock 1988) which allows forward and backward particle tracking. Pathlines or flowlines are calculated and can be displayed together with travel time markers, optional hydraulic head contours and groundwater flow velocity vectors.
- MT3D (Zheng 1990) and MT3DMS (Zheng and Wang 1998) allow the modeling of solute transport for the case that the solute does not significantly affect the groundwater flow field, so that the groundwater flow model can be established independently (using the MODFLOW code) from transport and used after its calibration for transport modeling which uses the results of the flow model calculated with MODFLOW. MT3D can simulate the transport of single species solutes in groundwater considering advection, dispersion and chemical reactions, which are limited to equilibrium-controlled linear or non-linear sorption, and first-order irreversible decay or biodegradation. MT3DMS, which is a further development of MT3D allows multi-species solute transport modeling.
- The MOC3D (Konikow *et al.* 1996) simulates the solute transport for a single species considering advective transport, hydrodynamic dispersion and simple chemical reactions, such as decay and linear sorption. MOC3D uses the characteristics method, which applies particle tracking, to solve the transport equation using the hydraulic gradients computed by MODFLOW. By applying MODFLOW as a built-in function, MOC3D can be modified to simulate density-dependent flow and solute transport.
- PEST (Doherty *et al.* 1994) and UCODE (Poeter and Hill 1998) are used for parameter estimation and model calibration. The codes allow to adjust model parameters and/or aquifer excitation data in order to minimize the differences between the model-generated numbers and the data observed in the field.

PMWIN comprises a state-of-the-art graphical user-interface, which allows a very user-friendly model construction with up to 80 layers and 250,000 cells in each model layer, and enables a professional output of the modeling results. Import and output of DXF-files permit the coupling to GIS Systems and other mapping software such as Autocad-Map.

6.8.7 *FEFLOW (Finite Element Subsurface Flow and Transport Simulation System)*

FEFLOW is an advanced Finite-Element subsurface **FLOW** and transport modeling system with an extensive list of functionalities, including variably saturated flow, variable fluid density mass and heat transport, and multi-species reactive transport. It has been established worldwide as a leading commercial software for modeling porous and fractured media. FEFLOW supports an impressive array of features of interest in subsurface flow and transport and is well documented, in terms of both peer-reviewed papers in the scientific literature and a comprehensive set of manuals and white papers. The program has been under development since 1979 by the Institute for Water Resources Planning and Systems Research Inc. (WASY GmbH) of Berlin, Germany, which has recently become a part of DHI Group.

FEFLOW contains pre- and post-processing functionality and an efficient simulation engine. A user-friendly graphical interface provides easy access to the extensive modeling options.

FEFLOW—in contrast to some of the competing products—is not a graphical front end for a separately developed simulation kernel. It is a completely integrated system from simulation engine to graphical user interface. It also includes a public programming interface for user code. For more information, see <http://www.feflow.info>. Key features of the software system are listed there in detail.

The following properties are emphasized:

Basics:

- Finite element method (FEM) for 3D and 2D (horizontal, vertical and axisymmetric plane), transient and steady-state problems.
- Modern GUI: interactive graphics, 3D and 2D visualization (OpenGL accelerated) with multiple simultaneous views and mouse/panel navigation.
- Data interfacing to GIS and CAD.
- Programming interface (C, C++).
- Multiple platforms: Windows and LINUX/UNIX.
- Parallel computing and 64-bit technology.

Flow:

- Darcy flow in porous media.
- Variably saturated flow with analytical formulae (such as van Genuchten/Mualem, Brooks-Corey, exponential and others) or full spline approximation (including a sophisticated spline formula editor to fit measured data) for retention and relative conductivity curves with and without hysteresis.
- Anisotropic hydraulic conductivity can be specified via axis-parallel, layer-oriented or full 3D anisotropy.
- Free surface flow modeled with fixed and moving mesh strategies.
- Variable-density flow: Boussinesq and extended Boussinesq approximations are selectable.
- Fracture flow with different laws of fluid motion: Darcy, Hagen-Poiseuille or Manning-Strickler.

Mass transport:

- Advection-dispersion solute transport with (Henry-, Freundlich- and Langmuir-type) sorption and chemical reaction.
- Single-species solute transport.
- Multi-species solute transport for mobile and immobile species.
- Reaction kinetics formula editor to specify rate expressions in a comprehensive manner coupled with a fast formula code interpreter.
- Density-dependent transport (e.g., saltwater intrusion), free and mixed convection.
- Double or multi-diffusive convection phenomena.
- Dispersion can be modeled either by a linear Fickian law or by a nonlinear non-Fickian law, useful for brine transport under high-concentration gradients.
- Fracture mass transport.

Heat transport:

- Advection-conduction heat transport.
- Free, forced, and mixed convection processes: Variable fluid density expansion for temperature effects is capable of solving large temperature ranges (including 4°C anomaly of water).
- Temperature- and mass-dependent fluid viscosity with a comprehensive viscosity formula editor.
- Thermohaline (coupled flow-mass-heat) convection.
- Borehole heat exchanger (BHE) modeling based on analytical and numerical solution strategies suited for single boreholes and arrays of BHE.
- Fracture heat transport.

Mathematical/numerical qualities:

- Flexible meshing: For 3D hexahedral and pentahedral elements of a trilinear and triparabolic approximation, for 2D quadrilateral and triangular elements of a bilinear and biparabolic accuracy are available.
- A fully adaptive meshing is provided for 2D based on mesh refinement and derefinement (AMR) techniques to enhance the reliability of the numerical simulation.
- Different time marching schemes can be chosen: Automatic time stepping schemes based on a predictor-corrector time integrator for second order (Adams-Bashforth/trapezoid rule) and first order (forward Euler/backward Euler) accuracy as well as Crank-Nicolson or fully implicit schemes at fixed (user-defined) time increments.
- Fast and stable equation solvers for large problems (among others: preconditioned conjugate gradient and algebraic multigrid solvers).
- Various upwind techniques are available to stabilize convection-dominated transport equations (e.g., streamline upwind, shock capturing, and PGLS).
- Parallel assembly of finite element matrices based on domain decomposition.
- Various types of boundary conditions can be specified. They can be time-constant or time-dependent. Specific boundary conditions refer to multi-layer well, BHE, integral flux, seepage, surface ponding and gradient-type conditions.
- Each boundary condition can be combined with constraints to formulate interrelated conditions (e.g., seepage faces, surface ponding or outflowing boundary conditions). Constraints can be time-constant or time-dependent (e.g., used for boundary conditions moving in space and time).
- Optionally, all material properties can also be time-dependent.
- Formula editor can be used to specify relationships for sink/source terms (e.g., implementing user-defined groundwater recharge formulae).
- Nonlinearities occurring in density and viscosity coupling phenomena, for unsaturated problems, free surface conditions, boundary constrained conditions and/or nonlinear adsorption or reaction kinetics are treated via Newton or Picard iterative techniques.
- Particle tracking methods for transient and steady-state flow fields in 3D and 2D.

The advanced interactive graphical working environment, the integration of powerful and modern numerical techniques together with tools highly useful in ‘daily’ handling of data and computational results, the network-based implementation, the power in parallel computing and the open data interface concept make FEFLOW very attractive in practice and research. The features of the package allow the solution of very complex and large problems. FEFLOW is continuously further developed and improved. Service and support of the package are worldwide.

6.8.8 *TOUGH, TOUGHREACT and related codes and modules*

The codes of the TOUGH family allow numerical simulations in a wide field of non-isothermal flows of multiphase, multi-component fluids in porous or fractured media with principal applications in geothermics, environmental remediation and nuclear waste disposal. The actual TOUGH (“Transport Of Unsaturated Groundwater and Heat”) codes were developed by Karsten Pruess at the Earth Sciences Division of the Lawrence Berkeley National Laboratory (LBNL) in Berkeley, California, at the beginning of the 1980s. The original MULKOM code implemented the fact that the governing equations for non-isothermal flows of multi-component and multiphase fluids are of the same mathematical form. This code served for multiple tests and allowed the development of TOUGH and TOUGH2 codes which are based on the integrated finite differences method (or finite volume method, section 5.3). The TOUGH code, which was released in 1987, is a reduced version of MULKOM for two-phase flow of water-air mixtures (Pruess 1987), whereas TOUGH2 code which was released in 1991 is a more comprehensive subset of MULKOM modules (Pruess 1991).

TOUGH2 allows the simulation of non-isothermal flows of multi-component, multiphase fluids in porous and fractured media in one, two, and three-dimensions. Main application

fields are in geothermal reservoir engineering, nuclear waste disposal, environmental assessment and remediation, geologic storage of greenhouse gases, and unsaturated and saturated zone hydrology. Later, TOUGH2 was updated to TOUGH2 version 2.0 (Pruess *et al.* 1999). Detailed information and updates of this code can be found at the homepage of the program: <http://www-esd.lbl.gov/TOUGH2/>. Written in Fortran 77, version 2.0 features several new fluid property modules and offers capabilities, such as coupled reservoir-wellbore flow, precipitation and dissolution effects, and multiphase diffusion. There are several modules or extensions of TOUGH2, which focus on environmental contamination problems with non-aqueous phase liquids (NAPLs) such as T2VOC module for three-phase flows of water, air and a volatile organic chemical (VOC) (Falta *et al.* 1995), the T2DM module for hydrodynamic dispersion in 2-D flow systems and TMVOC (Pruess and Battistelli 2002). These modules are included in the Version 2.0 package. The code iTOUGH2 allows inverse modeling, optimization, and sensitivity and uncertainty analysis (Finsterle 1999) whereas TOUGH-FLAC couples TOUGH2 with the commercial rock mechanics code FLAC3D (Rutqvist and Tsang 2002).

The code TOUGHREACT couples TOUGH2 Version 2 with a general chemical speciation and reaction progress package (Xu and Pruess 2001, Xu *et al.* 2006). Detailed information about this code can be found at the homepage <http://www-esd.lbl.gov/TOUGHREACT/>. Written in Fortran 77, TOUGHREACT allows simulations of chemically reactive non-isothermal flows of multiphase fluids in porous and fractured media. It allows modeling of numerous subsurface thermophysical-chemical processes under a wide range of pressure, temperature, water saturation, ionic strength, pH and Eh. Mineral-fluid interactions can occur under local equilibrium or kinetic rates and the gas phase can be chemically active. Rock porosity and permeability can be variable as function of precipitation and dissolution reactions. Based on these facilities, the code can be used for solving manifold geological and environmental tasks, including geothermal systems, groundwater quality, contamination and remediation, diagenetic and weathering processes, subsurface waste disposal and acid mine drainage and sequestration of carbon dioxide in deep aquifers.

6.8.9 STAR—General Purpose Reservoir Simulation System

The STAR reservoir simulation system (Pritchett 1995, 2002) has been in a state of continuous development and elaboration since the mid-1970s. At present (2010) is the newest version. The STAR codes were developed by John W. Pritchett at SAIC (Science Applications International Corporation, <http://www.saic.com>). STAR solves the set of nonlinear partial differential equations that describe the unsteady flow of fluid mass and of heat in heterogeneous rock formations. Most of the code is written in the FORTRAN 77 computer language, compatible with FORTRAN 90, with a few special-purpose components written in “C”. The code uses a fully implicit iterative line-successive-relaxation technique to simultaneously solve the highly nonlinear equations expressing the overall heat balance and multi-component, multiphase mass conservation relationships. Rock models available include the conventional “porous-medium” representation and the “MINC” model for flow in fractured rock systems. The principal applications for which STAR is intended are (1) geothermal reservoir simulation, (2) simulation of enhanced oil recovery (EOR) by steam- or hot-water-flooding, and (3) sequestration of carbon-dioxide in saline aquifers. The STAR simulator can operate in one-dimensional slab, cylindrical or spherical geometry, two-dimensional cartesian or axisymmetric geometry, or three-dimensional cartesian geometry. Considerable flexibility is provided for imposing various grid shapes, different types of boundary conditions, and realistic earth structure upon the finite-difference grid used. Advection of mass and energy are treated using a technique which is second-order accurate in space to minimize numerical dispersion effects. The term “phase” denotes one of the immiscible phases occupying the void spaces within the rock matrix (solid precipitates, oil, water, or gas) and the term “component” denotes a particular chemical species or mixture, such as H₂O, CO₂, air, NaCl, etc. The number of components that may be treated is in principle unbounded.

Choice of the equation-of-state package for use in the STAR calculations is determined by the specific application of interest (geothermal, carbon-dioxide sequestration, heavy oil). Fluid constitutive packages for geothermal applications include (1) single-phase, single-component, liquid water, (2) two-phase, single-component H₂O (water/steam), (3) two-phase, two-component liquid water/dissolved ideal gas/free ideal gas mixtures, (4) two-phase, two-component H₂O/CO₂ mixtures with steam mixed with free CO₂ as the gas phase and water with dissolved CO₂ as the liquid phase, (5) two-phase, two-component liquid brine/CH₄ mixtures with free CH₄ as the gas phase and water with dissolved NaCl and CH₄ as the liquid phase, and (6) three-phase, three component H₂O/CO₂/NaCl mixtures with steam mixed with free CO₂ as the gas phase and including the possibility of a solid precipitate (third phase). For hot water and steam-flooding EOR applications, available fluid constitutive packages are (1) three components (H₂O, heavy hydrocarbon, light hydrocarbon) and three phases (oil, water, gas), and (2) two components (H₂O and heavy hydrocarbon) and three phase (oil, water, gas).

An optional capability exists in STAR to treat tracers. The simulator permits the rock matrix to deform due to pore pressure and temperature, prior pressure history, and the sign of pore pressure change. Two different representations for production/injection wells are available in STAR. Both techniques use approximate methods to simulate the subgrid multiphase flow in the immediate neighborhood of the well. In the first representation, individual wells are treated, allowing flow between any given well and multiple computational grid blocks (or "layers"). The allocation of the flow among the various blocks is computed automatically. The STAR simulator system is also equipped with several special-purpose mathematical postprocessors.

6.8.9.1 *RIGHTS: Single-phase geothermal reservoir simulator*

There are many situations in which the fluid flow is single phase and the required calculations may be accurately treated and the computational costs significantly reduced by using SAIC's RIGHTS simulator which invokes the Boussinesq approximation. This approximation neglects fluid compressibility effects; the density of the fluid is assumed independent of pressure and depends only upon temperature and salinity. RIGHTS is a third generation simulation system for natural state modeling of liquid-dominated hydrothermal systems, reservoir response to geothermal fluid production/injection and energy storage applications.

6.8.9.2 *DIAGNS: Well test data diagnostics and interpretation*

DIAGNS is SAIC's PC-based tool for interactive analysis of pressure transient data from geothermal wells. The code has four major modules: PREPROC for preprocessing and conditioning flow and pressure data, DECON for calculating pressure response for unit flow rate using measured flow rate and pressure histories, TYPE for computing formation properties using traditional type curves, and INVERT for computing formation properties using field data and a variety of mathematical models. Each module is a freestanding interactive program that reads (and stores) data from a common database.

6.8.9.3 *GEOSYS: Data management and visualization system*

GEOSYS is a PC-based interactive, graphical, map-oriented computer system used to store, display and analyze large volumes of geothermal reservoir engineering data. The program provides access to all of the data that are collected related to a particular geothermal reservoir, and allows interactive extraction and display of these data in a wide variety of formats. More specifically, it allows storage, retrieval, and analysis of geographical data, well drilling data, well log data, well test data, production (chemical and flow) data, and multi-survey microgravity and self-potential data. GEOSYS also allows the user to display overlays of well locations, faults, and surface features on maps or topographic images.

6.8.10 COMSOL Multiphysics

COMSOL Multiphysics[®] (COMSOL 2008a) is a powerful interactive environment for modeling and solving many kinds of scientific and engineering problems based on partial differential equations (PDEs), by using the finite element method. With this software, it is easy to extend conventional models for one type of physics into multiphysics models that solve coupled physics phenomena simultaneously. With the built-in *physics modes* it is possible to build mathematical models by defining the equations and the relevant physical quantities, such as material properties, loads, constraints, sources, fluxes and boundary and initial conditions. COMSOL Multiphysics then internally compiles a set of PDEs representing the entire model. The user can access the power of COMSOL Multiphysics as a standalone product through a flexible graphical user interface, or by script programming in the COMSOL Script language. The software runs the finite element analysis together with adaptive meshing and error control using a variety of numerical solvers. COMSOL Multiphysics offers modeling and analysis power for many application areas. For several of the key application areas this software also provides optional modules.

The Earth Science Module (COMSOL 2008b) is an optional package that extends the COMSOL-Multiphysics modeling environment to quantitative investigation of geophysical and environmental phenomena. This module contains a set of application modes adopted for a broad category of simulations important in investigating the earth, which makes up a giant laboratory filled with an unlimited array of basic physics and multiphysics interactions. It is designed for researchers, engineers, developers, teachers, and students and suits single physics and interdisciplinary study. The contents of the Earth Science Module are a set of fundamental building blocks with which to pose and answer a wide array of physics questions. It is possible writing the own user's code, using the Earth Science Module as a springboard to learn and to explore a rich variety of physics modeling.

The *Earth Science Module Model Library* contains write-ups and documentation for a number of geophysical and environmental scenarios. In this library, the example models fall into five groups: fluid flow, solute transport, flow and deformation, heat transfer, and multiphysics. The models typically involve one or more application modes from the Earth Science Module. Others, such as the poroelasticity and electrokinetic volcano flow examples, utilize other application modes from elsewhere in COMSOL. The models serve as a reference and also provide a head start for particular analyses. The ready-to-run models come with theoretical background as well as instructions that illustrate how to set it up. The model files can be freely modified, for example changing the geometries and material properties, altering the equations, and adding new physics to the file.

The model descriptions range in detail. The *Earth Science Module User's Guide* covers the equation set up, offers some insights on the underlying physics, and includes some fundamental modeling techniques for each application mode. The interfaces, options, and functionalities in this module have been tailored especially to account for geologic processes terms. The heat transfer application modes also include options to automate the calculation of effective thermal properties for multicomponent systems. The fluid flow equations represent a wide range of possibilities. Included are Richard's equation which describes nonlinear flow in variably saturated porous media. The options for saturated porous media include Darcy's law for slow flow and the Brinkman equations where shear is non-negligible. The Navier-Stokes equations cover the free flows. The transport of chemicals and their reactions is also treated in the module. The solute transport application modes account for chemical transfer in solid, liquid, and gas phases for the free, saturated, and variably saturated fluid flows. A number of the examples in the model library link these application modes together.

6.9 CALIBRATION, VALIDATION AND SENSITIVITY ANALYSIS

Once the conceptual model has been converted to a grid-based numerical model, simulations can be carried out. However, before these can be used to simulate the future behavior of the

real aquifer system, the numerical model must be calibrated and validated. To that end, the model can be run to compare its simulation results against benchmarks numerical simulations or known field data on past water levels, and distributions of solute concentrations or temperatures. For practical reasons, the historical record used for calibration and validation is divided in two portions. For the first sub-period, calibration is performed with refinement of model parameters, whereas for the second the relevance of the calibrated model is checked through sensitivity analysis. Only a good calibration and validation gives confidence that the model is producing simulation results that are faithful to real-world conditions and that predictions of future water levels and/or distributions of solute concentrations or temperatures in groundwater will be reliable. Particular care must be taken with this step of elaborating numerical models. Calibration and validation of groundwater models is examined in detail, e.g., in the book of Hill and Tiedemann (2007).

6.9.1 *Model calibration*

The previously elaborated conceptual model is based on many assumptions and the spatial distribution and/or temporal variations of parameter values are based on discrete measurements. So, the exact values of the different parameters in the model domain may be quantified with varying degrees of confidence. Leakage coefficients, groundwater recharge by rainfall and irrigation, effective porosity, dispersion coefficients, and retardation factors are generally more difficult to know with precision as compared to the values of hydraulic conductivity (or transmissivity) and storage coefficients.

The calibration of a numerical groundwater flow and transport model is performed by varying the values of one or more of the model parameters and optimizing them, until agreement between simulation results and values measured in the field is obtained with acceptable precision. Hence, parameter value estimation can be used synonymously with calibration (see also chapter 7).

Since different combinations of parameter values can be used to obtain a calibrated model, there is no unique solution of the parameter-estimation problem. The existence of multiple solutions demands that great emphasis be placed on obtaining the most accurate field data possible. It is helpful if the value ranges of different parameters are known, and if their impact is known, the most important ones can be selected to be considered for calibration and delimit solutions to those fitting best for the field example.

Depending on model type, the calibration involves estimation of different parameters. For the calibration of stationary groundwater models, hydraulic conductivity (or transmissivity), groundwater recharge, and boundary fluxes are principal parameters for estimation. Thereby, the total water balance of the calibrated model domain must become zero (the total volume of inflowing water should be equal to the total volume of outflowing water). In the case of transient groundwater flow models, additionally the storage coefficient can be used as calibration parameters. Here, responses of hydraulic head to pumping tests or other aquifer stimulations can be used for calibration purposes.

In the case of transport models, at the first stage, a calibrated groundwater flow model should be established, which is then used for calibration using transport parameters as effective porosity, solute and heat sources, etc. The groundwater flow model can be re-calibrated accordingly to the transport model if it is needed, until the required accuracy is achieved. Calibration can be performed manually by parameter variation (trial-and-error method) or using automatic calibration tools provided by some of the existing modeling programs e.g., UCODE of the USGS and PEST.

In automatic methods, the optimization process is an intrinsic procedure, whereas in the trial-and-error method, the fitting is performed *post factum*. In inverse models, an inverse modeling routine will adjust input parameters and run the simulation repeatedly until agreement between

simulated and observed field data is obtained within a specified precision. Parameter estimation or solving the inverse problem through automatic model calibration is discussed separately in chapter 7.

The quality of the calibration, and therefore the accuracy of the model, can be expressed by comparing observed and simulated results in a diagram where observed values are plotted on one, and simulated values on the other axis (e.g., for hydraulic head, example see Figure 6.8). In these so-called scatter plots, the closer the heads fall on the straight line, the better the model is. Different statistical methods can be used for quantifying the deviation between observed and field-measured data such as the sum of squared residuals, residual mean, residual standard derivation, absolute mean error, and root mean squared error (see e.g., Thangarajan 2004).

In the example, a calibration shall be performed manually (trial-and-error method). From the regional water balance it is known that groundwater recharge through rainfall is of minor importance, and that hydraulic permeability and aquifer base height are well known parameters in comparison to boundary flow. For this reason, the model should be calibrated using boundary flow as the main calibration parameter. By varying boundary flow (for cells with boundary flux see Figure 6.7a), the optimal boundary flow has to be determined so that simulated and measured hydraulic heads of the model area are as similar as possible. In Figure 6.8 for all piezometer sites, the simulated hydraulic heads are compared with the hydraulic heads observed in the field (scatter plot) for the principal calibration steps indicated below (intermediate calibration steps were performed, but are not shown) and the deviation of the obtained points from the line $h_{\text{observed}} = h_{\text{simulated}}$ expressed as MSD (mean square deviation) is quantified. In Figure 6.9, the simulated hydraulic heads are plotted on the map of the model area and additionally, the differences between simulated and real hydraulic heads (interpolated from values measured in the piezometers) are shown.

Using initial K_H values with zone values corresponding to mean values of the respective K_H -ranges, a first numerical simulation is performed with a boundary flux of $Q_V = 0 \text{ m}^3/\text{s}$ per boundary cell (1st calibration step, Figs. 6.8a and 6.9a). The results show relatively good agreement between simulated and measured hydraulic heads for the topographically low areas, whereas in the higher-located areas (close to the mountain range), the simulated h values are several meters lower than the measured values.

These results from calibration step 1 call for introduction of a boundary flux coming from the mountain range and entering the model area in the NW. In a second calibration step, Q_V was therefore set equal $0.01 \text{ m}^3/\text{s}$ per boundary cell (Figs. 6.8b and 6.9b). The simulation results are approaching the measured h values, but are still too low in the area near to the mountain range. A further approximation with $Q_V = 0.05 \text{ m}^3/\text{s}$ (step 3; Figs. 6.8c and 6.9c) was too high, and some intermediate steps resulted in a best approach for $Q_V = 0.035 \text{ m}^3/\text{s}$ (step 4; Figs. 6.8d and 6.9d).

Until now, the K_H values were held constant. Now K_H values (within the given K_H ranges) will be modified to further improve the calibration. After intermediate steps the best approximation for K_H values shown for step 5 is obtained (Figs. 6.8e and 6.9e). Now again, Q_V is readjusted and the best results for $Q_V = 0.035 \text{ m}^3/\text{s}$ per boundary cell is obtained (step 6; Figs. 6.8f and 6.9f). This procedure can be continued until the desired maximum permitted error is obtained. In this case the differences between simulated and measured hydraulic heads are less than 20 cm in the entire model area (with exception of one measurement point near the river). So, the steady-state model can be considered as calibrated and accurate enough for prognosis according to the desired tasks.

6.9.2 Model validation (history matching)

As already mentioned in section 6.9.1, the selection of the parameter values and boundary conditions, which have been used for calibrating does not result in a unique solution, since other combinations of parameter values and boundary conditions may result in the same solution. Therefore, the calibrated model needs to be validated by history matching, in which the model

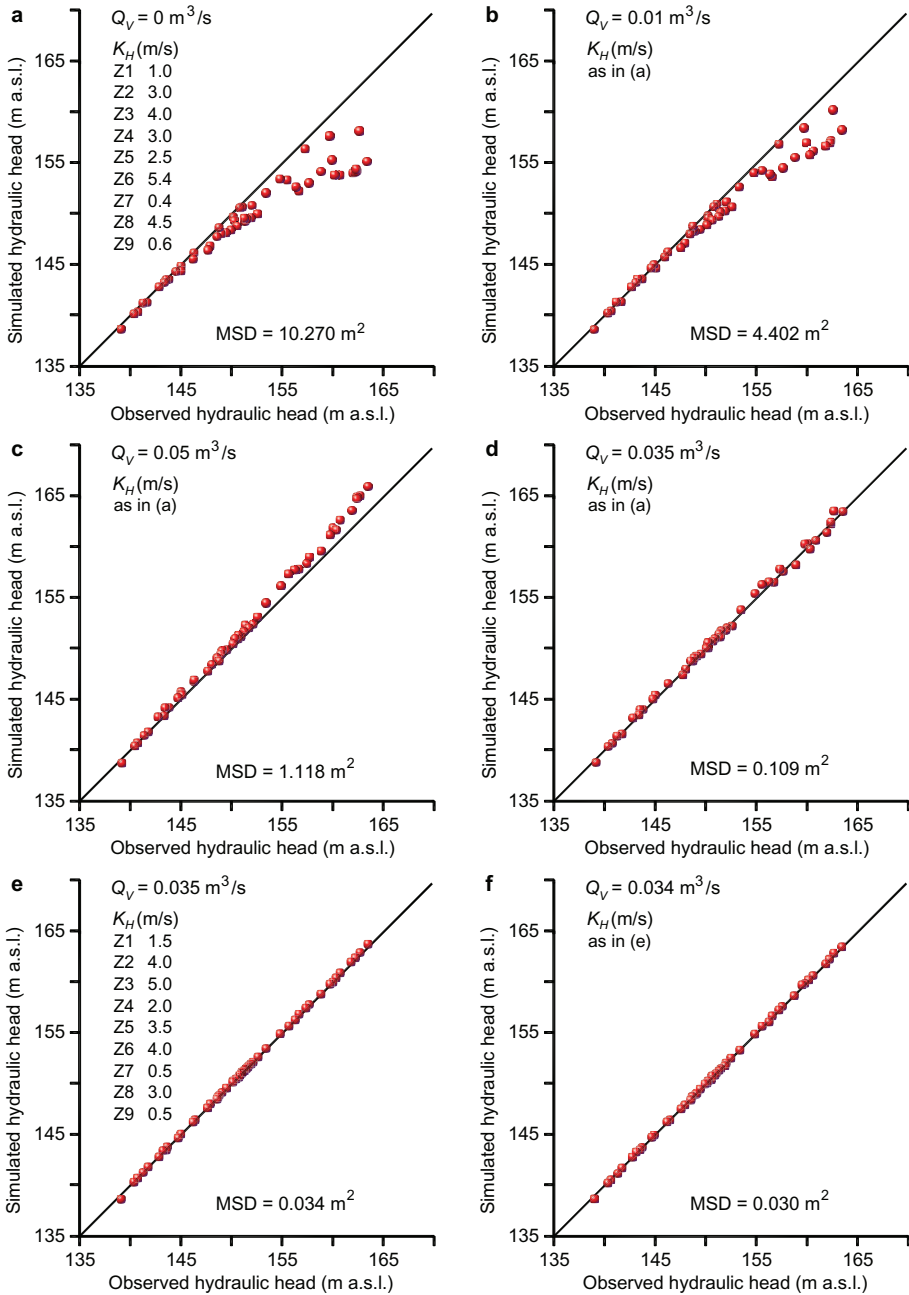


Figure 6.8. Regional groundwater flow modeling example: Comparison between measured and computed hydraulic heads for different calibration steps (Scatter plots); MSD (mean square derivation) quantifies the difference between modeled hydraulic heads and observed hydraulic head data; K_H is the hydraulic conductivity of the zones Z1 to Z9 and Q_V the boundary flux per each of the 31 boundary flux cells.

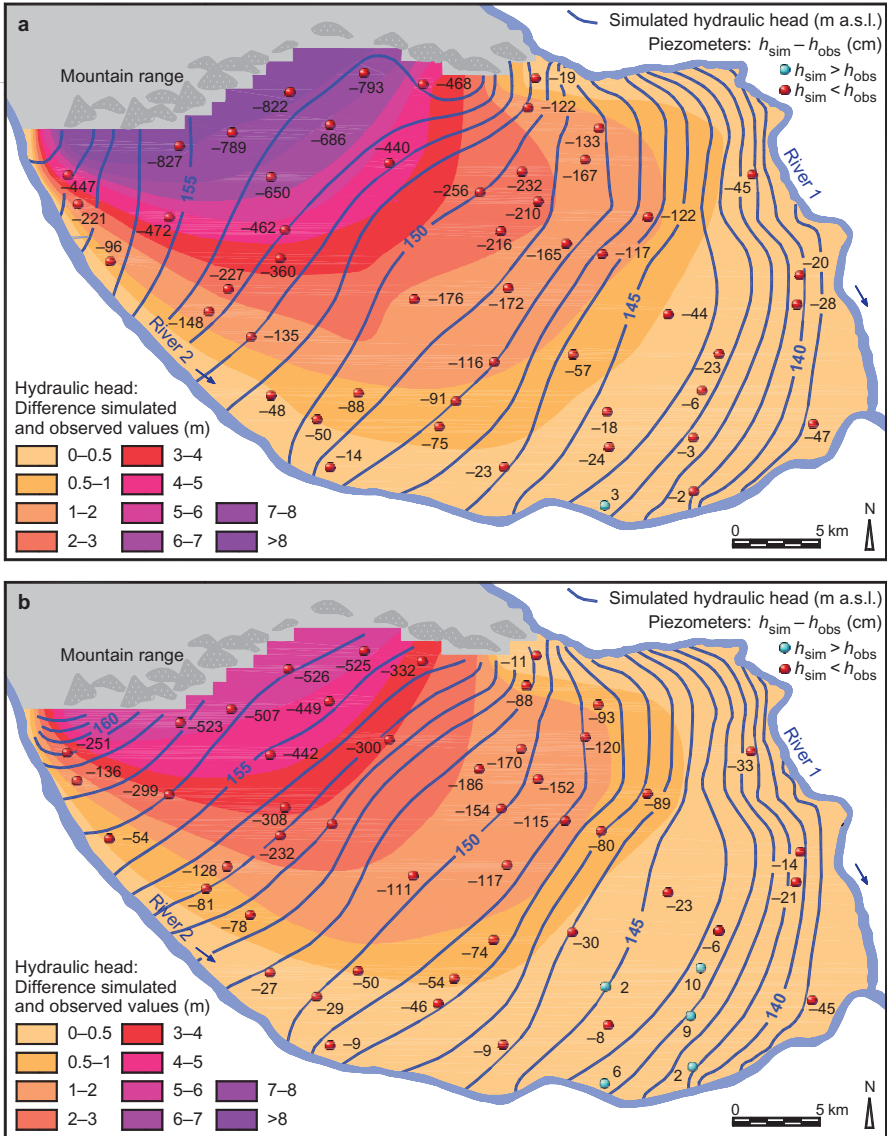


Figure 6.9. Simulation results of calibration steps: (a) Step 1: $Q_V = 0 \text{ m}^3/\text{s}$; (b) Step 2: $Q_V = 0.01 \text{ m}^3/\text{s}$; (c) Step 3: $Q_V = 0.05 \text{ m}^3/\text{s}$; (d) Step 4: $Q_V = 0.035 \text{ m}^3/\text{s}$; (e) Step 5: $Q_V = 0.35 \text{ m}^3/\text{s}$; (f) Step 6: $Q_V = 0.034 \text{ m}^3/\text{s}$ (values per boundary flux cell); Hydraulic conductivity K_H is constant for steps (a-d) and for (e-f), respectively.

is tested for some period in the past to prove whether the simulation results reproduce the known historic changes well enough: aquifer responses to pumping tests, changes of flow conditions, hydraulic heads, solute concentrations, or temperatures. For this purpose a time interval is used, which was not considered for the calibration process itself. If the model can be successfully validated, it is ready for predictive simulations. If it cannot be validated, then another conceptual model needs to be selected, or further calibration refinement with improved field data is required.

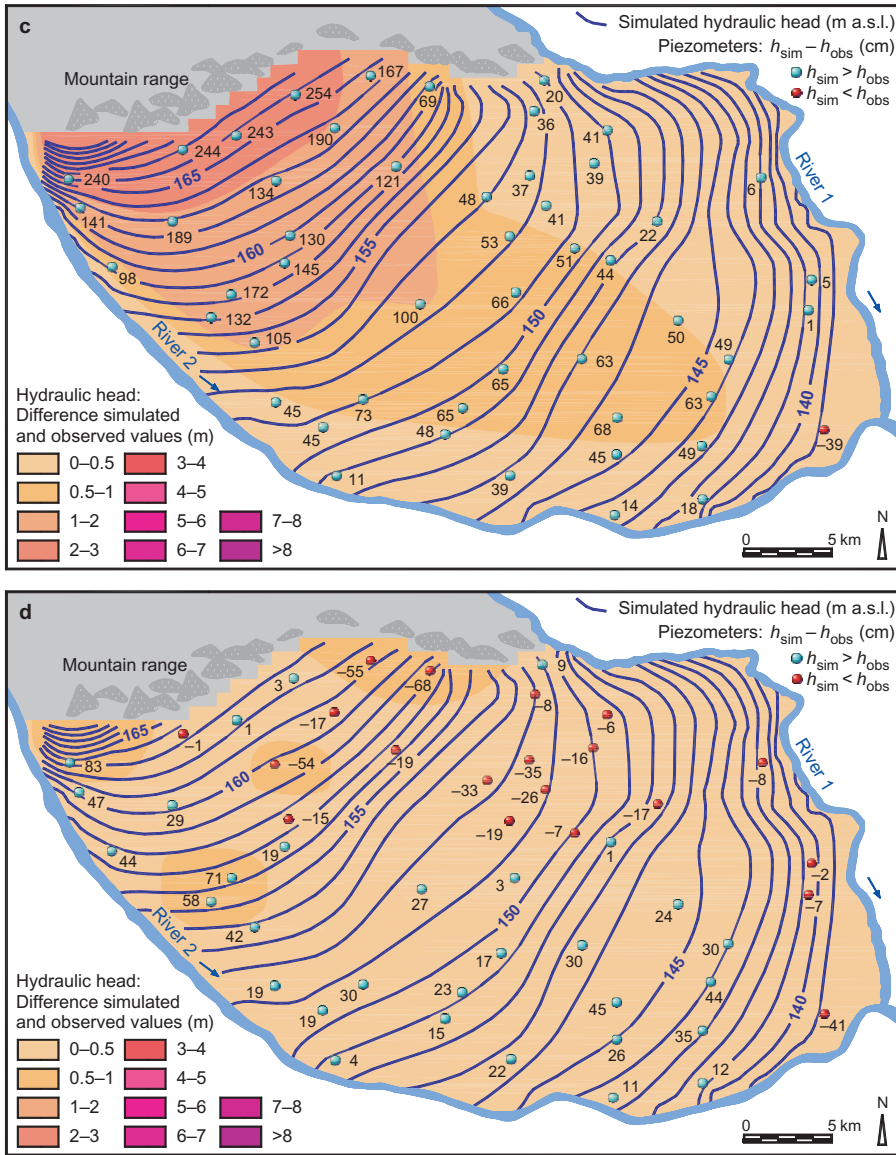


Figure 6.9. (Continued)

6.9.3 Sensitivity analysis

A sensitivity analysis is a systematic test to evaluate how changes in the parameters of a model affect the modeling results. Different parameters of the model are changing over a characteristic range, which is set by prior knowledge of the behavior of the parameter in the real world. The possible variations in the parameters are given by the uncertainty of the parameter observed in the field (see also section 6.12.1). The observed relative change in the model response in terms of the dependent variables (e.g., the hydraulic head, fluid flow rate, solute or heat flux), defines the most influencing parameters. Parameters for which the model is more sensitive require more

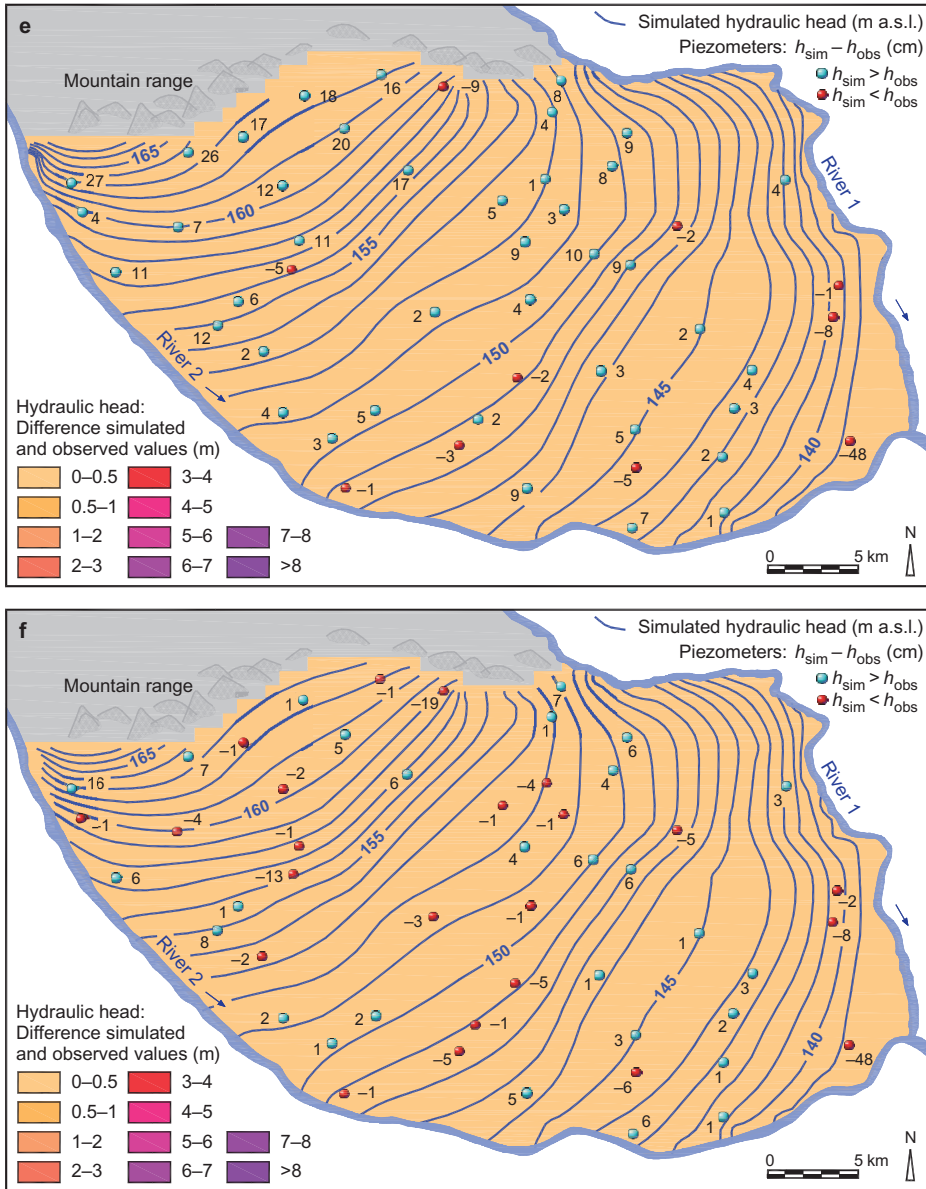


Figure 6.9. (Continued)

exact determination compared to others. It may be helpful to perform a preliminary sensitivity analysis before model calibration.

6.10 PERFORMING NUMERICAL SIMULATIONS

After all of the previous steps are complete, the numerical model can be used for making predictions and to answer the questions of our model. It can simulate and predict problems such as how groundwater extraction from wells or reduced groundwater recharge by reduced rainfall during

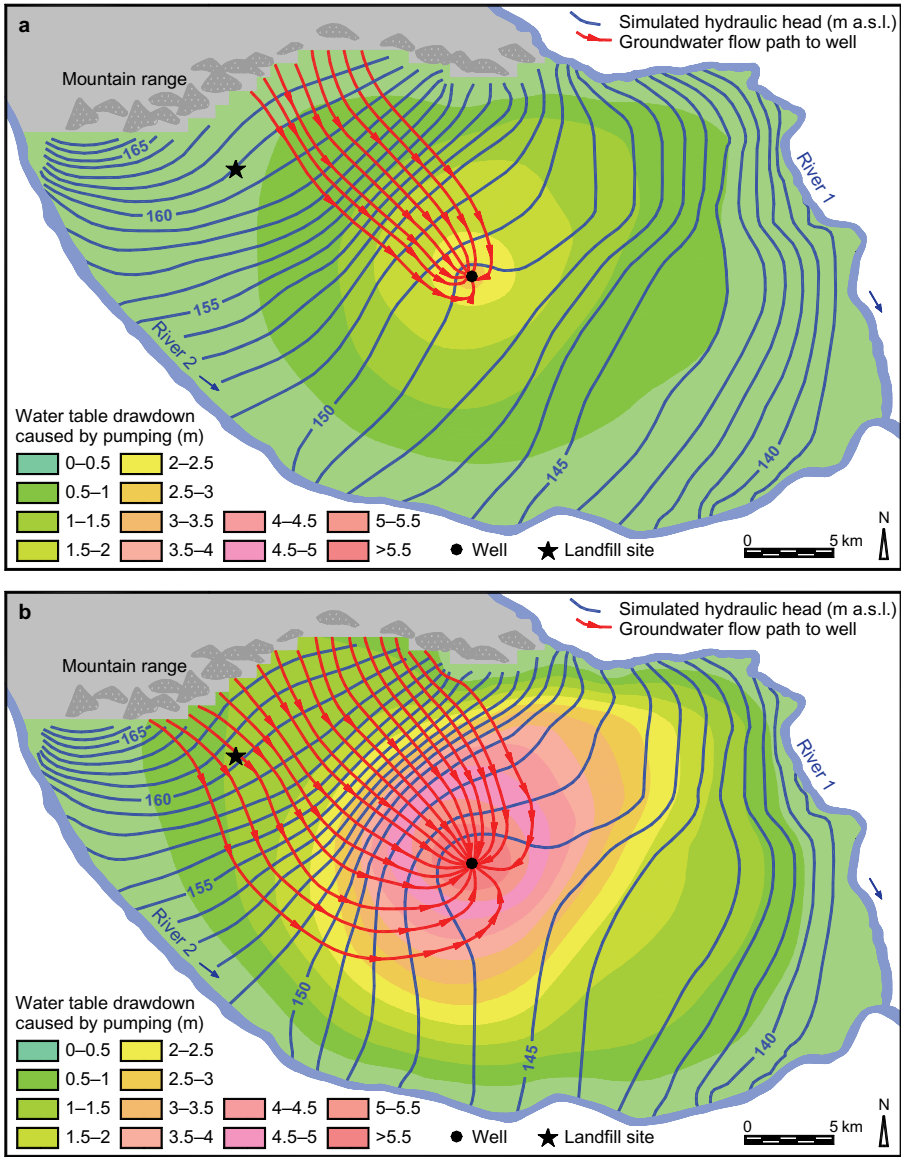


Figure 6.10. Capture zone for a drinking water well for different exploitation rates from a well field delimited by the outermost pathlines; time markers every 5 years: (a) $Q_{V\text{well}} = -0.4$; (b) -1.0 ; (c) $-0.7 \text{ m}^3/\text{s}$. Additionally, the plot of the drawdown of the water table caused by exploitation in the wellfield *versus* the natural initial groundwater table levels.

drought periods will influence local and regional water levels. It can predict propagation of contaminant plumes in aquifers, and heat transport in geothermal reservoirs. In this way, optimizing groundwater exploitation, remediation of contaminated aquifers, and optimizing exploitation of geothermal fields will be possible.

In the example, it shall be investigated whether a well field can be established at the site indicated in Figure 6.10. The question is whether contaminated water originating in the landfill can reach the well field and what would the maximum allowable exploitation rate be in order to

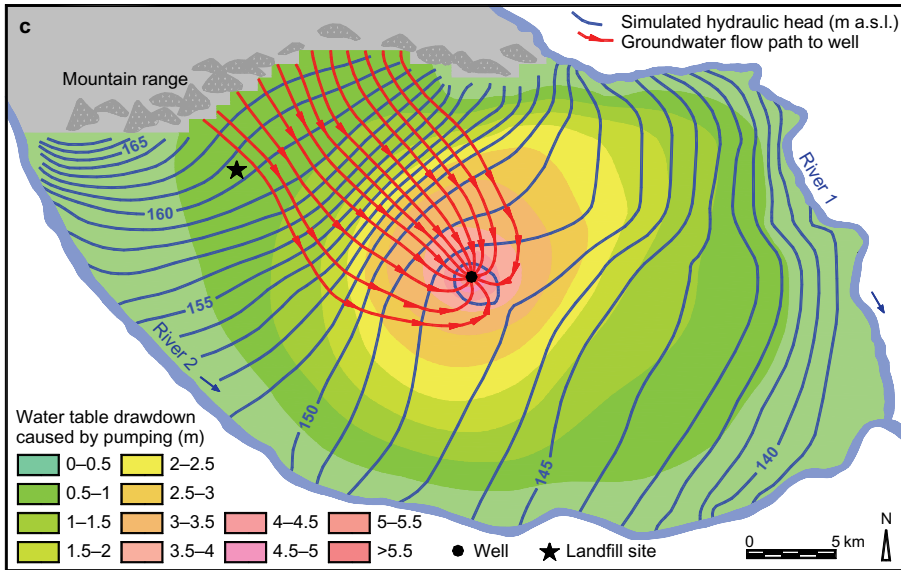


Figure 6.10. (Continued)

avoid that. Additionally, to obtain permission to exploit the field, the depression of the natural groundwater level caused by the withdrawal may not exceed 3.5 m outside an area delimited by a circle with a radius of 3 km around the well field.

This task can be solved using the previously calibrated numerical model and performing a series of numerical simulations using different exploitation rates $Q_{V\text{well}}$ for the well field. Figure 6.10 shows the capture zone for the well field for different exploitation rates. Simulations are performed for an effective aquifer porosity of $\varphi_{\text{eff}} = 0.08$ and a retardation factor of $R_d = 1$ (conservative tracer). Transversal dispersion of the contaminants is not to be considered. Additionally, plotted on the groundwater flow paths are time markers (every 5 years) indicating travel times. From the results generated varying $Q_{V\text{well}}$, a maximum value of $Q_{V\text{well}} = -0.7 \text{ m}^3/\text{s}$ is estimated as the maximum allowable withdrawal in the well field so that the landfill leachate does not come into its catchment area. In addition, the second condition of avoiding a depression of more than 3.5 m outside of a radius of 3 km is also fulfilled for that withdrawal rate.

6.11 HOW GOOD IS THE MODEL? ASSESSING UNCERTAINTIES

Numerical modeling of groundwater systems is associated with many uncertainties. There are two types of numerical model uncertainties, the uncertainty inherent to the selected conceptual model and the uncertainty of the model parameter values. The conceptual model, on which the numerical model is based, is a simplified description of the real field scale situation, which includes numerous simplifying approximations and assumptions, especially those regarding aquifer geometry and the estimated values of model parameters, sensitivity of variables, and the boundary locations and initial conditions and their variations in space and time.

The model domain boundaries are a source of uncertainties: the location of boundaries may shift through time or the boundary conditions (types) may change through time at the same location. The conditions of the boundaries (e.g., specific hydraulic heads or solute concentrations, boundary fluxes, etc.) may be functions of time. Boundary fluxes are difficult to measure and in consequence often highly uncertain. The spatial distributions of the values of parameters may vary over several orders of magnitude in a short distance. This behavior is caused by heterogeneities

on hydraulic conductivity, K_H , storage coefficient, S , effective porosity, φ_{eff} , and dispersivity, α , which all are approximated using discrete values from a few locations, where measurements were performed in the field. If two-dimensional horizontal models are used, the values at each point (in the horizontal plain) correspond additionally to an averaged value over the aquifer depth. Other values of parameters depend not only on space but also on time (e.g., hydraulic heads, groundwater recharge, solute concentrations, temperatures) and their uncertainty is due to missing temporal data measurements, or if the time dependence of these parameters is not recognized and considered, only the time-averaged values are used. Uncertainty is also related to sinks and sources of fluids and solids, which may be functions of time, and the ascribed transport mechanisms and transport parameters, including those describing processes of chemical reactions, sorption processes and decay, which depend additionally on solid phase composition, geochemical milieu, temperature, etc.

Different approaches have been developed to introduce uncertainty into the numerical modeling to account for the uncertainty of input parameters and conceptual model uncertainty. The evaluation of the conceptual model uncertainty in its predictive results is generally done by performing simulations with the different models available and evaluating the range of predictions obtained for the distinct models (e.g., Medina and Carrera 1996). The evaluation of the effect of parameter uncertainty on the modeling results can be established by various methods, which can be used to quantify the modeling result (prediction) uncertainty: Linear approximation, non-linear approximation, and Monte Carlo methods (see e.g., Carrera *et al.* 2005). In the latter, the various possibilities are represented in a large number of simulated realizations, and the statistical parameters of the parameter distribution of results is obtained (e.g., Carrera *et al.* 2005). Other approaches use stochastic models in which the various coefficients are represented as probability distributions.

6.12 MODEL MISUSE AND MISTAKES

During the different steps of numerical modeling, different types of mistakes and misuses may occur (see e.g. Mercer and Faust 1981, Mercer 1991). They can be divided into four groups: (1) Improper conceptualization of the problem to be considered, (2) selection of an inappropriate modeling code, (3) improper model application, and (4) misinterpretation of model results.

As already outlined, the first group, related to the elaboration of an accurate conceptual model properly reflecting the groundwater flow and solute and heat transport processes is a prerequisite for the elaboration of a suitable numerical model. If the conceptual model is wrong or not accurate enough, then the obtained simulation results do not reflect the behavior of the natural system. Principal mistakes during the elaboration of the conceptual model are predominantly related to an improper delimitation of the model domain area (aquifer geometry, location of boundaries, boundary types, and boundary values), wrong assumptions regarding homogeneity, isotropy and hydraulic parameters of the aquifer (and their respective spatial distribution and variation through time), wrong assumptions regarding the occurring transport processes, and an unsuitable selection of dimensionality (e.g., using a two-dimensional model, where a three-dimensional model is required).

With respect to the second group, it often can be observed that the modeler is using a highly sophisticated model program in situations, in which such a model is not required because there are not enough field data to support it or because the objectives do not require it.

Improper model applications occur if improper input data are used, and if the mesh or grid size and the intervals of the time steps are not properly selected. Also, sometimes the chosen model codes are not compatible with the chosen conceptual model. During model calibration the selection of unsuitable calibration parameters, calibration periods, and the use of a model that was calibrated under different conditions from those of the modeling time interval generate additional mistakes. These mistakes can lead to wrong results and incorrect interpretation of the modeling results.

6.13 EXAMPLE OF MODEL CONSTRUCTION—ASSESSMENT OF THE CONTAMINATION OF AN AQUIFER

In the following we present an idealized example, where we show the stepwise procedure of a modeling approach. It must be considered that several simplifications were made in order not to distract from the primary modeling objectives.

6.13.1 Situation and tasks

In the vicinity of the city of Las Palmas (15,000 inhabitants), groundwater is extracted from wells located at different properties. This water is primarily used as drinking water and secondarily used for irrigation (Fig. 6.11). Two years ago, a plastic materials factory whose production began in 1989 was built on the western border of the town (as a chronological reference, “today” corresponds to June 1991). The town itself receives its water supply from a water works located 3 km to the southeast (Fig. 6.11). This water works extracts water from a well at a constant rate of $Q_V = -0.05 \text{ m}^3/\text{s}$. Based on complaints presented by some farmers, who noted a decrease in the quality of the water compared to previous years, sampling and chemical analysis activities, commissioned by the town administration, were carried out in several wells on June 16, 1991.

Results showed a considerable increase, with regard to the values from neighboring areas, in the concentrations of sodium Na^+ (maximum 750 mg/l), chloride Cl^- (maximum 1030 mg/l), sulfates SO_4^{2-} (1348 mg/l) and hydroxyborate ions $\text{B}(\text{OH})_4^-$ (maximum 17.5 mg B/l) (Table 6.6, Figure 6.11a). The decrease in water quality is due, on the one hand, to the salty taste it has, and on the other hand, to the high mineralization and the concentrations of hydroxyborate ions, which prevent the use of groundwater for human consumption and irrigation as it has been used so far, or allows use of it to a much lesser extent.

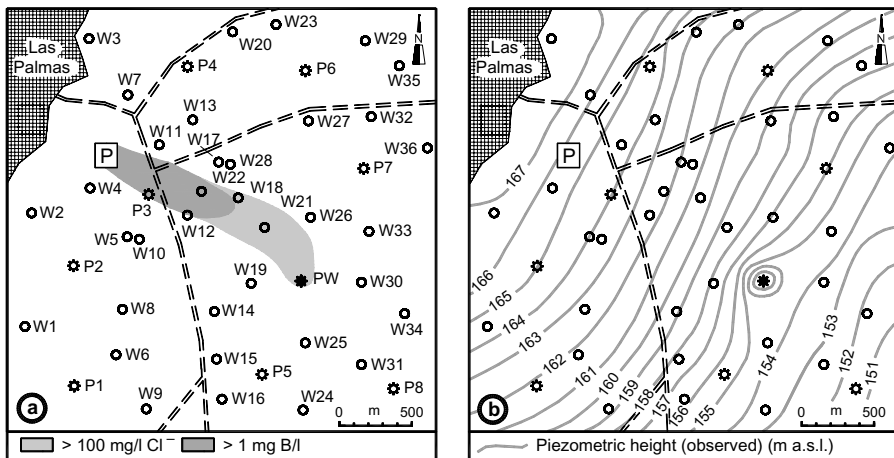


Figure 6.11. Field example from Las Palmas: (a) Location of the study area with the drilled wells W1 to W26, the piezometers, P1 to P7, the pumping well, PW, and the plastic materials industrial plant, P. Additionally shown are the areas with more than 100 mg/l of chloride, and more than 1 mg/l of boron (present as hydroxyborate anions found in groundwater); (b) Contour map showing mean values of the observed groundwater levels for the period between June 1990 and June 1991, measured at wells W1 to W36, piezometers P1 to P7, and pumping well PW of the water works (for data see Table 6.6).

Table 6.6. Field example from Las Palmas: chloride, sulfate, and hydroxyborate ion concentrations in groundwater. Samples were collected on June 16, 1991, and average piezometric measurements are for the period between June 1990 and June 1991 (measurements on June 11, 1990, September 15, 1990, December 1, 1990 and June 16, 1991).

Sampling point	Piezometric level (m a.s.l.)	Cl ⁻ (mg/l)	SO ₄ ²⁻ (mg/l)	B(OH) ₄ ⁻ (mg B/l)
W1	164.6	1.3	21.5	<0.1
W2	166.8	1.8	25.0	<0.1
W3	167.6	0.7	19.7	<0.1
W4	165.7	1.4	13.7	<0.1
W5	164.0	1.5	17.3	<0.1
W6	161.8	1.1	22.5	<0.1
W7	166.0	0.9	21.7	<0.1
W8	162.7	1.6	19.6	<0.1
W9	159.2	1.8	24.8	<0.1
W10	161.9	1.2	21.9	<0.1
W11	164.3	0.8	19.1	<0.1
W12	162.2	2.8	56.5	<0.1
W13	163.4	1.0	25.2	<0.1
W14	159.0	1.7	23.6	<0.1
W15	157.7	0.5	21.7	<0.1
W16	156.1	1.3	20.5	<0.1
W17	161.8	1.5	21.9	<0.1
W18	160.4	105.0	267	0.1
W19	157.6	1.5	23.4	<0.1
W20	162.9	1.4	26.0	<0.1
W21	158.6	1030.0	1348.0	<0.1
W22	162.0	780.0	1037.0	17.5
W23	162.0	0.9	23.7	<0.1
W24	153.5	1.8	19.5	<0.1
W25	154.4	1.3	17.8	<0.1
W26	156.8	1.3	14.9	<0.1
W27	158.8	1.8	21.1	<0.1
W28	160.5	1.7	23.7	<0.1
W29	159.2	1.6	25.0	<0.1
W30	153.7	1.1	24.8	<0.1
W31	132.6	1.5	12.9	<0.1
W32	156.6	1.3	21.8	<0.1
W33	154.5	1.3	25.7	<0.1
W34	151.8	1.6	21.6	<0.1
W35	157.4	0.9	15.8	<0.1
W36	154.2	1.6	23.7	<0.1
P1	—	1.0	19.8	<0.1
P2	—	1.5	17.7	<0.1
P3	—	10.5	56.8	0.4
P4	—	1.4	23.8	<0.1
P5	—	1.6	23.9	<0.1
P6	—	0.9	21.3	<0.1
P7	—	1.7	19.7	<0.1
PW	150.9	194	245.7	<0.1

In this case, there are numerous questions:

- Who causes contamination? Is the recently built industrial facility, presumably a polluting source, responsible for the situation? Can such responsibility be demonstrated? If the factory is not responsible, how do contaminants enter the system?

- Is there a severe or potential risk for the water works? If there is, how will contamination evolve in the future? When will the contamination plume reach the pumping well and when, if ever, will it disappear? These questions must be answered from two perspectives: on the one hand, considering the best-case scenario, that is, the contamination source is immediately closed; on the other, the worst-case scenario where the contamination process continues unchanged. For both cases, the concentrations that will reach the pumping well should be determined, both regarding the magnitude of its maximum values as well as regarding their distribution in time. The areas where contamination is apparent must be studied, as well as those where contamination is expected to occur. The same procedure must be carried out for farm wells.
- If necessary, is it possible or reasonable to take protective or sanitation measures to maintain the water supply to Las Palmas by the present water works? Which solutions are available to supply water to farms?

6.13.1.1 Existing field data and information

The only information available about the extent and lithologic characteristics of the unconfined aquifer results from 7 piezometers (P1 to P7) and a pumping well (PW) for which there are geological drilling profiles. They all reach the base of the Quaternary aquifer, composed of non-permeable massive limestone. The aquifer is composed of medium-grained sand with gravel and a percentage of silt below 5%. In 36 drilled wells, W1 to W36, the piezometric level can be measured, and systematic measurements have been carried out for one year, between June 1990 and June 1991. Mean values are presented in Table 6.6. On June 16, 1991, samples were taken and the corresponding analyses were performed. The concentration values obtained for Cl^- , SO_4^{2-} , and $\text{B}(\text{OH})_4^-$ (as B) are listed in Table 6.6.

6.13.2 Design of the investigation program

If models are used for the treatment of contamination accidents, it is recommended that a certain order should be followed, such as the one compiled by DVWK (1989):

- Preliminary research—contamination risk assessment
- Assessment methods—hydraulic head measurements and contaminant concentration determinations
- Simple models—ideal systems
- Flow time calculation—purely advective transport modeling as first approach
- Transport modeling considering dispersion, sorption, and other processes

6.13.3 Preliminary investigations—Contamination assessment

Chloride concentrations observed between Las Palmas and the water works are as high as 1030 mg/l, whereas those at the pumping well reach 194 mg/l (the threshold value is 250 mg/l), so contamination risk can be classified as acute. For this reason, research activities must be carried out in order to determine the real distribution of contaminants and their future propagation.

6.13.4 Acquisition of groundwater level and contaminant concentration

A preliminary rough assessment of contaminant propagation can be done by:

- Assessing the velocity and direction of the groundwater flow
- Using contaminants that are already present

In the first case, phreatic or piezometric groundwater level measurements are taken, whereas in the second, substance concentration values obtained in chemical analyses are used. For our example, the existing piezometric measurements can be used, as well as the analytical results for each ion to study. Based on piezometric data, a contour map can be drawn (Fig. 6.11b);

this map indicates a groundwater flow from approximately WNW to ESE. By observing the distributions of solute concentrations it can be shown that the contamination plumes corresponding to the different substances have a similar shape, with their source at the industrial plant (Fig. 6.11a). On the other hand, between the town, which may act as another potential contaminating source, and the suspected industrial plant, concentrations are low corresponding to the natural background values. Therefore, the industrial plant appears to be the sole source for contamination. Thus, the contamination source is localized and its starting time is known, June 1989. The water works is then directly downstream from the point source. The chloride contamination plume, whose mobility (retardation factor $R_d \approx 1$) is greater than that of the other solutes, has already reached it (Fig. 6.11a). Its Cl^- concentration, 194 mg/l, is still below the threshold value of 250 mg/l and the tasting threshold of approximately 350 mg/l. Groundwater flow average linear velocity (average pore velocity), v_A , between the source point of contamination and the water works can be approximately estimated based on the hydraulic gradient $i_h \approx 0.0072$, the approximate hydraulic conductivity of the aquifer media (medium sand with fine gravel), K_H , ($1 \times 10^{-3} \leq K_H \leq 1 \times 10^{-4}$ m/s) and effective porosity, φ_{eff} ($0.05 \leq \varphi_{\text{eff}} \leq 0.2$). Using $v_A = K_H i_h / \varphi_{\text{eff}}$, values between 3.6×10^{-6} and 1.4×10^{-3} m/s are obtained for v_A .

From this information the following conclusions can be drawn:

- It is possible to identify the responsible party causing the groundwater contamination, and this in turn allows determination of the contamination point source. The suspicions that contamination was caused by a recently settled plastic material industrial plant are confirmed.
- From its origin, the contamination plume advances in a WNW–ESE direction, and the propagation velocity of chloride can be assigned to that of groundwater at $3.6 \times 10^{-6} \leq v_A \leq 1.4 \times 10^{-3}$ m/s.
- The affected or potentially affected area is delimited.

6.13.5 *Groundwater flow and advective transport as a first approach*

Research activities carried out so far are only general approximations; to obtain a greater precision in the description of transport processes in the aquifer, the hydraulic situation needs to be studied and quantitatively described. This is essential to describe advective transport, which frequently plays a prevailing role in substance propagation in an aquifer, by using an analytical, or in our case, a numerical model. The determination of groundwater velocity pattern, together with other hydrogeological parameters, is of particular interest. With a simple numerical model, such as ASM modeling code (see section 6.8.3), groundwater flow can be simulated and flow times can be calculated for water particles based on the contamination source point and groundwater flow paths starting from this point.

6.13.5.1 *Delimitation of the area to model and aquifer geometry*

For a simple description of the model boundaries, the contaminated area to be modeled is placed so that two of its borders are parallel to the lines in the groundwater level contour map (NW and SE boundaries), with the other two borders in about perpendicular direction, which means that no groundwater flow occurs through these boundaries (impermeable NE and SW boundaries) (Fig. 6.12a). Then, the boundary conditions of the hydraulic head at the NW and SE boundaries correspond to those of the adjacent contour lines (Fig. 6.12a). Based on the data taken at the boreholes, an isodepth map of the aquifer base is drawn to be used as the vertical lower limit of the model (Fig. 6.12b).

6.13.5.2 *Hydrogeological parameters*

Hydraulic head (piezometric level) measurements performed in different seasons between June 1990 and June 1991 (measurements on June 11, 1990, September 15, 1990, December 1, 1990 and June 16, 1991) show that seasonal variations of the levels are below 0.5 m and they do not

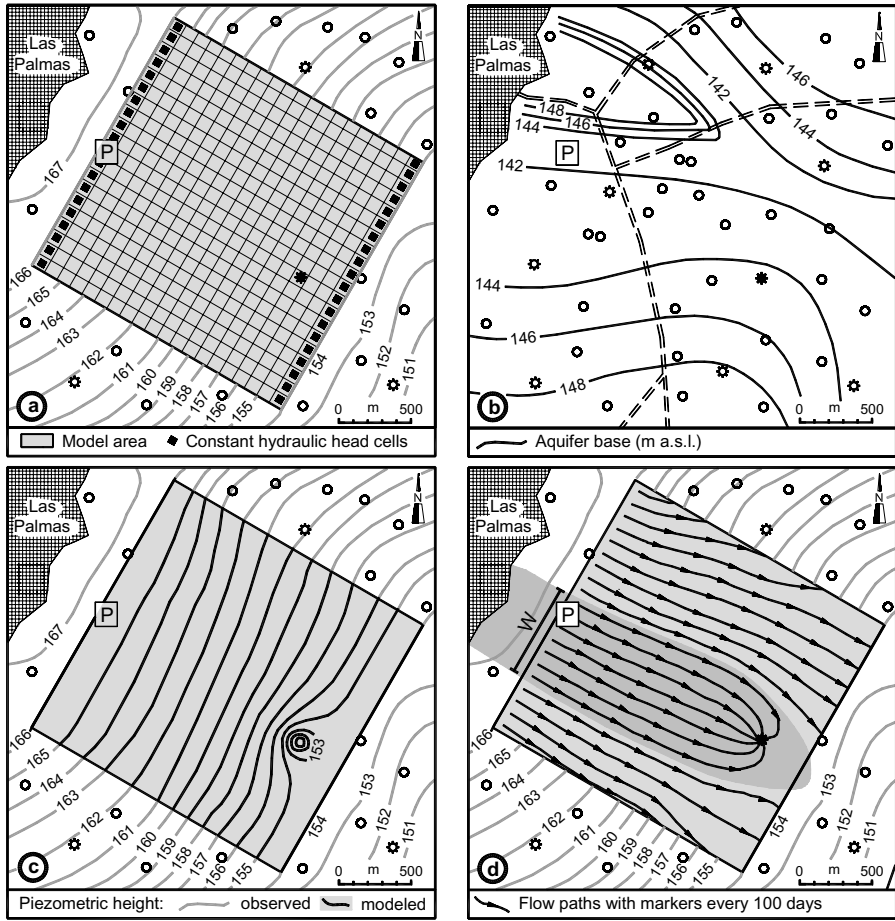


Figure 6.12. Field example from Las Palmas: (a) Position of the base of the aquifer, constructed with basement depth data from piezometers P1 to P7 and from well PW; (b) Position of the study and modeling area, with finite difference model cells; (c) Groundwater level contour map numerically modeled in the modeled area; (d) Simulated groundwater flow paths in the modeled area, with chronological demarcation every 100 days and catchment area of the well (darker gray). Figures (b) through (d) additionally show the groundwater contour maps located outside the modeled area, based on field data.

have a significant impact on groundwater flow velocity pattern. Hence, the numerical simulation is done assuming a stationary groundwater flow, using the average values from the piezometric levels (Table 6.7). To determine hydraulic properties, pumping tests were performed at piezometers P1 to P7, from which hydraulic conductivity, K_H , and storage coefficients, S , were obtained (Table 6.8). The K_H values range from 3.5×10^{-4} to 6×10^{-4} m/s, the S values, which correspond in the present phreatic aquifer to the effective porosity, vary from 0.08 to 0.14, and do not show a significant spatial pattern. However, recall that these values are based on few field measurements at discrete points. In practice, more measurements both within and outside of the modeling area need to be obtained. This will allow the modeler to delimit the range of values, in which discrete values can be expected. This, together with a sensitivity analysis, which evaluates the extent to which changes of the specific parameter value affect the simulation results,

Table 6.7. Field example from Las Palmas: Heights above sea level of the aquifer base for piezometers P1 to P7 and for pumping well PW.

Borehole/ piezometer	P1	P2	P3	P4	P5	P6	P7	PW
Aquifer base (m a.s.l.)	147.7	143.7	142.3	145.0	148.1	145.1	143.2	144.2

Table 6.8. Field example from Las Palmas: Hydraulic conductivity, K_H , and storage coefficient, S , obtained with pumping tests at piezometers P1 to P7; Aquifer thicknesses, b_a , obtained from the difference between piezometric levels and the base of the aquifer.

Well, piezometer	P1	P2	P3	P4	P5	P6	P7
Aquifer base (m below surface)	147.7	143.7	142.3	145.0	148.1	145.1	143.2
Piezometric level h (m a.s.l.)	161.8	165.0	164.0	164.4	155.4	160.1	156.1
Aquifer thickness b_a (m)	14.1	21.3	21.7	19.4	7.3	15.0	12.9
Hydr. conductivity K_H (10^{-4} m/s)	5.2	6.0	5.0	3.5	4.5	6.0	4.9
Storage coefficient S (ad)	0.10	0.14	0.11	0.08	0.10	0.11	0.08

can be used to obtain a range of possible solutions. Groundwater recharge from rainfall was neglected.

6.13.5.3 *Simulation of groundwater flow lines and flow times*

Using the data and information mentioned above, the numerical flow model can be constructed. After calibration, using K_H as the calibration parameter for matching simulated piezometric levels to those observed in the field, simulations can be carried out.

6.13.5.4 *Results*

The results obtained with groundwater flow velocity simulations are limited in their application to solute transport and interpretation of contaminant transport, but give an important first result. The reason is that solute dispersion effects and adsorption, desorption, and decomposition processes have not been considered. However, in the case of chloride as a contaminant, it may be assumed that it is not affected by sorption processes and behaves as an ideal tracer. In contrast, hydroxyborate ions undergo adsorption processes, which explains why the chloride plume has already reached the drinking water well, PW, whereas the boron concentration still corresponds to the background value (Table 6.6).

Based on our dispersion-free purely advective contaminant transport approach as a first approximation to our problem, we obtain the following results from our numerical modeling:

- According to flow lines and the time markers on them, water particles leaving from the contamination point source (100 m wide) take Δt_{SQ} 500 to 600 days to reach the pumping well of the water works. The same happens with substances that behave as ideal tracers, like Cl^- .
- The width of the capture zone of the pumping well can be determined from Figure 6.12d as $W = 700$ m. This means that the well receives water from a 700 m wide band that includes the contamination source and the entire plume (Fig. 6.12d). Based on the estimated values of chloride inflow, $C_{\text{Cl}} = 1000$ kg/day (11,574 mg/s), and hydroxyborate anions inflow, $C_B = 50$ kg B/day (579 mg B/s), and using the pumping rate of the production well $Q_V = -0.05$ m³/s (50 m³/s), the maximum expected concentrations at the pumping well can be estimated. From this calculation, maximum expected concentrations for chloride of $C_{\text{Clmax}} = C_{\text{Cl}}/Q_V = 231$ mg/l and for hydroxyborate anions of $C_{\text{Bmax}} = C_B/Q_V = 12$ mg B/l are obtained.

- Whereas maximum chloride concentrations C_{Clmax} are slightly below the threshold values admitted by the WHO and the EU (200 and 250 mg/l, respectively), maximum boron concentrations C_{Bmax} are well above the thresholds established by the EPA, not more than 1 mg/l of boron (WHO: 0.1 mg B/l in the year considered).
- The area affected by current and future contamination has been delimited; it spreads from the contamination point source to the drinking water well, where numerous contaminating particles are extracted from the aquifer through the pumping well, thus preventing contamination from going beyond this location.
- If the contamination point source is not eliminated, a quasi-stationary distribution of chloride and hydroxyborate anion concentrations will occur.
- If contamination is immediately interrupted, it will end in $\Delta t_{SQ} = 500$ to 600 days in case of chloride (ideal tracer).

6.13.6 *Transport model with dispersion, sorption, and resulting solutions*

6.13.6.1 *Introduction*

The elaboration of a transport model, which considers dispersion as well as sorption and other processes, requires much more information (see sections 6.5 and 6.7 on data need and data collection) as well as a denser sampling net and more frequent sampling. Therefore, when compared to the previous studies, it is considerably more difficult and more costly in terms of time and money. Each particular case must be carefully evaluated to determine whether the results obtained from the purely advective flow model constructed in section 6.13.5 are already enough to give all the answers for the problem or not. If, e.g. sorption needs to be considered, we need to know whether solute-specific sorption data can be taken from literature, or whether sorption experiments in the laboratory must be performed. The same applies for obtaining the longitudinal and the horizontal dispersivity values.

In the example of Las Palmas, the groundwater flow field is quite well known from the previous investigations (see 6.13.5), so one of the basic conditions for the elaboration of a solute transport model is fulfilled. On the contrary, information on solute concentrations is very limited (too limited for constructing a transport model), since sampling and analysis are available only for one time and since there are barely 6 sampling points in the area covered by the contamination plume. There are no data corresponding to the dispersion parameter of the aquifer. In regard to exchange processes between contaminants and aquifer materials and other substances dissolved in groundwater, only bibliographic references are available. According to these, chloride can be used as an ideal tracer, whereas boron, which at the present pH value is present as hydroxyborate anions, undergoes adsorption and desorption processes, being predominantly sorbed to clay minerals, iron, manganese hydroxides and oxides, and organic substances.

Based on this limited data scenario, there are two basic possibilities for the continuation of our study:

- A detailed survey can be carried out in accordance to what is described in section 6.5 and 6.6 on data need and data collection, to obtain the missing data, if possible within a given time frame. Usually, except for special cases, propagation models can only be elaborated on in areas that have been extensively studied during a prolonged period of time and therefore, have abundant data available to calibrate the model.
- For this reason, in practice, a compromise solution is usually applied and the lack of data is covered by estimations or assumptions (e.g., regarding sorption parameters and aquifer dispersivities). In these cases, a sensitivity analysis of the aquifer to be described can be done, varying different parameters so as to determine the influence of these parameters on the behavior of the system. Naturally, this methodology reduces the credibility of the obtained results. To produce a reliable quantitative prognoses, it should be possible to validate field measurements with the model, regarding flow pattern, concentration distributions, and their changes with time.

For the example, the stationary groundwater flow model from section 6.13.5 is used. Additionally two tracer tests are performed in order to obtain values for longitudinal and transversal dispersivity (for tracer tests see section 6.7.2.5). Again, we need to remember that these aquifer parameters were determined on the basis of field measurements from only two discrete points, and hence, even if the results are correct, they likely only apply to the small local area that was tested. In practice, more determinations are needed in order to determine the range of the values, which will allow the modeler to obtain a range of modeling results. For each tracer test, two wells/piezometers are used, one as an injection well and another as a sampling point. Without drilling new piezometers, tests are limited to a few potential locations, since most wells are separated by a distance that is greater than 100 days of groundwater particles' travel time. One of the tests is carried out between wells W5 and W10, whereas the second test is performed between wells W17 and W28 (Fig. 6.11). In both cases, the respective first well acts as the injection well and the second well acts as the sampling point. The evaluation of these tracer test yields values of effective porosity, φ_{eff} , and the longitudinal and transversal dispersivity, α_L and α_T , respectively (Table 6.9). The data obtained by means of tracer tests are valid for two discrete points in the modeling area, which must be taken into account when interpreting the modeling results. Since there is no information available on sorption materials in the aquifer matrix and on the geochemical conditions, and since time and resources do not allow the collection of this information, the sorption behavior of hydroxyborate anions shall be evaluated as a very rough approximation. This approximation will be obtained by comparing the boron plume with the chloride plume, which can be considered as an ideal tracer and undergoes no sorption and retardation. With this limited data we perform simulations for the contaminant transport for two possible scenarios, which correspond to the best- and worst-case situation:

- The contamination source keeps contaminating the aquifer unaltered.
- The contamination source is immediately shut down.

6.13.6.2 *Simulation of solute propagation with a permanent inflow of contaminants*

The calibrated numerical groundwater flow model elaborated in section 6.13.5 is now being extended to a transport model which considers dispersion and adsorption processes. However, this model has limited accuracy which needs to be considered when interpreting the simulation results. Calibration to fit the modeled solute distribution to the observed one is not accurate and a series of concentration measurements are necessary to achieve effectiveness. Using the average of the dispersivities obtained from the tracer tests, a simulation of the Cl^- propagation yields for the contamination plume at time $t = 730$ days a Cl^- concentration distribution that matches the distribution observed in the field (Fig. 6.13a). On the other hand, the propagation of boron is delayed compared to the Cl^- propagation. This indicates that hydroxyborate anions are being adsorbed by the aquifer media. Calibrating the model using the retardation factor R_d for hydroxyborate anions, and assuming linear adsorption, for a value of $R_d = 2.5$ the simulated contamination plume matches best with the observed (Fig. 6.13b).

Considering the assumptions mentioned above, the concentrations are simulated for some of the contaminated wells as a function of time. Curves for chloride concentrations show that contaminated wells W22, W21, W18, PW, and P3, located on the edge of the contamination plume,

Table 6.9. Field example from Las Palmas: Effective porosity and dispersivity values obtained by tracer tests.

Injection well for tracer I	W5	W17
Sampling and observation well U	W10	W28
Effective porosity φ_{eff} (ad)	0.12	0.095
Longitudinal dispersivity α_L (m)	12	9
Transversal dispersivity α_T (m)	1.0	0.7

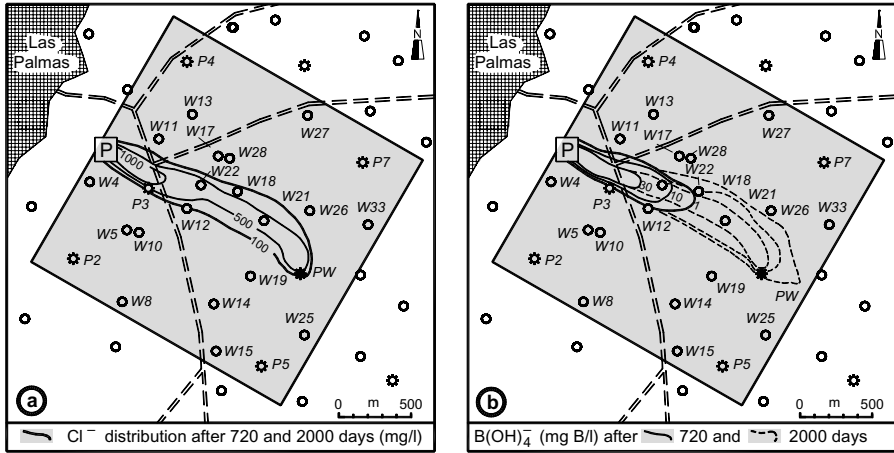


Figure 6.13. Field example from Las Palmas: Distribution of contaminants modeled for June 16, 1991 (=730 days) and 2000 days after the beginning of contaminant input: (a) for chloride, and (b) for hydroxyborate ions. The Cl^- distributions at 730 and 2000 days are identical.

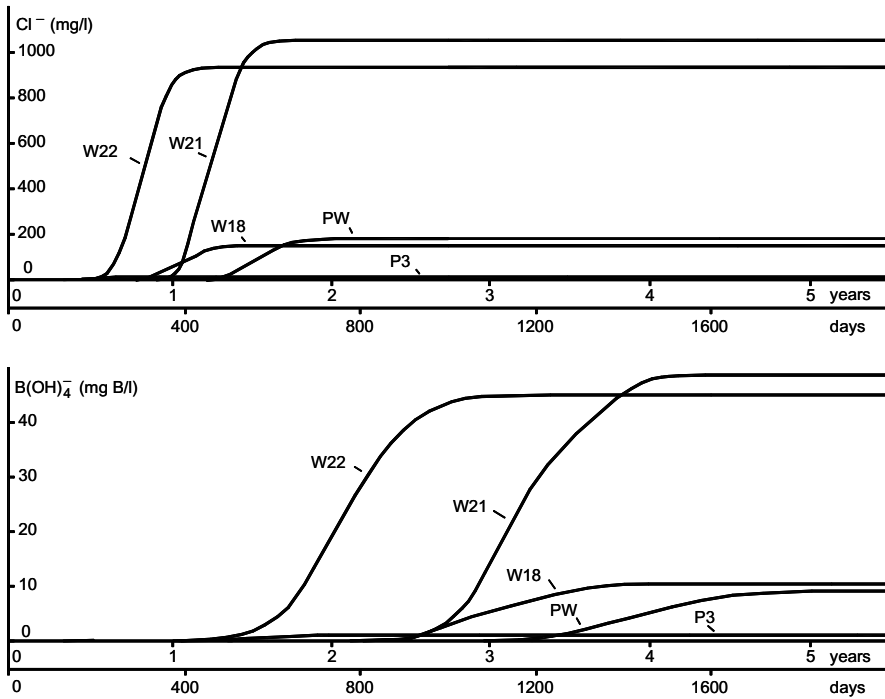


Figure 6.14. Evolution of solute concentrations, modeled for the affected sector: (a) chloride, (b) hydroxyborate anions (values as B) ($t = 0$ years corresponds to the beginning of contaminant inflow in June 1989; $t = 2$ years corresponds to the present time, June 1991).

are currently ($t = 2$ years) in a stationary stage, which means that chloride concentration will not vary in the future any more (Fig. 6.14). On the other hand, the concentration curves corresponding to boron show that these wells have not yet reached a stationary regime and concentrations will increase in the future (Fig. 6.14).

The following conclusions can therefore be drawn:

- Only wells W22, W21, W18, and PW show chloride concentrations of 860, 980, 135, and 180 mg/l that will not change in the future. Wells W22 and W21 are unusable and the remaining wells, including the pumping well, are below the threshold.
- The concentrations of hydroxyborate ions at wells W22, W21, W18, and PW, located within the affected area, reach (for time $t = 2$ years) values of 20, 0, 0.5, and 0.00 mg/l, respectively. These values will increase in the future until reaching 49, 41, 10, and 9.3 mg B/l, and numerous wells will be rendered useless. The pumping well at the water work will exceed the threshold value of 1 mg B/l at $t = 3.5$ years, that is, 1.5 years from now. Well W22, which is unusable due to its high concentration of chloride, already exceeds the maximum value for boron. Wells W21 and W18 will reach this threshold in approximately 7 months, at $t = 2.6$ years.

6.13.6.3 *Simulation of solute propagation with an immediate suspension of inflow of contaminants*

If the contamination source is immediately shut down (at $t = 730$ days), the following results are obtained:

- Chloride concentrations at wells W22, W21, W18, and PW, with 860, 980, 135, and 180 mg/l, are approximately constant for 0.5, 0.9, 1.0, and 1.5 years. After 1.1, 1.4, 1.2, and 1.7 years, the Cl^- background value will be reached. For wells W22 and W21, it will take 0.8 and 1.2 years, respectively, for the chloride concentration to go below the acceptable threshold level; after this both wells will be usable again.
- Due to the retardation effect of hydroxyborate ions, the high concentrations of wells W22, W21, W18, and PW with 2.8, 4.0, 3.7, and 4.5 mg B/l, respectively, will take considerably longer than the chloride to go below the admissible threshold value of 1 mg B/l.

When assessing these results, the contaminant concentrations and their variations in time, it must be taken into account that no accurate calibration of the transport model is possible because concentration measurements exist only for one discrete time. Hence, in the future, it will be necessary to collect new concentration data for comparison with the results obtained by modeling. In the case of a divergence, the model will have to be adapted to the new measured data and the results and prognosis will have to be adjusted accordingly.

6.13.6.4 *Water works: Diagnosis and recommended solutions*

The pumping well is only threatened by boron contamination and can be used for 1.5 more years before concentrations exceed the threshold level. If the industrial plant immediately stops contamination, the well would be unusable for 3 more years with concentrations of 9 mg/l. Different measures can be taken to present to ruling organizations. After a cost assessment study the most suitable option, or a combination of several options, will be chosen by them:

- The contamination source must be immediately shut down. It is recommended that the production liquid effluents ($10 \text{ m}^3/\text{day}$), with high concentrations of harmful substances, be diverted to evaporation pools with their bottoms sealed. Once the liquid is evaporated, the remaining solids should be deposited in suitable repositories. While these pools are built, effluents can be stored in tanks or suitable deposits.
- The water at the water work must be treated to reduce the boron concentrations, which are expected to remain for 3 years over the maximum threshold, in order to make the water potable.

- Additionally, a sanitation well may be drilled inside the contamination plume to extract and treat contaminated water.
- The water works can drill a new pumping well outside the contamination plume but in the vicinity of the one currently used. If this option is used, the new location will be determined by the elaborated simulation model. This possibility offers the following advantages: (1) Costs shall be paid by the contaminating industry; (2) After 4.5 years (when the old well is again suitable), the town of Las Palmas will have 2 additional wells for drinking water supply, which is important given the growing demand from the inhabitants. However, it needs to be considered that if the well that is currently being used is closed, then the contamination plume will extend further downstream. Therefore, studies must be carried out to determine if there is a contamination risk for other wells located downstream from this well. If so, it is recommended that the well remains in operation so that the contaminated aquifer is cleaned by removing all the contaminants.

6.13.6.5 *Farm wells: Diagnosis and recommended solutions*

Only wells W1, W22, W11, and W18 from all farm wells are or will be unusable. Since these farms require little water, it can be supplied by means of tank trucks while contamination lasts. The water needed for irrigation can be provided by wells located at neighboring farms (with the corresponding monetary compensation) and transported through temporary irrigation channels. A second alternative would be to suspend irrigation and file a claim against the party responsible for the contamination of indemnification to cover the reduced, or lack of agricultural production.

CHAPTER 7

Parameter identification and inverse problems

Longina Castellanos and Angel Pérez

“Inverse problems play a crucial role in geophysics because one of the main tasks in this field is to probe the Earth’s interior both for economic reasons, such as oil prospecting, and for the pursuit of academic knowledge about our planet.”

Roel Sniedery *et al.* (1998)*

7.1 INTRODUCTION

The scientific procedure to study an aquifer system, or any physical system in general, can be divided into three parts:

- Parameterization of the system: discovery of a minimal set of model parameters whose values completely characterize the system.
- *Direct problem* or *direct modeling*: discovery of the physical laws (e.g., groundwater flow equation, see chapter 4) allowing, for given values of the parameters (e.g., hydraulic conductivity of an aquifer, see section 4.3), predictions of some data parameters (e.g., hydraulic head) to be made.
- *Inverse modeling*: use of actual measurements of the observed parameters to infer the values of the model parameters (e.g., hydraulic conductivity). This inference problem is termed the *inverse problem*.

In chapter 5 we studied methods to obtain numerical solutions to the direct problem. These are, for instance, the finite element method, the line method and the finite difference method. In this chapter we study the inverse problem for parameter identification or reconstruction of unknown coefficients in a differential equation, from measurements of its solution.

In practice, conceptual models representing general behaviors of different states of the phenomenon in question are usually available (see chapters 6.3 and 6.4). Let us consider the simple differential model:

$$\frac{d\phi}{dt} = -x_1 e^{-t} + x_2 \cos(t) \quad (7.1)$$

Suppose the values for the parameters x_1 and x_2 are known. Then an approximate solution of equation (7.1) can be obtained using some adequate numerical method and thus a direct problem (DP) is solved: we know the *causes* (parameters x_1 and x_2) and evaluate the *effects* (the numerical values of $\phi(t)$) that allows us to know the state behavior as a function of time.

Suppose that we do not know the values of the parameters but that it is possible to obtain experimental measurements (data) of the values of $\phi(t)$ at m different times. The goal is to use these data to estimate the values of the parameters x_1 and x_2 from the most appropriate model. This is an inverse problem (IP): we know the effects ($\phi(t_i)$, $i = 1, \dots, m$) and we seek the causes (x_1 and x_2).

* Source: Roel Sniedery, Malcolm Sambridgez and Fernando Sansó: Inverse problems in geophysics: closing the gap between theory and practice. Guest editors’ introduction, *Inverse Problems* 14 (1998).

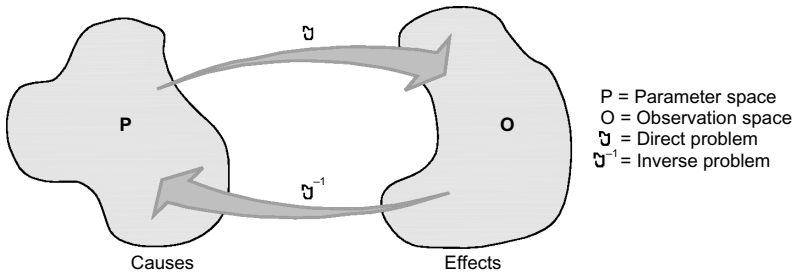


Figure 7.1. A graphic representation of the inverse-direct problems: causes are, e.g. hydraulic conductivity; effects are, e.g. hydraulic head.

We begin by simply defining the solution to an inverse problem as using the measurements of the effect to determine the cause. This view contrasts with the corresponding direct problem, whose solution involves finding effects based on a complete description of their causes. A graphic approach of the relationship between the inverse problem and the direct problem is presented in Figure 7.1.

These problems are usually divided into the terms:

- *Identification or reconstruction*, where one looks for the cause of an observed effect.
- *Control or design*, where one looks for ‘a’ possible cause of a desired effect.

Both problems are related, but there are also several mathematical consequences due to the different aims. In an identification problem a desirable property is uniqueness of a solution (identifiability), ideally there is a specific cause for the observed effect, which one would like to obtain. In a control or design problem, uniqueness is not really of importance, since non-uniqueness only means that the design goal can be reached by different strategies and hence, one has additional freedom (e.g., to incorporate further design goals).

Inverse problems may be classified as:

- *Continuous*: Most inverse problems are of this type. The parameter set to be estimated is a continuous function in several variables. For instance, the transmissivities in an aquifer are continuous functions of the space variables.
- *Discrete*: There are a finite number of model parameters to be estimated, for instance, the parameters x_1 and x_2 in the above example.

Sometimes the problem itself is continuous in nature (real world), but is discretized for computational reasons. For example, the partial differential equation (PDE) to find the hydraulic heads in an aquifer is discretized using a grid designed on the aquifer region, yielding a discrete system of equations.

The model function of an inverse problem, that might be the solution to a differential system of equations, as in example (7.1), may depend linearly or nonlinearly on the parameters. In equation (7.1), the analytic solution of the differential model is:

$$\varphi(x_1, x_2; t) = x_1 e^{-t} + x_2 \sin(t) \quad (7.2)$$

Suppose we have m data points y_i^{obs} of the behavior of φ at different times and we need to find x_1 and x_2 such that the distance from each of the y_i^{obs} to the corresponding model function $\varphi(t_i)$ for each t_i , $i = 1, \dots, m$, is minimized (see Fig. 7.2). In this example, the solution to the direct problem [the model function (7.2)] depends linearly on the parameters x_1 and x_2 , thus we need to solve a linear inverse problem.

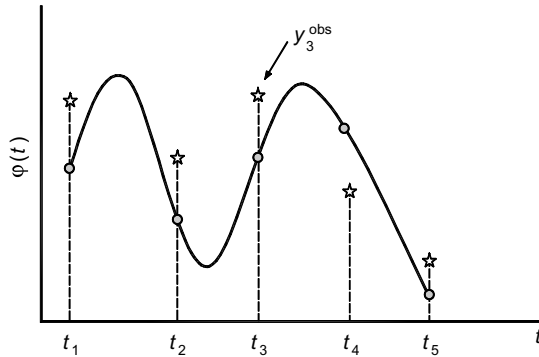


Figure 7.2. Model $\varphi(t)$ and observed data y_i^{obs} .

On the other hand, if the differential model is:

$$\frac{d\phi}{dt} = -x_1 e^{-x_1 t} + x_2 \text{Cos}(x_2 t) \tag{7.3}$$

the model function is then:

$$\varphi(x_1, x_2; t) = e^{-x_1 t} + \text{Sin}(x_2 t) \tag{7.4}$$

Thus, the solution to the direct problem [the model function (7.4)] depends nonlinearly on the parameters x_1 and x_2 , and we need to solve a nonlinear inverse problem. The goal in both, the linear and nonlinear cases, is to make the calculated solutions at each t_i , i.e., $\phi(x_1, x_2; t_i) = y_i^{\text{cal}}$ as close as possible to the observed data y_i^{obs} , for all $i = 1, \dots, m$.

In practice, the most common situation is that the analytic solution of a differential model is not available and the DP is solved numerically, thus it is difficult to establish whether the IP is linear or nonlinear. A parameter that appears linearly on a differential equation does not imply that it is also linear in the solution. For example, the equation:

$$\frac{d\phi}{dt} = -x_1 \phi$$

is a linear function of x_1 . However, its solution $\varphi(t) = e^{-x_1 t}$ is a nonlinear function of the parameter x_1 .

One way to measure the nearest solution is through the definition of some kind of distance. The most common, for several reasons, is the squared distance between the data points and the computed values. In this particular case, one would like to obtain the pair of values x_1 and x_2 such that the sum:

$$\sum_{i=1}^m (\varphi(x_1, x_2; t_i) - y_i^{\text{obs}})^2 = \sum_{i=1}^m (y_i^{\text{cal}} - y_i^{\text{obs}})^2 \tag{7.5}$$

is minimized, and the parameters x_1 and x_2 would be the ones for which the least value of the sum is reached.

The general mathematical formulation is the so-called least-squares problem (LSP) and it is as follows (the particular form in which the parameters appear in the model function makes the

term linear or nonlinear, accordingly):

$$\begin{aligned} \text{Minimize } F(\vec{x}) &\triangleq \frac{1}{2} \sum_{i=1}^m (\varphi(\vec{x}; t_i) - \bar{y}_i^{\text{obs}})^2 = \frac{1}{2} \|\vec{\Phi}(\vec{x}; t) - \bar{y}^{\text{obs}}\|_2^2 = \frac{1}{2} \|\vec{f}(\vec{x})\|_2^2 \\ \text{subject to } l_j &\leq x_j \leq u_j \\ & j=1, \dots, n \end{aligned} \quad (7.6)$$

with $\Phi(\vec{x}; t) = (\varphi(\vec{x}; t_1), \dots, \varphi(\vec{x}; t_m))^t$; $\bar{y}^{\text{obs}} = (y_1^{\text{obs}}, \dots, y_m^{\text{obs}})^t$;
 $\vec{f}(\vec{x}) = (f_1(\vec{x}), \dots, f_m(\vec{x}))^t$; $f_i(\vec{x}) = \varphi(\vec{x}; t_i) - y_i^{\text{obs}}$, $i = 1, \dots, m$

where $\varphi(\vec{x}; t)$ represents the desired model function, with t an independent variable and where the data $\{y_i^{\text{obs}}\}$ are measured and may be subject to experimental error. The independent variables $\{x_j\}$, $j = 1, \dots, n$, are the parameters of the problem to be manipulated in order to adjust the model to the observed data. The components of the vector function $\vec{\Phi}$ are the values of the model function $\varphi(\vec{x}; t)$ at each t_i , for $i = 1, \dots, m$.

If the model is to have any validity, we can expect that the function value at the solution of (7.6) will be small and that m , the number of data points, will be much greater than n . The vector function \vec{f} is called the residual vector. The variables l_j and u_j are the lower and upper bounds on the unknown parameters, respectively, which might not be present in the problem formulation, although they usually are in real problems, e.g. if we know the range of hydraulic conductivity values which can occur in a specific case.

The next sections will be devoted to the ill-posed inverse problem (section 7.2) and the methods used to solve the least-squares problem separately for the linear (section 7.3) and nonlinear case (section 7.4). We shall see their differences and similarities, the benefits of considering different methods for each type and also, the need for regularization in both cases. In what follows, we will use the two-norm and we omit the subscript.

7.2 ILL-POSEDNESS OF THE INVERSE PROBLEM

An obvious question when computing the minimizer of equation (7.6) is if this is a guarantee that the parameters are correct when identifiability is crucial (e.g., in parameter identification problems). Some authors call *model calibration* the process of estimating or identifying the proper parameters (see section 6.9). It is important to increase confidence in the solution making sure that the calculated parameters are correct within a certain range of measurement error. In any type of inverse problem one or more of the following Hadamard conditions may fail:

- 1st Hadamard condition: *Existence*: For all (suitable) data, there exists an appropriate solution to the problem.
- 2nd Hadamard condition: *Uniqueness*: For all (suitable) data, the solution is unique.
- 3rd Hadamard condition: *Stability*: The solution depends continuously on the data.

Is it then possible to obtain a good approximation to the correct values of the parameters if one of these conditions fails? We shall answer the question in this section and also in sections 7.3.3 and 7.4.3.

Inverse problems belong to the class of the so-called ill-posed problems. According to Jacques Hadamard (1865–1963), a mathematical problem is well-posed if the solution is unique and the data error is not amplified in the solution error. Thus, an ill-posed problem does not satisfy one of the Hadamard conditions. Neither existence nor uniqueness of a solution to an inverse problem is always guaranteed. Thus computing the least-squares solution of an inverse problem is a way to guarantee that there is always a solution.

As mentioned in section 7.1, non-uniqueness is sometimes advantageous, allowing the choice among several strategies for obtaining a desired effect (control or design case). Consequently the

third Hadamard's condition is not either important, since we are satisfied having small residuals for the solution parameters in order to reproduce the observed data.

If the level of the error in the data is large, the third condition of Hadamard does not matter either, even when the uniqueness of the solution is needed, because the exact problem and the problem with error are so distant from each other that they are simply different problems. In parameter identification or in any identifiability inverse problem, the third Hadamard condition must be addressed carefully.

In practical applications, the observed data are not exact, but instead contain noise owing to measurement errors and inaccuracies of the model itself. Even if the data noise is small, algorithms developed for well-posed problems could fail in case of a violation of the third Hadamard condition if they do not address the instability, since the data as well as the round-off errors may be amplified by an arbitrarily large factor in the solution error. Regularization methods, in which general terms of an ill-posed problem are replaced by a family of neighboring well-posed problems, are used in order to overcome this failure.

In the following sections we will study further failures of the fulfillment of Hadamard conditions in inverse problems.

7.2.1 Existence of a solution

If there is no solution one may ask: Does the model $\varphi(\vec{x}; t)$ really reflect the phenomenon measured by the data $\{y_i^{\text{obs}}\}$? Is there a set of parameters with $\varphi(\vec{x}; t)$, $i = 1, \dots, m$ sufficiently close to the observed data? This is because we are trying to fix a model function to some data that are not reproduced by the model. This may occur because the governing law for the phenomenon is not complete or simplifications or assumptions have been made that are not correct (e.g., developing a wrong or over-simplified conceptual model; see section 6.3). In this case the conceptual model should be reviewed for accuracy. For instance, if we suppose that the model function is:

$$\varphi(x_1; t) = t x_1^2 + 1$$

and the data is just the point $(1, 0)$, then x_1 is the solution to the equation:

$$\varphi(x_1; 1) = 1 x_1^2 + 1 = 0$$

which does not have a real solution. Nonetheless, if one looks for:

$$\underset{x_1 \in \mathbb{R}}{\text{Minimize}} F(x_1) = \|(x_1^2 + 1) - 0\|^2 = \|\varphi(x_1; 1) - 0\|^2$$

the solution is $x_1 = 0$ with $F(x_1) = 1$.

When a least-squares procedure is used to solve the inverse problem, as was shown in the above example, there is always a solution for any given model. However, if the available data are not enough, this method could produce large residuals and the solution parameters might give an inadequate model with incorrect estimated parameters even when non-uniqueness is not important, since the goal is to make the model function as close as possible to the observed data (Fig. 7.3). A rule of thumb is to obtain as much data as possible; although this is not always possible, may be because of financial restrictions or others, which hinder further data collection in the field (see chapter 6).

7.2.2 Uniqueness of the solution (identifiability)

If there is more than one solution, many non-desired solutions may be avoided by providing additional information. For example, finding the correct values of x_1 and x_2 in the model function $\varphi(x_1, x_2; t) = x_1 t + x_2$ to reproduce the data point $(2, 0)$, does not have a unique solution, but if in addition we have the condition $x_2 = 1$, the solution is uniquely identified.

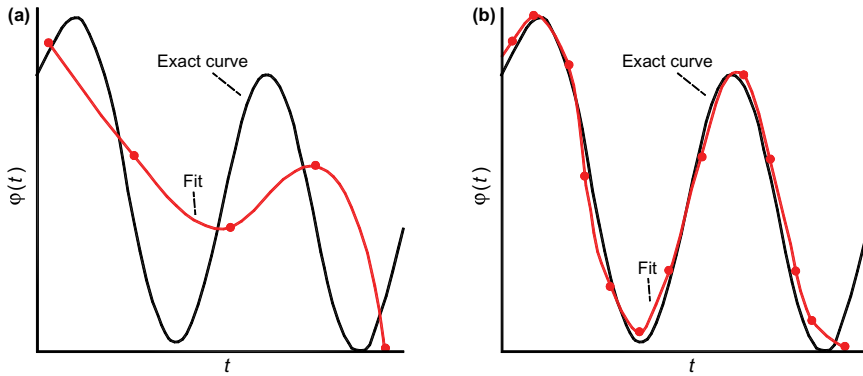


Figure 7.3. Effect of the number of data in the solution of an inverse problem: (a) few data, (b) many data.

In many cases, we can give a range for the values of the parameters based on experience or because of physical or chemical knowledge. Limits for the estimates contribute to a more restricted search space, coming closer to the uniqueness (see also chapter 6.9).

Constraints on the type of bounds of the parameters can be deduced *a priori*. Furthermore, a review of the model is advisable since the non-uniqueness of the solution might be due to an over-parameterization, e.g., some parameters might not be needed (e.g., we can neglect compressibility of the fluid if we consider shallow aquifers) (see also chapter 6).

In the following model:

$$\varphi(x_1, x_2, x_3; t) = x_1 t + 2x_2 t e^{-x_3 t}$$

if we have $x_3 = 0$, then the model becomes:

$$\varphi(x_1, x_2; t) = x_1 t + 2x_2 t = (x_1 + 2x_2)t$$

Thus, it is not necessary to compute two parameters; instead one sets a new parameter $\alpha = x_1 + 2x_2$ and seeks only for this single parameter.

A remedy for the non-uniqueness is choosing among the multiple solutions, for example, the least size solution, measured with some norm. But, is it a problem if we have a non-unique solution? In the introduction of this chapter we said that it depends on the circumstances:

- If it is ‘a’ cause that is needed to reproduce the desired effect then, rather than being a problem, having many solutions gives different scenarios from which to choose the most convenient solution under certain practical criteria (case of control or design).
- If on the other hand, ‘the’ cause of a given effect is needed, then uniqueness is of major interest (case of identification or reconstruction), e.g., computing the hydraulic conductivity in the flow equation of an aquifer.

7.2.3 Continuous dependency on the data

This condition might fail because most inverse problems arise from the discretization of a continuous setting producing ill-conditioned matrices if an accurate scheme is not used with care (see section 7.3.1). The error between the computed (approximate) solution and the solution with no error (exact but unknown) might be larger than the error in the data. Regularization strategies are needed to obtain a solution closer to the exact solution. We emphasize that this regularization is important in the case of identifiability and when the error in the observed data is small.

7.3 LINEAR LEAST-SQUARES (LLS)

As was pointed out in section 7.1, the definition of a least-squares problem as linear or nonlinear, depends on the way in which the parameters or functions to be estimated appear in the model function. If they appear in linear form, then the vector function $\vec{\Phi}(\vec{x}; t)$, whose i -th component is the model function $\varphi(\vec{x}; t_i)$, can be written as:

$$\vec{\Phi}(\vec{x}; t) = \mathbf{A}\vec{x}$$

where \mathbf{A} is an $m \times n$ matrix, and we have a linear least-squares (LLS) problem. Therefore the linear least-squares problem has the following mathematical statement:

$$\begin{aligned} \text{Minimize } F(\vec{x}) \triangleq \frac{1}{2} \|\mathbf{A}\vec{x} - \vec{y}^{\text{obs}}\|^2 \\ \mathbf{A} : m \times n \text{ matrix, } \vec{y}^{\text{obs}} : m\text{-data vector} \end{aligned} \tag{7.7}$$

where $\vec{r} = \mathbf{A}\vec{x} - \vec{y}^{\text{obs}}$ is known as the residual vector [called a residual function in the general setting of equation (7.6)].

In order to determine the parameters x_1 and x_2 in the model function (7.2), having m data points (t_i, y_i^{obs}) , we may set the vector function $\vec{\Phi}(\vec{x}; t)$ in the following matrix form:

$$\begin{aligned} \vec{\Phi}(\vec{x}; t) &= \begin{bmatrix} \varphi(\vec{x}; t_1) \\ \varphi(\vec{x}; t_2) \\ \vdots \\ \varphi(\vec{x}; t_m) \end{bmatrix} = \begin{bmatrix} x_1 e^{t_1} + x_2 \text{Sin}(t_1) \\ x_1 e^{t_2} + x_2 \text{Sin}(t_2) \\ \vdots \\ x_1 e^{t_m} + x_2 \text{Sin}(t_m) \end{bmatrix} = \mathbf{A} \begin{bmatrix} x_1 \\ x_2 \end{bmatrix} = \mathbf{A}\vec{x}; \\ \text{with: } \mathbf{A} &= \begin{bmatrix} e^{t_1} \text{Sin}(t_1) \\ e^{t_2} \text{Sin}(t_2) \\ \vdots \\ e^{t_m} \text{Sin}(t_m) \end{bmatrix} \end{aligned}$$

A solution (minimizer) of problem (7.7) necessarily satisfies $\vec{\nabla}F(\vec{x}^*) = \vec{0}$, that is:

$$\begin{aligned} \vec{\nabla}F(\vec{x}^*) &= \vec{\nabla} \left(\frac{1}{2} \|\mathbf{A}\vec{x}^* - \vec{y}^{\text{obs}}\|^2 \right) = \vec{0} \\ \Leftrightarrow \mathbf{A}^t(\mathbf{A}\vec{x}^* - \vec{y}^{\text{obs}}) &= \vec{0} \\ \Leftrightarrow \mathbf{A}^t\mathbf{A}\vec{x}^* &= \mathbf{A}^t\vec{y}^{\text{obs}} \end{aligned} \tag{7.8}$$

and the relations in the last row are the so-called normal equations.

A well-known result from linear algebra for a square system of linear equations is that if the matrix of the system is invertible (nonsingular), then the solution is unique; otherwise there are infinitely many solutions. We rewrite the well-known result for the LLS case (for details, see Golub and Van Loan 1989).

Result: If the matrix \mathbf{A} has linearly independent columns (thus $\mathbf{A}^t\mathbf{A}$ is nonsingular), the solution to the LLS problem is unique, otherwise $\mathbf{A}^t\mathbf{A}$ is singular and there are an infinite number of solutions.

Thus, in a linear parameter identification problem solved using LLS, the uniqueness of the solution is guaranteed if the system matrix has linearly independent columns but, is this sufficient for identifying the proper parameters? What about the third Hadamard condition? To answer these questions we need the definitions of the following section.

7.3.1 Condition number of an invertible square matrix

A definition that is closely related to errors is the condition number of an invertible square matrix, with respect to the solution of a system of equations $\mathbf{A}\vec{x} = \vec{y}$. This number is defined as:

$$\kappa(\mathbf{A}) = \|\mathbf{A}\| \|\mathbf{A}^{-1}\| \geq 1$$

and measures the largest possible effect that errors on the data or in the matrix of a linear equations system, can cause on the solution. The number $\kappa(\mathbf{A})$ is also a measure of how close a nonsingular (invertible) square matrix is to being singular. A ‘large’ condition number indicates that the solution is very far from the exact solution, even with small errors in the observed data.

In practice the linear system we really have is $\mathbf{A}_{\text{error}}\vec{x} = \vec{y}^{\text{obs}}$, with error in both, the matrix and the vector in the right hand side; the following inequalities hold:

$$\begin{aligned} \|\vec{x}^* - \vec{x}_{\text{exact}}^*\| &\leq \kappa(\mathbf{A}) \|\vec{y}^{\text{obs}} - \vec{y}\| \\ \|\vec{x}^* - \vec{x}_{\text{exact}}^*\| &\leq \kappa(\mathbf{A}) \|\mathbf{A}_{\text{error}} - \mathbf{A}\| \end{aligned}$$

where:

- \vec{x}_{exact}^* is the exact solution for the exact data \vec{y}
- \vec{x}^* is the approximated solution for the data with error \vec{y}^{obs}
- $\mathbf{A}_{\text{error}}$ is the matrix (linear model) with errors

In other words, the condition number of \mathbf{A} indicates the maximum effect of errors in the data \vec{y} or in the matrix \mathbf{A} , on the exact solution \vec{x}^* of the linear system. In this chapter we will refer only to errors in the observed data. More details on system matrix errors can be found in Golub *et al.* (1998); this technique is known as *total least-squares*.

When we solve inverse problems, the discrete formulation reflects the ill-posedness of the continuous underlying problem in the ill-conditioning of the associated matrix or matrices (in the nonlinear case), associated to their discretization, which corresponds to a large condition number.

The normal equations (7.8) solving the LLS problem have as matrix system $\mathbf{A}^t \mathbf{A}$. This matrix $\mathbf{A}^t \mathbf{A}$ has a condition number that is the square of $\kappa(\mathbf{A})$ (it is possible to define the condition number of a rectangular matrix in a similar manner using the definition of pseudo-inverse, see Golub and Van Loan 1989 for more details). It is advisable not to form this matrix product in order to avoid increasing the condition number of the system matrix and, consequently, making the error larger in the approximate solution of the LLS. Obviously, the ill-conditioning of \mathbf{A} is the cause of the failure of the third Hadamard condition in LLS problems and thus, in this case, the parameters of the model might not be correctly identified.

It is worthwhile to repeat that the condition number is defined for nonsingular matrices, and that we have uniqueness but not continuous dependency on the data whenever the condition number is large, which is the challenging case. In the next section we will see a method that avoids the construction of $\mathbf{A}^t \mathbf{A}$.

7.3.2 Linear least-squares solution: Direct method

The solution of LLS problems is usually obtained using some factorization of the matrix \mathbf{A} which is called a direct method. This avoids the formation of the product $\mathbf{A}^t \mathbf{A}$ and the increment of the condition number of the system matrix (section 7.3.1). The most popular method is the \mathbf{QR} factorization (Golub and Van Loan 1989), where \mathbf{Q} is an orthogonal $m \times m$ matrix ($\mathbf{Q}^t \mathbf{Q} = \mathbf{I}_m$) and \mathbf{R} is an upper triangular $m \times n$ matrix; the algorithm proceeds as follows:

1. Pre-multiplying the matrix \mathbf{A} by orthogonal matrices that nullify the entries under its diagonal, i.e:

$$\mathbf{H}_n \cdot \mathbf{H}_{n-1} \dots \mathbf{H}_1 \mathbf{A} = \mathbf{Q}^t \mathbf{A} = \begin{pmatrix} \mathbf{R}_{n \times n}^u \\ \mathbf{0}_{(m-n) \times n} \end{pmatrix}$$

2. Applying this factorization to the LLS problem and using the property of orthogonal matrices: $\|\mathbf{Q}\vec{x}\| = \|\vec{x}\|$, to obtain:

$$\|\mathbf{A}\vec{x} - \vec{y}^{\text{obs}}\| = \|\mathbf{Q}^t(\mathbf{A}\vec{x} - \vec{y}^{\text{obs}})\| = \|\mathbf{R}\vec{x} - \mathbf{Q}^t\vec{y}^{\text{obs}}\| = \left\| \begin{pmatrix} \mathbf{R}_{n \times n}^u \\ \mathbf{0}_{(m-n) \times n} \end{pmatrix} \vec{x} - \begin{pmatrix} (\mathbf{Q}^t\vec{y}^{\text{obs}})_{n \times 1} \\ (\mathbf{Q}^t\vec{y}^{\text{obs}})_{(m-n) \times 1} \end{pmatrix} \right\|$$

3. The minimum value of the LLS function is given by:

$$\vec{x}^* = (\mathbf{R}_{n \times n}^u)^{-1}(\mathbf{Q}^t\vec{y}^{\text{obs}})_{n \times 1}$$

Different commercial software is available for the LLS solution using the **QR** factorization technique, e.g. routine LSQR of the IMSL package (inline library of the Microsoft Visual FORTRAN, <http://www.vni.com/products/imsl>).

7.3.3 Tikhonov's regularization method

If a matrix is invertible and thus has a unique solution to the system of linear equations, but if the condition number $\kappa(\mathbf{A})$ is large (\mathbf{A} is ill-conditioned), then the presence of small errors in the data might produce large errors in the solution, i.e. the problem does not depend continuously on the data and does not fulfill the third Hadamard condition. This implies that:

$$\|\vec{y}^{\text{obs}} - \vec{y}\| < \delta \quad \text{but} \quad \|\vec{x}^* - \vec{x}_{\text{exact}}^*\| \gg \delta$$

We make the clarification at this point that this consideration is important when the level of error in the data is small and thus one expects to have a solution error of approximately δ . If the perturbation level in the observed data is large, then the problem being solved ($\mathbf{A}\vec{x} = \vec{y}^{\text{obs}}$) varies greatly from the exact problem ($\mathbf{A}\vec{x} = \vec{y}$) and it is not sensible to compare \vec{x}^* with \vec{x}_{exact}^* , because they represent the same model (the system matrix is the same), but with different goals (the data to which the model must be fixed).

The first step of regularization is to transform an ill-posed problem, by means of relevant information given by the knowledge of the user, into a well-posed one. Nonetheless, there are some mathematical methods that may regularize a problem even though there is no physical or practical information or if this information is insufficient. We emphasize the fact that the larger information is for a given problem, the better the solution is for the inverse problem.

When ill-conditioning is present, which usually happens in inverse problems, it might produce solutions quite far from the correct one, in the presence of small errors in the data. This effect is independent of the numerical stability of the algorithm (Golub and Van Loan 1989). Tikhonov (1963) proposed to substitute the solution of the ill-posed problem by a sequence of solutions to well-posed problems that depends on a parameter. When the parameter is close to zero, the solutions of this sequence tend toward the solution of the problem without error.

An application of Tikhonov's regularization method (Tikhonov 1963, Tikhonov *et al.* 1995), applied to the discrete LLS, solves this problem by adding a penalization term to the size of the solution vector to get a balance between the size of the residual vector and the size of the solution vector, solving the enhanced function:

$$\text{Minimize}_{\vec{x} \in \mathbb{R}^n} \frac{1}{2} \|\mathbf{A}\vec{x} - \vec{y}^{\text{obs}}\|^2 + \frac{\lambda^2}{2} \|\vec{x}\|^2 \tag{7.9}$$

The problem is to select the scalar λ which is a problem-dependent parameter. If the correct λ is found, then the solution obtained (the so-called regularized solution) is the best possible solution for the corresponding data error.

One usual way to accomplish this goal is to solve equation (7.9) for a decreasing sequence of λ , substituting the ill-posed problem by a sequence of well-posed problems; then plotting the λ -parametric curve of:

$$\|\mathbf{A}\vec{x}_\lambda^* - \vec{y}^{\text{obs}}\| \text{ vs } \|\vec{x}_\lambda^*\|$$

and selecting the point where both quantities are balanced since, as $\lambda \rightarrow 0$, the first quantity decreases and the second increases (Tikhonov *et al.* 1995). The basic iteration is as follows:

Tikhonov’s regularization method for LLS:

Given $\lambda^0 > \lambda^1 > \dots$, set $i = 0$

$$\left\{ \begin{array}{l} \text{Solve } \vec{x}_{\lambda_i}^* = \arg \min_{x \in \mathbb{R}^n} \left(\frac{1}{2} \|\mathbf{A}\vec{x} - \vec{y}^{\text{obs}}\|^2 + \frac{\lambda^i}{2} \|\vec{x}\|^2 \right) \\ \text{Set } i = i + 1 \end{array} \right.$$

Graph $\|\mathbf{A}\vec{x}_{\lambda_i}^* - \vec{y}^{\text{obs}}\|$ vs $\|\vec{x}_{\lambda_i}^*\|$ for $i = 0, 1, \dots$, and select the corner point $\vec{x}_{\lambda_c}^*$ as the best one.

The solution will be the one corresponding to the corner point of the parametric curve for λ (Fig. 7.4).

As a summary of the importance of regularization for the identification problem, we state the following two conclusions (Burger 2005):

- Without regularization and without further information, the error between the exact and the approximated solution can be arbitrarily large, even if the error in the data is arbitrarily small.
- Even with regularization, we can never achieve an error in the reconstruction or identification of parameters which is as low as the error in the observed data.

7.3.4 An iterative method for solving LLS: Linear conjugate gradients

The conjugate gradient method (Nemirovskii 1986) was originally designed to solve linear systems of equations with a symmetric positive definite coefficient matrix. This method was later extended to nonlinear problems. We refer to it here as the linear conjugate gradient (LCG) method, to emphasize that the method is used for the case of a linear system of equations. In the LLS problem we need to solve the system of normal equations:

$$\mathbf{A}^t \mathbf{A} \vec{x} = \mathbf{A}^t \vec{y}^{\text{obs}}$$

and whenever the matrix \mathbf{A} has linearly independent columns, satisfies the requirement of the LCG method pointed above. However, the application of this method is not direct and the procedure for solving the normal equations has many variations. Here, we consider the algorithm

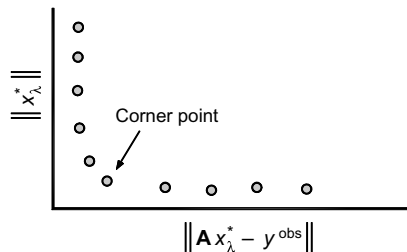


Figure 7.4. Corner point: solution for Tikhonov’s regularization method.

CGNE (conjugate gradient on the normal equations) given in Golub and Van Loan (1989), which experimentally is a good choice. The iterations will be \vec{x}_k , corresponding to the previous system of equations:

Linear conjugate gradient method for LLS: Algorithm CGNE:

Set $\vec{x}_0 = \vec{0}$, $\vec{r}_0 = \vec{y}^{\text{obs}} - \mathbf{A}\vec{x}_0$, $\vec{d}_0 = \mathbf{A}^t \vec{r}_0$

For $k = 1, 2, \dots$, until n or convergence, **do**

$$\left\{ \begin{array}{l} \alpha_k = \|\mathbf{A}^t \vec{r}_{k-1}\|^2 / \|\mathbf{A} \vec{d}_{k-1}\|^2 \\ \vec{x}_k = \vec{x}_{k-1} + \alpha_k \vec{d}_{k-1} \\ \vec{r}_k = \vec{r}_{k-1} - \alpha_k \mathbf{A} \vec{d}_{k-1} \\ \beta_k = \|\mathbf{A}^t \vec{r}_k\|^2 / \|\mathbf{A}^t \vec{r}_{k-1}\|^2 \\ \vec{d}_k = \mathbf{A} \vec{r}_k + \beta_k \vec{d}_{k-1} \end{array} \right.$$

Some interesting properties of this method are:

- Property 1: It is not necessary to store any matrix, only matrix-vector products are required.
- Property 2: In exact arithmetic, the convergence (i.e. $\|\vec{r}_k\| \approx 0$) is obtained in a number of iterations that is equal to the number of different eigenvalues of the matrix $\mathbf{A}^t \mathbf{A}$. This last fact permits using the method as a direct one. However, in practice, rounding errors produce the loss of this property and the method then behaves as an iterative one.
- Property 3: From the algorithm above, it can be seen that it is not necessary to form the matrix product $\mathbf{A}^t \mathbf{A}$.
- Property 4: For $\vec{x}_0 = \vec{0}$ the following properties hold:

$$\|\vec{x}_{k-1}\| < \|\vec{x}_k\| \quad \text{and} \quad \|\mathbf{A}\vec{x}_{k-1} - \vec{y}^{\text{obs}}\| > \|\mathbf{A}\vec{x}_k - \vec{y}^{\text{obs}}\|$$

- Property 5: On ill-conditioned problems, the first iterations approximate the exact solution.

The key to using the LCG method on ill-conditioned problems, as is usually the case for inverse problems, is the last property mentioned above: that the first iterations \vec{x}_k approximate the exact solution (Hansen 1998, Nemirovskii 1986). Thus, the importance of finding the iteration number k^* that gives the best possible approximation \vec{x}_{k^*} to the exact solution is clear. This is an alternative regularization way to the Tikhonov regularization method, in the sense that instead of solving problem (7.9) for a decreasing sequence of λ values, the regularization parameter is now given by the iteration number.

Algorithm CGNE is a very powerful tool for solving linear systems of equations, also because of its low memory requirement (property 1), thus it is quite useful in large-scale problems. A commercial code of the algorithm CGNE is available in the routine CGLS of the numerical toolbox of MATLAB (a high-performance language for technical computing, see the web site <http://www.mathworks.com>). The goal is now to correctly select the iteration number k^* . The next section is devoted to present a heuristic process to accomplish this objective.

7.3.4.1 L-curve regularization algorithm

The L-curve algorithm (Hansen 1998) was originally designed to compute the regularization parameter in Tikhonov's method (7.9); it can also be used to compute the iteration number k^* in the case of the LCG method. We describe the implementation for the latter case. Using property 4 from the introduction of section 7.3.4, we have that the norm of the LCG iterations $\|\vec{x}_k\|$, increases monotonically with k , and the residual norm $\|\mathbf{A}\vec{x}_k - \vec{y}^{\text{obs}}\|$, decreases monotonically with k . This behavior is important when using the L-curve which is described below (Hansen 1998).

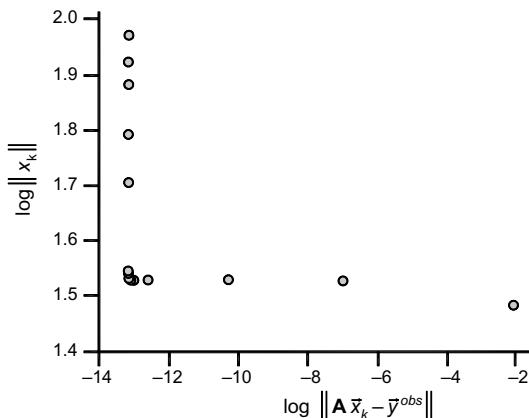


Figure 7.5. L-curve for the Foxgood example.

The main idea is to construct a parametric curve of the norm of the iterations $\|\vec{x}_k\|$ vs $\|\mathbf{A}\vec{x}_k - \vec{y}^{obs}\|$, where the parameter of this curve is the iteration index k . This curve is formed by discrete points and has a special shape, because these quantities increase and decrease respectively. The curve very often has an ‘L’ shape which gives the name to the algorithm. In Figure 7.5 the points of the L-curve are represented in a log-log scale, for a test example called Foxgood (Hansen 1998), with dimension $n = 64$ and considering a perturbation of order 10^{-6} in \vec{y}^{obs} , i.e. $\vec{y}^{obs} = \vec{y}^{exact} + 10^{-6}\xi(1, \dots, 1)^t$; where $\xi \in (0, 1)$ is a random number generated for each component value.

The corner of the L-curve balances the minimization of the residual norm and the norm of the LCG iterations (shown in Fig. 7.5). The placement of the points suggests that it is intuitively easy to determine the index k^* of the corner; however, its automatic detection requires a numerical algorithm that takes into consideration the different shapes that this curve may have when using a log-log scale. For a review of some ideas and algorithms to find the corner of an L-curve see Castellanos *et al.* (2002).

7.3.4.2 Linear preconditioned conjugate gradient method

In order to improve the conditioning of the matrix of a system of linear equations to accelerate the convergence of the conjugate gradient method, i.e., to equalize the largest number of eigenvalues as possible (see property 2 in the introduction to 7.3.4), it is convenient to use what is known as a pre-conditioner. We have the following equivalent system for the normal equations:

$$\mathbf{M}^t \mathbf{A} \vec{x} = \mathbf{M}^t \vec{y}^{obs} \tag{7.10}$$

where \mathbf{M} is the pre-conditioner. In this case it is said that a left preconditioning has been applied. The technique of preconditioning consists of doing a linear change of variables $\vec{x} = \mathbf{M}^t \vec{y}$ and then minimizing the function:

$$h(\vec{y}) = f(\vec{x}) = \frac{1}{2} \|\mathbf{A} \vec{x} - \vec{y}^{obs}\|^2 = \frac{1}{2} \|\mathbf{A} \mathbf{M}^t \vec{y} - \vec{y}^{obs}\|^2$$

$$\nabla h(\vec{y}) = (\mathbf{A} \mathbf{M}^t)^t (\mathbf{A} \mathbf{M}^t \vec{y} - \vec{y}^{obs})$$

Using the necessary conditions for a minimizer, i.e., $\nabla h(\vec{y}) = \vec{0}$ we obtain (7.10):

$$(\mathbf{A} \mathbf{M}^t)^t \mathbf{A} \mathbf{M}^t \vec{y} = (\mathbf{A} \mathbf{M}^t)^t \vec{y}^{obs} \Leftrightarrow \mathbf{M}^t \mathbf{A} \mathbf{M}^t \vec{y} = \mathbf{M}^t \vec{y}^{obs} \Leftrightarrow \mathbf{M}^t \mathbf{A} \mathbf{x} = \mathbf{M}^t \vec{y}^{obs}$$

The simplest pre-conditioner is a diagonal matrix, e.g. to give the same order of magnitude to each parameter that can be measured in different units system. For instance, if $\vec{x} = (x_1, x_2)^t$ and x_1 is measured in kilometers and x_2 in meters, it is advisable to set both numbers to the same system of units, which is equivalent to put $\vec{x} = \mathbf{D}\vec{y}$ with $\mathbf{D} = \text{diag}(10^{-2}, 1)$ setting both to meters.

The ideal pre-conditioner would be the inverse of the system matrix because the solution is just the matrix-vector product: $\vec{x}^* = (\mathbf{A}^t \mathbf{A})^{-1} \mathbf{A}^t \vec{y}^{\text{obs}}$ which is obtained in one single step in this method. Thus, the closer to the inverse system matrix the pre-conditioner is, the faster the execution of the method, at least in terms of the speed of convergence. However, for ill-conditioned matrices the inverse will be also ill-conditioned and it is not a good choice to select a matrix too close to it.

Appropriate preconditioning techniques are often very problem-specific and are still subject to intense research; examples can be found in Hanke (1999).

When the LCG method is applied to the preconditioned system of equations (7.10), it becomes the ‘linear preconditioned conjugate gradient’ (LPCG) method (see Nocedal *et al.* 1999 for details).

A FORTRAN implementation of a LPCG algorithm can be found in the IMSL package, in routines PCGRC and DPCGRC (inline library of the Microsoft Visual FORTRAN, or in <http://www.vni.com/products/imsl/>). However, for the LLS problem, these routines need the formation of the matrix product $\mathbf{A}^t \mathbf{A}$ which, as mentioned in section 7.3.1, is not recommended.

7.4 NONLINEAR LEAST-SQUARES (NLS)

Although the problem (7.6) for a function F that does not depend linearly on the vector of parameters \vec{x} , can be minimized using a general optimization method, in most circumstances, the properties of the function F make it worthwhile to use methods designed specifically for the nonlinear least-squares problem. Using again the model function in example (7.4), for determining the parameters x_1 and x_2 :

$$\varphi(x_1, x_2; t) = e^{-x_1 t} + \text{Sin}(x_2 t)$$

Thus:

$$\vec{\Phi}(\vec{x}; t) = \vec{\Phi}(x_1, x_2; t) = \begin{bmatrix} e^{x_1 t_1} + \text{Sin}(x_2 t_1) \\ e^{x_1 t_2} + \text{Sin}(x_2 t_2) \\ \vdots \\ e^{x_1 t_m} + \text{Sin}(x_2 t_m) \end{bmatrix} \quad \text{and} \quad \vec{y}^{\text{obs}} = \begin{bmatrix} y_1^{\text{obs}} \\ y_2^{\text{obs}} \\ \vdots \\ y_m^{\text{obs}} \end{bmatrix}$$

$$\vec{f}(\vec{x}) = \vec{\Phi}(\vec{x}; t) - \vec{y}^{\text{obs}} = (f_1(\vec{x}), f_2(\vec{x}), \dots, f_m(\vec{x}))^t; \quad F(\vec{x}) = \|\vec{f}(\vec{x})\|^2$$

$$f_i(\vec{x}) = \varphi(\vec{x}; t_i) - y_i^{\text{obs}}$$

The Jacobian matrix of the vector function $\vec{f}(\vec{x})$ is:

$$\mathbf{J}(\vec{x}) = \begin{pmatrix} \frac{\partial f_1}{\partial x_1} & \dots & \frac{\partial f_1}{\partial x_n} \\ \vdots & \ddots & \vdots \\ \frac{\partial f_m}{\partial x_1} & \dots & \frac{\partial f_m}{\partial x_n} \end{pmatrix}_{m \times n}$$

The gradient vector and Hessian matrix of the scalar function $F(\vec{x}) = \|\vec{f}(\vec{x})\|^2$ are:

$$\begin{aligned}\nabla F(\vec{x}) &= \mathbf{J}'(\vec{x})\vec{f}(\vec{x}) \\ \nabla^2 F(\vec{x}) &= \mathbf{J}(\vec{x})^t \mathbf{J}(\vec{x}) + \sum_{i=1}^m f_i(\vec{x}) \nabla^2 f_i(\vec{x})\end{aligned}$$

If the vector of residuals $\vec{f}(\vec{x})$ of the solution is supposed to be ‘small’ at the solution, i.e. $\vec{f}(\vec{x}^*) \approx \vec{0}$, the second term of the Hessian matrix at the solution could then be approximated by: $\nabla^2 F(\vec{x}^*) \approx \mathbf{J}(\vec{x}^*)^t \mathbf{J}(\vec{x}^*)$. If this approximation uses a Newton’s method, it becomes the well-known Gauss-Newton method (Nocedal *et al.* 1999) and the basic iteration is the following:

Newton’s method for NLS (Gauss-Newton):

Given \vec{x}_0

For $k = 0, \dots$, until convergence, do

Solve the linear system of Gauss-Newton equations

$$\nabla^2 F(\vec{x}_k) \vec{s}_k = -\nabla F(\vec{x}_k) \Leftrightarrow \mathbf{J}(\vec{x}_k)^t \mathbf{J}(\vec{x}_k) \vec{s}_k = -\mathbf{J}(\vec{x}_k)^t \vec{f}(\vec{x}_k) \quad (7.11)$$

Set $\vec{x}_{k+1} = \vec{x}_k + \vec{s}_k$

Notice that the Gauss-Newton equations (7.11) are the normal equations of the linear least-squares problem:

$$\underset{\vec{s}_k \in \mathbb{R}^n}{\text{Minimize}} \quad \frac{1}{2} \left\| \mathbf{J}(\vec{x}_k) \vec{s}_k + \vec{f}(\vec{x}_k) \right\|^2 \quad (7.12)$$

Thus, the application of the Newton method to solve a NLS problem, under the assumption of small residuals, can be viewed as an iterative solution to the LLS problem, whose solution gives the vector of movement to a better approximation of the NLS solution.

In general, the methods linearize the nonlinear problem at each iteration, i.e., they approximate $\vec{f}(\vec{x}_k + \vec{s}_k) \approx \vec{f}(\vec{x}_k) + \mathbf{J}(\vec{x}_k) \vec{s}_k$ to obtain the LLS sub-problem (7.12) and solve the problem to get a better approximation than the previous iteration in the sense of descent of the nonlinear function, in order to obtain, within some permissible number of iterations, the desired solution with minimal function value.

In what follows we will use the following notation: \vec{f}_k for $\vec{f}(\vec{x}_k)$; \vec{g} for $\vec{g}(\vec{x}_k)$ and \mathbf{J}_k for $\mathbf{J}(\vec{x}_k)$, to make easier the presentation of the methods to solve NLS problems.

7.4.1 The Levenberg-Marquardt method

The Levenberg-Marquardt (L-M) method (Moré 1977) has been used with great success to solve the NLS problem, since it takes advantage of the specific form of the function to be minimized. In other words, it exploits the particular form of the gradient and the possibility of approximating the true Hessian matrix at each iteration by $\mathbf{J}_k^t \mathbf{J}_k$, under the assumption of small residuals. This method also overcomes the drawback of the Gauss-Newton method, concerning the possible singularity of the matrix $\mathbf{J}_k^t \mathbf{J}_k$. The advantage of the L-M method is that it includes a globalization strategy to enforce convergence from most initial points. No iterative method can guarantee the convergence to a solution from any initial point but, it is possible to make it more probable.

The linearization of the function \vec{f}_k around the current point \vec{x}_k is a first order Taylor expansion and thus, it is correct for an unknown Δ_k neighborhood of it. Then the appropriate formulation

would be:

$$\text{Minimize}_{\|\vec{s}_k\| \leq \Delta_k} \frac{1}{2} \|\mathbf{J}_k \vec{s}_k + \vec{f}_k\|^2 \tag{7.13}$$

Hence the solution to (7.13) would be correct for the NLS problem in the sense that the nonlinear function value would also be decreased at each iteration.

The L-M method belongs to those known as ‘trust region’ type methods; the search direction is the solution of (7.13) and has the following properties:

$$\begin{aligned} (\mathbf{J}'_k \mathbf{J}_k + \lambda_k \mathbf{I}) \vec{s}_k &= -\mathbf{J}'_k \vec{f}_k \\ \lambda(\|\vec{s}_k\| - \Delta_k) &= 0 \\ \mathbf{J}'_k \mathbf{J}_k + \lambda_k \mathbf{I} &\geq 0 \text{ (positive semi-definite)} \end{aligned}$$

where λ_k is a non-negative scalar and \mathbf{I} is the identity matrix of order n . The second equation means that for $\lambda \neq 0$ the solution satisfies $\|\vec{s}_k\| = \Delta_k$, i.e., it is located at the boundary. A unit step is always taken along \vec{s}_k , giving the next iteration as:

$$\vec{x}_{k+1} = \vec{x}_k + \vec{s}_k$$

The following two cases arise in the computation of the correct value of λ_k , once the adequate value of Δ_k has been chosen:

Case 1: $\lambda = 0$ and $\mathbf{J}'_k \mathbf{J}_k$ nonsingular: Compute Gauss-Newton direction

$$\vec{s}^{GN} = -(\mathbf{J}'_k \mathbf{J}_k)^{-1} \mathbf{J}'_k \vec{f}_k$$

If $\|\vec{s}^{GN}\| \leq \Delta_k$ then $\vec{s}_k = \vec{s}^{GN}$ (the solution is inside the trust region)

Case 2: If $\mathbf{J}'_k \mathbf{J}_k$ is singular or $\|\vec{s}^{GN}\| > \Delta_k$: Compute $\lambda > 0$, the root of $\|\vec{s}(\lambda)\| - \Delta_k = 0$, then

$$\vec{s}_k = \vec{s}(\lambda) = -(\mathbf{J}'_k \mathbf{J}_k + \lambda \mathbf{I})^{-1} \mathbf{J}'_k \vec{f}_k \text{ (solution is at the boundary of the trust region)}$$

The difficulty in this approach is to perform an appropriate strategy for choosing Δ_k , which must rely on heuristic considerations. Most standard strategies (Dennis *et al.* 1996, Moré 1977) have originally been developed to ‘globalize’ the convergence of the Gauss-Newton iteration for well-posed minimization problems and basically rely on some criteria about the agreement between the nonlinear model (7.6) and the linear one (7.12).

The constrain on the size of the solution of problem (7.13), when the matrix $\mathbf{J}'_k \mathbf{J}_k$ is nonsingular, causes that the solution would be at the boundary and thus, the problem turns out into:

$$\text{Minimize}_{\|\vec{s}_k\| = \Delta_k} \frac{1}{2} \|\mathbf{J}_k \vec{s}_k + \vec{f}_k\|^2 \tag{7.14}$$

which is equivalent to the solution of the unconstrained problem:

$$\text{Minimize}_{\vec{s}_k \in \mathbb{R}^n} \frac{1}{2} \|\mathbf{J}_k \vec{s}_k + \vec{f}_k\|^2 + \frac{\lambda}{2} (\|\vec{s}_k\|^2 - \Delta_k^2) \tag{7.15}$$

This is the same problem solved in the Tikhonov regularization method (7.9), except that in the L-M method, a bound on the size of the solution is imposed. Although this bound is usually due to optimization considerations, it controls the iteration size from growing too much. This seems to be the reason for the good behavior of the L-M method on noisy problems (i.e., with errors in the observed data), since the method will compute the regularized linear solution many times.

A very efficient and robust FORTRAN implementation of the unconstrained Levenberg-Marquardt method can be found in the MINPACK-2, available at <http://www-fp.mcs.anl.gov/otc/minpack/summary.html>.

7.4.2 Using an optimization routine (TRON) to solve NLS problems

In practice the NLS problems are usually subject to bound constraints, i.e., the parameters can only be sought within certain lower and upper values. This makes sense since most of the times the unknown parameters are physical, chemical or biological quantities. Thus it is necessary to use a method that can deal with such restrictions, which are mathematically posed as:

$$\begin{array}{l} \text{Minimize } F(\vec{x}) \\ \text{subject to } l_j \leq x_j \leq u_j \\ j=1, \dots, n \end{array}$$

where F is a nonlinear smooth scalar function depending on a vector in \mathbb{R}^n , and l_j and u_j are the lower and upper bounds of the parameters, respectively. This is known as a bound constraint nonlinear optimization problem. Of course, the function F could be of the least-squares type, as in equation (7.6), but the optimization methods do not have the same performance on any nonlinear function as we shall see immediately.

The IMSL software package of routines (inline library of the Microsoft Visual FORTRAN, <http://www.vni.com/products/imsl/>) has an implementation of the Levenberg-Marquardt method with bound constraints, although the technique used to deal with the constraints may result inefficient in large-scale problems, when too many parameters are involved.

On the other hand, using general routines for optimization in the solution of NLS, can have the inconvenience that they do not take advantage of the particular structure of the function of the NLS problem, which happens in quasi-Newton's methods. These methods usually approach the Hessian matrix or its inverse at each iteration, which can be useful when the function is 'very' nonlinear or when the residual vector norm in the solution is very large. However, the most typical case is that of small residuals, when these general methods are inefficient.

A trust region version of Newton's method for general nonlinear minimization of bound constrained problems is called TRON (Moré 1999). This technique is equivalent to the Levenberg-Marquardt method but it can deal with the bound constraints. This is the method we are going to present and use in one of the application examples of section 7.5.1. The basic iteration of the trust region Newton (TRON) method is:

Trust region Newton's method:

Given \vec{x}_0

For $k = 0, \dots$, until convergence, do

<p>Solve</p> $\begin{array}{l} \text{Minimize } \frac{1}{2} \vec{s}_k^t \nabla^2 F_k \vec{s}_k + \vec{s}_k^t \vec{g}_k \\ \text{subject to } \ \vec{s}_k\ \leq \Delta_k \end{array}$ <p>Set $\vec{x}_{k+1} = \vec{x}_k + \vec{s}_k$</p>

When this algorithm is applied to the NLS problem (7.6) using the true Hessian matrix only approximated with the first order information ($\nabla^2 F_k \approx \mathbf{J}_k^t \mathbf{J}_k$), it becomes a Levenberg-Marquardt method, since at each iteration the nonlinear least-squares problem is approximated by the solution of the associated linear least-squares problem. The basic iteration of the TRON method for NLS is then:

Trust Region Newton's Method for NLS:

Given \vec{x}_0

For $k = 0, \dots$, until convergence, do

Solve $\text{Minimize } \frac{1}{2} \vec{s}_k^t (\mathbf{J}_k^t \mathbf{J}_k) \vec{s}_k + \vec{s}_k^t (\mathbf{J}_k^t \vec{f}_k) = \frac{1}{2} \ \mathbf{J}_k \vec{s} + \vec{f}_k\ ^2$ subject to $\ \vec{s}_k\ \leq \Delta_k$ Set $\vec{x}_{k+1} = \vec{x}_k + \vec{s}_k$	(7.16)
---	--------

The treatment of the bound constraints is not shown here, since it requires a more mathematical background on this subject, the reader is referred to Moré and Lin (1999) for details. To solve the constrained LLS sub-problem (7.16), the vector \vec{s}_k is obtained using a linear preconditioned conjugate gradient method (LPCG, see section 7.3.4.2).

Since the TRON method solves the same sub-problem (7.16) as the L-M method, when applied to a NLS problem using the approximate Hessian matrix $\mathbf{J}_k^t \mathbf{J}_k$, the equivalence to the Tikhonov regularization method is also valid for this technique. Therefore its performance is similar to the L-M method, besides the advantage of dealing with bound constraints, which makes it an attractive option for most real problems. The projected search strategy used for the treatment of the bound constraints makes the difference on performance in comparison to the IMSL routines mentioned in the second paragraph of this section.

The main drawback of this method for the NLS problem is the formation of the product $\mathbf{J}_k^t \mathbf{J}_k$ which increases the ill-conditioning. This may be avoided by redesigning the code for the specific NLS problem and is a work in progress by the authors of this chapter.

The routine DTRON that implements this method is freely available from the home page of the Argonne National Laboratories (<http://www-unix.mcs.anl.gov/~more/tron/>).

7.4.3 Regularization techniques in NLS

As we have pointed out, the selection of the trust region radii Δ_k , which is related to the parameter λ_k , is based on optimization considerations. Thus, it does not take into account, neither for the L-M method nor for the TRON method, the possible ill-posedness of the inverse problem. We emphasize again the fact that the more information about a problem is available, the best is the solution obtained. This is the first kind of regularization. Since the TRON method is able to deal with bound constraints, the knowledge of effective ranges of the parameters can be used and thus, the solution could be better approximated.

One practical way to regularize a NLS problem is to use the Tikhonov regularization method:

Tikhonov's regularization method for NLS:
 Given $\lambda^0 > \lambda^1 > \dots$, set $i = 0$

Solve $\vec{x}_{\lambda_i}^* = \arg \min_{\vec{x} \in \mathbb{R}^n} \left(\frac{1}{2} \ \vec{f}(\vec{x})\ ^2 + \frac{\lambda^i}{2} \ \vec{x}\ ^2 \right)$ Set $i = i + 1$

Graph $\|\vec{f}(\vec{x}_{\lambda_i}^*)\|$ vs $\|\vec{x}_{\lambda_i}^*\|$ for $i = 0, 1, \dots$, and select the corner point $\vec{x}_{\lambda_c}^*$ as the best one

It is possible to use, for instance, the L-curve algorithm to determine the corner point. This schema might be prohibitive for some practical problems with too many parameters, or too expensive evaluations of the model function, because it would be necessary to execute the optimization algorithm as many times as there are tested values of λ . At each execution at least one evaluation of the function and one of the gradient are needed by iteration.

Another option might be to introduce the regularization into the linear part of the TRON method that uses a LPCG to solve the linear least-squares sub-problem (7.16). This heuristic approach is still under research, but initial results for practical applications are promising.

Another way of possible regularization is to consider a multiscale scheme which will be explained in one of the application examples in section 7.5. To get more insight into regularization techniques the reader may see Engl *et al.* (1996).

7.5 APPLICATION EXAMPLES

7.5.1 Groundwater modeling

A fundamental problem in the modeling of groundwater systems is to obtain reliable estimates of flow parameters for the functions appearing in various differential equations (see chapter 4). Those parameters (e.g., hydraulic conductivity) are difficult to determine and more information on their effects is needed (e.g., hydraulic head). The computational difficulties associated with their estimation appear because this inverse problem is ill-posed, and are aggravated by the sparseness of well sites and the inherent measurement errors.

To simplify the exposition we consider the flow equation in a non-homogeneous isotropic confined horizontal plane aquifer with the dimensions (x, fy) :

$$Q_V(x, y, t) + S(x, y, t) \frac{\partial h(x, y, t)}{\partial t} = \frac{\partial}{\partial x} \left(T_v(x, y) \frac{\partial h(x, y, t)}{\partial x} \right) + \frac{\partial}{\partial y} \left(T_v(x, y) \frac{\partial h(x, y, t)}{\partial y} \right) \quad (7.17)$$

The direct problem is to compute the state variable hydraulic head $h(x, y, t)$, with known parameter functions $S(x, y, t)$ (storage coefficient), $T_v(x, y)$ (transmissivity) and $Q_V(x, y, t)$ (a groundwater source term), i.e., to solve the differential equation with the corresponding initial and boundary conditions.

The inverse problem related to this differential model is to estimate one or several of the parameter functions, using measurements of the function $h(x, y, t)$ and/or some additional data. These data could be, for example, some real range of the values of $T_v(x, y)$ and $S(x, y, t)$ in some zones of the aquifer. We might want to find $Q_V(x, y, t)$, $T_v(x, y)$ and/or $S(x, y, t)$ which would be the parameters to be identified in the whole region occupied by the aquifer.

This inverse problem is ill-posed since its solution is highly sensitive, because it could change a lot with small perturbations of the observed hydraulic heads, which is a common practical situation. Therefore some regularization technique is required (section 7.4.3).

Groundwater modeling has its own peculiarities:

- These models are expensive since the solution of the direct problem requires solving large systems of equations for each model run.
- State variables are time dependent, for example, the hydraulic head $h(x, y, t)$ in equation (7.17).
- Heterogeneity: Values of hydraulic conductivity (transmissivity $T_v(x, y)$ in the case of a 2-dimensional confined aquifer) which is often the dominant hydraulic property may vary several orders of magnitude within the model domain.
- There are different types of parameters.
- The data measured in the field (the hydraulic head) are discrete values and hence they represent often only small sections of the whole aquifer.
- Model uncertainty: Geometry of the aquifer and heterogeneity patterns are controlled by the geology, which is never known accurately. This fact increases the uncertainty in the conceptual model (see section 6.11).
- Low sensitivity: Depending on the problem, state variables may display low sensitivity. Observing different sets of transmissivity values, the hydraulic heads do not differ significantly. This is the symptom of the great ill-posedness of this problem.

Because of the above features, the aquifer model prediction is highly uncertain for both, the conceptual model and the model parameters. The purpose of this application example is to solve the latter practical problem.

The earliest methods in inverse groundwater modeling (Sun 1994) substituted the hydraulic heads, $h(x, y, t)$, which were assumed to be known, into the flow equation (7.17). This substitution leads to a first order partial differential equation for the transmissivity $T_v(x, y)$. Then, using a numerical solver, its values were obtained.

This approach has several drawbacks. Firstly, it requires the accurate knowledge of hydraulic heads, groundwater recharge, $Q_V(x, y, t)$, storage coefficient $S(x, y, t)$ and boundary conditions over the whole domain in space and time. This can only be achieved through interpolation of the discrete values obtained from field measurements, which introduces errors. Secondly, it is unstable since each component of the system matrix generated in the discretization of the flow equation, depends on the hydraulic heads that are contaminated by measurements and interpolation errors. That is why although this method is a direct approach to compute the transmissivity, it is not recommended.

To overcome the interpolation error on the hydraulic heads, most recent methods use the indirect approach, in which the parameters are found by minimizing an objective function, such as the least-squares function. For example the indirect approach formulation for the estimation of the parameter function $T_v(x, y)$ is:

$$\text{Minimize } F(\vec{T}) = \left\| \vec{h}^{\text{cal}} - \vec{h}^{\text{obs}} \right\|^2 \tag{7.18}$$

$l_j \leq T_j \leq u_j$
 $j=1, \dots, nx \times ny$

This equation represents a huge computational task, because at each iteration of the minimization procedure, the partial differential equation (7.17) must be solved for the current values of the transmissivities as shown in the flow chart in Figure 7.6. Thus, the cost of a single evaluation of the least-squares function is very high, and its dimension will be equal to the size of the grid used to compute the hydraulic heads, let's say $nx \times ny$.

In order to regularize the solution of the inverse problem identifying the parameter function $T_v(x, y)$, a number of approaches may be used, such as: (1) the Tikhonov regularization, (2) providing additional types of data, and (3) reducing the number of parameters to be estimated (which also reduces the dimension of the least-squares procedure).

7.5.1.1 Multiscale optimization

If the optimization represented by equation (7.18) is carried out directly over the entire grid of the physical region of the aquifer used to solve the direct problem, there would be $nx \times ny$ unknowns (the grid size). The ill-conditioning of the problem in the presence of noise could produce oscillatory solutions, corresponding to a transmissivity function with great variations.

In order to regularize the solution, multiscale optimization solves a sequence of better conditioned sub-problems, generated by refining the discretization: beginning with a grid of lower dimension the transmissivities are computed on this coarse grid in the optimization procedure. After refining the grid, the initial values of the transmissivities are obtained from the interpolation of those acquired to the new nodes, until the last grid is obtained (the one with the same dimension as for the PDE solver).

Each grid is obtained by applying successive subdivisions: starting from a coarse grid $m = 0$ whose size is $nx_0 \times ny_0$ until the final grid $m = mscale$ is achieved (Fig. 7.7). The number of intervals and their size depend on the number of refinements $mscale$. For $0 \leq m \leq mscale$ the finite dimensional parameter space E^m is the vector space of parameter distributions [for example transmissivity $T_v(x, y)$], which are continuous piecewise bi-linear segments over the elements of the grid. Then, from dichotomy we have that $E^{m-1} \subset E^m$. For a description of multiscale grids, the reader is referred to Gómez *et al.* (1998).

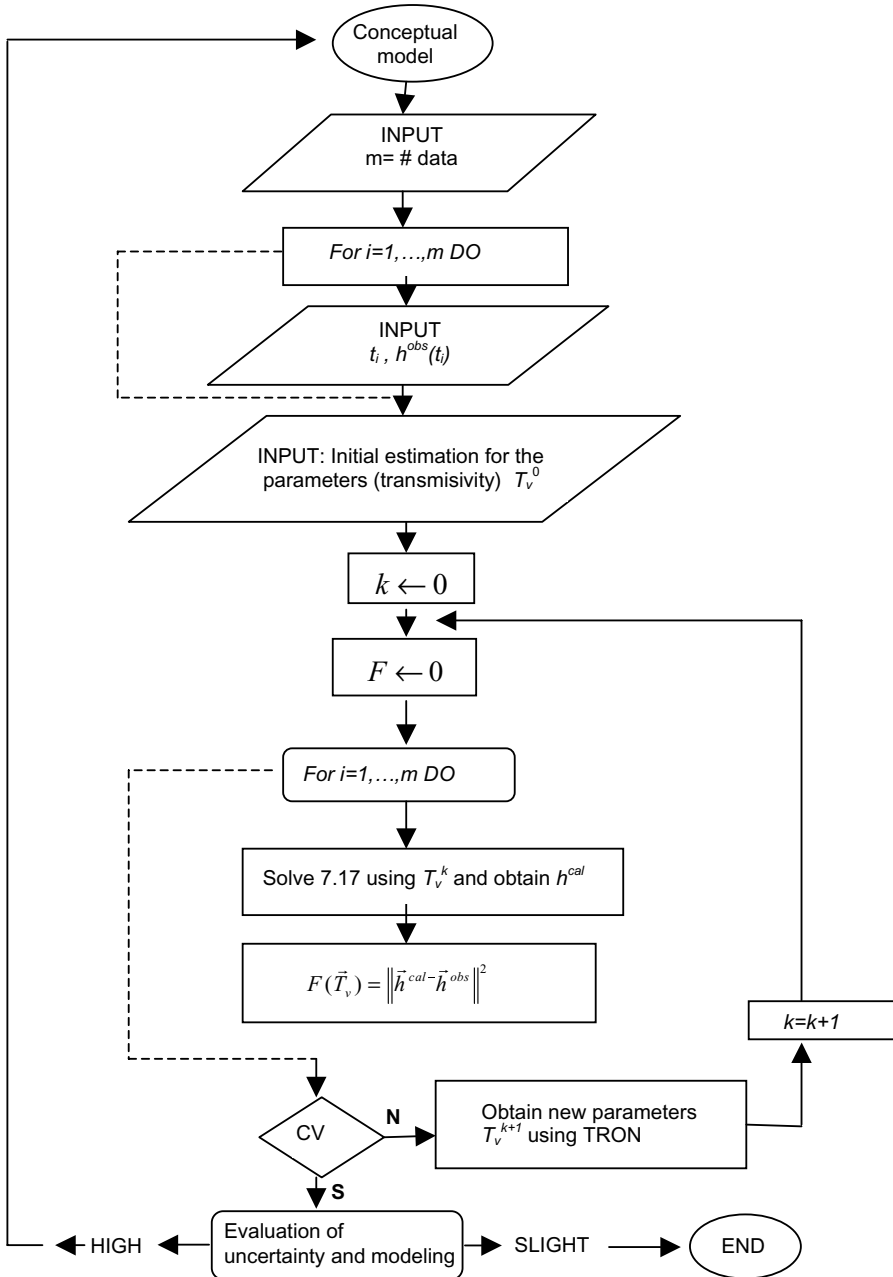


Figure 7.6. Procedure to estimate the transmissivity in the flow equation.

Thus, the parameterization of $T_v(x, y)$ is made in the following way. Given a profile $\bar{T}_v^{m-1} \in E^{m-1}$ can be represented in E^m by its coordinates $\alpha_{i,j}^m$ on a basis $\bar{e}_{i,j}^m$ of E^m (multiscale basis):

$$\bar{T}_v^m(x, y) = \sum_{m=0}^{mscale} \sum_i^{nx} \sum_j^{ny} \alpha_{i,j}^m \bar{e}_{i,j}^m(x, y)$$

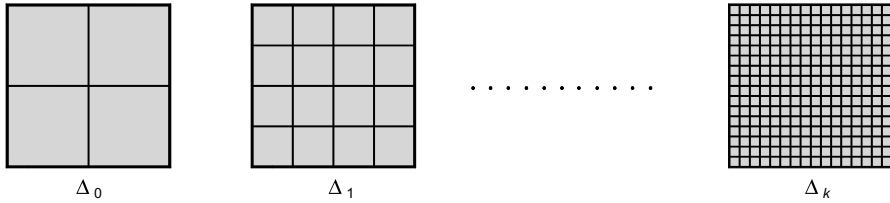


Figure 7.7. Multiscale grids: Basic sequence.

where $m = 0$ or i is odd or j is odd. We then have to solve, for each m , the finite dimensional problem which implies finding the coefficient matrices $\mathbf{A}^m = (\alpha_{i,j}^m)$.

Multiscale optimization consists of growing gradually the initial iterate and approaching the solution by finding first a good approximation to the coefficient α_i , which is associated to the high sensitivity over coarse grids. Using this approximation (the optimal coefficients) as starting points, it is possible to find the coefficients associated to the non-linearity (Gómez *et al.* 1998). This process can be described as follows:

Given an initial guess \tilde{T}_0 , solve problem (7.18) in the coarser grid $m = 0$ to find \tilde{T}_*^0 . Then, for every grid generated by refinement, do:

For $m = 1$ until *mscale* do

- Take as the initial approximation $\tilde{T}_{v0}^m = \tilde{T}_{v*}^{m-1} \oplus \tilde{T}_v^m \tilde{T}_v^m \in W^m$ where W^m is a supplementary space of E^m such that $E^m = E^{m-1} \oplus W^m$ and \tilde{T}_v^m is obtained from \tilde{T}_{v*}^{m-1} by interpolation.
- Use a local bounded optimization method to find $\tilde{T}_{v*}^m \in E^m$.

7.5.1.2 An elementary example

Let us consider the aquifer shown in Figure 7.8a and the transmissivity estimations $T_v(x, y)$ in equation (7.17). The investigations and experiments performed in this aquifer with an area of 78.2 km², using a trial and error method (the values of transmissivities are fixed, the PDE is solved to obtain values of the hydraulic heads, they are compared with those observed and, based on a wide knowledge of the aquifer, new transmissivities are fixed, repeating the process a finite number of times until the calculated hydraulic heads ‘approach’ to those observed), resulted in the delimitation of three zones with individual constant transmissivity values (Fig. 7.8a). The objective of the experiment presented next is to see which method best reproduces these values of transmissivities.

For the simulation of the direct problem we use an irregular grid inscribed into a squared region and for the multiscale schema, *mscale* = 3. The storage coefficient is 0.0015. The initial and boundary conditions are shown in Figure 7.8a. In this implementation we used a complete final grid of 16 × 16 cells to solve the direct problem. Throughout the procedure, including the first two grids of 4 × 4 and 8 × 8 cells, respectively, we used the source codes of MODFLOW 2000 (USGS 2000).

7.5.1.2.1 Experimental results

Data with error: Using the transmissivity values obtained by trial and error, the PDE solver was run for a grid consisting of 16 × 16 cells. The hydraulic heads were obtained for each cell. Then they were taken as the experimental measurements and thus, the exact solution is known.

In order to test the performance of the multiscale method, a random error of order 10⁻⁴ was added to the hydraulic heads, to see if the known transmissivity values could be reproduced.

Figure 7.8b–d shows that the multiscale method achieved a better approximation to the optimal parameters compared to the method not using multiscaling. The graphic of the optimal transmissivity obtained in each case (Fig. 7.8c,d) compared with the exact solution (Fig. 7.8b) and

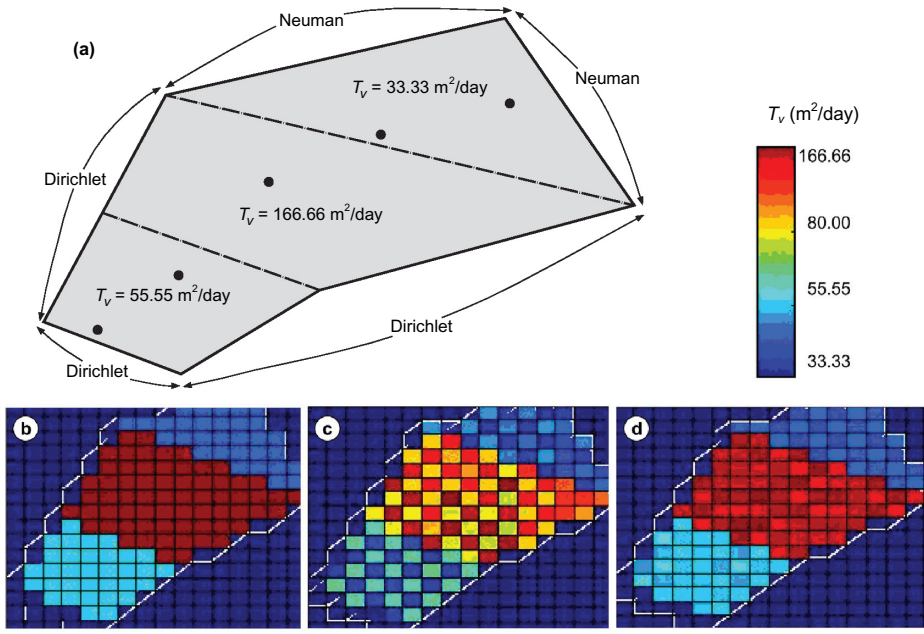


Figure 7.8. (a) Aquifer example composed of three zones with constant values of transmissivity $T(x, y)$ obtained from ‘trial and error’; (b–d) Transmissivity maps obtained with: (b) Exact solution; (c) No multiscale, TRON method in the grid scale of 16×16 ; (d) Multiscale using TRON method in the optimization at each scale of the procedure, $NR2 = \|\vec{T}_v^{\text{exact}} - \vec{T}_v^* \| / \|\vec{T}_v^{\text{exact}}\|$.

the value of the error between the exact and the approximated solution ($\|\vec{T}_v^{\text{exact}} - \vec{T}_v^* \| / \|\vec{T}_v^{\text{exact}}\|$, demonstrate this result. Additionally, the residual obtained with both runs is small, which is typical in the problem of identification. The practical regularization effect of multiscale grids is presented in this example and also studied further in Gómez *et al.* (1998).

7.5.2 Inverse problems in geophysics

A geophysical field u (seismic, electromagnetic, gravitational, etc.) is defined by the distribution of the earth’s physical parameters χ (density, electrical conductivity, elasticity, etc.). The field and the parameter of the medium are usually related via a nonlinear operator A that is defined by the mathematical model of the medium, i.e.:

$$A\chi = u \quad u \in U, \quad \chi \in X \tag{7.19}$$

The inverse problem of geophysical prospecting is to determine the distribution of the physical parameters χ inside the earth (and, hence, the crust’s structure and composition) from the measured geophysical field u . In order to solve this problem we need special physical observations. The development of automated systems for processing geophysical data put the interpretation of the prospecting result on an industrial basis. The efficiency of this prospecting has also thus being significantly improved. Naturally, an automated system must be based on methods for solving the inverse problem in geophysics.

The feature of the geophysical inverse problem is that the observed fields are the integral effect of all the sources, comprising the non uniform medium under investigation. The variations compensate each other and therefore the observed fields are weakly sensitive to variations in

the set of parameters. This means that the geophysical inverse problems are unstable, i.e., two different sets of parameters can produce a similar external field. If ignored, this instability can lead to very erroneous interpretations of the observed data. Thus, we must determine an approximate solution to the inverse problem close to the real one. This can be done by applying the methods for regularizing ill-posed problems. The features of this type of inverse problem indicate that regularizing algorithms must be an intrinsic and necessary component of automated systems for processing and interpreting data.

A measured geophysical field always contains certain errors, i.e. the initial information u_δ always differs from the true geophysical field:

$$\|u - u_\delta\|_U \leq \delta \tag{7.20}$$

where δ is the measurement error. The value of δ consists of two parts $\delta = \delta_u + \delta_m$, where δ_u is due to apparatus distortions and pick-ups and δ_m is due to the fact that the real distribution of the medium's parameters χ does not correspond to the class of media for which the operator A is defined. In geophysical prospecting, the model errors δ_m (geological pick-ups) are usually much larger than the measurement error δ_u . This is why the efficiency of geological prospecting can be improved more by applying efficient methods for processing and interpreting data than by developing more accurate instrumentation.

Given that the available information about the geophysical field is not precise, instead of using equation (7.19), we must use the following condition to determine the parameter χ :

$$\|A\chi - u_\delta\|_U \leq \delta \tag{7.21}$$

That is, we try to satisfy equation (7.19) with the accuracy δ at which the field was measured. All the medium parameters χ_δ that satisfy (7.21) comprise a set X_δ of equivalent solutions of the inverse problem. If the inverse problem is well-posed, then all the equivalent parameters $\chi_\delta \in X_\delta$ will be close to each other; in other words, there will be a maximum deviation between equivalent parameters:

$$\varepsilon(\delta) = \sup_{\chi_\delta \in X_\delta} \left\| \chi_\delta^{(1)} - \chi_\delta^{(2)} \right\|_X$$

The value of $\varepsilon(\delta)$ characterizes the maximum error in the solution of the inverse problem. On the other hand, if the problem is ill-posed $\varepsilon(\delta)$ will tend to infinity, i.e., small errors in the geophysical field result in arbitrary errors in the medium parameters.

In geophysics, we say that the geophysical inverse problem is the problem of making inferences about the physical parameters of the earth's systems from observed data. Since nearly all data are subject to some uncertainty, these inferences are usually statistical. Furthermore, since one can only record finitely many (noisy) data and since geophysical systems are usually modeled by the continuum equations of physics, no geophysical inverse problem is really uniquely solvable: if there is a single model that fits the data there will be infinity of them.

We are often forced to make compromises between what information we desire to get from a solution and the kind of information that in fact is contained in the data. These compromises lead to other kinds of 'answers' that are less direct than the parameter estimation. Indeed a major part of the practice of inverse theory is to identify what features of a solution are most valuable and then make the compromises that help emphasize these features.

7.5.2.1 An elementary geophysical inverse problem

Thermal regimes and regional fluid flows are critical factors in the formation and maturation of petroleum, gas and coal deposits. In Figure 7.9a a sketch of a petroleum window limited by the geothermal gradients and other parameters appropriate for the formation and accumulation of oil deposits in a given area, is shown.

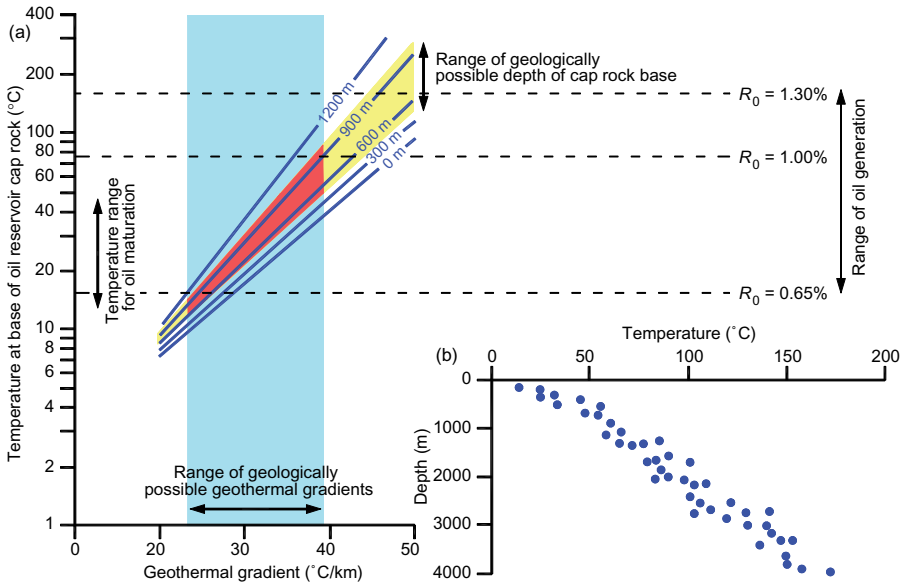


Figure 7.9. (a) Sketch of a petroleum window limited by the geothermal gradients and other parameters. The range of oil generation is given by R_0 (in %) with values of 0.65, 1.00, and 1.30%, respectively; (b) Temperature observations vs depth.

Suppose you are assigned the task of determining the geothermal gradient in an oil field from one of its deep wells. One may proceed as follows:

- Get your gear (thermal probe and depth measuring device) and head to the target well;
- Make measurements of the temperature T (°C) in the borehole at regular depth intervals, say $z = 100$ m;
- Get back to the office and begin the chore of numerical computation.

The starting point is to plot the temperature measurements (data observations) vs depth z which may look like the plot shown in Figure 7.9b. Clearly the relation between depth and temperature is a linear one (assumed that there is a constant geothermal gradient), so that you may choose a straight line as the system model. That is to say the physics of the problem at hand is such that:

$$T = a + bz \tag{7.22}$$

In ordinary situations, we know the numerical values of $\{a; b\}$ and by inserting a set of depth values $\{z_i\}$ we compute the corresponding temperatures $\{T_i\}$ at each depth; thus we go from right to left of the model equation. This is the ‘forward’ or ‘direct’ problem or modeling, as we have discussed in the beginning of this chapter. T -values computed in this manner are called ‘predicted data’ or ‘model response’.

The situation at hand, however, is quite different. We have already spent time in the field to measure temperatures T at predetermined set of z -values. We seek now how to find the numerical estimates of $\{a; b\}$, the model parameters that will best-fit the observational data. This is the essence of the inverse problem. We want to proceed from right to left in the model. This brings us to the next task in our computational agenda.

7.5.2.2 Formulation of the inverse problem

In Table 7.1, we show the first 10 measurements of the temperatures that were made from some well. By selecting equation (7.23) as our model, we are implicitly asserting that there is a set

Table 7.1. Measurements of the temperatures T vs depth z performed in a well.

z (m)	0	100	200	300	400	500	600	700	800	900	1000
T (°C)	21.57	12.74	34.45	39.48	28.13	55.21	58.69	49.58	57.17	59.27	59.23

of model parameters $\{a; b\}$ such that for every depth value listed in Table 7.1, they yield the corresponding temperature measurement observed in the field.

Hence, we may write the following set of equations:

$$T_i = a + b z_i, \quad i = 1, \dots, m$$

If we place all the T -values (our observed data) in a column vector:

$$\vec{d} = [T_1, T_2, T_3, \dots, \dots, \dots, T_N]^t$$

and place the model parameters in another column vector:

$$\vec{m} = [a, b]^t$$

then we may write the set of equations in matrix form as:

$$\begin{bmatrix} d_1 \\ d_2 \\ \vdots \\ d_m \end{bmatrix} = \begin{bmatrix} 1 & z_1 \\ 1 & z_2 \\ \vdots & \vdots \\ 1 & z_m \end{bmatrix} \begin{bmatrix} a \\ b \end{bmatrix}$$

set $\mathbf{G} = \begin{bmatrix} 1 & z_1 \\ 1 & z_2 \\ \vdots & \vdots \\ 1 & z_m \end{bmatrix}$ and then have $\vec{d} = \mathbf{G} \vec{m}$

This is the inverse problem that we need to solve to complete our project. Note that in the above equation both, the data (\vec{d}) and the model parameters (\vec{m}) are in separate vectors of their own. This is the main feature of the so-called explicit linear inverse problem (LIP), which may be solved using the methods presented in this chapter.

CHAPTER 8

Groundwater modeling application examples

“Anybody who can solve the problems of water will be worthy of two Nobel Prizes, one for peace and one for science.”

John F. Kennedy

In this chapter, we present some possible applications in which numerical modeling can be applied to solve practical problems. However, we need to consider that these examples are simplified, especially regarding geometry and data variability. We often assume homogeneous and isotropic aquifers to show the principal behavior of aquifers caused by stresses such as pumping. In many situations, this leads to solutions that are adequate for preliminary observations. However, we must recognize that there may be more subtle complexities inherent to real world conditions, e.g., in which parameter values are complex functions of space and time. The problems may become ill-posed, so that solutions to these problems are no longer unique. Together with the knowledge of the sensitivity of the modeling result to the different parameters' values and distributions, in practice, we will obtain a set of possible modeling solutions from which we need to select the one, which best describes the real world problem.

8.1 PERIODICAL EXTRACTION OF GROUNDWATER

8.1.1 *Situation and tasks*

At the center of a square-shaped 500×500 m study area (borders parallel to N–S and E–W directions), there is an industrial plant (Fig. 8.1) that needs to exploit groundwater from a shallow aquifer. Thereby a minimum discharge rate $Q_V = -0.03$ m³/s (injection into the aquifer are indicated by ‘+’ and extraction by ‘-’ symbols) has to be extracted during a 12-hour period. The 12-hour period represents the working hours of the factory; the rest of the time, the pumps are inactive. To avoid subsidence at the foundations of the buildings located to the east and to the west of the industrial plant, groundwater levels should in no case decrease more than 0.6 m in an area of >100 m to the west and to the east of the well. Numerical modeling will be used to investigate whether this is possible.

8.1.2 *Aquifer specifications*

The unconfined aquifer used for water withdrawal can be considered as homogeneous and isotropic, with a hydraulic conductivity of $K_H = 1 \times 10^{-4}$ m/s and a storage coefficient determined from pumping tests of $S = 0.08$ in the entire study area. Through water level measurement in piezometers, the hydraulic heads are known to be unaffected by the pumping for the following areas: 200 m a.s.l. on the northern border of the study area, and 225 m a.s.l. on the southern border. No groundwater flow through the western and eastern borders occurs. The base of the aquifer is horizontal and is located at 140 m a.s.l. Groundwater recharge by rainfall is constant in time and amounts to 250 mm/year in the entire study area.

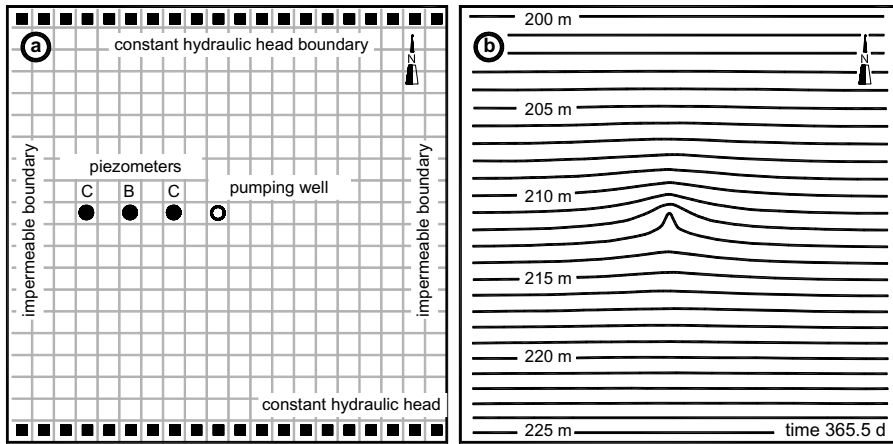


Figure 8.1. (a) Study area (500×500 m, 20×20 cells, boundary conditions, location of the pumping well, and observation piezometers located 50, 100 and 150 m to the west of the well; (b) Simulated hydraulic heads after a pumping phase (at $t = 376.5$ days).

8.1.3 Tasks

Step 1: Elaborate a hydraulic groundwater flow model, which describes the present situation. Locate piezometers A, B, and C at 50, 100 and 150 m respectively to the west of the industrial plant. Take into account that the north–south axis that crosses the industrial plant is the axis of symmetry. Carry out the simulation and plot the piezometry (hydraulic head–time curves) for points A, B and C. Perform the simulation starting at $t = 0$ for a period of 365 days with no pumping, to establish a stationary groundwater flow field, and finally, after $t = 365$ days, simulate a periodical pumping until $t = 376.5$ days.

Step 2: Discuss the simulated piezometry and evaluate the following issues of interest:

- What are the magnitudes of the maximum depressions of the water table at piezometers A, B, and C with a periodic discharge of $Q_V = -0.03 \text{ m}^3/\text{s}$?
- Is it possible to extract the required $0.03 \text{ m}^3/\text{s}$ without exceeding the maximum allowed depression of water table? If not, what is the maximum allowed flow $Q_{V \text{ max}}$? Is the static (natural) water table recovered at the different piezometers between two pumping phases?
- How many pumping cycles does it take for the piezometers to reach a state in which levels only present periodic variations?
- Determine the magnitude of water table oscillations and the gap between the maximum piezometric levels in a period of time $375 < t < 376$ days.

Step 3: Calculate water balances for the entire modeling area in a period of time $375 < t < 376$ days and compare and interpret the results for the following situations:

- At the end of the first time interval.
- 1 pumping phase.
- 1 rest phase.
- 1 pumping phase and the rest phase immediately after it.

8.1.4 Elaboration of a numerical model and problem solution

8.1.4.1 Elaboration of the numerical flow model

We select the simulation code ASM (see section 6.8.3) to construct a simple numerical 2-dimensional horizontal groundwater flow model. The transient groundwater flow in an unconfined homogeneous and isotropic aquifer is represented on 20×20 equally sized cells covering

the 500×500 m square of the study area (Fig. 8.1a). Complete model input data are listed in Table 8.1. The base of the aquifer is set to 140 m a.s.l. for all cells of the modeling area.

The well of the industrial plant is located in the middle of the model area and 3 piezometers, A, B, and C are introduced 50, 100, and 150 m to its west, respectively. According to the available information on the aquifer, the N–S directed model margins are impermeable for groundwater flow, and at the northern and southern boundaries hydraulic heads are prescribed on the boundaries with values of 200 m a.s.l. at the northern and 225 m a.s.l. at the southern border.

For simulation of the time-dependent groundwater withdrawal and the resulting impact on the aquifer monitored in the observation piezometers, we select 24 time intervals with distinct pumping rates. The first interval is selected long enough (365 days) to establish a stationary groundwater flow field, corresponding to the natural conditions in the modeled area, which we can use as a starting point for our simulation with periodic pumping. This is done by selecting 23 intervals with a duration of 12 hours each, with alternating pumping rates of $Q_V = -0.03 \text{ m}^3/\text{s}$ and $Q_V = 0 \text{ m}^3/\text{s}$, corresponding to pumping phases and rest periods without pumping.

Table 8.1. Input data for the groundwater flow model.

• Type of model ¹⁾ :		• extraction rate for the different time/pumping intervals (m^3/s)	
• stationary (0/1)	[1]	• $Q_{V1}, Q_{V3}, Q_{V5}, \dots, Q_{V23}$	[0]
• confined/free (0/1)	[1]	• $Q_{V2}, Q_{V4}, Q_{V6}, \dots, Q_{V24}$	[-0.3]
• anisotropy (K_{Hy}/K_{Hx})	[1]		
• Model grid:		• Piezometer location:	
• number of cells on x	[20]	• piezometer #1	
• number of cells on y	[20]	• x index of cell	[4]
• size of cells on x (m)	[25]	• y index of cell	[10]
• size of cells on y (m)	[25]	• piezometer #2	
• Time parameters:		• x index of cell	[6]
• number of time/pumping intervals (1/24)	[24]	• y index of cell	[10]
• number of time steps within a time/pumping interval	[24]	• piezometer #3	
• duration of a time/pumping interval:		• x index of cell	[8]
• interval 1 (day):	[365]	• y index of cell	[10]
• interval 2 (day):	[0.5]	• Aquifer parameters:	
• interval 3 (day):	[0.5]	• hydraulic conductivity K_H (m/s)	$[10^{-4}]$ for entire model area
• ..	• ..	• storage coefficient S (ad)	[0.08] for entire model area
• ..	• ..	• initial piezometric heads h (m)	[200] on N boundary [220] on S boundary [200] in the rest area
• ..	• ..	• mean groundwater recharge $Q_{V\text{recharge}}$ ($\text{m}^3/\text{s}/\text{m}^2$)	$[7.9 \times 10^{-9}]$ for entire modeling area
• interval 24 (day):	[0.5]	• aquifer base (m above reference)	[140] for entire modeling area
• Injection/pumping well:		• boundary flux $Q_{V\text{boundary}}$ ($\text{m}^3/\text{s}/\text{m}^2$)	[0] for entire modeling area
• number wells	[1]		
• location, injection (+) or extraction (-) in m^3/s			
• for well #1			
• x index of cell	[10]		
• y index of cell	[10]		

¹⁾ Note that the values listed for “type of model” are specified as “1” if a given attribute is true or as “0” if it is false; N: North, S: South.

Along with this information all known field data have been introduced into the model. When performing the simulation, we will obtain a simulation result of the groundwater flow field for the end of each time interval, as shown in Figure 8.1b as example for $t = 365.5$ days, after 12 hours of pumping with a rate of $Q_V = -0.3 \text{ m}^3/\text{s}$.

8.1.4.2 *Evaluation of the piezometric pattern*

The evolution of piezometric levels in time at the observation points A, B, and C is shown in Figure 8.2 only in the interval $364 < t < 376.5$ days, which is of interest for solving our specific problem. From Figure 8.2 (or the respective data files), we can determine the maximum depressions in piezometers A, B, and C amounting 0.80, 0.46 m, and 0.34 m, respectively. Since, the maximum depression in B, which corresponds to the point 100 m west of the well is less than the maximum tolerable depression of 0.60 m required to avoid subsidence of buildings, we can confirm that it is possible to extract the required $0.03 \text{ m}^3/\text{s}$. However, the original (natural) groundwater level at the piezometers is never recovered between two pumping phases, and after 8 pumping phases, groundwater levels present only periodic oscillations around a mean value.

8.1.4.3 *Evaluation of the water balance of the model area*

From the model area, water can be added (or removed) by different types of fluxes: (1) at cells of prescribed hydraulic head, (2) at cells with defined boundary fluxes, (3) at cells with withdrawal or injection wells, (4) at cells of groundwater recharge or evaporation on the surface, and (5) at leakage cells. The sum of all these fluxes corresponds to the total water balance of the entire model area. In the case of steady-state groundwater flow model the total balance must be zero (plus or minus the tolerable error), otherwise, the model is either not properly calibrated or is caused by improper specification of parameters in the numerical description of the problem. As we can see from the value of the total water balance at the end of the first time interval ($Q_{V\text{total}} = 1.4 \times 10^{-6} \text{ m}^3/\text{s}$), which corresponds to zero flux in practice at $t = 365$ days, the model has reached a solution corresponding to a stationary groundwater flow field. Thereby all the groundwater, which is recharged by rainfall, $Q_{V\text{recharge}} = 1.78 \times 10^{-2} \text{ m}^3/\text{s}$, leaves the model areas at the northern and southern boundaries at the cells with prescribed hydraulic head cells $Q_{V\text{pot}} = -1.78 \times 10^{-3} \text{ m}^3/\text{s}$. Analyzing the total balances in the time interval $375 \text{ days} < t < 376$

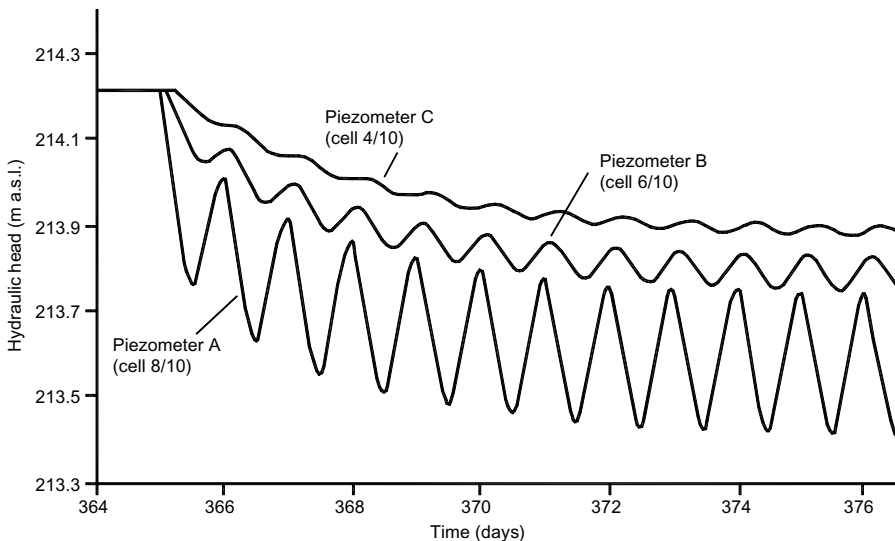


Figure 8.2. Simulated piezograms of the observation points A, B, and C with periodical extraction of groundwater from the well.

Table 8.2. Water balance for the modeling area (in m^3/s) for time intervals 22 (pumping phase; a) and 23 (rest phase; b) corresponding to the time interval 375 days $< t < 376$ days.

Component		(a)	(b)
Horizontal fluxes	Q_V^{hor}	≈ 0	≈ 0
Contributions and losses through wells	Q_V^{well}	-3.00×10^{-2}	0
Contributions and losses at prescribed hydraulic head cells	Q_V^{pot}	1.26×10^{-2}	1.31×10^{-2}
Contributions and losses through boundaries	Q_V^{boundary}	0	0
Infiltration recharge	Q_V^{recharge}	1.78×10^{-3}	1.78×10^{-3}
Contributions and losses through leakage	Q_V^{leakage}	0	0
Global balance	Q_V^{total}	-1.57×10^{-2}	1.48×10^{-2}

days, we obtain $Q_V^{\text{total-pump}} = -1.57 \times 10^{-2} \text{ m}^3/\text{s}$ at the end of the pumping phase (time step 22; at $t = 375.5$ days), and $Q_V^{\text{total-rest}} = 1.48 \times 10^{-2} \text{ m}^3/\text{s}$ at the end of the following rest phase (time step 23; at $t = 376$ days) (Table 8.2). We can see that in a pumping phase, about half of the quantity of water pumped from the well $Q_V^{\text{well}} = -3.00 \times 10^{-2} \text{ m}^3/\text{s}$ originates from a water influx through the model boundaries with prescribed head cells ($Q_V^{\text{pot}} = 1.26 \times 10^{-2} \text{ m}^3/\text{s}$), and less than 10% from recharge by rainfall ($Q_V^{\text{recharge}} = 1.78 \times 10^{-3} \text{ m}^3/\text{s}$). The water balance for the time interval 375 days $< t < 376$ days, corresponding to one pumping and one rest phase, is obtained as the sum $Q_V^{\text{total-pump}} + Q_V^{\text{total-rest}} = -9 \times 10^{-4} \text{ m}^3/\text{s}$, which shows that both these water fluxes practically compensate each other, corresponding to steady-state conditions, in which only periodic oscillations of water levels around a mean value occur.

8.2 WATER EXCHANGE BETWEEN AN AQUIFER AND A SURFACE WATER BODY BY LEAKAGE

8.2.1 Problem and tasks

A water works located to the west of a middle-sized city found evidence of the presence of a toxic organic compound in its wells. This compound can only come from an industrial effluent treatment plant, which is discharging its treated water to a river located in the recharge area of the wells used by the water works. To determine the severity of the problem, the authorities requested the percentage of the volume extracted by the water works corresponding to filtration from the river determined by performing infiltration tests along the river course and by using numerical modeling of the groundwater-surface water system.

8.2.2 Hydrogeological setting, available data and measurements

Figure 8.4 shows the study area, with the location of wells used by the water works and the piezometers available for groundwater levels monitoring and sampling. The alluvial aquifer is considered to be homogeneous and with an impermeable base at 50 m a.s.l. By the means of pumping tests and based on a regional model, a hydraulic conductivity value of $K_H = 5 \times 10^{-4} \text{ m/s}$ was deduced. The wells produce a total of 20,000 m^3/d , which translates as 0.026 m^3/s for each of the 9 wells. There are 7 piezometers, P_1 to P_7 , with groundwater level measurements dating from October 1990 (Table 8.3).

8.2.3 Formulating surface water-groundwater interactions by leakage

Water exchange between bodies of groundwater and surface water, can be described as leakage. Using the leakage factor L , defined as the vertical hydraulic conductivity K_{HL} of the base of the

Table 8.3. Spatial coordinates of the piezometers 1 to 7 and measured groundwater levels; the point ($x = 0$, $y = 0$) corresponds to the lower left corner of the map in Figure 8.4).

Piezometer	P ₁	P ₂	P ₃	P ₄	P ₅	P ₆	P ₇
x coordinate (m)	6855.3	4897.3	8841.3	9778.4	5274.9	9205.0	5065.1
y coordinate (m)	6696.7	10723.3	9395.1	7486.6	2502.2	12610.8	4683.3
h groundwater level (m a.s.l.)	83.03	82.88	84.10	84.97	83.90	85.35	82.99

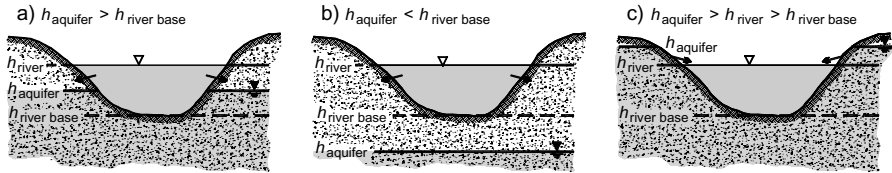


Figure 8.3. Water exchange between an aquifer and a surficial water body for different positions of the groundwater table.

river divided by its thickness b_s ($L = K_{HL}/b_s$), exfiltration and infiltration flows Q_{VL} can be formulated as follows:

$$Q_{VL} = \begin{cases} L(h_{\text{river}} - h_{\text{aquifer}}) & \text{for } h_{\text{aquifer}} > h_{\text{base-river}} \\ L(h_{\text{river}} - h_{\text{base-river}}) & \text{for } h_{\text{aquifer}} < h_{\text{base-river}} \end{cases}$$

If the groundwater level h_{aquifer} is higher than that of the surface water h_{river} (e.g., river or lake), water flow from the aquifer towards the surface water occurs (exfiltration) (Fig. 8.3). On the other hand, if the level of the surface water is above the groundwater level, then the water flow will be from the river towards the aquifer (infiltration). In the case of river water infiltration to the aquifer, Q_{VL} values will be positive, whereas they will be negative in the case of exfiltration.

If the piezometric level in the aquifer h_{aquifer} is higher than the base level of the river $h_{\text{base-river}}$, the leakage factor is independent from $h_{\text{base-river}}$ and dependent only on the water level in the river h_{river} . If the piezometric level in the aquifer h_a is lower than the base level of the river $h_{\text{base-river}}$, the leakage factor depends on $h_{\text{base-river}}$, and not on the water level in the river (Fig. 8.3).

8.2.4 Execution of infiltration tests along the river

Along the course of the river, infiltration tests were performed, and at the respective sites the water level of the river was measured. Respective real measured data were interpolated and adapted to the cell numbers as given in Figure 8.4 of the numerical model and are listed in Table 8.4. The level of the river base was estimated by subtracting an averaged water column of 0.44 m (corresponding to the average water depth in the river) from the river water level. Since the area A , from where leakage from the river towards the aquifer occurs, does not necessarily cover the entire area of a respective cell of the numerical grid, the leakage factors L must be corrected. In each cell, only the part which is covered by the river must be considered, that means only the area A corresponding to the product:

length a of the river stretch at each cell \times width b of the river

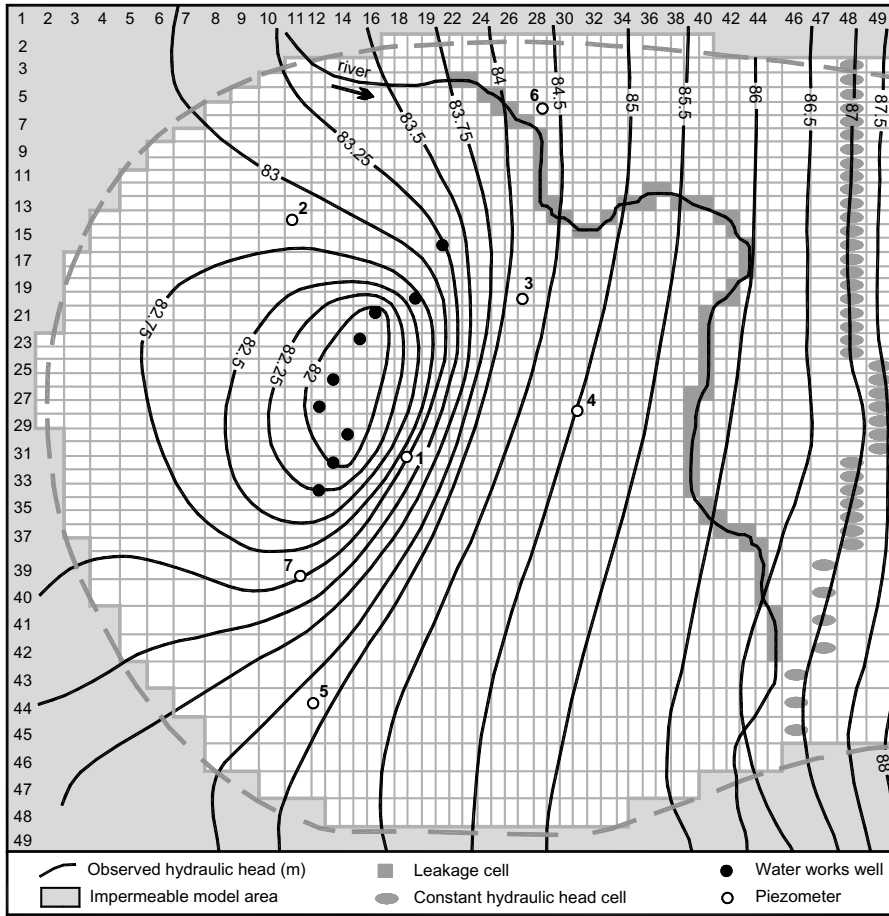


Figure 8.4. Model area (16,000 × 15,500 m) with the location of the river from where surface water infiltrates into the aquifer, the wells used by the water works, location of piezometers, the groundwater level contour lines, and the design of the numerical model grid, including respective cell numbers.

Table 8.4. Leakage parameters.

Cell index (x, y)	River base (m a.s.l.)	Surface water level (m a.s.l.)	$L = K_{HL}/b_s$ ($\times 10^{-9}/s$)	b (m)	a (m)	Az (m^2)	$L^* = L(ab)/Az$ ($\times 10^{-9}/s$)
22/4	84.16	84.60	1164.60	7.80	150	15625	87.21
23/4	84.17	84.61	1164.60	7.80	75	15625	43.60
24/5	84.18	84.62	1164.60	7.80	75	15625	43.60
25/5	84.18	84.62	1164.60	7.80	125	15625	72.67
25/6	84.19	84.63	1164.60	7.80	50	15625	29.07
26/6	84.20	84.64	1164.60	7.80	125	15625	72.67
26/7	84.21	84.65	1164.60	7.80	50	15625	29.07
27/7	84.26	84.70	1164.60	7.80	150	15625	87.21
28/8	84.31	84.75	13333.30	7.30	175	15625	1090.13
28/9	84.38	84.82	13333.30	7.30	125	15625	778.66

(Continued)

Table 8.4. (Continued)

Cell index (x, y)	River base (m a.s.l.)	Surface water level (m a.s.l.)	$L = K_{HL}/b_s$ ($\times 10^{-9}/s$)	b (m)	a (m)	Az (m^2)	$L^* = L(ab)/Az$ ($\times 10^{-9}/s$)
28/10	84.45	84.89	13333.30	7.30	150	15625	934.40
28/11	84.52	84.96	13333.30	7.30	125	15625	778.66
28/12	84.59	85.03	13333.30	7.30	150	15625	934.40
28/13	84.66	85.10	13333.30	7.30	100	15625	622.93
29/13	84.70	85.14	13333.30	7.30	75	15625	467.20
29/14	84.74	85.18	13333.30	7.30	100	15625	622.93
30/14	84.78	85.22	13333.30	7.30	125	15625	778.66
31/15	84.82	85.26	13333.30	7.30	125	15625	778.66
32/15	84.87	85.31	16000.00	7.30	175	15625	1308.16
33/14	84.92	85.36	16000.00	7.30	175	15625	1308.16
34/13	84.96	85.40	16000.00	7.30	150	15625	1121.28
35/13	85.00	85.44	16000.00	7.30	125	15625	934.40
36/13	85.04	85.48	16000.00	7.30	50	15625	373.76
36/12	85.08	85.52	16000.00	7.30	75	15625	560.64
37/12	85.12	85.56	16000.00	7.30	150	15625	1121.28
38/13	85.16	85.60	16000.00	7.30	125	15625	934.40
39/13	85.20	85.64	16000.00	7.30	125	15625	934.40
40/13	85.25	85.69	16000.00	7.30	150	15625	1121.28
41/14	85.29	85.73	16000.00	7.30	125	15625	934.40
42/14	85.33	85.77	16000.00	7.30	75	15625	560.64
42/15	85.37	85.81	16000.00	7.30	125	15625	934.40
43/16	85.42	85.86	16000.00	7.30	125	15625	934.40
43/17	85.47	85.91	6545.50	7.00	150	15625	439.86
43/18	85.51	85.95	6545.50	7.00	125	15625	366.55
42/19	85.56	86.00	6545.50	7.00	150	15625	439.86
42/20	85.60	86.04	6545.50	7.00	75	15625	219.93
41/20	85.64	86.08	6545.50	7.00	125	15625	366.55
42/20	85.68	86.12	6545.50	7.00	150	15625	439.86
40/21	85.72	86.16	6545.50	7.00	150	15625	439.86
40/22	85.76	86.20	6545.50	7.00	150	15625	439.86
40/23	85.80	86.24	6545.50	7.00	125	15625	366.55
40/24	85.84	86.28	6545.50	7.00	150	15625	439.86
40/25	85.88	86.32	10142.90	7.80	125	15625	632.92
40/26	85.91	86.35	10142.90	7.80	75	15625	379.75
40/27	85.94	86.38	10142.90	7.80	75	15625	379.75
39/27	85.98	86.42	10142.90	7.80	125	15625	632.92
39/28	86.02	86.42	10142.90	7.80	125	15625	632.92
39/29	86.06	86.50	10142.90	7.80	125	15625	632.92
39/30	86.09	86.53	10142.90	7.80	125	15625	632.92
39/31	86.13	86.57	10142.90	7.80	125	15625	632.92
39/32	86.16	86.60	10142.90	7.80	125	15625	632.92
39/33	86.20	86.64	10142.90	7.80	125	15625	632.92
39/34	86.26	86.70	10142.90	7.80	175	15625	886.08
40/35	86.29	86.73	10142.90	7.80	50	15625	253.17
40/36	86.34	86.78	10142.90	7.80	150	15625	759.50
41/36	86.39	86.83	10142.90	7.80	150	15625	759.50
42/37	86.42	86.86	10142.90	7.80	50	15625	253.17
43/37	86.46	86.90	10142.90	7.80	75	15625	379.75
44/38	86.51	86.95	10142.90	7.80	125	15625	632.92
44/39	86.59	87.03	10142.90	7.80	250	31250	632.92
44/40	86.68	87.12	10142.90	7.80	250	31250	632.92
45/41	86.77	87.21	10142.90	7.80	275	31250	696.21
45/42	86.86	87.30	12637.90	7.90	300	31250	958.46

By multiplying L with the ratio of this surface $A = ab$ related to the entire area of the cell Az corresponding to the percentage of the river surface ab with respect to the surface A of the cell we obtain a new leakage factor L^* , as input for our numerical model.

8.2.5 Elaboration of a numerical model and problem solution

A numerical 2-dimensional horizontal model covering $16,000 \times 15,500$ m was used to represent an unconfined homogeneous and isotropic aquifer with stationary groundwater flow. It is constructed using ASM modeling code (see section 6.8.3) with the grid shown in Figure 8.4. With the exception of the right model boundary, the boundaries were selected in such a way that the model margin is about perpendicular to the groundwater level contours (parallel to flow lines), and hence impermeable (Fig. 8.4). Therefore, cells outside of the desired boundary were made inactive by setting their K_H value to zero. Using the same method, the right model boundary was adjusted in such way that it is approximately parallel to the groundwater level contours of 87 and 87.5 m a.s.l. (Fig. 8.4), so that at these prescribed hydraulic head cells, a groundwater flow perpendicular across this model boundary occurs. The model input data are listed in Table 8.5.

Table 8.5. Input data for the groundwater flow model.

• Type of model ¹⁾ :		• for well #5	
• stationary (0/1)	[0]	• x index of cell	[13]
• confined/free (0/1)	[1]	• y index of cell	[26]
• anisotropy (K_{Hy}/K_{Hx})	[1]	• for well #6	
• Model grid:		• x index of cell	[12]
• number of cells on x	[49]	• y index of cell	[12]
• number of cells on y	[49]	• for well #7	
• size of cells on x (m)		• x index of cell	[14]
cell 1–11	[500]	• y index of cell	[30]
cell 12–45	[250]	• for well #8	
cell 46–49	[500]	• x index of cell	[13]
• size of cells on y (m)		• y index of cell	[32]
cell 1–2	[500]	• for well #9	
cell 3–38	[250]	• x index of cell	[12]
cell 39–49	[500]	• y index of cell	[34]
• Injection/pumping well:		• extraction rate	
• number wells	[9]	• Q_1 – Q_9	[–0.026]
• location, injection (+) or extraction (–) in m^3/s		• Aquifer parameters:	
• for well #1		• hydraulic conductivity	$[5 \times 10^{-4}]$ for all active cells ²⁾
• x index of cell	[21]	• storage coefficient	[0]
• y index of cell	[16]	• initial hydraulic heads h (m)	[87 and 87.5] on E at prescribed hydraulic head cells [80] in the rest area [50] for entire model area
• for well #2		• aquifer base (m above reference)	
• x index of cell	[19]		
• x index of cell	[20]		
• for well #3			
• x index of cell	[16]		
• y index of cell	[21]		
• for well #4			
• x index of cell	[15]		
• y index of cell	[23]		

¹⁾ Note that the values listed for “type of model” are specified as “1” if a given attribute is true or as “0” if it is false.

²⁾ K_H will later used as calibration parameter.

Step 1: Model without leakage from river: Before introducing the river and the river water infiltration by leakage, we will construct a numerical model considering only the water withdrawal in the wells and calibrate this model. Since the hydraulic conductivity K_H is only known very roughly from regional studies, this parameter will be selected as the calibration parameter of the flow model (K_H shall be determined within the margin of error, 1×10^{-4} m/s). Therefore, the first model run is performed using $K_H = 5 \times 10^{-4}$ m/s for the entire model area (with the exception of the inactive cells). For comparing the simulated and the real situation, we use the groundwater levels observed at the piezometers P₁ to P₇, and compare them with the modeling results as we have done in section 6.9.1. We use scatter plots and compare the numerically simulated hydraulic heads with those measured in the field at the sites of the 7 piezometers P₁ to P₇. For the initial value of the calibration parameter $K_{H1} = 5 \times 10^{-4}$ m/s, the deviation between simulated and measured hydraulic heads is given by a mean square derivation value of $MSD_1 = 20.7 \text{ m}^2$. We can see that for all piezometer locations the simulated hydraulic heads are lower than the measured ones, so that we need to increase the hydraulic conductivity in the next calibration step. We double K_H and obtain for the new $K_{H2} = 1 \times 10^{-3}$ m/s a much better agreement between simulated and measured heads ($MSD_2 = 0.36 \text{ m}^2$), but the simulated hydraulic heads are still slightly lower than the measured ones. To further improve the K_H value, we increase K_H slightly stepwise by 1×10^{-4} m/s. For $K_{H3} = 1.1 \times 10^{-3}$ m/s we obtain for the derivation $MSD_3 = 0.20 \text{ m}^2$ and for $K_{H4} = 1.2 \times 10^{-3}$ m/s we obtain a MSD_4 of 0.25 m^2 ; so that $K_{H3} = 1.1 \times 10^{-3}$ m/s, is the most appropriate value for hydraulic conductivity for the established calibration target.

Step 2: Model with leakage from river: Now, we implement the river and the groundwater surface interactions expressed as leakage. Therefore, we introduce in the leakage cells along the river the values of surface water level and river base level, and the corrected leakage factors L^* determined in section 8.2.4 (Table 8.4). Since it is likely that the conditions have been modified after introducing the leakage, we need to re-calibrate the model by adjusting again the K_H value. For $K_{H3} = 1.1 \times 10^{-3}$ m/s we obtain a $MSD'_3 = 0.28 \text{ m}^2$ and the values of the simulated hydraulic heads are slightly greater than the observed ones so that we need to reduce the hydraulic conductivity value. Doing so in steps of 1×10^{-4} m/s, we obtain stepwise $K_{H5} = 9 \times 10^{-4}$ m/s as hydraulic conductivity value with the smallest $MSD_5 = 0.10 \text{ m}^2$.

With this calibrated groundwater flow model, in which groundwater recharge is through the mechanisms of groundwater inflow ($Q_{V_{gw}}$) from the eastern model boundary and from infiltration through leakage from the contaminated river ($Q_{V_{river}}$), we can now establish the balance of both fluxes. For this purpose, we need to determine the water fluxes through leakage from the river towards the aquifer (according to eq. 8.1 positive values of Q_V), excluding these leakage cells where groundwater infiltrates from the aquifer into the river (negative values of Q_V). The sum of leakage fluxes from all leakage cells with river water infiltration into the aquifer amounts $Q_{V_{river}} = 0.15 \text{ m}^3/\text{s}$, so about 65% of the water exploited in the wells ($Q_{V_{well}} = 0.23 \text{ m}^3/\text{s}$) of the water works corresponds to contaminated riverwater. Hence, the simulation results of the numerical model have proven the influx of river water contaminated by an organic toxic compound into the wells and quantified the severity of the problem allowing now to formulate corresponding counter measures.

8.3 SCENARIO MODELING OF MULTI-LAYER AQUIFERS AND DISTRIBUTION OF GROUNDWATER AGES CAUSED BY EXPLOITATION

8.3.1 *Problem*

The public water works of a city with one million inhabitants is exploiting groundwater from wells located in an urban area. The aquifers are located in highly inhomogeneous complex structured Quaternary alluvial sediments of about 100 m thickness lying over impermeable Tertiary bedrock. Over time, water from shallow wells has become more and more affected by contamination, so

water works providers are considering two alternatives. One option is to drill deeper wells within the urban areas of around 100 m depth, and the other is to install a new water works outside of the urban area in an anthropogenically unaffected region. The latter solution requires much more investment.

To assist in the decision making, information is needed about whether the groundwater exploitation of deeper, not yet contaminated aquifers, is a suitable long-term option. To decide this, two principal questions must be answered:

- Are the deeper layers of the aquifer system sufficiently protected by the clay layers and lentils to hinder, under natural flow conditions, the inflow of shallow contaminated groundwater within the urban area, or can we expect that within a short time the exploited deeper groundwater will become contaminated too?
- Which choice impacts the groundwater exploitation from deeper aquifers on the vertical groundwater flow field of the whole aquifer system including the shallow contaminated layer? Does the pumping in deep not yet contaminated aquifers, which may cause an increase of the hydraulic gradient towards the deeper aquifer, accelerate the inflow of shallow contaminated groundwater into the exploited deep aquifer?

To estimate the potential of the clay layers and lentils in protecting the deeper aquifer from contamination and potential influences of the urban groundwater exploitation from deeper aquifers on the whole aquifer system and the contamination hazard potential, numerical simulations shall be conducted. Since the complex structured heterogeneous Quaternary aquifer systems composed of intercalated layers or lenses of gravel, sand, silt and clay, are not known in great detail, and consequently, few field data exist on them, no numerical model of the entire system can be elaborated. As consequence, a variety of 2-dimensional vertical-plane multilayer aquifer models (scenarios), using different geometric model configurations which are adapted to the typical situations found in the study area, shall be elaborated. They will be used to estimate the manner in which the aquifer geometry, the presence of additional clay layers and lenses, and the groundwater exploitation, influences the groundwater flow pattern, as well as the groundwater balance at the different levels of the aquifer, and the distribution in residence time (groundwater age). Therefore, models are constructed of two or three layers, including additional clay layers and lenses, with a total thickness of 100 m in different configurations. Simulations shall be performed with and without groundwater extraction from the deepest aquifer. The results shall be compared to determine the impact of the exploitation on the groundwater flow field and the propagation of the contaminant originating from the contaminated shallow urban aquifer. The geometric aquifer configurations will be investigated to find which has the greatest impact, and which configurations have reduced or negligible influence. The modeling results can be considered as the range of potential scenarios in the study area and can be used to assist in decision making.

8.3.2 *Aquifer specifications*

The water works provides the modeler with a set of typical geometries of cross-sections found in the alluvial aquifer. On this base, a vertical cross-section of a 100 m thick unconfined alluvial aquifer with a horizontal extension of 10,000 m shall be modeled. The left border and the base of the cross-section area are impermeable to water. The right border of the model is open to the inflow and outflow of groundwater. Here, all groundwater shall leave the model area in a horizontal direction. Groundwater is recharged through rainfall with a constant seasonal rate of $Q_V = 157.7$ mm/year (5×10^{-9} m³/s/m²) throughout the surface of the model. The hydraulic head presents a slope from left to right. The thickness of the saturated aquifer is approximately 100 m and varies slightly according to the piezometric level.

The 100 m thick aquifer system is composed of two (model I) or three (model II and III) horizontal layers with the same porosity, $\varphi_{\text{eff}} = 0.2$, but different hydraulic conductivities, K_H , and thicknesses, b_a :

- Model I: A high conductivity layer (thickness $b_a = 40$ m, $K_H = 10^{-3}$ m/s) underlying a layer that is 10 times less permeable ($b_a = 60$ m, $K_H = 10^{-4}$ m/s).
- Model II: A high conductivity layer at the top and bottom of the aquifer (each $b_a = 20$ m, $K = 10^{-3}$ m/s) are separated by a $b_a = 60$ m thick layer whose conductivity is three orders of magnitude lower ($K_H = 10^{-6}$ m/s).
- Model III: The structure of the model is similar to that of Model II, with the only difference that the conductivity of the lowermost layer is now 10 times lower ($K_H = 10^{-4}$ m/s).

For each of the three models I–III, 4 different configurations of clay layers and clay lenses ($K_H = 10^{-9}$ m/s) may be present in the aquifer (variants 1 to 4), resulting in 12 different configurations. Clay lenses and horizons of varying extent and location are found according to the following specification, where point $x = 0$, and $y = 0$, corresponds to the upper left corner of the cross-section area:

- Variant 1: no clay layer is present.
- Variant 2: there is one clay layer ($b_a = 4$ m) that spreads over 80% of the width of the model and has one 1200 m wide window and a second 800 m wide window. The base of the clay layer is at $y = 60$ m, and its horizontal extension: $1200 \leq x \leq 6800$ m and $7600 \leq x \leq 10,000$ m.
- Variant 3: there is one clay layer ($b_a = 4$ m) that spreads over 68% of the width of the model and has one 4200 m wide window. The base of clay layer is at $y = 60$ m, and its horizontal extension: $4200 \leq x \leq 10,000$ m.
- Variant 4: The following clay layers of $M = 2$ m are added to the variant 2.
 - base of clay layer $y = 16$ m: $9400 \leq x \leq 10,000$ m;
 - base of clay layer $y = 18$ m: $5800 \leq x \leq 8000$ m; $8800 \leq x \leq 10,000$ m;
 - base of clay layer $y = 20$ m: $5200 \leq x \leq 7800$ m; $8600 \leq x \leq 9600$ m;
 - base of clay layer $y = 28$ m: $4000 \leq x \leq 10,000$ m;
 - base of clay layer $y = 30$ m: $3800 \leq x \leq 10,000$ m;
 - base of clay layer $y = 32$ m: $3200 \leq x \leq 10,000$ m;
 - base of clay layer $y = 44$ m: $5600 \leq x \leq 7000$ m; $7800 \leq x \leq 10,000$ m;
 - base of clay layer $y = 48$ m: $2800 \leq x \leq 5000$ m;
 - base of clay layer $y = 46$ m: $2200 \leq x \leq 5000$ m; $5600 \leq x \leq 6800$ m; $8000 \leq x \leq 10,000$ m.

8.3.3 *Objectives of the modeling*

In each of the 3 models, I–III, and their respective variants, 1–4, resulting in the 12 model scenarios, simulations of the steady-state groundwater flow field shall be performed with and without groundwater withdrawal by the well from the lower layer. Well discharge shall correspond to 50% of the natural groundwater recharge by rainfall (in the examples where this yield is not possible, a smaller withdrawal shall be used instead) to perform the following investigations:

1. Determine for each of the three models, I–III (with no clay layers), the mass balance of the groundwater circulating under natural conditions in each layer in relation to the total groundwater recharge by rainfall. Evaluate how the design and the hydraulic conductivity of the different layers influence the groundwater flow in each layer.
2. Evaluate for the different model configurations the influence of the groundwater extraction by the well on the groundwater flow and the groundwater balance in the different layers. Groundwater shall thereby be exploited in a well only from the lowermost layer with the following location and extension of filter section:

- Model I: variants 1, 2, and 4: well at $x = 6100$ m; variant 3: $x = 7100$ m; filter section for all variants $y = 66$ to 86 m depth.
- Model II and III: all variants: well at $x = 7100$ m; filter section from $y = 82$ to 98 m depth.

Well discharge shall amount to 50% of the water recharged by rainfall at the earth's surface; where this yield is not possible, a suitable lower value shall be used instead.

3. Estimate the contamination hazard of the deep aquifer by the shallow contaminated groundwater in the urban area. Thereby, the contamination hazard shall be evaluated and compared for scenarios without and with the pumping of groundwater from the lowermost layer. The evaluation shall be performed using groundwater balances for the different layers as well as the groundwater flow paths and isochrones, which indicate groundwater ages. For interpretation, it will be considered that severe contamination of the shallow aquifer within the urban area started about 60 years ago. This means that areas in the modeled cross-sections with water younger than 60 years should be considered contaminated (hydrodynamic dispersion is not considered). Estimate the areas in the cross-sections which are expected to become contaminated during the next 40 years.

8.3.4 Elaboration of a numerical model

A numerical 2-dimensional vertical-plane model corresponding to a cross-section through the unconfined inhomogeneous aquifer with stationary groundwater flow is constructed. The grid of the $10,000 \times 100$ m model area is composed of 50 cells in x -direction (cell width: 200 m) and 50 cells in y -direction (cell width: 2 m) (Fig. 8.5).

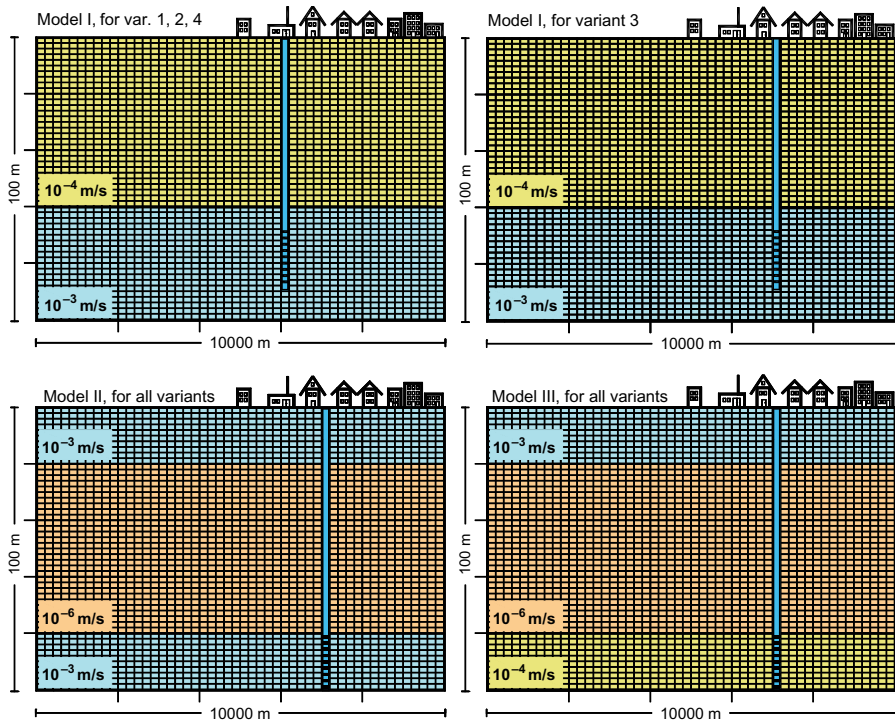


Figure 8.5. Model grid of the $10,000 \times 200$ m covering cross-section areas of models I, II, and III with the distribution of the different sediment layers and their respective hydraulic conductivities. Additionally shown is the position of the pumping well and the cells corresponding to the well filter sections from where groundwater is extracted.

8.3.4.1 Aquifer properties

The models are designed according to the specifications given in 8.3.2 for the 3 models and the 4 variants, obtaining an aquifer system. The designs of models I to III with 2 or 3 principal layers and their conductivities are shown in Figure 8.5. Each of the three models is subdivided into four variants that are differentiated by the position of the clay layers and lenses (Fig. 8.6). These have a hydraulic conductivity of $K_H = 10^{-9}$ m/s; the x and y indices of cells corresponding to clay are (cell index $x = 0, y = 0$ corresponds to the upper left cell in the model area):

- Variant 1: no clay layer is present
- Variant 2:
 - $y = 29: x = 7-34$ and $39-50$
 - $y = 30: x = 7-34$ and $39-50$
- Variant 3:
 - $y = 29: x = 22-50$
 - $y = 30: x = 22-50$
- Variant 4; in addition to the clay layer of variant 2:
 - $y = 8: x = 58-60$
 - $y = 9: x = 29-40$ and $44-50$
 - $y = 10: x = 26-39$ and $43-48$
 - $y = 14: x = 20-50$
 - $y = 15: x = 19-50$
 - $y = 16: x = 16-50$
 - $y = 22: x = 28-35$ and $39-50$
 - $y = 23: x = 11-25, 28-34$ and $40-50$
 - $y = 24: x = 14-25$

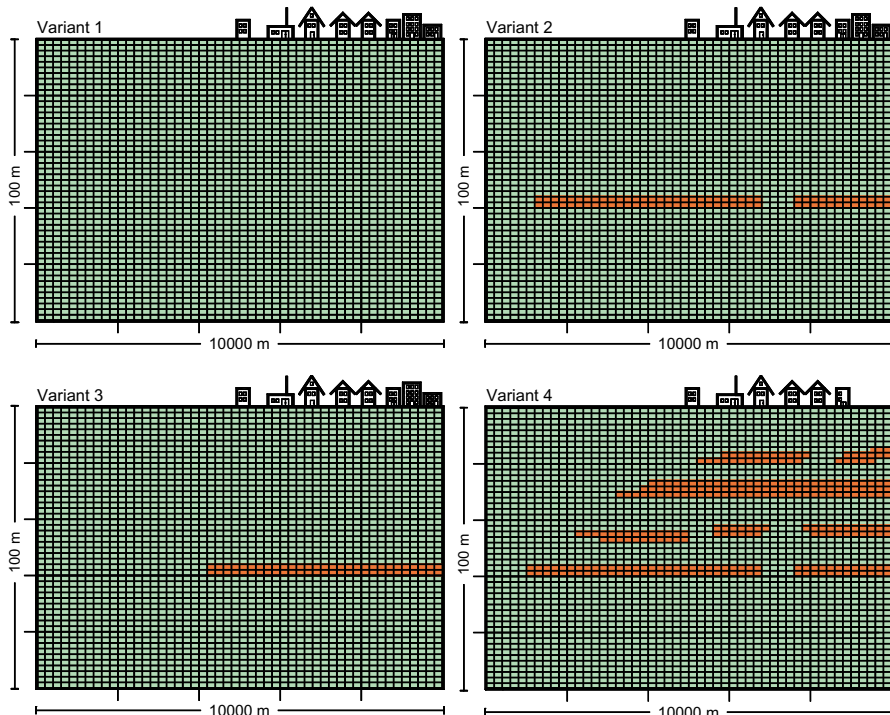


Figure 8.6. Model grid of the cross-section area with the spatial distribution of the clay layers and lenses (red) of model variants 1 to 4.

8.3.4.2 Boundary conditions

The left and lower boundaries of the model are impermeable, whereas recharge by rainfall at the upper horizontal margin is simulated by a constant boundary flow of $Q_V = 5 \times 10^{-9} \text{ m}^3/\text{s}/\text{m}^2$ corresponding to recharge by rainfall of 157.7 mm/year. The right model boundary, where groundwater can flow out, is represented by prescribed hydraulic head.

For the determination of the water balances in the different layers, groundwater must leave the model area at the right model boundary in horizontal direction. Then, water flows can be determined in these boundary cells for each layer which corresponds to the water flow component of the respective layer. For that purpose, an additional 500 m wide high-conductivity column will be added ($K_H = 10^{-1} \text{ m/s}$) to the right border of the model. This will prevent vertical flow at this boundary and will allow a horizontal flow of groundwater so as to be able to univocally separate the water volumes corresponding to the flows in the individual layers leaving at the right model boundary.

8.3.4.3 Groundwater extraction

50% of the recharged water will be extracted from the deepest layer of the aquifer system. The location of the wells is shown in Figure 8.5 and the x and y indices of the extraction cells are:

- Model I: variants 1, 2, and 4: cells $x = 31$; variant 3: $x = 36$; for all variants filter section from $y = 34$ to 44.
- Model II and III: all variants: well at $x = 36 \text{ m}$; filter section from $y = 42$ to 49.

8.3.5 Results

For the 12 model configurations (models I–III and respective variants 1–4) groundwater flow was simulated in the cross-sections using Sutra modeling code (Voss 1984; see section 6.8.4). The volumes of the groundwater flowing through the different layers towards the right margin of the model and their share of total groundwater recharge on the earth's surface is calculated for both scenarios without and with groundwater exploitation from the lowermost layer by the well. Together with flowpaths and groundwater isochrones the results are presented in Figures 8.7–8.10, 8.11–8.14, and 8.15–8.18 for models I, II, and III, respectively.

8.3.5.1 Groundwater balance in models with two or three geological layers

The vertical groundwater flow field in the cross-section of the aquifer is mainly controlled by the geometry and the hydraulic properties of the 2 or 3 geological layers.

- If a less permeable layer is located over a layer with 10 times higher hydraulic conductivity (model I), then most of the recharged groundwater flows almost vertically through the upper layer and reaches the lower layer where it flows horizontally.
- If there is a layer between two other layers that are 1000 times more permeable than the layer in the middle (model II), similar volumes of water flow horizontally in the upper and lower layers.
- If the hydraulic conductivity of the lower layer in model II is reduced by factor 10 (model III), the inflow of water to the lower layer is significantly reduced, and most of the water flows in the upper layer in a horizontal direction.

8.3.5.2 Influence of groundwater exploitation

A comparison of simulation results with and without groundwater extraction from the lower layer indicates that exploitation can severely affect the natural groundwater flow pattern:

- In the case of model I, where under natural conditions most of the groundwater flows in the lower layer (77–54%), the extraction of groundwater from the lower layer by means of the well causes only a small increase of water influx into that layer (11–16% in variants 1–4; Table 8.6).

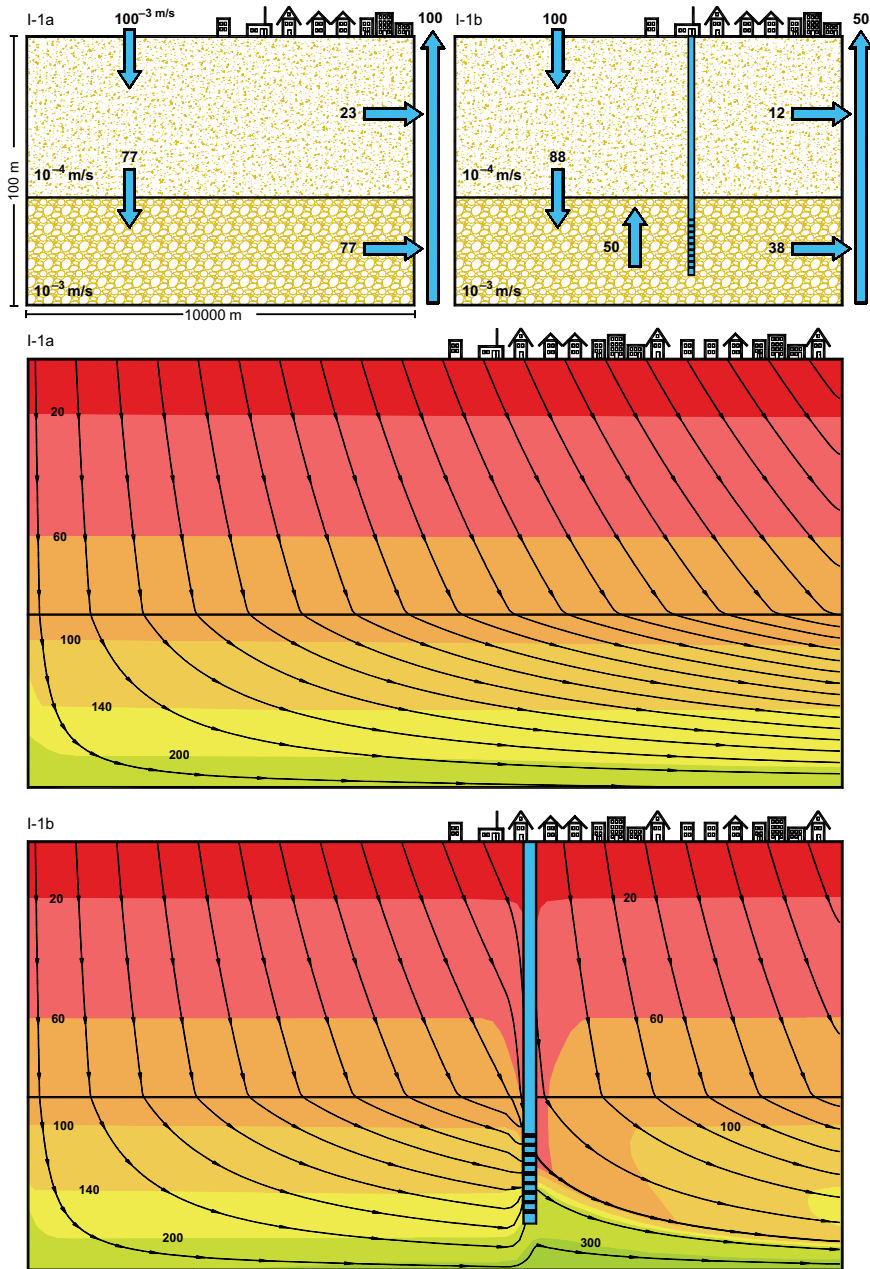


Figure 8.7. Model I, variant 1, simulation results: (a) without, (b) with groundwater withdrawal from the deeper layer. In the model configuration with a 10-times higher hydraulic conductivity layer forming the deeper layer most of the groundwater recharged at the earth's surface flows through the less permeable upper layer and reaches the deeper layer, where it flows towards the right model margin or is exploited in the well. The arrows indicate the mass balances of the groundwater flowing through the different layers towards the right model margin (as percentage of total recharged groundwater). Both lower figures show the groundwater flowpaths originating from the earth's surface and the groundwater isochrones (groundwater ages in years) for the scenario with and without groundwater exploitation, respectively.

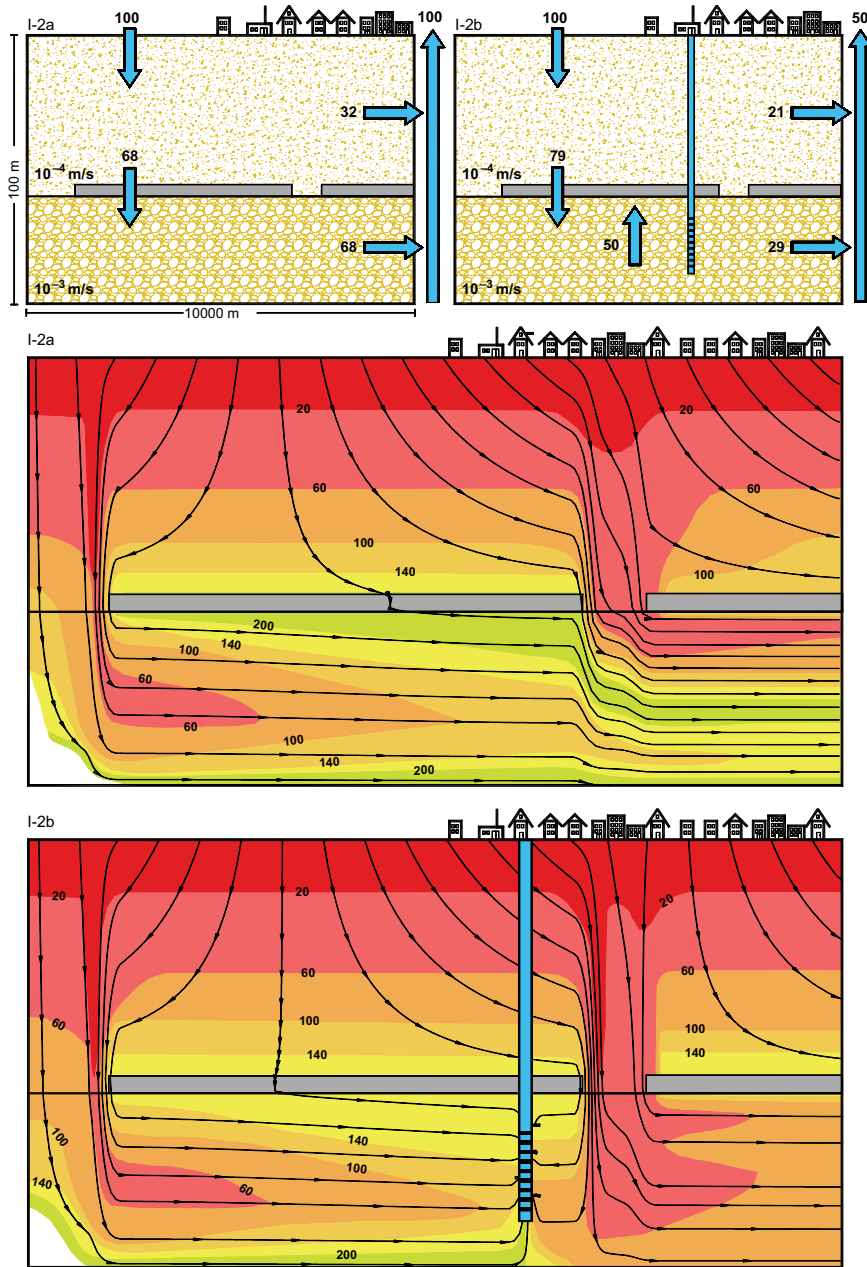


Figure 8.8. Model I, variant 2, simulation results: Most of the recharged groundwater flows around the two clay layers and reaches the deeper aquifer through the two windows in the clay layers. Correspondingly, two “fingers” of today’s contamination delimited by the 60 year isochrone (severe superficial contamination started 60 years ago) can be found. In the forecasted 40 year period nearly the entire deep layer becomes contaminated. Compared to variant I, without the clay layer, the clay layers increase the contamination of the deeper aquifer instead of protecting it as might have been expected. The reason is that the window in the clay layer is located downstream of the pumping well. For further explanations, see Figure 8.7.

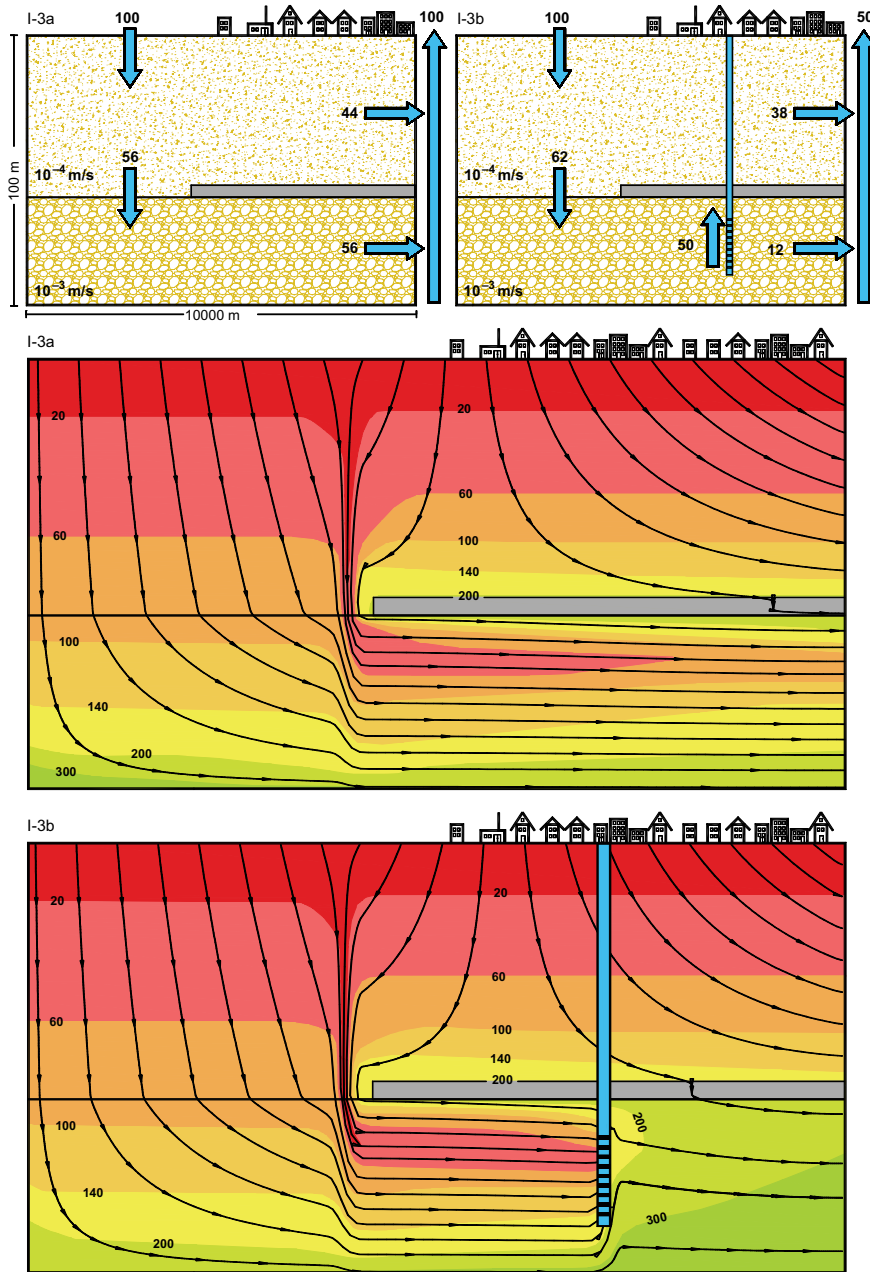


Figure 8.9. Model I, variant 3, simulation results: Compared to variant 1, we have now only one window in the clay layer located upstream of the well, through which most of the recharged groundwater reaches the deeper layer (56 and 62% for the scenario without and with pumping, respectively), hence slightly less compared to variant 2, where the fluxes into the deeper layer were 68 and 79%, respectively). For the case without pumping, the distribution of contamination after 60 and 100 years (delimited by the 60 and 100 year isochrones) shows a similar extension as in variant 1. In contrast to the variant with pumping, it can be seen that the well is extracting the entire contamination plume reaching the deeper layer. For further explanations, see Figure 8.7.

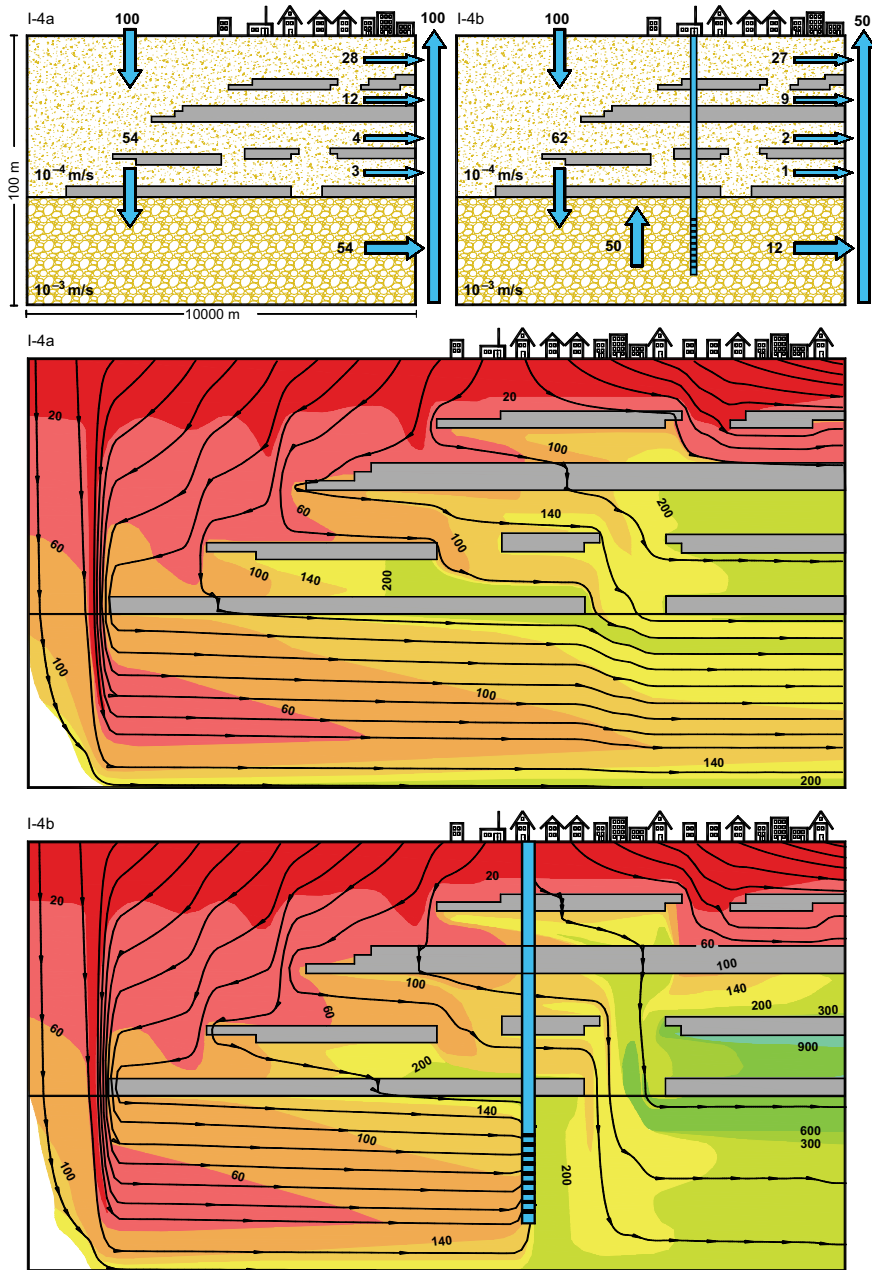


Figure 8.10. Model I, variant 4 simulation results: Here variant 2 with the two clay layers was modified by adding some more clay layers in the upper layer, which significantly reduce the groundwater influx into the deeper layer through the right window. However, the water flow through the left window is increased compared to variant 2, and in total 54% (without pumping) and 62% (with pumping) of the recharged groundwater reaches the deeper layer. This results in more contamination in the area upstream of the well location compared to variant 2. As already observed in variant 3, the well extracts most of the contamination plume. For further explanations, see Figure 8.7.

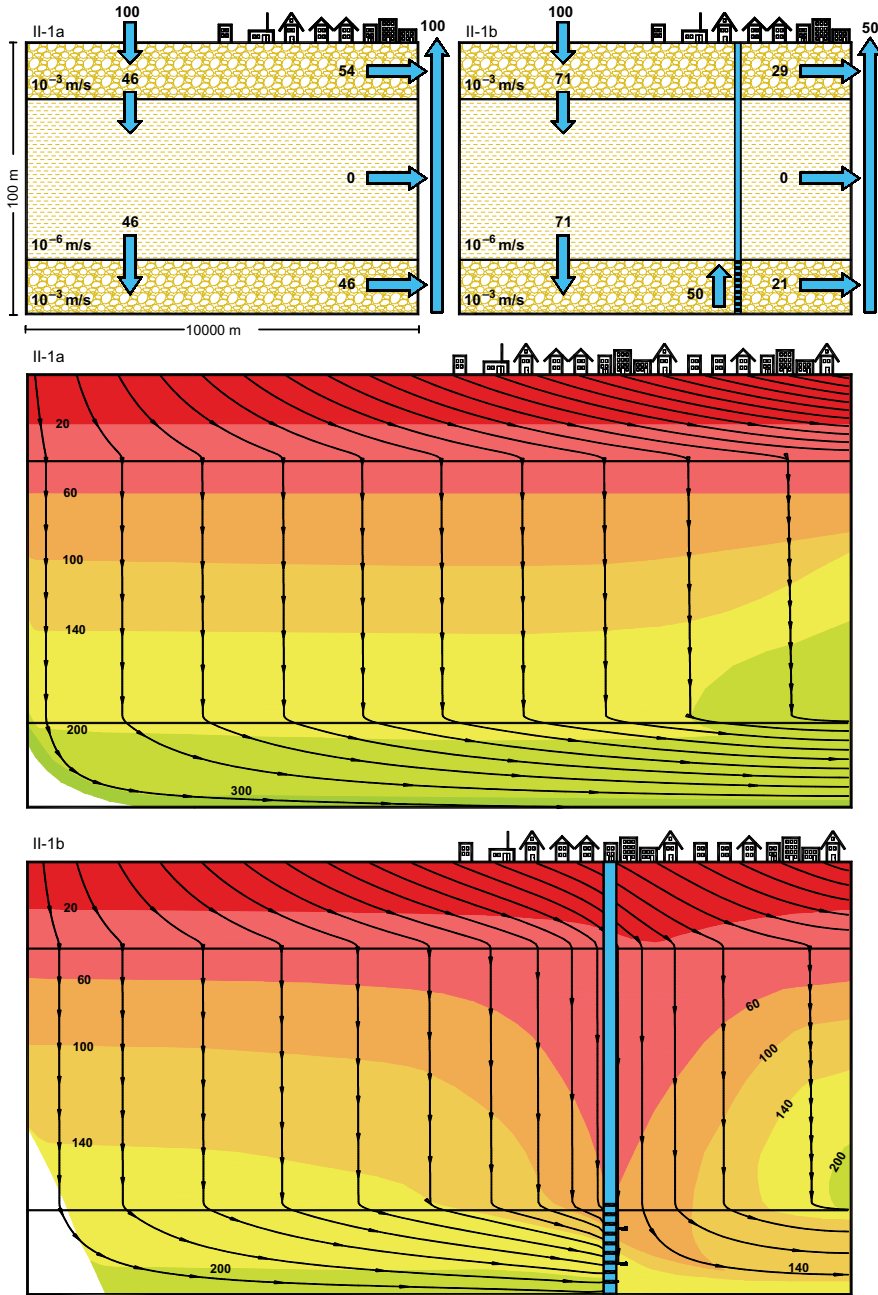


Figure 8.11. Model II, variant 1, simulation results: In model II, with 2 higher hydraulic conductivity layers in the top and bottom of the cross-section separated by a 1000-times less permeable layer, the water balance becomes significantly different for the scenario without and with pumping from the deep layer, as compared to model I, where this difference was small. So, in model II under natural conditions only 46% of the recharged groundwater reaches the lower level, whereas with pumping 71% reaches this layer. Under natural flow conditions, no contamination of the deeper layer can be observed for the present day situation and the forecasted 40 year period. In contrast, the additional influx caused by exploitation contaminates the well, and the deeper aquifer is shown by the 60 and 100 year isochrones. For further explanations, see Figure 8.7.

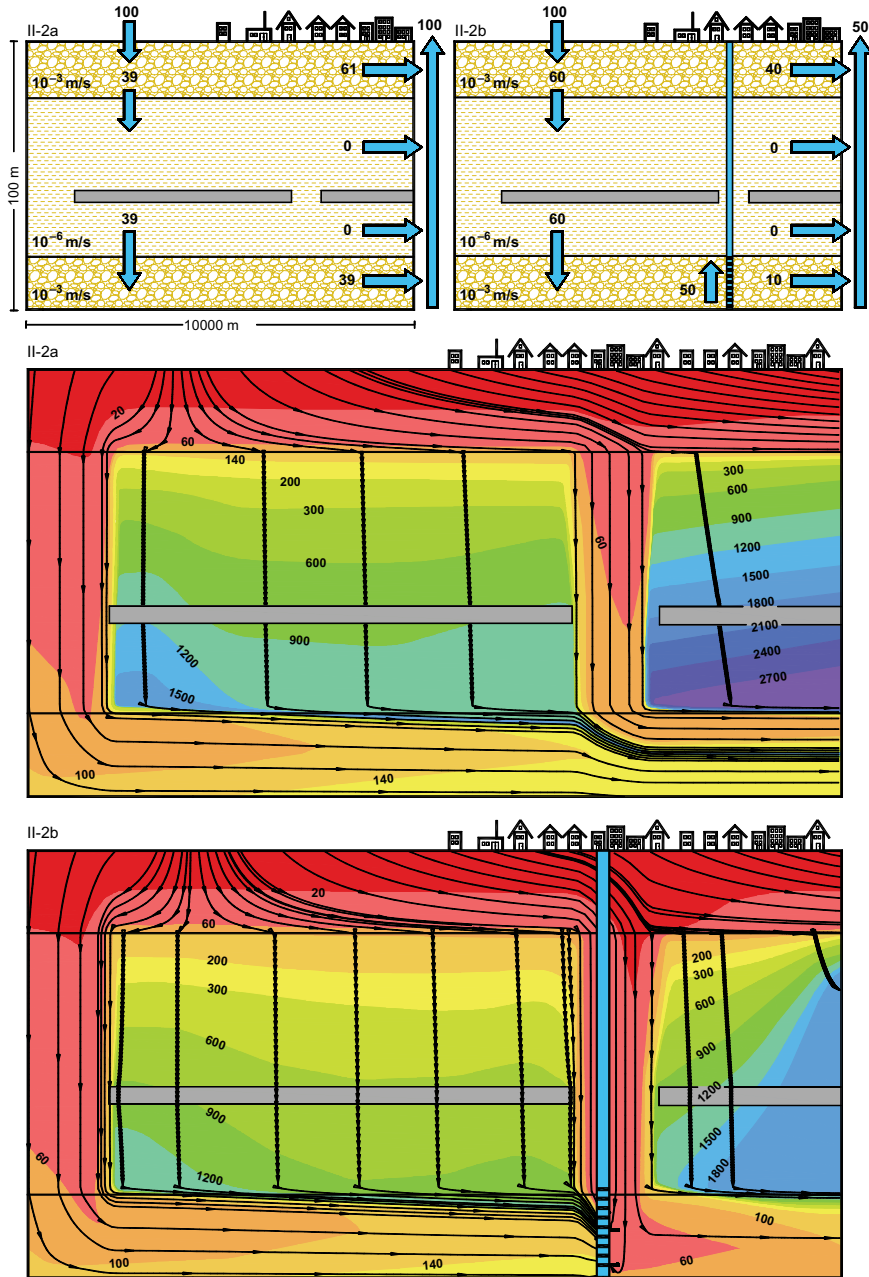


Figure 8.12. Model II, variant 2, simulation results: The two added clay layers in the middle layer reduce the influx into the deeper layer to 39 and 60% of the groundwater recharge for the scenarios with and without pumping (without clay layers in variant 1, 46, and 71%, respectively). However, since this influx is restricted to the areas of the windows in the clay layers, the influx causes contamination of the deeper layer for both cases without and with groundwater exploitation. However, contamination of the deeper layer is significantly larger since here 60% of shallow contaminated groundwater reaches the deeper layer compared to only 39% under natural flow conditions. For further explanations, see Figure 8.7.

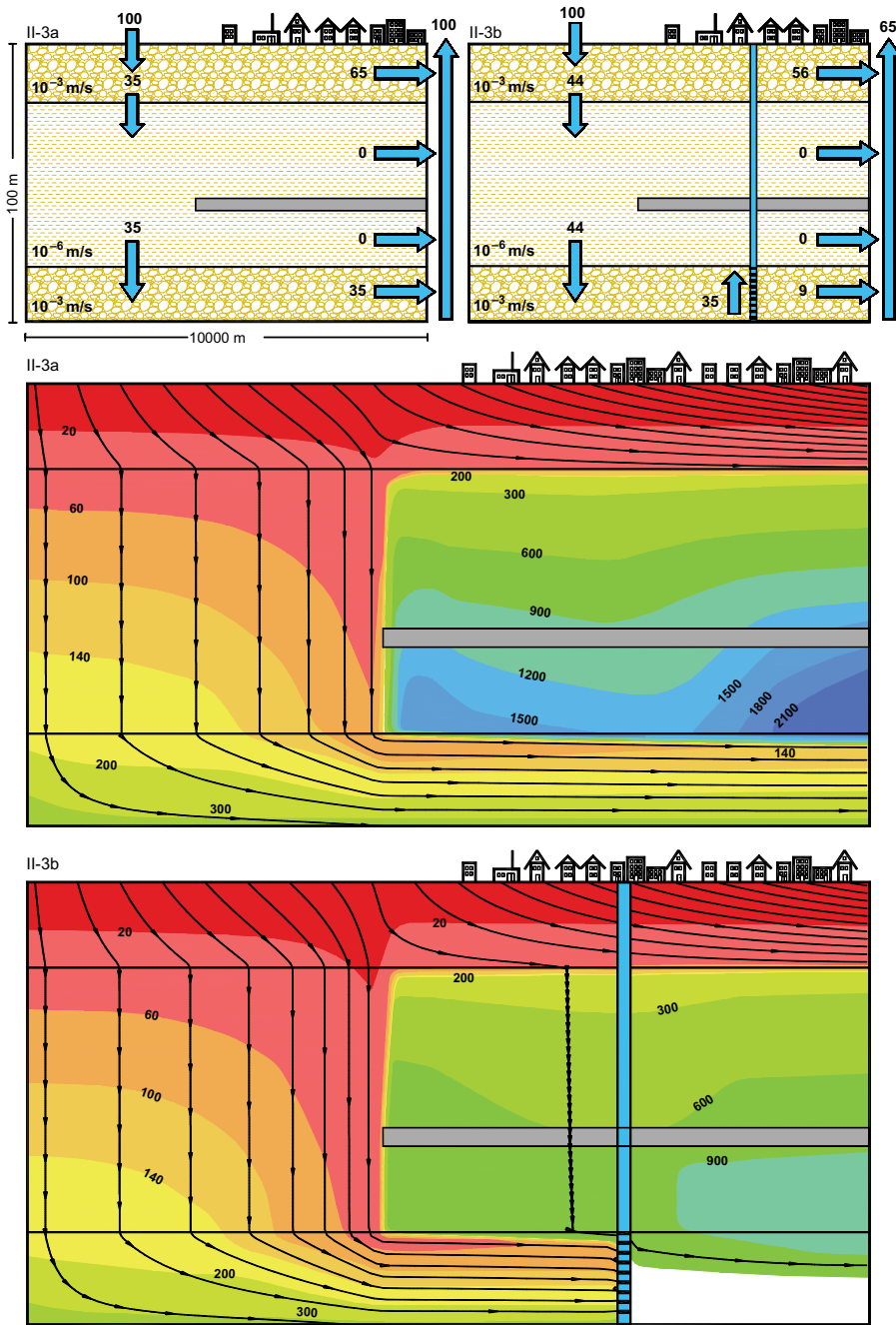


Figure 8.13. Model II, variant 3, simulation results: With the presence of only one clay layer, the water influx into the deeper layer is further reduced compared to previous variants of model I. Under natural flow conditions only 35% reaches the lower layer. The clay layer hinders enough water reaching the well to maintain a withdrawal corresponding to 50% of the groundwater recharge, so that the simulation was performed with a value of 35%. The present-day contamination plume did not reach the well, but reached the deeper aquifer with the addition of pumping. Under natural flow conditions, the contamination did not reach the deeper layer today (60 year isochrone), but is expected to do so in the 40 year forecast period (100 year isochrone). For further explanations, see Figure 8.7.

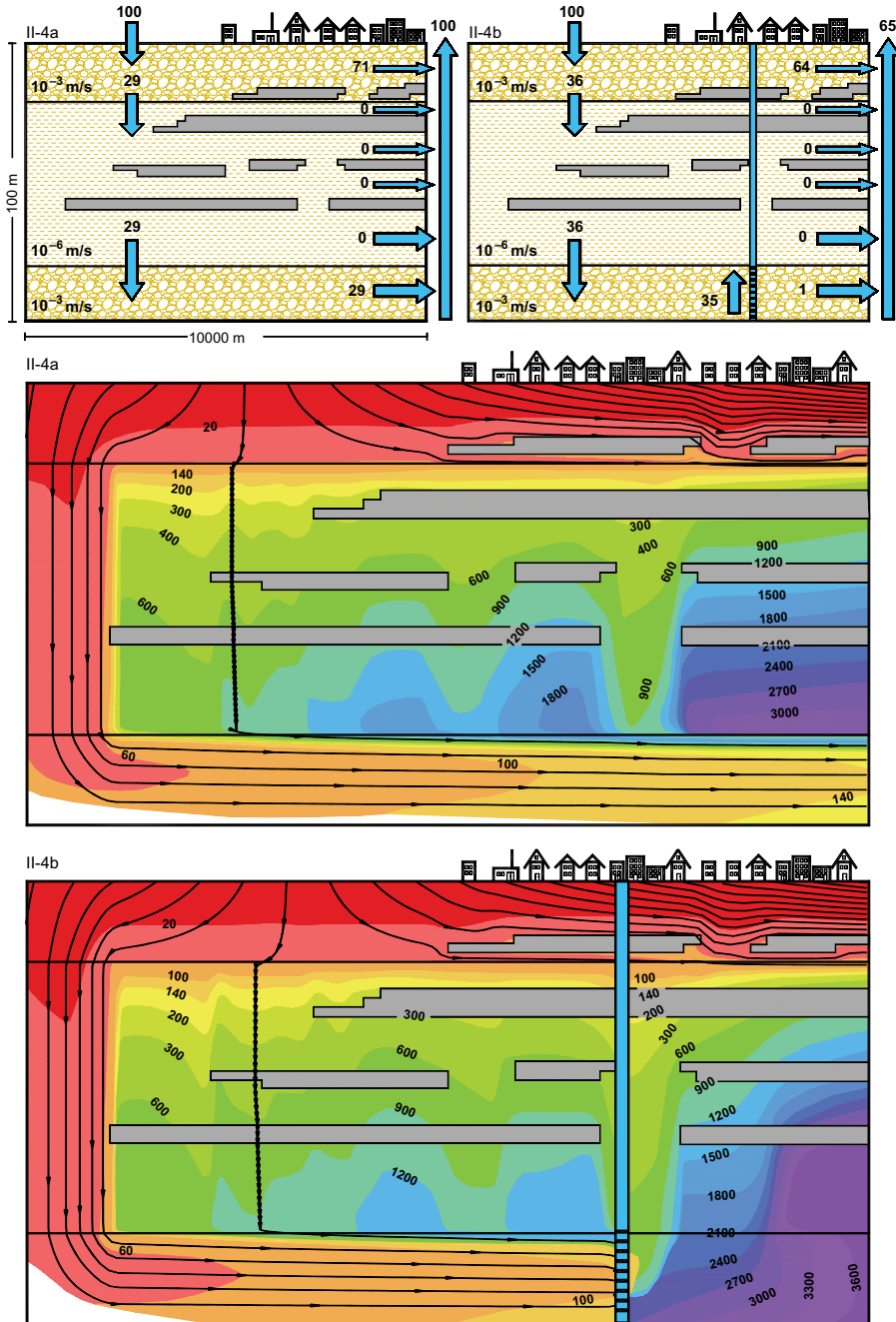


Figure 8.14. Model II, variant 4, simulation results: The addition of more clay layers and lenses to those of variant 2, further reduces water influx into the deeper layer compared to the previous variants and only 29 and 36% of the groundwater recharge reaches the deeper layer under natural conditions and with pumping, respectively. However, water influx through the left window in the clay layer is increased compared to variant 2, resulting in higher contamination in the area groundwater upstream. As in previous variant, the clay layer and lenses hinder enough water reaching the well to maintain a withdrawal corresponding to 50% of the groundwater recharge, and the simulation was performed with 35%. For further explanations, see Figure 8.7.

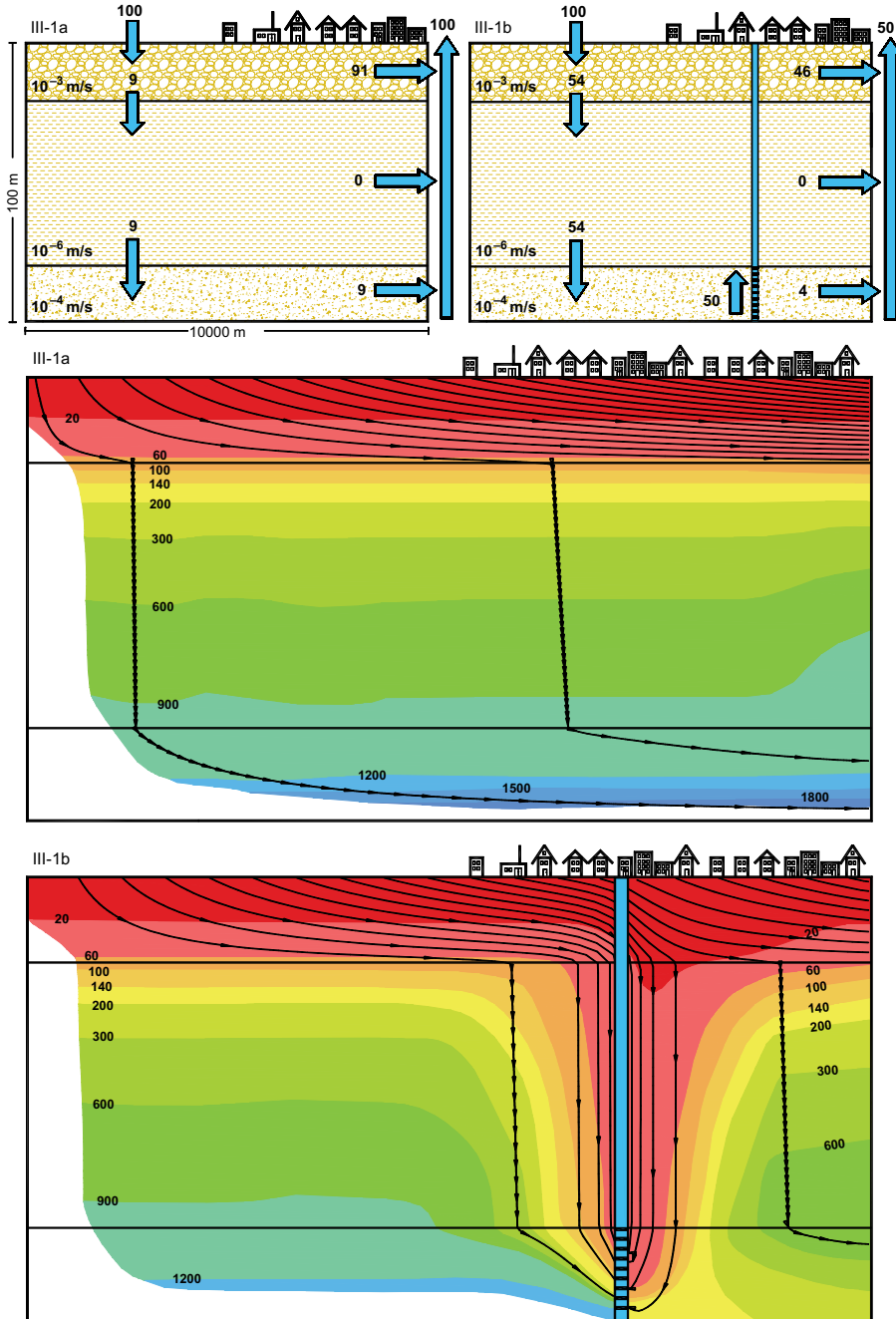


Figure 8.15. Model III, variant 1, simulation results: In model III, the hydraulic conductivity of the lowermost layer of model II is reduced by a factor of 10, so that now the uppermost layer has the highest hydraulic conductivity. In this model, under natural flow conditions, most of the recharged groundwater flows within the uppermost layer towards the right model boundary and the effect of pumping from the deepest layer is highest. In variant 1, under natural conditions, only 9% of groundwater recharge reaches the deeper layer and contamination remains restricted to the uppermost aquifer, whereas groundwater exploitation causes an influx of 54% of the recharge and the well becomes contaminated. For further explanations, see Figure 8.7.

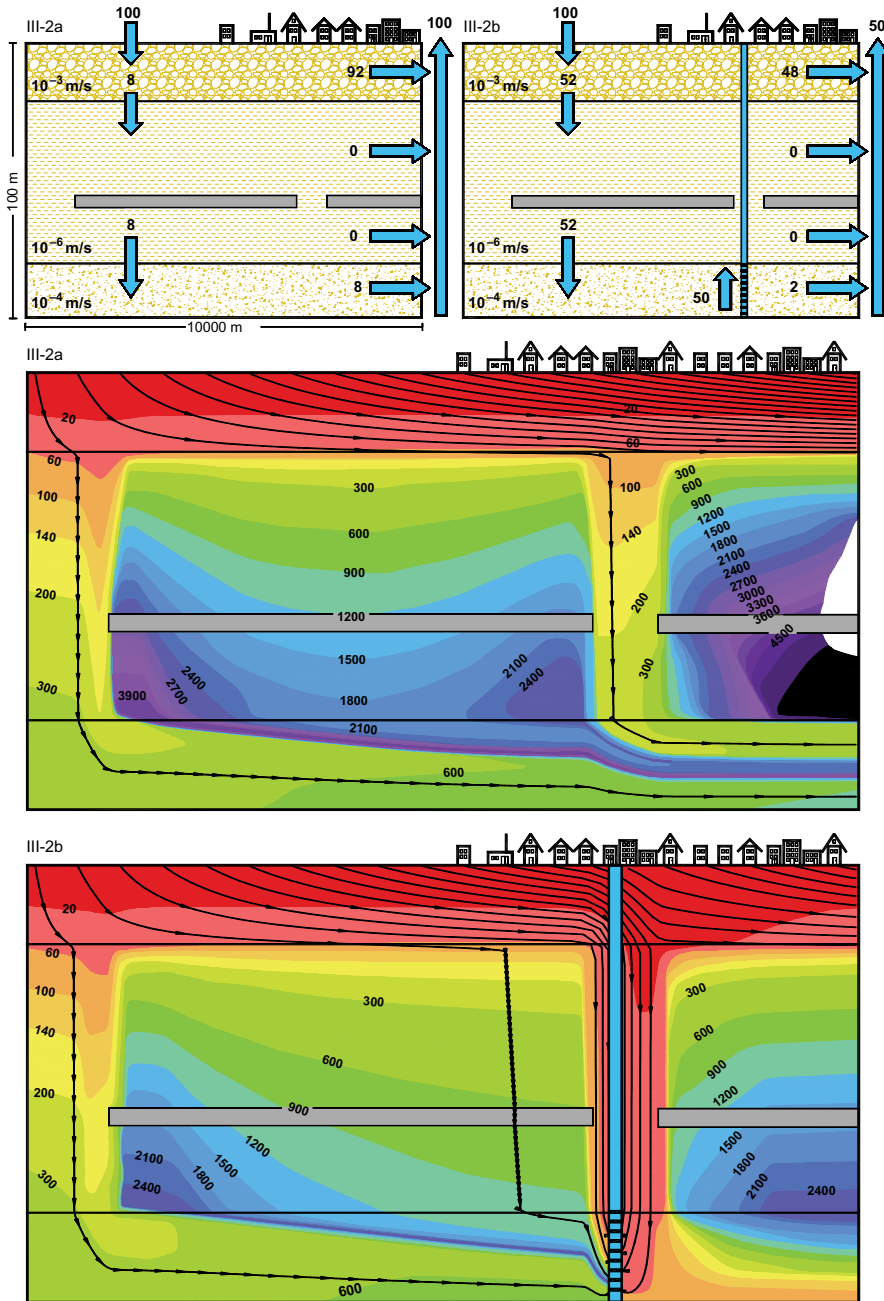


Figure 8.16. Model III, variant 2, simulation results: The impact of the two clay layers on the groundwater influx into deeper layers is minimal. Under natural flow conditions, 8% of the recharged groundwater reaches the lower layer (as compared to 9% without clay layers, variant 1), whereas under pumping conditions a much higher volume of 52% (54% without clay layers) reaches the deeper layer. Most of the recharged groundwater flows around the two clay layers and reaches the deeper aquifer. Due to the low influx under natural conditions, the lower layer is not contaminated, whereas contamination exists under the condition of pumping. For further explanations, see Figure 8.7.

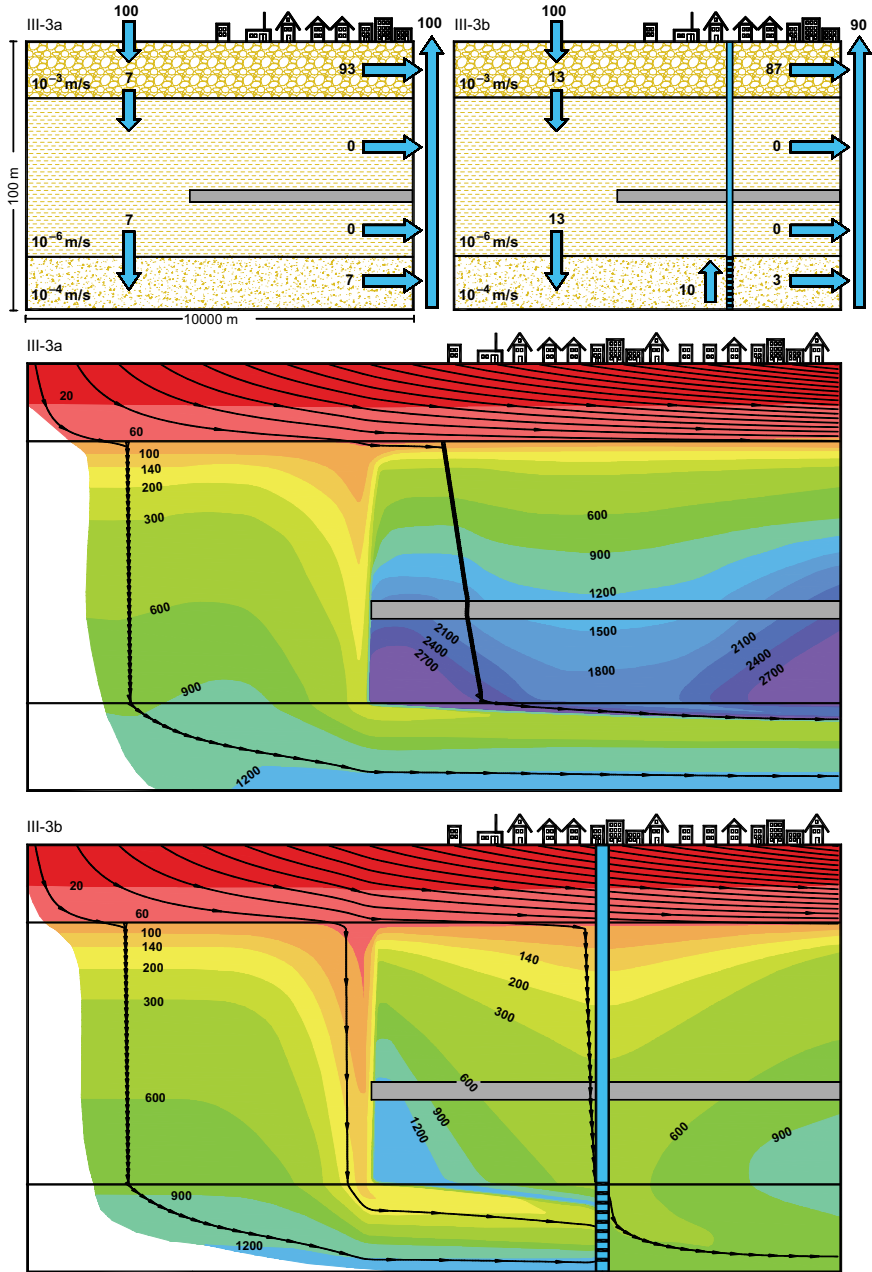


Figure 8.17. Model III, variant 3, simulation results: With only one clay layer present, water influx into the deeper layer is similar as under natural flow conditions, 7% compared to 8 and 9% in previous variants of model III. In contrast, there are significant differences under pumping conditions, where the clay layer hinders enough water reaching the well to maintain a withdrawal of 50% of groundwater recharge, and a value of only 10% was used. Present-day contamination (60 year isochrone) did not reach the lower layer, but under pumping conditions is expected to do so in the 40 year forecast period (100 year isochrone). However, due to the low influx rates in the deep layer, contamination propagation is much slower compared to previous variants and those found in models I and II.

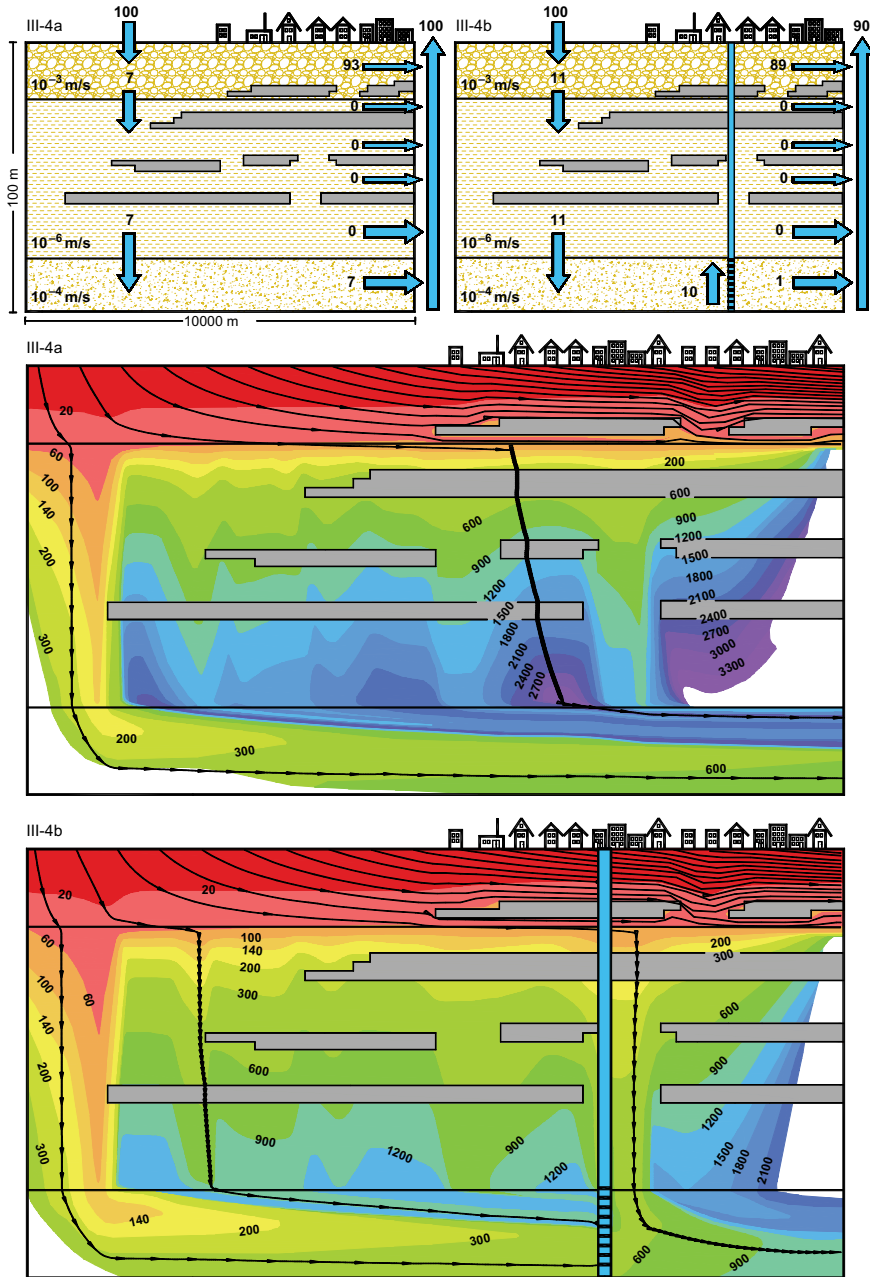


Figure 8.18. Model III, variant 4, simulation results: The addition of more clay layers and lenses to those of variant 2 shows similar water influx as previous variant 3 of 7% under natural flow conditions and 11% under pumping conditions (withdrawal 10% of recharge). This influx into the deeper layer occurs at the left window in the clay layer and the contamination plume for the 40 year forecast (100 year isochrone) reaches the lower layer. However, due to the low flow velocities, contamination (due to the low influx rates in the deep layer) propagation is much slower compared to variants 1 and 2 and compared to those found in models I and II.

Table 8.6. Influence of groundwater extraction on the water balance of the model. An increased flow is observed into the lower layer as a result of the extraction of water from this layer. The Δ corresponds to the increase (percentage) of the flow into the lower layer as compared to the scenario with no pumping (=100%). Unless otherwise indicated, groundwater extraction by the well represents 50% of the total recharge to the modeled area from rainfall.

	Variant 1	Variant 2	Variant 3	Variant 4
Model I	77 → 88% $\Delta = 14\%$	68 → 79% $\Delta = 16\%$	56 → 62% $\Delta = 11\%$	54 → 62% $\Delta = 15\%$
Model II	46 → 71% $\Delta = 54\%$	39 → 60% $\Delta = 54\%$	(35 → 44%) ($\Delta = 26\%$) (well discharge 35%)	(29 → 36%) ($\Delta = 24\%$) (well discharge 35%)
Model III	9 → 54% $\Delta = 500\%$	8 → 52% $\Delta = 550\%$	(7 → 13%) ($\Delta = 86\%$) (well discharge 10%)	(7 → 11%) ($\Delta = 57\%$) (well discharge 10%)

- In the case of model II, where groundwater flow under natural conditions is similar in the upper and lower layers (46–29% in the lower layer), the extraction of groundwater results in a greater increase (as compared to model I) of groundwater flow into the lower layer (54% in variants 1 and 2; the values of variants 3 and 4 can not be compared since in these model configurations the exploitation rate of 50% of the superficial recharge can not be obtained; Table 8.6).
- In the case of model III, where groundwater flow under natural conditions occurs mainly in the upper layer (91–93%), the extraction of groundwater by means of the well results in the greatest increase of groundwater flow in the lower layer (as compared to models I and II). Exploitation here results in a multiple increase of groundwater flow in the lower layer (variant 1: 500%; variant 2: 2550%; as in the case of model 2, the values from variant 3 and 4 are not comparable; Table 8.6).

8.3.5.3 *Influence of clay layers*

In order to determine the potential of the clay layers and lenses present in typical situations in the study area, the simulation results of variants 2 to 3 are compared with those of variants where clay layers are absent. The results show that the clay layers and lenses in models I, II, and III result in moderate changes in the natural groundwater flow field. For the model configuration without pumping, we obtain the following results:

- In models II and III, in which a low hydraulic conductivity layer is located between two higher conductivity layers, the additional clay layers found inside the intermediate layer limit the vertical flow through this layer to the vertical sections above and below the windows in the clay layers. The consequence is a significant change in groundwater flow pattern. Compared to variant 1 (no clay layers), variants 2, 3, and 4, where groundwater flows in the lower layer, present a reduction of 15, 24 and 37%, respectively, in model II, and 11, 22 and 37%, respectively, in model III (Table 8.7).
- In model I (without pumping), where clay layers are found in the high hydraulic conductivity layers (as compared to models II and III), the reduction of flow into the lower layer is similar to models II and III. The values are 12, 27, and 30% for variants 2, 3, and 4 respectively (as compared to variant 1 with no clay layers).

Pumping does not significantly influence the results of model I, and the clay layers in the variants 2 to 4 lead to similar water flow reduction as in the case without a well. In models II and III, only the results from variant 2 of the pumping models can be compared (Table 8.7). Whereas for model II, variant 2 shows similar results for the model without and with pumping

Table 8.7. Groundwater flow reduction into the lower layer (as compared to variant 1 without clay) caused by the presence of additional clay layers and lenses present in variants 2, 3, and 4 with different location of clay layers and lenses. The Δ corresponds to the percentage reduction of the flow in the lower layer as compared to the variant with no clay layers or lenses (=100%). Unless otherwise indicated, groundwater extraction by the well represents 50% of the total recharge to the modeled area.

	Without well			With well		
	Variant 2	Variant 3	Variant 4	Variant 2	Variant 3	Variant 4
Model I	77 → 68% $\Delta = 12\%$	77 → 56% $\Delta = 27\%$	77 → 54% $\Delta = 30\%$	88 → 79% $\Delta = 10\%$	88 → 62% $\Delta = 30\%$	88 → 62% $\Delta = 30\%$
Model II	46 → 39% $\Delta = 15\%$	46 → 35% $\Delta = 24\%$	46 → 29% $\Delta = 37\%$	71 → 60% $\Delta = 15\%$	(71 → 44%) ($\Delta = 38\%$) ¹⁾	(71 → 36%) ($\Delta = 49\%$) ³⁾
Model III	9 → 8% $\Delta = 11\%$	9 → 7% $\Delta = 22\%$	9 → 7% $\Delta = 22\%$	54 → 52% $\Delta = 4\%$	(54 → 13%) ($\Delta = 76\%$) ²⁾	(54 → 11%) ($\Delta = 80\%$) ²⁾

¹⁾ discharge 35%; ²⁾ discharge 10%; ³⁾ discharge 35%.

(a 15% reduction of the water inflow into the deepest layer caused by the clay layer), for model III the reduction is about 3 times less for the model with pumping (4%) compared to the model without pumping (11%) (Table 8.7).

In general, it can be concluded that the influence of clay layers and lenses in the vertical flow of groundwater is greater if such clay layers or lenses are located within layers with a relatively low hydraulic conductivity. The influence is smaller if clays are located within more permeable layers where groundwater can easily flow around them.

8.3.5.4 Contamination threat for deeper aquifers

Simulations have been performed using a very simplified two-dimensional model with stationary groundwater flow and exploitation of the deep aquifer using just one well corresponding to typical scenarios occurring in the study area. When using the results to assess the contamination threats to the deep aquifer, it must be kept in mind that the modeling of different scenarios is in a 2-dimensional cross-section; this means that the flow pattern used in the calculations might differ significantly from the actual 3-dimensional (more or less axi-symmetric) flow pattern, as in the case of a well. Groundwater pathlines and groundwater balances of the different layers have been used to evaluate contaminant transport, which is a very simplified approach. Consideration must be given to the fact that the vulnerability of groundwater is a complicated issue that is somehow arbitrary and not directly measurable and related to the specific contaminants and their concentrations. These are responsible for rock-water interactions which may cause retardation of the contaminant particles compared to groundwater flow velocity, while our approach would correspond to a contaminant, whose propagation is not affected by water-rock interactions.

However, our simplified approach is accurate enough to address the objectives. The results obtained from our scenario modeling are sufficiently clear to indicate that for many of the model configurations, which do represent typical situations in the study area, the clay layers and lenses do not protect the deeper aquifer in a sufficient manner against contamination by an inflowing contaminated shallow aquifer. Depending on the hydraulic properties, the influx of contaminated shallow groundwater is further accelerated if groundwater is extracted from the deeper aquifer:

- If the upper layer is more permeable than the lower layers (model III), most of the groundwater flows naturally in the upper layer and the contamination threat to the lower aquifers is low. In this case, the exploitation of groundwater from the lower layers has the greatest impact. The exploitation causes a multiple increase in the flow of the lower layers, and as a consequence, the threat of contaminating the lower aquifers increases the most.

- If the lower layer is more permeable than the upper ones (model I), under natural conditions most of the water flows in the lower layer. As a consequence, there is a greater flow of surface contaminants as compared to model III. In this case, the exploitation of groundwater from the lower layer increases the threat of contaminating the lower aquifer only slightly compared to the situation under natural conditions.
- If the upper and the lower layers have the same conductivity and there is a third layer of lower conductivity between them (model II), the results obtained are similar to those yielded by model III.

The areas of the cross-sections affected by contamination, considering that severe contamination of the shallow aquifer within the urban area started about 60 years ago, can be delimited by groundwater isochrones. Areas with mean groundwater ages of less than 60 years can be considered affected by the contamination (not considering hydrodynamic dispersion). These areas are shown in Figures 8.7, 8.8, and 8.9 in reddish colors. It can be recognized that in different model configurations the present-day contamination has already reached sections of the deep aquifer (see Figures 8.7–8.10, 8.11–8.14, and 8.15–8.18 for models I, II, and III and respective variants). The extent of the contamination for the next 40 years corresponds to the area between the isochrones 60 and 100 years, which is shown in dark orange in the cross-sections and which covers large areas of the deep aquifer in most of the model configurations. As a consequence, the use of the deep aquifer within the urban area can not be considered as a mid-term option, and the choice of constructing a new water works outside of the city, which lies groundwater-upstream in an anthropogenically unaffected area is recommended as a solution.

8.4 POINT SOURCE CONTAMINATION AND AQUIFER REMEDIATION

8.4.1 *Situation*

A water works extracts a continuous discharge of $Q_V = -0.2 \text{ m}^3/\text{s}$ from a gravel and sand aquifer. In the vicinity of the water works, a traffic accident occurred at time $t = 0$, and as a result, an amount, $C_0 = 100 \text{ kg}$, of a toxic water-miscible contaminant seeped into the groundwater upstream of the well used by the water works. The authorities were informed about the accident only at time $\Delta t = 22$ days after the accident happened. For selecting appropriate counter-measures to prevent contamination of the water works well (WWW), they requested a consulting company to perform numerical modeling. This model will be used to estimate the contamination hazard for the WWW, and if confirmed, to define appropriate counter-measures.

8.4.2 *Aquifer specifications*

The aquifer is isotropic, the conductivity K_H for the entire area is $1.5 \times 10^{-4} \text{ m/s}$, and effective porosity is $\varphi_{\text{eff}} = 0.15$. The aquifer is unconfined and groundwater flow can be considered stationary. Piezometric heads unaffected by pumping for the area are known through piezometers: 190 m a.s.l. on the northern edge, and 220 m a.s.l. on the southern edge; there is no groundwater flow into the system from the east or the west (Fig. 8.19a). The base of the aquifer presents a uniform slope to the north. It is located 159 m a.s.l. along the 220 m hydraulic head contour line and 140 m a.s.l. along the 190 m hydraulic head contour line. Groundwater recharge through rainfall is 250 mm/year in the entire area. Longitudinal dispersivity is $\alpha_L = 10 \text{ m}$, transverse dispersivity is $\alpha_T = 1 \text{ m}$.

8.4.3 *Objectives*

To determine the contamination hazard and countermeasures to prevent contamination of the WWW, a simple numerical transport model shall be constructed. This model will use the available field data on the groundwater flow pattern, which shall be considered as stationary, and the amount

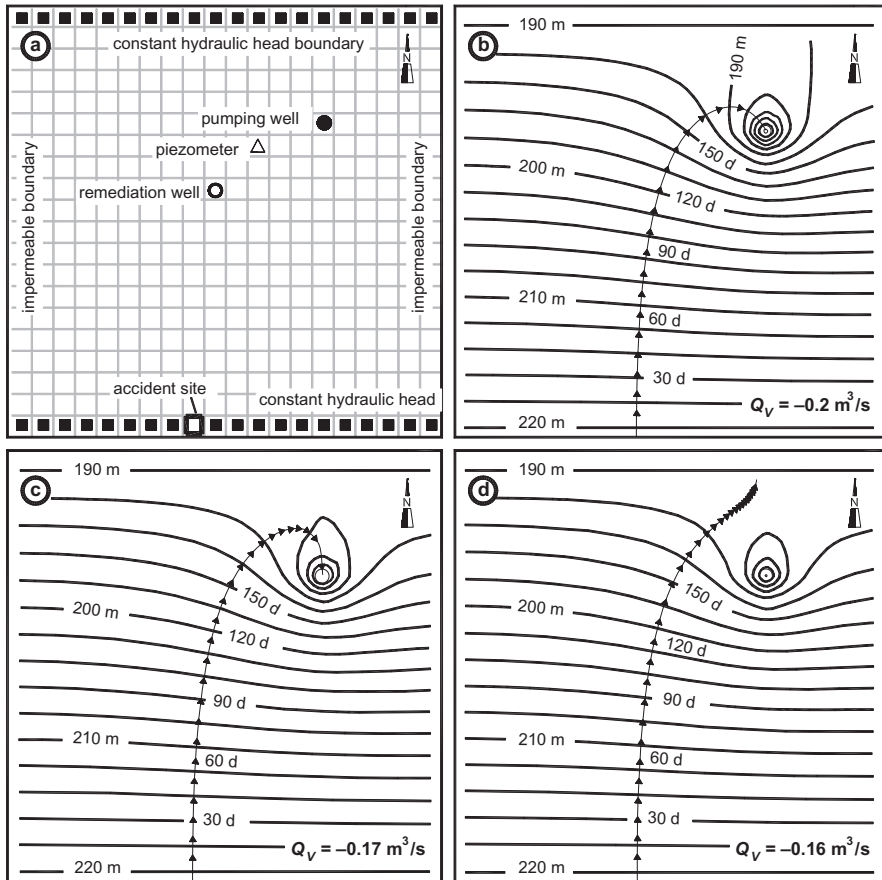


Figure 8.19. Aquifer remediation modeling example: (a) Study area ($400 \times 400 \text{ m}$, 20×20 cells); pumping well (WWW), remediation well, observation piezometer, and accident site (contamination point source); (b–d) Hydraulic head contours and flow lines with time marks every 10 d (days) for the contaminant coming from the site of the accident (contaminant retardation factor $R_d = 4$) for different Q_V of the WWW.

of contaminants released during the accident into the groundwater. The following problems shall be addressed:

- Determine whether the contamination reaches the WWW, considering its regular pumping rate of $Q_V = -0.2 \text{ m}^3/\text{s}$. If it does reach the well, determine when this is expected to occur (not considering dispersion of the contaminant). Determine the maximum pumping rate for which the contaminant does not reach the WWW (with an accuracy of $0.01 \text{ m}^3/\text{s}$).
- Determine the 50-day line around the WWW for the contaminant, that is, determine the isochrone from where the contaminant takes 50 days to reach the well. Additionally, isochrones for the period of time $0 < t < 100$ days with an equidistance of 12.5 days shall be plotted.
- In order to maintain a water supply, it is not possible to reduce discharge from the water works. For this reason, a remediation well to catch contamination before it reaches the pumping well, needs to be built. Select a suitable location for the remediation well. Determine minimum extraction and how long the remediation well should operate (considering dispersion of the contaminant)? An additional 2 days shall be considered necessary for this remediation well to be ready to operate. To answer these questions, contaminant concentrations at the WWW,

the remediation well and the piezometer located between them must be determined for different extraction rates at the remediation well.

- Determine the isochrones around the WWW and the remediation well for the obtained optimal exploitation rate in the remediation well (time $0 < t < 100$ days; equidistance between isochrones: 12.5 days).

8.4.4 Elaboration of a numerical model and problem solution

A simple numerical horizontal 2-dimensional model 400×400 m is constructed using the ASM code (see section 6.8.3) with the grid shown in Figure 8.19a. The N–S directed boundaries are impermeable to water. At the northern and southern boundaries, hydraulic heads are prescribed: 190 m a.s.l. at the northern, and 220 m a.s.l. at the southern borders. The complete model input data is listed in Table 8.8. The model is used to simulate stationary groundwater flow in an unconfined homogeneous and isotropic aquifer, and contaminant transport originating at the accident site and starting at time $t = 0$ as a function of time.

8.4.4.1 Groundwater flow pattern

To determine whether contamination reaches the well of the water works, the groundwater flow pattern (flow lines) from the site of the accident is simulated. Using this problem approach, which does not consider dispersion of the contaminant particles, the simulation shows that with a regular discharge rate of $Q_V = -0.2 \text{ m}^3/\text{s}$ at the water works, contamination does reach the pumping well (Fig. 8.19b). If the discharge rate is reduced to $Q_V = -0.16 \text{ m}^3/\text{s}$ the flow line originating from the accident site does not reach the well, whereas for $Q_V = -0.17 \text{ m}^3/\text{s}$ it still reaches the

Table 8.8. Input data for the groundwater flow and transport model.

<ul style="list-style-type: none"> • Type of model¹⁾: <ul style="list-style-type: none"> • stationary (0/1) [0] • confined/free (0/1) [1] • anisotropy (T_{yy}/T_{xx}) [1] • Model grid: <ul style="list-style-type: none"> • number of cells on x [20] • number of cells on y [20] • size of cells on x (m) [20] • size of cells on y (m) [20] • Injection/pumping well: <ul style="list-style-type: none"> • number wells [1, 2²⁾] • location, injection (+) or extraction (-) in m^3/s • for well #1 <ul style="list-style-type: none"> • x index of cell [15] • y index of cell [6] • extraction rate [-0.2] • for well #2²⁾ <ul style="list-style-type: none"> • x index cell [\square²⁾] • y index of cell [\square²⁾] • extraction rate [\square²⁾] 	<ul style="list-style-type: none"> • Piezometer location: <ul style="list-style-type: none"> • x index of cell [\square³⁾] • y index of cell [\square³⁾] • Aquifer parameters: <ul style="list-style-type: none"> • hydraulic conductivity K_H (m/s) [1.5×10^{-4}] for entire model area • storage coefficient S (ad) [0] for entire model area • initial piezometric heights h (m) [190] on N boundary [220] on S boundary [200] in the rest area • mean groundwater recharge ($\text{m}^3/\text{s}/\text{m}^2$) [$7.9 \times 10^{-9}$] for entire model surface • aquifer base (m above reference) [140] on N boundary [159] on S boundary • boundary flux ($\text{m}^3/\text{s}/\text{m}^2$) [0] for entire model area
--	---

¹⁾ Note that the values listed for “type of model” are specified as “1” if a given attribute is true or as “0” if it is false; ²⁾ Well 2 is the remediation well, whose need and optimal location (cell numbers) and extraction rate will be determined by modeling; ³⁾ Location of the piezometer will be determined during modeling; N: North, S: South.

well (Fig. 8.19c,d). Using the time marks on the flow line, the time elapsed between the accident and the arrival of the contaminant to the well can be estimated at 180 days for $Q_V = -0.2 \text{ m}^3/\text{s}$ (based on groundwater velocity and on the retardation factor $R_d = 4$ for the contaminant, which means that the propagation of the contaminant is 4 times slower than the groundwater flow).

8.4.4.2 Isochrones

Figure 8.20 shows 8 isochrones around the WWW from where the travel time of the contaminant to the well is constant, corresponding to the value of the respective isochrone (period of time $0 < t < 100$ days; equidistance between isochrones 12.5 day). For example, for all points lying on the 50-days isochrone, the contaminant takes 50 days to reach the well.

8.4.4.3 Designing the remediation well

The remediation well should be located on the flow line of the water particles that start their run at the site of the accident. This line corresponds to the flow line calculated for the contaminant (Fig. 8.19b) with the difference that, due to the retardation, time marks have an equidistant spacing of 2.5 days (contaminant propagation is retarded by factor $R_d = 4$ compared to groundwater flow velocity). On the other hand, it should be placed at a location not yet reached by contamination at the time $\Delta t = 25$ days which is the time elapsed since the accident. This will be used to file the report as well as for the location and construction of the well. Also, the well should not be too far away from the contamination point source in order to prevent the propagation of the contamination plume by transverse dispersivity. Based on the flow line (Fig. 8.19b) and its time marks, a possible location can be selected in cell 10/12.

Discharge rate from the remediation well: Including the remediation well at the position established simulations are performed for different discharge rates in the $Q_{V\text{rem}}$ in the remediation well. Dispersion of the contaminant in the direction of groundwater flow (longitudinal dispersion) and perpendicular to water flow (transverse dispersion) are considered. Using the random-walk approach for contaminant propagation of ASM code, where the propagation of contaminant particles is simulated using a stochastic approach, superposed on the above-constructed groundwater flow model, the discharge rate $Q_{V\text{rem}}$ in the remediation well is modified until most of the contaminant particles are captured in the remediation well, thus preventing them from reaching the water works. Figure 8.21 shows concentrations at the remediation well, the piezometer,

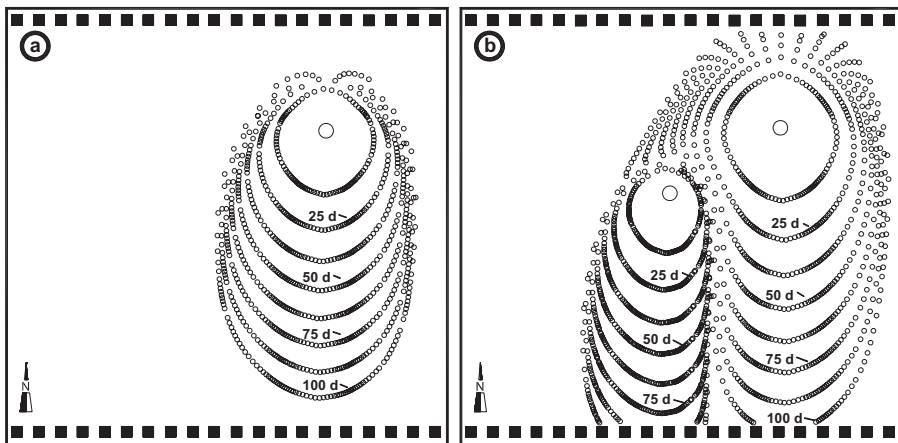


Figure 8.20. Aquifer remediation modeling example: (a) Isochrones around the pumping well with an equidistance of 12.5 d (days), between 0 and 100 d; (b) Isochrones around the water works well and the remediation well with an interval of 12.5 days for the period of time between 0 and 100 days.

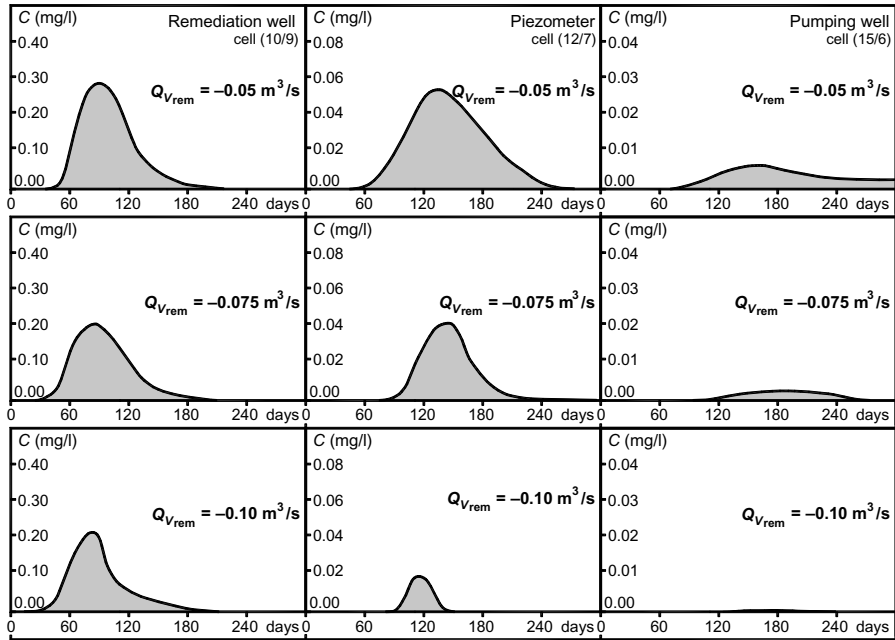


Figure 8.21. Aquifer remediation modeling example: Contaminant concentrations C at the WWF, at the piezometer, and at the remediation well for different discharge rates at the remediation well ($Q_{Vrem} = -0.1, -0.075$ and $-0.05 \text{ m}^3/\text{s}$). Contamination concentrations, as well as the resulting averaged curves, corresponding to 1000 particles of contaminant, have been represented with time increments of $\Delta t = 1$ day, and based on the “random walk” method.

and the WWF for different extraction rates in the remediation well as functions of time. The pumping rate that prevents contamination from reaching the water works is $Q_{Vrem} = -0.1 \text{ m}^3/\text{s}$ (keeping the WWF in production with $Q_V = -0.2 \text{ m}^3/\text{s}$). The groundwater isochrones around both these extraction wells are shown in Figure 8.20. The remediation well should operate for at least 150 days (=180 days after the accident) (Fig. 8.21).

8.5 BORON CONTAMINATION PROPAGATION

8.5.1 Situation and objectives

A factory producing boric acid has contaminated the groundwater resources of a Quaternary aquifer system (up to 6.2 mg B/l). Since boron is toxic to crops, the use of this contaminated groundwater for irrigation poses a danger. The potential of this hazard, especially for the future, shall be estimated by numerical modeling. This modeling will be used to forecast the transport of borate ions coming from the contamination point source without carrying out additional field studies. The areas that will be affected in the future should be delimited, and the contamination risk for areas used for agricultural activities should be assessed. To this end, a simple hydrogeological transport model shall be created to simulate the propagation of borate ions from when contamination started until the present time. Thereby, it must be considered that for crop toxicity the concentration of boron in irrigation water is not as relevant as the absolute amount of boron provided to crops (0.5 kg B/ha per year in sensitive crops and 3.0 kg B/ha per year in tolerant crops for the edaphic and climatic conditions of the studied area). For this reason, no general concentration threshold can be established for irrigation water, since toxicity depends

points during the same period. Whereas non-contaminated areas have boron concentrations of less than 0.2 mg B/l in the groundwater, concentrations in the contaminated area reach 6.2 mg B/l. The mean boron concentrations in the groundwater from the February 1991 to February 1992 observation period are shown in Figure 8.22. The considered shallow aquifer is about 20 m thick and the regional hydraulic conductivity is $K_H = 1.10^{-3}$ m/s, whereas effective porosity is roughly estimated as $\varphi_{\text{eff}} \approx 0.2$. Recharge of the aquifer through rainfall can be neglected.

8.5.3 *Elaboration of a numerical model*

The numerical simulation of boron transport shall be performed using the SUTRA modeling code (see section 6.8.4). According to the goals of obtaining a rough approximation of the future propagation of the contaminant and the lack of information regarding aquifer parameters and piezometric levels, groundwater flow shall be considered as stationary and in a horizontal direction only. The small variations in piezometric level for one year (<1 m) and the low thickness of the aquifer (≈ 20 m) compared to its horizontal extent allow for these simplifications. The rectangular mesh of the model area is composed of 40 elements in the W–E direction and 32 elements in the N–S direction with an extent of 13.4 and 10 km, respectively. The right boundary (eastern) is the principal river of the region (river 1), the receiving stream of river 2 (Fig. 8.23a). The piezometric levels of the northern, southern, and western boundaries are obtained from interpolations of groundwater level measurements. The aquifer is assumed to have an average thickness of 20 m, and to be horizontal and isotropic; effective porosity is 0.2. The piezometric levels of the eastern boundary are those of the average water level in river 1. There is no recharge of the aquifer through rainfall. The infiltration of effluents at the boric acid factory is simulated with an input rate of 1.0 l/s, and with a concentration of 250 mg B/l. This corresponds to the total estimated annual amount of boron influx of 7888 kg/year (or 21.6 kg/day). Since it is not possible to determine the amount of boron-rich water coming from river 2, boron input to the aquifer is simulated by the means of fixed concentration nodes located along the course of the riverbed. Concentration is set, based on field data, at 1 mg B/l. The regional background value is taken as the initial concentration value for the entire modeled area: 0.1 mg B/l. The adsorption of borate ions in different subsoil materials has, at first instance, been neglected. For the hydraulic conductivity, first, an initial value of $K_H = 10^{-3}$ m/s, corresponding to the regional known K_H value, is used for the entire model area. Thereafter, the K_H value is locally modified during the calibration process so that the simulated boron concentrations will match those measured in the field (Fig. 8.23a), obtaining the hydraulic conductivity zones shown in Figure 8.23b.

8.5.4 *Results of the simulations*

The simulated stationary groundwater flow field of the study area is shown in Figure 8.23 together with the propagation of the boron contamination front, defined as 0.6 mg B/l, which corresponds to the present conditions of the maximum tolerable boron concentration in the irrigation water. The contamination front is shown for 4, 7, 10, and 13 years after the boric acid factory started its production. It can be seen that the boron moves towards the east and then the southeast before most of it enters the receiving stream (river 1 in Fig. 8.23). This means that the area that will be affected by boron contamination in the future, making the water unsuitable for irrigation, will be confined to an area limited by river 2 to the north, by river 1 to the east, and by an imaginary NW–SE line joining the boric acid factory with river 1 (Fig. 8.23). It should be mentioned that although the model is very simple and describes the actual situation in a very simplified manner, it allows the estimation of the contamination threat in the region and delimitation of the affected area relatively accurately. This in turn, allows for the rational planning of future agricultural projects within the study area.

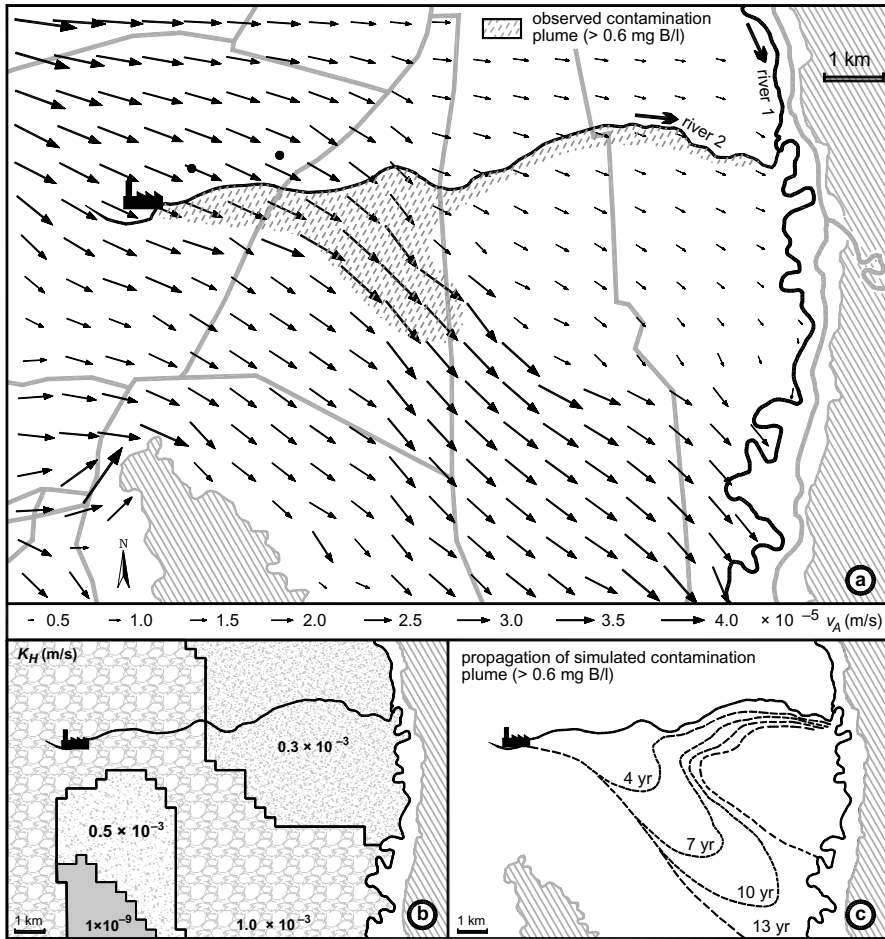


Figure 8.23. Aquifer contamination modeling setup and simulation results: (a) simulated groundwater flow field with groundwater flow velocity vectors. Additionally plotted area with groundwater boron concentrations exceeding 0.6 mg B/l as observed from concentration measurements (after 4.5 years of starting boric acid production), which is the maximum tolerable boron concentration in the irrigation water considering the specific crops and amount of irrigation water volume applied in the area of the case study; (b) Zones of different hydraulic conductivity obtained by model calibration; (c) Extension of the modeled contamination plume (>0.6 mg B/l) after 4, 7, 10, and 13 years since the beginning of boric acid production in the factory. For other symbols see Figure 8.22.

8.6 ANNUAL TEMPERATURE OSCILLATIONS IN A SHALLOW STRATIFIED AQUIFER

8.6.1 Introduction and objectives

Groundwater temperatures can vary both in time and space and are influenced by atmospheric conditions, subsurface heat sources, and the characteristics of the soil and rocks. Whereas heat transport processes in deep aquifers, especially those related to geothermal energy exploration, are quite well studied and modeled, the studies of the much more complex heat transport in shallow aquifers are few.

The major variables and parameters that affect groundwater temperature $T(x, y, z)$ of shallow aquifers are:

- Heat sources, the most important being the sun and the interior of the earth. The time-variable source is thermal energy from the sun, absorbed by the earth, which causes a heat flow in soil and rock layers with transport mechanisms such as conduction, convection, dispersion, and thermodiffusion. This flow of energy varies in time in a complex way, but only those variations with an annual periodic component will be considered in our example. In addition to this, there is a heat flow coming from inside the earth that can be considered to be constant in time (with the exception of thermally active regions). The chemical and biochemical reactions that occur in the soil and in groundwater are yet another source of heat, but they will be neglected in our example.
- Morphological characteristics of the earth's surface.
- Depth of the groundwater level.
- Properties of aquifer components and the non-saturated zone, such as: kind of materials, total porosity, effective porosity, water saturation, hydraulic conductivity, fluid density and viscosity, thermal conductivity (fluid and solid), specific heat capacity (fluid and solid), thermal dilatation coefficient, and compressibility (fluid and solid).
- Characteristics of the groundwater flow field (flow velocities and directions).
- Mixing effects: mixing of groundwaters of different temperatures from different aquifers, or mixture by surface water infiltrating into an aquifer.
- Geometric and hydrogeological data of the aquifer.

The effect of some of these factors on groundwater temperature shall be studied in detail in our example. A coupled numerical flow and heat transport model will be used to simulate the effect of the principal parameters on the groundwater and on the springwater temperatures and their variation in time using modeling example scenarios as similar as possible to typical natural conditions. One of the objectives of these simulations will be to analyze temporal and spatial variations of groundwater temperature with depth and as function of the groundwater flow field. Simulations will be performed for a vertical two-layer aquifer that is affected by temperature variations of the earth's surface. These simulations are aimed at studying the interdependence between groundwater flow and temperature fields in an aquifer system, and spring water temperatures and their tight relation with aquifer geometry, hydraulic properties, and the depth of the phreatic groundwater level below earth's surface.

Eight model scenarios with a 1000 m wide and about 20 m high cross-section of an unconfined aquifer composed of two layers with thicknesses b_{a1} and b_{a2} , and hydraulic conductivities K_{H1} and K_{H2} which are varied in the different scenarios (Table 8.9), shall be performed. For each modeling scenario, simulations will be performed for several depths of the phreatic level GF ($GF = 0.5, 1, 2, 4$ and 7 m below the earth's surface).

The following simulations shall be performed and interpreted for scenarios 1–8:

- Balance of the water masses flowing in each layer towards the right model boundary as percentage of total groundwater recharge.
- Simulate spring water temperatures. Determine the annual amplitude, AMP , of the springwater temperature (indicating the annual periodic temperature variations), and the phase difference, $\Delta\varphi$, between the maximum and minimum surface and corresponding spring water temperatures. Perform the respective simulations for different GF . Analyze the influence of groundwater flow field and depth to groundwater table on spring water temperatures as characterized by AMP and $\Delta\varphi$.

For scenarios 1 and 3 the following additional simulations shall be performed:

- Simulate the groundwater flow field and the respective temperature field for a given time (May 1st), for a depth to water table of $GF = 2$ m.

Table 8.9. Thickness of upper (M_1) and lower (M_2) layer and respective hydraulic conductivities K_{H1} and K_{H2} (m/s) with a reference temperature of 9°C for the simulation scenarios 1 to 8.

Scenario	$b_{a1} = 5 \text{ m}; b_{a2} = 15 \text{ m}$		Scenario	$b_{a1} = 15 \text{ m}; b_{a2} = 5 \text{ m}$	
	K_{H1} (m/s) (upper layer)	K_{H2} (m/s) (lower layer)		K_{H1} (m/s) (upper layer)	K_{H2} (m/s) (lower layer)
1	10^{-3}	10^{-6}	5	10^{-3}	10^{-5}
2	10^{-3}	10^{-4}	6	10^{-3}	10^{-4}
3	10^{-5}	10^{-3}	7	10^{-5}	10^{-3}
4	10^{-4}	10^{-3}	8	10^{-4}	10^{-3}

- Simulate the spring water temperatures for the time interval November–October for different values of GF , and compare the different depths of water table for the obtained values of AMP and $\Delta\varphi$.

8.6.2 Elaboration of a numerical model

8.6.2.1 Geometry

The aquifer system is considered a vertical cross-sectional setup, and is comprised of two horizontal layers of different thickness (b_{a1} , b_{a2}) and hydraulic conductivity (K_{H1} , K_{H2}) (Table 8.9). The horizontal extent of the modeled area is $\Delta x = 1000 \text{ m}$. The left and right vertical boundary, and the base of the model are impermeable to water (Fig. 8.24). At the top border the model area groundwater recharge through rainfall occurs with a seasonably variable rate. In the upper right corner of the vertical plain model domain, all groundwater leaves the model area at a spring. There is an incoming vertical, constant, terrestrial heat flow through the lower border. The phreatic surface drops from left to right. The thickness of the saturated area is, according to the formation of the phreatic surface, approximately 20 m. The thickness of the overlying non-saturated layer will vary between $GF = 0.5$ and $GF = 7 \text{ m}$ (not included in the model area) to show the influence of the depth of the groundwater level on the groundwater temperature field and on the temperature of the water from the spring. The temperature at the earth's surface is mainly influenced by weather conditions with seasonal variations, and will be approximated by means of a Fourier series. The earth's surface shall be assumed to be parallel to the groundwater table, so that the depth from the earth's surface to the groundwater level is constant all over the model area. By varying the conductivity and thickness of each layer, different flow fields will be generated, in turn affecting the temperature distribution, and spring water temperatures.

8.6.2.2 Aquifer properties

The individual layers of the aquifer are considered to be homogeneous and isotropic. For the calculation of the effective thermal conductivity, $k_{T\text{eff}}$, of the solid matrix-water set, the arithmetic mean values obtained for $k_{T\text{eff}}$ using the “series approach” (eq. 8.1) and the “parallel approach” (eq. 8.2) will be used with the two thermal conductivities of each component: $k_{T_w} = 0.59 \text{ W/m/K}$ for water and $k_{T_s} = 3.5 \text{ W/m/K}$ for the solid matrix; total porosity is φ_{total} :

$$k_{T\text{eff}} = \varphi_{\text{total}} k_{T_w} + (1 - \varphi_{\text{total}}) k_{T_s} \quad \text{series approach} \quad (8.1)$$

$$\frac{1}{k_{T\text{eff}}} = \frac{\varphi_{\text{total}}}{k_{T_w}} + \frac{1 - \varphi_{\text{total}}}{k_{T_s}} \quad \text{parallel approach} \quad (8.2)$$

To show the principles, the choice of the absolute values used is of no relevance. An increase in thermal conductivity of granular particles would result in an increase in effective thermal

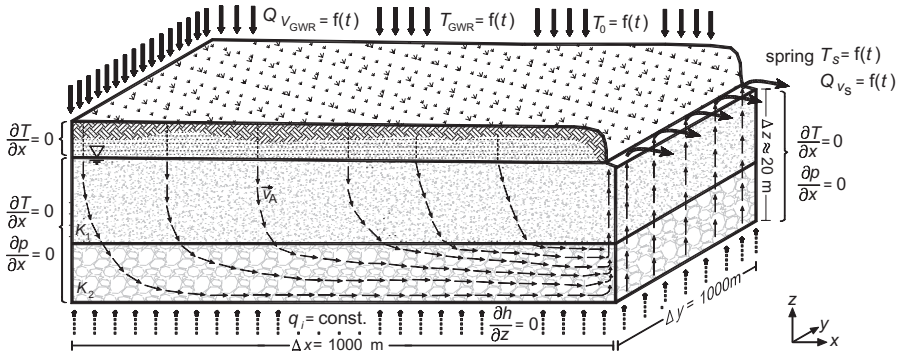


Figure 8.24. Organization of the model and boundary values.

conductivity, whereas an increase in porosity would translate to a decrease in effective thermal conductivity. On the other hand, a decrease in effective porosity, φ_{eff} , means an increase in real flow velocity, and average groundwater residence times decrease. The specific heat capacity, c_p , of the water-saturated grain structure is the result of the addition of the individual heat capacities, c_{pw} , of water and c_{ps} , of the solid, according to:

$$c_p = \varphi_{\text{total}} \rho_w c_{pw} + (1 - \varphi_{\text{total}}) \rho_s c_{ps} \tag{8.3}$$

where ρ_w , ρ_s are the specific densities of the water and fluid, respectively. The heat capacity of water is $c_{pw} = 4190 \text{ J/kg/K}$, whereas that of solid components such as quartz and clay minerals is $c_{ps} = 758 \text{ J/kg/K}$. Viscosity, μ_f , and fluid density, ρ_w , depend on water temperature according to the following equations (Voss 1984):

$$\begin{aligned} \rho_w(T) &\approx \rho_0 - \rho_0 \beta_T (T - T_0) \\ \text{with } \rho_0 &= \text{fluid density at reference} \\ &\text{temperature } T_0 = 20^\circ\text{C} \\ \beta_{w0} &= \text{thermal expansion coefficient at } T_0 \end{aligned} \tag{8.4}$$

$$\mu(T) \approx (237.0 \times 10^{-7}) 10^{\frac{248.37}{T+133.152}} \tag{8.5}$$

8.6.2.3 Boundary conditions

First-order boundaries (Dirichlet type): for the upper border of the model, temperature is prescribed. Its time dependence is given by a Fourier series; the amplitude of the annual period temperature variation is 9 K, and mean annual temperature is 8°C. Groundwater upwelling at the right border is represented by a Dirichlet type boundary condition with $p = 0 \text{ Pa}$.

Second-order boundaries (Neumann type): This boundary type is selected for groundwater flow for all boundaries of the model area except of the upper right corner of the vertical cross-section, corresponding to the spring (Fig. 8.24). The boundaries, which are impermeable to water, are a special case of this boundary type. A water flow entering through the upper border of the model is the recharge of groundwater that appears on the phreatic surface. Therefore, the temperature of this incoming water has to be set as a Dirichlet boundary condition. To define a value for the temperature of the recharged groundwater, different simulations with time-dependent temperature functions are performed. Temperatures that would be found at depths between 0.1 and 1 m below the earth's surface if heat transport were strictly conductive, are used. It is demonstrated that the selected function does not cause substantial modifications in the temperature field of the studied aquifer, and that it only produces significant changes in spring water temperature during events

that lead to short-term recharge peaks. Since we study only annual changes, and short-term effects are not within our objectives, recharge water temperature will not be studied in detail, and it will be approximated by using the soil temperature at 0.5 m below the surface.

Groundwater recharge rate on the surface caused by rainfall varies in time. It is represented by means of a rectangular function of annual periodicity, where winter months (November to May) present a recharge of 160 mm, and summer months (June to October) have a recharge of 40 mm. This is equivalent to an annual recharge of 200 mm. Through the base of the modeled area there is a constant heat inflow of 70 mW/m.

8.6.2.4 Initial conditions

At the beginning of each simulation, pressure and temperature distributions are required. Since all time-dependent parameters follow annual functions, a 5 year pre-simulation is carried out to initialize these fields (before our real simulation starts). During this period, from a constant temperature of 8°C in the entire model area and a pressure field equivalent to the hydrostatic pressures, a distribution of temperatures and pressures is generated; this distribution will be used as the starting point of the main simulation.

8.6.3 Simulations of spring water temperatures and their results (scenarios 1–8)

The simulations carried out for scenarios 1 to 8 yield spring water temperatures whose amplitudes, AMP , and phase displacements, $\Delta\varphi$, together with the water balances for the corresponding model scenarios, are represented in Figure 8.25.

8.6.3.1 Groundwater flow field

Groundwater flow field configuration in shallow free aquifers with surface recharge is controlled by their stratigraphy (Fig. 8.25). If the lower layer of a horizontal aquifer system is less permeable than the overlying layer, little water gets through to the lower layers and water mainly circulates in the overlying layer. Since little water gets to the lower areas, real velocities are small and groundwater residence times are long. The differences correspond to the relation between the conductivities of the different layers. When more permeable layers are found at deeper levels in the aquifer, water passes vertically through the upper, less permeable layers, and circulates in the lower layers.

8.6.3.2 Annual periodic oscillations of spring water temperature

Spring water temperatures can be characterized by the amplitude AMP of their annual periodic oscillations, as well as by the phase difference, $\Delta\varphi$, between earth's surface and spring water maximum (or minimum) temperature values. Figure 8.25 shows the dependency of these parameters for scenarios 1 through 8, which differ in the pattern of their groundwater circulation systems in the aquifer with its two layers of variable hydraulic conductivity and thickness.

Maximum annual spring water temperature variations (highest amplitudes) are observed in scenarios 1, 2, 5, and 6, where water movement mainly occurs on the upper layer of the aquifer (Fig. 8.25). Temperature varies within the upper layer which is only 5 m thick, between 7.5 and 0.2 K for depths of $GF = 0.5$ m and 7 m, respectively (scenario 1). The corresponding phase differences, $\Delta\varphi$, vary between 0.8 and 8.2 months. If the thickness of the upper layer is increased to 15 m (scenarios 5 and 6), amplitudes of only 3.8 K as a maximum are reached (with $GF = 0.5$), whereas values higher than 1.8 months are obtained for $\Delta\varphi$. If the upper layer has higher hydraulic conductivity, the thickness of this layer is a significant factor in the evolution of spring water temperature.

8.6.3.3 Results summary

A thin layer, only a few meters in thickness with low conductivity that overlays a second more permeable layer, is enough to produce a strong cushioning effect on spring water temperature variations. The thickness of the lower layer is then of little relevance.

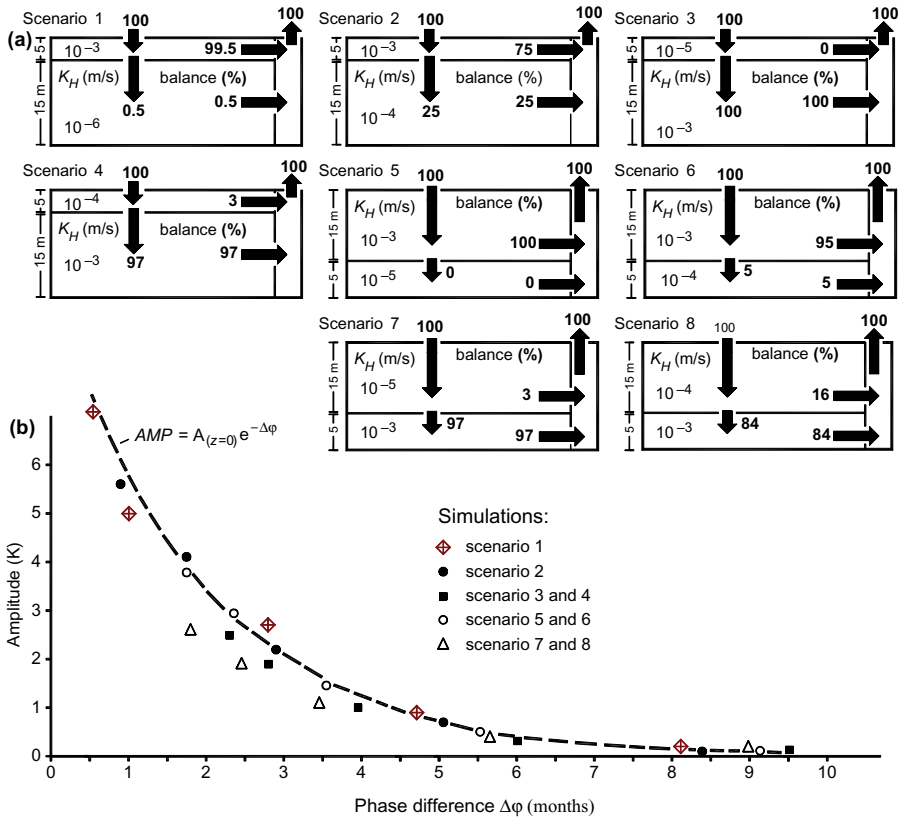


Figure 8.25. Spring water temperatures for model scenario 1 through 8: (a) Aquifer configuration and water masses in each layer; (b) Relation between the annual amplitude, AMP , and phase difference, $\Delta\phi$, between earth's surface and spring water temperatures. The curve shown with broken lines represents the relationship, independent of materials, between AMP and $\Delta\phi$ for a purely conductive transport of heat in an aquifer with water at rest.

If water movement occurs mainly in the upper layer of the aquifer, at equal depths of the phreatic layer, temperature amplitude is always greater and $\Delta\phi$ values are always lower than in the previous case. Here, the thickness of the upper layer is significant.

As a summary, it can be said that for the evolution of spring water temperature in time, both the depth of the phreatic layer as well as the role of the first meters of the aquifer system in groundwater circulation are essential.

8.6.4 Scenario 1 and 3: Simulations and results

Simulations of scenario 1 and 3, which do not differ in the model geometry, but in the hydraulic conductivity of the distinct layers, are performed using the Sutra modeling code (Voss 1984; see section 6.8.4). For each scenario, simulations are carried out for different depths of the phreatic surface ($GF = 0.5, 1, 2, 4$ and 7 m).

The modeling results are shown in Figure 8.26 for scenario 1, and Figure 8.27 for scenario 3, each divided into five parts (a–e) corresponding to:

- Model area showing groundwater flow paths and values of groundwater flow velocity.
- Water volumes, which are flowing in each individual layer towards the right model boundary in relation to total recharge. A 60 m wide high permeable column on the right boundary of

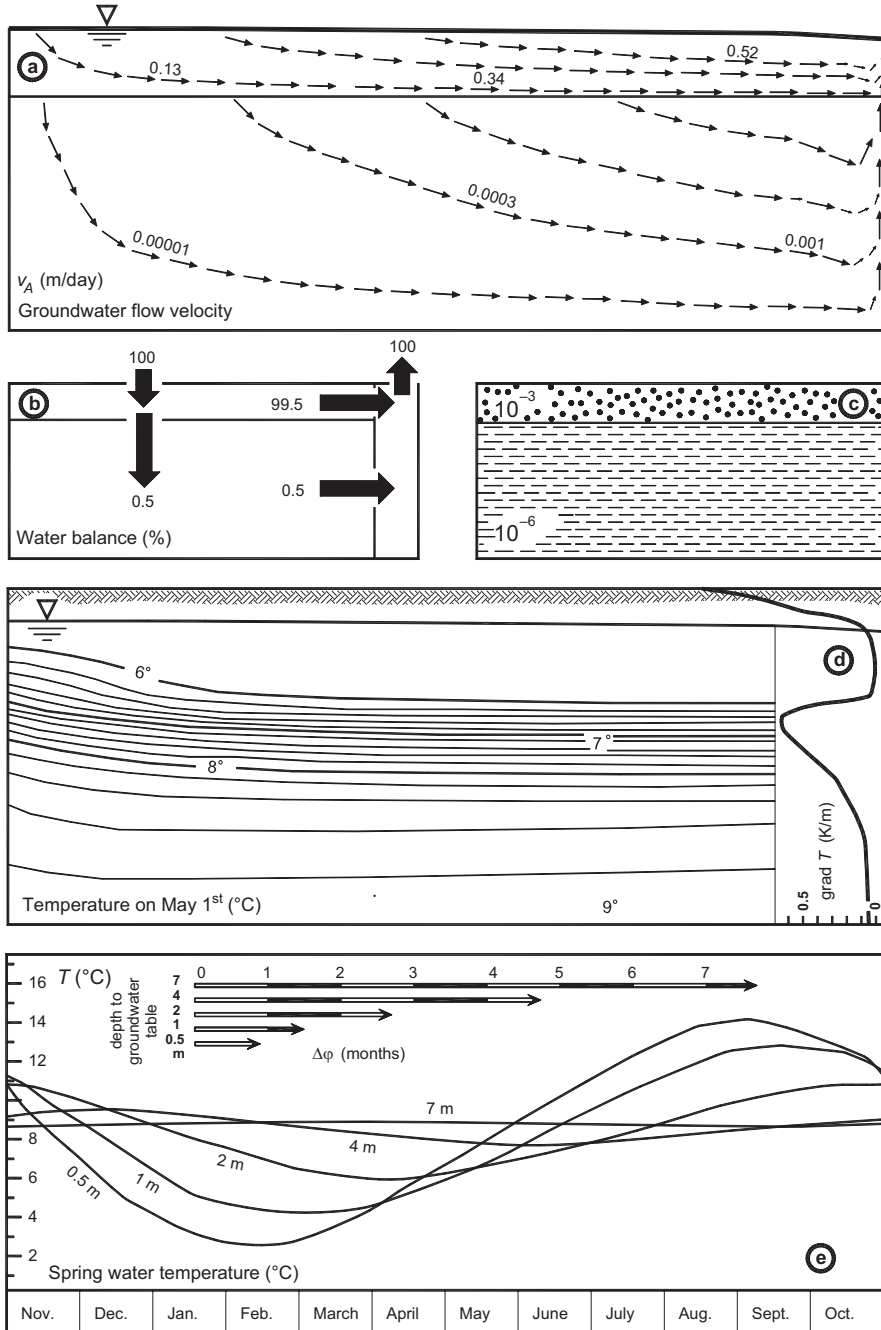


Figure 8.26. Scenario 1: (a) Groundwater flow pattern; (b) Water balance for each layer of the system; (c) Aquifer configuration; (d) Spatial distribution of temperatures in the aquifer system for $GF = 2$ m; (e) Spring water temperatures as a function of time. (Horizontal model extent 1000 m, vertical extent 20 m; cross-section 16× exaggerated; for details see text).

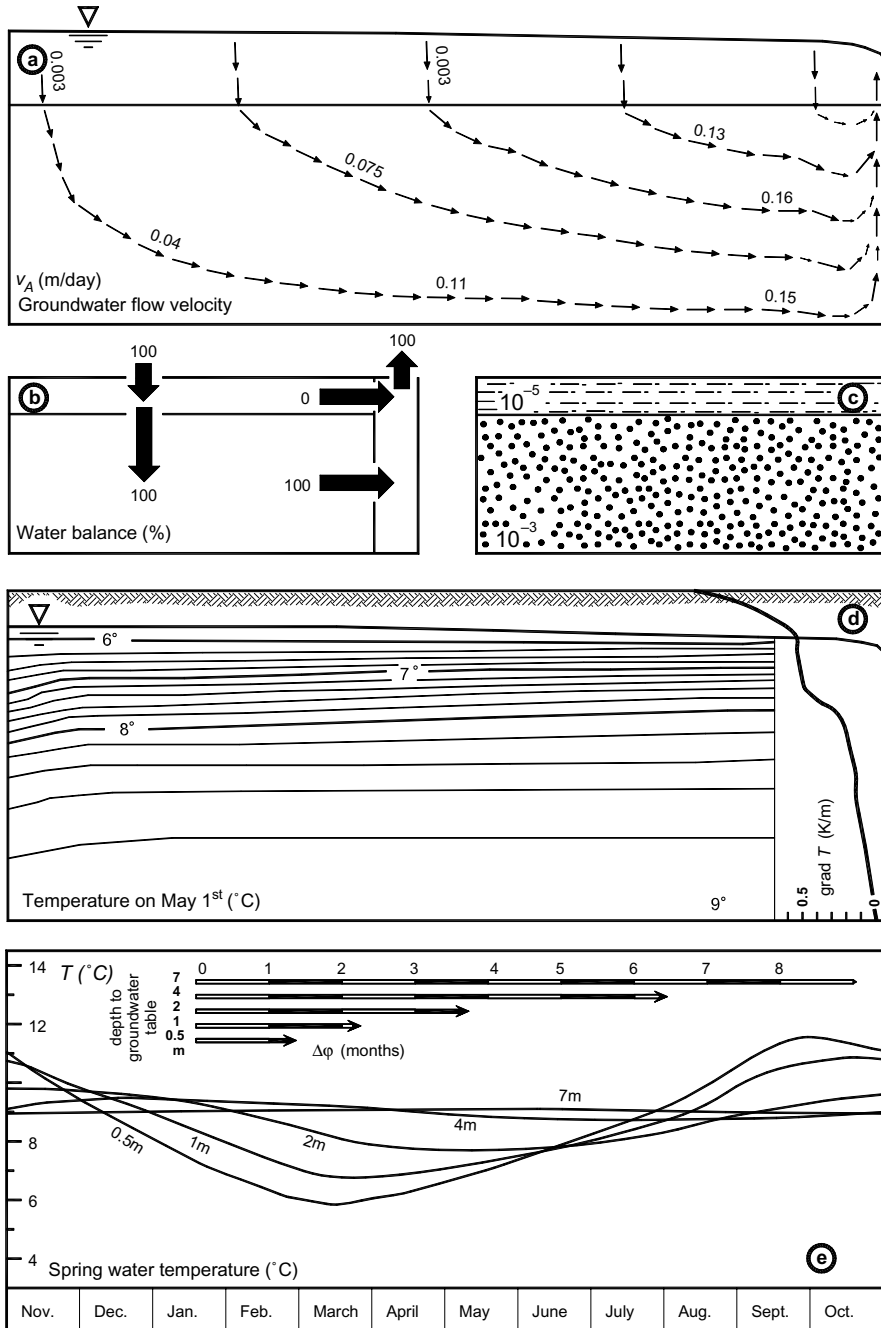


Figure 8.27. Scenario 3: (a) Groundwater flow pattern; (b) Water balance for each layer of the system; (c) Aquifer configuration; (d) Spatial distribution of temperatures in the aquifer system for $GF = 2$ m; (e) Spring water temperatures as a function of time. (Horizontal model extent 1000 m, vertical extent 20 m; cross-section 16× exaggerated; for details see text).

the model is used as a separation from the balance viewpoint between the horizontal flow that takes place at each layer, and the ascending vertical flow that occurs in the spring.

- Geometry, thickness, and hydraulic conductivity K_H values for each layer. The K_H values correspond to a mean aquifer temperature of 9°C.
- The temperature field in the aquifer is represented as isotherms on May 1st, with a phreatic level depth of 2 m. On the right border, temperature gradient is given as a function of depth, including the non-saturated area.
- Temperature variation of spring water for different depths of the phreatic surface. The arrows show the displacement of (phase difference, $\Delta\varphi$) between the minimum values of spring temperatures as compared to the minimum values of earth surface temperatures for different phreatic surface depths.

8.6.4.1 Scenario 1

8.6.4.1.1 Aquifer configuration, flow field and water balance

The aquifer system is formed by a 5 m thick, high permeable layer ($K_{H1} = 10^{-3}$ m/s), with an underlying 15 m thick layer whose hydraulic conductivity is 1000 times lower ($K_{H2} = 10^{-6}$ m/s) (Fig. 8.26). As a result, 99.5% of groundwater recharge remains in the upper layer and flows horizontally towards the discharge area (spring).

8.6.4.1.2 Temperature field

The present groundwater flow field significantly modifies the temperature field due to convective heat transport. The non-distorted temperature field that would correspond to the distribution of temperatures on the left border extrapolate to the rest of the model, and the isotherms of the upper layer are displaced downwards in such a way that constant temperatures are recorded in the entire layer ($\Delta T < 0.1$ K); the vertical component of the temperature gradient is therefore ≈ 0 K/m. As a consequence, the isotherms corresponding to the upper portion of the underlying layer are concentrated, and a maximum of 0.6 K/m in the temperature gradient is recorded. As depth increases, this gradient decreases first linearly, and then almost exponentially, as it approaches a value of 0.03 K/m. The flow velocities in the lower layer, 1000 times lower, are so low that they do not visibly affect the temperature field. With the exception of the left area of the modeled region, isotherms are horizontally disposed.

8.6.4.1.3 Spring water temperature

Since 99.5% of the recharged groundwater flows within the upper layer that is only 5 m thick, the influence of terrestrial surface temperature on the temperature field of this layer, and therefore on the spring water temperature, is high. As a direct consequence of this influence, values between 7.1 and 0.15 K are obtained for annual spring water temperature amplitudes for the different depths of the phreatic surface (0.5 to 7 m). The annual arithmetic mean of the spring water temperature is 8.3°C for a depth of 0.5 m, and 8.8°C for a depth of 7 m of the groundwater table. Phase difference, $\Delta\varphi$, between corresponding extreme temperature values of the terrestrial surface, and spring water, varies according to the different simulated depths of the groundwater table between 0.5 and 8.4 months.

8.6.4.2 Scenario 3

8.6.4.2.1 Aquifer configuration, flow pattern and water balance

Opposed to the previous scenario, the lower layer is more permeable ($K_{H2} = 10^{-3}$ m/s) than the overlying layer ($K_{H1} = 10^{-5}$ m/s). The recharged groundwater flows through the upper layer in a vertical direction and almost 100% reaches the lower layer where it takes a horizontal direction towards the spring (Fig. 8.27).

8.6.4.2.2 Temperature field

Unlike the previous scenario, in this flow field the lower layer mainly affects the temperature field. As distance from the left margin increases, temperature isotherms are displaced towards the upper layer, resulting in a concentration, and as a consequence a maximum temperature gradient

of 0.55 K/m. The lower layer, on the contrary, presents increasing distances between isotherms. At the boundary with the lower layer which is better drained, the temperature gradient suffers a sudden variation from 0.5 to 0.25. As temperature increases, it approximates 0.02 K/m, which is the value reached at the base of the model.

8.6.4.2.3 Spring water temperature

The total volume of recharged groundwater flows through the lower layer towards the spring. Conditioned by the greater circulation depths, and by the upward displacement of isotherms which leads to an additional increase of temperatures in the lower layer, the mean annual value for spring water temperatures, increases. This is demonstrated by the fact that when phreatic depth is increased, temperature goes up from 8.4 to 9.1°C, which is a significantly greater increase than in scenario 1. If temperature variations are compared, the present scenario has more of a cushioning effect due to its greater circulation depth. For the studied depths of the groundwater table, spring water temperature amplitudes of 2.5 and 0.05 K are recorded, values that are significantly lower than in the previous scenario. The corresponding phase difference between corresponding temperature extremes at the earth's surface and the spring water $\Delta\varphi$, varies between 1.7 and 9.5 months.

CHAPTER 9

Geothermal systems modeling examples

“Deeper physical insight combined with theoretical simplicity provides the short-cuts leading immediately to the core of extremely complex problems and to straightforward solutions. This cannot be achieved by methods which are sophisticated and ponderous even in simple cases.”

Maurice A. Biot (1962)*

In this chapter, we present a few applications where numerical modeling can be applied to solve practical problems occurring in the exploration and exploitation of geothermal resources. First, we give in section 9.1 a short and very simplified introduction to geothermal energy, its applications for direct uses and for power generation and its benefits compared with other renewable energy resources and with fossil fuels. In that section we also give a simplified description of geothermal reservoirs. The descriptions presented here are very fundamental and are only aimed to introduce those readers, who are not familiar with geothermal energy or geology to these topics and to indicate them those references where they can find more detailed information.

9.1 WHAT IS GEOTHERMAL ENERGY?

Geothermal heat (or geothermal energy) is the heat contained in the solid Earth and its internal fluids. It originates from sources within the Earth itself predominantly from (1) radiogenic heat due to decay of radioactive isotopes, (2), original heat which corresponds to the heat present in the Earth directly after its formation, (3) potential energy released in form of heat during the formation of new crust, accumulation of heavy metals in the mantle of the Earth, or formation of its iron core and (4) frictional heat resulting from elastic energy released during earthquakes (for details see Clauser 2007).

The Earth's crust, whose thickness ranges typically from the Earth's surface to depths of 25–40 km, includes the depths of geothermal resources which can be technically tapped. Within the Earth's crust, heat transport is predominantly by conduction, and in presence of fluids (magma, water) by convection. The combination of these two different heat transport mechanisms results in an irregular temperature-depth distribution with large lateral variations. Further, the content of radioactive minerals, which produce heat within the Earth's crust itself have an influence on the temperature distribution. Average heat flow amounts 87 mW/m^2 (continent 67 mW/m^2 ; oceans: 101 mW/m^2). However, large anomalies occur along tectonic plate boundaries, where moving fluids such as magma and water can transport heat (Clauser 2007). This contributes to the genesis of the many high-temperature geothermal reservoirs, which are found on the continents along active plate boundaries such as subduction zones, continental rifts and continental collision zones. Examples for these type of high-temperature hydrothermal geothermal reservoirs, which are mostly located in depths from 1–3 km, are the Mexican geothermal reservoirs that we present in section 9.1.1. In marine areas, along the mid-ocean ridges, and in volcanic areas related to subduction zones, where magma is upwelling, we have high positive thermal anomalies.

* Speech of Maurice A. Biot during the Acceptance speech of Timoshenko Award. American Society of Mechanical Engineers, *Applied Mechanics Reviews* 16:2, 1963.

These geothermal resources in the ocean are not yet commercially tapped. The Gulf of California (Mexico) is presented in sections 9.5.2.1 as example for such submarine geothermal reservoirs.

In practice, geothermal energy can be considered as an infinite heat source. Specific technology can be used to drill wells into the reservoir, bring its hot fluids to the surface, take the underground heat and transform it into electricity (Figure 9.1). It is a natural, renewable and reliable domestic source of energy with environmental and cost advantages over other energy sources. Besides electricity generation, this natural heat source may also be used directly in several applications.

As already mentioned in the introduction to this book (chapter 1), there are many practical benefits of using geothermal energy:

- Geothermal energy from hydrothermal and conductive systems is an optimal option to cover part of the future electricity demand and to guarantee energy security. Since the geothermal resources are domestic, their use makes countries independent from fossil fuel imports and the related problems caused by their world market price fluctuations, and so contributes to energy independence for both developing and developed countries.
- The use of geothermal heat replaces the need for large amounts of combustible hydrocarbons. Millions of barrels of fossil fuels are saved each year in countries where geothermics is employed in different forms.
- The production of only 45 MW_e of electricity from geothermal reservoirs is equivalent to burning one million barrels of oil each year for the same purpose.
- Geothermal power plants do not burn any fossil fuel and consequently very few gaseous emissions are produced. The emissions of CO₂, sulfur oxides (SO_x) and nitrogen oxides (NO_x) from a geothermal plant, are less than 2% compared to fossil fuel based power plants (UNFCCC 1997).
- Considering the total cost of energy generated from geothermal resources, which comprise installation costs and generation costs, electricity from geothermal power plants is competitive in comparison to electricity produced by fossil fuel power plants or power plants using other renewable energy resources.
- The residual heat from geothermal power plants can be used for several direct uses such as those listed below. In case of power plants, whose residual water exceeds a temperature of 80°C, this water also can be used for electric power generation applying binary technology process.

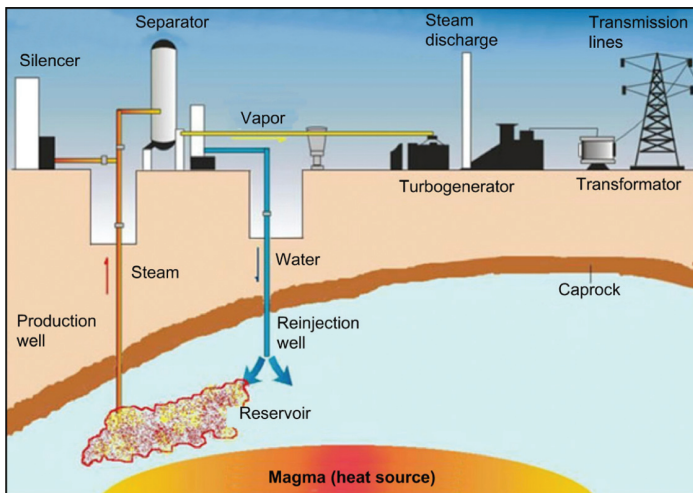


Figure 9.1. A simplified scheme of a geothermal field showing the main parts of the underground reservoir and surface equipment (adapted from Maya-González and Gutiérrez-Negrín 2007).

- Geothermal heat can be directly used for space heating and cooling, providing hot water for houses and industrial purposes, snow and ice melting, bathing, heating greenhouses, aquaculture, drying of fruits, etc.
- The silica in the brine is useful for the fabrication of construction materials.

Geothermal energy is abundant worldwide, either as high- or low-enthalpy resources if we classify them according to their temperature, or as convection or conduction dominated systems if we classify them according to the principal heat transport mechanism. Today (2010), the planet has an installed geothermal capacity of 10,715 MW_e distributed in 24 countries for electricity production (Table 9.1) (Bertani 2010), and 50,583 MW_t (thermal MW; year 2009) for direct uses in 78 countries (Lund *et al.* 2010). There are plans in many countries to increase this capacity. Exploitation of geothermal energy currently saves around 450 billion barrels of oil each year.

The main characteristics of geothermal fields will be illustrated using the Mexican volcanic reservoirs subjected to exploitation as examples (Fig. 9.1). Other carefully selected examples

Table 9.1. Worldwide installed geothermal capacity and geothermal electric power generation in 2010 compared with the respective 2005 values (Bertani 2005, 2010).

	Installed geothermal capacity in		Geothermal electricity generation			
	2010 (2005)	2010	2005	2005	2005	2010
	MW _e	% of world geothermal capacity	(GWh)	% of world geothermal power generation	% of total national power generation	(GWh)
USA	3093 (2564)	28.87	16840	30.23	0.5	16603
Philippines	1904 (1930)	17.77	9253	16.61	19.1	10311
Indonesia	1197 (797)	11.17	6085	10.92	6.7	9600
Mexico	958 (953)	8.94	6282	11.28	3.1	7047
Italy	843 (791)	7.87	5340	9.59	1.9	5520
New Zealand	628 (435)	5.86	2774	4.98	7.1	4055
Japan	536 (535)	5.20	3467	6.22	0.3	3064
Iceland	575 (202)	5.37	1483	2.66	17.2	4597
El Salvador	204 (151)	1.90	967	1.74	22	1422
Costa Rica	166 (163)	1.55	1145	2.06	15	1131
Kenya	167 (129)	1.56	1088	1.95	19.2	1430
Russia	82 (79)	0.77	85	0.15	0	441
Nicaragua	88 (77)	0.82	271	0.49	9.8	310
Turkey	82 (20)	0.77	105	0.19	0	490
Papua-New Guinea	56 (6)	0.52	17	0.03	n/a	450
Guatemala	52 (33)	0.49	212	0.38	3	289
China (Tibet)	24 (28)	0.22	96	0.17	30 ¹⁾	150
Portugal (Azores)	29 (16)	0.27	90	0.16	n/a	175
France (Guadeloupe, Alsace)	16 (15)	0.15	102	0.18	9.0 ²⁾	95
Ethiopia	7.3 (7.3)	0.07	17	0.03	n/a	10
Germany	6.6 (0.2)	0.06	1.5	0	negl.	50
Austria	1.4 (1.1)	0.01	3.2	0.01	negl.	3.8
Australia	1.1 (0.2)	0.01	0.5	0.02	negl.	0.5
Thailand	0.3 (0.3)	0	1.8	0	negl.	2
Total	10715 (8933)	100	55709	100		67246

¹⁾ referred to Tibet,

²⁾ referred to Guadeloupe; negl.: negligible; n/a: not available.

of not traditionally used geothermal systems are presented in this chapter. Further information can be found at the following online resources: Geothermal Education Office (GEO 2009), International Geothermal Association (IGA 2009a), Geothermal Resources Council (GRC 2009) and the Geothermal Conference Papers Database (IGA 2009b).

9.1.1 Characteristics of geothermal reservoirs in Mexico as examples of heterogeneous non-isothermal aquifers

The first geothermal well in Mexico was drilled in 1954, and in 1959 the first commercial plant came into operation (Pathe, Hidalgo state) having a capacity of 3.5 MW_e (electric megawatt). Today (2009) Mexico occupies the fourth place worldwide in installed geothermal electric capacity (Table 9.1) and the fourth place in geothermal electric power generation. In 2009, the total installed geothermal capacity of the country was 958 MW_e and the energy produced in 2008 was 7047 GWh (Gutiérrez-Negrín *et al.* 2010) distributed between four reservoirs (Table 9.2, Fig. 9.2). This figure represents almost 2.5% of the total installed electric capacity in Mexico, which is operated by the federal utility *Comisión Federal de Electricidad* (CFE: 38,474 MW_e total installed capacity in 2009; Gutiérrez-Negrín *et al.* 2010). The total quantity of electricity generated for public service in Mexico during 2008 was 234,096 GWh (Gutiérrez-Negrín *et al.* 2010); geothermal generation represented about 3.0% of this total. There are also private electricity producers in Mexico with a total installed capacity of 21,127 MW_e, generating 46,893 GWh in the year 2008 (Gutiérrez-Negrín *et al.* 2010), although none of them produces geothermal electricity.

Table 9.2. Main geothermal fields in Mexico, installed geothermal capacity and electricity generation (data updated by Gutiérrez-Negrín *et al.* 2010).

Field	Installed capacity in year 2009 (MW _e)	Electricity generation in year 2008 (GWh)
Cerro Prieto	720	5175
Los Azufres	188	1517
Los Humeros	40	313
Las Tres Virgenes	10	41.2
Total	958	7047

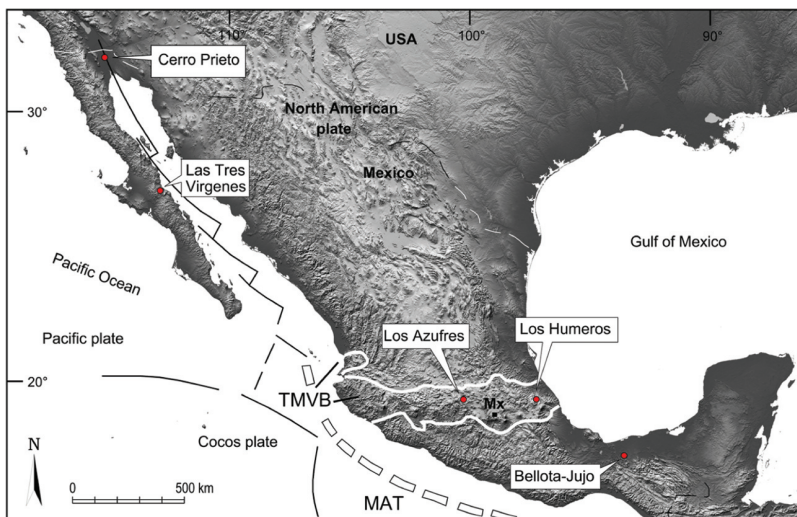


Figure 9.2. The main high-enthalpy geothermal fields in Mexico and location of the Bellota-Jujo oil reservoir complex related to low-enthalpy geothermal aquifers. TMVB: Transmexican Volcanic Belt, MAT: Middle American Trench.

9.1.1.1 Cerro Prieto, Baja California

The Cerro Prieto field (Fig. 9.3a) is the second largest geothermal reservoir in the world. It is located in the southern part of the Salton trough, about 30 km south of the US-Mexico border in Baja California state, Mexico (Fig. 9.2). The existence of this reservoir is closely related to the San Andreas fault system. Its fluids are stored in sandstones, intercalated with shales, which are located over a granitic basement forming the only currently exploited sedimentary-type geothermal reservoir in Mexico (Fig. 9.4) (Birkle and Verma 2002). The conceptual model of the Cerro Prieto reservoir, indicates that geothermal brine may have formed in coastal lagoons similar to modern sabkhas by seawater evaporation to about six times its normal salinity. Parts of them migrated to the bottom of the sediments in the southern part of the Salton trough. The opening of the pull-apart basin caused their upward rise and mixing with Colorado River water saturating overlying sediments (Truesdell *et al.* 1981) (Fig. 9.4). Production of the field is through two fault zones (indicated as “L” and “H” fault in Figure 9.4) (Halfman *et al.* 1984, Lippmann *et al.* 1991).

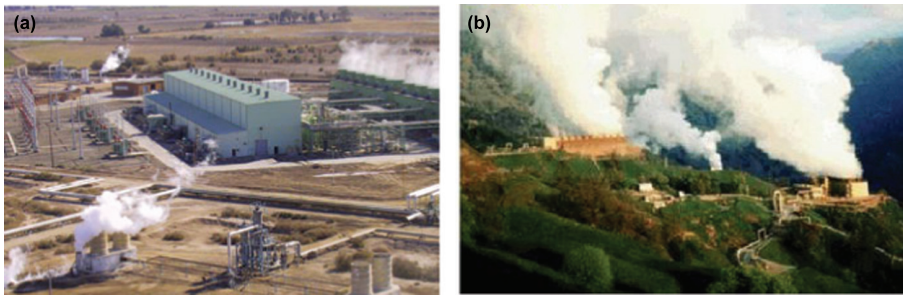


Figure 9.3. Aerial view of (a) the Cerro Prieto geothermal field, located to the north of Baja California, Mexico and (b) Los Azufres geothermal field, located in the state of Michoacán, Mexico.

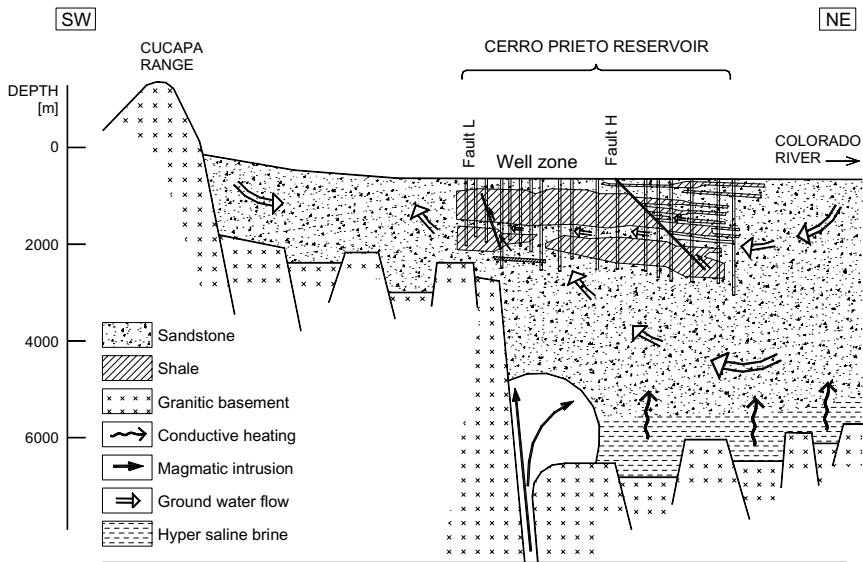


Figure 9.4. Conceptual model of the Cerro Prieto geothermal reservoir indicating that the reservoir is recharged with water from the Colorado river, which infiltrates into the underground where it is conductively heated up by a deep heat source (modified from Birkle and Verma 2002, based on Halfman *et al.* 1984, Lippmann *et al.* 1991).

The geothermal field was already known in prehispanic times (Suárez *et al.* 1999) and its commercial exploitation started in 1973. Currently it has an installed capacity of 720 MW_e distributed in thirteen units, which are fed from 168 wells with an average depth of 2500 m. The extraction wells produce 52.6 million metric tons of steam per year (6000 tons/h. About 70 million tons of brine per year are reinjected into the reservoir through 15 injection wells (Maya-González and Gutiérrez-Negrín 2007). In April 2009, Cerro Prieto achieved 36 years of uninterrupted commercial electricity generation. Annually, this field generates about 5000 GWh, satisfying 70% of the demand on the electricity grid of the main cities located in the northern region of Baja California, Mexico.

9.1.1.2 Los Azufres, Michoacán

Los Azufres geothermal field (Fig. 9.3b) is located in central Mexico, in the central-western part of the Transmexican Volcanic Belt (Fig. 9.2), at an average altitude of 2800 m a.s.l. The development of this reservoir, discovered in 1972, was initiated in 1975. Los Azufres is a volcanic hydrothermal reservoir, formed by a 2700 m thick interstratification of upper Miocene to Pliocene lava flows of andesitic to basaltic composition (Dobson and Mahood 1985). This field presents several faults and intense fracturing (Fig. 9.5). Up to 1000 m thick silicic sequences (rhyolitic to dacitic) of Pleistocene age seal the geothermal aquifer from the surface, allowing the system to pressurize (Birkle and Verma 2002, Fig. 9.4). There are about 65 drilled wells with wellhead elevations between 2700 and 3200 m a.s.l. There are two fractured subsystems defining two connected sectors: Maritaro in the north and Tejamaniles in the south. At shallow levels (<500 m), hydrothermal alteration under low temperature conditions (170°C) caused argillitization with smectite, zeolite, calcite and chlorite as the principal mineral assemblage (González *et al.* 2000). Below 1500 m, epidote, amphibole, prehnite and garnet indicate temperatures above 250°C and pressure conditions between 15 and 20 MPa. In Tejamaniles a narrow convective zone produces fumaroles, steam plumes, hot springs, mud lakes and steaming ground. The liquid

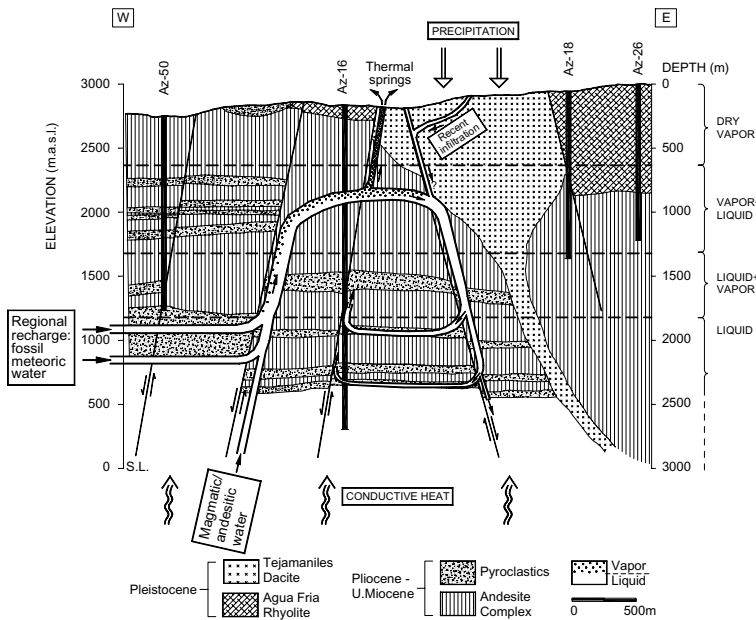


Figure 9.5. Conceptual model of the Los Azufres geothermal reservoir (after Birkle and Verma 2002, geological information after González *et al.* 2000a).

extracted is mostly reinjected into the reservoir to avoid contamination of the environment and land subsidence. Additionally, this injection serves to recharge the reservoir.

Los Azufres was the first geothermal field in Mexico to produce electricity from fluids stored in volcanic rocks. From the electrical production point of view, this field is second in importance in Mexico after Cerro Prieto. In 2009, the Los Azufres geothermal field (Fig. 9.3b) had an installed capacity of 188 MW_e, and was producing 1517 GWh in the year 2008 using 14 generating units (Gutiérrez-Negrín *et al.* 2010). The main thermodynamic properties of this volcanic reservoir are indicated in Table (9.3) and the characteristics of the production wells are shown in Table (9.4). Since the middle of the 1980s, measurements of petrophysical properties have been carried out in cores extracted from wells of the Los Azufres geothermal reservoir. A number of parameters were measured: rock density, effective porosity, permeability, thermal conductivity and specific heat (Table 3.8 in chapter 3).

Table 9.3. Characteristics of the Los Azufres geothermal field (Suarez 1991, 1997).

Type of rocks	Rhyolites (shallow layers and caprock); andesites and basalts (production layers), local basement (unknown)
Type of water	Sodium-chloride waters
Average thermodynamic state	p_m : 10 MPa, T_m : 310°C, h_m : 1400 kJ/kg (compressed liquid, average properties). Above 1600 m a.s.l. there is a two-phase zone; at some few zones, there is a steam phase alone
Steam quality	Very heterogeneous, between 0 and 100%
Porosity	Between 0.7 and 24% (measured from drill cores)
Permeability	Heterogeneous; faults, fractures and matrix acting together; The values range from microdarcys to 1000 millidarcys
Volume and capacity	49 km ³ (N) 23 km ³ (S), 320 MW _e during 20 years

Table 9.4. Characteristics of wells, (N and S) in the Los Azufres geothermal field (Suarez 1991, 1997).

Wells in Tejamaniles (South)					Wells in Maritaro (North)				
Well	WHP (MPa _g)	Steam (T/h) ¹⁾	Water (T/h) ¹⁾	Gas %w	Well	WHP (MPa _g)	Steam (T/h) ¹⁾	Water (T/h) ¹⁾	Gas %w
Az-02	2.0	73	211	0.7	Az-04	1.2	50	89	1.4
Az-06	1.1	27	0	4.2	Az-05	1.0	83	56	1.4
Az-16	1.0	32	92	0.9	Az-09	0.7	31	36	0.5
Az-16D	1.2	20	11	4.0	Az-13	1.1	64	15	1.9
Az-17	0.9	52	0	2.2	Az-28	1.0	24	37	0.3
Az-18	1.1	71	35	9.0	Az-32	1.0	52	2	2.0
Az-22	2.0	85	104	0.8	Az-41	1.0	36	–	–
Az-26	1.0	88	180	4.5	Az-42	1.0	126	203	0.5
Az-33	1.2	40	70	2.5	Az-43	1.2	50	35	1.0
Az-34	1.0	50	0	7.0	Az-48	1.0	38	43	0.3
Az-35	1.5	37	0	3.0	Az-51	1.0	47	105	0.4
Az-36	1.1	36	27	2.4	Az-56	0.9	20	15	0.5
Az-37	1.2	49	0	2.0					
Az-38	1.1	105	0	2.8					
Az-46	1.1	52	109	1.4					
Az-55	1.0	38	48	0.8					
Total		855	1007	–	Total		621	636	–

¹⁾ At 0.8 MPa_g separation pressure; WHP = Well head pressure (in MPa); MPa_g = gauge pressure; %_w = percentage by weight.

9.1.1.3 Los Humeros, Puebla

The Los Humeros geothermal reservoir was discovered in 1968; its development was initiated in 1980 and in 1990 the first power plant was constructed. The field is located between the states of Puebla and Veracruz, in the eastern portion of the Transmexican Volcanic Belt, some 200 km to the east of Mexico City (Fig. 9.2, Fig. 9.6a).

The Los Humeros is a volcanic hydrothermal system presenting several faults and fractures, embedded in large calderic structure (Los Humeros and Los Potreros calderas), aged about 460,000 years (Fig. 9.7). The reservoir consists of complex geological units of limestone, ignimbrites and andesites, with some dacites and rhyolites. Mainly andesitic rocks form the caldera structure over a basement including granitic rocks, limestone and metamorphic rocks (skarn and hornfels). The reservoir's caprock is formed by ignimbrites covered by postcalderic products (tuff, ash, etc.). At this field, neither hot springs nor mud ponds are found and there is only steaming ground.

Los Humeros geothermal reservoir is formed by andesitic rocks and additional limestone in the lower part of the reservoir (Fig. 9.7). The sedimentary basement rocks show low permeability characteristics, whereas the heat source is still very hot and nearby to the reservoir (Birkle and

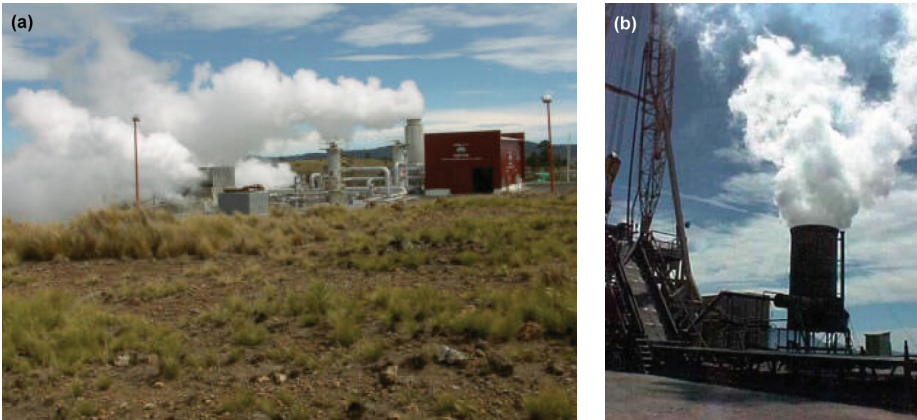


Figure 9.6. (a) View of the Los Humeros geothermal field (Puebla, Mexico) and (b) Las Tres Virgenes (Baja California, Mexico) geothermal field.

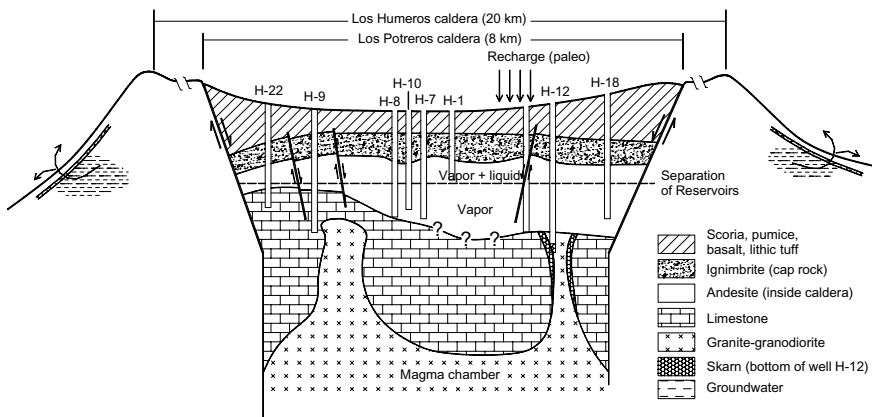


Figure 9.7. Conceptual model of the Los Humeros geothermal reservoir (after Birkle and Verma 2002).

Verma 2002). This produces superheated steam and HCl vapor (Bischoff *et al.* 1996). Ignimbrite layers act as caprock.

Two geothermal reservoirs can be distinguished (Fig. 9.7): a shallow one containing vapor and liquid and a deeper one, the main reservoir, with superheated steam (Barragán *et al.* 1991; Tello 1992, 1994; Portugal *et al.* 1994, Verma *et al.* 1998).

The shallow reservoir is found in andesitic rocks from a depth of 400 to 600 m in the central caldera collapse structure. It has an average temperature of 150°C and contains water of sodium-bicarbonate type.

The deeper reservoir is located at depth between 1400 and 2000 m. It has an average thickness of 700 m, including a zone with acidic water, corresponding to a rock volume of 21 km³. The effective average porosity is 12.3%. Therefore, the volume of hot fluid present is approximately 2.6 km³. If the acidic zone is not considered, the average thickness is equal to 460 m and the useful hot fluid volume is 1.7 km³. The deeper reservoir contains sodium-chloride type waters of high enthalpy at 320°C and 12.0 MPa. In some portions of the field, measured temperatures are close to 400°C (well H-29, 390°C at 2050 m depth).

The production of HCl vapor is due to water-rock interaction at high temperature, (300–350°C), high salinity (3000–7000 ppm), low pH and low volume of water (Barragán *et al.* 1989).

The properties of the Los Humeros geothermal field are summarized in Table 9.5.

In this field, there are 33 drilled wells, with depths ranging from 1450 to 3250 m. Most of them produce dry steam. The field began to generate electricity in 1991 and today there are seven back-pressure portable units of 6 MW_e each, giving a total installed capacity of 40 MW_e. The waste liquid is injected back into the reservoir to avoid environmental contamination. Additionally, the reinjection serves to recharge the reservoir and to maintain its pressure. Production data for this field are presented in Table 9.6. An important conclusion from these data is that a significant problem at Los Humeros is neither permeability nor porosity, but the lack of available water, which for unknown reasons the system was unable to retain in its geological past. The geochemical data show that there is no significant natural recharge and this system has a relatively small volume of water stored.

In 1988 measurements of petrophysical properties were made in wells of the Los Humeros geothermal field (Contreras *et al.* 1990). Eighteen cores from 15 wells were divided into 39 fragments and analyzed. The range of depths of the cores was between 616 m and 2847 m. The measured parameters were rock densities, porosities, absolute permeability, rock compressibility, module of elasticity, specific heat, thermal conductivity and thermal diffusivity. These properties were measured in dry rock and in water-saturated rock at the ambient temperature of 25°C. The confining pressures were within a range of [10, 40] MPa. Data obtained from measurements using water-saturated rock samples are shown in Table 3.7 (chapter 3).

Table 9.5. Characteristics of the Los Humeros geothermal field (Suarez 1991, 1997).

Lithological column	Scorias, pumice, basalt, lithic tuff (shallow layers); ignimbrites (intermediate layers); andesites (production layers); local basement (deep layers)
Type of water	Sodium-chloride waters are found in most wells; In a few wells (H-1, H-16 and H-18) the water is of sodium-bicarbonate type and produced from shallow zones of the reservoir
Average thermodynamic state	p_m : 12.5 MPa, T_m : 320°C, h_m : 1500 kJ/kg (compressed liquid, close to the two-phase zone. Steam phase: alone at some portions. Maximum T = 400°C (measured))
Steam quality	Between 85 and 100% in most wells
Porosity	Between 4% and 24% (measured in drill cores)
Permeability	Very heterogeneous: Faults, fractures and matrix acting together; K: 5×10^{-15} m ² (matrix average), 10^{-12} m ² (in fractures)
Volume and capacity	21 km ³ , 75 MW _e predicted; 40 MW _e installed

Table 9.6. Production data for the Los Humeros geothermal field (Suarez 1991, 1997).

Wells in Tejamaniles (South)					Wells in Marítaro (North)				
Well	WHP ¹⁾ (MPa _g)	Steam (tons/h)	Water (tons/h)	Enthalpy (kJ/kg)	Well	WHP ¹⁾ (MPa _g)	Steam (tons/h)	Water (tons/h)	Enthalpy (kJ/kg)
H-01	1.24	12	12	1543	H-16	2	31	11	2044
H-06	2.62	37	11	2148	H-17	1.45	16	0.5	2595
H-07	5.1	40	–	2662	H-20	1.45	40	–	2662
H-08	1.45	27	4	2341	H-28	2.34	20	7	1983
H-09	1.45	86	–	2662	H-29	1.79	18	–	2662
H-10	1.09	11	–	2662	H-30	2	20	1	2600
H-11	0.57	8	5	1751	H-31	2.31	48	2	2583
H-12	3.79	47	4	2300	H-32	1.64	11	6	1863
H-13	1.90	18	6	2106	H-33	1.86	33	–	2662
H-15	1.88	19	3	2297					

¹⁾ WHP = Well head pressure (in MPa); MPa_g = gauge pressure.

9.1.1.4 *Las Tres Virgenes, Baja California*

The Las Tres Virgenes geothermal reservoir is contained in a geological complex formed by three volcanoes of Quaternary age (Maya-González and Gutiérrez-Negrín 2007). The volcanism in this region of Mexico is closely related to tectonic processes that are separating the peninsula of Baja California on the Pacific plate from the North American plate (spreading rate ~5 cm/year), probably as a lateral extension of the San Andreas fault system, initiated at the end of the Miocene (Coletta and Angelier 1981) (Fig. 9.2). The fluids of this reservoir are stored in granodiorite-type basement rocks and probably in the overlying, sedimentary Grupo Comondú (Portugal *et al.* 2000). The commercial exploitation of this field started in 2001 with two plants of 5 MW_e each (Fig. 9.6b). The fluid is extracted from two wells producing 38 metric tons/h. The residual brine accompanying the steam is reinjected into the reservoir for recharge purposes.

9.1.1.5 *Cerritos Colorados (La Primavera), Jalisco*

The Cerritos Colorados (formerly La Primavera) geothermal reservoir is located in the central portion of the Transmexican Volcanic Belt (Fig. 9.2), inside a volcanic caldera of 12 km diameter. Its fluids are stored in andesites. Thirteen wells were drilled during the 1980s and six of these were producers with an average fluid rate of 40 tons/h. Because of political conflicts with local opposition groups, development activities in this field were suspended in 1989.

The average reservoir pressure is 12 MPa, the average temperature 304°C, the maximum measured temperature 355°C, and the initial thermodynamic state of the reservoir was compressed liquid. The minimum volume of the reservoir is 6 km³; the volumetric estimation of its electric capacity is 125 MW_e (Suárez 1997).

Measurements of petrophysical properties have been carried out in cores from this field: rock density, effective porosity, thermal conductivity, compressibility and specific heat were determined. The cores were collected from seven wells. The effective porosity values of the cores are dispersed, but most of them are high. The thermal conductivity is proportional to density, i.e. highly dense rocks with low porosity have good thermal conductivity. In general, high porosity values (>10%) are observed in rocks located at depths below 1000 m, with few exceptions. Below a depth of 1500 m the measured porosities are generally lower (average: 6%). Diffusivity, thermal conductivity and specific heat were measured in four different cores. Measurements were made in both dry rock and water-saturated rock at normal atmospheric pressure and temperature conditions (0.1 MPa, 20°C). Higher values of thermal conductivity are found in deeper parts of the reservoir containing rock with larger compaction and smaller porosity.

The thermal diffusivity, in dry and in saturated rock, are very close to 10^{-6} m²/s, whereas rock specific heat values are around 1 kJ/kg/°C. The petrophysical data are shown in Table 3.6 of section 3.8.1.

9.2 TRANSIENT RADIAL-VERTICAL HEAT CONDUCTION IN WELLS

In spite of great advances in the study of heat flow in the terrestrial surface, precise knowledge of the thermal behavior of the Earth's crust is still lacking. To accurately estimate the temperature distribution as a function of depth, it is necessary to know the thermal conductivity of the underground material and the position of the heat source or the distribution of heat flow at the profound boundary. The deep flow of heat coming from the planet's interior, together with the heterogeneous thermal diffusivity, are the main mechanisms that preclude temperature uniformity in the upper layers of the Earth's crust. From a geothermal point of view, drilling wells causes irreversible local thermal alterations, forming punctual discontinuities in the crust. The study of these artificial discontinuities permits the inference of some natural thermal parameters of the local rock.

Geothermal wells exchange heat with the surrounding porous rock. This transmission of thermal energy between the well casing and the rock formation is essentially conductive. Its study is important because the loss/gain of heat can influence the wellbore fluid thermodynamic conditions and the prediction of its natural original state. In addition, the first thermal data obtained during drilling contains valuable information concerning rock thermal parameters, thermal conductivity and specific heat. The analysis of anomalies in heat transmission provides indirect information about the extension and abundance of fractured areas. When drilling the well, the unknown vertical distribution of temperature is altered by the mechanical perforation itself and by the introduction of mud and water into the borehole. In low permeability volcanic reservoirs, this thermal interference spreads approximately in radial form, locally affecting an unknown volume of the reservoir (Fig. 9.5). The well dimensions, thermal parameters measured in cores and the inlet and outlet mud temperatures are the only available data when drilling.

In this section we present a practical radial-vertical conduction model for numerical analysis of the transient heat flow. This model provides a practical solution of the type $T(r, z, t)$ which results from coupling three solutions in two independent dimensions. To estimate the effect of the thermal disturbance in the well's neighboring formation, the model uses the available thermal information in flexible form. The central objective is to quantify the amount of energy lost radially by conduction through the well at any depth. If the natural heat flow outside the borehole is purely conductive, estimation of these variables can be very accurate. If there are convective anomalies, the quantification of discrepancies will permit the location of areas of convection and consequently, of probable high permeability. Coupling our analytic model to a well simulator could complement the study of this complex phenomenon.

9.2.1 Transient radial-vertical flow of heat

Conductive heat transfer from the well towards the rock formation is not negligible (Ramey 1962). Kanev *et al.* (1997) showed that when heat loss from the wellbore is not considered, the calculated wellhead temperature could diverge by 30°C from measurements. This loss can influence the well thermodynamics. Ramey (1962) developed an approximate solution to the transient heat conduction in wellbores with hot fluids. With his model the fluid and casing temperatures can be estimated as functions of depth and time. Several well simulators exist in the geothermal market; some reach great numerical sophistication (Garg and Combs 1998), including diverse correlations for the calculation of friction, phase changes, two-phase feed zones, etc. The model we introduce focuses on the problem of pure heat conduction between the pipe and the cement in the annular column and the formation.

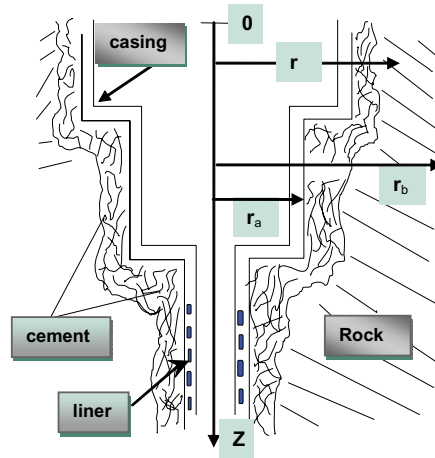


Figure 9.8. Simplified drawing of a geothermal well showing its main parts. The figure is not to scale.

The heat disturbance can travel up to a radial distance r_b inside the reservoir (Fig. 9.8). This distance depends on depth. Initially, in any geothermal reservoir zone, the temperature has an unknown vertical profile which, in the span of human life, can be considered stationary. Before well construction ($t = 0$) there exists a natural temperature distribution at each point of the future perforated zone. At some time $t > 0$ drilling causes a complex vertical disturbance that also spreads in the radial direction, inducing a second temperature profile at each depth. Both temperatures are coupled in a common boundary around the well (Fig. 9.8). When drilling is completed, the perforated area has lost heat. This is reflected in the temperature difference between the formation and the borehole. The movement of hot water inside the well produces a convective heat flow, which creates a new initial thermal state in the borehole, generating another temperature profile inside the well. Due to the high thermal conductivity of metal (25–50 W/m°C), the vertical flow of heat inside the casing is very high. At the same time the transient temperature differential between the fluid and the casing is insignificant. Therefore, the water and casing can be assumed to be at approximately the same temperature. This hypothesis does not hold for the cement and the reservoir rock, because both have smaller thermal conductivities (Suárez and Samaniego 1999).

Figure 9.8 shows the region of the space included in the model. The radial transient conduction at each depth $z > 0$ is obtained by overlapping the solutions corresponding to several infinite hollow cylinders, embracing a region formed by the cement in contact with the formation from an inner radius r_a to an external radius r_b at temperatures $T_a(z)$ and $T_b(z)$, respectively. Both temperatures are independent of the radius, but are functions of depth. The initial temperature distribution in the domain or region of interest $\Omega = \{r_a < r < r_b\}$, is given by $T(r, z, 0) = T_i(r, z)$, which can be assumed linear as a first approximation. The internal well temperatures can be measured at each time t . At distances larger than r_b , the reservoir temperature is stationary and only a function of depth. T_0 is the boundary condition in an arbitrary plane Z_0 and the bottom boundary condition is T_H at depth $z = H$. The mathematical form of the model that fulfils all these requirements is constructed as follows. In cylindrical coordinates the differential model in the domain Ω occupied by the well has the form:

$$\Delta T = \frac{1}{r} \frac{\partial}{\partial r} \left(r \frac{\partial T}{\partial r} \right) + \frac{\partial^2 T}{\partial z^2} = \frac{1}{\delta_T} \frac{\partial T}{\partial t} \text{ in } \Omega \quad (9.1a)$$

$$T(r, z, t) \quad \forall t > 0, \quad T(r, z, 0) = T_i(r, z)$$

At the boundary $\partial\Omega$:

$$\left\{ \begin{array}{l} T(r_a, z, t) = T_a(z), T(r_b, z, t) = T_b(z) \\ T(r, z_0, t) = T_0(r); T(r, z_H, t) = T_H(r) \\ T(r_a, z_0, t) = T_{0a}; T(r_a, z_H, t) = T_{Ha} \\ T(r_b, z_0, t) = T_{0b}; T(r_b, z_H, t) = T_{Hb} \end{array} \right\}$$

where $\partial\Omega$ represents the boundary of the well and the parameter δ_T [m²/s] is the thermal diffusivity of the medium (section 2.1.8). The dependence on θ is assumed negligible; at every plane of coordinate $z = \text{constant}$, the unknown function $T(r, z, t)$ is composed of two parts:

$$T(r, z, t) = U(r, z_0) + V(r, t) \tag{9.2}$$

To simplify this solution, we assume *a priori* that: $\frac{\partial^2 T}{\partial z^2} = 0$ and look for $U(r)$ and $V(r)$.

9.2.1.1 *Radial portion of the model*

Each one of the functions in equation (9.2) is the solution of different models. Note that both functions U and V must have the same units as T [°C]. $U(r)$ is a stationary radial model describing the temperature distribution between $r_a < r < r_b$:

$$\frac{1}{r} \frac{d}{dr} \left(r \frac{dU}{dr} \right) = 0 \tag{9.3}$$

$$U(r_a) = T_a(z), \quad U(r_b) = T_b(z)$$

The solution of $U(r)$ is elementary:

$$U(r) = T_a + \frac{T_b - T_a}{\text{Ln}(r_b/r_a)} \text{Ln} \left(\frac{r}{r_a} \right) \tag{9.4}$$

The function $V(r, t)$ corresponds to a transient radial heat flow inside an infinite hollow cylinder, defined by an inner radius r_a , an outer radius r_b , initial temperature $T_i(r)$ and boundary conditions at zero temperature:

$$\frac{1}{\delta_T} \frac{\partial V}{\partial t}(r, t) = \frac{1}{r} \frac{\partial}{\partial r} \left(r \frac{\partial V}{\partial r} \right); \quad \left\{ \begin{array}{l} V(r_a, t) = V(r_b, t) = 0 \\ V(r, 0) = T_i(r) \end{array} \right\} \tag{9.5}$$

A general solution to problem (9.5) was proposed by Carslaw and Jaeger in 1959, in terms of an important special function of an infinite series. For the solution of equation (9.5) we use a similarity function to integrate, in a single variable, the radial space and the time. The following change of function transforms equation (9.5) into a first kind Bessel differential equation of order 0:

$$\tau(r) = V(r, t)e^{\delta_T \alpha^2 t} \Rightarrow r^2 \frac{d^2 \tau}{dr^2} + r \frac{d\tau}{dr} + (\alpha r)^2 \tau = 0 \tag{9.6}$$

The general solution of equation (9.6) is:

$$\tau(r) = C J_0(\alpha r) + D Y_0(\alpha r) \tag{9.7}$$

where C and D are constants that can be deduced from the boundary conditions; both constants must have units of temperature [°C]; α is a parameter related to the roots of the cross product Bessel functions defined below. The auxiliary function $\tau(r)$ must have units of temperature;

thus the parameter α has units of $[m^{-1}]$ in order to have a dimensionless exponential. The two conditions in equation (9.7) imply that:

$$D = -C \frac{J_0(\alpha r_a)}{Y_0(\alpha r_a)} \Rightarrow J_0(\alpha r_a) Y_0(\alpha r_b) - J_0(\alpha r_b) Y_0(\alpha r_a) = 0 \tag{9.8}$$

The last expression in equation (9.8) is valid for any constant C . Consequently, there exists a function U_0 (Fig. 9.9) that we call the cross product Bessel function of order 0 (Abramowitz and Segun 1972), defined by:

$$U_0(\alpha r) = J_0(\alpha r) Y_0(\alpha r_b) - J_0(\alpha r_b) Y_0(\alpha r) \tag{9.9}$$

Note that always $U_0(\alpha_j r_b) = 0$ while $U_0(\alpha_j r_a) = 0$ if and only if α_j is a solution of equation (9.8) (Fig. 9.9). Given the nature of J_0 and Y_0 , the roots of (9.9) are infinite in number (Abramowitz and Segun 1972). Then each solution of (9.7) has the same form, differing only in the value of $\alpha_j (j = 1, \infty)$. Applying the principle of superposition and replacing the solutions in equation (9.7):

$$\tau_j(r) = -C_j \frac{U_0(\alpha_j r)}{Y_0(\alpha_j r_b)}; \quad j = 1, \infty \Rightarrow V(r, t) = \sum_{j=1}^{\infty} C_j \frac{U_0(\alpha_j r)}{Y_0(\alpha_j r_b)} e^{-\delta_T \alpha_j^2 t} \tag{9.10}$$

The constants C_j are calculated using the orthogonality properties of $U_0(\alpha r)$ (Carslaw and Jaeger 1959) and the initial condition of equation (9.5). Multiplying by U_0 and integrating both sides of the equation between r_a and r_b :

$$\begin{aligned} \int_{r_a}^{r_b} r T_i(r) U_0(\alpha_m r) dr &= \sum_{j=1}^{\infty} \frac{C_j}{Y_0(\alpha_j r_b)} \int_{r_a}^{r_b} r U_0(\alpha_j r) U_0(\alpha_m r) dr \\ &= \sum_{j=1}^{\infty} \frac{2\delta_{jm} C_j}{Y_0(\alpha_j r_b)} \frac{J_0^2(\alpha_j r_a) - J_0^2(\alpha_j r_b)}{\pi^2 \alpha_j^2 J_0^2(\alpha_j r_a)} = \frac{2C_j [J_0^2(\alpha_j r_a) - J_0^2(\alpha_j r_b)]}{Y_0(\alpha_j r_b) \pi^2 \alpha_j^2 J_0^2(\alpha_j r_a)} \end{aligned} \tag{9.11}$$

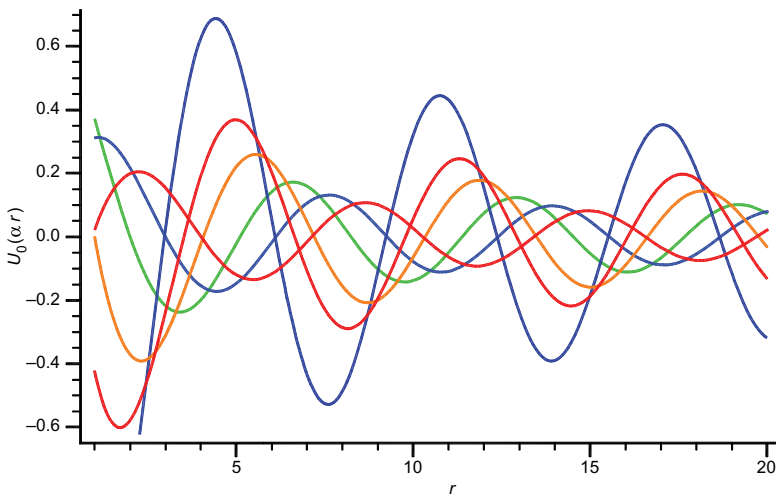


Figure 9.9. The function $U_0(\alpha r)$ showing some roots and the argument dependence of its roots position. The largest amplitude corresponds to the largest $\alpha = 4, 3, 2, 1, 0.5, 0.1$.

The final series is reduced to a single term (when $j = m$) and from this expression all the constants C_j can be deduced ($\forall r_a < r_b$):

$$C_j = \frac{\pi^2 \alpha_j^2 J_0^2(\alpha_j r_a) Y_0(\alpha_j r_b)}{2[J_0^2(\alpha_j r_a) - J_0^2(\alpha_j r_b)]} \cdot \int_{r_a}^{r_b} r T_i(r) U_0(\alpha_j r) dr \quad (9.12)$$

Equation (9.12) completes the solution of equation (9.5). It is important to note that the zeros of $U_0(\alpha r)$ are infinite, real and positive (Fig. 9.9). The numerical precision of the model depends closely on the exact calculation of all of them. Their numerical evaluation must be performed carefully in double precision (Suárez and Samaniego, 1999). Expression (9.12) also shows that the constants C_j have the same units as $T_i(r)$ [$^{\circ}\text{C}$]. Finally, the complete equation that models the radial conduction of heat from the cylindrical interior of a geothermal well to the surrounding formation is a coupled result formed by equations (9.4) and (9.10):

$$T(r, z, t) = T_a + \frac{T_b - T_a}{\text{Ln}(r_b/r_a)} \text{Ln}\left(\frac{r}{r_a}\right) + \sum_{j=1}^{\infty} C_j \frac{U_0(\alpha_j r)}{Y_0(\alpha_j r_b)} e^{-\delta_T \alpha_j^2 t} \quad (9.13)$$

It is simple to prove that equation (9.13) is the unique solution of the partial differential equation (9.1). The internal temperature T_a is a function of depth that can be obtained by direct well measurements. Different problems can be solved with model (9.13):

- Up to what radial distance does well drilling perturb the natural distribution of temperatures in the reservoir?
- What is the distribution and evolution of temperature in the region $r_a < r < r_b$?
- How is the temperature in the cement affected by the vertical flow of heat?
- How much heat is exchanged radially between the wellbore and the reservoir?

In the following section we illustrate the use of this model with two different applications to a well located in the Los Azufres, Mexico hydrothermal field. Codes were written in FORTRAN-77 (HeatWellR.for) and in *Mathematica* language (HeatWellM.nb) for the mathematical model (9.13). Both are free and available at the following internet address: <http://www.fismat.umich.mx/~marioc/>. The programs are applicable to a large variety of problems at different scales, including well completions.

First we examine the effect of heat transfer between the casing and the formation, calculating the temperature distribution inside the cement. A second group of applications is focused on the distribution of temperature in the surrounding rock and the radial heat loss effects, from the bottom hole to the wellhead.

9.2.1.2 Radial temperature distribution inside the cement

To illustrate the use of the model, the effect of possible heat transfer between the casing and the formation was examined. The cementing of a geothermal well fixes the pipe to the rock and provides zonal isolation of the wellbore to exclude other non-geothermal fluids present in the reservoir. Its primary objective is not the thermal isolation of the well. The thermal conductivity of cement is not constant and depends almost exclusively on its density (Nelson 1990). Usually light cement is used in hot deep areas, while more dense cement is used in cold superficial areas. Consequently, the radial heat loss is higher in shallow strata, because of a major conductivity gradient. We applied the model to the initial cementing conditions of well Az-01 of the Los Azufres, Mexico geothermal field. This cement has a thermal conductivity of 1.0–1.21 W/m/ $^{\circ}\text{C}$, a density of 1906 kg/m³, and specific heat of 879 J/kg/ $^{\circ}\text{C}$. The boundary temperatures inside the well come from several logs obtained in 1980. The cement joins the metallic pipe to the rock, between an internal radius $r_a = 0.17$ m and an external radius $r_b = 0.25$ m. The two boundary conditions are fixed and indicated in the vertical axis (Fig. 9.8). Figure 9.10a shows

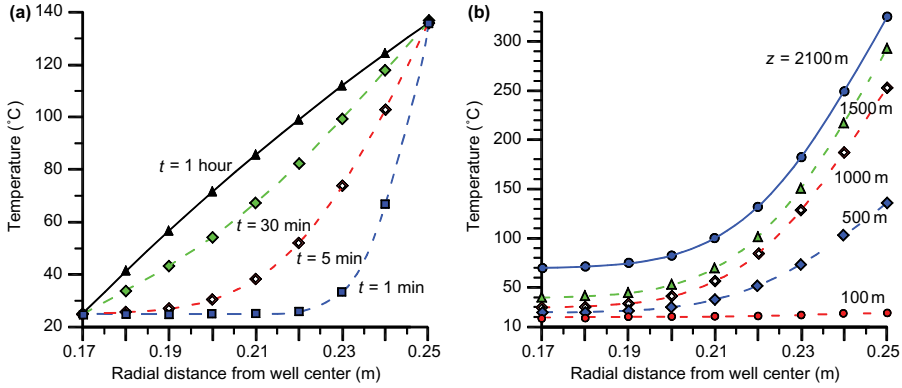


Figure 9.10. (a) Distribution of temperature inside the cement joining the pipe and the rock at 500 m depth for different times t after the geothermal fluid started to flow; (b) Radial distribution of temperature inside the cement at different depths z .

the distribution of temperature inside the cement at 500 m depth at different temperature after the geothermal fluid started to flow.

The evolution of T occurred between one minute and one hour, when T becomes stationary. Figure 9.10b shows the temperature distribution inside the cement at different depths, with geothermal fluid flowing for 30 minutes. A practical result of this analysis is the estimation of thermo-mechanical stresses generated by the high thermal gradients inside the cement. This effect linked to the presence of air bubbles, could explain the origin of cement failure and borehole collapse observed in some wells. For well Az-01, the thermal stress starts to be important at a depth of 500 m. The highest calculated temperature is 260°C at 2100 m. A second group of applications was focused on the distribution of temperature in the surrounding rock and the radial heat loss effects, that can be deduced from this distribution, from the bottom hole to the wellhead.

9.2.1.3 Vertical portion of the model

The internal and external temperatures, T_a and T_b respectively, can be linear functions of depth z satisfying the imposed boundary conditions in equation (9.1). Any piecewise linear function of z ($z_1 \leq z \leq z_2$), is also appropriate for this model. Figure 9.11 shows two vertical temperature profiles measured in well Az-01 of the Los Azufres, Mexico geothermal field.

Equating to zero the second partial derivative of $T(r, z, t)$ with respect to z in equation (9.13), we can deduce a general form of the vertical heat flow solution that satisfies the partial differential equation (9.1) with this imposed condition:

$$0 = \frac{\partial^2}{\partial z^2} T(r, z, t) = \frac{\partial^2 T_a}{\partial z^2} + f(r) \left(\frac{\partial^2 T_b}{\partial z^2} - \frac{\partial^2 T_a}{\partial z^2} \right) + 0 \quad (9.14)$$

$$\text{where: } f(r) = \frac{\ln(r/r_a)}{\ln(r_b/r_a)} = f_r$$

Therefore:

$$\frac{d^2 T_a}{dz^2} + f_r \frac{d^2 T_b}{dz^2} - f_r \frac{d^2 T_a}{dz^2} = 0 \Leftrightarrow \left(1 - \frac{1}{f_r} \right) \frac{d^2 T_a}{dz^2} = \frac{d^2 T_b}{dz^2}$$

$$\Leftrightarrow \frac{d^2}{dz^2} \left[\left(1 - \frac{1}{f_r} \right) T_a - T_b \right] = 0 \Leftrightarrow \left(1 - \frac{1}{f_r} \right) T_a - T_b = -A_1 z - A_2 \quad (9.15)$$

$$\Leftrightarrow T_b(z) = \left(1 - \frac{1}{f_r} \right) T_a(z) + A_1 z + A_2$$

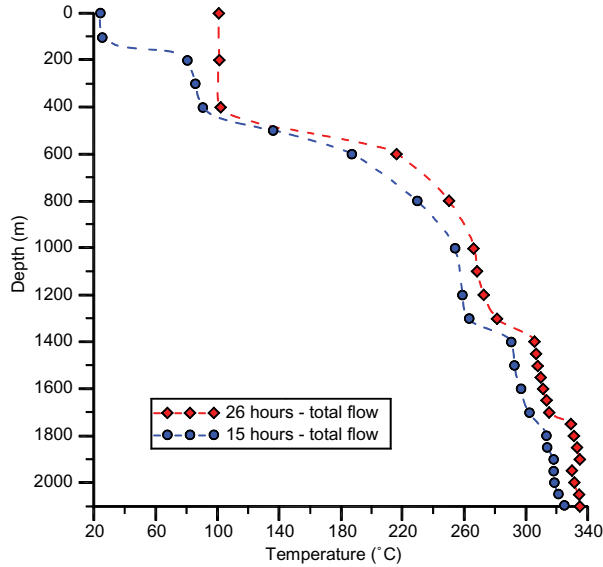


Figure 9.11. Vertical distributions of temperature measured in well Az-01 of the Los Azufres, Mexico geothermal reservoir.

where A_1 and A_2 are two integration constants that can be deduced from the boundary conditions of model (9.1):

$$\begin{aligned} \text{in } \partial\Omega: \quad & \{T_a(0) = T_{0a}, T_b(0) = T_{0b}, T_a(H) = T_{Ha}, T_b(H) = T_{Hb}\} \\ \Rightarrow \quad & A_1 = -\frac{\left(1 - \frac{1}{f_r}\right)(T_{Ha} - T_{0a}) - T_{Hb} + T_{0b}}{H}, \quad A_2 = T_{0b} - \left(1 - \frac{1}{f_r}\right)T_{0a} \end{aligned} \quad (9.16)$$

In the following application model (9.13) was used to calculate the evolution and distribution of temperature between well Az-01 and the surrounding reservoir rock until the thermal disturbance reaches a maximum distance of 11 m. We assume that this approximate value corresponds to the initial temperatures measured in February 1980, after the well was completed. Figure 9.12a shows the temperature evolution of the well, in the span of one year, in the interval [0.5, 10.5] m at 500 m depth. Figure 9.12b shows the temperature distribution in the same interval for $t = 30$ days at different depths. The following averaged parameters were used for the porous rock/water system: thermal conductivity 2.5 W/m/°C, density 2500 kg/m³, specific heat 1320 J/kg/°C, porosity 0.1.

9.2.1.4 The well-rock radial flow of heat

The radial component of the heat flow is calculated directly from its definition:

$$\begin{aligned} Q_r(r, t) &= -k_T \frac{\partial T}{\partial r} = -k_T \left(\frac{\partial U}{\partial r} + \frac{\partial V}{\partial r} \right) \\ &= -\frac{k_T}{r} \frac{(T_a - T_b)}{\ln(r_b/r_a)} - k_T \sum_{j=1}^{\infty} C_j \frac{U_1(\alpha_j r)}{Y_0(\alpha_j r_b)} e^{-\delta_T \alpha_j^2 t} \end{aligned} \quad (9.17)$$

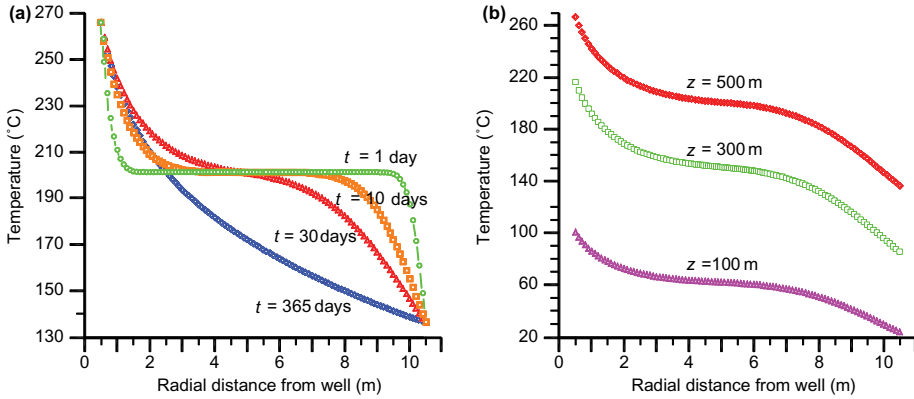


Figure 9.12. (a) Radial distribution of temperature in the interval [0, 11] m: (a) between the pipe and the rock formation; (b) at different depths, for $t = 30$ days.

where U_1 is the radial derivative of U_0 :

$$U_1(\alpha r) = \frac{d}{dr} U_0(\alpha r) = -\alpha J_1(\alpha r) Y_0(\alpha r_b) + \alpha J_0(\alpha r_b) Y_1(\alpha r) \tag{9.18}$$

because: $\frac{d}{dr} J_0(\alpha r) = -\alpha J_1(\alpha r)$, $\frac{d}{dr} Y_0(\alpha r) = -\alpha Y_1(\alpha r)$

Note that $Q_r(r, t)$ has one stationary component and another transitory component, and both have units of $[W/m^2]$. After some time has elapsed, the well-rock radial heat flow will reach steady state. For example, using the data obtained in section 2.1.8 for the thermal diffusivity of volcanic rocks, $6.62 \times 10^{-7} \leq \delta_T [m^2/s] \leq 1.12 \times 10^{-6}$, assuming that for $e^{-10} = 0.000045$ the terms in the infinite series become negligible and taking $\alpha \approx 1 \text{ m}^{-1}$, then $t \geq 1/\delta_T/1^2$. Thus, it will take between 10 and 18 days for the radial heat conduction to become stationary, after the flow of fluid inside the well has thermally stabilized. This result is just an approximated example; to obtain accurate values of steady-state conditions it is necessary to solve equation (9.17) with parameters corresponding to each particular case. The radial flow of heat in each interval Δz is calculated directly from equation (9.17). For example, at 500 m depth the stationary portion of the heat flow is $Q_S = 19.2 \text{ W/m}^2$.

9.3 THE MODEL OF AVDONIN

9.3.1 Transient radial flow of hot water in 1D

An important aspect of the management of geothermal reservoirs is the reinjection of cooled water into the reservoir or the injection of hot water into a colder aquifer. For isothermal water injection the pressure change in the aquifer can be estimated with the Theis solution given by equation (4.55). This classical solution shows that the pressure is proportional to the fluid dynamic viscosity. On the other hand, in section 2.3.4.4 we showed that water viscosity depends strongly on temperature (Fig. 2.19a). Thus, the validity of the Theis model (eq. 4.55) is seriously affected by this parameter. For the non-isothermal case, the injection of colder water into a geothermal reservoir is a moving boundary differential problem. The cold temperature front moves outwards from the injection well in a radial direction. A similar situation occurs if the injected water is hotter than the water of the aquifer and during hot fluid injection in oil reservoirs. In both cases heat transfer occurs at the boundary between the cold and the hot fluid and it is important to

estimate the temperature profile. The boundary between both fronts is a gradual transition zone dependent on the aquifer's thickness and its diffusivity which increases with time.

Many important transient problems, associated with flow to or from wellbores, are represented by the convection-diffusion equation (4.104a). This equation also appears in a wide range of heat and mass transport problems. Applications include geothermal production with reinjection, thermal energy storage in packed beds and permeable formations, thermal methods for oil recovery, miscible flooding, oil recovery by hot fluid injection and energy extraction from hot dry rocks using specific injection-extraction techniques.

Avdonin (1964) developed a classical model to solve the problem of finding the temperature field of a conductive plaque enclosed by two confining mineral beds, when injecting hot incompressible liquid through a unitary hole. Avdonin found an integral solution to the problem with the addition of longitudinal diffusion, while considering the horizontal thermal conductivity of the minerals below and above the plaque negligible. Fluid properties are held constant in Avdonin's solution. This problem is equivalent to the transmission of a temperature front during hot fluid injection into an aquifer with cold water; it involves radial flow of fluid and heat in a liquid-saturated porous media. Water at constant temperature is injected into a reservoir that is initially at a different temperature, and the flow occurs from the orifice of a well at zero radius to an outer boundary at some finite distance. The solution is one-dimensional in Cartesian coordinates.

Consider a horizontal porous layer of thickness b_a which is bounded above and below by relatively impermeable layers. A vertical wellbore of radius r_w intersects the porous layer. Fluid at temperature T_{in} is injected into the formation at a constant volume flow rate Q_w . The fluid is assumed incompressible with constant heat capacity. To progress uniformly into the porous medium displacing the previous pore fluid, the water and the porous solid are assumed to be in local thermal equilibrium. Fluid flow is approximately in steady-state and is transported by conduction and convection. The transient form of this process is represented by the following two-dimensional mathematical model (adapted from Avdonin 1964):

$$\begin{aligned}
 u(r, z, t) &= \frac{T - T_0}{T_l - T_0}; \quad k_{T_r} \frac{\partial^2 u}{\partial z^2} = \rho_r c_r \frac{\partial u}{\partial t}; \quad \text{for } z > 0 \quad \text{and} \quad t > 0 \\
 k_{T_s} \frac{\partial^2 u}{\partial r^2} - \frac{v_l \rho_l c_l}{r} \frac{\partial u}{\partial r} + \frac{2k_{T_r}}{b_a} \frac{\partial u}{\partial z} &= \rho_s c_s \frac{\partial u}{\partial t}; \quad z = 0, \quad r > 0 \quad \text{and} \quad t > 0 \\
 u(r, z, 0) = 0, \quad \forall r > 0; \quad u(r, 0, t) = 1, \quad \text{if } r = z = 0; \quad \lim_{z^2+r^2 \rightarrow \infty} u(r, z, t) &= 0
 \end{aligned} \tag{9.19}$$

In this model, $u(r, z, t)$ is the normalized temperature of the aquifer, T_0 is its initial temperature, T_l is the temperature of the fluid injected and $T(r, z, t)$ is the transitory temperature of the aquifer warmed up by the injection. k_{T_s} and k_{T_r} are the thermal conductivities of the solid rock and of the fluid-rock system, respectively; ρ_l , ρ_s and ρ_r , are densities, c_l , c_s and c_r are the specific heats of the liquid, rock and fluid-rock system, respectively; b_a is the aquifer thickness and v_l represents the velocity of the injected liquid. The units of both partial differential equations in model (9.19) are [J/s/m³/°C]. The solution of model (9.19) was constructed by Avdonin (1964) using a similarity method and the Laplace transform:

$$\begin{aligned}
 u(\xi, \tau) &= \frac{\xi}{\sqrt{\pi \tau}} \int_0^1 \exp \left[- \left(s \gamma \sqrt{\tau} - \frac{\xi}{2s\sqrt{\tau}} \right)^2 \right] \cdot \operatorname{erfc} \left[\frac{\alpha s^2 \sqrt{\tau}}{2\sqrt{1-s^2}} \right] \frac{ds}{s^2} \\
 \text{where: } \xi &= \frac{2r}{b_a}; \quad \tau = \frac{4k_{T_s} t}{c_s \rho_s b_a^2}; \quad \gamma = \frac{Q_w c_l \rho_l}{4k_{T_s}}; \quad \alpha = \sqrt{\frac{k_{T_r} c_r \rho_r}{k_{T_s} c_s \rho_s}}
 \end{aligned} \tag{9.20}$$

Note that Q_w [m³/s/m] is the volumetric constant rate of hot water injection per unit length. The integral in this model should be evaluated numerically. The following approximation of the

complementary error function (Abramowitz and Stegun 1972) is useful in the practical application of Avdonin's model:

$$\operatorname{erfc}(y) = [0.3480242x - 0.0958798x^2 + 0.7478556x^3]e^{-z^2} + \varepsilon(x) \quad (9.21)$$

where: $x = \frac{1}{1 + 0.47047y}$; and the error is: $|\varepsilon(x)| \leq 2.5 \times 10^{-5}$

equation (9.20) is a classic model that requires few experimental data to calculate the radial flow of hot/cold water in confined aquifers.

9.4 THE INVASION OF GEOTHERMAL BRINE IN OIL RESERVOIRS

The production of petroleum together with connate water is a common phenomenon in oil and gas reservoirs. This water is unusable, and its management is, in general, quite expensive. The magazine *Oilfield Review* (Arnold *et al.* 2004) reported that in the USA ten barrels (1.6 m³) of water are extracted for each barrel of oil. The world average is three barrels of water produced per barrel of oil. The disposal cost of this water is between 5 and 10 thousand million dollars in the USA, and approximately 40 thousand million dollars per year in the entire world. Even using the most advanced disposal techniques, water can represent 90% of the total extracted fluids, which can seriously affect the commercial feasibility of the oil field. As it currently has no commercial utility, this water should be reinjected into the formation to maintain reservoir pressure. Another possible future use of this water is treatment to make it usable for the water supply of the cities close to the oil field.

On the southern coast of the Gulf of Mexico, some oil reservoirs are associated with deep hot aquifers in such a way that their wells are invaded by geothermal brine, producing a variable mixture of oil and hot water. Although oil is extracted from wells completed in the upper boundary of the oil reservoir, the total volume of water produced equals or exceeds oil production in some cases. The handling of this additional hot water becomes a serious practical problem. The main goal of this example is the understanding of the water invasion mechanism and estimation of the critical volumetric rate in oil wells when the invasion of the geothermal brine starts.

A new numerical model (developed by Suárez *et al.* 2007) is required to predict the critical oil exploitation rate at which wells can be totally invaded by geothermal brine. The objective is to estimate the optimum mass rate for producing wells in order to minimize the production of water, or to achieve an oil-water mixture extraction where oil always prevails. For construction of the model, classic laws and equations are applied. Standard published formulae for both relative permeability and capillary pressure are used. We obtain a single non-linear partial differential equation (PDE) which depends only on water saturation, space and time. This PDE is a 3D generalization of the classical 1D Buckley-Leverett model. This new PDE is solved using finite elements. The numerical results reproduce the effect of water invasion: after some time elapses, the original oil volume diminishes abruptly, displacing the boundary of the water-oil contact and the transition zone in the vertical direction.

9.4.1 *Geothermal aquifers and oil reservoirs: Available data*

Geothermal areas related to hydrocarbon reservoirs exist in different parts of the world. The presence of interstitial hot water in the pores alters several parameters of the reservoir. Non-isothermal conditions affect the effective saturations and the relative permeability of both immiscible phases. The non-isothermal conditions, produced by the moving brine, affect the effective saturations of the phases (oil and brine) and the relative permeability of both immiscible phases. The relative permeability of oil is increased by the raised temperature due to the presence of geothermal water. This effect reduces the residual saturation of heavy oils. At the same time, the dynamic viscosities

of water and oil diminish, affecting the displacement of both fluids. The geothermal brine in the rock formation has quite different physical behavior compared to hydrocarbons. Water acts like a substance having a molecular weight larger than 18, because its inter-molecular forces are stronger than those in petroleum (Pedersen *et al.* 2006). Due to superficial tension, a great amount of oil is held in the pores of the rock in such a way that the mobility of the invasion water prevails. For heavier and more viscous oils, the mobility of water will dominate in the immiscible mixture of these fluids.

With the purpose of illustrating the model developed in this section, we consider the case of the Bellota-Jujo hydrocarbon complex, located in the southern coast of the Gulf of Mexico (Fig. 9.2). The Port Ceiba reservoir, which is part of this system, is associated with an geothermal aquifer. It contains hot brine and hydrocarbons and is a remarkable example of coupled processes of this type. The water in this oil field flows vertically from a aquifer located at 6000 m depth through conductive fractured zone and a fault, up to the oil bearing layers with the oil production wells located in a depth of 5000–6000 m. The water of the aquifer is geothermal brine at 150°C, with a density of 1150 kg/m³.

Port Ceiba’s wells are oil producers, but some are invaded by brine, producing a variable mixture of water and oil. Although the oil is extracted at the upper zone of the oil-water contact (OWC), the total volume of water produced equals or exceeds oil production. The effect of water invasion, together with oil extraction, produces a gradual decrease in the original volume of oil and a vertical displacement of the OWC. In this way the well receives more and more water until it becomes completely invaded. The handling of this water in the formation is a serious practical problem costing the company millions of dollars every year.

To study this problem, the simultaneous flow of two immiscible fluids, oil and water, in a three-dimensional porous medium is considered. The capillary pressure and relative permeability needed in this problem are discussed in sections 2.3.7 and 2.3.9. For construction of the partial differential equation it is assumed that:

- There is no transfer of mass between fluids.
- The law of Darcy is applicable to both phases.
- The system is hot but isothermal.
- Rock permeability k , densities ρ_w, ρ_o and viscosities μ_w, μ_o , are constants.

The available information from this oilfield is summarized in Table 9.7.

A fundamental formula relating capillary pressure and capillary height is:

$$p_c(S_w) = h_c \Delta\rho g, \quad \Delta\rho = \rho_w - \rho_o, \quad g = 9.8 \text{ m/s}^2 \quad (9.22)$$

where h_c is the height over the plane of capillary pressure $p_c = 0$. This surface is the boundary of the oil-water contact (COW) where $S_w \approx 1, S_o \approx 0$. The transition area is the location where

Table 9.7. Physical parameters from well PC-115 of the Puerto Ceiba oil reservoir (Suárez *et al.* 2007, Suárez and Samaniego 2007).

Average pressure	$p_a = 940 \text{ kg/cm}^2$
Bottom flowing pressure	$p_{wbf} = 700 \text{ kg/cm}^2$
Volumetric rate	$q_0 = 11000 \text{ Bce/D}$
Oil density	$\rho_o = 770 \text{ kg/m}^3$
Water density	$\rho_w = 1145 \text{ kg/m}^3$
Pressure difference Δp_w	$p_a - p_{wbf} = 240 \text{ kg/cm}^2$
Vertical distance between well and OWC	$\Delta h = 375 \text{ m}$
Brine temperature	$T = 150^\circ\text{C}$
Capillary pressure	$p_c(S_w) = p_o - p_w$
Saturations	$S_w + S_o = 1$

both phases coexist. The residual saturation of water S_{wi} is reached at the point of the reservoir where $S_o \approx 1$.

9.4.2 A general 3D mathematical model

Using a traditional cartesian reference system, the immiscible flow of oil and water takes place in a plane formed by an inclined fault, forming an angle θ between 0 and $\pi/2$ radians, with the vertical. The fluids enter the fault from the rock formation and from the aquifer at an initial constant velocity. To simplify the writing of equations we define the following variables:

$$\begin{aligned} \vec{v}_w &= \vec{w} && \text{velocity of water} \\ \vec{v}_o &= \vec{v} && \text{velocity of oil} \\ \vec{u} &= \vec{w} + \vec{v} && \text{velocity of both phases} \end{aligned} \tag{9.23}$$

that means: $\vec{u} = \begin{pmatrix} u_x \\ u_y \\ u_z \end{pmatrix} = \begin{pmatrix} w_x + v_x \\ w_y + v_y \\ w_z + v_z \end{pmatrix}$

Using the continuity equations for both phases:

$$\begin{aligned} \rho_w \vec{\nabla} \cdot \vec{w} + \varphi \rho_w \frac{\partial S_w}{\partial t} &= 0; \quad \rho_o \vec{\nabla} \cdot \vec{v} + \varphi \rho_o \frac{\partial S_o}{\partial t} = 0 \\ \Rightarrow \quad \vec{\nabla} \cdot \vec{w} + \varphi \frac{\partial S_w}{\partial t} &= 0; \quad \vec{\nabla} \cdot \vec{v} + \varphi \frac{\partial S_o}{\partial t} = 0 \\ \Rightarrow \quad \vec{\nabla} \cdot (\vec{w} + \vec{v}) + \varphi \frac{\partial}{\partial t} (S_w + S_o) &= 0 \\ \Rightarrow \quad \vec{\nabla} \cdot (\vec{w} + \vec{v}) = \vec{\nabla} \cdot \vec{u} = 0; & \text{ (because } S_w + S_o = 1) \\ \Rightarrow \quad \vec{u}(t_0) = \vec{u}_0 = \vec{u} \quad \Rightarrow \quad \vec{u} = \text{constant} \end{aligned} \tag{9.24}$$

The last equation results from both the continuity and the fact that the initial total velocity is constant. We assume that the rock permeability tensor is the constant matrix:

$$\mathbf{K} = \begin{pmatrix} k_x & 0 & 0 \\ 0 & k_y & 0 \\ 0 & 0 & k_z \end{pmatrix} \tag{9.25}$$

Darcy's law for each phase is:

$$\begin{aligned} \vec{w} &= -\frac{k_{rw}}{\mu_w} \mathbf{K} (\vec{\nabla} p_w - \rho_w \vec{g}) = -\lambda_w \begin{pmatrix} k_x \frac{\partial p_w}{\partial x} \\ k_y \frac{\partial p_w}{\partial y} \\ k_z \frac{\partial p_w}{\partial z} - k_z \rho_w g \cos \theta \end{pmatrix} = \begin{pmatrix} w_x \\ w_y \\ w_z \end{pmatrix} \\ \vec{v} &= -\frac{k_{ro}}{\mu_o} \mathbf{K} (\vec{\nabla} p_o - \rho_o \vec{g}) = -\lambda_o \begin{pmatrix} k_x \frac{\partial p_o}{\partial x} \\ k_y \frac{\partial p_o}{\partial y} \\ k_z \frac{\partial p_o}{\partial z} - k_z \rho_o g \cos \theta \end{pmatrix} = \begin{pmatrix} v_x \\ v_y \\ v_z \end{pmatrix} \end{aligned} \tag{9.26}$$

the mobilities are: $\lambda_w = \frac{k_{rw}}{\mu_w}$; $\lambda_o = \frac{k_{ro}}{\mu_o}$; $\frac{1}{\lambda} = \frac{1}{\lambda_w} + \frac{1}{\lambda_o}$

From these vectorial equations, the pressure gradients are deduced:

$$\vec{\nabla} p_w = \begin{pmatrix} \frac{\partial p_w}{\partial x} \\ \frac{\partial p_w}{\partial y} \\ \frac{\partial p_w}{\partial z} \end{pmatrix} = \begin{pmatrix} -\frac{w_x}{\lambda_w k_x} \\ -\frac{w_y}{\lambda_w k_y} \\ \frac{-w_z}{\lambda_w k_z} + \rho_w g \cos \theta \end{pmatrix}; \quad \vec{\nabla} p_o = \begin{pmatrix} \frac{\partial p_o}{\partial x} \\ \frac{\partial p_o}{\partial y} \\ \frac{\partial p_o}{\partial z} \end{pmatrix} = \begin{pmatrix} -\frac{v_x}{\lambda_o k_x} \\ -\frac{v_y}{\lambda_o k_y} \\ \frac{-v_z}{\lambda_o k_z} + \rho_o g \cos \theta \end{pmatrix} \quad (9.27)$$

Next, we define the fractional velocities:

$$\begin{aligned} u_x = w_x + v_x &\Rightarrow 1 = \frac{w_x}{u_x} + \frac{v_x}{u_x} = f_x + g_x \\ u_y = w_y + v_y &\Rightarrow 1 = \frac{w_y}{u_y} + \frac{v_y}{u_y} = f_y + g_y \\ u_z = w_z + v_z &\Rightarrow 1 = \frac{w_z}{u_z} + \frac{v_z}{u_z} = f_z + g_z \end{aligned} \quad (9.28)$$

or: $w_x = u_x f_x$; $w_y = u_y f_y$; $w_z = u_z f_z$

The capillary pressure gradient is the vector:

$$\vec{\nabla} p_C = \vec{\nabla} p_o - \vec{\nabla} p_w = \begin{pmatrix} \frac{\partial p_C}{\partial x} \\ \frac{\partial p_C}{\partial y} \\ \frac{\partial p_C}{\partial z} \end{pmatrix} = \begin{pmatrix} \frac{u_x f_x}{\lambda k_x} - \frac{u_x}{\lambda_o k_x} \\ \frac{u_y f_y}{\lambda k_y} - \frac{u_y}{\lambda_o k_y} \\ \frac{u_z f_z}{\lambda k_z} - \frac{u_z}{\lambda_o k_z} + (\rho_o - \rho_w)g \cos \theta \end{pmatrix} \quad (9.29)$$

After some algebraic manipulations:

$$\begin{aligned} f_x &= \frac{\lambda k_x}{u_x} \left[\frac{dp_c}{dS_w} \frac{\partial S_w}{\partial x} + \frac{u_x}{\lambda_o k_x} \right] = \frac{\lambda k_x}{u_x} \frac{dp_c}{dS_w} \frac{\partial S_w}{\partial x} + \frac{\lambda}{\lambda_o} \\ &\quad \leftarrow F_x \rightarrow \\ f_y &= \frac{\lambda k_y}{u_y} \left[\frac{dp_c}{dS_w} \frac{\partial S_w}{\partial y} + \frac{u_y}{\lambda_o k_y} \right] = \frac{\lambda k_y}{u_y} \frac{dp_c}{dS_w} \frac{\partial S_w}{\partial y} + \frac{\lambda}{\lambda_o} \\ &\quad \leftarrow F_y \rightarrow \\ f_z &= \frac{\lambda k_z}{u_z} \left[\frac{dp_c}{dS_w} \frac{\partial S_w}{\partial z} + \frac{u_z}{\lambda_o k_z} + (\rho_w - \rho_o)g \cos \theta \right] \\ &= \frac{\lambda k_z}{u_z} \frac{dp_c}{dS_w} \frac{\partial S_w}{\partial z} + \frac{\lambda k_z}{u_z} (\rho_w - \rho_o)g \cos \theta + \frac{\lambda}{\lambda_o} \\ &\quad \leftarrow F_z \rightarrow \quad \leftarrow G_z \rightarrow \\ \text{and: } \frac{\lambda}{\lambda_o} &= \frac{\lambda_w}{\lambda_w + \lambda_o} = \frac{1}{1 + \frac{\lambda_o}{\lambda_w}} = \left(1 + \frac{k_{ro}}{k_{rw}} \frac{\mu_w}{\mu_o} \right)^{-1} \end{aligned} \quad (9.30)$$

We define the following auxiliary functions:

$$\begin{aligned}
 F_x &= \frac{\lambda k_x}{u_x} \frac{dp_c}{dS_w}; & F_y &= \frac{\lambda k_y}{u_y} \frac{dp_c}{dS_w}; \\
 F_z &= \frac{\lambda k_z}{u_z} \frac{dp_c}{dS_w}; & G_z &= \frac{\lambda k_z}{u_z} (\rho_w - \rho_o) g \cos \theta
 \end{aligned}
 \tag{9.31}$$

The fractional velocities can be expressed as:

$$f_x = F_x \frac{\partial S_w}{\partial x} + \frac{\lambda}{\lambda_o}; \quad f_y = F_y \frac{\partial S_w}{\partial y} + \frac{\lambda}{\lambda_o}; \quad f_z = F_z \frac{\partial S_w}{\partial z} + G_z + \frac{\lambda}{\lambda_o}
 \tag{9.32}$$

Using these components in the equation of continuity for water (9.24), we deduce a final partial differential equation for water saturation, with the initial distribution and boundary conditions already described:

$$\begin{aligned}
 &\varphi \frac{\partial S_w}{\partial t} + \vec{\nabla} \cdot (\mathbf{F} \cdot \vec{\nabla} S_w) + \vec{G} \cdot \vec{\nabla} S_w = 0 \\
 &\mathbf{F}(S_w), \vec{G}(S_w), S_w(\vec{x}, t), \\
 &\vec{x} = (x, y, z) \in \Omega \subset \mathbb{R}^3, \quad \forall t > 0 \\
 &S_w(\vec{x}, 0) = S_w^0(\vec{x}) \\
 &S_w(\vec{x}, t) = 1 \quad \forall \vec{x} \in \Gamma_w \\
 &S_w(\vec{x}, t) = 0 \quad \forall \vec{x} \in \Gamma_o \\
 &\Gamma_o \cup \Gamma_w = \Gamma = \partial\Omega
 \end{aligned}
 \tag{9.33}$$

The auxiliary coefficients are of tensorial nature and are expressed as:

$$\mathbf{F} = \begin{pmatrix} u_x F_x & 0 & 0 \\ 0 & u_y F_y & 0 \\ 0 & 0 & u_z F_z \end{pmatrix}; \quad \vec{G} = \begin{pmatrix} u_x \frac{\partial}{\partial S_w} \left(\frac{\lambda}{\lambda_o} \right) \\ u_y \frac{\partial}{\partial S_w} \left(\frac{\lambda}{\lambda_o} \right) \\ u_z \frac{\partial}{\partial S_w} \left(\frac{\lambda}{\lambda_o} \right) + u_z \frac{\partial G_z}{\partial S_w} \end{pmatrix}
 \tag{9.34}$$

\mathbf{F} is the tensor of relative mobility of both phases $\left[\frac{\text{N}}{\text{Pa} \cdot \text{s}} \right]$

\vec{G} is the vector of mobility of both phases $\left[\frac{\text{m}}{\text{s}} \right]$

9.4.2.1 The one-dimensional Buckley-Leverett model

Using the functions defined in (9.34) and the general equation (9.33) in one dimension, let us say the vertical direction OZ, we obtain by direct substitution:

$$\begin{aligned}
 &\varphi \frac{\partial S_w}{\partial t} + K \frac{\partial}{\partial z} \left(\frac{k_{rw} k_{ro}}{k_{rw} \mu_o + k_{ro} \mu_w} \right) \frac{\partial p_c}{\partial z} + u_z \frac{\partial}{\partial z} \left(\frac{k_{rw}}{k_{rw} + k_{ro} \mu_w / \mu_o} \right) + \\
 &+ K \frac{\partial}{\partial z} \left(\frac{k_{rw} k_{ro}}{k_{rw} \mu_o + k_{ro} \mu_w} \right) (\rho_w - \rho_o) g \cos \theta = 0; \quad S_w = S_w(z, t)
 \end{aligned}
 \tag{9.35}$$

In 1942 Buckley and Leverett discovered that the displacement of oil by water cannot be solved by simplified, stationary solutions. They tackled this problem by neglecting the actions of capillary forces (Marle 1981). Assuming the same hypothesis, for $\theta = 0$ in previous equation, we obtain:

$$\varphi \frac{\partial S_w}{\partial t} + u_z \frac{\partial}{\partial z} \left(\frac{k_{rw}}{k_{rw} + k_{ro}} \frac{\mu_w}{\mu_o} \right) + K \frac{\partial}{\partial z} \left(\frac{k_{rw} k_{ro}}{k_{rw} \mu_o + k_{ro} \mu_w} \right) (\rho_w - \rho_o) g = 0 \quad (9.36)$$

With some algebra, we can simplify this equation:

$$\begin{aligned} \varphi \frac{\partial S_w}{\partial t} + u_z \frac{\partial}{\partial z} \left(\frac{\frac{\mu_o}{k_{ro}}}{\frac{\mu_w}{k_{rw}} + \frac{\mu_o}{k_{ro}}} \right) + \frac{\partial}{\partial z} \left(\frac{K(\rho_w - \rho_o)g}{\frac{\mu_w}{k_{rw}} + \frac{\mu_o}{k_{ro}}} \right) &= 0 \\ \Rightarrow \varphi \frac{\partial S_w}{\partial t} + u_z \frac{\partial}{\partial z} \left(\frac{\frac{\mu_o}{k_{ro}} + \frac{K(\rho_w - \rho_o)g}{u_z}}{\frac{\mu_w}{k_{rw}} + \frac{\mu_o}{k_{ro}}} \right) &= 0 \end{aligned} \quad (9.37)$$

Defining a special function $\Phi(S_w)$ we finally obtain:

$$\text{with: } \Phi(S_w) = \frac{\frac{\mu_o}{k_{ro}} + \frac{K(\rho_w - \rho_o)g}{u_z}}{\frac{\mu_w}{k_{rw}} + \frac{\mu_o}{k_{ro}}} \quad \Rightarrow \quad \boxed{\varphi \frac{\partial S_w}{\partial t} + u_z \frac{d\Phi}{dS_w} \frac{\partial S_w}{\partial z} = 0} \quad (9.38)$$

This equation is the classic form of the Buckley-Leverett (1942) model with non-stationary solutions for the displacement of oil by water in one dimension, when the action of capillary forces is neglected. Therefore, equation (9.38) is a special case of the general model represented by equation (9.33).

9.4.3 Formulation and numerical solution using the finite element method

The model represented by equation (9.33) is non-linear (see section 5.2), but it only depends on water saturation. We can formulate this model using finite elements (Zienkiewicz and Taylor 1991, Reddy and Gartling 2001). Multiplying both sides of equation (9.33) by a test-function w_j of an appropriate functional space E_T defined over the solution domain $\Omega \subset \mathbb{R}^3$ and integrating:

$$\int_{\Omega} w_j \phi \frac{\partial S_w}{\partial t} d\Omega = - \int_{\Omega} w_j \vec{\nabla} \cdot (\mathbf{F} \cdot \vec{\nabla} S_w) d\Omega - \int_{\Omega} w_j \vec{G} \cdot \vec{\nabla} S_w d\Omega \quad (9.39)$$

Let S be an approximated function of $S_w \approx S$ with the residual $R = S_w - S$. Substituting this relationship in equation (9.39), assuming that the terms containing R are zero (Ritz-Galerkin hypothesis) we obtain:

$$\begin{aligned} \int_{\Omega} \phi w_j \frac{\partial S}{\partial t} d\Omega &= - \int_{\Omega} w_j \vec{\nabla} \cdot \vec{H} d\Omega - \int_{\Omega} w_j \vec{G} \cdot \vec{\nabla} S d\Omega \\ \Leftrightarrow \int_{\Omega} w_j f(R) d\Omega &= 0, \quad \forall w_j \in E_T(\Omega), \quad \vec{H} = \mathbf{F} \cdot \vec{\nabla} S = \begin{pmatrix} F_x \partial_x S \\ F_y \partial_y S \\ F_z \partial_z S \end{pmatrix} \end{aligned} \quad (9.40)$$

We can transform one of the integrals:

$$\begin{aligned}
& \text{with: } \frac{\partial}{\partial x_i}(w_j H_i) = \frac{\partial w_j}{\partial x_i} H_i + w_j \frac{\partial H_i}{\partial x_i}, \quad x_i = x, y, z \\
& \Rightarrow \int_{\Omega} w_j \vec{\nabla} \cdot \vec{H} \, d\Omega = \int_{\Omega} \left(w_j \frac{\partial H_x}{\partial x} + w_j \frac{\partial H_y}{\partial y} + w_j \frac{\partial H_z}{\partial z} \right) d\Omega \\
& = \int_{\Omega} \left(\frac{\partial}{\partial x}(w_j H_x) + \frac{\partial}{\partial y}(w_j H_y) + \frac{\partial}{\partial z}(w_j H_z) \right) d\Omega \\
& \quad - \int_{\Omega} \left(\frac{\partial w_j}{\partial x} H_x + \frac{\partial w_j}{\partial y} H_y + \frac{\partial w_j}{\partial z} H_z \right) d\Omega \\
& \Rightarrow \int_{\Omega} w_j \vec{\nabla} \cdot \vec{H} \, d\Omega = \int_{\Omega} \vec{\nabla} \cdot (w_j \vec{H}) \, d\Omega - \int_{\Omega} \vec{\nabla} w_j \cdot \vec{H} \, d\Omega
\end{aligned} \tag{9.41}$$

Using the divergence theorem in the second integral:

$$\int_{\Omega} w_j \vec{\nabla} \cdot \vec{H} \, d\Omega = \int_{\Gamma} w_j \vec{H} \cdot \vec{n} \, d\Gamma - \int_{\Omega} \vec{\nabla} w_j \cdot \vec{H} \, d\Omega \tag{9.42}$$

This relationship leads to a transformation of the equation (9.40) to obtain the weak form of the differential original model. As a result, the weak formulation of equation (9.33) is:

$$\int_{\Omega} \phi w_j \frac{\partial S}{\partial t} \, d\Omega = \int_{\Omega} \vec{\nabla} w_j \cdot \vec{H} \, d\Omega - \int_{\Gamma} w_j \vec{H} \cdot \vec{n} \, d\Gamma - \int_{\Omega} w_j \vec{G} \cdot \vec{\nabla} S \, d\Omega \tag{9.43}$$

This formula can also be deduced by direct application of the general Green theorem to equation (9.39). We define an interpolation function of the form:

$$S(x, y, z, t) = \sum_{i=1}^N s_i(t) w_i(x, y, z) \tag{9.44}$$

where $\{s_i(t), i = 1, N\}$ are N time-dependent unknown coefficients and w_i are N test functions in the same space E_T . Substituting this interpolation in all the terms of equation (9.43):

$$\begin{aligned}
& \varphi \sum_{i=1}^N \frac{ds_i}{dt} \int_{\Omega} w_i w_j \, d\Omega = \sum_{i=1}^N s_i \int_{\Omega} \mathbf{F} \cdot \vec{\nabla} w_i \cdot \vec{\nabla} w_j \, d\Omega \\
& \quad - \sum_{i=1}^N s_i \int_{\Gamma} w_j \mathbf{F} \cdot \vec{\nabla} w_i \cdot \vec{n} \, d\Gamma - \sum_{i=1}^N s_i \int_{\Omega} w_j \vec{G} \cdot \vec{\nabla} w_i \, d\Omega \\
& \Rightarrow \varphi \sum_{i=1}^N M_{ij} \frac{ds_i}{dt} = \sum_{i=1}^N N_{ij} s_i - \sum_{i=1}^N L_{ij} s_i - \sum_{i=1}^N G_{ij} s_i
\end{aligned} \tag{9.45}$$

where the matrices are all symmetrical and defined as follows:

$$\begin{aligned}
 M_{ij} &= \int_{\Omega} w_i w_j d\Omega, & N_{ij} &= \int_{\Omega} \mathbf{F} \cdot \vec{\nabla} w_i \cdot \vec{\nabla} w_j d\Omega, & L_{ij} &= \int_{\Gamma} w_j \mathbf{F} \cdot \vec{\nabla} w_i \cdot \vec{n} d\Gamma \\
 G_{ij} &= \int_{\Omega} w_j \vec{G} \cdot \vec{\nabla} w_i d\Omega, & \text{and: } K_{ij} &= N_{ij} - L_{ij} - G_{ij}
 \end{aligned} \tag{9.46}$$

These formulae allow the construction of an ordinary differential system that approximates the model (9.33) by the finite element method (q_{α} is a source term):

$$\mathbf{M} \cdot \frac{d\vec{S}}{dt} + \mathbf{K} \cdot \vec{S} = \vec{Q}; \quad \text{where: } Q_j = \int_{\Omega} q_{\alpha} w_j, \quad \text{and: } \vec{S} = (s_1, s_2, \dots, s_N) \tag{9.47}$$

After solving this system by classical techniques (Reddy and Gartling 2001) we obtain an approximate numerical solution of the model representing the water saturation (see chapter 5 for further details).

9.4.4 Numerical simulation of brine invasion

To illustrate the use of our model, we made numeric simulations in two dimensions of a hypothetical oil extraction zone presenting brine invasion. We used data from well PC-115 (Table 9.7) located in Port Ceiba reservoir of the Bellota-Jujo complex (Fig. 9.2). We assume the fault as a porous medium of very high permeability ($\sim 10^3$ Darcy), located at the center of the production region. The lateral boundaries are at constant pressure and zero flow. The changes only occur in the vertical direction. To represent in a simple form the geometry of the area of interest, of dimensions $6000 \times 800 \text{ m}^2$, a non-structured mesh (Fig. 9.13a) of 552 triangular elements and 2640 degrees of freedom was constructed. The interpolants used are quadratic Lagrange polynomials. To perform the computations we used the COMSOL-Multiphysics software (COMSOL 2008a).

The oil-water contact (OWC) boundary is located at $Y = 0 \text{ m}$ or 6000 m below the surface of the oil field. The initial condition at $t = 0$ is $S_w = 0$ in the porous medium column and $S_w = 1$ below the OWC, in the aquifer. The zone was subjected to various production rates in the interval (3000, 8000) B_o/day until brine invasion was observed. Several permeability values were tested; all were different, but always approximately 10^3 Darcy. For the parameters and data already described, we obtained a critical constant volumetric rate equal to $7057 \text{ B}_o/\text{day}$ for which the brine invasion is massive. This invasion occurs abruptly after a transition region was established, where $S_w, S_o \neq 0$ and $S_w + S_o = 1$ Figure 9.14 shows the evolution of oil saturation at one representative point. Figures 9.13b–d are two-dimensional surfaces of the simulated area, illustrating the evolution of both distributions $S_o = S_{nw}$ (non wetting phase) and S_w (wetting phase) in the whole modeled region.

The general conclusion of this example is that the presence of water in hydrocarbon reservoirs is a serious practical problem. On global scale, the estimate of the current cost of brine handling oscillates between 5 and 50 cents (world average in US dollars) per barrel of water and ascends to \$4 US per barrel of petroleum in wells producing oil with 80% water content. To deal with this problem the mathematical model herein introduced (Suárez *et al.* 2007) permits the approximate representation of brine invasion in wells producing oil. This numerical model is useful to estimate the critical oil extraction rate at which the water invasion becomes massive. We have applied the model to data from a well located in a high permeability zone in the Gulf of Mexico. Once the geothermal brine entered the production zone, and for the critical oil rate of $7057 \text{ B}_o/\text{day}$, an abrupt oil saturation depression of 80% is obtained in a lapse of 6 days after 52 days of continuous production.

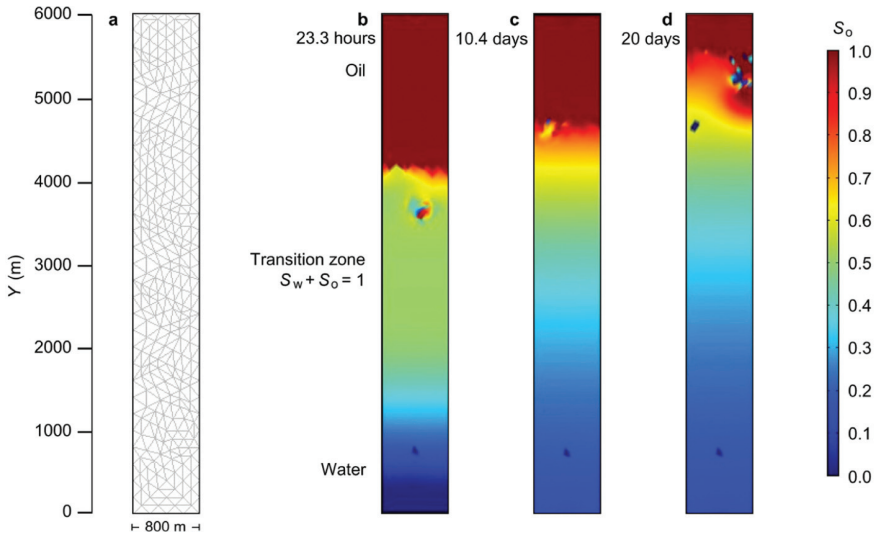


Figure 9.13. (a) Non-structured mesh, with 552 finite elements, of the simulated porous medium; oil (S_o) and brine saturation (S_w). Simulation times of 23.3 hours (b); 10.4 days (c) and 20 days (d), after a transitional zone was established.

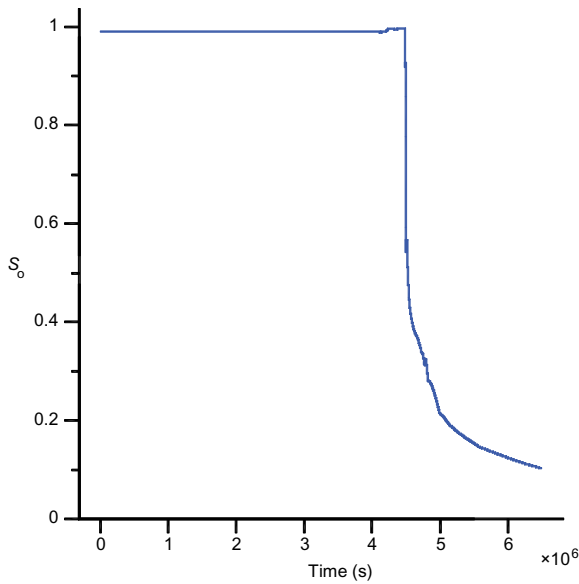


Figure 9.14. Oil saturation affected by brine invasion at the point (150, 5500) m, after 52 days of production.

9.5 MODELING SUBMARINE GEOTHERMAL SYSTEMS

Submarine geothermal reservoirs have a practically infinite energy potential. This deep submarine energy source is related to the existence of hydrothermal vents emerging in many places along the oceanic spreading centers between tectonic plates (Fig. 9.15). These systems have a total length

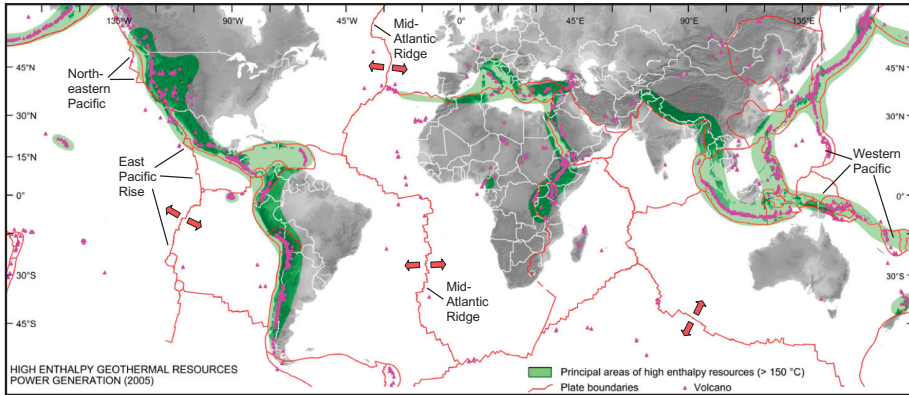


Figure 9.15. Simplified plate tectonical world map indicating principal mid-ocean ridges as sites for marine geothermal resources and areas with high enthalpy geothermal resources located on continents (modified from Chandrasekharam and Bundschuh 2008).

of about 65,000 km in the Earth's oceanic crust (Marshall 1979). Some are located at more than 2000 m below sea level, while other shallow submarine geothermal fields are related to faults and fractures near continental platforms and are found at depths of between one and 50 m (Suárez Bosché *et al.* 2000, Suárez and Samaniego 2005, 2006). In this section we will present examples of the Gulf of California, Mexico.

The specific chemical characteristics of the submarine hydrothermal deep fluids indicate that water-oceanic rock interactions occur at high temperature and pressure conditions. Hydrothermal fluid at 350–400°C exits the seafloor through natural chimneys (Fig. 9.16) at velocities of about 0.70 to 2.36 m/s and mixes with seawater at 4°C (Humphris *et al.* 1995). The thermal fluxes measured at some chimneys range from 1 to 93 MW_T (thermal megawatts) with an average value for a single orifice of about 8 MW_T. Some heat fluxes of about 1000 MW_T have been detected in some vent fields. In the following sections (9.5.1 and 9.5.2), we present models, descriptions, and preliminary estimations of the amount of geothermal energy contained in some submarine systems that is escaping through fissures in the ocean floor.

9.5.1 Brief description of submarine geothermal systems

Hydrothermal circulation at the deep ridges on the seafloor (ocean-spreading centers) is a fundamental complex process controlling mass and energy transfer from the interior of the Earth through the oceanic lithosphere, to the hydrosphere and the atmosphere. The properties and behavior of such a complex system cannot be thoroughly explained by the isolated understanding of its individual components, but it is necessary to consider the interactions of all their parts. Submarine hydrothermal interactions influence the composition of the oceanic crust and the chemistry of the ocean. The circulating fluid is chemically altered due to processes occurring during its passage through the oceanic crust at elevated temperatures and pressures. This mechanism produces hydrothermal vent fields, which support unique and diverse biological communities, from microbial populations to worms, and crabs, that link the transfer of the chemical energy of dissolved inorganic chemical species to the production of organic carbon, (Corliss and Ballard, 1977, Humphris *et al.* 1995). The eventual transfer of gases liberated by hydrothermal activity from the ocean to the atmosphere, extend its influence far beyond the oceans themselves. The understanding of this mass and energy flows between these complex geological, chemical, geophysical and biological subsystems requires the development of integrated numerical models that take account of these interactions.

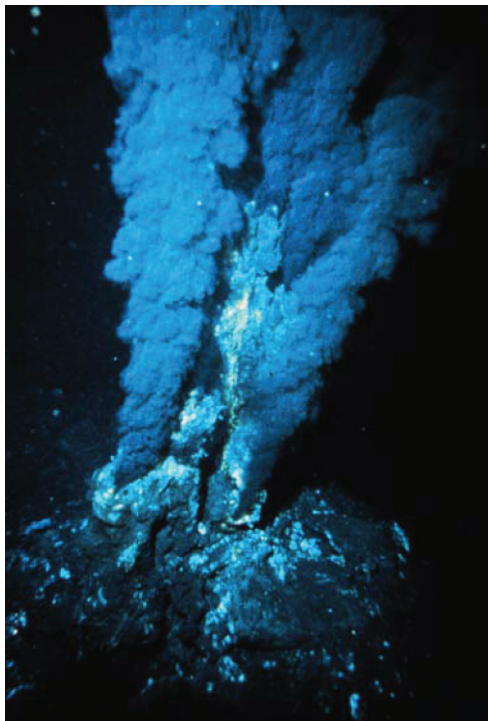


Figure 9.16. A natural chimney or black smoker discharging fluids along the ocean-spreading center, in the Atlantic Ocean.

9.5.1.1 *Geothermal discharge chimneys and plumes*

Most of the known hydrothermal vents in the ocean are found along the mid-ocean ridge systems (MORS) located in the deep sea (Damm 1995). The crest of the MORS is the place where a new lithosphere is created through igneous activity. Such magmatic processes provide the energy to drive hydrothermal circulation of seawater through the oceanic crust, producing rock-seawater interactions at temperatures of between 200 and 400°C, (Grijalva 1986, Mercado 1990, Damm 1995). The resulting mechanism gives rise to venting at seafloor depths, of between 840 and 3600 m and contributes considerably to the global balance of the total Earth's heat (Fornari and Embley 1995). This venting is associated with fissures located directly above magma injection zones. The observed vent fields are typically tens of meters in diameter, ranging between 4 to 800 m² in area, (Hessler and Kaharl 1995). The heat input from these systems affects the mid-depth circulation of the oceans.

Many vent fields have vertical structures forming chimneys built of materials which precipitate from the heated vent fluid as it mixes with seawater (Fig. 9.16). Black smoker chimney walls are formed as hydrothermal fluid mixes turbulently with seawater. This occurs because it is the subsequent dominance of horizontal transport across the wall, mineral dissolution and precipitation within pore spaces of the wall, and deposition of Cu-Fe sulfide along the inside of the flow conduit, (Fornari and Embley 1995). Initial models describing the formation of black smoker chimneys were based on petrologic studies of samples recovered from deposits venting 350°C fluid at 21°N on the East Pacific Rise (Kingston 1995).

Hydrothermal plumes are created by the thermal and chemical input from fluid escaping submarine hot spring systems into the deep sea. The plumes' active discharge orifices cover only a minute percentage of the seafloor, but there is an enormous range of temporal and spatial scales involved in these events. Baker *et al.* (1995) found that the hydrothermal fluids discharged from

vents, form plumes that are rapidly diluted in the seawater and the mixture rises hundreds of meters and spreads laterally from tens to thousands of kilometers.

9.5.1.2 Models to compute the heat flux related to the plumes

Plumes formed by mixing of seafloor vent fluids and ambient seawater are easily detectable using physical and chemical tracers. This is why the careful study of plumes is a useful tool for hydrothermal exploration. Many measurements have been made to calculate the vertical heat flow in a buoyant plume. Turner (1973) established a useful equation to estimate the maximum height Z_M of rise of a plume as a function of the buoyancy flux F_0 and frequency N_B :

$$Z_M = 5 \left(\frac{F_0}{\pi} \right)^{\frac{1}{4}} N_B^{-\frac{3}{4}} \tag{9.48}$$

The variable N_B is the Brunt-Väisälä buoyancy frequency. Figures 9.17a,b correspond to a plume from a black smoker with a heat flux of about 60 MW_T, venting into an ocean with a constant density gradient given by the following equation (Lupton 1995):

$$N_B^2 = -\frac{g}{\rho_0} \frac{d\rho}{dz} = 1.5 \times 10^{-6} \text{s}^{-2} \tag{9.49}$$

where $g = 9.81 \text{ m/s}^2$ is the acceleration due to gravity, and $\rho_0 \approx 10^3 \text{ kg/m}^3$ is the average local density; therefore the vertical density gradient is $d\rho/dz \approx -1.53 \times 10^{-4} \text{ kg/m}^4$. From measurements reported by Lupton (1995), we obtain $F_0 = 0.174 \text{ m}^4/\text{s}^3$. Using $N_B = 1.224745 \times 10^{-3}/\text{s}$ as the value of the frequency, it is possible to estimate the maximum height of the plume: $Z_M \approx 370 \text{ m}$ above seafloor. According to these models, a plume of 750 m height will correspond to a heat flux of about 1000 MW_T. Using the available data we have identified a direct relationship between the heat flux $Q(Z)$ and $Z_M(F_0)$ (Suárez and Samaniego 2005).

$$Q(Z) = 0.0576591 Z - 0.000173826 Z^2 + 3.33284 \times 10^{-9} Z^4 \tag{9.50}$$

Other thermal fluxes measured in black smokers range from 1 to 93 MW_T, with an accepted average value for a single orifice of about 8 MW_T, (Lupton 1995, Bemis *et al.* 1993). In 1986 a mega-plume was discovered in the region of the Juan de Fuca ridge in the Pacific Ocean

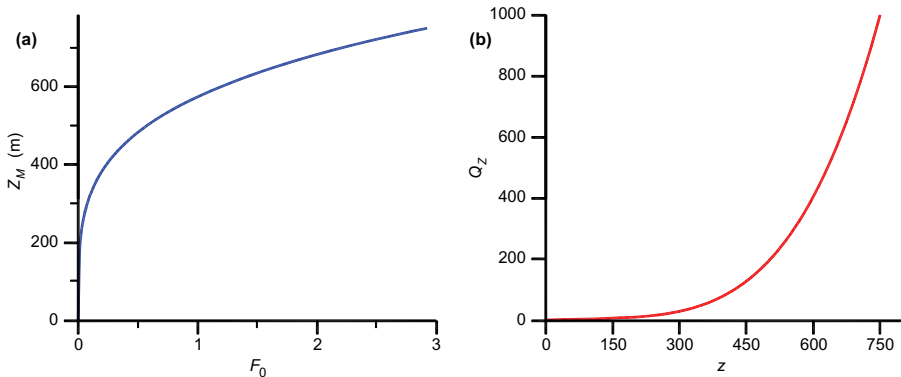


Figure 9.17. (a) Maximum height Z_M of a plume as a function of the buoyancy flux F_0 in the interval $[0, 3] \text{ m}^4/\text{s}^3$; (b) Total heat flux $Q(Z)$ in MW_T as a function of the height of a plume in the interval $[0, 750] \text{ m}$.

(JFR) with a horizontal extension of 20 km, a thickness of 600 m and of excess heat of about 10^{11} MJ. Bemis *et al.* (1993) collected data at different locations close to a vent source on the JFR and calculated the vertical heat flow in a buoyant plume. Their results approximately agree with values obtained with our model (Suárez and Samaniego 2005). The weak dependence of Z_M on the effective heat flux (eq. 9.50) indicates that the megaplume observed in the JFR region in 1986, was able to affect the water column up to 1000 m above the seafloor. Other megaplumes have since been observed, supporting the conclusion that the total convective heat outflowing from the ocean is discharged in the form of both continuous steady-state venting and megaplumes. Alt (1995) estimated that submarine hydrothermal discharges remove about 30% of the heat lost from the whole oceanic crust. Stein *et al.* (1995) predicted an average hydrothermal heat loss in some places of the oceanic crust of about $1.5 \text{ W}_T/\text{m}^2$. The same parameter predicted just for the ridges is between 2 and 100 MW_T/km (per unit ridge length); the former value is for a slow flow ridge while the latter corresponds to a plume with a heat content of 1000 MW_T .

9.5.1.3 *Modeling the radial heat conduction in chimneys*

The model developed for geothermal wells in section 9.2 and represented by equation (9.13), can also be used to compute the radial conduction of heat in submarine chimneys. Assuming that the chimney is approximately cylindrical, it is only necessary to employ the appropriate initial and boundary conditions. An application of this model to a submarine chimney with conduction and convection was published recently (Suárez and Samaniego 2005).

9.5.2 *Submarine geothermal potential*

Using the available information extracted from different sources, it is possible to make preliminary estimations of the volumetric submarine geothermal potential. Simple mathematical models, traditionally employed for terrestrial reservoirs may be used to estimate the capacity of submarine reservoirs (Suárez 2000). We applied this volumetric technique to estimate the available energy in two different systems located in the Gulf of California, Mexico.

9.5.2.1 *Submarine potential of the Gulf of California*

Some submarine thermal areas are located offshore from the port of Ensenada, Baja California, where temperatures of up to 102°C have been measured at 20 m depth, less than 100 m from the coast. In addition, a submarine geothermal reservoir is located in the Wagner Depression (Fig. 9.18) at less than 30 m depth. Both geothermal zones are accessible to exploitation by installing offshore platforms, similar to those used by the oil industry. Rough estimates indicate that the geothermal potential of this submarine zone could be 100 times larger than that of the Cerro Prieto, Mexico reservoir (Grijalva 1986, Mercado 1990).

In the following equations we use the parameters defined in previous sections: φ is the porosity, ρ is density, S_j is saturation ($j = l$ for liquid, $j = v$ for vapor), and h_f is the specific fluid enthalpy. The coefficients c_w and c_r are water and rock isobaric heat capacities respectively. T is temperature in $^\circ\text{C}$ and V_r is the solid rock volume in m^3 . For the fluid energy density:

$$\begin{aligned} \text{volumetric internal fluid energy: } E_{\text{fluid}} &= \frac{\text{fluid energy}}{\text{fluid volume}} \\ \text{single phase fluid: } E_{\text{fluid}} &= \varphi \rho_f h_f \quad \left[\frac{\text{kJ}}{\text{m}^3} \right] \\ \text{two-phase fluid: } E_{\text{fluid}} &= \varphi (S_l \rho_l h_l + S_v \rho_v h_v) \quad \left[\frac{\text{kJ}}{\text{m}^3} \right] \end{aligned} \quad (9.51)$$

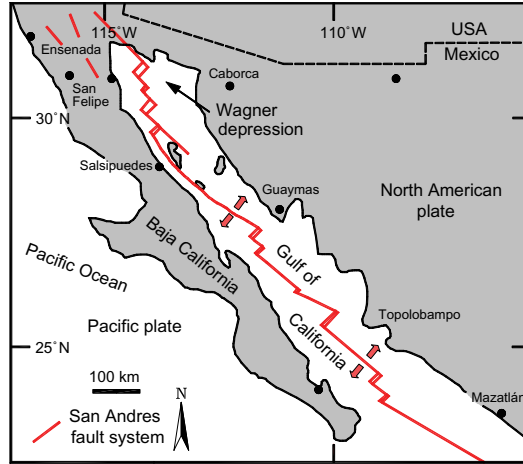


Figure 9.18. The Gulf of California and its tectonic setting, Mexico.

For the rock energy density:

$$E_{\text{rock}} = \frac{\text{rock energy}}{\text{solid volume}} = (1 - \varphi) \rho_r c_r T_r \left[\frac{\text{kJ}}{\text{m}^3} \right] \quad (9.52)$$

The total initial energy in the submarine geothermal reservoir is:

$$E_0 = (E_{\text{fluid}} + E_{\text{rock}}) \cdot V_B \quad [\text{kJ}] \quad (9.53)$$

It is assumed that the initial energy in place coincides with a liquid phase state. We suppose that the final energy, after exploitation and heat and fluid extraction, corresponds to the thermodynamic state at some lower temperature. The real value of this hypothetical final energy should be estimated and adapted for every specific case. Assuming constant rock parameters, the algebraic difference between the final and the initial state is equal to the available energy, given by the following formulae (Suárez and Samaniego 2005):

$$\begin{aligned} \text{For the rock: } \Delta E_{\text{rock}}]_{\text{initial}}^{\text{final}} &\approx (1 - \varphi) \rho_r C_r (T_{\text{initial}} - T_{\text{final}}) \\ \text{For the fluid: } \Delta E_{\text{fluid}}]_{\text{initial}}^{\text{final}} &\approx (\varphi \rho_f h_f)]_{\text{liquid}}^{\text{initial}} - (\varphi \rho_f h_f)]_{\text{2-phase}}^{\text{final}} \\ \text{total energy available: } \Delta E_{\text{total}} &= \Delta E_{\text{rock}} + \Delta E_{\text{fluid}} \end{aligned} \quad (9.54)$$

To compute the available energy that can be used directly in the form of heat (MW_T), over a given period, we need the time-coefficient C_E , defined as the inverse of the number of seconds in a sidereal year (365.25 days) multiplied by the number of years of energy extraction:

$$C_E = \frac{1}{365.25 \times 86400 \times t_E} = \frac{1.0 \times 10^{-6}}{31.5576 t_E} = \frac{3.16881}{t_E} \times 10^{-8} \text{ [s}^{-1}] \quad (9.55)$$

where t_E is the payoff time of the investment realized for the hypothetical submarine project. To calculate the geothermal electric power of the reservoir it is necessary to multiply the available

energy from equation (9.54), by the coefficient C_E given by equation (9.55) and by the conversion factor f_E of recoverable electric energy (Suárez 2000):

$$G_P = f_E \cdot C_E \Delta E_{\text{Total}} \quad [\text{MW}_e] \quad (9.56)$$

For the application of this model, we considered a density average of volcanic rock of 2500 kg/m³, porosity of 10%, rock specific heat c_r of 1000 J/kg/°C and a fixed rock volume of one cubic kilometer (1.0×10^9 m³). This is because the volume of porous hot rock is the main unknown in this type of system. Table 9.8 summarizes the available data and the results.

The thermodynamic properties of Punta Banda were estimated using a linear model constructed from the available data (z is the sea depth in meters):

$$p(z) = 1.0 + 0.1 z(\text{bar}); \quad T(z) = 97.082 + 0.246 z(^{\circ}\text{C}) \quad (9.57)$$

The results shown in Table 9.8 are restricted to the submarine region defined by the following coordinates: latitudes between 32°N and 23°N; longitudes between 117°W and 106°W (Fig. 9.18). The units of the geothermal potential are MW_T per km³ of oceanic rock in the vicinity of the hydrothermal vents. Considering that only 1% of the thermal submarine energy may be transformed into electricity ($f_E = 0.01$), during a payoff time $t_E = 30$ years, and using the available data, the minimum geothermal electric power that may be obtained from these submarine resources is approximately 26,100 MW_e.

9.5.2.2 *Using the boundary element method to estimate the initial conditions of submarine geothermal systems*

Because of the complexity of submarine reservoirs and the scarcity of real field data, the modeling and simulation of such systems is cumbersome and uncertain. The boundary element method (BEM) introduced in chapter 5 (section 5.4) is a numerical technique for solving elliptic and convection-diffusion partial differential equations. The BEM relates known boundary data and boundary integral equations to the unknown values of the internal points of the solution domain in a very effective and accurate way. Therefore, this is a suitable method to estimate quickly several possible initial states when little data on the geothermal system are available. In this example, we show the potential advantages of the BEM in elliptic problems and suggest a way in which it

Table 9.8. Two submarine geothermal systems in Baja California, Mexico.

Average fluid properties				
Pressure (MPa)	Temperature (°C)	Density (kg/m ³)	Enthalpy (kJ/kg)	c_w (J/kg/°C)
5	220	842.6	944.3	4594
22	360	568.1	1719	9449
Thermodynamic rock properties				
Porosity %	Temperature (°C)	Density (kg/m ³)	Enthalpy (kJ/kg)	c_r (J/kg/°C)
10	220	2400	471.75	1142.2
10	360	2650	639.04	1247.6
Potential energy of each zone				
Region	Energy density (MJ/m ³)	Available energy (10 ¹⁵ J)	Geothermal potential (MW _T /km ³)	Rock volume (km ³)
Punta Banda	574	232	245	?
Gulf of California	906	832	880	?

can be coupled to other numerical methods like finite elements or integrated finite differences. Although we apply this technique to an oceanic system, it is obvious that the same method could also be used to study terrestrial geothermal or cold groundwater reservoirs.

To model the natural state of submarine reservoirs, the initial mathematical problem is expressed in terms of boundary integral equations, fundamental solutions and boundary conditions of mixed type (section 5.4). The main field functions are pressure and temperature. The versatility and power of the BEM permits the efficient treatment of very complex or unknown reservoir geometry, without requiring discretization of the whole domain occupied by the system. This permits the efficient testing of different boundary conditions to estimate several possible initial thermodynamic states at any interior point of the domain occupied by the reservoir under specific conditions. The classic BEM is limited to single-phase flow in homogeneous media and cannot be fully applied to flow problems in heterogeneous systems. In this latter case there is no fundamental solution. To overcome this difficulty after an initial state is estimated, a more general reservoir simulator such as TOUGH2 (Pruess *et al.* 1999) can be used to improve and complete the initial simulation.

The few available data on hydrothermal vents are very useful to estimate the amount of energy flowing from the ocean floor. It is possible to estimate initial conditions knowing only heat fluxes and temperatures at fissures and chimneys using a hybrid technique. The PDE describing the natural state of a geothermal reservoir is approximately elliptic, because the transient changes are very slow (see section 4.6.1). By equalling to zero the corresponding transient terms for the heat equation (4.83) in a homogeneous and isotropic reservoir, we obtain a simplified PDE for the temperature of the domain, similar to equation (5.112):

$$\begin{aligned} \Delta T &= \frac{\partial^2 T}{\partial x^2} + \frac{\partial^2 T}{\partial y^2} = f(x, y), \quad \forall \vec{P} = (x, y) \in \Omega \subset \mathbb{R}^2 \\ T(\vec{P}) &= u_T(\vec{P}), \quad \forall \vec{P} \in \Gamma = \partial\Omega \end{aligned} \tag{9.58}$$

We assume that $f=0$ to solve the Laplace problem, obtaining a solution similar to equation (5.180). Applying these results to the PDE (9.58):

$$\begin{aligned} T(\vec{P}) &= \int_{\partial\Omega} \left(T(\vec{q}) \frac{\partial v(\vec{q}, \vec{P})}{\partial n} - v(\vec{q}, \vec{P}) \frac{\partial T(\vec{q})}{\partial n} \right) ds \\ \forall \vec{P}, \quad \vec{P}_0 &\in \Omega \subset \mathbb{R}^n, \quad \vec{q} \in \partial\Omega = \Gamma = \Gamma_T + \Gamma_N \subset \mathbb{R}^{n-1}, \quad n = 1, 2, 3 \end{aligned} \tag{9.59}$$

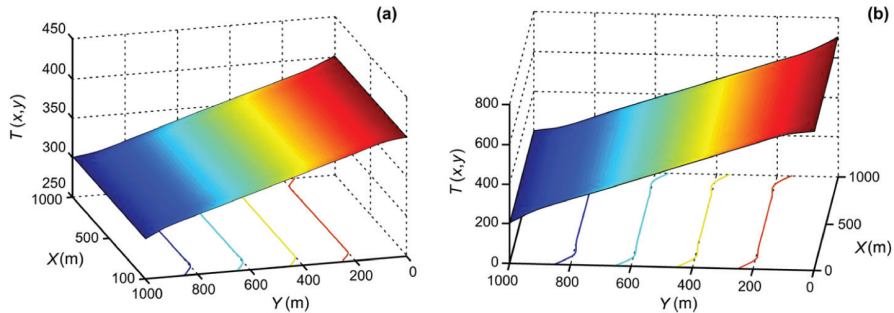
This equation was programmed and solved in Fortran/90 code (Katsikadelis 2002), using the Gauss-Legendre quadrature to solve the line integrals of equation (5.130). We assumed a squared submarine reservoir of $(1000 \times 1000)\text{m}^2$ in 2D. Forty boundary elements were sufficient to estimate the temperature distribution in this reservoir using the BEM. The boundary conditions were zero heat flow at the lateral boundaries and constant but different temperatures at the bottom and top of the reservoir. To calculate the temperature we chose 81 internal points uniformly distributed in the square. Although this number could be larger, 81 are sufficient to draw the surfaces and illustrate the results. We considered the numerical values shown in Table 9.9. The average thermal conductivity is $3.0 \text{ W/m}^\circ\text{C}$ (Suárez *et al.* 2006).

This is a simple application of this idea: knowing the range of possible temperatures, we can ask what should be the fixed temperatures at the top and bottom of the reservoir able to reproduce the measured conductive heat flow. We considered two simulations, one for the conductive heat flow measured in the Gulf of California ($0.3 \text{ W}_T/\text{m}^2$) and a second for the estimated average hydrothermal heat loss from some areas the oceanic crust of about $1.5 \text{ W}_T/\text{m}^2$ (see section 9.5.1.2). The results for a single initial state are shown in Figures 9.19a,b.

The main purpose of the simulation problem we have presented is to illustrate the easy and efficient use of the BEM in the estimation of the natural state of submarine geothermal reservoirs,

Table 9.9. Some parameters of submarine reservoirs.

Field function	Minimum	Maximum
Pressure	19 MPa	30 MPa
Temperature	200°C	700°C
Fluid flow rate	0.7 m/s	2.5 m/s
Heat flux	0.34 W _T /m ²	1.50 W _T /m ²

Figure 9.19. Temperature distribution that fits (a) the heat flow of the Gulf of California and (b) the average oceanic crust heat loss reported by Stein *et al.* (1995) for some areas.

knowing few parameters. The same technique can be applied to any elliptic or Poisson problem described in chapters 2 and 4.

9.6 MODELING PROCESSES IN FRACTURED GEOTHERMAL SYSTEMS

Our understanding of transport processes that occur in naturally fractured geothermal systems is far from complete. Often, evaluation and numerical simulations of fractured geothermal reservoirs are carried out by assuming equivalent porous media and homogeneous petrophysical properties within big matrix blocks.

The main mathematical problem in fractured reservoirs is the difficulty in representing the dimensions and spatial distribution of fractures. Most of the successful fractured hydrothermal systems presented in this section share an essential characteristic: the good producer wells tend to intersect permeable faults or they are drilled in or in the vicinity of intensely fractured regions related to faults. These wells cross, at different depths, zones of high permeability ($k \approx 10^{-10} \text{ m}^2$), which correspond neither to fresh volcanic rock ($k \approx 10^{-18} \text{ m}^2$), nor to fractures ($k \approx 10^{-13} \text{ m}^2$). The contrast in these values affects the behavior of the reservoir and the immediate response of the wells. Volcanic fractured rock forming these systems is anisotropic and comprise high permeability zones alongside very low or null permeability regions. Several phenomena detected in these systems can neither be explained nor reproduced if only single porosity models are considered. For example, abrupt pressure changes between the well and the reservoir are observed. There are zones under compressed liquid thermodynamic conditions, but wells completed there produce high quality steam from the rock formation. In these zones a large enthalpy difference exists between the well's feed interval and the reservoir. Continuous fluid production has also been observed in some wells that remain in a quasi-stationary state for years, maintaining the concentrations of non-condensable gases at a practically constant level.

9.6.1 Single porosity and fractured volcanic systems

There are essential differences between fractured reservoirs with faults and simple porous media (SP). Non-fractured volcanic reservoirs have never been found and single porosity systems of volcanic origin do not exist. The genesis of a volcanic system occurs by pyroclastic eruptions, magma flows, cooling and solidification of lava, tectonics, seismicity, resurgence, and creation of faults with intense fracturing. During these processes, water remains trapped, producing the hydrothermal system. Because of the internal topology of the fractured rock, the thermodynamic functions change abruptly, introducing discontinuities at the boundaries between the solid matrix and each fracture and fault. Pressure and temperature are not the only variables experiencing changes. There are also abrupt variations in mass and energy flows, in the steam distribution and in the behavior of non-condensable gases.

In a single porosity medium, none of these processes occurs. The matrix has primary porosity and the thermodynamic properties vary continuously and smoothly within the same rock unit; fluid transport in the small pores obeys Darcy's law and phase changes occur gradually. In fractured media the situation is further complicated by the impossibility of performing direct measurements of the key parameters. To illustrate the points raised above and put them into context we now briefly describe two approaches by which to model fractured reservoirs.

9.6.2 The double porosity model

Double porosity media (DP) are a classic topic in the literature on fractured reservoirs. The first models for slightly compressible liquid and pseudo-steady-state matrix-flow appeared in the 1960s (Barenblatt *et al.* 1960, Warren and Root 1963). Subsequently in the 1970s and 1980s the transient matrix-fracture flow and the effect of conductive faults were considered (de Swaan 1976, Cinco Ley and Meng 1988). Similar problems of double porosity were studied in geothermal reservoirs but, due to phase change and non-linearity in the basic equations, analytic solutions are scarce (Zimmerman *et al.* 1993). Double porosity in fractured geothermal media was generalized and solved numerically by means of the MINC (multiple interacting continua) concept by Pruess and Narasimhan (1985). The concept of "double porosity" assumes that fluid diffusivity is higher in the fractures than in the matrix blocks. In the study of Pruess and Narasimhan (1985) a transient transfer of heat and mass via matrix-fractures is considered. An essential feature of this double porosity model is the possibility of performing a detailed numerical treatment of the interporosity flow between the two media. In some cases, the matrix blocks are traversed by faults and are frequently exposed to non-uniform boundary conditions because of alternate injection of liquid at low temperature over a long period.

9.6.3 The triple porosity model

Figure 9.20 shows a 10 cm diameter core from the Los Azufres geothermal field, Mexico geothermal field at 2679 m depth, which is crossed by one sealed fault. It clearly shows the intense network of fractures surrounding the main structure. The fault itself has a width of 1.5 cm. Fractures present an average opening of 0.1 cm. The location of non-producing wells in the same field suggests that fracturing diminishes when the distance to faults increases at any depth. Other cores from the same well which do not intersect the fault show a total absence of fractures. This indicates that far from the fault, the matrix blocks increase their size and fractures become even more widely spaced (Fig. 9.21). In order to explain empirically the behaviour of heterogeneous reservoirs, we introduced the triple porosity/permeability (TP) concept (Suárez and Samaniego 1995), which is applicable to fractured systems traversed by penetrating open faults. In this concept the intensity of fracturing is very high near the fault, intermediate in the fractured medium and very low or negligible in the matrix blocks. In these media an abrupt permeability contrast exists between the matrix, fractures and faults. The available evidence strongly suggests that fluid transport in this type of system occurs in four stages (Fig. 9.21):

$$\text{Matrix } (10^{-18} \text{ m}^2) \rightarrow \{\text{micro} \rightarrow \text{fractures}\} (10^{-13} \text{ m}^2) \rightarrow \text{Fault } (10^{-10} \text{ m}^2) \rightarrow \text{Well}$$



Figure 9.20. Rock core (diameter 10 cm) from Los Azufres geothermal field (Mexico) which is crossed by a 1.5 cm wide sealed fault and a network of fractures with openings of about 0.1 cm.

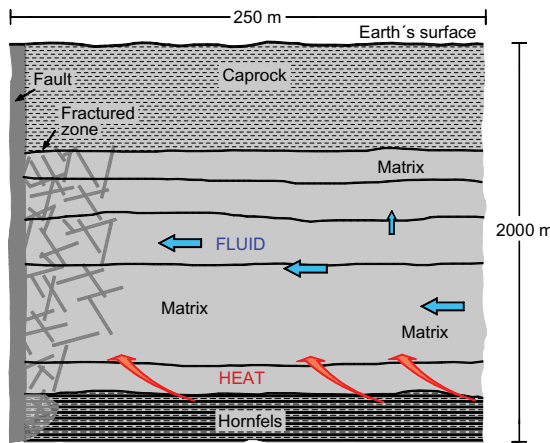


Figure 9.21. A triple-porosity system, showing the direction of flows from the matrix to the fault.

The preceding permeability values reveal the highly contrasting properties of matrix, fractures and faults of the Los Azufres geothermal field. Experimental data show that matrix blocks are very small in the vicinity of the fault, with fractures separated by a few centimeters. The matrix blocks are very large far from the fault where only distant and isolated fractures can be found. In this triple porosity model, fluid diffusivity attains its maximum value within the fault; it is higher in the fractures than in the matrix. Flow towards the wells occurs in such a way that the initial response in the extraction zone is detected immediately in the fault, then it is observed in the fractured network and later in the rock matrix. Matrix, fractures and fault are three interacting continua clearly distinguishable by their respective petrophysical parameters. Mass and energy

interaction is carried out through special transport functions that depend on the form and size of the blocks, on the intensity of fracturing and on the communication with the fault.

9.6.4 Fluid transport through faults

In 1991, liquid injection in well Az-8 (Fig. 9.22) of the Los Azufres geothermal reservoir decreased from 200 tons/h to 10 tons/h (Suárez *et al.* 1992). Over the same period, the liquid produced at well Az-46, located 1290 m to the east (Fig. 9.22), diminished. Faults oriented E–W are communicating both zones. In February 1992 injection in Az-8 was rapidly increased from 10 to 225 tons/h. At that moment, liquid produced at Az-46 reached a minimum value of 8 tons/h (Fig. 9.23).

Liquid injected in Az-8 took approximately 21 days to arrive at the production zone. The injection well is completed 1330 m deeper than the production well. The total distance between the wells is 2620 m. Average flow speed between the two zones is about 124.8 m/day or $1.44 \cdot 10^{-3}$ m/s. Assuming that flow takes place in a plane defined by both wells, a pressure gradient of 0.0054 MPa/m was estimated. From Darcy’s law a global permeability of 1.16×10^{-11} m² (≈ 11 Darcy) is inferred. This value was obtained following the assumption of zero tortuosity and two-dimensional transport. The actual vectorial distance between the two wells must be higher.

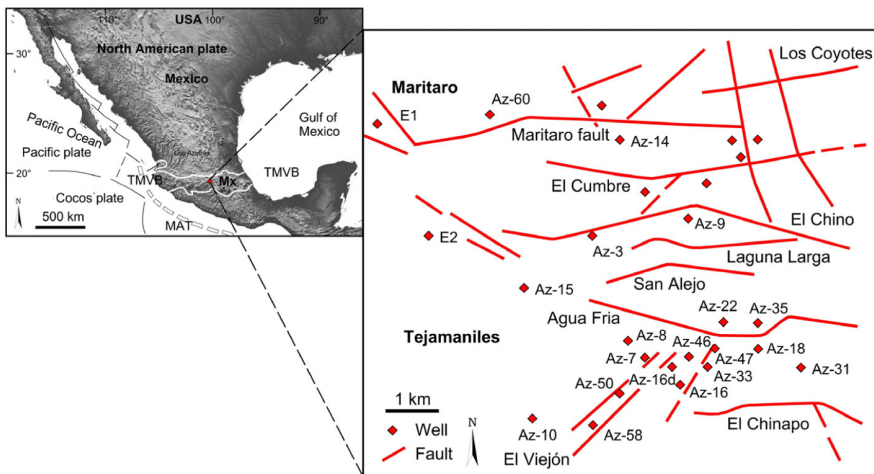


Figure 9.22. Location of the Los Azufres geothermal field with its main faults and wells.

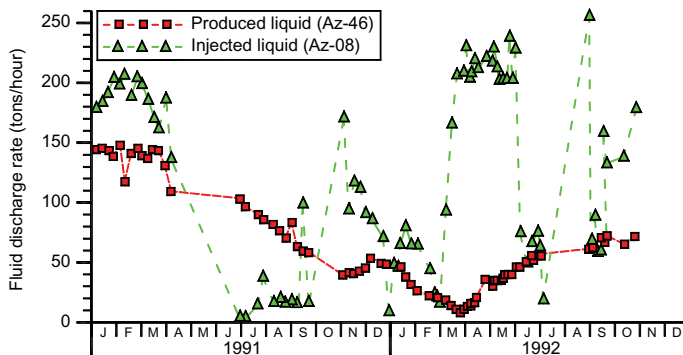


Figure 9.23. Liquid injection in well Az-08 and produced liquid at well Az-46 in the years 1991 and 1992.

We deduce that the velocity and permeability inside the zone delimited by wells Az-8 and Az-46 correspond to the transport of liquid through faults and fractures.

9.6.5 *General equations for single, double and triple porosity models*

The triple porosity/permeability concept (Suárez and Samaniego 1995) describes flow through porous media with different porosities: single (SP), double (DP) and triple (TP), which all approximately obey the same differential equations. The difference between these three media resides in the dimension and number of equations required. SP requires one equation for mass and one for heat. DP requires two equations for each medium, whereas TP, formed by three interconnected continua, requires three pairs of equations (Suárez and Samaniego 1995). In any of these three cases, the transient flow of mass and energy is theoretically described by the equations derived in chapter 4 and rewritten here for the three models:

$$\begin{aligned} \frac{\partial(\varphi_j \rho_j)}{\partial t} + \vec{\nabla} \cdot (\rho_j \vec{v}_j) &= q_j, \quad \left[\frac{\text{kg}}{\text{s m}^3} \right], \quad (\text{for mass}) \\ \frac{\partial U_j}{\partial t} + \vec{\nabla} \cdot (\rho_j h_j \vec{v}_j - k_{Tj} \cdot \vec{\nabla} T_j) &= h_j q_j, \quad \left[\frac{\text{J}}{\text{s m}^3} \right], \quad (\text{for energy}) \end{aligned} \quad (9.60)$$

$$\forall j = m, f, F$$

The subindex j represents flow in the matrix (m), in the fractures (f) and in the fault (F), respectively. The variables and functions are as defined in previous sections: ρ_j is density, φ_j is porosity, v_j is Darcy's velocity, U_j is total internal energy (eq. 4.98), h_j is specific enthalpy, k_{Tj} is thermal conductivity, and T_j is the temperature of each medium. We assume that there is thermal equilibrium at the initial state of the reservoir and thus the three temperatures are the same at the beginning of the simulation. The term q_j is a function that represents the mutual exchange of fluid between the three continua.

9.6.6 *Numerical comparison between single porosity and fractured media*

In this example, we present a comparison between results obtained from numerical studies of a naturally fractured reservoir treated as a simple porous medium, and the simulation of some real aspects of the fractured reservoir using double and triple porosity models. This exercise highlights the great practical importance of considering, even approximately, the true nature of such systems. The homogeneous simplified evaluation of the energy resource in a fractured system can result in unrealistic estimates of its longevity and of the capacity of the reservoir to generate electricity. The three models discussed above were applied to the simulation of Tejamaniles, the southern sector of the Los Azufres field, Mexico (Fig. 9.22), using real reservoir data. This sector possesses a number of essential aspects for modeling (Suárez *et al.* 1992): wide and rich production history, simultaneous reinjection since the beginning of exploitation, and fluid extraction is concentrated in a straight corridor with penetrating faults and intense fracturing located between San Alejo and El Chinapo faults (Fig. 9.22). Models were numerically solved with the TOUGH simulator (Pruess 1991) for three different 3D problems related to the same sector, varying the details of its geometry. In all cases, the objective of the simulation was to reproduce the first eleven years of the reservoir's exploitation. The first problem was to simulate a single porous medium without fractures. A mesh of 115 horizontal elements was created, with seven vertical strata, for a total of 805 elements.

The next problem was the evaluation of the same zone considering double porosity (DP) and employing the MINC method coupled to the TOUGH code (Pruess 1991). This technique, applied to the previous mesh, would generate a minimum of 8000 finite volumes in five vertical strata (Fig. 9.24), unnecessarily complicating the problem. The extraction of fluid in this zone is

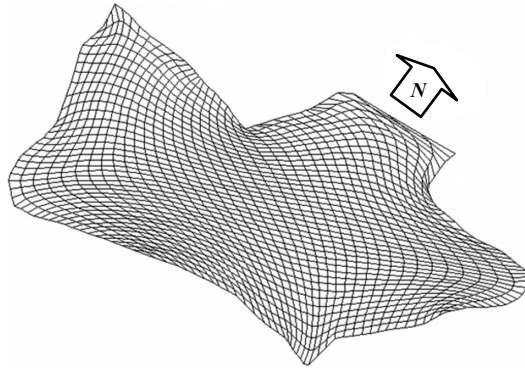


Figure 9.24. A general mesh of the southern sector of the Los Azufres geothermal field with 1600 cells in each vertical stratum (horizontal extension: ~ 8 km).

75% concentrated in the aforementioned corridor defined by faults oriented W--E. Wells outside this area seem not to be affected by extraction in the corridor. We proceeded to simulate by DP only this corridor by creating a system of three parallel fractures penetrating up to a layer located 1600 m a.s.l. Each original matrix block was partitioned into five nested volume elements; this DP model generated a mesh of 116 volumes per fracture. The corridor's lateral walls were supposed impervious; this simplification permitted the elimination of elements and wells outside the principal volume.

The third model considered triple porosity (TP) inside the same corridor, simulating the fault's width up to a zone of direct influence of 1 m wide. The fractured network is very intense in the immediate vicinity of the fault within a 5 m radius. There is a transition zone of 10 m, with less fractures and minor permeability, connected to regular matrix blocks at growing distances up to 400 m in total width.

The corridor thus defined is horizontally closed: it only admits fluid and heat from the deep vertical strata. A mesh of 241 elements with 15 active wells was processed. This experiment showed that it is possible to reduce the number of elements in a fractured mesh, without losing essential attributes of the real medium.

An essential difficulty found in the simulation of this type of fractured media was the representation of the fluid rate distribution among the three media. Strictly speaking, a geological fault is a deep open channel having porosity values close to 100% and extremely high hydraulic conductivity. More realistic simulations should use the Navier-Stokes equations (4.10) and/or the Forchheimer equation (4.76).

Flow occurs in a two-dimensional space defined through the fault's plane; tortuosity is insignificant and only the walls' roughness could influence the transport. Flow inside the fractured mesh is three-dimensional and tortuosity could be important. Wells presenting high flow rates have to distribute their production among matrix, fractures and the fault, defining a fault's zone of influence. A key unknown is the percentage of fluid rate corresponding to each portion of the system.

In our DP and TP models we assigned by trial and error, a mass rate extraction proportionally distributed in each medium. Another practical aspect is the importance of detailing the production and injection history, because a coarse averaged history could mask the true response of the fractured medium. In our treatment we considered time steps of between 2 and 30 days, depending on the rapidity of mass rate changes. We performed various series of numerical experiments employing known reservoir parameters (Table 9.10). Unknown property values were obtained by trial and error when fitting the system's initial state and during the history matching of the field. Permeability distribution is tensorial and was obtained from several sources (pressure tests, core measurements, experiments); its decrease is exponential with depth in non-fractured zones. The specific heat of saturated rock is homogeneous and equal to 1165 J/kg/°C.

Table 9.10. Some key reservoir parameters used in the simulations.

Strata (m a.s.l.)	Rock density (kg/m ³)	Porosity (%)	k_X (m ²) (W-E)	k_Y (m ²) (N-S)	k_Z (m ²)	k_T (W/m/°C)
Caprock (2950)	2251	0.1	10^{-17}	10^{-18}	10^{-25}	0.18
B (2300)	2355	11.9	248×10^{-15}	10^{-16}	248×10^{-15}	1.93
C (2000)	2434	8.3	48×10^{-15}	10^{-17}	48×10^{-15}	2.09
D (1600)	2528	5.5	7.4×10^{-15}	10^{-18}	7.4×10^{-15}	1.62
E (1200)	2677	2.9	10^{-15}	10^{-18}	10^{-15}	1.69
F (400)	2900	1.0	10^{-25}	10^{-25}	10^{-19}	2.01
Fractures	2000	50.0	5.5×10^{-13}	10^{-17}	5×10^{-13}	1.93
Fault	1528	80.0	1.5×10^{-9}	10^{-18}	10^{-12}	1.62

At Los Azufres, thirty-nine reservoir pressure measurements were made in several wells, over the period 1982–1993. Sufficient data are available for comparison with the calculated values. The observed enthalpy in some selected wells differs by a maximum of 4% between the wellhead and bottom hole. Fluid entering wells Az-18, –33 and –46 is two-phase at the feeding point. Measured enthalpy is supposed to represent enthalpy in the fractured zone in the well's neighborhood (Suárez *et al.* 1992).

9.6.6.1 *Graphical results of the simulations*

Figures 9.25a,b show a comparison between SP and DP pressures and temperatures at the production zone of well Az-18. It is apparent that the pressure curve calculated with SP underestimates the measured pressure decline in the reservoir. Pressure oscillations are observed in the fracture. This behavior is absent in the SP case. Fluctuations reflect the complex history of liquid injection. At the 5th matrix block in the DP model, the pressure curve is almost parallel to the SP curve, since the beginning until 1989. In that year, fluid extraction was increased.

The enthalpy augmented smoothly from 1600 kJ/kg in 1983 to 2200 kJ/kg in 1993 (Fig. 9.25c). During the first years, the SP model underestimates enthalpy evolution and then it increases abruptly, over-estimating measured values. Subsequently, enthalpy falls abruptly, reflecting the arrival of more liquid. The DP model reproduces the real evolution quite well. This match was achieved taking into account the simultaneous contribution of fluid from fractures and nearest matrix block. The TP model was unnecessary to reproduce this behavior.

Another interesting example comes from well Az-33 located in the same Tejamaniles sector of the Los Azufres field. Its evolution was analyzed using the three models. Fault pressures calculated using the TP model reproduced accurately, the measured pressures until 1989 (Fig. 9.26a). From then on, the calculated depression in the fault is higher than the measured values: almost double the real pressure decrement in 1992. This result exemplifies typical behavior when fluid is extracted directly from a fault. In reality, mass rate must somehow be simultaneously distributed among the fractures and block matrix surrounding the fault. The pressure is higher at the beginning because the initial pressures in the fault, fractures and matrix are different.

In 1988, fluid extraction was increased to feed a 50 MWe power plant. As soon as the fault started to feed several wells, its global mass rate increased. This explains the abrupt depression in the fault in the TP model. Nevertheless, in the fractured mesh and in matrix blocks, there is sufficient fluid and the depression is lower. We conclude that the well's feeding zone receives fluid mass from different media under different thermodynamic conditions. Table 9.11 shows a summary of comparative values.

For this problem, the three models reproduce quite accurately the final pressure (Fig. 9.26a), but not the enthalpy. Figure 9.26b compares the real enthalpy with values calculated using the SP and DP models. Real behavior was not reproduced in either cases. DP liquid enthalpy started at 1250 kJ/kg, but soon increased. Fluid evolving steam in the fractures dominated. The TP model

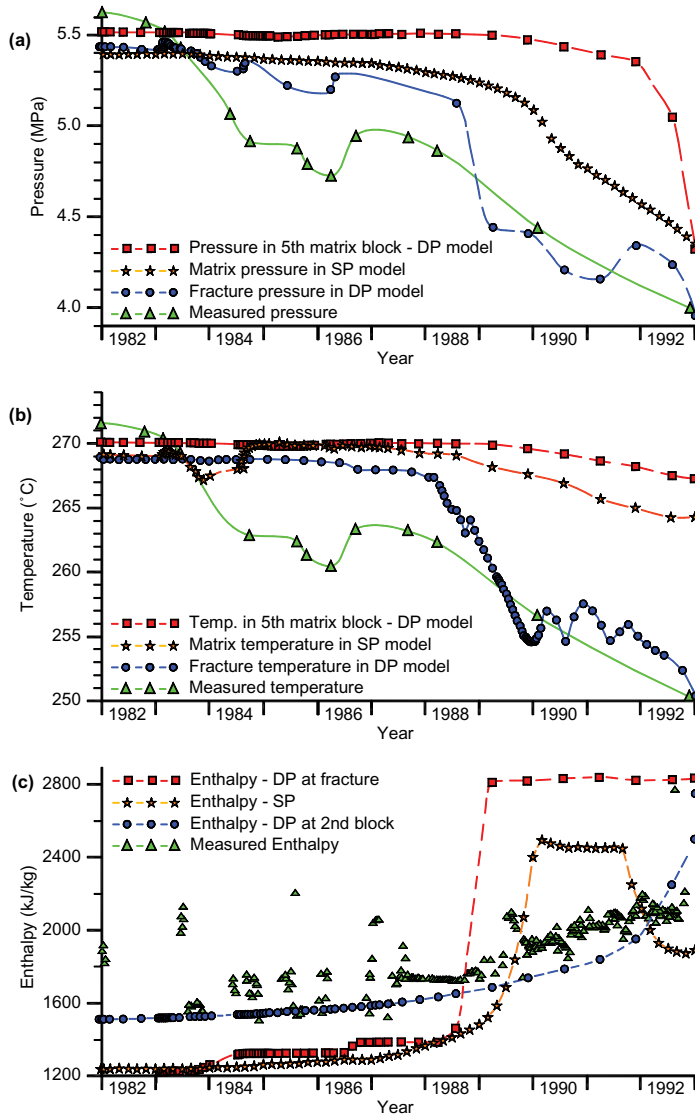


Figure 9.25. Los Azufres geothermal field, well Az-18: Comparison of single porosity (SP) versus double porosity (DP) model: (a) pressure, (b) temperature and (c) enthalpy.

reproduces general enthalpy changes reasonable well (Fig. 9.26c). This match was obtained by superposing the evolution of various zones of the TP media. The first part of the curve corresponds to fluid extracted in the fault, the second portion, to the fractured network and the third part corresponds to fluid in the matrix-fractures interface.

The triple porosity mechanism explains why, when extraction starts, pressure differences are introduced between the reservoir and the well's feeding point. Pressure gradients induce the creation of a boiling front starting at the matrix-fractures interface. Apparently, a parallel mechanism of phase segregation appears, allowing the migration of more vapor towards the well, even if the reservoir's natural state corresponds to compressed liquid.

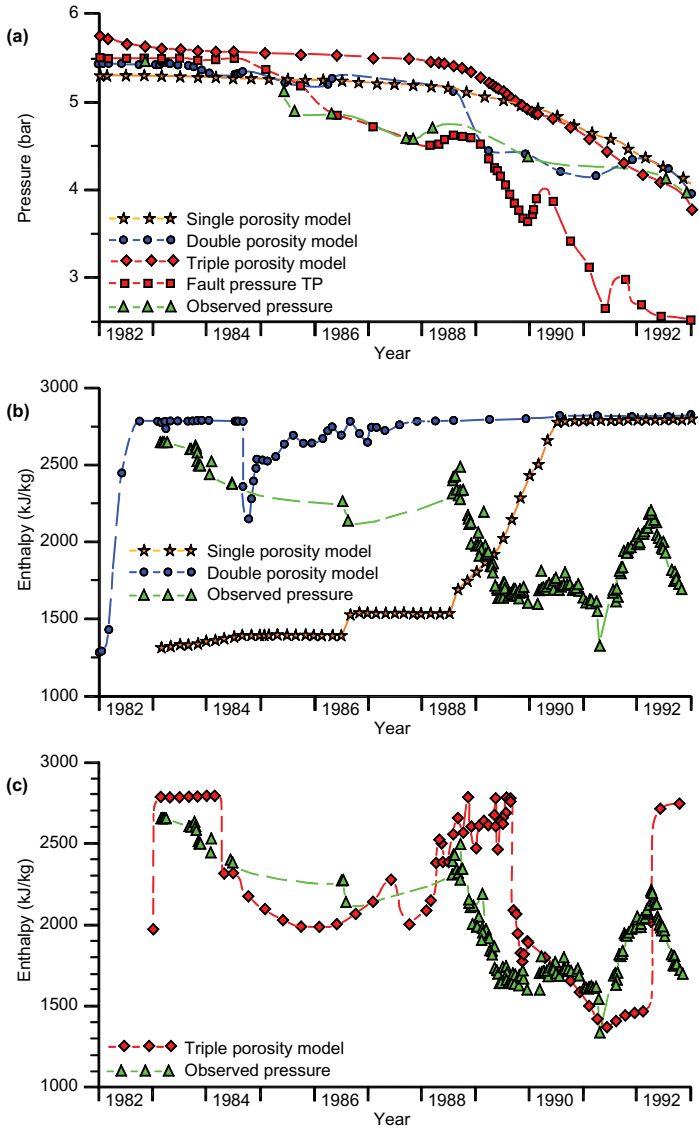


Figure 9.26. Los Azufres geothermal field, well Az-33: Comparison of pressures (a) and enthalpies (b, c) of single porosity (SP) versus double porosity (DP) and triple porosity (TP) models.

As a final example, we examine the evolution in time of the spatial distribution of pressure, temperature and steam saturation around another well intersecting the same fault, at approximately 800 m depth. Figure 9.27 shows several curves, calculated using the triple porosity model and representing different depths in the three media, and are plotted simultaneously. In Figures 9.27a,b, it can be seen that the measured values of pressure and temperature correspond to some kind of average values among the fault, the fractures and the matrix. The lowest values are in the fault, while the highest are in the matrix and in deep zones far from the feeding point.

Figure 9.27c shows that steam is distributed in a complicated form among the three media. In the fault, the evolution of high quality steam takes place very rapidly. This phenomenon coexists

Table 9.11. Results comparing measured and calculated values at wells AZ-18 and AZ-33 from Loz Azufres geothermal field.

	p_{initial} (MPa)	p_{final} (MPa)	Δp (MPa)	T_{initial} (°C)	T_{final} (°C)
Well Az-18					
Single porosity	5.40	4.35	1.05	269	255
Double porosity	5.45	3.95	1.50	269	264
Measured	5.63	4.00	1.63	271 ¹⁾	?
Well Az-33					
Single porosity	5.30	4.07	1.23	268	252
Double porosity	5.40	4.00	1.40	269	264

¹⁾ Assuming that fluid was 2-phase.

with zones containing less vapor and even matrix blocks and profound zones that could remain in a compressed liquid state.

From the results of this study, a number of conclusions may be drawn:

- In the simulation of a geothermal fractured reservoir as a single porosity medium, there is a tendency to underestimate the real pressure fall-off in production zones. Under these conditions, making long-term extrapolations about the behavior of production zones, may lead to overestimation of the capacity of a planned geothermal power plant, because the natural longevity of wells, could be shorter.
- Detailed simulations using double or triple porosity modeling may also be subject to difficulties. If the behavior of the fault is the only aspect considered, there is a tendency to exaggerate the pressure fall-off. A realistic analysis should take into account the simultaneous contribution of the fault, the fractured mesh and some matrix blocks in the zone of influence of the conductive fault.
- Evolution of production enthalpy could become very complicated in wells subjected to intensive long-term injection. The matching of this behavior can be achieved only if double or, even better, triple porosity models are considered. The single porosity model does not necessarily give bad results, but it fails systematically to reproduce reinjection effects in fractured zones.
- Simulating fluid extraction from faults requires simultaneous extraction from distinct producing strata under different thermodynamic conditions. In the examples presented, the best enthalpy fit was obtained using double and triple porosity models.
- Real pressure fluctuations originate from the production/injection history of the analyzed field. Pressure oscillations were numerically detected in fractures and in the fault. This phenomenon is absent in the matrix blocks and in single porosity models. Including details of faults and fractures in a simulation, results in an increase of the number of matching possibilities. Mathematical models can only be an approximate representation of reality. For any complex fractured system, an idealized equivalent system will contain the principal features of some part of the phenomenon, in some portion of the space, during certain time.

9.6.7 Effective thermal conductivity and reservoir natural state; Flow problem with CO₂

The Los Azufres geothermal field is a convective reservoir, formed by fractured andesites and some dacites. Andesites show several degrees of hydrothermal alteration (Viggiano and Gutiérrez-Negrín 1988). An impervious cap rock is formed by rhyolites having negligible or very low local permeability. The cap rock obstructs the escape of mass and convective heat. However, energy loss by conduction is only partially prevented by the rhyolites. The temperature difference between the top and bottom of the reservoir is remarkable. One of the deepest drilled wells, Az-47 has a temperature of 358°C at 2964 m depth, while at the surface the average temperature is 15°C.

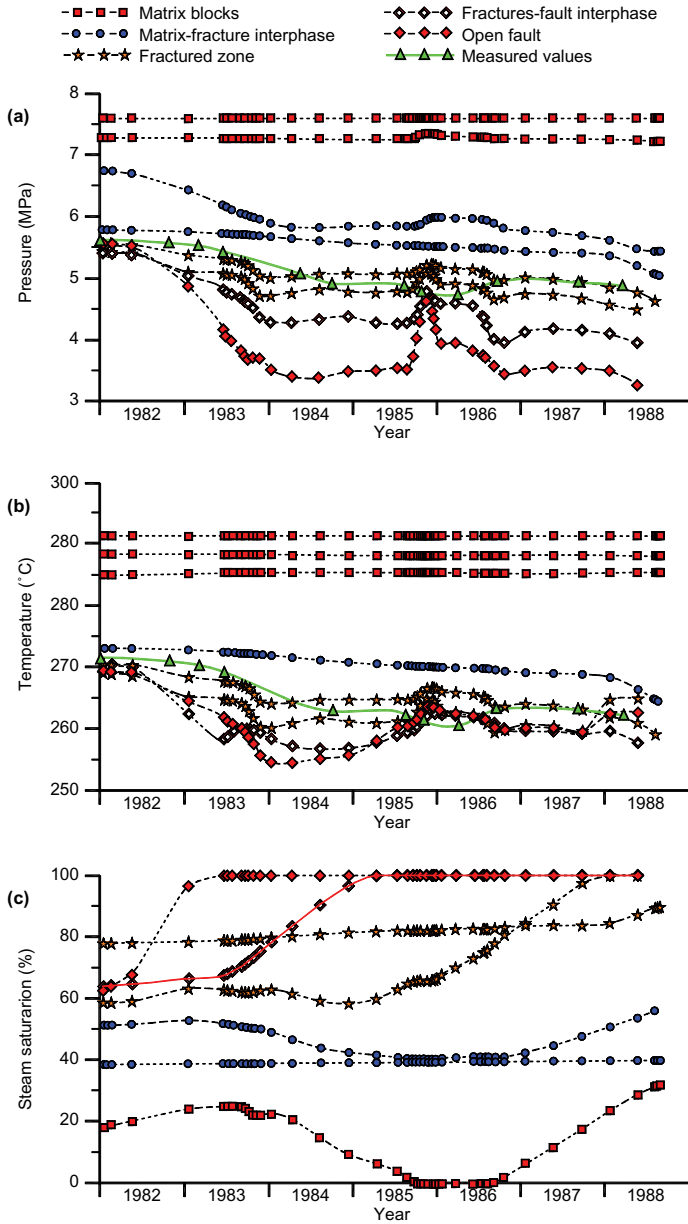


Figure 9.27. Los Azufres geothermal field: (a) Pressure, (b) temperature and (c) steam distribution in the neighborhood of a fault, triple porosity model (TP).

Measured thermal conductivity in cores ranges between 1 and 2.34 W/m/°C (Contreras *et al.* 1988). The average conductive heat flow is about 0.22 W/m², corresponding to an average thermal gradient of 0.12°C/m, four times larger than the normal geothermal gradient (0.03°C/m).

The portion of the reservoir under study corresponds to a real zone of the Los Azufres geothermal field (Fig. 9.28). The complex real geology of the field was reduced to a vertical section having a cross sectional area of 6.3×10^4 m² and a total depth of 3000 m. A conductive fault is

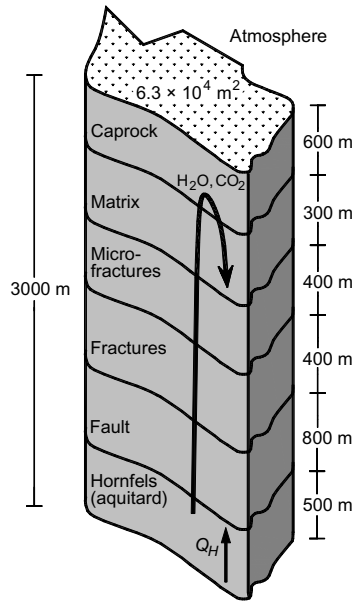


Figure 9.28. A simplified vertical model of the southern sector of the Los Azufres geothermal field representing a natural convective heat pipe mechanism.

Table 9.12. Parameters used in the numeric simulations¹⁾.

Thickness (m)	Element	Rock density (kg/m ³)	Porosity (%)	Vertical permeability (m ²)	Thermal conductivity (W/m/°C)
600	Caprock	2251	1.95	1.0×10^{-20}	1.05
1900	Matrix	2528	11.95	1.0×10^{-15}	2.19
1000	Micro-fractures	2434	8.32	1.0×10^{-14}	1.65
1000	Fractures	2300	25.5	1.0×10^{-13}	1.63
1900	Fault	1677	50	1.0×10^{-12}	1.66
500	Hornfels	2834	1.59	1.0×10^{-18}	1.82

¹⁾ General parameters: initial fluid pressure and temperature 5.5 MPa and 265°C, respectively; initial CO₂ partial pressure: 0.5 MPa; Bottom boundary conditions: 17.0 MPa and 350°C; Fluid extraction rate is -20 kg/s; Rock specific heat is 1165 J/kg/°; Diffusive steam flux coefficient is 1.38×10^{-5} m²/s. Corey's relations are used as relative permeabilities; Capillary pressure was neglected. Vertical thermal conductivity was approximated by the regression formula: $k_T(z) = 1.87 - 1.76 \times 10^{-4} z$, $z \in [-79, 1850]$ m a.s.l.; $R^2 = 0.93$; $k_T(Z) = 7.65 - 2.66 \times 10^{-3} z$, $z \in [1850, 2850]$ m a.s.l.; $R^2 = 1.0$, both in W/m/°. R^2 is the correlation coefficient.

located to the west, while the eastern boundary is impervious and located 250 m from the fault (Fig. 9.22). The northern and southern boundaries are closed. The geometric model is formed mostly by single-porosity elements. The deeper Hornfels element is 500 m thick and acts as a continuous heat source with constant temperature boundary conditions (Table 9.12). The caprock is represented by a very low permeability top block of 600 m total thickness. A 20 m region near the fault, contains both fractures and microfractures. An intensely fractured region is located close to the fault and has a width of 5 m.

In these systems, reservoir fluid contain several components whose dynamics are affected by petrophysical heterogeneity in different ways. For example, rock absolute permeability and thermal conductivity at the matrix-fractures interface are key parameters in coupled processes of conductive and convective thermal energy flow with transport of multicomponent fluid, because both parameters differ greatly in value between matrix, microfractures and fractures. Through numerical experiments, we show that the interporosity flow of fluid could be controlled at the interface between matrix and fractures by averaged properties. On the other hand, effective thermal conductivity averaged at shallow strata can cause radical changes in the natural state of non-isothermal reservoirs.

We performed several numeric experiments testing different averages of various petrophysical parameters (Suaréz 1993). The main parameters used in the numerical simulations are given in Table 9.12. Calculations were performed using the finite volume method, contained in the code TOUGH (developed at the Lawrence National Berkeley Laboratory), for a water-carbon dioxide

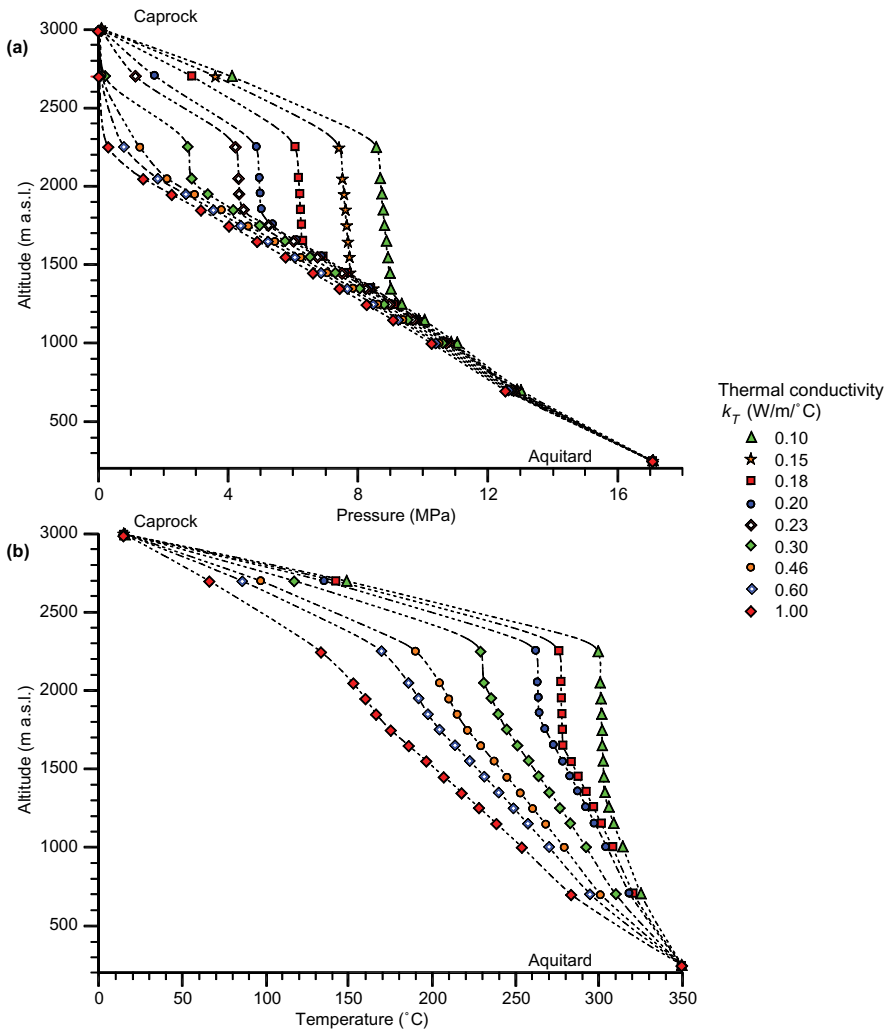


Figure 9.29. Vertical distributions of pressure (a) and temperature (b) as a function of the average thermal conductivity at the caprock.

equation of state (Pruess 1987, 1988, 1995, 1998). The general coupled transport equations solved by this code are given in section 5.3. Rock thermal conductivity in any non-isothermal reservoir is a key parameter affecting the conductive heat flow, the distribution of temperatures and the definition of a barrier to hold the accumulated energy. Several simulations were performed for different thermal conductivity averages between the caprock and the top of the reservoir. Different steady-state conditions were obtained and, some are shown in Figures 9.29a,b, and 9.30.

The natural state observed at Los Azufres, shows small vertical pressure and temperature gradients between 1800 and 2250 m a.s.l., close to vaporstatic conditions. But from 0 to 1800 m a.s.l. the observed gradients correspond to boiling hydrostatic conditions. This system exhibits pressure and temperature profiles characterized by a discontinuity in its vertical gradient (Figs. 9.29a,b). This discontinuity also appears in the vertical distribution of thermal conductivity at the same depth. Our numerical results suggest that the vertical location of this point of discontinuity is controlled by the thermal conductivity average existing between the limit of the reservoir and the caprock. Thermal conductivities that are too high could produce liquid-dominated reservoirs, while values that are too low could be the cause of vapor-dominated reservoirs (Fig. 9.29). Non-condensable gases such as CO₂ tend to accumulate in a condensation zone at the upper limit of the reservoir (Fig. 9.30). The best average methods that reproduce the observed reservoir behavior are obtained using both the general geometric mean (A_{gG}) and the serial average for three components (A_s) shown in Table 3.1, for rock, water and carbon dioxide.

9.6.8 Simultaneous heat and mass flow in fractured reservoirs: Conclusions

In this section (9.6) we presented some results obtained by using different averages of petrophysical parameters in the numerical simulation of a fractured geothermal reservoir located in central Mexico. This field contains multicomponent fluid: brine in two phases, liquid, vapor, dissolved carbon dioxide and other non-condensable gases. We show different equilibrium and evolution states obtained by using different averages. We presented herein graphical results for fluid pressure and temperature, and carbon dioxide partial pressure. We observe that rock absolute permeability and thermal conductivity at the matrix-fracture interfaces, are the key parameters in coupled processes of conductive and convective thermal energy flow with transport of multicomponent fluids.

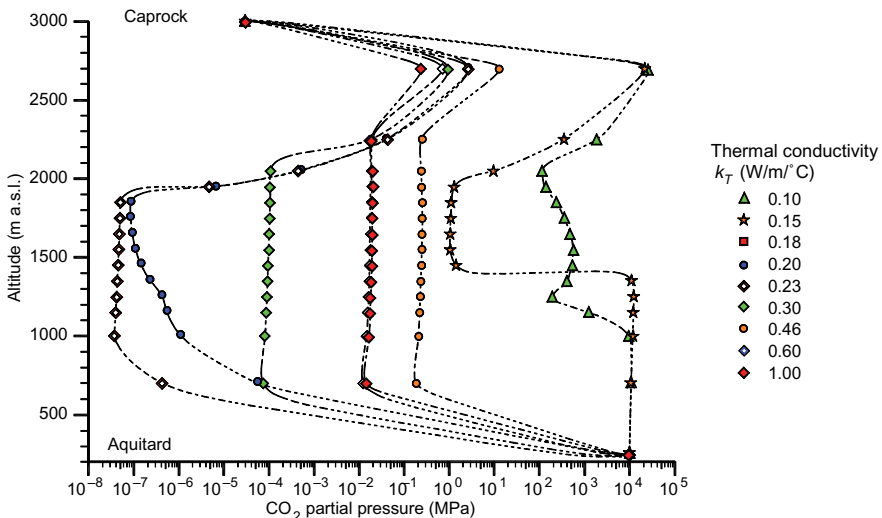


Figure 9.30. CO₂ partial pressure profile as a function of the average thermal conductivity at the caprock.

This coupling, associated with the latent heat of vaporization liberated during convection, accelerates the formation of caprocks. This occurs because internal heat is transported towards the Earth's surface, increasing the temperature in anomalous geothermal zones and causing hydrothermal alteration of rock at several depths. Similar heat-mass coupling processes provide mechanisms for the formation of hydrocarbon reservoirs, which can only be created under appropriate pressure and temperature conditions.

APPENDIXES

A: Mathematical appendix

... *Mathematics is a basis for the scientific study of the world. However, why is this abstract mathematics lying so far from our specific, touchable, and beautiful world so essential for world study? Why then upon studying it are we capable of studying the world? Finally, what is, after all, mathematics?*

Juri I. Neimark (2003)*

A.1 INTRODUCTION TO INTERPOLATION TECHNIQUES

The description of groundwater flow and transport of solutes and heat require mathematics. In this Appendix, we present the main results needed to understand several mathematical aspects of this book. To go deeper into every one of these subjects, interested readers may consult specialized literature. In applied mathematics, it is necessary to approximate functions for different reasons (Abramowitz and Stegun 1965). Newton and his pupil Taylor discovered around 1670 that many important functions could be approximated by simple polynomials, if these functions are sufficiently differentiable in a given domain $[a, x]$. This is Taylor's theorem (Haaser *et al.* 2001):

$$f(x) = \sum_{k=0}^n \frac{(x-a)^k}{k!} f^{(k)}(a) + \int_a^b f^{(n+1)}(t) \frac{(x-t)^n}{n!} dt \quad (\text{A.0})$$

The integral formula in equation A.0 is an expression of the error or residual in Taylor's expansion. The following are some examples of approximations of classical functions obtained from Taylor's theorem. They are useful in different parts of the book:

$$e^x \approx \sum_{i=0}^n \frac{x^i}{i!} = 1 + x + \frac{x^2}{2!} + \frac{x^3}{3!} + \dots + \frac{x^n}{n!}, \quad \forall x \in \mathbb{R}$$

$$\frac{1}{1+x} \approx \sum_{k=0}^n (-1)^k x^k = 1 - x + x^2 - x^3 + \dots + (-1)^n x^n, \quad \forall |x| < 1$$

$$(1+x)^r \approx 1 + rx + \frac{r(r-1)}{2!} x^2 + \dots + \frac{r(r-1) \dots (r-n+1)}{n!} x^n + \dots, \quad \forall r \in \mathbb{R}, |x| < 1$$

$$a^x \approx \sum_{k=0}^n \frac{(x \text{ Lna})^k}{k!} = 1 + \frac{(x \text{ Lna})^1}{1} + \frac{(x \text{ Lna})^2}{2!} + \dots + \frac{(x \text{ Lna})^n}{n!}, \quad \forall a > 0$$

$$\text{Ln}(x) \approx \sum_{j=0}^n \frac{2}{2j+1} \left(\frac{x-1}{x+1} \right)^{2j+1} = 2 \frac{x-1}{x+1} + \frac{2}{3} \left(\frac{x-1}{x+1} \right)^3 + \frac{2}{5} \left(\frac{x-1}{x+1} \right)^5 + \dots, \quad \forall x > 0$$

$$\text{Sin}(x) \approx \sum_{k=0}^n (-1)^k \frac{x^{2k+1}}{(2k+1)!} = x - \frac{x^3}{3!} + \frac{x^5}{5!} + \dots + (-1)^n \frac{x^{2n+1}}{(2n+1)!} + \dots$$

* Juri I. Neimark: *Mathematical Models in Natural Science and Engineering*. Springer-Verlag, Berlin, 2003.

$$\begin{aligned}\cos(x) &\approx \sum_{k=0}^n (-1)^k \frac{x^{2k}}{(2k)!} = 1 - \frac{x^2}{2!} + \frac{x^4}{4!} - \dots + (-1)^n \frac{x^{2n}}{(2n)!} + \dots \\ \tan(x) &\approx x + \frac{x^3}{3} + \frac{2x^5}{3 \cdot 5} + \frac{17x^7}{3^2 \cdot 5 \cdot 7} + \frac{62x^9}{3^2 \cdot 5 \cdot 7 \cdot 9} + \dots, \quad \forall |x| < \frac{\pi}{2}\end{aligned}$$

If $f(x)$ is a periodic function in the interval $[-L, L]$ m, then it can be represented by an infinite series of complex exponentials or by an infinite series of sine and cosine functions, even if $f(x)$ is discontinuous. This approximation is very important in the analytic solution of the heat equation (section 4.6.1):

$$\begin{aligned}f(y) &= \sum_{n=-\infty}^{+\infty} c_n e^{iny} = \dots c_{-2} e^{-i2y} + c_{-1} e^{-iy} + c_0 + c_1 e^{iy} + c_2 e^{i2y} + c_3 e^{i3y} + \dots \\ \text{where: } c_n &= \frac{1}{2\pi} \int_{-\pi}^{\pi} f(y) e^{-iny} dy; \quad \forall n \in \mathbb{Z} \text{ (complex Fourier series)} \\ \text{for } y = \frac{\pi x}{L}: f(y) &\approx \frac{a_0}{2} + a_1 \cos y + b_1 \sin y + \dots + a_n \cos ny + b_n \sin ny \quad (\text{A.1}) \\ \Rightarrow f(x) &= \frac{a_0}{2} + \sum_{n=1}^{\infty} \left[a_n \cos\left(\frac{n\pi x}{L}\right) + b_n \sin\left(\frac{n\pi x}{L}\right) \right] \text{ (classic Fourier series)} \\ \text{and: } a_n &= \frac{1}{L} \int_{-L}^L f(x) \cos\left(\frac{n\pi x}{L}\right) dx; \quad b_n = \frac{1}{L} \int_{-\pi}^{\pi} f(x) \sin\left(\frac{n\pi x}{L}\right) dx, \quad \forall n \geq 0\end{aligned}$$

A.1.1 *Approximation and basis of interpolation in one dimension*

The FEM employs interpolation as a technique of approximation. Therefore, the understanding of the bases of this method requires knowing what interpolation is. When measuring any variable in hydrogeology, such as pressure, permeability or temperature, the measurements can be done only in a finite number of points. It is physically impossible to quantify the variable continuously, everywhere. Thus, it is necessary to estimate these variables in other ways. Interpolation is an approximation technique to construct new data knowing only a discrete set of measured data points within the range of available information. The interpolation functions, which are known *a priori*, must reproduce exactly all the measured points, allowing to approximate the unknown points that have not been measured. The total number of known data points is the available information and determines the order of the approximation.

The mathematical representation of a general interpolation function, also called *interpolator*, is any linear combination of simpler basis functions selected *a priori*. These interpolators can be linear, quadratic, cubic polynomials, etc., or trigonometric functions, or splines, or radial functions, or any group of functions forming a basis of interpolation (see section A.2). The following functions are examples of common bases for interpolators that have the general form: $\{b_0(x), b_1(x), b_2(x), \dots, b_n(x)\}$.

$$\begin{aligned}\{b_0(x) = 1, b_1(x) = x, b_2(x) = x^2, \dots, b_k(x) = x^k\}, \\ \{b_0(x) = 1, b_1(x) = e^x, b_2(x) = e^{2x}, \dots, b_n(x) = e^{nx}\}, \\ \{b_0(x) = 1, b_1(x) = \sin x, b_2(x) = \sin 2x, \dots, b_n(x) = \sin nx\}, \\ \{b_0(x) = T_0(x), b_1(x) = T_1(x), b_2(x) = T_2(x), \dots, b_n(x) = T_n(x)\}, \\ \{b_0(x) = H_0(x), b_1(x) = H_1(x), b_2(x) = H_2(x), \dots, b_n(x) = H_n(x)\}\end{aligned} \quad (\text{A.2})$$

The last examples $T_n(x)$ and $H_n(x)$ are the Tchebyshev and Hermite polynomials respectively. They are defined recursively as follows (Abramowitz and Stegun 1965):

$$\begin{aligned}
 T_n(x) &= \text{Cos}(n \text{Arcos } x) \quad \Rightarrow \quad T_0(x) = 1, T_1(x) = x \\
 T_{n+1}(x) - 2x T_n(x) + T_{n-1}(x) &= 0, \quad \forall n \geq 1, x \in [-1, 1] \\
 H_{n+1}(x) - x H_n(x) + n H_{n-1}(x) &= 0, \quad \forall n \geq 1, x \in (-\infty, \infty) \\
 H_0(x) = 1, \quad H_1(x) = x, \quad \frac{dH_n(x)}{dx} &= n H_{n-1}(x)
 \end{aligned}
 \tag{A.3}$$

A.1.2 Basis of a linear functional space

Let E_{01} be the space of linear polynomials defined in the interval $[0, 1]$; its elements are $E_{01} = \{f_1(x) = c_0 + c_1x \mid x \in [0, 1]\}$. E_{01} is a vectorial space of dimension two, because $\{1, x\}$ is a functional basis of this space. Any function of E_{01} can be written as a linear combination of 1 and x ; the couple of constants (c_0, c_1) are the coordinates of $f_1(x)$ in E_{01} . For example, the coordinates of $f_1(x) = x$ are $(0, 1)$, those of $f_1(x) = 1$ are $(1, 0)$, those of $f_1(x) = 1 - x$ are $(1, -1), \dots$, etc. The functions $b_0(x) = 1 - x, b_1(x) = x$, both are in E_{01} . Any function $f_1 \in E_{01}$ is represented by: $f_1(x) = c_0 + c_1x = c_0(1 - x) + (c_0 + c_1)x = f(0) b_0(x) + f(1) b_1(x)$. The functions $\{b_0, b_1\}$ are linearly independent; therefore, they also form another basis of the vectorial space E_{01} , (Ericsson *et al.* 1996, Weisstein 2003).

A.1.2.1 Karl Weierstrass approximation theorem (1885)

We know that any continuous function on a closed and bounded interval can be uniformly approximated on that interval by polynomials to any degree of accuracy. This fact is rigorously established by the following general theorem of Karl Weierstrass (Weisstein 2003):

- “If f is a continuous real-valued function on the interval $[a, b]$ and if any number $\varepsilon > 0$ is given, then there exists a polynomial $P(x)$ on $[a, b]$ such that $|f(x) - P(x)| < \varepsilon$ for all $x \in [a, b]$.”

Let f be a function that we want to interpolate and let $b_i(x)$ be a functional basis, then:

$$f(x) \approx P_n(x) = c_0 b_0(x) + c_1 b_1(x) + \dots + c_n b_n(x) = \sum_{i=0}^n c_i b_i(x)
 \tag{A.4}$$

where $P_n(x)$ is the generalized polynomial of order n approximating the function $f(x)$. The constants $c_i = \{c_0, c_1, c_2, \dots, c_n\}$ are the coordinates of the approximation and the set formed by $\{b_i(x), i = 0, n\}$ is the *basis of the interpolation*. If we define E_n as the space where these polynomials are living, then the dimension of E_n is equal to $n + 1$ because we need $n + 1$ numbers to get the representation of $P_n(x)$.

A.1.3 Support and matrix of the interpolation

To interpolate a function, the generalized polynomial (A.4) should reproduce exactly the $n + 1$ conditions imposed by the data of the available information:

$$P_n(x_k) = f(x_k), \quad \forall k = 0, n
 \tag{A.5}$$

The set of data points $S_n = \{x_0, x_1, x_2, \dots, x_n\}$ where the function $f(x)$ is known, is called the *interpolation support*. This support contains the points where there is accurate numeric information on $f(x)$. The support is local if S_n is smaller than the function domain. The support is global

We build up the interpolation matrix by computing the system (A.6) replacing the corresponding numerical data:

$$\begin{aligned} c_0 \sin(0.785397) + c_1 \sin(2 \times 0.785397) + c_2 \sin(3 \times 0.785397) &= 0.35355 \\ c_0 \sin(1.570795) + c_1 \sin(2 \times 1.570795) + c_2 \sin(3 \times 1.570795) &= 1.00000 \\ c_0 \sin(2.356193) + c_1 \sin(2 \times 2.356193) + c_2 \sin(3 \times 2.356193) &= 0.35356 \end{aligned}$$

Thus, the interpolation matrix is:

$$\mathbf{B} = \begin{pmatrix} 0.707106 & 1 & 0.707106 \\ 1.00000 & 0 & -1.00000 \\ 0.707106 & -1 & 0.707106 \end{pmatrix}, \quad \vec{C} = \begin{pmatrix} c_0 \\ c_1 \\ c_2 \end{pmatrix}, \quad \vec{F} = \begin{pmatrix} 0.35355 \\ 1.00000 \\ 0.35356 \end{pmatrix}$$

The exact solution of this system is:

$$\vec{C} = \mathbf{B}^{-1} \cdot \vec{F} = \begin{pmatrix} 0.354 & 0.5 & 0.354 \\ 0.5 & 0 & -0.5 \\ 0.354 & -0.5 & 0.354 \end{pmatrix} \cdot \begin{pmatrix} 0.354 \\ 1.000 \\ 0.354 \end{pmatrix} = \begin{pmatrix} 0.751 \\ 0.000 \\ -0.249 \end{pmatrix}$$

Therefore the interpolation polynomial is:

$$P_3(x) = \vec{C} \cdot \vec{b}(x) = \mathbf{B}^{-1} \cdot \vec{F} \cdot \vec{b}(x) = 0.751 \sin x - 0.249 \sin 3x$$

Let compute an “unknown” value of the original function, for example $x = 3\pi/8$. The interpolated value is: $f(3\pi/8) \approx P_3(3\pi/8) = 0.78912$. In this case we can compare this result with the real value $\sin^3(3\pi/8) = 0.78858$. Thus, the absolute error of the interpolation is 0.00054 for this particular example. Notice that the point $3\pi/8$ is inside the range of the support. If we use this interpolation to estimate other values of the function outside the support $x \notin [x_1, x_3]$ we perform an extrapolation.

A.1.4.2 Example 2

We have a support of three points (x_0, x_1, x_2) :

x_k	$x_0 = 0.0$	$x_1 = 4.0$	$x_3 = 6.0$
$f(x_k)$	$f_0 = 1.0$	$f_2 = 2.0$	$f_3 = 3.0$

We consider the basis formed by the monomials $\{b_0(x) = 1, b_1(x) = x, b_2(x) = x^2\}$, the system (A.7) becomes:

$$\mathbf{B} \cdot \vec{C} = \vec{F} \Leftrightarrow \begin{pmatrix} 1 & x_0 & x_0^2 \\ 1 & x_1 & x_1^2 \\ 1 & x_2 & x_2^2 \end{pmatrix} \cdot \begin{pmatrix} c_0 \\ c_1 \\ c_2 \end{pmatrix} = \begin{pmatrix} f_0 \\ f_1 \\ f_2 \end{pmatrix} \tag{A.10}$$

The determinant of the matrix is $\det \mathbf{B} = D = 48$. The inverse matrix \mathbf{B}^{-1} is:

$$\begin{aligned} \mathbf{B}^{-1} &= \frac{1}{D} \begin{pmatrix} x_1 x_2 (x_2 - x_1) & x_0 x_2 (x_0 - x_2) & x_0 x_1 (x_1 - x_0) \\ x_1^2 - x_2^2 & x_2^2 - x_0^2 & x_0^2 - x_1^2 \\ x_2 - x_1 & x_0 - x_2 & x_1 - x_0 \end{pmatrix} \\ \Rightarrow c_0 &= \frac{x_1 x_2 (x_2 - x_1)}{D} f_0 + \frac{x_0 x_2 (x_0 - x_2)}{D} f_1 + \frac{x_0 x_1 (x_1 - x_0)}{D} f_2 = 1 \\ c_1 &= \frac{x_1^2 - x_2^2}{D} f_0 + \frac{x_2^2 - x_0^2}{D} f_1 + \frac{x_0^2 - x_1^2}{D} f_2 = 0.083 \\ c_2 &= \frac{x_2 - x_1}{D} f_0 + \frac{x_0 - x_2}{D} f_1 + \frac{x_1 - x_0}{D} f_2 = 0.042 \end{aligned} \quad (\text{A.11})$$

The interpolator of $f(x)$, which is only known in three different points, is the quadratic polynomial:

$$f(x) \approx P_2(x) = \sum_{i=0}^2 c_i b_i(x) = c_0 + c_1 x + c_2 x^2 = 1 + 0.083 x + 0.042 x^2$$

It is easy to estimate an unknown value $f(5) \approx 1 + 0.083 \cdot 5 + 0.042 \cdot 25 = 2.465$. The interpolation based on the classic polynomials $P_n(x) = c_0 + c_1 x + c_2 x^2 + \dots + c_n x^n$, is useful because of the simplicity of the functions involved. These interpolators are very important in finite elements and deserve a special attention.

A.1.5 *The Lagrange interpolation polynomials*

These classical polynomials conform the most simple and useful technique to interpolate functions. The basis is formed by the monomials $\{1, x, x^2, \dots, x^n\}$. The use of this basis to construct interpolators is called Lagrange interpolation. The general form of the interpolation based on Lagrange polynomials is (Legras 1973):

$$\begin{aligned} P_n(x) &= \sum_{j=0}^n L_j(x) f(x_j), \quad \text{where:} \\ L_j(x) &= \prod_{\substack{i=0 \\ j \neq i}}^n \frac{x - x_i}{x_j - x_i}; \quad L_j(x_j) = 1; \quad L_j(x_i) = 0 \end{aligned} \quad (\text{A.12})$$

Lagrange interpolation is a fundamental technique in the FEM. All the Lagrange polynomials can be deduced using equation (A.12); the most useful are linear, quadratic and cubic.

Any function known only in two different points (x_0, f_0) and (x_1, f_1) can be interpolated with the linear polynomial $P_1(x)$. Using the general formula (A.12) for $n = 0, 1$, two linear Lagrange polynomials are deduced (Fig. A.1):

$$\begin{aligned} L_0(x) &= \frac{x - x_1}{x_0 - x_1}, \quad \left\{ \begin{array}{l} L_0(x_0) = 1 \\ L_0(x_1) = 0 \end{array} \right\}, \quad L_1(x) = \frac{x - x_0}{x_1 - x_0}, \quad \left\{ \begin{array}{l} L_1(x_0) = 0 \\ L_1(x_1) = 1 \end{array} \right\} \\ P_1(x) &= \sum_{j=0}^1 L_j(x) f(x_j) = L_0(x) f_0 + L_1(x) f_1 \end{aligned} \quad (\text{A.13})$$

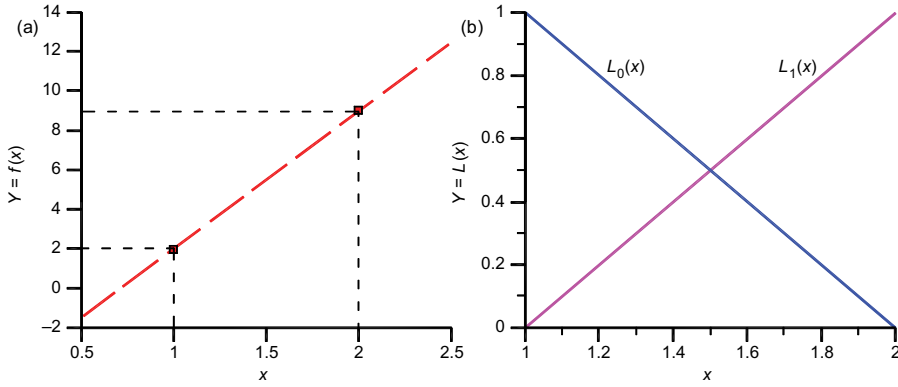


Figure A.1. Interpolation using the linear Lagrange polynomials: (a) Interpolation of $f(x)$ with linear Lagrange polynomials; (b) The linear Lagrange polynomials $L_0(x)$ and $L_1(x)$.

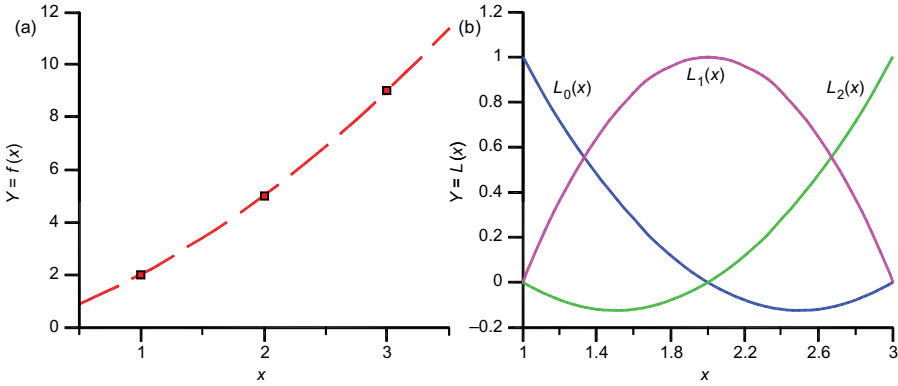


Figure A.2. Interpolation with the quadratic Lagrange polynomials: (a) Interpolation of $f(x)$ with quadratic Lagrange polynomials; (b) The quadratic Lagrange polynomials.

Any function known in three different points (x_0, f_0) , (x_1, f_1) , (x_2, f_2) can be interpolated with the polynomial $P_2(x)$. There are three quadratic Lagrange polynomials (Fig. A.2):

$$L_0(x) = \frac{x - x_1}{x_0 - x_1} \frac{x - x_2}{x_0 - x_2}, \quad L_1(x) = \frac{x - x_0}{x_1 - x_0} \frac{x - x_2}{x_1 - x_2}, \quad L_2(x) = \frac{x - x_0}{x_2 - x_0} \frac{x - x_1}{x_2 - x_1}$$

$$L_i(x_i) = 1, \quad L_i(x_j) = 0, \quad \text{or: } L_i(x_j) = \delta_{ij}, \tag{A.14}$$

$$\text{and: } P_2(x) = \sum_{j=0}^2 L_j(x) f_j = L_0(x) f_0 + L_1(x) f_1 + L_2(x) f_2$$

Any function known in four different points (x_0, f_0) , (x_1, f_1) , (x_2, f_2) and (x_3, f_3) can be interpolated using the cubic polynomial $P_3(x)$. For $n = 0, 1, 2, 3$ there are four Lagrange

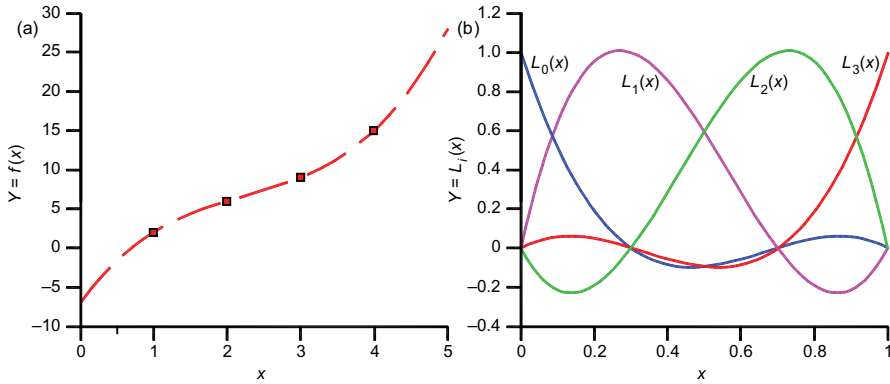


Figure A.3. Interpolation with the cubic Lagrange polynomials: (a) $f(x)$ interpolated with cubic Lagrange polynomials; (b) The cubic Lagrange polynomials.

polynomials. Note again that $L_i(x_j) = \delta_{ij}$ (Fig. A.3):

$$\begin{aligned}
 L_0(x) &= \frac{(x - x_1)(x - x_2)(x - x_3)}{(x_0 - x_1)(x_0 - x_2)(x_0 - x_3)}, & L_1(x) &= \frac{(x - x_0)(x - x_2)(x - x_3)}{(x_1 - x_0)(x_1 - x_2)(x_1 - x_3)} \\
 L_2(x) &= \frac{(x - x_0)(x - x_1)(x - x_3)}{(x_2 - x_0)(x_2 - x_1)(x_2 - x_3)}, & L_3(x) &= \frac{(x - x_0)(x - x_1)(x - x_2)}{(x_3 - x_0)(x_3 - x_1)(x_3 - x_2)}
 \end{aligned}
 \tag{A.15}$$

A.1.5.1 Example 1

Build the Lagrange interpolation polynomial of degree three for a function $f(x)$ whose known values are the following:

x_i	0	1	3	4
$f(x_i)$	1	3	2	5

By direct application of formula (A.15):

$$\begin{aligned}
 f(x) \approx P_3(x) &= \sum_{j=0}^3 L_j(x) f(x_j) = \sum_{j=0}^3 \frac{(x - x_0)(x - x_1)(x - x_2)}{(x_j - x_0)(x_j - x_1)(x_j - x_2)} f_j \\
 &= \frac{(x - 1)(x - 3)(x - 4)}{(1 - 0)(3 - 0)(4 - 0)} \cdot 1 + \frac{x(x - 3)(x - 4)}{1(1 - 3)(1 - 4)} \cdot 3 + \frac{x(x - 1)(x - 4)}{3(3 - 1)(3 - 4)} \cdot 2 \\
 &\quad + \frac{x(x - 1)(x - 3)}{4(4 - 1)(4 - 3)} \cdot 5 \quad \text{then: } f(x) \approx P_3(x) = 1 + 4.33x - 2.83x^2 + 0.5x^3
 \end{aligned}$$

In the FEM the Lagrange polynomials are commonly used for $n = 1, 2, 3$ and are very helpful in solving flow problems in one, two or three dimensions. However, these polynomials are practical only for lower degree interpolations; with $n > 4$ they become oscillating, especially if the nodes of the support are equidistant. This behavior is known as the Runge’s phenomenon and is illustrated in the following example.

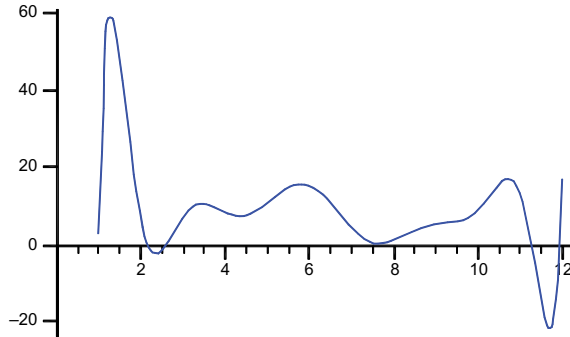


Figure A.4. Oscillations of a high order Lagrange interpolation polynomial for the function $f(x)$.

A.1.5.2 Example 2

Let $f(x)$ be a function known in the values below. We apply a Lagrange interpolation of order 12 to observe oscillations close to the extremes of the support. Two interpolated results are completely outside the range of measured values (Fig. A.4):

x_i	1	2	3	4	5	6	7	8	9	10	11	12
$f(x_i)$	3	6	7	8.5	11	15	4.2	1.1	5.5	9	13	17

A.2 INTERPOLATION IN TWO AND THREE DIMENSIONS

The mathematical representations of general interpolators in two and three dimensions are also linear combinations of basis functions selected *a priori*. These interpolators can be bilinear, quadratic, or cubic polynomials, trigonometric functions, or any group of functions in two or three variables forming bases of interpolation. Let f be a function defined in a two or three-dimensional space. We want to interpolate $f(\vec{x})$ using the basis $b_i(\vec{x})$, here the variable is the vector $(\vec{x}) = (x, y)$ or $(\vec{x}) = (x, y, z)$ then:

$$f(\vec{x}) \approx P_n(\vec{x}) = \sum_{i=0}^n c_i b_i(\vec{x}) = c_0 b_0(\vec{x}) + c_1 b_1(\vec{x}) + \dots + c_n b_n(\vec{x})$$

$$P_n(\vec{x}_k) = f(\vec{x}_k), \quad \forall k = 0, n \quad \Leftrightarrow \quad \mathbf{B} \cdot \vec{C} = \vec{F} \tag{A.16}$$

where the support is: $\{\vec{x}_0, \vec{x}_1, \vec{x}_2, \dots, \vec{x}_n\}$; $\vec{x}_k = (x_k, y_k, z_k)$

$P_n(\vec{x})$ is the generalized polynomial of order n approximating the function $f(\vec{x})$. The constants $c_i = \{c_0, c_1, c_2, \dots, c_n\}$ are the coordinates of the approximation and the set formed by $\{b_i(\vec{x}), i = 0, n\}$ is the basis of the multidimensional interpolation. The generalized polynomial (A.16) should reproduce exactly the $n+1$ conditions imposed by the available data. The solution of the system (A.16) has the same form as in equation (A.8). The inverse matrix equation of (A.16) is the general solution of the multidimensional interpolation problem. Thus, the only difference with the interpolation in one dimension is the construction of the basis in two and three

dimensions. The following functions are examples of common multidimensional bases:

$$\{1, x, y, xy, x^2, y^2, x^2y, xy^2, x^2y^2, \dots, x^p y^q\} \quad \forall p, q = 0, 1, 2, 3, \dots$$

$$\{1, \sin x, \sin y, \sin x \sin y, \sin x \sin 2y, \sin 2x \sin 2y, \dots, \sin px \sin qy\} \quad (\text{A.17})$$

$$\{1, T_1(x), T_1(y), T_1(x)T_1(y), T_1(x)T_2(y), T_2(x)T_2(y), \dots, T_p(x)T_q(y)\}$$

The two- or three-dimensional interpolation base can be written in a general form:

$$\{b_p(x)b_q(y)b_r(z), \forall p, q, r = 0, 1, 2, 3, \dots\} \quad (\text{A.18})$$

where b_p , b_q and b_r are any of the basis functions defined in equation (A.2) for the variables x , y , z , respectively. The case of Lagrange interpolators for two and three dimensions is particularly important. For two dimensions, the bilinear interpolation is:

$$\begin{aligned} f(x, y) &\approx P_1(x, y) = \sum_{k=0}^1 L_k(x, y) f(x_k, y_k) = \sum_{k=0}^1 L_k(x) \cdot L_k(y) f_k \\ &= L_0(x) \cdot L_0(y) f_0 + L_1(x) \cdot L_1(y) f_1 = \frac{x - x_1}{x_0 - x_1} \cdot \frac{y - y_1}{y_0 - y_1} f_0 + \frac{x - x_0}{x_1 - x_0} \cdot \frac{y - y_0}{y_1 - y_0} f_1 \end{aligned} \quad (\text{A.19})$$

For three dimensions, the trilinear interpolation is:

$$\begin{aligned} f(x, y, z) &\approx P_1(x, y, z) = \sum_{k=0}^1 L_k(x) \cdot L_k(y) \cdot L_k(z) f_k \\ &= L_0(x) \cdot L_0(y) \cdot L_0(z) f_0 + L_1(x) \cdot L_1(y) \cdot L_1(z) f_1 \\ &= \frac{x - x_1}{x_0 - x_1} \cdot \frac{y - y_1}{y_0 - y_1} \cdot \frac{z - z_1}{z_0 - z_1} f_0 + \frac{x - x_0}{x_1 - x_0} \cdot \frac{y - y_0}{y_1 - y_0} \cdot \frac{z - z_0}{z_1 - z_0} f_1 \end{aligned} \quad (\text{A.20})$$

The construction of multidimensional Lagrange polynomials of higher degree can be easily extended following these two examples in equations (A.14) and (A.15).

A.3 ELEMENTS OF TENSOR ANALYSIS

In mathematical terminology (Weisstein 2003) three orthonormal vectors $\{\vec{e}_1, \vec{e}_2, \vec{e}_3\}$ define a vectorial basis in the three-dimensional space \mathbb{R}^3 . Any vector \vec{v} in \mathbb{R}^3 can be represented as a linear combination of the basic vectors: $v = v_1 \vec{e}_1 + v_2 \vec{e}_2 + v_3 \vec{e}_3$. We say that this basis “*generates*” the vectorial space \mathbb{R}^3 . A basis of a higher dimensional vector space V is defined as a subset $\vec{b}_0 = \{\vec{e}_1, \vec{e}_2, \dots, \vec{e}_n\}$ of vectors in V that are linearly independent and generate V . These vectors form a basis if and only if every $v \in V$ can be uniquely written as: $v = v_1 \vec{e}_1 + v_2 \vec{e}_2 + \dots + v_n \vec{e}_n$; where the numbers v_1, v_2, \dots, v_n are called the coordinates of vector v . All these concepts are extended to vectorial spaces of real functions. The vector space V will have many different bases, but there is always the same number of basis vectors in each of them. The number of basis vectors in V is called the dimension of V . In this book, we used specifically the index notation to represent vectors and tensors in two, three, or four dimensions.

A.3.1 Index notation for vectors and tensors

The advantage of the index notation is that a vectorial or tensorial function comprising many components can be represented by only one. For example any vector in \mathbb{R}^3 has three components

$v = v_1\vec{e}_1 + v_2\vec{e}_2 + v_3\vec{e}_3$. Any of its coordinates (v_1, v_2, v_3) can be represented by v_i with one index and thus, it represents the vector itself for $i = 1, 2, 3$. We say that v_i constitutes a tensor of the first order. We define a second-order tensor as a linear operator \mathbf{T} of the space V into itself, $\mathbf{T}: V \rightarrow V$. In more advanced terms, a tensor is a transformation of one coordinate system to another, in the same space, according to certain laws. This definition involves invariant properties, which are very important in the mathematical representation of continuum physical laws. A second-order tensor in \mathbb{R}^3 is a matrix that can be constructed with the tensorial product of two vectors:

$$\vec{u} \otimes \vec{v} = \begin{pmatrix} u_1 \\ u_2 \\ u_3 \end{pmatrix} \begin{pmatrix} v_1 & v_2 & v_3 \end{pmatrix} = \begin{pmatrix} u_1v_1 & u_1v_2 & u_1v_3 \\ u_2v_1 & u_2v_2 & u_2v_3 \\ u_3v_1 & u_3v_2 & u_3v_3 \end{pmatrix} = \begin{pmatrix} T_{11} & T_{12} & T_{13} \\ T_{21} & T_{22} & T_{23} \\ T_{31} & T_{32} & T_{33} \end{pmatrix} = (T_{ij}) \quad (\text{A.21})$$

Note that in the index notation, T_{ij} has two indices ($i, j = 1, 2, 3$) representing the six components of a matrix \mathbf{T} . Using the vectors of the orthonormal basis in equation (A.21) $\{\vec{e}_1 = (1, 0, 0), \vec{e}_2 = (0, 1, 0), \vec{e}_3 = (0, 0, 1)\}$ the tensorial product becomes:

$$\mathbf{T} = \vec{u} \otimes \vec{v} = u_i\vec{e}_i \otimes v_j\vec{e}_j = u_iv_j\vec{e}_i \otimes \vec{e}_j = T_{ij}\vec{e}_i \otimes \vec{e}_j \quad (\text{A.22})$$

Any term in which an index is repeated, for example i (or j), denotes a sum of all terms obtained by assigning ($i = 1, 2, 3$). This is the summation convention for tensors. Thus, equation (A.22) is equivalent to the expression:

$$\begin{aligned} u_iv_j\vec{e}_i \otimes \vec{e}_j &= u_1v_1 \begin{pmatrix} 1 \\ 0 \\ 0 \end{pmatrix} \begin{pmatrix} 1 & 0 & 0 \end{pmatrix} + u_1v_2 \begin{pmatrix} 1 \\ 0 \\ 0 \end{pmatrix} \begin{pmatrix} 0 & 1 & 0 \end{pmatrix} \\ &+ \dots + u_3v_3 \begin{pmatrix} 0 \\ 0 \\ 1 \end{pmatrix} \begin{pmatrix} 0 & 0 & 1 \end{pmatrix} \end{aligned} \quad (\text{A.23})$$

The scalar product of two vectors, using index notation is:

$$\vec{u} \cdot \vec{v} = u_i\vec{e}_i \cdot v_j\vec{e}_j = u_iv_j\vec{e}_i \cdot \vec{e}_j = u_iv_j\delta_{ij} = u_iv_i = u_1v_1 + u_2v_2 + u_3v_3 \quad (\text{A.24})$$

The symbol δ_{ij} is the unit second-order tensor, also known as the Kronecker delta, and defined as follows:

$$\delta_{ij} = \begin{cases} 1, & \text{if } i = j \\ 0, & \text{if } i \neq j \end{cases} \quad \Leftrightarrow \quad \vec{e}_i \cdot \vec{e}_j = \delta_{ij} \quad (\text{A.25})$$

The dot product of a tensor by a vector $\mathbf{T} \cdot \vec{x}$ becomes:

$$\begin{pmatrix} T_{11} & T_{12} & T_{13} \\ T_{21} & T_{22} & T_{23} \\ T_{31} & T_{32} & T_{33} \end{pmatrix} \cdot \begin{pmatrix} x_1 \\ x_2 \\ x_3 \end{pmatrix} = (T_{ij}\vec{e}_i \otimes \vec{e}_j) \cdot x_k\vec{e}_k = T_{ij}x_k\vec{e}_i \otimes \vec{e}_j \cdot \vec{e}_k = T_{ij}x_k\vec{e}_i\delta_{jk} = T_{ij}x_j\vec{e}_i \quad (\text{A.26})$$

A.3.2 Differential operators in curvilinear coordinates

The differential operators used in this book can be written in different coordinate systems for any function u : cartesian, cylindrical and spherical.

Cartesian coordinates $u(x, y, z), \vec{v} = (v_x, v_y, v_z)$

$$\text{Gradient: } \vec{\nabla}u = \left(\frac{\partial u}{\partial x}, \frac{\partial u}{\partial y}, \frac{\partial u}{\partial z} \right); \nabla_x u = \frac{\partial u}{\partial x}, \nabla_y u = \frac{\partial u}{\partial y}, \nabla_z u = \frac{\partial u}{\partial z}$$

$$\text{Divergence: } \operatorname{div}(\vec{v}) = \vec{\nabla} \cdot \vec{v} = \frac{\partial v_x}{\partial x} + \frac{\partial v_y}{\partial y} + \frac{\partial v_z}{\partial z} = \partial_i v_i$$

$$\text{Laplacian: } \nabla^2 u = \operatorname{div}(\vec{\nabla}u) = \vec{\nabla} \cdot \vec{\nabla}u = \frac{\partial^2 u}{\partial x^2} + \frac{\partial^2 u}{\partial y^2} + \frac{\partial^2 u}{\partial z^2} = \partial_i (\partial_i u)$$

Cylindrical coordinates $u(r, \theta, z), \vec{v} = (v_r, v_\theta, v_z)$

$$\text{Gradient: } \vec{\nabla}u = \left(\frac{\partial u}{\partial r}, \frac{1}{r} \frac{\partial u}{\partial \theta}, \frac{\partial u}{\partial z} \right); \nabla_r u = \frac{\partial u}{\partial r}, \nabla_\theta u = \frac{1}{r} \frac{\partial u}{\partial \theta}, \nabla_z u = \frac{\partial u}{\partial z}$$

$$\text{Divergence: } \operatorname{div}(\vec{v}) = \vec{\nabla} \cdot \vec{v} = \frac{1}{r} \frac{\partial}{\partial r}(rv_r) + \frac{1}{r} \frac{\partial v_\theta}{\partial \theta} + \frac{\partial v_z}{\partial z}$$

$$\text{Laplacian: } \nabla^2 u = \vec{\nabla} \cdot \vec{\nabla}u = \frac{1}{r} \frac{\partial}{\partial r} \left(r \frac{\partial u}{\partial r} \right) + \frac{1}{r^2} \frac{\partial^2 u}{\partial \theta^2} + \frac{\partial^2 u}{\partial z^2}$$

Spherical coordinates $u(r, \theta, \varphi), \vec{v} = (v_r, v_\theta, v_\varphi)$

$$\text{Gradient: } \vec{\nabla}u = (\nabla_r u, \nabla_\theta u, \nabla_\varphi u); \nabla_r u = \frac{\partial u}{\partial r}, \nabla_\theta u = \frac{1}{r} \frac{\partial u}{\partial \theta}, \nabla_\varphi u = \frac{1}{r \sin \theta} \frac{\partial u}{\partial \varphi}$$

$$\text{Divergence: } \operatorname{div}(\vec{v}) = \vec{\nabla} \cdot \vec{v} = \frac{1}{r^2} \frac{\partial}{\partial r}(r^2 v_r) + \frac{1}{r \sin \theta} \frac{\partial}{\partial \theta}(v_\theta \sin \theta) + \frac{1}{r \sin \theta} \frac{\partial v_\varphi}{\partial \varphi}$$

$$\text{Laplacian: } \nabla^2 u = \operatorname{div}(\vec{\nabla}u) = \frac{1}{r^2} \frac{\partial}{\partial r} \left(r^2 \frac{\partial u}{\partial r} \right) + \frac{1}{r^2 \sin \theta} \frac{\partial}{\partial \theta} \left(\sin \theta \frac{\partial u}{\partial \theta} \right) + \frac{1}{r^2 \sin^2 \theta} \frac{\partial^2 u}{\partial \varphi^2}$$

A.3.3 Tensorial notation for differential operators in cartesian coordinates

$$\vec{\nabla}u = \left(\frac{\partial u}{\partial x_i} \vec{e}_i \right); \frac{\partial u}{\partial n} = \vec{\nabla}u \cdot \vec{n} = \frac{\partial u}{\partial x_i} n_i; \operatorname{div} \vec{v} = \vec{\nabla} \cdot \vec{v} = \frac{\partial v_i}{\partial x_i}; \nabla^2 u = \Delta u = \frac{\partial^2 u}{\partial x_i \partial x_i}$$

$$\vec{\nabla} \vec{v} = \left(\frac{\partial v_i}{\partial x_j} \vec{e}_i \otimes \vec{e}_j \right); \nabla^2 \vec{v} = \left(\frac{\partial^2 v_i}{\partial x_j \partial x_j} \vec{e}_i \right); \quad (\text{gradient and Laplacian of a vector})$$

A.4 THE INTEGRAL THEOREM OF STOKES

Stokes' theorem states that the integral of the differential of a function dw over a domain Ω is equal to the integral of the function $w(x, y, z)$ along the boundary $\partial\Omega$ of the domain:

$$\int_{\Omega} dw = \int_{\partial\Omega} w \tag{A.27}$$

This integral theorem is one of the most important general results of calculus. It holds in all dimensions, but it is particularly useful for three-dimensional domains. In more rigorous

mathematical terms, w is a differential form with compact support and dw is called the exterior derivative of w (Weisstein 2003). If the domain Ω is of dimension n , then its boundary $\partial\Omega$ is of dimension $n - 1$. Stokes' general theorem is connected to several particular but powerful integral theorems, which involve the differential operators divergence, gradient and Laplacian. These specific results allow transforming the integrals that lead to the weak form of PDEs in the finite element method.

A.4.1 Riemann's theorem

Let $w(x, y) = f \, dy - g \, dx$ be a differential form in two dimensions. Applying directly Stoke's theorem (Fig. A.5):

$$\int_{\Omega} dw = \int_{\Omega} \left(\frac{\partial f}{\partial x} + \frac{\partial g}{\partial y} \right) dx \, dy = \int_{\partial\Omega} (f \, dy - g \, dx) \tag{A.28}$$

If (f, g) are the components of the gradient of a known function $F(x, y)$:

$$\begin{aligned} \vec{\nabla}F &= \left(\frac{\partial F}{\partial x}, \frac{\partial F}{\partial y} \right) = (f, g) \quad \text{and:} \quad \vec{n} = (n_x, n_y), \quad \vec{\tau} = (-n_y, n_x) = \left(\frac{dx}{ds}, \frac{dy}{ds} \right) \\ \Rightarrow \int_{\Omega} \left(\frac{\partial f}{\partial x} + \frac{\partial g}{\partial y} \right) dx \, dy &= \int_{\Omega} \left(\frac{\partial^2 F}{\partial x^2} + \frac{\partial^2 F}{\partial y^2} \right) dx \, dy = \int_{\partial\Omega} (fn_x + gn_y) \, ds \tag{A.29} \\ &= \int_{\partial\Omega} \left(\frac{\partial F}{\partial x} n_x + \frac{\partial F}{\partial y} n_y \right) ds = \int_{\partial\Omega} \vec{\nabla}F \cdot \vec{n} \, ds \quad \Leftrightarrow \quad \boxed{\int_{\Omega} \nabla^2 F \, dx \, dy = \int_{\Gamma} \frac{\partial F}{\partial n} \, ds} \end{aligned}$$

A.4.2 Green's first identity

This formula is a consequence of result (A.28) applied to the following change of functions (Fig. A.5):

$$\begin{aligned} f &= u \frac{\partial v}{\partial x}, \quad g = u \frac{\partial v}{\partial y} \quad \Rightarrow \quad \frac{\partial^2 F}{\partial x^2} = \left(\frac{\partial u}{\partial x} \frac{\partial v}{\partial x} + u \frac{\partial^2 v}{\partial x^2} \right), \quad \frac{\partial^2 F}{\partial x^2} = \left(\frac{\partial u}{\partial x} \frac{\partial v}{\partial x} + u \frac{\partial^2 v}{\partial x^2} \right) \\ \Rightarrow \quad \nabla^2 F &= \vec{\nabla}u \cdot \vec{\nabla}v + u \nabla^2 v, \quad \text{and} \quad \vec{\nabla}F \cdot \vec{n} = u \frac{\partial v}{\partial x} n_x + u \frac{\partial v}{\partial y} n_y = u \vec{\nabla}v \cdot \vec{n} \end{aligned}$$

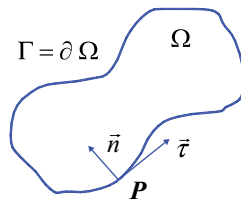


Figure A.5. A domain Ω showing its boundary with normal \vec{n} and tangent $\vec{\tau}$ vectors at any point $P(x, y)$ of $\Gamma = \partial\Omega$.

Replacing these relationships into Riemann's theorem (A.28) we obtain the first integral formula of Green, which is valid in two and three dimensions:

$$\int_{\Omega} (\vec{\nabla}u \cdot \vec{\nabla}v + u \nabla^2 v) d\Omega = \int_{\partial\Omega} u \vec{\nabla}v \cdot \vec{n} dA = \int_{\Gamma} u \frac{\partial v}{\partial n} ds \quad (\text{A.30})$$

A.4.3 *Green's second identity*

This second formula is a simple consequence of equation (A.29). By applying previous result (A.28) to the following functions:

$$\begin{aligned} f &= v \frac{\partial u}{\partial x}, \quad g = v \frac{\partial u}{\partial y} \quad \Rightarrow \quad \frac{\partial^2 F}{\partial x^2} = \left(\frac{\partial u}{\partial x} \frac{\partial v}{\partial x} + v \frac{\partial^2 u}{\partial x^2} \right), \quad \frac{\partial^2 F}{\partial x^2} = \left(\frac{\partial u}{\partial x} \frac{\partial v}{\partial x} + v \frac{\partial^2 u}{\partial x^2} \right) \\ \Rightarrow \quad \nabla^2 F &= \vec{\nabla}u \cdot \vec{\nabla}v + v \nabla^2 u, \quad \text{and} \quad \vec{\nabla}F \cdot \vec{n} = v \frac{\partial u}{\partial x} n_x + v \frac{\partial u}{\partial y} n_y = v \vec{\nabla}u \cdot \vec{n} \\ \Rightarrow \quad \int_{\Omega} (\vec{\nabla}u \cdot \vec{\nabla}v + v \nabla^2 u) d\Omega &= \int_{\partial\Omega} v \vec{\nabla}u \cdot \vec{n} dA \end{aligned}$$

Subtracting this result from (A.29) we obtain:

$$\begin{aligned} \int_{\Omega} (\vec{\nabla}u \cdot \vec{\nabla}v + u \nabla^2 v - \vec{\nabla}u \cdot \vec{\nabla}v - v \nabla^2 u) d\Omega &= \int_{\partial\Omega} (u \vec{\nabla}v \cdot \vec{n} - v \vec{\nabla}u \cdot \vec{n}) dA \\ \int_{\Omega} (u \nabla^2 v - v \nabla^2 u) d\Omega &= \int_{\partial\Omega} (u \vec{\nabla}v - v \vec{\nabla}u) \cdot \vec{n} dA = \int_{\Gamma} \left(u \frac{\partial v}{\partial n} - v \frac{\partial u}{\partial n} \right) ds \end{aligned} \quad (\text{A.31})$$

This last equation is known as the Green's second formula. Both identities are useful in the finite element method.

A.4.4 *The divergence theorem*

This theorem is another very important integral property, which derives directly from Green's second identity for the following particular functions:

$$\begin{aligned} u &= 1 \quad \text{and} \quad \vec{v} = \vec{\nabla}v \quad \Rightarrow \quad \vec{\nabla}u = \vec{0}, \quad \nabla^2 u = 0, \quad \nabla^2 v = \text{div } \vec{v} \\ \Rightarrow \quad \int_{\Omega} \text{div } \vec{v} d\Omega &= \int_{\partial\Omega} \vec{v} \cdot \vec{n} dA \end{aligned} \quad (\text{A.32})$$

A.4.5 *The Dirac distribution*

The distributions are special operators also called "generalized functions". The Dirac distribution is known in physics as the "impulse function". In one dimension it is defined with the symbol

$\delta(x)$, $x \in \mathbb{R}$ and it has the following properties:

$$\delta(x) = \begin{cases} \infty, & x = 0 \\ 0, & x \neq 0 \end{cases}, \quad \int_{-\infty}^{\infty} \delta(x) dx = 1 \quad (\text{A.33})$$

An explicit construction of this distribution is given in the next example:

$$f_m(x) = \begin{cases} \frac{m}{2}, & |x| < \frac{1}{m} \\ 0, & |x| \geq \frac{1}{m} \end{cases} \Rightarrow \delta(x) = \lim_{m \rightarrow \infty} f_m(x) \quad (\text{A.34})$$

$$\int_{-\infty}^{\infty} \delta(x) dx = \lim_{m \rightarrow \infty} \int_{-m}^m \frac{m}{2} dx = \lim_{m \rightarrow \infty} \left. \frac{m}{2} x \right|_{-m}^m = \lim_{m \rightarrow \infty} \frac{m}{2} \left(\frac{1}{m} + \frac{1}{m} \right) = 1$$

Another important property is the effect it has on real functions that are integrables:

$$\forall h : \mathbb{R} \rightarrow \mathbb{R} : \int_{-\infty}^{\infty} \delta(x) h(x) dx = h(0), \quad \int_{\mathbb{R}} \delta(x - x_0) h(x) dx = h(x_0) \quad (\text{A.35})$$

Where $h(x)$ is any continuous function defined in a finite interval, which contains x_0 . The Dirac distribution can be defined also in two-dimensions:

$$\text{If } \vec{P}, \vec{P}_0 \in \mathbb{R}^2 \Rightarrow \delta(\vec{P} - \vec{P}_0) = \begin{cases} 0, & \text{if } \vec{P} \neq \vec{P}_0 \\ \infty, & \text{if } \vec{P} = \vec{P}_0 \end{cases} \quad (\text{A.36})$$

$$\text{Then: } \int_{\Omega} \delta(\vec{P} - \vec{P}_0) d\Omega = 1, \quad \int_{\Omega} \delta(\vec{P} - \vec{P}_0) h(\vec{P}) d\Omega = h(\vec{P}_0)$$

A similar definition holds in three-dimensions. Two explicit constructions are given in the following examples. Let r be a radial variable such that:

$$r^2 = |\vec{P} - \vec{P}_0|^2 = (x - x_0)^2 + (y - y_0)^2 \geq 0 \Rightarrow$$

$$f_m(r) = \begin{cases} \frac{m^2}{\pi}, & \text{if } r < \frac{1}{m} \\ 0, & \text{if } r \geq \frac{1}{m} \end{cases}; \quad f_m(r) = \frac{m}{\pi} e^{-mr^2} \Rightarrow \delta(\vec{P} - \vec{P}_0) = \lim_{m \rightarrow \infty} f_m(r) \quad (\text{A.37})$$

$$\text{and : } \delta(\vec{P} - \vec{P}_0) = \delta(x - x_0) \delta(y - y_0)$$

These results are necessary in the boundary element method developed in Chapter 5.

B: Tabulated thermal conductivities

Table B1. Thermal conductivity k_T (W/m/K) of the principal rock-forming minerals of the upper earth's crust as function of direction in the crystal lattice and of temperature. Values of k_T are given in bold as averages over the data n (where $n > 1$; standard deviation is also given even if statistically not significant). The experimental temperature is T ; where unknown, RT stands for room temperature without specification. The directional dependence of the measured unidirectional value of k_T , which is caused by the anisotropy of the minerals due to its specific crystal lattice, is indicated alternatively by: (1) the crystal's optical axes $\{100\}$, $\{010\}$ and $\{001\}$, (2) the diagonal elements k_{T11} , k_{T22} and k_{T33} of the tensor \mathbf{k}_T , with k_{T33} being parallel to the $\{001\}$ axis, and the $\{100\}$ axis lying in the k_{T11} and k_{T22} plane, and (3) the components of k_T parallel (\parallel) or perpendicular (\perp) to the crystals direction of highest k_T . Where this information is absent, "x" indicates measurements on single crystals, and "a" on single-mineral aggregates. Mean values k_{Tm} are calculated after Popov *et al.* (1987) as $k_{Tm} = 1/3(k_{T\{100\}} + k_{T\{010\}} + k_{T\{001\}})$. Data sets from different authors are separated by "—", and authors are given by number in square brackets. [1] Sass (1965), [2] Horai (1971), [3] Dreyer (1974), [4] Popov *et al.* (1987), [5] Popov *et al.* (1999), [6] Diment and Pratt (1988), [7] Horai and Baldrige (1972), [8] Birch and Clark (1940), [9] Clark (1966), [10] Birch (1954), [11] Ratcliffe (1959). Chemical formulas are from Ralph (2003). (Compiled from Clauser 2006).

Crystalline orientation, **thermal conductivity** k_T , (data number n , Temperature T), [reference]

Silicates

actinolite $\text{Ca}_2(\text{Mg}, \text{Fe}^{2+})_5[\text{Si}_8\text{O}_{22}][\text{OH}]_2$
 \parallel : **5.34 \pm 0.12** (2; 31°C), \perp : **2.96** (1; RT) [6]—a: **3.64 \pm 0.50** (2; RT) [4,5]

albite $\text{NaAlSi}_3\text{O}_8$
a: **2.34** (1; 25°C) [1]—a: **2.14 \pm 0.22** (4; RT) [2]— k_{T11} : **2.1** (?; RT) [3]— k_{T33} : **2.9** (?; RT), k_{Tm} : **2.04 \pm 0.25** (6; RT) [4,5]

allanite $(\text{Y}, \text{Ce}, \text{Ca})_2(\text{Al}, \text{Fe}^{3+})_3[\text{SiO}_4]_3[\text{OH}]$
 k_{Tm} : **1.44** (1; RT) [4,5]

almandine $\text{Fe}_3\text{Al}_2[\text{SiO}_4]_3$
a: **3.56** (1; RT) [6]—a: **3.31** (1; RT) [2]— k_{T11} : **3.6** (?; RT) [3]— $\{100\}$: **3.53 \pm 0.14** (3; 27°C), $\{010\}$: **3.53 \pm 0.14** (3; 27°C), $\{001\}$: **3.53 \pm 0.14** (3; 27°C) [4,5]

andalusite Al_2SiO_5
a: **6.56 \pm 0.45** (8; 35°C) (<5% quartz impurity) [6]—a: **7.58** (1; RT) [2]

anorthite $\text{CaAl}_2\text{Si}_2\text{O}_8$
a: **2.72** (1; 25°C) [1]—a: **1.68** (1; RT) [2]

augite $(\text{Ca}, \text{Na})(\text{Mg}, \text{Fe}, \text{Al}, \text{Ti})(\text{Al}, \text{Si})_2\text{O}_6$
a: **4.20 \pm 0.05** (3; 35°C) [6]

beryl $\text{Be}_3\text{Al}_2\text{Si}_6\text{O}_{18}$
x: **3.93 \pm 0.08** (2; RT), k_{Tm} : **4.16** (1; RT), a: **3.87** (1; RT), $\{100\}$: **3.81 \pm 0.09** (2; 27°C), $\{010\}$: **3.81 \pm 0.09** (2; 27°C), $\{001\}$: **4.31 \pm 0.19** (2; 27°C) [4,5]

biotite $\text{K}(\text{Mg}, \text{Fe})_3(\text{Al}, \text{Fe}^{3+})\text{Si}_3\text{O}_{10}(\text{OH}, \text{F})_2$
 \parallel : **3.14** (2; 33°C), \perp : **0.52 \pm 0.01** (2; 32°C) [6]—a: **2.02 \pm 0.32** (2; RT) [2]— k_{Tm} : **2.29 \pm 0.26** (2; RT), x: **2.10** (1; RT), $\{100\}$: **2.61** (1; 27°C), $\{010\}$: **2.61** (1; 27°C), $\{001\}$: **1.30** (1; 27°C) [4,5]

cancrinite $\text{Na}_6\text{Ca}_2\text{Al}_6\text{Si}_6\text{O}_{24}[\text{CO}_3]_2$
 k_{Tm} : **1.36** (1; RT) [4,5]

chalcedony SiO_2
a: **3.17** (1; RT) [4,5]

(Continued)

Table B1. (Continued)

Crystall latter orientation, **thermal conductivity** k_T , (data number n , Temperature T), [reference]*Silicates (Continued)*chlorite $(\text{Mg,Fe})_3[(\text{Si,Al})_4\text{O}_{10}[\text{OH}]_2] \cdot (\text{Mg,Fe,Al})_3[\text{OH}]_6$ a: **3.06 ± 1.32** (5; 30°C) [6]—a: **5.2** (?; RT), k_{T11} : **5.5** (?; RT), k_{T33} : **5.1** (?; RT) [3]—a: **5.15 ± 0.94** (3; RT) [2]— k_{Tm} : **3.77** (1; RT), x: **7.87** (1; RT), {100}: **11.1** (1; 27°C), {010}: **11.1** (1; 27°C), {001}: **1.38** (1; 27°C) [4,5]chrysotile $\text{Mg}_3\text{Si}_2\text{O}_5[\text{OH}]_4$ a: **1.95** (1; RT) [4,5]clinochlore $(\text{Mg,Fe}^{2+})_5\text{Al}[\text{Si}_3\text{Al}]\text{O}_{10}[\text{OH}]_8$ ||: **10.34 ± 0.57** (2; 29°C), ⊥: **1.97 ± 0.06** (2; 29°C) [6]cordierite $(\text{Mg,Fe})_2\text{Al}_4\text{Si}_5\text{O}_{18}$ ||: **3.33 ± 0.04** (3; 35°C), ⊥: **3.06 ± 0.03** (2; RT) [6]— k_{Tm} : **2.41** (1; RT) [4,5]diopside $\text{CaMgSi}_2\text{O}_6$ a: **4.40 ± 0.42** (2; 35°C) [6]—a: **4.66 ± 0.31** (4; RT) [2]— k_{Tm} : **4.05 ± 0.03** (3; RT) [4,5]enstatite $\text{Mg}_2\text{Si}_2\text{O}_6$ a: **4.47 ± 0.35** (4; RT) [2]epidote $\text{Ca}_2(\text{Al,Fe})_3[\text{SiO}_4]_3[\text{OH}]$ ||: **3.10** (1; 32°C), ⊥: **2.93** (1; 32°C), a: **2.51 ± 0.03** (2; 31°C) [6]—a: **2.83 ± 0.3** (2; RT) [2]eudialyte $\text{Na}_4(\text{Ca,Ce})_2(\text{Fe}^{2+},\text{Mn,Y})\text{ZrSi}_8\text{O}_{22}(\text{OH,Cl})_2$ a: **1.14** (1) [4,5]fayalite Fe_2SiO_4 a: **3.85 ± 0.08** (4; 30°C) (dunite, mostly fayalite Fa) [6]—a: **3.16** ($\text{Fo}_4\text{Fa}_{96}$) (1; RT) [2]— k_{Tm} : **3.30** (1; RT) [4,5]forsterite Mg_2SiO_4 a: **4.68 ± 0.38** (3; 30°C) (dunite, 97%; 92% forsterite (Fo): 8% fayalite (Fa): $\text{Fo}_{92}\text{Fa}_8$) [8]—a: **5.03 ± 0.2** (5; RT) ($\text{Fo}_{98-91}\text{Fa}_{2-9}$) [2]grossular $\text{Ca}_3\text{Al}_2[\text{SiO}_4]_3$ a: **5.32** (1; RT) [6]—a: **5.48 ± 0.24** (3; RT) [2]—{100}: **5.90** (1; 27°C), {010}: **5.90** (1; 27°C), {001}: **5.90** (1; 27°C) [4,5]hornblende $\text{Ca}_2(\text{Mg,Fe}^{2+})_4(\text{Al,Fe}^{3+})[\text{Si}_7\text{Al}]\text{O}_{22}[\text{OH}]_2$ ||: **2.75 ± 0.18** (2; RT), ⊥: **1.88** (1; 35°C) [6]—a: **2.91 ± 0.09** (2; 20°C) [9]—a: **2.81 ± 0.27** (2; RT) [2]— k_{T11} : **3.0** (?; RT), k_{T33} : **2.4** (?; RT) [3]— k_{Tm} : **1.82 ± 0.01** (2; RT) [4,5]ilvaite $\text{CaFe}_2^{2+}\text{Fe}^{3+}[\text{SiO}_4]_2[\text{OH}]$ k_{Tm} : **1.84** (1; RT) [4,5]jadeite $\text{Na}(\text{Al,Fe})\text{Si}_2\text{O}_6$ a: **5.59 ± 1.22** (2; 34°C) [6]—a: **5.64 ± 1.44** (2; RT) [2]kyanite Al_2SiO_5 a: **7.15 ± 0.17** (4; 35°C), a: **12.45 ± 0.71** (3; 35°C) (<5% quartz impurity) [6]—a: **14.16** (1; RT) [2]labradorite $(\text{Ca,Na})(\text{Si,Al})_4\text{O}_8$ a: **1.71** (1; RT) [4,5]microcline KAlSi_3O_8 {001}: **2.04** (1; RT) [1]—a: **2.49 ± 0.10** (3; RT), [2]—a: **2.41 ± 0.11** (3; RT) [4,5]monticellite CaMgSiO_4 a: **3.25 ± 0.04** (3; 35°C) [6]muscovite $\text{KAl}_2[\text{Si}_3\text{Al}]\text{O}_{10}[\text{OH}]_2$ ||: **3.89 ± 0.0** (2; 30°C), ⊥: **0.62 ± 0.13** (4; 42–45°C) [6]—a: **2.28 ± 0.07** (3; RT) [2]— k_{Tm} : **2.34** (1; RT), x: **2.88** (1; RT), {100}: **3.80** (1; 27°C), {010}: **3.80** (1; 27°C), {001}: **1.03** (1; 27°C) [4,5]natrolite $\text{Na}_2\text{Al}_2\text{Si}_3\text{O}_{10} \cdot 2\text{H}_2\text{O}$ k_{Tm} : **1.73** (1; RT) [4,5]nepheline $(\text{Na,K})\text{AlSiO}_4$ a: **1.39 ± 0.15** (3; 35°C) [6]—a: **1.36** (1; RT) [4,5]oligoclase $(\text{Na,Ca})(\text{Si,Al})_4\text{O}_8$ k_{Tm} : **2.11** (1; RT) [4,5]

(Continued)

Table B1. (Continued)

Crystall lattice orientation, **thermal conductivity** k_T , (data number n , Temperature T), [reference]*Silicates (Continued)*olivine (Fa_{x-y}: contains x-y% fayalite (Fa): Fe₂SiO₄)a: Fa₀₋₁₀: **5.10**, Fa₁₀₋₃₀: **4.27**, Fa₃₀₋₅₀: **3.60**, Fa₅₀₋₇₀: **3.18**, Fa₇₀₋₉₀: **3.05**, Fa₉₀₋₁₀₀: **3.14** (all RT) [7]orthoclase KAlSi₃O₈||: **2.34 ± 0.11** (2; 30°C), {010}: **2.68** (1; 30°C), {001}: **2.30 ± 0.3** (2; 30°C) [1]—a: **2.31** (1; RT)[2]—†: **2.9**, ||₁: **4.2**, ||₂: **4.6**, k_{T11} : **2.94**, k_{T22} : **4.2**, k_{T33} : **4.63** (1; all RT) [3]—a: **2.15 ± 0.05** (2 RT) [4,5]pargasite NaCa₂(Mg,Fe²⁺)₄Al[Si₆Al₂]O₂₂[OH]₂ k_{Tm} : **2.65** (1; RT) [4,5]phlogopite KMg₃Si₃AlO₁₀(F,OH)₂||: **4.01** (3; 30°C), †: **0.48 ± 0.02** (4; 30°C) [6]— k_{Tm} : **1.57** (1; RT) [4,5]plagioclase (An_{x-y}: contains x-y% anorthite: CaAl₂Si₂O₈)a: An₀₋₅: **2.34**, An₅₋₁₅: **1.92**, An₁₅₋₃₀: **1.63**, An₃₀₋₅₀: **1.46**, An₅₀₋₇₀: **1.46**, An₇₀₋₈₅: **1.59**, An₈₅₋₁₀₀: **1.72**, (all RT) [7]prochlorite (Mg,Fe²⁺,Al)₆Al[Si_{2.5}Al_{1.5}]O₁₀[OH]₈a: **2.61 ± 0.40** (10; 29–34°C) [6]pyrophyllite Al₂Si₄O₁₀[OH]₂||: **6.17 ± 0.73** (5; 30°C), †: **1.12 ± 0.42** (2; 30°C), a: **4.47 ± 0.47** (7; 30–35°C) [6]—||: **4.98** (0°C), **4.17**(100°C), **3.59** (200°C), **3.14** (300°C), **2.81** (400°C) [9]pyroxene (Fs_{x-y}: contains x-y% ferrosillite (Fs): Fe₂Si₂O₆)a: Fs₀₋₁₀: **4.73**, Fs₁₀₋₃₀: **4.93**, Fs₃₀₋₅₀: **3.43**, Fs₅₀₋₇₀: **3.18**, Fs₇₀₋₉₀: **3.14**, Fs₉₀₋₁₀₀: **3.22** (?; RT) [7]quartz (α) SiO₂||: **10.17** (1; 30°C) [8]—†: **6.15** (1; 30°C) [11]—a: **8.1** (?; RT), k_{T11} : **6.5** (?; RT), k_{T33} : **11.3** (?; RT)[3]—a: **7.69** (1; RT) [2]—x: **7.60 ± 0.0** (4; RT), {100}: **6.05 ± 0.0** (4; 27°C), {010}: **6.05 ± 0.0**(4; 27°C), {001}: **10.7 ± 0.0** (4; 27°C) [4,5]

temperature range 0–350°C:

†: x: **6.82** (0°C), **5.65** (50°C), **4.94** (100°C), **4.44** (150°C), **4.06** (200°C), **3.73** (250°C), **3.52** (300°C), **3.31** (350°C) [8]||: x: **11.43** (0°C), **9.38** (50°C), **7.95** (100°C), **7.03** (150°C), **6.32** (200°C), **5.69** (250°C), **5.15** (300°C), **4.73** (0°C) [8]rhodonite (Mn²⁺,Fe²⁺,Mg,Ca)SiO₃ k_{Tm} : **2.35** (1; RT) [4,5]sanidine (K,Na)(Si,Al)₄O₈ k_{Tm} : **1.73** (1; RT) [4,5]scapolite (Na,Ca)₄(Si,Al)₁₂O₂₄(Cl,CO₃,SO₄)x_X: **1.76 ± 0.00** (3; 35°C), x_Z: **1.95 ± 0.04** (2; 35°C) [6]—x: **1.42** (1; RT), {100}: **1.34** (1; 27°C), {010}:**1.34** (1; 27°C), {001}: **1.59** (1; 27°C) [4,5]serpentine (antigorite) (Mg,Fe)₃[Si₂O₅][OH]₄||: **2.76 ± 0.03** (4; RT), †: **2.41 ± 0.15** (2; 32°C), a: **2.61 ± 0.40** (10; 30–34°C) [6]—a: **2.1** (?; RT), k_{T11} : **2.6** (?; RT), k_{T33} : **2.3** (?; RT) [3]—a: **3.53 ± 1.57** (3; RT) [2]—a: **2.80 ± 0.20** (4; RT), k_{Tm} :**2.78** (1; RT) [4,5]sillimanite Al₂SiO₅a: **10.73 ± 0.64** (3; 35°C) [6]—a: **9.10** (1; RT) [2]sodalite Na₄Al₃Si₃O₁₂Cla: **3.16 ± 0.12** (3; 35°C) [6]spessartine Mn₃Al₂[SiO₄]₃a: **3.06 ± 0.10** (3; 35°C) [6]—{100}: **3.66** (1; 27°C), {010}: **3.66** (1; 27°C), {001}: **3.66** (1; 27°C) [4,5]spodumene LiAlSi₂O₆ k_{Tm} : **5.28 ± 0.77** (2; RT) [4,5]talc Mg₃Si₄O₁₀[OH]₂||: **10.69 ± 1.50** (5; 29–34°C), †: **1.76 ± 0.0** (2; 30°C) [6]—a: **2.97** (1; 30°C) [10]—a: **6.1 ± 1.27**(2; RT) [2]— k_{T11} : **3.1** (?; RT), k_{T33} : **2.9** (?; RT) [3]titanite CaTiSiO₅a: **2.34** (1; RT) [2]

(Continued)

Table B1. (Continued)

Crystall latter orientation, **thermal conductivity** k_T , (data number n , Temperature T), [reference]*Silicates (Continued)*topaz $\text{Al}_2\text{SiO}_4(\text{F},\text{OH})_2$ k_{Tm} : **20.9** (1; RT) [4,5]tourmaline (schorl) $\text{NaFe}_3^{2+}\text{Al}_6[\text{BO}_3]_3\text{Si}_6\text{O}_{18}[\text{OH}]_4$ x: **3.97 ± 0.47** (2; RT), k_{Tm} : **3.64** (1; RT), {100}: **4.36 ± 0.40** (2; 27°C), {010}: **4.36 ± 0.40** (2; 27°C), {001}: **3.19 ± 0.59** (2; 27°C) [4,5]tremolite $[\text{Ca}_2\text{Mg}_5][\text{Si}_8\text{O}_{22}][\text{OH}]_2$ ||: **5.79 ± 0.28** (2; 31°C), ⊥: **4.54 ± 0.14** (2; 32°C) [6]vesuvianite $\text{Ca}_{10}\text{Mg}_2\text{Al}_4[\text{SiO}_4]_5[\text{Si}_2\text{O}_7]_2[\text{OH}]_4$ x: **2.31 ± 0.23** (2; RT), a: **2.86** (1; RT), {100}: **2.17 ± 0.22** (3; 27°C), {010}: **2.17 ± 0.22** (3; 27°C), {001}: **2.34 ± 0.18** (3; 27°C) [4,5]zircon ZrSiO_4 k_{T11} : **3.9** (?; RT), k_{T33} : **4.8** (?; RT) [3]—a: **5.54** (?; RT) [2]*Oxides*cassiterite SnO_2 k_{Tm} : **12.3** (1; RT) [4,5]chromite FeCr_2O_4 a: **2.20 ± 0.27** (3; 35°C) [3]—a: **2.52** (1; RT) [2]—a: **2.62** (1; RT) [4,5]corundum Al_2O_3 ||: **18.37 ± 3.86** (5; 26–70°C), ⊥: **17.70 ± 3.60** (4; 23–77°C) [6]— k_{T11} : **31.2** (?; RT), k_{T33} : **38.9** (?; RT) [3]hematite Fe_2O_3 a: **12.42 ± 1.74** (3; 30 °C) [9,10]— k_{T11} : **14.7** (?; RT), k_{T33} : **12.1** (?; RT) [3]—a: **11.28** (1; RT) [2]— k_{Tm} : **18.25 ± 1.25** (2; RT), [4,5]ilmenite FeTiO_3 a: **2.50 ± 0.02** (3; 35°C) [6]—a: **2.38 ± 0.25** (2; RT) [2]—a: **2.92** (1; RT) [4,5]magnetite $\text{Fe}^{2+}\text{Fe}_2^{3+}\text{O}_4$ a: **4.61 ± 0.39** (8; 22–33°C) [6]— k_{T11} : **9.7** (?; RT) [3]—a: **5.10** (1; RT) [2]— k_{Tm} : **4.34 ± 0.90** (2; RT) [4,5]pyrochlore $(\text{Na},\text{Ca})_2\text{Nb}_2\text{O}_6(\text{OH},\text{F})$ a: **1.52** (1; RT) [4,5]rutile TiO_2 ⊥: **7.95 ± 1.19** (2; 44–67°C), ||: **13.19 ± 0.89** (2; 36–67°C), a: **4.90 ± 0.21** (3; RT) [6,9]— k_{T11} : **9.3** (?; RT), k_{T33} : **12.9** (?; RT) [3]—a: **5.12** (1; RT) [2]—x: **4.89** (1; RT), {100}: **4.38** (1; 27°C), {010}: **4.38** (1; 27°C), {001}: **5.92** (1; 27°C) [4,5]scheelite CaWO_4 k_{Tm} : **2.53 ± 0.20** (4; RT) [4,5]spinel MgAl_2O_4 a: **12.14 ± 1.51** (3; 35–70°C) [9]— k_{T11} : **13.8** (?; RT) [3]—a: **9.48** (1; RT) [2]wolframite $(\text{Fe},\text{Mn})\text{WO}_4$ k_{Tm} : **2.81 ± 0.38** (5; RT) [4,5]wulfenite PbMoO_4 k_{Tm} : **1.82** (1; RT) [4,5]*Sulfides*arsenopyrite FeAsS a: **7.24** (1; RT) [4,5]chalcopyrite CuFeS_2 a: **7.55 ± 0.33** (3; 35°C) [6]—a: **10.7** (1; RT) [4,5]galena PbS a: **2.76 ± 0.22** (3; 35°C) [6]—a: **2.28** (1; RT) [2]—a: **1.99** (1; RT), x: **2.02** (1; RT), {100}: **2.02** (1; 27°C), {010}: **2.02** (1; 27°C), {001}: **2.02** (1; 27°C) [4,5]

(Continued)

Table B1. (Continued)

Crystall lattice orientation, **thermal conductivity** k_T , (data number n , Temperature T), [reference]*Sulfides (Continued)*pyrite FeS₂a: **23.15 ± 2.45** (3; 35°C) [6]—a: **19.21** (1; RT) [2]—a: **23.7** (1; RT), {100}: **41.4** (1; 27°C), {010}: **41.4** (1; 27°C), {001}: **41.4** (1; 27°C) [4,5]—x: **41.4** (1; RT), k_{T11} : **37.9** (?; RT) [3]

pyrrhotite FeS

a: **3.53 ± 0.06** (3; 35°C) [6]—a: **4.60** (1; RT) [2]—a: **3.52** (1; RT), {100}: **3.43** (1; 27°C), {010}: **3.43** (1; 27°C), {001}: **3.71**(1; 27°C) [4,5]sphalerite, (Zn,Fe²⁺)Sa: **11.20 ± 0.02** (3; 35°C) [6]sphalerite (marmatite), (Zn,Fe²⁺)Sa: **18.9** (1; RT) [4,5]

sphalerite (cleiophane), ZnS

a: **4.67** (1; RT) [4,5]

wurtzite (Zn,Fe)S

a: **4.19** (1; RT) [4,5]*Sulfates*anhydrite CaSO₄a: **5.36 ± 0.30** (6; 25–35°C) [6]—a: **4.76** (1; RT) [2]barite BaSO₄||: **2.92 ± 0.09** (4; 25–100°C), ⊥: **2.07 ± 0.03** (2; 25–100°C), a: **1.72 ± 0.05** (4; 25–35°C) [6]—a: **1.51 ± 0.12** (2; RT) [4,5]celestine SrSO₄||: **1.38** (1; 35°C), ⊥: **1.29 ± 0.11** (3; 35°C) [6]— k_{Tm} : **1.32** (1; RT) [4,5]gypsum CaSO₄ · 2H₂Oa: **1.30** (1; RT) [6] a: **1.22** (1; RT) [4,5]—⊥: **1.6**, ||₁: **2.5**, ||₂: **3.8**, k_{T11} : **2.6**, k_{T22} : **1.6**, k_{T33} : **3.7** (all 1; RT) [3]*Carbonates*aragonite CaCO₃a: **2.37 ± 0.23** (11; 25–100°C) [6]—a: **2.24** (1; RT) [2]calcite CaCO₃ k_{T11} : **4.2** (?; RT), k_{T33} : **5.0** (?; RT) [3]—x: **3.13** (1; RT), {100}: **3.21** (1; 27°C), {010}: **3.21** (1; 27°C), {001}: **3.50** (1; 27°C) [4,5]— k_{Tm} : **3.28 ± 0.04** (2; RT), a: **3.59** (1; RT) [2]

temperature range 0–400°C:

||: x: **4.00** (0°C), **3.63** (30°C), **3.40** (50°C), **2.99** (100°C), **2.73** (150°C), **2.55** (200°C), **2.41** (250°C), **2.29** (300°C), **2.20** (350°C), **2.13** (0°C) [8]⊥: x: **3.48** (0°C), **3.16** (30°C), **3.00** (50°C), **2.72** (100°C), **2.52** (150°C), **2.37** (200°C), **2.25** (250°C), **2.16** (300°C), **2.09** (350°C), **2.06** (400°C) [8]cerussite PbCO₃a: **1.35 ± 0.02** (3; 35°C) [6]dolomite CaMg[CO₃]₂a: **4.85 ± 0.26** (73; 25–35°C) [6]— k_{T11} : **4.7** (?; RT), k_{T33} : **4.3** (?; RT) [3]—a: **5.51** (1; RT) [2]—a: **5.97 ± 0.44** (2; RT) [4,5]magnesite MgCO₃||: **7.86 ± 0.20** (4; 25–100°C), ⊥: **7.32 ± 0.36** (4; 25–100°C), a: **8.18 ± 1.34** (5; 34–35°C) [6]—a: **5.84** (1; RT) [2]siderite FeCO₃a: **2.99 ± 0.15** (3; 35°C) [6]—a: **3.01** (1; RT) [2]strontianite SrCO₃a: **1.38 ± 0.07** (4; 35°C) [6]witherite BaCO₃a: **2.26 ± 0.02** (3; 35°C) [6]

(Continued)

Table B1. (Continued)

Crystall latter orientation, **thermal conductivity** k_T , (data number n , Temperature T), [reference]

Phosphates

apatite $\text{Ca}_5[\text{PO}_4]_3(\text{F},\text{Cl},\text{OH})$

a: 1.27 ± 0.02 (3; 35°C) [6]—a: 1.38 ± 0.01 (2; RT) [2]—x: 1.58 ± 0.06 (3; RT), {100}: 1.53 ± 0.07 (3; 27°C), {010}: 1.53 ± 0.07 (3; 27°C), {001}: 1.70 ± 0.07 (3; 27°C) [4,5]

Halides

fluorite CaF_2

x: 8.62 ± 1.11 (6; 0–36°C) [6]— k_{T11} : 10.1 (?; RT) [3]—a: 9.51 (1; RT) [2]—a: 8.64 (1; RT) [4,5]

halite NaCl

x: 5.55 ± 1.09 (8; 0–35°C) [9]—a: 6.1 (?; RT) [3]—a: 5.88 (1; RT), k_{Tm} : 5.90 (1; RT), {100}:

5.89 ± 0.01 (2; 27°C), {010}: 5.89 ± 0.01 (2; 27°C), {001}: 5.89 ± 0.01 (2; 27°C) [4,5]

temperature range 0–400°C:

x: 6.11 (0°C), 5.02 (50°C), 5.44 (70°C), 4.21 (100°C), 3.59 (150°C), 3.12 (200°C), 2.76 (250°C), 2.49 (300°C), 2.30 (350°C), 2.09 (400°C) [8]

sylvite KCl

x: 6.74 ± 0.3 (2; 0–12°C) [9]— k_{T11} : 6.4 (?; RT) [3]

Nomenclature

Though we have defined each parameter or variable where it occurs for the first time in the text, we provide in the following a list of the most important symbols used in the book. We include the principal parameters and variables, which describe the physical processes. This list is not intended to be complete. In contrast, we want to include only the physically relevant parameters and variables rather than all the mathematical ones which are used within the book and which are defined in each section individually.

Note 1: Indices (or subindices) of parameters indicate if not otherwise stated:

B	bulk	eff	effective	F	fault	f	fluid	g	gas	l	liquid
o	oil	r	rock	S	Skeleton	s	solid	v	vapor	w	water

Note 2: In case of a matrix or vector, the units are give for the respective matrix or vector components.

Symbol	Meaning	Units (SI)
A	Area	m^2
A_r	Flow area	m^2
A_0	Initial area	m^2
\vec{a}	Vectorial acceleration (eq. 2.79a)	m/s^2
[ad]	Dimensionless parameter	ad
AMP	Annual temperature amplitude in spring- and groundwater	K
B	Skempton coefficient (chapter 2)	ad
b	Biot-Willis coefficient (chapter 2)	ad
b_a	Aquifer thickness	m
b_k	Unitary basis for interpolation	ad
b_s	Thickness of semiconfining layer	m
b_0	Constant parameter associated with the rock pore size	ad
C	Biot poroelastic coefficient (chapter 2)	Pa
$C(x)$	Molecular concentration of the substance	mol/m^3
C_B	Matrix of the poroelastic coefficients	Pa
C_B	Drained bulk compressibility	$1/Pa$
C_D	Consolidation diffusion coefficient	m^2/s
C_f	Isothermal compressibility of the fluid	$1/Pa$
C_m	Mass fraction of NaCl	$kg/kg = ad$
C_p	Heat capacity at constant pressure	J/K
C_s	Non-jacketed volumetric compressibility	$1/Pa$
C_{sol}	Solute concentration in the source fluid (volume referred: mol/m^3 or kg/m^3)	mol/kg or $kg/kg = ad$
C_T	Bulk isothermal compressibility	$1/Pa$
C_U	Undrained bulk compressibility	$1/Pa$
C_V	Volumetric heat capacity at constant volume	$J/m^3/K$
C_w	Isothermal compressibility of water	$1/Pa$
C_0	Experimental constant	ad
C_Φ	Unjacketed compressibility of the pore volume	$1/Pa$

c	Experimental parameter (eq. 2.154)	ad
c_k	Compaction coefficient	1/m
c_i	Specific heat capacity at constant pressure ($i = f, l, r, s, v, w$)	J/kg/K
c_m	Salinity concentration (mass fraction)	% or ad
c_p	Isobaric specific heat capacity	J/kg/K
c_V	Specific heat capacity at constant volume	J/kg/K
Co_i	Courant's magnitude ($i = x, y$)	ad
D	Tensor of molecular diffusion (section 4.8.1) or dispersion tensor (section 4.8.2 and 4.8.3)	m ² /s
D/Dt	Advective derivative	1/s
D^*	Molecular diffusivity	m ² /s
D_f	Fractal dimension	–
D_I	Eigenvalues of the diffusion tensor D ($I = X, Y, Z$)	m ² /s
D_m	Mechanical or hydrodynamic dispersion coefficient	m ² /s
D_v	Symmetrical tensor of spatial changes of fluid velocity	1/s
d_g	Representative grain diameter for the porous medium	m
d_{ni}	Nodal distance	m
d_0	Initial diameter	m
dp_w/dt	Pressure drawdown in the well	Pa/s
dS	Differential surface or area	m ²
dT/dz	Temperature gradient	K/m
dV_i	Differential volume ($i = f, B, s$)	m ³
dV_Φ	Differential porous volume	m ³
E	Young's modulus of elasticity (chapter 2)	Pa
E_{rr}^2	Error of quadratic order in the approximation	–
\vec{E}_i	Energy flow ($i = f, l, r, v$)	J/m ² /s
E_1	Vector space of linear functions on the mesh \mathcal{M}_1	–
$E_1(u)$	Exponential integral	–
e_i	Volumetric internal energy of ($i = f, l, v, r, s$)	J/m ³
F	Force	N
\vec{F}_{E1}	Total energy flow, single-phase fluid	J/m ² /s
\vec{F}_{E2}	Total energy flow, two-phase fluid	J/m ² /s
F_e	Electrical resistivity factor	ad
\vec{F}_i	Vectorial flow of mass ($i = l, v, r$)	kg/m ² /s
\vec{F}_{M1}	Momentum of the fluid, per unit volume of porous rock	kg/m ² /s
\vec{F}_{M2}	Momentum of the two-phase fluid, per unit volume of rock	kg/m ² /s
F_{ni}	Average flux at the interface S_{ni}	kg/m ² /s
F_s	Helmholtz free internal energy	J
F_x	Force in the x direction	N
f_f	Volumetric Helmholtz potential or free energy ($i = f, s, w$)	J/m ³
f_v	Volumetric fraction of incondensable gas in the gaseous phase	ad
f_φ	Friction factor	ad
G	Shear or rigidity modulus (chapter 2)	Pa
G_P	Electric geothermal power (electric Watt)	W _e
G_S	Gibbs free internal enthalpy	J
G_U	Rigidity undrained modulus	Pa
GF	Depth of groundwater table below earth's surface	m
g	Acceleration of gravity	m/s ²
g_f	Gibbs specific free enthalpy of the fluid	J/m ³
g_S	Volumetric Gibbs potential of the skeleton	J/m ³
H	Inverse of the poroelastic expansion coefficient	Pa
$H(x)$	Heaviside distribution	–

H_G	Geothermal energy	J
H_S	Skeleton enthalpy	J
h	Hydraulic head, piezometric or hydraulic height (water level in the well in hydraulics)	m
h_i	Specific enthalpy ($i = f, l, w, r, s, S, v$)	J/kg
h_T	Heat transfer coefficient	J/s/m ² /K
h_{well}	Water level in the well	m
I	Unit matrix	–
i_h	Hydraulic gradient	m/m = ad
J	Joule-Thomson coefficient	K/Pa
$J(t)$	Determinant of the Jacobian matrix	–
K	Tensor of absolute permeability at any point (x, y, z) of the porous medium	m ²
K_B	Bulk modulus of the porous rock	Pa
K_d	Distribution coefficient	kg/kg = ad
K_H	Hydraulic conductivity tensor	m/s
K_{HL}	Vertical conductivity of the semiconfining layer	m/s
K_I	Principal value of the hydraulic conductivity tensor K_H (matrix coefficient) ($I = X, Y, Z$)	m/s
K_i	Bulk modulus of the fluid ($i = w, f$)	Pa
K_s	Elastic modulus of the solid phase (chapter 2)	Pa
K_U	Elastic undrained bulk modulus	Pa
k	Intrinsic permeability	m ²
k_e	Effective permeability	m ²
k_i	Absolute permeability (1 Darcy = 9.86923×10^{-13} m ²)	m ²
k_{ni}	Average permeability of the medium at the interface S_{ni}	m ²
k_{rg0}	Gas relative permeability for imbibition	ad
k_{ri}	Relative permeability ($i = l, w, o, g, s, v$)	ad
k_{rj}	Relative permeability: ($j = nw = \text{non-wetting phase}$, $w = \text{wetting phase}$)	ad
k_{rw0}	Water relative permeability for drainage	ad
k_{T_i}	Thermal conductivity tensor for anisotropic media ($i = l, w, o, g, s, v, r$)	W/m/K
k_{T_i}	Thermal conductivity ($i = l, w, o, g, s, v, r$)	W/m/K
$k_{T_{ni}}$	Thermal conductivity at the interface S_{ni}	W/m/K
k_z	Kozeny constant (≈ 0.5 m ²) (eq. 2.2b)	m ²
L	Tensorial differential operator	–
L	Dripping or leakage factor	1/s
L_j^k	Linear Lagrange polynomials of j -rank in the interval I_k	–
L_v	Latent heat of vaporization	J/mol or J/kg
M	Biot coefficient characterizing the fluid elastic properties	Pa
M_i	Mass of ($i = f, l, v, r, w$)	kg
M₁	Mesh of the reservoir	–
$M\varphi$	Multiple-porosity reservoir	–
m_f	Fluid mass content per unit reference volume	kg/m ³
m_0	Fluid mass content (reference or initial)	kg/m ³
[mD]	Millidarcy (1mD = 10^{-3} D = 9.86923×10^{-16} m ² $\approx 10^{-15}$ m ²)	–
N	Biot Tangent modulus	Pa
$N^*(x)$	Concentration of the diffusive substance	number of molecules/m ³
N_M	Number of molecules of the substance	number of molecules
N_V	Number of finite volumes	–

n	Experimental parameter (eq. 2.155)	ad
\vec{n}	Unit normal vector	—
Nk	Multiple permeability reservoir	m^2
P	Parameter space (chapter 7)	—
P_A	Arithmetic average	—
P_{B1}	Budiansky's average 2D	—
P_{B2}	Budiansky's average 3D	—
P_C	Continuity average	—
P_G	Geometric average	—
P_{gA}	General arithmetic average	—
P_{gG}	General geometric average	—
P_{HS}	Hashin-Shtrikman average 2D	—
P_{HS2}	Hashin-Shtrikman average 3D	—
P_L	Linear average	—
P_{L1}	Linear Lagrange average	—
P_p	Parallel average	—
P_s	Serial average	—
P_w	Weighted average	—
P_{wG}	Weighted geometric average	—
p_a	Atmospheric pressure	Pa
p_B	Fluid pressure in the Brinkman region	Pa
p_C	Capillary pressure in a porous medium	Pa
p_{Ce}	Entry capillary pressure	Pa
p_{Cmax}	Maximum capillary pressure	Pa
p_D	Fluid pressure in the Darcy region	Pa
p_d	Differential pressure	Pa
p_E	Equilibrium pressure	Pa
p_e	Effective pressure	Pa
p_f	Pore pressure of the fluid	Pa
p_{Fmax}	Maximum fracture capillary pressure	Pa
p_i	Pressure ($i = S, l, w, o, g, s, v$)	Pa
p_k	Confining lithostatic pressure	Pa
p_{NS}	Pressure in the Navier-Stokes region	Pa
p_{nw}	Non-wetting pressure	Pa
p_{sv}	Vapor saturation pressure for a flat interface	Pa
p_U	Non-isothermal undrained fluid pressure	Pa
\bar{p}	Average reservoir pressure	Pa
\bar{Q}	Heat exchanged between the system and its surroundings	J
\vec{Q}_f	Vectorial flow of convective energy related to the fluid movement	W/m^2
Q_E	Thermal energy	J
Q_H	Volumetric heat generation	W/m^3
Q_n	Flow rate averaged in each V_n	kg/s
Q_{ni}	Averaged flow rate at the interface	kg/s
Q_{VT}	Total volumetric pumping rate	m^3/s
Q_V	Volumetric fluid extraction or injection rate	m^3/s
q^*	Solute flux	number of molecules/ m^2/s
\vec{q}_D	Vector of convective-dispersive flux of the dissolved solute	$kg/m^2/s$
q_D	Convective-dispersive flux of the solutes dissolved in the fluid of the porous rock	$kg/m^2/s$
q_{Di}	Convective-dispersive flux of the solutes dissolved in the fluid of the porous rock in i direction ($i = x, y, z$)	$kg/m^2/s$

q_f	Volumetric extraction or injection of fluid mass in the reservoir	kg/m ³ /s
q_H	Power of a heat source	W
q_{ij}	Interaction between medium V_i and V_j	kg/m ³ /s
q_N	Rate of recharge/extraction in the reservoir	m/s
q_n	Normal component of the heat flow	J/m ² /s
\vec{q}_T	Vectorial heat flow	W/m ²
q_V	Volumetric flow rate per unit volume of the sources or sinks of water	1/s
R	Inverse of the unconstrained storage coefficient	Pa
R_d	Retardation factor	ad
R_e	Reynolds number	ad
R^e	Error or residual of the approximation u^e	–
R_g	Ideal gas constant (8.314472 J/K/mol)	J/K/mol
R_I	Resistivity index	ad
R_j	Rate of solute production in the reaction number j of a total of N_R different reactions	kg/m ³
r	Radial distance	m
\vec{r}	Position vector of a fluid particle in V_Φ	m
r_C	Radius of the well casing	m
r_M	Average radius of curvature of the interface	m
r_w	Radius of the well	m
S	Entropy (thermodynamics)	J/K
S	Storativity of an aquifer (or storage coefficient)	ad
S_e	Effective liquid saturation	ad
S_{gc}	Critical gas saturation	ad
S_i	Saturation ($i = w$: wetting phase, nw : non-wetting phase)	ad
S_j	Saturation ($j = o, w, g, l$)	ad
S_{ni}	Boundary at the interface	m ²
S_{nw}	General normalized wetting-phase saturation	ad
S_{nwi}	Initial saturation of the non-wetting phase	ad
S_{nwimb}	Normalized water saturation by imbibition	ad
S_p	Storage for pressure and neglecting gravity (eq. 4.56b)	m · s ² /kg
S_{rg}	Water saturation at irreducible gas saturation	ad
S_{rl}	Irreducible water saturation	ad
S_{rs}	Residual steam saturation by imbibition	ad
S_{rw}	Residual water saturation	ad
S_{sp}	Specific storage of an aquifer (or specific storage coefficient)	1/m
S_V	Steam saturation	ad
S_w	Wetting-phase saturation	ad
$S_w^{drainaje}$	Drainage water saturation	ad
$S_w^{imbibition}$	Imbibition water saturation	ad
S_{wc}	Critical water saturation	ad
S_{wcg}	Critical water saturation for gas	ad
S_{wi}	Irreducible water saturation	ad
S_{wr}	Residual saturation of S_w	ad
s_i	Volumetric entropy ($i = S, s, f, w$)	J/K/m ³
T_A	Characteristic average reservoir temperature	°C or K
T_i	Temperature ($i = f, l, r, s, v, w$)	°C or K
T_j	Average temperature ($j = f, l, v, r, w$)	°C or K
T_{sat}	Saturation temperature	°C or K
\mathbf{T}_V	Transmissivity tensor of the aquifer	m ² /s

T_{va}	Average aquifer transmissivity	m^2/s
T_0	Reference temperature (initial temperature)	$^{\circ}C$ or K
t	Time	s
\vec{t}	Unit tangential vector	—
t_E	Commercial exploitation time of the reservoir	s
$t_{0.5}$	Value of half-life for the radioactive substance	s
U	Internal energy	J
U_s	Solid internal energy	J
U_T	Total thermal energy	J
\vec{u}	Vector displacement	m
$u(x)$	Continuous function u of the space E_1 (chapter 5)	—
\vec{u}_f	Vector displacement of the fluid particles	m
\vec{u}_s	Vector displacement of the solid particles	m
u_x	Pore fluid velocity	m/s
V_i	Arbitrary volume of phase i	m^3
V_j	Volume ($i = B, F, f, l, r, s, v, w$)	m^3
V_P	Volume of the pores	m^3
V_{Φ}	Effective pore volume	m^3
V_0	Initial volume	m^3
ν	Poisson's coefficient (chapter 2)	ad
ν_A	Average pore velocity of the fluid through the porous material	m/s
ν_B	Brinkman fluid velocity	m/s
ν_C	Velocity of the contaminant	m/s
ν_D	Darcy fluid velocity	m/s
ν_f	Darcy flux, or volumetric discharge per unit area, or Darcy velocity, or seepage velocity	m/s
$\vec{\nu}_i$	Vectorial velocity ($i = f, s$)	m/s
ν_i	Speed component in the direction of the turbulence	m/s
ν_{NS}	Navier-Stokes fluid velocity	m/s
ν_r	Radial flow velocity	m/s
ν_s	Speed of sound	m/s
ν_x	Darcy velocity (eq. 4.111)	m/s
W	Work done by the system ($W < 0$) or on the system ($W > 0$)	J
$W(u)$	Well function	ad
$w(x, y)$	Weight function	—
X_l	Liquid quality	ad
X_v	Steam quality	ad
\vec{x}	Position vector	m
z_0	Reference depth	m
$\vec{\nabla}T$	Vector thermal gradient	K/m
$\nabla_x p$	Pressure gradient vector in one dimension	Pa/m

Greek symbols	Meaning	Unit (SI)
α	Experimental correction coefficient (eq. 2.155)	ad
α_A	Areal thermal expansion coefficient at constant pressure	1/K
α_L	Longitudinal dispersivity	m
α_{ij}	Dimensionless constant	ad
α_T	Transverse dispersivity	m
α_x	Linear thermal expansion	1/K

α_φ	Porosity variation of the skeleton when temperature changes	1/K
β_F	Volumetric fraction of fractures	ad
β_f	Experimental factor (eq. 4.81)	ad
β_{ij}	Thermoelastic tensor	Pa/K
Γ	Boundary of domain $\Omega(\partial\Omega)$	—
γ_a	Coefficient of molecular diffusion	m ² /s
γ_C	Composed thermal expansivity	1/K
γ_i	Thermal expansivity ($i = B, w, f$)	1/K
γ_m	Global pore-fluid thermal expansion coefficient	1/K
γ_U	Undrained thermal expansivity	1/K
γ_φ	Thermal expansivity of the pores	1/K
Δe_f	Change in internal energy	J
ΔG_S	Useful energy able to be totally transformed into work	J
ΔH_s	Skeleton-stored enthalpy	J
Δh	Drawdown or change in hydraulic head	M
Δh_f	Change in fluid enthalpy	J
$\Delta h/\Delta z$	Hydraulic gradient	m/m = ad
Δm_f	Change in fluid mass content	kg/m ³
$\Delta p/\Delta x$	Pressure gradient in one dimension	Pa/m
$\Delta q_z/\Delta z$	Heat flow vertical gradient	W/m
ΔU_s	Matrix-stored energy	J
ΔV_B	Representative elementary volume (REV)	m ³
$\Delta \rho_f$	Change of fluid density	kg/m ³
$\Delta \varphi$	Change in effective porosity	ad
$\Delta \varphi$	Phase difference between the maximum and minimum Earth's surface and corresponding groundwater temperatures (chapter 8)	K or °C
$\delta(x)$	Dirac distribution	—
δ_H	Hydraulic diffusivity	m ² /s
δ_{ij}	Unit tensor	—
δQ	Heat exchanged per unit volume	J/m ³
δ_T	Thermal diffusivity	m ² /s
δW	Volumetric work	J/m ³
δ_w	Diffusivity of water	m ² /s
δz_n	Small normal compression of the fracture relative to z	m
$\partial\Omega = \Gamma$	Boundary of the domain Ω	—
ε	Overall volumetric strain	ad
ε_i	Volumetric strain of ($i = B, s, f$)	ad
ε_j	Evaporation rate ($j = v$) and condensation rate ($j = l$)	kg/m ² /s
ε_l	Condensation rate	ad
ε_n	Volumetric strain in direction n	ad
ε_s	Volumetric deformation of the solid phase	ad
$\vec{\varepsilon}_T$	Total vectorial strain	ad
ε_t	Volumetric strain in direction t	ad
ε_V	Volumetric deformation	ad
ε_x	Axial strain	ad
ε_z	Vertical strain	ad
ν_f	Fluid kinematic effective viscosity	m ² /s
ζ	Biot variation of fluid content	ad
η	Mobility	m · s/kg
η_G	Geothermal-electricity conversion factor	ad (or as %)
η_H	Hydraulic diffusion coefficient	m ² /s
θ	Angular component	—

θ_{ni}	Angle between gravity and the vector orthogonal to S_{ni}	–
Λ_n	Matrix of flow coefficients in the finite volume method	Λ
λ	Drained Lamé coefficient (chapter 2)	Pa
λ_f	Coefficient of fluid viscosity of dilatation or compression	Pa · s
λ_{ijkl}	Thermoelastic tensor	Pa
λ_R	Radioactive decay constant	1/s
λ_U	Undrained Lamé modulus	Pa
λ_φ	Pore size distribution coefficient	ad
μ_e	Effective viscosity	Pa · s
μ_f	Fluid dynamic viscosity	Pa · s
μ_{ij}	Fluid viscosity when crossing S_{ij}	Pa · s
\vec{v}	Phase velocity field (vector)	m/s
v_{ni}	Phase velocity between two finite volumes V_n and V_i	m/s
ν_U	Undrained Poisson's coefficient	ad
ρ	Global density	kg/m ³
ρ_b	Bulk density of the rock	kg/m ³
ρ_i	Density ($i = f, g, l, r, s, v, w$)	kg/m ³
ρ_{ij}	Fluid density when crossing S_{ij}	kg/m ³
ρ_T	Average density	kg/m ³
ρ_0	Fluid density in a reference state	kg/m ³
σ	Stress	Pa
$\boldsymbol{\sigma}$	Stress tensor	Pa
$\boldsymbol{\sigma}_B$	Bulk stress tensor	Pa
σ_{dry}	Stress in dry rock	Pa
$\boldsymbol{\sigma}_f$	Fluid stress tensor	Pa
σ_H	Hydrostatic stress	Pa
σ_{lg}	Liquid-gas stress	Pa
σ_M	Average of the stress tensor $\boldsymbol{\sigma}$ components	Pa
σ_{sg}	Solid-gas stress	Pa
σ_{sl}	Solid-liquid stress	Pa
$\boldsymbol{\sigma}_T$	Symmetric two-order tensor in four dimensions	Pa
$\vec{\sigma}_T$	Total poroelastic stress vector	Pa
σ_w	Surface tension of water	Pa
σ_X	Axial stress	Pa
σ_Y	Lateral confining stress	Pa
σ_Z	Vertical stress	Pa
σ_Z^s	Vertical solid stress	Pa
σ_0	Superficial tension	Pa
τ	Tangential shear stress	Pa
τ_f	Tortuosity factor	ad
τ_{dry}	Tangential stress in dry rock	Pa
τ_{ij}	Terzaghi effective stresses	Pa
τ_w	Tangential stress	Pa
v	Specific volume ($i = f, g, l, r, s, v, w$)	m ³ /kg
ν_M	Liquid phase molar volume	m ³ /mol
Φ	Differential model of model function φ (chapter 7)	–
$\varphi = \varphi_{eff}$	Effective porosity	ad (or as %)
$\varphi(t)$	Model function; effects of causes (chapter 7)	–
φ_F	Fracture porosity	ad
φ_k	Unitary basis function $\{k = 0, n\}$	–
φ_M	Matrix porosity	ad
φ_s	Solid volume fraction	ad

φ_0	Porosity at zero stress (eq. 2.2d)	ad (or as %)
φ_1	Surface reference porosity	ad (or as %)
χ	Earth's physical parameter (density, electrical conductivity, elasticity, etc.) (chapter 7)	–
Ψ_S	Energy dissipation function	Pa/s
Ψ_{1M}	Total volumetric flow rate (single-phase) exchanged between V_n and its surroundings	kg/m ³ /s
Ψ_{2M}	Total volumetric flow rate (two-phase) exchanged between V_n and its surroundings	kg/m ³ /s
Ω	Spatial domain occupied by the porous rock	–
Ω^e	Finite element volume	–
ω	Boltzmann's transformation	ad

References

- Aaheim, A. and Bundschuh, J.: The value of geothermal energy for developing countries. In: D. Chandrasekharam and Bundschuh, J. (eds): *Geothermal energy for developing countries*. Balkema Publisher, Lisse, The Netherlands, pp. 37–52, 2002.
- Abramowitz, M.Y. and Stegun, I. (eds): *A handbook of mathematical functions*. Dover, New York, NY, 1965.
- Abramowitz, M. and Stegun, I.A. (eds): Handbook of mathematical functions with formulas, graphs, and mathematical tables. National Bureau of Standards, *Applied Mathematics Series 55*, issued June 1964, tenth printing, December 1972, with corrections, <http://www.math.sfu.ca/~cbm/aands/> (accessed August 2009).
- Advonin, N.A.: Some formulas for calculating the temperature field of a stratum subject to thermal injection. *Neft' i Gaz* 3 (1964), pp. 37–41.
- AIAA (American Institute of Aeronautics and Astronautics): Guide for the verification and validation of computational fluid dynamics simulations, AIAA-G-077-1998, Reston, VA, 1998.
- Alonso, M. and Finn, E.J.: *Fundamental university physics*, Vol. I. *Mechanics*, Vol. II *Fields and waves*. Addison-Wesley Pub. Co., Palo Alto, CA, 1967.
- Alt, J.: Subseafloor processes in mid-ocean ridge hydrothermal systems. *Geophys. Monogr.* 91, American Geophysical Union, 1995, pp. 85–114.
- Ameen, M.: *Boundary element analysis: Theory and programming*. Narosa Publishing House, London, UK, 2001.
- Anand, J., Somerton, W. and Gomaa, E.: Predicting thermal conductivities of formations from other known properties. *SPE Journal* 13 (1973), pp. 267–273.
- Aqtesolv: Ver. 4.0 Professional, Software, HydroSOLVE, Inc., Reston, VA, 2006.
- Aquifer Test Pro: Ver. 4.1: Scientific Software Group, Sandy, UT, 2007.
- Aquifer^{win32}: Software, Scientific Software Group, Sandy, UT.
- Archer, R.: *Computing flow and pressure transients in heterogeneous media using boundary element methods*. PhD Thesis, Department of Petroleum Engineering, Stanford University, CA, 2000.
- Archer, R., Horne, R. and Onyejekwe, O.: Petroleum reservoir engineering applications of the dual reciprocity boundary element method and the Green element method. *Proceedings 21st World Conference on the BEM*, 25–27 August 1999, Oxford University, Oxford, UK, 1999.
- Archie, G.E.: The electrical resistivity log as an aid in determining some reservoir characteristics. *AIME Petroleum Tech.* (1942), pp. 1–8.
- Arnold, R., Burnett, D., Elphick, J., Feeley, T., Galbrun, M., Hightower, M., Jiang, Z., Khan, M., Lavery, M., Luffey, F. and Verbeek, P.: Managing water—From waste to resource. *Oilfield Review* 16:2 (2004), Schlumberger, pp. 26–41.
- ASME: Brief history of the ASME Properties of Steam Subcommittee. ASME Center for Research & Technology Development, Washington, DC, 2005, http://crted.asme.org/wsts/steam_history.pdf (accessed August 2009).
- Asszonyi, C. and Richter, R.: *The continuum theory of rock mechanics*. Trans Tech Publications, CH-8712 Stäfa-Zürich. Switzerland, 1979.
- Auset, M. and Keller, A.A.: Pore-scale processes that control dispersion of biocolloids in saturated porous media. *Water Resour. Res.* 40:3 (2004), W03503.
- Auset, M., Keller, A.A., Brissaud, F. and Lazarova, V.: Intermittent filtration of bacteria and colloids at pore and column scales. *Water Resour. Res.* 41:9 (2005), W09408.
- Avdonin, N.A.: Some formulas for calculating the temperature field of a stratum subject to thermal injection. *Neft' i Gaz* 7:3 (1964), pp. 37–41.
- Axelsson, G., Flovenz, O.G., Hauksdottir, S., Hjartarson, A. and Liu, J.: Analysis of tracer test data, and injection-induced cooling, in the Laugaland geothermal field, N-Iceland. *Geothermics* 30:6 (2001), pp. 573–589.
- Bai, M., Elsworth, D. and Roegiers, J.-C.: Multiporosity/multipermeability approach to the simulation of naturally fractured reservoirs. *Water Resour. Res.* 29:6 (1993), pp. 1621–1633.

- Baker, E., German, C. and Elderfield, H.: Hydrothermal plumes over spreading-center axes: Global distributions and geological inferences. *Geophys. Monogr.* 91, American Geophysical Union, 1995, pp. 47–71.
- Balhoff, M.T.: *Coupling pore-scale and simulation-scale models: A method for multiscale modeling in porous media*. University of Texas at Austin, ICES, Austin, TX, 2006, http://www.ticam.utexas.edu/subsurface/files/Affiliates_2006/Affiliates_2006_Balhoff.pdf (accessed April 2007).
- Barberi, F. and Carapezza, M.L.: Helium and CO₂ soil gas emission from Santorini (Greece). *Bull. Volcanology*, 56 (1994), pp. 335–342.
- Barenblatt, G., Zheltov, Y. and Kochina, I.: Basic concepts in the theory of seepage of homogeneous liquids in fissured rocks. *J. Appl. Math. Mech.* 24 (1960), pp. 1286–1303.
- Barragán, R.M., Nieva, D., Santoyo, E., González, E., Verma, M.P. and López, J.M.: Geoquímica de fluidos del campo geotérmico de Los Humeros, (México). *Geotermia* 7 (1991), pp. 23–47.
- Batu, V.: *Aquifer hydraulics: A comprehensive guide to hydrogeologic data analysis*. Wiley-Interscience; book and disk edition, New York, NY, 1998.
- Batu, V.: *Applied flow and solute transport modeling in aquifers—Fundamental principles and analytical and numerical methods*. CRC Press/Taylor & Francis, Boca Raton, FL, 2006.
- Bear, J.: *Dynamics of fluids in porous media*. Dover, New York, NY, 1972.
- Bear, J.: *Hydraulics of groundwater*. Dover Publications, New York, NY, 1979.
- Bear, J. and Bachmat, Y.: Transport phenomena in porous media—Basic equations. In: J. Bear and Y. Corapcioglu (eds): *Fundamentals of transport phenomena in porous media*. Vol. 82, *NATO ASI Series E: Applied Sciences*, M. Nijhoff Publishers, Dordrecht, The Netherlands, 1984, pp. 3–61.
- Bear, J. and Bachmat, Y.: *Introduction to modeling of transport phenomena in porous media*. Kluwer, Dordrecht, The Netherlands, 1990.
- Bear, J. and Berkowitz, B.: Groundwater flow and pollution in fractured rock aquifers. In: P. Novak (ed): *Development of hydraulic engineering*. *Elsevier Applied Science* Vol. 4, Oxford, UK, 1987.
- Bear, J. and Veruijt, A.: *Modeling groundwater flow and pollution*. Reidel Publ. Co., Dordrecht, The Netherlands, 1987.
- Bear, J., Beljin, M.S. and Ross, R.R.: *Fundamentals of groundwater modeling*, United States Environmental Protection Agency, EPA/540/S-92/005, 1992.
- Bear, J., Tsang, C.-F. and de Marsily, G. (eds): *Flow and contaminant transport in fractured rock*. Academic Press, New York, NY, 1993.
- Beardsmore, G.R. and Cull, J.P.: *Crustal heat flow—A guide to measurement and modelling*. Cambridge University Press, Cambridge, UK, 2001.
- Bemis, K., von Herzen, R. and Mottl, M.: Geothermal heat flux from hydrothermal plumes on the Juan de Fuca Ridge. *J. Geophys. Res.* 98 (1993), pp. 6351–6365.
- Bertani, R.: World geothermal power generation in the period 2001–2005. *Geothermics* 34 (2005), pp. 651–690.
- Bertani, R.: Geothermal power generation in the world 2005–2010 update report. *Proceedings World Geothermal Congress 2010*, 25–29 April 2010, Bali, Indonesia, 2010.
- Bhattacharya, P., Mukherjee, A.B., Bundschuh, J., Zevenhoven, H.R. and Loeppert, R.H. (eds): Arsenic in soil and groundwater environment. In: *Trace Metals and other Contaminants in the Environment*, Volume 9, Elsevier, Amsterdam, The Netherlands, 2007a.
- Bhattacharya, P., Welch, A.H., Stollenwerk, K.G., McLaughlin, M., Bundschuh, J. and Panaullah, G.: Arsenic in the environment: Biology and Chemistry. *Sci. Total Envir.* 379:2–3 (2007b), pp. 109–265.
- Bhattacharya, P., Ramanathan, A.L., Mukherjee, A.B., Bundschuh, J., Chandrasekharam, D. and Keshari, A.K.: *Groundwater for sustainable development: Problems, perspectives and challenges*. Balkema Publisher/Francis and Taylor, Leiden, The Netherlands, 2008.
- Biot, M.A.: General theory of three-dimensional consolidation. *J. Appl. Physics* 12 (1941), pp. 155–164.
- Biot, M.A.: Theory of elasticity and consolidation for a porous anisotropic solid. *J. Appl. Physics* 26 (1955), pp. 182–185.
- Biot, M.A.: Theory of propagation of elastic waves in a fluid saturated porous solid. Part I: Low-frequency range. *J. Acoustic Soc. Am.* 28 (1956a), pp. 168–178.
- Biot, M.A.: Theory of propagation of elastic waves in a fluid saturated porous solid. Part II: Higher-frequency range. *J. Acoustic Soc. Am.* 28 (1956b), pp. 179–191.
- Biot, M.A.: Mechanics of deformation and acoustic propagation in porous media. *J. Appl. Physics* 33:4 (1962), pp. 1482–1498.
- Biot, M.A.: Theory of finite deformations of porous solids. *Indiana Univ. Math. J.* 21:7 (1972), pp. 597–620.
- Biot, M.A. and Willis, D.G.: The elastic coefficients of the theory of consolidation. *J. Appl. Mech.* 24 (1957), pp. 594–601.

- Birch, F.: Thermal conductivity, climatic variation, and heat flow near Calumet, Michigan. *Am. J. Sci.*, 252:1 (1954), pp. 1–25.
- Birch, F. and Clark, H.: The thermal conductivity of rocks and its dependence upon temperature and composition, Part 1. *Am. J. Sci.* 238:8 (1940), pp. 529–558.
- Birkle, P. and Verma, M.P.: Geothermal development in Mexico. In: D. Chandrasekharam and J. Bundschuh (eds): *Geothermal energy for developing countries*. Balkema Publisher, Lisse, The Netherlands, pp. 385–404, 2002.
- Bisson, R.A.: Space age integrated exploration and treatment of renewable regional sources of pristine groundwater in fractured rock “megawatersheds”. *Desalination* 99 (1994), pp. 257–273.
- Blès, J.L. and Feuga, B.: *The fracture of rocks*. Bureau de Recherches Géologiques et Minières, Elsevier, New York, NY, 1986.
- Bloomfield, K.K. and Moore, J.N.: Modeling hydrofluorocarbon compounds as geothermal tracers. *Geothermics* 32 (2003), pp. 203–218.
- Bodvarsson, G.S., O’Sullivan, M. and Tsang, Ch.: The sensitivity of geothermal reservoir behavior to relative permeability parameters. *Proceedings of the 6th Workshop on Geothermal Reservoir Engineering*, Stanford University, Stanford, CA, 1980, pp. 224–237.
- Boonstra, J.: *SATEM, Selected aquifer test evaluation methods, a microcomputer program*. Book and disk edition, Int. Inst. Land Reclam, Wageningen, The Netherlands, 1989.
- Bouwer, H.: The Bouwer and Rice slug test—An update. *Ground Water* 27:3 (1989), pp. 304–309.
- Bouwer, H. and Rice, R.C.: A slug test method for determining hydraulic conductivity of unconfined aquifers with completely or partially penetrating wells. *Water Resour. Res.* 12:3 (1976), pp. 423–428.
- Brassington, F.C.: *Field hydrogeology*. 2nd ed, Wiley, New York, NY, 1998.
- Brebbia, C.A. and Ferrante, A.J.: *Computational methods for the solution of engineering problems*. Pentech Press Ltd., London, UK, 1978.
- Brodkey, R.S.: *The phenomena of fluid motions*. Addison-Wesley Co., Menlo Park, CA, 1967.
- Brooks, R.H. and Corey, A.T.: Properties of porous media affecting fluid flow. *J. Irrig. Drain. Div.* 6 (1966), pp. 61–68.
- Brownell, D., Garg, S. and Pritchett, J.: Governing equations for geothermal reservoirs. *Water Resour. Res.* 13 (1977), pp. 929–934.
- Brownell, D.H., Garg, S.K. and Pritchett, J.W.: Computer simulation of geothermal reservoirs. *Proceedings 45th Annual California Regional Meeting of the SPE of AIME*, paper No. 5381, 1975, pp. 1–9.
- Buckley, S.E. and Leverett, M.C.: Mechanism of fluid flow in sands. *Trans. AIME* 146, 1942, pp. 107–116.
- Bundschuh, J.: Modeling annual variations of spring and groundwater temperatures associated with shallow aquifer systems. *J. Hydrology* 142: (1992), pp. 427–444.
- Bundschuh, J.: Modeling the heat transport from the earth’s surface through aquifers to springs: Theoretical examples and case studies. In: *Exchange processes at the land surface for a range of space and time scales*, IAHS publication 212, Wallingford, UK, 1993a, pp. 205–213.
- Bundschuh, J.: Using heat to trace shallow aquifer systems: Numerical models of theoretical examples and case studies. In: *Tracers in hydrology*, IAHS publication 215, Wallingford, UK, 1993b, pp. 341–342.
- Bundschuh, J.: Flächenhafter Wärmeeintrag in Aquifere als Tracer und Indikator für das Kontaminations-Gefährdungspotential: Modelle und Geländebeispiele Süddeutschlands. *Z. dt. Geol. Ges.* 146 (1995), pp. 425–441.
- Bundschuh, J. and Chandrasekharam, D.: The geothermal potential of the developing world. In: D. Chandrasekharam and J. Bundschuh (eds): *Geothermal energy for developing countries*. Balkema Publisher, Lisse, The Netherlands, pp. 53–62, 2002.
- Bundschuh, J. and Coviello, M.: Geothermal energy: Capacity building and technology dissemination. In: D. Chandrasekharam and J. Bundschuh (eds) (2002): *Geothermal energy for developing countries*. Balkema Publisher, Lisse, The Netherlands, pp. 77–90, 2002.
- Bundschuh, J., Alvarado, G.E., Rodriguez, J.A., Roldán, A.R., Palma, J.C., Zuñiga, A., Reyes, E., Castillo, G. and Salgado, R.M.: Resources and policy of geothermal energy in Central America. In: D. Chandrasekharam and J. Bundschuh (eds): *Geothermal energy for developing countries*. Balkema Publisher, Lisse, The Netherlands, pp. 313–364, 2002.
- Bundschuh, J., Bhattacharya, P. and Chandrasekharam, D. (eds): *Natural arsenic in groundwater: Occurrence, remediation and management*. Balkema Publisher, Leiden, The Netherlands, 2005.
- Bundschuh, J., Birkle, P., Aaheim, A. and Alvarado, G.E.: Geothermal resources for development—valuation, present use and future opportunities. In: Bundschuh, J. and Alvarado G.E. (eds):

- Central America: Geology, resources and hazards* (2 Volumes). Balkema Publisher, Lisse, The Netherlands, pp. 869–894, 2007.
- Bundschuh, J., Armienta, M.A., Birkle, P., Bhattacharya, P., Matschullat, J. and Mukherjee, A.B. (eds): Natural arsenic in groundwater of Latin America. In: J. Bundschuh and P. Bhattacharya (series eds): *Arsenic in the environment*, Volume 1. CRC Press/Balkema Publisher, Boca Raton, FL, 2009.
- Burger, M.: Parameter Identification. Lecture notes, Fifth Winter School in Computational Mathematics: Inverse Problems and Parameter Identification for PDE Models, 20–25 February 2005, Geilo, Norway, 2005, <http://www.math.sintef.no/vskoler/2005/notes/Burger.pdf> (accessed August 2009).
- Butler, J.J., Jr.: *The design, performance and analysis of slug tests*. Lewis Publishers, Boca Raton, FL, 1998.
- Byrnes, A.P.: Aspects of permeability, capillary pressure, and relative permeability properties and distribution in low-permeability rocks important to evaluation, damage, and stimulation. *Proceedings Rocky Mountain Association of Geologists—Petroleum Systems and Reservoirs of Southwest Wyoming Symposium*, 19 September 2003, Denver, CO, 2003.
- Carrera, J., Alcolea, A., Medina, A., Hidalgo, H. and Slooten, L.J.: Inverse problem in hydrogeology. *Hydrogeology J.* 13 (2005), pp. 206–222.
- Carslaw, H.S. and Jaeger, J.C.: *Conduction of heat in solids*. 2nd ed, Oxford Clarendon Press, Oxford, UK, 1959.
- Castellanos, J.L., Gómez, S. and Guerra, V.: The triangle method for finding the corner of the L-curve. *Appl. Numer. Math.* 43 (2002), pp. 359–373.
- Chandrasekharam, D. and Bundschuh, J. (eds): *Geothermal energy resources for developing countries*. A.A. Balkema, Lisse, The Netherlands, 2002.
- Chandrasekharam, D. and Bundschuh, J.: *Low-middle enthalpy geothermal systems for power generation*. CRC Press/Taylor & Francis/Balkema, Boca Raton, FL, 2008.
- Chang, C.P., Chang, T.Y., Want, C.T., Kuo, C.H. and Chen, K.S.: Land-surface deformation corresponding to seasonal ground-water fluctuation, determining by SAR interferometry in the SW Taiwan. *Math. Comput. Simul.* 67 (2004), pp. 351–359.
- Chen, H.Y., Teufel, L.W. and Lee, R.L.: Coupled fluid flow and geomechanics. In: *Reservoir study, I. Theory and governing equations*. Paper SPE 30752 presented at the SPE Annual Technical Conference & Exhibition, 22–25 October 1995, Dallas, TX, 1995, pp. 507–519.
- Cheng, A., Detournay, E. and Abousleiman, Y.: A tribute to Maurice A. Biot. *Int. J. Solids Structures* 35 (1998), pp. 4515–4517.
- Chevron Corporation: <http://www.willyoujoinus.com/> (accessed November 2009).
- Chiang, W.-H.: 3D-Groundwater Modeling with PMWIN: A simulation system for modeling groundwater flow and transport processes. 2nd ed., Springer, Berlin, Germany, 2005.
- Chiang, W.-H. and Kinzelbach, W.: PMPATH for Windows. User's manual. Scientific Software Group, Washington, DC, 1994.
- Chiang, W.-H. and Kinzelbach, W.: Processing Modflow: A simulation system for modeling groundwater flow and pollution. Manual for MPWIN code, 1998a; <http://www.ifu.ethz.ch/publications/software/pmwin/pm5.pdf>.
- Chiang, W.-H. and Kinzelbach, W.: PMPATH 98. An advective transport model for Processing Modflow and Modflow, 1998b.
- Chiang, W.-H. and Kinzelbach, W.: 3D-Groundwater Modeling with PMWIN. Springer, Berlin, Germany, 2005.
- Chiang, W.-H., Kinzelbach, W. and Rausch, R.: *ASM6: Aquifer simulation model for Windows*. Schweizerbart, Stuttgart, Germany, 1997.
- Chiang, W.-H., Kinzelbach, W. and Rausch, R.: *Aquifer simulation model for Windows—Groundwater flow and transport modeling, an integrated program*. Gebrüder Borntraeger, Berlin, Stuttgart, Germany, 1998.
- Cinco Ley, H. and Meng, H.Z.: Pressure transient analysis of wells with finite conductivity fractures in double porosity reservoirs. Paper SPE 6019 presented at the SPE Annual technical Conference and Exhibition, New Orleans, Oct. 3–6, 1988.
- Clark, Jr., S.P.: Thermal conductivity. In: S.P. Clark, Jr. (ed): *Handbook of physical constants*. Memoir 97, Geological Society of America, New York, NY, 1966, pp. 459–482.
- Clark, I.D. and Fritz, P.: *Environmental isotopes in hydrogeology*. CRC Press, Boca Raton, FL, 1997.
- Clauser, C.: Geothermal energy. In: K. Heinloth (ed): Landolt-Börnstein, Group VIII: *Advanced materials and technologies*, Vol. 3: *Energy technologies*, Subvol. C: *Renewable energies*. Springer, Heidelberg-Berlin, Germany, 2006, pp. 480–595.
- Clough, R.W.: The finite element in plane stress analysis. *Proceedings 2nd ASCE Conference on Electronic Computation*, Pittsburg, PA, 1960.

- Clough, R.W.: The finite element in structural mechanics. In: O.C. Zienkiewicz and G.S. Holister (eds): *Stress analysis*. Wiley, New York, NY, 1965.
- Colback, P.S. and Wiid, B.L.: Influence of moisture content on the compressive strength of rock. *Proc. Rock Mech. Symp. Can.*, Dept. of Mines & Tech. Surveys, Ottawa, Canada, 1965.
- Coletta, B. and Angelier, J.: Faulting evolution of Santa Rosalía Basin, Baja California Sur, Mexico. In: L. Ortlieb and J. Roldan (eds): *Field Guides and Papers: Geology of Northwestern and Southern Arizona*. Inst. Geol., UNAM, Mexico City, Mexico, 1981, pp. 265–274.
- COMSOL: COMSOL Multiphysics® software and User's Guide, version 3.5. COMSOL AB, Stockholm, Sweden, 2008a.
- COMSOL: Earth Science Module User's Guide version 3.5. COMSOL AB, Stockholm, Sweden, 2008b.
- COMSOL: Pore-scale flow solved with COMSOL Multiphysics® 3.5a. COMSOL AB, Stockholm, Sweden, 2008c, <http://www.comsol.com/showroom/gallery/488/> (accessed August 2009).
- COMSOL: Fluid flow to wells: Wellbore storage solved with COMSOL Multiphysics® 3.5a. COMSOL AB, Stockholm, Sweden, 2008d, <http://www.comsol.com/showroom/gallery/502/> (accessed August 2009).
- COMSOL: Coupled flow laws solved with COMSOL Multiphysics® 3.5a. COMSOL AB, Stockholm, Sweden, 2008e, <http://www.comsol.com/showroom/gallery/609/> (accessed August 2009).
- COMSOL: COMSOL AB, Stockholm, Sweden, 2009, <http://www.comsol.com/showroom/gallery> (accessed August 2009).
- Contreras, E., Domínguez, B., Iglesias, E., García, A. and Huitrón, R.: Compendio de resultados de mediciones petrofísicas en núcleos de perforación del campo geotérmico Los Azufres. *Geotermia* 4:2 (1988), pp. 79–105.
- Contreras, E., Domínguez, B. and Rivera, O.: Mediciones petrofísicas en núcleos de perforación del campo geotérmico de Los Húmeros. *Geotermia* 6:1 (1990), pp. 7–42.
- Contreras, E., Guevara, M. and Rentería, D.: Estudio y evaluación de metodologías para estimar propiedades termofísicas de rocas a partir de análisis químicos y estudios petrográficos. Project No. 5568, Inf. IIE/11/5568/101/F, Instituto de Investigaciones Eléctricas IIE, Cuernavaca, Mor., Mexico, 1994.
- Cooper, H.H. Jr., Bredehoeft, J.D. and Papadopoulos, I.S.: Response of a finite-diameter well to an instantaneous charge of water. *Water Resour. Res.* 3:1 (1967), pp. 263–269.
- Corey, A.T.: The interrelation between gas and oil relative permeabilities. *Producer's Monthly* 1:19 (1954), pp. 38–41.
- Corliss, J.B. and Ballard, R.D.: Oases of life in the cold abyss. *Nat. Geogr. Mag.* 152:2 (1977), pp. 441–453.
- Courant, R.: Variational methods for the solution of problems of equilibrium and vibrations. *Bull. Am. Math. Soc.* 49 (1943), pp. 1–23.
- Courant, R., Friedrichs, K. und Lewy, H.: Über die partiellen Differentialgleichungen der mathematischen Physik. *Math. Ann.* 100 (1928), pp. 32–74.
- Coussy, O.: *Mécanique des milieux poreux*. Ed. Technip, Paris, France, 1991.
- Coussy, O.: *Poro mechanics*. John Wiley & Sons, New York, NY, 2004.
- Crank, J. and Nicolson, P.: A practical method for numerical evaluation of solutions of partial differential equations of the heat conduction type. *Proc. Camb. Phil. Soc.* 43 (1947), pp. 50–67.
- Cruse, T. and Rizzo, F.: Boundary integral equation method: Computational applications in applied mechanics. *Applied Mechanics Conf. AMD* Vol. 11, The Applied Mechanics Division, ASME. Rensselaer Polytechnic Institute, New York, NY, 1975.
- Cunha, C., Bonet, E.J. and Corrêa, A.C.: Water alternating gas injection: Laboratory measurements and comparison with analytical calculation. *J. Porous Media* 2:2 (1999), pp. 143–151.
- D'Yakov, E.: The method of variable directions in solving systems of finite difference equations. *Soviet Math. Dokl.* 2 (1961), pp. 577–580. TOM 138, 271–274.
- Dagan, G.: Solute transport in heterogeneous porous formations. *J. Fluid Mech.* 145 (1984), pp. 151–177.
- Damm, K.: Controls on the chemistry and temporal variability of seafloor hydrothermal fluids. *Geophys. Monogr.* 91, American Geophysical Union, 1995, pp. 222–247.
- Dandekar, A.Y.: *Petroleum reservoir rock and fluid properties*. CRC Press/Taylor & Francis, Boca Raton, FL, 2006.
- Darcy, H.: *Les fontaines publiques de la Ville de Dijon*. Dalmont, Paris, France, 1856.
- Dawson, K.J. and Istok, J.D.: *Aquifer testing: design and analysis of pumping and slug tests*. Lewis Publishers, Boca Raton, FL, 1991.
- Day-Lewis, F.D., Person, M.A. and Konikow, L.F.: Computer program (MACPUMP) for interactive aquifer-test analysis. US Geological Survey Water-Resources Investigations Report 95-4012, US Geological Survey, Reston, VA, 1995.
- de Marsily, G.: *Quantitative hydrogeology*. Academic Press, Orlando, FL, 1986.

- De Swaan, A.: Analytical solutions for determining naturally fractured reservoir properties by well testing. *SPE Journal* 16 (1976), AIME, pp. 117–122.
- De Wiest, R. (ed): *Flow through porous media*. Academic Press, New York, NY, 1969.
- Dennis, J.E. and Schnabel, R.B.: Numerical methods for unconstrained optimization and nonlinear equations. *SIAM*, Philadelphia, PA, 1996.
- Detournay, E. and Cheng, A.H.-D.: Fundamentals of poroelasticity. In: C. Fairhurst (ed): *Comprehensive rock engineering: Principles, practice and projects*, Vol. II: *Analysis and design method*. Pergamon Press, Oxford, UK, pp. 113–171.
- Dietrich, P., Helmig, R., Hötzl, H., Kongeter, J. and Teutsch, G.: *Flow and transport in fractured porous media*. Springer, Berlin, Germany, 2005.
- Dill, E.H.: *Continuum mechanics: Elasticity, plasticity, viscoelasticity*. CRC Press Taylor & Francis Group, Boca Raton, FL, 2007.
- Diment, W.H. and Pratt, H.R.: *Thermal conductivity of some rock-forming minerals: a tabulation*. Open File Report 88-690, US Geological Survey, Denver, CO, 1988.
- Diodato, D.M.: *A compendium of fracture flow models—1994*. Center for Environmental Restoration Systems, Energy Systems Division, Argonne National Laboratory, Aragonne, IL, 1994.
- Diomampo, G.P., Chen, C.-Y., Li, K. and Horne, R.N.: (2002), Relative permeability through fractures. *Proceedings of the 27th Workshop on Geothermal Reservoir Engineering*, 28–30 January 2002, Stanford University, Stanford, California, SGP-TR-171, 2002, pp. 21–38.
- Dobson, P.F. and Mahood, G.A.: Volcanic stratigraphy of the Los Azufres geothermal area, Mexico. *J. Volcanol. Geotherm. Res.* 25 (1985), pp. 273–287.
- Doherty, J., Brebber, L. and Whyte, P.: PEST-Model-independent parameter estimation. User's manual. Watermark Computing, Australia, 1994.
- Domenico, P.A. and Schwartz, F.W.: *Physical and chemical hydrogeology*. John Wiley and Sons, New York, NY, 1990.
- Dreyer, W.: *Materialverhalten anisotroper Festkörper: Thermische und elektrische Eigenschaften*. Springer, Vienna, Austria, 1974.
- Duc, J. and Bellet, D.: *Mécanique des solides reels*. Editions Cepadues, Toulouse, France, 1976.
- Dullien, F.A.: *Porous media, fluid transport and pore structure*. Academic Press, New York, NY, 1979.
- DVWK: Stofftransport im Grundwasser. *DVWK Schriften* 83, Paul Parey, Hamburg, Germany, 1989.
- EIA (Energy Information Administration): International energy outlook 2007. Energy Information Administration, Office of Integrated Analysis and Forecasting, US Department of Energy, Washington, DC, DOE/EIA-0484(2007), 2007, <http://www.eia.doe.gov/oiaf/ieo/index.html> (accessed July 2007).
- Ellsworth, T.R., Shouse, P., Skaggs, T.H., Jobs, J.A. and Fargerlund, J.: Solute transport in unsaturated soil: Experimental design, parameter estimation and model discrimination. *Soil Sci. Soc. Am. J.* 60 (1996), pp. 397–407.
- Engelen, G.B. and Vennecker, R.G.W.: A distributed hydrological system approach to mountain hydrology. *Memories of the 22nd Congress of IAH*, Vol. XXII, Lausanne, Switzerland, 1990, pp. 837–845.
- Engl, H., Hanke, M. and Neubauer, A.: *Regularization of inverse problems*. Kluwer, Dordrecht, The Netherlands, 1996.
- Eriksson, K., Estep, D., Hansbo, P. and Johnson, C.: *Computational differential equations*. Studentlitteratur, Lund, Sweden, 1996.
- Fairwater, G., Gourlay, A. and Mitchell, A.: Some high accuracy difference schemes with a splitting operator for equations of parabolic and elliptic type. *Numer. Math.* 10 (1967), pp. 56–66.
- Falta, R.W., Pruess, K., Finsterle, S. and Battistelli, A.: T2VOC user's guide. Rep. LBL-36400. Lawrence Berkeley Natl. Lab., Berkeley, CA, 1995.
- Farmer, I.W.: *Engineering properties of rocks*. E. & F.N. Spon Ltd. London, UK, 1968.
- Faust, C.R. and Mercer, J.W.: Mathematical modeling of geothermal systems. *Proceedings of the United Nations Meeting*, San Francisco, CA, 1975, pp. 1635–1641.
- Felippa, C.A.: Nonlinear finite element methods. Course manual, ASEN 5107, Fall 2007, Department of Aerospace Engineering Sciences, University of Colorado at Boulder, Boulder, CO, 2007, <http://www.colorado.edu/engineering/Aerospace/CAS/courses.d/NFEM.d/> (accessed August 2009).
- Felippa, C.A.: Advanced finite element methods. Course manual, ASEN 6367, Spring 2009, Department of Aerospace Engineering Sciences, University of Colorado at Boulder, Boulder, CO, 2009a, <http://www.colorado.edu/engineering/Aerospace/CAS/courses.d/AFEM.d/> (accessed August 2009).
- Felippa, C.A.: Introduction to finite element methods. Course manual, ASEN 5007, Fall 2009, Department of Aerospace Engineering Sciences, University of Colorado at Boulder, Boulder, CO, 2009b, <http://www.colorado.edu/engineering/Aerospace/CAS/courses.d/IFEM.d/> (accessed August 2009).

- Ferris, J.G., Knowles, D.B., Brown, R.H. and Stallman, R.W.: Theory of aquifer tests (PDF). Water Supply Paper 1536-E, US Geological Survey, 1962.
- Finsterle, S.: iTOUGH2 user's guide. Rep. LBNL-40040. Lawrence Berkeley Natl. Lab., Berkeley, CA, 1999.
- Fish, J. and Belytschko, T.: *A first course in finite elements*. John Wiley & Sons, New Jersey, NJ, NY, 2007.
- Fjaer, E., Holt, R., Horsrud, P. and Risnes, R.: Petroleum related rock mechanics. *Dev. Petrol. Sci.* 33, Elsevier, Amsterdam, 1992.
- Forchheimer, P.: Wasserbewegung durch Boden. *Zeitschrift des Vereines Deutscher Ingenieure* 45 (1901), pp. 1736–1741 and pp. 1781–1788.
- Fornari, D. and Embley, R.: Tectonic and volcanic controls on hydrothermal processes at the mid-ocean ridge: An overview based on near-bottom and submersible studies. *Geophys. Monogr.* 91, American Geophysical Union, 1995, pp. 1–46.
- Forsythe, G.E. and Wasnow, W.R.: *Finite-difference methods for partial differential equations*. John Wiley & Sons, Inc., New York, NY, 1960.
- Fox, L.: *Numerical solution of ordinary and partial differential equations*. Pergamon Press, Oxford, UK, 1962.
- Franke, O.L., Reilly, T.E. and Bennett, G.D.: Chapter B5: Definition of boundary and initial conditions in the analysis of saturated ground-water flow systems—An introduction (PDF), Book 3: Applications of hydraulics. US Geological Survey, 1987.
- Freyberg, D.L.: A natural gradient experiment on solute transport in sand aquifer: 2. Spatial moments and the advection and dispersion of nonreactive tracers. *Water Resour. Res.* 22:13 (1986), pp. 2031–2046.
- Galerkin, B.G.: Series solution of some problems of elastic equilibrium of rods and plates (in Russian). *Vestnik Inzhenerov Tech.* 19 (1915), pp. 897–908.
- Garabedian, S.P., LeBlanc, D.R., Gelhar, L.W. and Celia, M.A.: Large-scale natural gradient tracer test in sand and gravel, Cape Cod, Massachusetts: 2. Analysis of spatial moments for a nonreactive tracer. *Water Resour. Res.* 27:5 (1991), pp. 911–924.
- García, A., Contreras, E. and Domínguez, B.: Estudios petrofísicos en cuatro núcleos de perforación del campo geotérmico La Primavera: Propiedades térmicas. *Geotermia* 7:1 (1991), pp. 59–68.
- García, G.H.: *Modelo del estado térmico inicial del campo geotérmico de Los Azufres, Michoacán, México*. PhD Thesis, Instituto de Geofísica, Universidad Nacional Autónoma de México UNAM, Mexico City, Mexico, 2000.
- Garg, S.K.: Pressure transient analysis for two-phase (water/steam) geothermal reservoirs. *Society of Petroleum Engineering Journal (SPEJ)*, 1980, pp. 206–214. Paper SPE 7479, first presented at the SPE 53rd Annual Fall technical conference, Houston October 1–3, 1978. Reprinted from June 1980 issue of SPEJ.
- Garg, S.K.: Formation compaction associated with thermal cooling in geothermal reservoirs. *Energy Sources* 9 (1984), pp. 261–268.
- Garg, S.K.: On formation compaction and energy balance law for liquid-saturated porous media reservoirs. *Adv. Water Resour.* 8 (1985), pp. 22–25.
- Garg, S.K. and Combs, J.: Mathematical modeling of mass and energy transport in geothermal boreholes with two-phase feedzones. *Geothermal Resources Council Transactions* 22, 1998, pp. 547–555.
- Garg, S.K. and Pritchett, J.: On pressure-work, viscous dissipation and the energy balance relation for geothermal reservoirs. *Adv. Water Resour.* 1 (1977), pp. 41–47.
- Gassmann, F.: Über die Elastizität poröser Medien. *Vier. der Natur. Gesellschaft in Zürich* 96 (1951), pp. 1–23.
- Gelhar, L.W. and Axness, C.L.: Three-dimensional stochastic analysis of macrodispersion in aquifers. *Water Resour. Res.* 19 (1983), pp. 161–180.
- Gelhar, L.W., Welty, C. and Rehfeldt, K.R.: A critical review of data on field-scale dispersion in aquifers. *Water Resources Res.* 28:7 (1992), pp. 1955–1974.
- GEO: Web page of the Geothermal Education Office, 2009, <http://geothermal.marin.org/> (accessed October 2009).
- GRC: Web page of the Geothermal Resources Council, 2009, <http://www.geothermal.org/> (accessed October 2009).
- Germain, P.: *Mécanique des milieux continus*, Tome 1: *Théorie générale*. Masson et Cie. Éd., Paris, France, 1973.
- Giggenbach, W.F.: Geothermal solute equilibria: Derivation of Na-K-Mg-Ca geoindicators. *Geochim. Cosmochim. Acta* 52 (1988), pp. 2749–2765.
- Gockenbach, M.S.: *Partial differential equations: Analytical and numerical methods*. SIAM-Society for Industrial and Applied Mathematics, 2002.

- Goldscheider, N. and Drew, D.: Methods in Karst Hydrogeology. *IAH International Contributions to Hydrogeology* 26, Taylor & Francis, London, UK, 2007.
- Golub, G.H. and Van Loan, C.F.: *Matrix computations*. Johns Hopkins University Press, Baltimore, MD, 1989.
- Golub, G.H., Hansen, P.C. and O'Leary, D.P.: Tikhonov regularization and total least squares. Technical report, CS-TR-3829, UMIACS-TR-97-65, Computer Science Department, University of Maryland, College Park, MD, 1998, <http://hdl.handle.net/1903/913> (accessed August 2009).
- Gómez, S., Pérez, A. and Alvarez, R.M.: The multiscale optimization for aquifer parameter identification with noisy data. *Computational Methods in Water Resources* XII, Vol. 2, Computational Mechanics Publication, 1998, <http://library.witpress.com/pages/PaperInfo.asp?PaperID=6357> (accessed January 2009).
- González, E.P., Birkle, P. and Torres-Alvarado, I.S.: Evolution of the hydrothermal system at the geothermal field of Los Azufres, Mexico, based on fluid inclusion, isotopic and petrologic data. *J. Volcanol. Geotherm. Res.* 104:1–4 (2000), pp. 277–296.
- Goranson, R.W.: Heat capacity: heat of fusion. In: F. Birch, J.F. Schairer and H.C. Spicer (eds): *Handbook of physical constants*. Special Paper 36, Geological Society of America, New York, NY, 1942. pp. 223–242.
- Grijalva, N.: Investigación de la energía geotérmica en la Depresión de Wagner en el Golfo de California, latitud 31°00' al 31°15' y longitud 113°50' al 114°10'. Unpublished reports prepared for the Comisión Federal de Electricidad under Contract No. CCP-CLS-002/ 86 (date of 1st report: 10/1/86, date of 2nd report: 11/22/86), Cerro Prieto, B.C., Mexico, 1986.
- Gueguen, Y. and Bouteca, M. (eds): Mechanics of fluid-saturated rocks. *International Geophysics Series* 89, Elsevier-Academic Press, New York, NY, 2004.
- Gunderson, R., Parini, M. and Sirad-Azwar, L.: Fluorescein and naphthalene sulfonate liquid tracer results at the Awibengkok geothermal field, West Java, Indonesia. *Proceedings 27th Workshop on Geothermal Reservoir Engineering*, Stanford, CA, 2002.
- Gutiérrez-Negrín, L.C.A.: 1997–2006: A decade of geothermal power generation in Mexico. *Transactions of the Geothermal Resources Council* 31, 2007, pp. 167–171.
- Gutiérrez-Negrín, L.C.A., Maya-González, R. and Quijano-León, J.L.: Current status of geothermics in Mexico. *Proceedings World Geothermal Congress 2010*, 25–29 April 2010, Bali, Indonesia, 2010.
- Habana, M.D.: Relative permeability of fractured rock. SGP-TR-172, Stanford Geothermal Program, Stanford, CA, 2002.
- Hadjidimos, A.: On some high accuracy difference schemes for solving elliptic equations. *Numer. Math.* 13 (1969), pp. 396–403.
- Halfman, S.E., Lippmann, M.J., Zelweer, R. and Howard, J.H.: Geologic interpretation of geothermal fluid movement in Cerro Prieto Field, Baja California, Mexico. *Am. Ass. Petrol. Geol. Bull.* 68 (1984), pp. 18–30.
- Halihan, T. and Wicks, C.M.: Modeling of storm responses in conduit flow aquifers with reservoirs. *J. Hydrol.* 208 (1998), pp. 82–91.
- Hall, P. with a contribution by Chen, J.: *Water well and aquifer test analysis*. A book and disk edition, Water Resources Publications LLC, Highlands Ranch, CO, 1996.
- Han, N.W., Bhakta, J. and Carbonell, R.G.: Longitudinal and lateral dispersion in packed beds: Effect of column length and particle size distribution. *AIChE J.* 31 (1985), pp. 277–288.
- Hanke, M. and Vogel, C.R.: Two-level preconditioners for regularized inverse problems, I. *Theory, Numer. Math.* 83 (1999), pp. 385–402.
- Hannington, M., Jonasson, I., Herzig, P. and Petersen, S.: Physical and chemical processes of seafloor mineralization at mid-ocean ridges. *Geophys. Monogr.* 91, American Geophysical Union, 1995, pp. 115–157.
- Hansen, P.C.: Rank-deficient and discrete ill-posed problems. *SIAM*, Philadelphia, PA, 1998.
- Hantush, M.S.: Analysis of data from pumping test in leaky aquifers. *Trans. American Geophysical Union* 37, 1956, pp. 702–714.
- Harvey, A.H., Peskin, A.P. and Klein, S.A.: NIST/ASME steam properties, Version 2.21, Users' Guide. Physical and Chemical Properties Division, National Institute of Standards and Technology, Gaithersburg, MD, March 2004.
- Hashin, Z. and Shtrikman, S.: A variational approach to the theory of the effective magnetic permeability of multiphase materials. *J. Appl. Physics* 33:10 (1962), pp. 3125–3131.
- Hessler, R. and Kaharl, V.: The deep-sea hydrothermal vent community: An overview. *Geophys. Monogr.* 91, American Geophysical Union, 1995, pp. 72–84.

- Hill, M.C. and Tiedeman, C.R.: *Effective groundwater model calibration: With analysis of data, sensitivities, predictions, and uncertainty*. Wiley, New York, NY, 2007.
- Holzbecher, E.: *Modeling density-driven flow in porous media: Principles, Numerics, Software*. Springer, Berlin, New York, 1998.
- Honarpour, M.M., Koederitz, L. and Harvey, A.H.: Relative permeability of petroleum reservoirs. CRC Press, Boca Raton, FL, 1986.
- Horai, K.: Thermal conductivity of rock-forming minerals. *J. Geophys. Res.* 76:5 (1971), pp. 1278–1308.
- Horai, K. and Baldrige, W.S.: Thermal conductivity of nineteen igneous rocks, II: Estimation of the thermal conductivity of rock from the mineral and chemical compositions. *Phys. Earth Planet. Interiors* 5 (1972), pp. 157–166.
- Humphris, S.E., Zierenberg, R.A., Mullineaux, L.S. and Thomson, R.E. (eds): Seafloor hydrothermal systems: Physical, chemical, biological and geological interactions. *Geophys. Monogr.* 91, American Geophysical Union, 1995, pp. 1–466.
- Huntoon, P.W.: Is it appropriate to apply porous media groundwater circulation models to karstic aquifers? In: A.I. El-Kadi (ed): *Groundwater models for resources analysis and management*. Pacific Northwest/Oceania Conference, Honolulu, HI, 1995, pp. 339–358.
- Huyakorn, P.S., Lester, B.H. and Faust, C.R.: Finite element techniques for modeling ground water flow in fractured aquifers. *Water Resour. Res.* 19:4 (1983), pp. 1019–1035.
- Hvorslev, M.J.: Time lag and soil permeability in ground-water observations. *Bull.* 36, Waterways Exper. Sta. Corps of Engrs., US Army, Vicksburg, MS, 1951, pp. 1–50.
- IAEA: *Isotope and radiation techniques in soil physics and irrigation studies*. International Atomic Energy Agency, Vienna, Austria, 1984a.
- IAEA: *Isotope techniques in the hydrogeological assessment of potential sites for the disposal of high-level radioactive wastes*. International Atomic Energy Agency, Vienna, Austria, 1984b.
- IAEA: *Isotope techniques in water resources development*. International Atomic Energy Agency, Vienna, Austria, 1988.
- IAEA: *Isotopic and chemical techniques in geothermal exploration, development and use: Sampling methods, data handling, interpretation*. International Atomic Energy Agency, Vienna, Austria, 2001.
- IGA: Website of the International Geothermal Association, 2009a, <http://iga.igg.cnr.it/index.php> (accessed September 2009).
- IGA: IGA Geothermal Conference Papers Database. 2009b, http://pangea.stanford.edu/ERE/db/IGA_standard/default.htm (accessed September 2009).
- IPCC: Intergovernmental Panel on Climate Change. http://ipcc-wg1.ucar.edu/wg1/FAQ/wg1_faq-2.1.html (accessed November 2009).
- Javandel, I., Doughty, C. and Tsang, C.F.: Groundwater transport: Handbook of mathematical models. *Water Resources Monograph Series* 10, American Geophysical Union, third printing, 1987.
- Jeannin, P.-Y.: Modeling flow in phreatic and epiphreatic karst conduits in the Holloch Cave, Muotatal, Switzerland. *Water Resour. Res.* 37 (2001), pp. 191–200.
- JICA: La Primavera geothermal development project in United Mexican States. Japan International Cooperation Agency, Final Report, Tokyo, Japan, 1989.
- Kanev, K., Ikeuchi, J., Kimura, S. and Okajima, A.: Heat loss to the surrounding rock formation from a geothermal borehole. *Geothermics* 26:3 (1997), pp. 329–349.
- Käss, W.: *Lehrbuch der Hydrogeologie*, Vol. 9: *Geohydrologische Markierungstechnik*. Bornträger, Berlin, Germany, 1992.
- Katsikadelis, J.T.: *Boundary elements: Theory and applications*. Elsevier, Amsterdam, The Netherlands, 2002.
- Keller, A.A. and Auset, A.: A review of visualization techniques of biocolloid transport processes at the pore scale under saturated and unsaturated conditions. *Adv. Water Resour.* 30:6/7 (2007), pp. 1392–1407.
- Kestin, J.: Sourcebook on the production of electricity from geothermal energy. US Dept. of Energy, Washington, DC, 1980.
- Kingston, M.: Modeling chimney growth and associated fluid flow at seafloor hydrothermal vent sites. *Geophys. Monogr.* 91, American Geophysical Union, 1995, pp. 158–177.
- Kinzelbach, W.: Numerische Methoden zur Modellierung des Transportes von Schadstoffen im Grundwasser. *Schriftenreihe Wasser-Abwasser*, R. Oldenbourg Verlag, München, Wien, 1987.
- Kinzelbach, W. and Rausch, R.: ASM, Aquifer Simulation Model, Version 1.0. International Groundwater Modeling Center, IGWMC-BAS 27, Indianapolis, IN, 1989.

- Kinzelbach, W. and Rausch, R.: *Grundwassermodellierung—Eine Einführung mit Übungen*. Gebrüder Borntraeger, Berlin, Stuttgart, Germany, 1995.
- Kirsch, R.: *Groundwater geophysics: A tool for hydrogeology*. Springer, Berlin, Germany, 2006.
- Konikow, L.F., Goode, D.J. and Homberger, G.Z.: A three-dimensional method-of characteristics solute-transport model. U.S. Geological Survey, Water Resources Investigations Report 96-4267, 1996.
- Krasny, J. and Sharp, J.M.: Groundwater in fractured rocks. *IAH Selected Paper Series* 9, Francis and Taylor Group, London, UK, 2007.
- Kresic, N.: Remote sensing of tectonic fabric controlling groundwater flow in Dinaric Karst. *Remote Sens. Environ.* 53 (1995), pp. 85–90.
- Kresic, N.: *Hydrogeology and groundwater modeling*. CRC Press/Taylor & Francis Group, Boca Raton, FL, 2007.
- Krishnamurthy, J., Mani, A., Jayaraman, V. and Manivel, M.: Groundwater resources development in hard rock terrain—An approach using remote sensing and GIS techniques. *JAG* 2:3/4 (2000), pp. 204–215.
- Kruseman, G.P. and de Ridder, N.A.: *Analysis and evaluation of pumping test data*. 2nd ed, International Institute for Land Reclamation and Improvement, Wageningen, The Netherlands, 1991.
- Lang, S.: *Linear algebra*. Addison-Wesley Co., Columbia University, New York, NY, 1969.
- Lautrup, B.: *Physics of continuous matter*. Institute of Physics Publishing IOP, Bristol, UK, 2005.
- León Diez, F. (ed): AGUA. Special edition *LaJornada*, 2005, Mexico.
- Lerner, D.N., Issar, A.S and Simmers, I.: Groundwater recharge, a guide to understanding and estimating natural recharge. *IAH International Contributions to Hydrogeology* 8, Hans Heise, Hannover, Germany, 1990.
- Li, K. and Horne, R.N.: Calculation of steam-water relative permeability using capillary pressure data. *Proceedings 27th, Workshop on Geothermal Reservoir Engineering*, Stanford University, SGP-TR-171, Stanford, CA, 2002, pp. 119–124.
- Li, K. and Horne, R.N.: Universal capillary pressure and relative permeability model from fractal characterization of rock. *Proceedings, 29th Workshop on Geothermal Reservoir Engineering*, 26–28 January 2004, Stanford University, CA, 2004, pp. 103–110.
- Li, K. and Horne, R.N.: Inferring relative permeability from resistivity well logging. *Proceedings, 30th Workshop on Geothermal Reservoir Engineering*, Stanford University, Stanford, CA, January 31–February 2, 2005, SGP-TR-176. 2005, pp. 58–63.
- Li, K. and Horne, R.N.: Fractal modeling of capillary pressure curves for The Geysers rocks. *Geothermics* 35 (2006), pp. 198–207.
- Li, K. and Horne, R.N.: Systematic study of steam-water capillary pressure. *Geothermics* 36 (2007), pp. 558–574.
- Lienhard IV, J.H. and Lienhard V, J.H.: *A heat transfer textbook*. 3rd edition, Massachusetts Institute of Technology, Version 1.31, 2008, available online at <http://web.mit.edu/lienhard/www/ahtt.html> (accessed August 2009).
- Lippmann, M., Narasimhan, T. and Witherspoon, P.: Numerical simulation of reservoir compaction in liquid dominated geothermal systems. *Int. Assoc. of Hydrological Sciences* Pub. No. 121, 1977, pp. 179–189.
- Lippmann, M.J., Truesdell, A.H., Halfman-Dooley, S.E. and Mañón, A.: A review of the hydrogeologic-geochemical model for Cerro Prieto. *Geothermics* 20 (1991), pp. 39–52.
- Liu, G.R. and Quek, S.: *The finite element method—A practical course*. Butterworth-Heinemann, Bristol, UK, 2003.
- Long, J.C.S., Remer, J.S., Wilson, C.R. and Witherspoon, P.A.: Porous medium equivalents for networks of discontinuous fractures. *WWR* 18, 1992, pp. 645–648.
- Lund, J.W., Freeston, D.H. and Boyd, T.L.: Direct utilization of geothermal energy 2010 worldwide review. *Proceedings World Geothermal Congress 2010*, 25–29 April 2010, Bali, Indonesia, 2010.
- Lupton, J.: Hydrothermal plumes: Near and far field. *Geophys. Monogr.* 91, American Geophysical Union, 1995, pp. 317–346.
- Magaña, M.I., Lopez, D.L., Barrios, L.A., Pérez, N.M., Padron, E. and Henríquez, E.: Diffuse and convective degassing of soil gases and heat at the TR-6-Zapotillo hydrothermal discharge zone, Berlin geothermal field, El Salvador. *Geothermal Resources Council Transactions* 28, 2004, pp. 485–488.
- Manzella, A.: Geophysical methods in geothermal exploration. *Ciencia Abierta* 12 (2000), (electronical journal), Chile, http://cabierta.uchile.cl/revista/12/articulos/pdf/A_Manzella.pdf. (accessed May 2007).
- Marle, C.M.: *Multiphase flow in porous media*. Editions Technip, Institut Français du Pétrole, Rueil-Malmaison, France, 1981.
- Marshall, N.B.: Hydrothermal Oases. In: *Developments in deep-sea biology*. Blandford Press, London, UK, 1979, pp. 284–307.
- Mase, T. and Mase, G.: *Continuum mechanics for engineers*. 2nd ed, CRC Press, Boca Raton, FL, 1999.

- Mavko, G., Mukerji, T. and Dvorkin, J.: *The rock physics handbook: Tools for seismic analysis in porous media*. Cambridge University Press, Cambridge, UK, 2003.
- Maya-González, R. and Gutiérrez-Negrín, L.C.A. Recursos geotérmicos para generar electricidad en México". *Revista Digital Universitaria* [online] 8:12 (2007), <http://www.revista.unam.mx/vol.8/num12/art91/int91.htm> (accessed September 2009).
- Medina, A. and Carrera, J.: Coupled estimation of flow and solute transport parameter. *Water Resour. Res.* 32:10 (1996), pp. 3063–3076.
- Mercado, S.: Manifestaciones hidrotermales marinas de alta temperatura (350°C) localizadas a 21°N, a 2600 m de profundidad en la elevación este del Pacífico. *Geotermia* 6:3 (1990), pp. 225–263.
- Mercado, S.: Geotermoquímica de manifestaciones hidrotermales marinas de alta temperatura. *Geotermia* 9:2 (1993), pp. 155–164.
- Mercer, J.W.: Common mistakes in model applications. *Proceedings ASCE Symposium on Ground Water*, July 29–August 2, 1991, Nashville, Tennessee, 1991.
- Mercer, J.W. and Faust, C.R.: *Ground-water modeling*. National Water Well Association (NWWA), Worthington, OH, 1981.
- MIT: The future of geothermal energy—Impact of enhanced geothermal systems (EGS) on the United States in the 21st Century. An assessment by an MIT-led interdisciplinary panel, Massachusetts Institute of Technology, 2006, <http://geothermal.inel.gov> and http://www1.eere.energy.gov/geothermal/egs_technology.html (accessed July 2007).
- Mongillo, M.A.: *Remote sensing techniques for geothermal investigation and monitoring in New Zealand*. PhD thesis, University of Auckland, New Zealand, 2002, <http://hdl.handle.net/2292/2141/> (accessed December 2007).
- Mook, W.: Introduction to isotope hydrology featuring the isotopes of hydrogen, oxygen and carbon. *IAH International Contributions to Hydrogeology* 25, Taylor & Francis, London, UK, 2005.
- Moore, J.E.: *Field hydrogeology: A guide for site investigations and report preparation*. CRC Press, Boca Raton, FL, 2002.
- Moré, J.J.: The Levenberg-Marquardt algorithm: Implementation and theory. In: G.A. Watson (ed): *Numerical Analysis. Lecture Notes in Mathematics* 630, Springer, Berlin, Germany, 1977, pp. 105–116.
- Moré, J.J. and Lin, C.J.: Newton's method for large-scale bound constrained optimization problems. *SIAM Journal on Opt.* 4 (1999), pp. 1100–1127.
- Morland, L.W., Foulser, R. and Garg, S.K.: A mixture theory for a fluid-saturated isotropic elastic matrix. *Int. J. Geomech.* 4:3 (2004), pp. 207–215.
- Muskat, M.: The flow of homogeneous fluids through porous media. *International Series in Physics*, McGraw-Hill, New York. 2nd printing J.W. Edwards Inc., Ann Arbor, MI, 1937, reprinted ed. 1946.
- Muskat, M., Wyckoff, R.D., Botset, H. and Meres, M.: Flow of gas-liquid mixtures through sands. *Transactions of AIME* 123, 1937, pp. 69–96.
- Narasimhan, T.N.: Numerical modeling in hydrogeology. In T.N. Narasimhan (ed): *Recent trends in hydrogeology*. Special Paper 189 Geological Society of America, Boulder, CO, 1982, pp. 273–296.
- Narasimhan, T. and Witherspoon, P.: An integrated finite difference method for analyzing fluid flow in porous media. *Water Resour. Res.* 12:1 (1976), pp. 57–64.
- National Research Council: *Rock fractures and fluid flow*. National Academies Press (NAP), Washington, DC, 1996.
- Nelson, E.B. (ed): *Well cementing*. Schlumberger Educational Services, Dowell Schlumberger, Houston, TX, 1990.
- Nemirovskii, A.S.: The regularization properties of the adjoint gradient method in ill-posed problems. *USSR Comput. Math. Phys.* 26:2 (1986), pp. 332–347.
- Neuman, S.P.: Stochastic continuum representation of fractured rock permeability as an alternative to the REV and fracture network concepts. In: E. Custodio, A. Gurgui and J.P. Lobo-Ferreira (eds): *NATO Advanced Workshop on Advances in Analytical and Numerical Groundwater Flow and Quality Modelling, NATO ASI Series, Series C: Mathematical and Physical Sciences*, Vol. 224. Reidel Publications, Dordrecht, The Netherlands, 1987, pp. 331–362.
- Nickolson, N.: *Geothermal fluids: Chemistry and exploration techniques*. Springer, Berlin, Germany, 1993.
- Nocedal, J. and Wright, S.J.: *Numerical optimization*. Springer, Berlin, Germany, 1999.
- Noel, N., Urmeneta, A., Fitzgerald, S. and Horne, R.N.: The role of capillary forces in the natural state of fractured geothermal reservoirs. *Proceedings 23rd Workshop on Geothermal Reservoir Engineering*, 26–28 January 1998, Stanford University, Stanford, CA, SGP-TR-158, 1998, pp. 100–109.
- Oil-Price.Net: <http://www.oil-price.net/> (accessed March 2010).

- Ortega, J.M., and Reinboldt, W.C.: *Iterative solution of nonlinear equations in several variables*. Academic Press, New York, NY, 1970.
- Pachepsky, Y., Benson, D. and Rawls, W.: Simulating scale dependent solute transport in soils with the fractional advection-dispersion equation. *Soil Sci. Soc. Am. J.* 64 (2002), pp. 1234–1243.
- Padrón, E., López, D.L., Magaña, M.I., Marrero, R. and Pérez, N.M.: Diffuse degassing and relation to structural flow paths at Ahuachapán geothermal field, El Salvador. *Geothermal Resources Council Transactions* 27, 2003, pp. 325–330.
- Pankow, J.F., Johnson, R.L., Hewetson, J.P. and Cherry, J.A.: An evaluation of contaminant migration patterns at two waste disposal sites on fractured porous media in terms of the equivalent porous medium (EPM) model. *J. Contaminant Hydrol.* 1 (1986), pp. 65–76.
- Passmore, M.J. and Archer, J.S.: Thermal properties of reservoir rocks and fluids. In: R.Y. Dawe and D. Wilson (eds): *Developments in petroleum engineering* 1. Elsevier, Amsterdam, The Netherlands, 1985, pp. 265–290.
- Peaceman, D. and Rachford, J.H.H.: The numerical solution of parabolic and elliptic differential equations. *J. Soc. Indust. Appl. Math.* 3 (1955), pp. 28–41.
- Pedersen, K.S. and Christensen, P.L.: *Phase behavior of petroleum reservoir fluids*. CRC Press/Taylor & Francis Group, Boca Raton, FL, 2006.
- Pinder, G.F. and Bredehoft, J.D.: Application of the digital computer for aquifer evaluation. *Water Resour. Res.* 4 (1968), pp. 1069–1093.
- Pinder, G.F. and Gray, W.G.: *Finite element simulation in surface and subsurface hydrology*. Academic Press, New York, NY, 1977.
- Piri, M.: *Pore-scale modelling of three-phase flow*. PhD Thesis, Centre for Petroleum Studies, Department of Earth Science and Engineering, Imperial College London, London, UK, 2003.
- Pita, C.R.: *Calculo vectorial*. Prentice—Hall Hispanoamericana, S.A., Mexico City, Mexico, 1995.
- Poeter E.P. and Hill, M.C.: Documentation of UCODE, a computer code for universal inverse modeling, U.S. Geological Survey, Water-Resources Investigations Report 98-4080, 1998.
- Pollock, D.W.: Semianalytical computation of path lines for finite difference models. *Ground Water* 26:6 (1988), pp. 743–750.
- Popov, Y.A., Berezin, V.V., Soloviev, G.A., Romushkevich, R.A., Korostelev, V.M., Kostyrin, A.A. and Kulikov, I.V.: Thermal conductivity of minerals. *Izvestia, Physics of the Solid Earth* 23:3 (1987), pp. 245–253.
- Popov, Y.A., Pribnow, D., Sass, J.H., Williams, C.F. and Burkhardt, H.: Characterisation of rock thermal conductivity by high-resolution optical scanning. *Geothermics* 28:2 (1999), pp. 253–276.
- Poronet: A tribute to Maurice A. Biot (1905–1985). PoroMechanics Internet Resources Network, <http://www.olemiss.edu/sciencenet/poronet/piobiot.html> (accessed July 2009).
- Porro, I., Wierenga, P.J. and Hills, R.G.: Solute transport through large uniform and layered soil columns. *Water Resour. Res.* 29 (1993), pp. 1321–1330.
- Portugal, E., Verma, M.P. Barragán, R.M. and Mañón, A.: Geoquímica isotópica de ^{13}C , D y ^{18}O de fluidos del sistema geotérmico Los Humeros, Puebla, (México). *Geofís. Int.* 33 (1994), pp. 607–618.
- Portugal, E., Birkle, P., Barragán, R.M., Arellano, V.M., Tello, E. and Tello, M.: Hydrochemical-isotopic and hydrogeological conceptual model of the Las Tres Vírgenes geothermal field, Baja California Sur, México. *J. Volcanol. Geotherm. Res.* 101 (2000), pp. 223–244.
- Powell, T. and Li, K.: A depletion mechanism for the behavior of noncondensable gases at The Geysers. *Geotherm. Resour. Council Trans.* 27, 2003, pp. 771–778.
- Pozrikidis, C.: *Boundary element methods*. Chapman & Hall/CRC Press, Boca Raton, FL, 2002.
- Pritchett, J.W.: STAR: A geothermal reservoir simulation system. *Proc. World Geothermal Congress*, Florence, Italy, 1995, pp. 2959–2963.
- Pritchett, J.W.: STAR user's manual, Version 9.0. Science Applications International Corp. Report SAIC-02/1055, San Diego, CA, 2002.
- Prickett, T.A., Naymik, T.G. and Lonquist, C.G.: A “random walk” solute transport model for selected groundwater quality evaluations. *Illinois State Water Survey Bull.* 65, Champaign, IL, 1981.
- Pruess, K.: TOUGH User's guide. Prepared for the Division of Waste Management—US Nuclear Regulatory Commission, NUREG/CR-4645, SAND86-7104, LBL-20700, UC-251, Lawrence Berkeley Laboratory, Berkeley, CA, 1987.
- Pruess, K.: SHAFT, MULKOM, TOUGH: A set of numerical simulators for multiphase fluid and heat flow. *Geothermia* 4:1 (1988), pp. 185–202.

- Pruess, K.: *TOUGH2—A general-purpose numerical simulator for multiphase fluid and heat flow*. LBL 29400, Lawrence Berkeley Laboratory, University of California, Berkeley, CA, 1991.
- Pruess, K. (ed): *TOUGH2—A general-purpose numerical simulator for multiphase fluid and heat flow*. Proceedings of the TOUGH Workshop '95, Lawrence Berkeley Laboratory, LBL-37200, UC-1240, Berkeley, CA, 1995.
- Pruess, K. (ed): *TOUGH2—A general-purpose numerical simulator for multiphase fluid and heat flow*. Proceedings of the TOUGH Workshop '98, Lawrence Berkeley National Laboratory, LBNL-41995, CONF-980559, Berkeley, CA, 1998.
- Pruess, K.: Numerical simulation of leakage from a geologic disposal reservoir for CO₂, with transitions between super- and sub-critical conditions. *Proceedings, TOUGH Symposium 2003*, Berkeley, CA. Lawrence Berkeley Natl. Lab., Berkeley, CA, 2003.
- Pruess, K. (ed): *Proceedings of TOUGH Symposium 2006*. Lawrence Berkeley National Laboratory, Berkeley, CA, 2006.
- Pruess, K. and Battistelli, A.: TMVOC, a numerical simulator for three-phase non-isothermal flows of multicomponent hydrocarbon mixtures in saturated-unsaturated heterogeneous media. Rep. LBNL-49375. Lawrence Berkeley Natl. Lab., Berkeley, CA, 2002.
- Pruess, K. and Narasimhan, T.N.: A practical method for modeling fluid and heat flow in fractured porous media. *Soc. Pet. Eng. J.* 25 (1985), pp. 14–26.
- Pruess, K. and O'Sullivan, M.: The effects of capillarity and vapor adsorption in the depletion of vapor-dominated reservoirs. *Proceedings Stanford Geothermal Workshop 17*, Stanford, CA, 1992.
- Pruess, K., Wang J.S.Y. and Tsang, Y.W.: On thermohydrologic conditions near high-level nuclear wastes emplaced in partially saturated fractured tuff: 1. Simulation studies with explicit consideration of fracture effects. *Water Resour. Res.* 26:6 (1990a), pp. 1235–1248.
- Pruess, K., Wang, J.S.Y. and Tsang, Y.W.: On thermohydrologic conditions near high-level nuclear wastes emplaced in partially saturated fractured tuff: 2. Effective continuum approximation. *Water Resour. Res.* 26:6 (1990b), pp. 1249–1261.
- Pruess, K., Oldenburg, C. and Moridis, G.: *TOUGH2 User's Guide, Version 2.0*. Report LBNL-43134, Lawrence Berkeley National Laboratory, Berkeley, CA, 1999.
- Raghavan, R.: *Well test analysis*. Prentice Hall, Englewood Cliffs, NJ, 1993.
- Ralph, J.: *Mindat.org mineral data base*. <http://www.mindat.org/>, 2003 (accessed April 2009).
- Ramey, H. Jr.: Wellbore heat transmission. *J. Petrol. Technol.* 225 (1962), pp. 427–435.
- Ramey, H. Jr., Brigham, W., Chen, H., Atkinson, P. and Arihara, N.: Thermodynamic and hydrodynamic properties of hydrothermal systems. *Proceedings of the NSF Conference on the Utilization of Volcano Energy*, 4–8 February 1974, Hilo, HI, 1974, pp. 509–587.
- Ratcliffe, E.H.: Thermal conductivities of fused and crystalline quartz. *Brit. J. Appl. Phys.* 10 (1959), pp. 22–25.
- Rausch, R., Schäfer, W., Therrien, R. and Wagner, C.: *Solute transport modelling: An introduction to models and solution strategies*. Borntraeger-Science Publishers, Berlin, Stuttgart, Germany, 2005.
- Rayleigh, J.W.: *The theory of sound*. 2nd ed, Macmillan, London, UK, 1896.
- Reddell, D.L. and Sunada, D.K.: Numerical simulation of dispersion in groundwater aquifers. *Hydrology Paper 41*, Colorado State University, Fort Collins, CO, 1970, pp. 1–77.
- Reddy, J.N. and Gartling, D.K.: *The finite element method in heat transfer and fluid dynamics*. 2nd ed, CRC Press, Boca Raton, FL, 2001.
- Reed, J.E.: Chapter B3: Type curves for selected problems of flow to wells in confined aquifers (PDF), Book 3: Applications of hydraulics, US Geological Survey, 1980.
- Rehfeldt, K., Tompson, A., Hassan, A., Reimus, P. and Halford, K.: The role of dispersion in radionuclide transport—Data and modeling requirements. Stoller-Navarro Joint Venture, Las Vegas, NV, prepared for US Department of Energy under Contract No. DE-AC52-03NA99205, 2004, <http://www.osti.gov/bridge/servlets/purl/821405-4YpuJd/native/821405.pdf> (accessed August 2009).
- Repsold, H.: Well logging in groundwater development. *IAH International Contributions to Hydrogeology 9*, Hans Heise, Hannover, Germany, 1989.
- Rice, J.R. and Cleary, M.P.: Some basic stress diffusion solutions for fluid-saturated elastic porous media with compressible constituents. *Rev. Geophys.* 14 (1976), pp. 227–241.
- Richtmeyer, R.D. and Morton, K.W.: *Difference methods of initial-value problems*. J. Wiley & Sons, New York, NY, 1967.
- Ringrose, S., Vanderpost, C. and Matheson, W.: Evaluation of vegetative criteria for near-surface groundwater detection using multispectral mapping and GIS techniques in semi-arid Botswana. *Appl. Geogr.* 18:4 (1998), pp. 331–354.

- Ritz, W.: Über eine neue Methode zur Lösung gewisser Variationsprobleme der mathematischen Physik. *J. Reine Angew. Math.* 135 (1908), pp. 1–61.
- Roache, P.J.: *Computational fluid dynamics*. Hermosa Publishers, Albuquerque, NM, 1972.
- Robinson, B.A. and Tester, J.W.: Dispersed fluid flow in fractured reservoirs: An analysis of tracer-determined residence time distributions. *J. Geoph. Res.* 89:B12 (1984), pp. 10,374–10,384.
- Rutqvist, J. and Tsang, C.-F.: A study of caprock hydromechanical changes associated with CO₂ injection into a brine formation. *Environ. Geol.* 42 (2002), pp. 296–305.
- S. Arriaga, M.C. and Verduzco, F.S.: On the natural collapse of fractures in rocks with low fluid. *Int. J. Rock Mechanics Mining Sci.* 35:4/5 (1998), pp. 500–501.
- Sass, J.H.: The thermal conductivity of fifteen feldspar specimens. *J. Geophys. Res.* 70:16 (1965), pp. 4064–4065.
- Satik, C.: A measurement of steam–water relative permeability. In: *Proceedings of the 23rd Workshop on Geothermal Reservoir Engineering*, Stanford University, Stanford, CA, 1998, pp. 120–126.
- Sato, K.: *Accelerated perturbation boundary element model for flow problems in heterogeneous reservoirs*. PhD Thesis, Department of Petroleum Engineering, Stanford University, CA, 1992.
- Scheffer, F. and Schachtschabel, P.: *Lehrbuch der Bodenkunde*. Ferdinand Enke, Stuttgart, Germany, 1989.
- Scheidegger, A.E.: *The physics of flow through porous media*. 3rd ed, University of Toronto Press, Toronto, Canada, 1974.
- Schlumberger: Visual MODFLOW Pro 9.1 User's Manual, Schlumberger Water Service, Waterloo, Ontario, Canada, 2009a.
- Schlumberger: The oilfield glossary. An on-line information source, 2009b, <http://www.glossary.oilfield.slb.com/> (accessed August 2009).
- Schmidt, E. and Grigull, U.: *Properties of water and steam in SI-units, 0–800°C and 0–1000 bar*. 2nd ed, Springer, Berlin, Germany, 1979.
- Schulz, V., Kehrwald, D., Wiegmann, A. and Steiner, K.: Flow, heat conductivity, and gas diffusion in partly saturated microstructures. *NAFEMS Seminar: Simulation of Complex Flows (CFD), Niedernhausen/Wiesbaden*, 25–26 April 2005.
- Schwarze, H., Jaekel, U. and Vereecken, H.: Estimation of macrodispersion by different approximation methods for flow and transport in randomly heterogeneous media. *Transp. Porous Media* 43 (2001), pp. 265–287.
- Seiler, K.-P.: *Groundwater recharge from run-off, infiltration and percolation*. Springer, Berlin, Germany, 2007.
- Shaban, A., Khawlie, M., Abdallah, C. and Faour, G.: Geologic controls of submarine groundwater discharge: Application of remote sensing to north Lebanon. *Environ. Geol.* 47 (2004), pp. 512–522.
- Shook, G.M. and Forsmann, J.H.: Tracer interpretation using temporal moments on a spreadsheet. Idaho National Laboratory, Geothermal Technologies Program, INL/EXT-05-00400, prepared for the US Department of Energy Assistant Secretary for Energy Efficiency and Renewable Energy, Contract DE-AC07-05ID14517, Idaho Falls, ID, 2005.
- Singhal, B.B. and Gupta, R.P.: *Applied hydrogeology of fractured rocks*. Springer, Berlin, Germany, 1999.
- Smith, G.D.: *Numerical solution of partial differential equations: Finite difference methods*. 2nd ed, Clarendon Press, Oxford, UK, 1978.
- Smith, S.E., El-Shamy, I. and Monsef, H.A.: Locating regions of high probability for groundwater in the Wadi El-Arish Basin, Sinai, Egypt. *J. Afric. Earth Sci.* 25:2 (1997), pp. 253–262.
- Sobolev, S.L.: *Applications of functional analysis in mathematical physics*. Leningrad, Russia, English translation by the American Mathematical Society, Providence, Rhode Island, Princeton University Press, Princeton, NJ, 1950.
- Solomon, S., Quin, D., Manning, M., Marquis, M., Averyt, K., Tignor, M., Miller, H.L. and Chen, Z. (eds): *Climate Change 2007: The physical science basis*. Contribution of Working Group I to the 4th Assessment Report of the Intergovernmental Panel on Climate Change. Cambridge University Press, UK, 2007.
- Sonntag, R.E. and van Wylen, G.: *Introduction to thermodynamics classical & statistical*. 2nd edition, John Wiley & Sons, New Jersey, NJ, 1982.
- Sree Devi, P.D., Srinivasulu, S. and Kesava Raju, K.: Hydrogeomorphological and groundwater prospects of the Pageru river basin by using remote sensing data. *Environ. Geol.* 40 (2001), pp. 1088–1094.
- Stallman, R.W.: Chapter B1: Aquifer-test design, observation, and data analysis (PDF), Book 3: *Applications of hydraulics*. US Geological Survey, 1971.
- Stein, C., Stein, S. and Pelayo, A.: Heat flow and hydrothermal circulation. *Geophys. Monogr.* 91, American Geophysical Union, 1995, pp. 425–445.
- Strang, G. and Fix, J.: *An analysis of the finite element method*. Prentice Hall, Englewood Cliffs, NJ, 1973.

- Struckmeier, W. and Margat, J.: Hydrogeological maps, a guide and a standard legend. *IAH International Contributions to Hydrogeology* 17, Hans Heise, Hannover, Germany, 1995.
- Suárez, M.C.: Cálculo analítico de propiedades térmicas del agua pura I. *Geotermia* 1:1 (1985), pp. 74–77.
- Suárez, M.C.: Rock thermal conductivity at the caprock and initial conditions in two-phase volcanic hydrothermal systems. *Proceedings 18th Workshop on Geothermal Reservoir Engineering*, Stanford Geothermal Program, Stanford University, Stanford, CA, 1993.
- Suárez, M.C.: Modelo conceptual integrado del yacimiento geotérmico de Los Humeros, Puebla. Internal technical report No. YI-HU1295, Dpto. de Yacimientos, Subgerencia de Estudios, Comisión Federal de Energía CFE, Mexico City, Mexico, 1995.
- Suárez, M.C.: Deep geothermal systems in Mexico: An integral diversified resource for the energy of the future. *Transactions Geothermal Resources Council* 22, 1998, pp. 327–331.
- Suárez, M.C.: Flujo de fluidos no-isotermicos en reservorios fracturados con porosidad y permeabilidad multiples. PhD Thesis, National University of Mexico (UNAM), 2000a.
- Suárez, M.C.: Modelo volumétrico para la evaluación de reservorios geotérmicos con información incipiente. Technical report DEX-013/2000, Dpto. de Exploración, Comisión Federal de Energía CFE, Mexico City, Mexico, 2000b.
- Suárez, M.C.: Evaluación del potencial, biogénesis y características esenciales de los sistemas geotérmicos submarinos en México—Norte de la costa Mexicana del Océano Pacifico y Golfo de California. *Geotermia* 17:1 (2004), pp. 31–43.
- Suárez, M.C. and Mañón, A.M.: Injection of cold water and air into a two-phase volcanic hydrothermal system. *TOUGH Workshop—First International Symposium on Numerical Simulation of Multicomponent Systems*, preprints, Lawrence Berkeley Laboratory, Berkeley, CA, 1990.
- Suárez, M.C. and Samaniego, F.V.: Triple-porosity/permeability flow in faulted geothermal reservoirs: Two-dimensional effects. *Proceedings of the Second International Workshop on Multicomponent Systems, TOUGH'95*, 20–22 March 1995, Lawrence Berkeley Laboratory, Berkeley, CA, 1995, pp. 113–118.
- Suárez M.C. and Samaniego, F.: A practical solution for the radial-vertical heat conduction in geothermal wells. *Proceedings, 24th Workshop on Geothermal Reservoir Engineering*, Stanford University, Stanford, CA, 1999.
- Suárez, M.C. and Samaniego, F.: Evolution of helium and argon at a volcanic geothermal reservoir. *Proceedings of the 28th Workshop on Geothermal Reservoir Engineering*, Stanford University, Stanford, CA, 2003. pp. 1–8.
- Suárez, M.C. and Samaniego, F.: A preliminary evaluation of the convective energy escaping from submarine hydrothermal chimneys. *Proceedings, 30th Workshop on Geothermal Reservoir Engineering*, January 31–February 2, 2005, Stanford University, Stanford, CA, SGP-TR-176, 2005, pp. 1–8.
- Suárez, M.C. and Samaniego, F.: TOUGH and the boundary element method in the estimation of the natural state of geothermal submarine systems. *TOUGH Symposium Proceedings*, Vol. 1/1, Lawrence Berkeley National Laboratory, Berkeley, VA, 2006, pp. 1–6.
- Suárez, M.C. and Samaniego, F.: Geothermal brine invasion in oil reservoirs: A 3D generalization of the Buckley-Leverett model using non-linear finite elements. Stanford University Geothermal Program 32/1 (SGP-TR-183), Stanford, CA, 2007, pp. 233–239.
- Suárez, M.C. and Viggiano, J.L.: Recovery factors and unused energy in a fractured reservoir. In: Federation of Icelandic Industries (ed): *Proceedings International Conference on Industrial uses of Geothermal Energy*, Reykjavik, Iceland, 1992.
- Suárez, M.C., Pruess, K. and Lippmann, M.: Preliminary modeling studies on Los Azufres geothermal field. In: M. Ramirez and J.E. Mock (eds): *Proceedings Symposium in the Field of Geothermal Energy*. Agreement between US Department of Energy and the Comision Federal de Electricidad, Mexico, (1986–1989), San Diego, CA, 1989.
- Suárez, M.C., Tello, M.L., Del Rio, L. and Gutiérrez, H.: The long-term observed effect of air and water injection into a fractured hydrothermal system. *Proceedings 17th Workshop on Geothermal Reservoir Engineering*, Stanford Geothermal Program, Stanford University, Stanford, CA, 1992.
- Suárez, M.C., Cataldi, R. and Hodgson, S.: Stories from a Heated Earth. In: R. Cataldi, S. Hodgson and J. Lund (eds): *Our Geothermal Heritage*. Published by the Geothermal Resources Council and the International Geothermal Association, 1999.
- Suárez, M.C., Samaniego, F. and Pacheco, R.: Ingeniería del activo Bellota-Jujo. Unpublished report 2, Diseño de Explotación, PEMEX-Exploración-Producción, Comalcalco, Tab., Mexico, 2006.

- Suárez, M.C., Tsompanakis, Y. and Samaniego, F.: Geothermal manifestations and earthquakes in the Caldera of Santorini, Greece: An historical perspective. *Proceedings, 33rd Workshop on Geothermal Reservoir Engineering*, 28–30 January 2008, Stanford University, CA, SGP-TR-185, 2008, pp. 1–8.
- Suárez Arriaga, M.C.: Evaluación del sistema hidrotermal de Los Azufres, Michoacán: Parte I: Características y capacidad energética del sector Tejamaniles. Technical report No. IYAZ.28/91, Gerencia de Proyectos Geotermoeléctricos, Comisión Federal de Electricidad, Mexico City, Mexico, 1991.
- Suárez Arriaga, M.C.: Simulación numérica y evaluación de Maritaro, sector norte del Campo geotérmico de Los Azufres, Michoacán. Technical report No. OMM-AZ.02/97, Gerencia de Proyectos Geotermoeléctricos, Comisión Federal de Electricidad, Mexico City, Mexico, 1997.
- Suárez Arriaga, M.C.: The interfacial interaction problem in complex multiple porosity fractured reservoirs., *Seventh Granada Lectures, AIP Conference Proceedings*, volume 661, American Institute of Physics, New York, NY, 2003.
- Suárez Arriaga, M.C. and Samaniego, V., F.: A petrophysical parameters average and numerical simulation of simultaneous heat and mass flow in fractured reservoirs. Preprints of the International Symposium on Coupled Phenomena in Civil, Mining & Petroleum Engineering, 1–3 November 1999, Sanya, Hainan Island, People's Republic of China, 1999, pp. 11–20.
- Suárez Arriaga, M.C., Samaniego, F. and Bundschuh, J.: Geothermal water in oil reservoir: A new 2D model solved with Comsol. *Proceedings Comsol Conference*, 4–6 October 2007, Boston, MA, 2007, pp. 203–209.
- Suárez Arriaga, M.C., Tsompanakis, Y. and Samaniego, V., F.: Geothermal manifestations and earthquakes in the caldera of Santorini, Greece: An historical perspective. *Stanford Geothermal Program (SGP-TR-185)*, Vol. 33 No. 1, 1–7, January 2008, Stanford, CA, 2008.
- Suárez Arriaga, M.C., Samaniego, F. and Bundschuh, J.: Numerical modeling of the coupled flow of brine and oil in hydrocarbon reservoirs. In: M.C. Suárez-Arriaga, J. Bundschuh, and F.J. Dominguez-Mota (2008): Numerical modeling of coupled phenomena in science and engineering—Practical use and examples. In: J. Bundschuh and M.C. Suárez-Arriaga (series eds): *Multiphysics modeling, Volume 1*. Balkema/CRC Press/Francis & Taylor, The Netherlands, 2009, pp. 335–346.
- Suárez Bosché, N., Suárez Bosché, K. and Suárez Arriaga, M.C.: A submarine geothermal system in Mexico. *Proceedings of the World Geothermal Congress*, 28 May–10 June 2000, Kyushu-Tohoku, Japan, 2000, pp. 3889–3893.
- Suárez-Bosche, N.E., Suárez-Arriaga, M.C., Samaniego, F. and Delgado, V.: Fundamental characteristics of hydrothermal submarine systems and preliminary evaluation of its geothermal potential in Mexico. *Proceedings World Geothermal Congress 2005*, Antalya, Turkey, Paper Number: 1604.
- Sun, N.-Z.: *Inverse problems in groundwater modeling*. Kluwer Academic Publishers, Dordrecht, The Netherlands, 1994.
- Tangarajan, M.: *Regional groundwater modeling*. Capital Publishing Company, New Delhi, Kolkata, Bangalore, India, 2004.
- Teeuw, R.M.: Groundwater exploration using remote sensing and a low-cost geographical information system. *Hydrogeology J* 3:3 (1995), pp. 21–30.
- Tello, E.: Características geoquímicas e isotópicas de los fluidos producidos por los pozos de Los Humeros, Puebla, México. In: *Geothermal Investigations with Isotope and Geochemical Techniques in Latin America*, IAEA-TECDOC-641, San José, Costa Rica. 1992, pp. 423–438.
- Tello, E.: Características geoquímicas de agua y gases de Los Humeros, Pue. I. Implicaciones de equilibrio. CFE Internal Report GQ-010-94, Morelia, Mich., Mexico, 1994.
- Terry, R.E.: *Manual for tracer test design and evaluation*. Univ. of Kansas, Seneca, KS, 1981.
- Terzaghi, K.: *Theoretical soil mechanics*. John Wiley, New York, NY, 1943.
- Thauvin, F. and Mohanty, K.: Modeling of non-Darcy flow through porous media. *SPE* 38017, 1997, pp. 313–314.
- Theis, C.V.: The relation between the lowering of the piezometric surface and the rate and duration of discharge of a well using ground-water storage. *Transactions, American Geophysical Union* 16, 1935, pp. 519–524.
- Tiedeman, C.R. and Hsieh, P.A.: Evaluation of longitudinal dispersivity estimates from simulated forced- and natural-gradient tracer tests in heterogeneous aquifers. *Water Resour. Res.* 40 (2004), W01512.
- Tikhonov, A.N., Goncharsky, A.V., Stepanov, V.V. and Yagola, A.G.: *Numerical methods for the solution of ill-posed problems*. Kluwer, Dordrecht, The Netherlands, 1995.

- Tikhonov, A.N.: Solution of incorrectly formulated problems and the regularization method. *Soviet Math. Dokl.* 4, pp. 1035–1038; English translation of *Dokl. Akad. Nauk SSSR* 151 (1963), pp. 501–504.
- Truesdell, A.H., Thompson, J.M., Coplen, T.B., Nehring, N.L. and Janik, C.J.: The origin of the Cerro Prieto geothermal brine. *Geothermics* 10:3/4 (1981), pp. 225–238.
- Truesdell, C. (ed): *Encyclopedia of physics: Fluid dynamics II*, Volume 8/part 2. Springer, Berlin, Germany, 1963.
- Turner, J.S.: *Buoyancy effects in fluids*. Cambridge University Press, Cambridge, UK, 1973.
- Turner, M.J., Clough, R.W., Martin, H.C. and Topp, L.C.: Stiffness and deflection analysis of complex structures. *J. Aero Sci.* 23 (1956), pp. 805–823.
- UNEP: Vital Water Graphics. United Nations Environmental Programme, UNEP, Nairobi, Kenya, <http://www.unep.org/dewa/assessments/ecosystems/water/vitalwater/> (accessed November 2000).
- UNFCCC: El Hoyo-Monte Galán geothermal project. United Nations Framework Convention of Climate Change, USIJI Uniform Reporting Document: Activities implemented jointly under the pilot phase. UNFCCC, Bonn, Germany, 1997, <http://www.unfccc.int/program/aij/aijact/nicusa01.html> (accessed May 2004).
- USGS: MODFLOW-2000: The US Geological Survey modular ground-water model user guide to the observation, sensitivity, and parameter estimation processes and three post-processing programs. USGS Open-File Report 00-184, Denver, CO, 2000.
- Van Genuchten, M.T.: A closed-form equation for predicting the hydraulic conductivity of unsaturated soils. *Soil Sci. Soc. Amer. J.* 44:5 (1980), pp. 892–898.
- Verma, M.P., Tello, E., Arellano, V. and Nieva, D.: Acidic fluid in Los Humeros geothermal reservoir. *Proceedings 23rd Workshop on Geothermal Reservoir Engineering*, Stanford University, Stanford, CA, 1998, pp. 234–239.
- Verruijt, A.: Elastic storage of aquifers. In: R. DeWiest (ed): *Flow through porous media*. Academic Press, New York, NY, 1969, pp. 331–376.
- Viggiano, J.C. and Gutiérrez-Negrín, L.C.A.: Análisis petrográficos estadísticos de núcleos en el campo geotérmico de Los Azufres, Mich. *Geotermia* 4:2 (1988), pp. 7–37.
- Voss, C.I.: SUTRA-Saturated unsaturated transport, a finite element simulation model for saturated-unsaturated, fluid-density-dependent groundwater flow with energy transport or chemically-reactive single-species solute transport. US Geological Survey Water-Resources Investigations Report 84-4369, Denver, CO, 1984.
- Voss, C.I. and Provost, A.M.: SUTRA—a model for saturated-unsaturated variable-density ground-water flow with solute or energy transport: US Geological Survey Water-Resources Investigations Report 02-4231, Denver, CO, 2002.
- Vougioukalakis, G.: *Santorini guide to the volcano*. Scientific advisors: M. Fytikas, P. Dalambakis and N. Kolios. Published by The Institute for the Study and Monitoring of the Santorini Volcano (I.S.M.O.S.A.V.), Thira, Greece, 2007.
- Vrba, J. and Zaporozec, A.: Guidebook on mapping groundwater vulnerability. *IAH International Contributions to Hydrogeology* 16, Hans Heise, Hannover, Germany, 1994.
- Wagner, W. and Pruss, A.: The IAPWS Formulation 1995 for the thermodynamic properties of ordinary water substance for general and scientific use. *J. Phys. Chem. Ref. Data* 31 (2002), pp. 387–535.
- Wagner, W. et al.: The IAPWS Industrial Formulation 1997 for the thermodynamic properties of water and steam. *ASME J. Eng. Gas Turbines and Power* 122 (2000), pp. 150–182.
- Walton, W.C.: *Aquifer test analysis with WindowsTM software*. Taylor & Francis, London, UK, 1996.
- Wang, H., Persaud, N. and Zhou, X.: Specifying scale-dependent dispersivity in numerical solutions of the convection—dispersion equation. *Soil Sci. Soc. Am. J.* 70 (2006), pp. 1843–1850.
- Wang, H.F.: *Theory of linear poroelasticity—with applications to geomechanics and hydrogeology*. Princeton University Press, New Jersey, NJ, 2000.
- Warren, J.R. and Root, P.J.: The behavior of naturally fractured reservoirs. *Soc. of Petrol. Engin. J.* 3: 3 (1963), pp. 245–255.
- Watanabe, K.: *Release on the IAPWS Formulation 1995 for the thermodynamic properties of ordinary water substance for general and scientific use*. Fredericia, Denmark, 1996.
- Waterloo Hydrogeologic Inc.: *Visual MODFLOW v.3.1 User's Manual*, Waterloo, Canada, 2003.
- Weight, W.D. and Sonderegger, J.L.: *Manual of applied field hydrogeology*. McGraw-Hill, New York, NY, 2001.

A.1.4	Numerical examples of interpolation	410
A.1.4.1	Example 1	410
A.1.4.2	Example 2	411
A.1.5	The Lagrange interpolation polynomials	412
A.1.5.1	Example 1	414
A.1.5.2	Example 2	415
A.2	Interpolation in two and three dimensions	415
A.3	Elements of tensor analysis	416
A.3.1	Index notation for vectors and tensors	416
A.3.2	Differential operators in curvilinear coordinates	417
A.3.3	Tensorial notation for differential operators in cartesian coordinates	418
A.4	The integral theorem of Stokes	418
A.4.1	Riemann's theorem	419
A.4.2	Green's first identity	419
A.4.3	Green's second identity	420
A.4.4	The divergence theorem	420
A.4.5	The Dirac distribution	420
B:	Tabulated thermal conductivities	422
	Nomenclature	429
	References	439
	Book series page	479

Multiphysics Modeling

Series Editors: Jochen Bundschuh & Mario César Suárez Arriaga

ISSN:1877-0274

Publisher: CRC/Balkema, Taylor & Francis Group

1. Numerical Modeling of Coupled Phenomena in Science and Engineering

Editors: M.C. Suárez Arriaga, J. Bundschuh & F.J. Domínguez-Mota

2009

ISBN: 978-0-415-47628-7

2. Introduction to the Numerical Modeling of Groundwater and Geothermal Systems

Editors: J. Bundschuh & M.C. Suárez Arriaga

2010

ISBN: 978-0-415-40167-8

This book provides an introduction to the scientific fundamentals of groundwater and geothermal systems. In a simple and didactic manner the different water and energy problems existing in deformable porous rocks are explained as well as the corresponding theories and the mathematical and numerical tools that lead to modeling and solving them. This approach provides the reader with a thorough understanding of the basic physical laws of fluid flow in thermoporoelastic rocks, the partial differential equations representing these laws and the principal numerical methods, which allow finding approximate solutions of the corresponding mathematical models. The book also presents the form in which specific useful models can be generated and solved. The text is introductory in the sense that it explains basic themes of the systems mentioned in three areas: engineering, physics and mathematics. All the laws and equations introduced in this book are formulated carefully based on fundamental physical principles. This way, the reader will understand the key importance of mathematics applied to all the subjects. Simple models are emphasized and solved with numerous examples. For more sophisticated and advanced models the numerical techniques are described and developed carefully.

This book will serve as a synoptic compendium of the fundamentals of fluid, solute and heat transport, applicable to all types of subsurface systems, ranging from shallow aquifers down to deep geothermal reservoirs. The book will prove to be a useful textbook to senior undergraduate and graduate students, postgraduates, professional geologists, hydrogeologists and geophysicists, engineers, mathematicians and others working in the vital areas of groundwater and geothermal resources.

MULTIPHYSICS MODELING – VOLUME 2

ISSN 1877-0274

The book series addresses novel mathematical and numerical techniques with an interdisciplinary focus that cuts across all fields of science, engineering and technology. A unique collection of worked problems provides understanding of complicated coupled phenomena and processes, its forecasting and approaches to problem-solving for a diverse group of applications in physical, chemical, biological, geoscientific, medical and other fields. The series responds to the explosively growing interest in numerical modeling of coupled processes in general and its expansion to ever more sophisticated physics. Examples of topics in this series include natural resources exploration and exploitation (e.g. water resources and geothermal and petroleum reservoirs), natural disaster risk reduction (earthquakes, volcanic eruptions, tsunamis), evaluation and mitigation of human-induced phenomena as climate change, and optimization of engineering systems (e.g. construction design, manufacturing processes).

SERIES EDITORS

Jochen Bundschuh & Mario-César Suárez Arriaga



CRC Press
Taylor & Francis Group
an informa business
www.crcpress.com

6000 Broken Sound Parkway, NW
Suite 300, Boca Raton, FL 33487
Schipholweg 107C
2316 XC Leiden, NL
2 Park Square, Milton Park
Abingdon, Oxon OX14 4RN, UK



an **informa** business